

INSTITUTE OF PHYSICS
SERIES IN CONDENSED MATTER PHYSICS

THE MAGNETOCALORIC EFFECT AND ITS APPLICATIONS

A M TISHIN
Y I SPICHKIN

The Magnetocaloric Effect and its Applications

Series in Condensed Matter Physics

Series Editors: **J M D Coey, D R Tilley and D R Vij**

Other titles in the series

Field Theories in Condensed Matter Physics
Sumathi Rao (ed)

Nonlinear Dynamics and Chaos in Semiconductors
K Aoki

Permanent Magnetism
R Skomski and J M D Coey

Modern Magneto optics and Magneto optical Materials
A K Zvezdin and V A Kotov

Theory of Superconductivity
A S Alexandrov

Other titles of interest

Handbook of Superconducting Materials
D Cardwell and D Ginley (eds)

Superconductivity of Metals and Cuprates
J R Waldram

Superfluidity and Superconductivity
D R Tilley and J Tilley

Topics in the Theory of Solid Materials
J M Vail

Series in Condensed Matter Physics

The Magnetocaloric Effect and its Applications

A M Tishin

Physics Department,

M V Lomonosov Moscow State University, Moscow, Russia

and

Y I Spichkin

Advanced Magnetic Technologies and Consulting Ltd,

Moscow, Russia

IOP

Institute of Physics Publishing
Bristol and Philadelphia

© IOP Publishing Ltd 2003

All rights reserved. No part of this publication may be reproduced, stored in a retrieval system or transmitted in any form or by any means, electronic, mechanical, photocopying, recording or otherwise, without the prior permission of the publisher. Multiple copying is permitted in accordance with the terms of licences issued by the Copyright Licensing Agency under the terms of its agreement with Universities UK (UUK).

British Library Cataloguing-in-Publication Data

A catalogue record for this book is available from the British Library.

ISBN 0 7503 0922 9

Library of Congress Cataloging-in-Publication Data are available

Commissioning Editor: Tom Spicer

Production Editor: Simon Laurenson

Production Control: Sarah Plenty

Cover Design: Victoria Le Billon

Marketing: Nicola Newey and Verity Cooke

Published by Institute of Physics Publishing, wholly owned by The Institute of Physics, London

Institute of Physics Publishing, Dirac House, Temple Back, Bristol BS1 6BE, UK

US Office: Institute of Physics Publishing, The Public Ledger Building, Suite 929, 150 South Independence Mall West, Philadelphia, PA 19106, USA

Typeset by Academic + Technical, Bristol

Printed in the UK by MPG Books Ltd, Bodmin, Cornwall

Contents

Preface	ix
Acknowledgments	x
1 Introduction	1
2 Physics and models of magnetocaloric effect	4
2.1 General thermodynamic approach	4
2.2 Magnetocaloric effect in the frames of the theory of second-order phase transitions	9
2.3 Statistical and mean-field model of a magnetic material	10
2.4 Entropy, its change and magnetocaloric effect	14
2.5 MCE at the first-order transitions	28
2.6 MCE in ferrimagnetic and antiferromagnetic materials	32
2.7 MCE in the vicinity of magnetic phase transitions	36
2.8 MCE in inhomogeneous ferromagnets	42
2.9 MCE in superparamagnetic systems	44
2.10 Anisotropic and magnetoelastic contributions to the MCE	49
2.11 Heat capacity	52
2.12 MCE and elastocaloric effect	58
2.13 Adiabatic demagnetization	62
3 Methods of magnetocaloric properties investigation	69
3.1 Direct methods	69
3.1.1 Measurements in changing magnetic field	69
3.1.2 Measurements in static magnetic field	74
3.1.3 Thermoacoustic method	77
3.2 Indirect methods	81
3.2.1 Magnetization measurements	81
3.2.1.1 Isothermal magnetization measurements	81
3.2.1.2 Adiabatic magnetization measurements	84

3.2.2	Heat capacity measurements	86
3.2.2.1	Heat pulse calorimetry	90
3.2.3	Other methods	94
4	Magnetocaloric effect in 3d metals, alloys and compounds	96
4.1	Ferromagnetic 3d metals	96
4.2	Alloys and compounds	105
4.3	3d thin films	123
5	Magnetocaloric effect in oxides	126
5.1	Garnets	126
5.1.1	Rare earth iron garnets	126
5.1.2	Rare earth gallium and aluminium garnets	131
5.2	Perovskites	137
5.2.1	Rare earth orthoaluminates	137
5.2.2	Other RMeO ₃ perovskites	142
5.2.3	Manganites and related compounds	143
5.3	3d oxide compounds	168
5.4	RXO ₄ compounds	175
6	Magnetocaloric effect in intermetallic compounds	179
6.1	Rare earth–nonmagnetic element compounds	179
6.1.1	Rare earth–aluminium compounds	179
6.1.2	Rare earth–Cu, Zn, Ga, Rh, Pd, Ag, In	193
6.2	Rare earth–nickel	200
6.3	Rare earth–iron	211
6.3.1	RFe ₂ , RFe ₃ and R ₂ Fe ₁₇ compounds	211
6.3.2	LaFe ₁₃ compounds	220
6.3.3	Other rare earth–iron compounds	225
6.4	Rare earth–cobalt	225
6.5	Rare earth–manganese	244
7	Magnetocaloric effect in rare earth–metalloid compounds	247
7.1	Compounds with Sb and As	247
7.2	Silicides and germanides	250
7.2.1	Ternary compounds of rare earths with Si and Ge	250
7.2.2	Magnetocaloric effect in R ₅ (Si–Ge) ₄ alloys	258
8	Magnetocaloric effect in rare earth metals and alloys	276
8.1	Rare earth metals	277

8.1.1	Gadolinium	277
8.1.2	Terbium	284
8.1.3	Dysprosium	294
8.1.4	Holmium	302
8.1.5	Erbium	303
8.1.6	Thulium	306
8.1.7	Neodimium	308
8.1.8	Theoretically available MCE in heavy rare earth metals	309
8.2	Rare earth alloys	316
8.2.1	Tb–Gd alloys	316
8.2.2	Gd–Dy, Gd–Ho and Gd–Er alloys	321
8.2.3	Dy–Y, Tb–Y, Er–La and Er–Pr alloys	322
8.2.4	Tb–Dy alloys	326
9	Magnetocaloric effect in amorphous materials	330
9.1	Amorphous alloys based on RE metals	330
9.2	Amorphous alloys based on transition metals	336
10	Magnetocaloric effect in the systems with superparamagnetic properties	338
10.1	Nanocomposite systems	338
10.2	Molecular cluster systems	343
11	Application of the magnetocaloric effect and magnetic materials in refrigeration apparatuses	351
11.1	Passive magnetic regenerators	351
11.1.1	Rare earth intermetallic compounds in passive regenerators	353
11.1.2	Rare earth metals and their alloys in passive regenerators	362
11.2	Magnetic refrigeration	365
11.2.1	General consideration	365
11.2.2	Active magnetic regenerator refrigerators	374
11.2.3	Magnetically augmented regenerators in gas refrigerators	387
11.2.4	Hybrid magnetic working bodies	389
11.2.5	Magnetic refrigerators working on the Ericsson cycle	391
11.2.6	Magnetic refrigerators working on the Carnot cycle	393
11.3	Working materials for magnetic refrigerators	401

12 Conclusion	418
Appendix 1 Units used in the book	422
Appendix 2 Magnetic, thermal and physical properties of some metals, alloys, compounds and other materials	428
References	440
Index	463

Preface

This book is devoted to one of the most exciting directions of investigation in the condensed matter physics field—the magnetocaloric effect (MCE) and possible applications of this phenomenon in refrigeration technology. For a long time the effect was used as a powerful tool for investigation of magnetic materials, especially in the area of magnetic phase transitions accompanying various spin structure transformations and in low temperature physics to obtain temperatures below 1 K. It is also convenient for theoretical simulation in the framework of various models.

Although the magnetocaloric effect, which displays itself in the changing of a magnetic material temperature under magnetization in adiabatic conditions, was discovered a long time ago, in recent years it has attracted the attention of investigators and the amount of papers in this direction increases practically exponentially. First of all this is related to practical application of the MCE and magnetic materials in refrigeration devices and, especially, in magnetic refrigerators, which work on magnetic refrigeration cycles instead of conventional vapour–gas cycles. Recently a series of acting magnetic refrigerator prototypes have been developed and created. The particular importance is that the created prototypes work at room temperature and have significant potential to be incorporated into the marketplace. Magnetic refrigerators are characterized by compactness, high effectiveness, low energy consumption and environmental safety. The further development of such devices is related to progress in permanent magnets, which can replace such cumbersome sources of magnetic fields requiring liquid helium superconducting magnets. It is expected that in the near future the energy product of permanent magnets will at least double. We suggest that the first commercially available models of magnetic refrigerators will appear rather sooner in spite of essential competition which they will have to withstand from existing vapour–gas refrigeration technology.

One of the most important parts of the magnetic refrigerator is its working body—a magnetic material—which should have high magnetocaloric properties, in particular, high MCE value. The working body in

many respects determines the characteristics of the whole refrigeration device. At the present time the energies of many scientific groups working in the field of MCE are directed on searching for the most effective magnetic working body. This is the field where the scientific interests of investigators intersect with practical applications. That is why this book considers in detail the physics of MCE and the experimental and theoretical results obtained to date in this field. We also believe that in future the MCE will find other, as yet unknown, applications.

It should be noted that, as far as we know, this book is the first one where the results of long-term investigations of the MCE and related quantities (such as heat capacity, thermal conductivity, etc) and also information on magnetic refrigerators, working principles and designs are summarized. We hope that this book will be useful for a wide circle of scientists and engineers working in the field of MCE and magnetic material investigations and magnetic refrigerator development. Unfortunately we were not able to present in the book all of the large amount of selected material and the increasing number of papers issued during the time that the book was in press.

**A M Tishin
Y I Spichkin**

Acknowledgments

The authors wish to thank all colleagues who work, and have worked, at the Physics Department of the M V Lomonosov Moscow State University who jointly conducted studies on magnetic and magnetothermal properties of rare earth metals, alloys and compounds for rather useful collaboration, and especially Professor K P Belova, who was influential at the beginning of the investigation of the magnetocaloric effect at Moscow State University, and Professor S A Nikitin, who was head of the group where the authors began their magnetocaloric studies. The authors would like to express their gratitude to Professors K A Gschneidner, Jr and V K Pecharsky for helpful discussions, which led to a more deeper understanding of some of the fundamental and applied aspects of the magnetocaloric effect. AMT also thanks Professor K A Gschneidner for much assistance in the collection of literature used in this book and for support of activity in this direction in recent years. The authors thank Dr A O Pecharsky for assistance with experimental investigations and calculation of some properties of magnetic materials discussed in this book. The authors also thank A S Chernishov, M I Ilyn and A S Mishenko for technical assistance during the preparation of illustrations for this book. YIS gratefully acknowledges Advanced Magnetic Technologies and Consulting Ltd for support of his work for recent years.

Chapter 1

Introduction

Investigation of magnetothermal phenomena in magnetic materials is of great importance for solving fundamental problems of magnetism and solid state physics, as well as for technological applications. These phenomena have a strong influence on such physical values as entropy, heat capacity and thermal conductivity, and reflects by itself transformations taking place in spin structure of a magnetic material. This book presents an attempt to give an overview of theoretical and experimental investigations and also technological applications of the phenomena made by the authors with more than 20 years' experience in this field.

The book is mainly devoted to the experimental results on the magnetocaloric effect (MCE) and influence of magnetic field on the entropy. MCE, discovered by Warburg in 1881 (Warburg 1881) in iron, displays itself in emitting or absorption of heat by a magnetic material under the action of a magnetic field. Under adiabatic conditions a magnetic field can cause cooling or heating of the material as a result of variation of its internal energy. It has to be noted that the term MCE can be considered more widely by its application not only to temperature variation of the material, but also to variation of the entropy of its magnetic subsystem under the effect of the magnetic field.

To illustrate the reasons for the MCE arising, let us consider a system of spins, which is paramagnetic or ferromagnetic near its magnetic ordering temperature. The entropy of such a system can be considered as a sum of two contributions—the entropy related to magnetic ordering and the entropy related to the temperature of the system. Application of a magnetic field will order the magnetic moments comprising the system, which are disordered by thermal agitation energy, and, consequently, the entropy depending on the magnetic ordering (the magnetic entropy) will be lowered. If a magnetic field is applied under adiabatic conditions when any heat exchange with the surroundings is absent, then the entropy related to the temperature should increase in order to preserve the total entropy of the system constant. Increasing of this entropy implies the system heating up, and an increase in its temperature. The opposite process—adiabatic

removal of the magnetic field (demagnetization)—will cause cooling of the magnetic system under consideration. The described temperature change is the manifestation of the MCE. A magnetic material can be roughly presented as consisting of magnetic, lattice and conduction electron subsystems, and these systems contribute to the total entropy of the material (see chapter 2 for details).

On the basis of MCE it is possible to create magnetic refrigerators—the machines where magnetic materials are used as working bodies instead of a gas, and magnetization/demagnetization is used instead of compression/expansion in conventional refrigerators. To realize any cooling process it is necessary to have a system in which entropy depends on temperature and some external parameter. In the case of a gas this parameter is pressure, and in the case of a magnetic material it is a magnetic field. Langevin (1905) was the first to demonstrate that the changing of a paramagnet magnetization causes in general a reversible temperature change. Debye (1926) and Giauque (1927) proposed to use reversible temperature change in paramagnetic salts to obtain low temperatures by adiabatic demagnetization. The first experiments to realize this idea were conducted by Giauque and MacDougall (1933), de Haas *et al* (1933a–c) and Kurti and Simon (1934). These experiments are considered more thoroughly in section 2.13.

The interest in investigation of MCE has increased in recent decades, on the one hand due to the possibility of obtaining information about the magnetic state and magnetic phase transformations in magnetic materials that is hard to obtain by other methods and, on the other hand, because of the prospects of the creation of magnetic cooling machines using magnetic materials as working bodies. Research work on MCE and related magneto-thermal properties in various magnetic materials, including 3d and 4f magnetic metals, and their alloys and compounds is carried out in many universities and research centres all over the world. The number of publications devoted to MCE is growing rapidly—in 1999 about 21 articles were published on this theme, in 2000 about 41, and in 2001 there were 91 publications. In 2002 about 10 works on MCE were issued every month. Since the beginning of the MCE investigations about 900 articles directly related to this theme have appeared. Recently Coey (2001), in his review devoted to the application of magnetic materials, noted cost-effective magnetic materials with a large magnetocaloric effect suitable for magnetic refrigerators among ten desirable new practical magnetic materials.

The scope of the book embraces materials with magnetic moments of either band or localized nature and various types of magnetic ordering—ferro-, antiferro- and ferrimagnetic and also more complex, such as helicoidal, magnetic structures. The character of MCE, magnetic entropy change and heat capacity behaviour in the materials is reviewed and discussed.

Chapter 2 of the book is devoted to the models and approaches, which are usually used for description of the MCE. Among them the thermodynamic

approach, Landau's theory of second-order phase transitions and mean field approximation are considered. In chapter 3 the reader can find information about various experimental apparatus and methods of the MCE measurement and determination, their errors and limitations. In chapters 4–10 the experimental and theoretical data about MCE in different classes of magnetic materials are regarded and discussed, among which one can mention 3d transition and rare earth metals, various alloys and compounds on their basis. The emphasis in these chapters is put on understanding the physical nature of the observed magnetocaloric phenomena and their relation with the processes in magnetic subsystems of the materials. A large amount of experimental material is reviewed, systematized and presented in figures and tables.

Chapter 11 is dedicated to the application of the MCE and magnetic materials in refrigeration devices, and also to the operational principles and design of such devices. Both passive (in regenerators of conventional gas cryocoolers) and active (in magnetic refrigerators) applications have been considered. This theme is the second, besides fundamental scientific interest, reason for high attention paid to the MCE investigations at the present time. Since the time of the first adiabatic demagnetization experiments, essential progress has been made in magnetic refrigeration in cryogenic as well as in room-temperature ranges. In May 2002 the Astronautics Corporation of America and Ames Laboratory demonstrated a room-temperature wheel-type magnetic refrigerator with gadolinium as a working body and a permanent magnet. The interest in magnetic refrigerators is related to their energy- and cost-saving potential, high efficiency and reliability. Such refrigerators do not need a compressor and can have a long lifetime because of low operational frequency and a minimum number of moving parts. The working bodies of magnetic refrigerators are solid magnetic materials with low toxicity, which can be easily utilized or recycled. Room-temperature magnetic refrigerators are also preferable from the environmental point of view—they do not use volatile liquid refrigerants which have a negative influence on the Earth's atmosphere. Magnetic refrigerators and cryocoolers can be used in various fields such as hydrogen liquefiers, high-speed computers and SQUIDs cooling, building air conditioning, cooling systems for vehicles, domestic and plant fridges etc. The recent achievements of the Astronautics Corporation of America and Ames Laboratory in magnetic refrigerator development and design show that an era of wide use of the magnetic cooling devices in life and industry is coming.

Various types of magnetic refrigerators and cryocooler designs for different temperature ranges are considered and discussed in chapter 11. The aspect of magnetic working materials, including complex magnetic bodies and principles of their development, are also regarded.

We hope that with the help of this book a reader will get a comprehensive overview of the physics of the magnetocaloric effect and other related magnetothermal phenomena, and their possible technological applications.

Chapter 2

Physics and models of magnetocaloric effect

In this chapter the main terms and conceptions about magnetocaloric effect (MCE) are introduced. The models and approaches usually used for description of MCE, such as thermodynamic and statistic approaches, mean field approximation and Landau's theory of second-order phase transitions, are considered. The main contributions to the MCE and the peculiarities of the MCE near second- and first-order magnetic transitions, in antiferromagnets, nonhomogeneous and superparamagnetic systems, are also regarded. Finally attention is paid to such related properties as heat capacity and elastocaloric effect.

2.1 General thermodynamic approach

For the description of magnetothermal effects in magnetic materials the following thermodynamic functions are used: the internal energy U , the free energy F and the Gibbs free energy G .

The internal energy U of the system can be represented as a function of the entropy S , the volume V and the magnetic field H (Swalin 1962, Bazarov 1964, Vonsovskii 1974):

$$U = U(S, V, H) \quad (2.1a)$$

or as a function of S , V and magnetic moment M :

$$U = U(S, V, M). \quad (2.1b)$$

Correspondingly, the total differential of U can have the forms

$$dU = T dS - p dV - M dH \quad (2.2a)$$

$$dU = T dS - p dV - H dM \quad (2.2b)$$

where p is the pressure and T is the absolute temperature.

The magnetic field H is usually used as an external parameter in the free energy F and Gibbs free energy G .

The free energy F , which is a function of T , V and H , is used for systems with constant volume and is defined as (Swalin 1962, Bazarov 1964, Vonsovskii 1974)

$$F = U - TS. \quad (2.3)$$

Its total differential has the form

$$dF = -S dT - p dV - M dH. \quad (2.4)$$

The Gibbs free energy G is a function of T , p and H and is used for systems under constant pressure (Swalin 1962, Bazarov 1964, Vonsovskii 1974):

$$G = U - TS + pV - MH \quad (2.5)$$

with the total differential

$$dG = V dp - S dT - M dH. \quad (2.6)$$

For the free energy F the internal parameters S , p and M (generalized thermodynamic quantities), conjugated to the external variables T , V and H , can be determined by the following equations of state (Swalin 1962, Bazarov 1964, Vonsovskii 1974):

$$S(T, H, V) = -\left(\frac{\partial F}{\partial T}\right)_{H,V} \quad (2.7a)$$

$$M(T, H, V) = -\left(\frac{\partial F}{\partial H}\right)_{V,T} \quad (2.7b)$$

$$p(T, V, H) = -\left(\frac{\partial F}{\partial V}\right)_{H,T}. \quad (2.7c)$$

Analogously, for the Gibbs free energy we have the following equations (Swalin 1962, Bazarov 1964, Vonsovskii 1974):

$$S(T, H, p) = -\left(\frac{\partial G}{\partial T}\right)_{H,p} \quad (2.8a)$$

$$M(T, H, p) = -\left(\frac{\partial G}{\partial H}\right)_{T,p} \quad (2.8b)$$

$$V(T, H, p) = \left(\frac{\partial G}{\partial p}\right)_{T,H}. \quad (2.8c)$$

If the magnetic moment M is chosen in G as an external variable instead of the magnetic field H , then

$$H = \left(\frac{\partial G}{\partial M}\right)_{T,p}. \quad (2.8d)$$

So-called Maxwell equations can be obtained from equations (2.8a) and (2.8b), equations (2.8a) and (2.8c), and equations (2.8a) and (2.8d) (Kittel 1958,

Swalin 1962, Bazarov 1964, Vonsovskii 1974):

$$\left(\frac{\partial S}{\partial H} \right)_{T,p} = \left(\frac{\partial M}{\partial T} \right)_{H,p} \quad (2.9a)$$

$$\left(\frac{\partial S}{\partial p} \right)_{T,H} = - \left(\frac{\partial V}{\partial T} \right)_{H,p} \quad (2.9b)$$

$$\left(\frac{\partial S}{\partial M} \right)_{T,p} = - \left(\frac{\partial H}{\partial T} \right)_{M,p}. \quad (2.9c)$$

The heat capacity C at constant parameter x is defined as (Swalin 1962, Bazarov 1964)

$$C_x = \left(\frac{\delta Q}{dT} \right)_x \quad (2.10)$$

where δQ is the heat quantity changing the system temperature on dT . Using the second law of thermodynamics (Swalin 1962, Bazarov 1964):

$$dS = \frac{\delta Q}{T} \quad (2.11)$$

and the heat capacity can be represented as

$$C_x = T \left(\frac{\partial S}{\partial T} \right)_x. \quad (2.12)$$

The bulk thermal expansion coefficient $\alpha_T(T, H, p)$ can be defined as (Swalin 1962, Bazarov 1964)

$$\alpha_T(T, H, p) = \frac{1}{V} \left(\frac{\partial V}{\partial T} \right)_{H,p} \quad (2.13a)$$

or, using equation (2.9b),

$$\alpha_T(T, H, p) = - \frac{1}{V} \left(\frac{\partial S}{\partial p} \right)_{T,H}. \quad (2.13b)$$

The total differential of the total entropy of the magnetic system expressed as a function of T , H and p can be written as

$$dS = \left(\frac{\partial S}{\partial T} \right)_{H,p} dT + \left(\frac{\partial S}{\partial H} \right)_{T,p} dH + \left(\frac{\partial S}{\partial p} \right)_{T,H} dp. \quad (2.14)$$

Using equations (2.9a), (2.12), (2.13b) and (2.14), one can obtain for an adiabatic process ($dS = 0$) the following equation:

$$\frac{C_{H,p}}{T} dT + \left(\frac{\partial M}{\partial T} \right)_{H,p} dH - \alpha_T V dp = 0 \quad (2.15)$$

where $C_{H,p}$ is the heat capacity under constant magnetic field and pressure.

Under an adiabatic-isobaric process ($dp = 0$, this process is usually realized in magnetocaloric experiments) the temperature change due to the change of the magnetic field (the magnetocaloric effect) can be obtained from equation (2.15) as

$$dT = -\frac{T}{C_{H,p}} \left(\frac{\partial M}{\partial T} \right)_{H,p} dH. \quad (2.16)$$

For an adiabatic-isochoric process ($dV = 0$) the total differential of $V(T, H, p)$ has the form

$$dV = \alpha_T V dT + \left(\frac{\partial V}{\partial H} \right)_{T,p} dH - V \kappa^{-1} dp \quad (2.17)$$

where κ is the bulk elastic modulus:

$$\frac{1}{\kappa} = -\frac{1}{V} \left(\frac{\partial V}{\partial p} \right)_{T,H}. \quad (2.18)$$

The equation for an adiabatic-isochoric process can be derived from equations (2.15) and (2.17):

$$\left\{ \frac{C_{H,p}}{T} - \alpha_T^2 \kappa V \right\} dT + \left[\left(\frac{\partial M}{\partial T} \right)_{H,p} - \alpha_T \kappa \left(\frac{\partial V}{\partial H} \right)_{T,p} \right] dH = 0. \quad (2.19)$$

Because the second term in the brackets is small and can be neglected (Kuz'min and Tishin 1992), the equation for the magnetocaloric effect has the form

$$dT = -\frac{T}{C_{H,p}} \left[\left(\frac{\partial M}{\partial T} \right)_{H,p} - \alpha_T \kappa \left(\frac{\partial V}{\partial H} \right)_{T,p} \right] dH \quad (2.20)$$

where the second term is due to the internal magnetostriction tensions arising from the change in magnetic state of the system keeping the volume constant.

Using equation (2.14), the general expression for the magnetocaloric effect dT arising in a magnetic material under isobaric conditions and adiabatic magnetization by a field dH can be obtained:

$$\frac{dT}{dH} = -\frac{(\partial S / \partial H)_{T,p}}{(\partial S / \partial T)_{H,p}}. \quad (2.21)$$

The total differential of the total entropy considered as a function of T , M and p can be written as

$$dS = \left(\frac{\partial S}{\partial T} \right)_{M,p} dT + \left(\frac{\partial S}{\partial M} \right)_{T,p} dM + \left(\frac{\partial S}{\partial p} \right)_{T,M} dp. \quad (2.22)$$

From equations (2.9c), (2.12) and (2.22) one can obtain the expression for the magnetocaloric effect caused by an adiabatic-isobaric change of

magnetization:

$$dT = \frac{T}{C_{M,p}} \left(\frac{\partial H}{\partial T} \right)_{M,p} dM. \quad (2.23)$$

By integration of equations (2.16) or (2.23) the finite temperature change $\Delta T = T_2 - T_1$ (here T_2 and T_1 are the final and the initial temperatures, respectively) under adiabatic magnetization can be calculated.

From equation (2.22) one can derive a general equation connecting dT and dM at isobaric conditions, analogous to equation (2.21):

$$\frac{dT}{dH} = - \frac{(\partial S / \partial M)_{T,p}}{(\partial S / \partial T)_{M,p}}. \quad (2.24)$$

In this section we consider general thermodynamic equations in which no assumptions were made on the system structure and microscopic interactions inside the system. To obtain more concrete magnetocaloric properties of the system one should know the form of its thermodynamic functions F or G , which requires some model assumptions.

F and G can be established using nonequilibrium thermodynamic potential $\Phi(T, H, M, p, V)$, in which the internal parameters M and V or p are regarded as independent variables. To obtain the equilibrium Gibbs free energy G or equilibrium free energy F one should minimize Φ with respect to M and V or M and p :

$$G(T, H, p) = \min_{M,V} \Phi(T, H, M, p, V) \quad (2.25a)$$

$$F(T, H, V) = \min_{M,p} \Phi(T, H, M, p, V). \quad (2.25b)$$

Then, with the help of the thermodynamic equations (2.7) and (2.8), the equilibrium internal parameters of a system can be obtained. The form of the nonequilibrium potential Φ can be determined by symmetry and/or microscopic consideration.

The general equations (2.16) and (2.23) describing the MCE take into account contributions corresponding to various processes occurring under magnetization, including contributions from paraprocesses and magneto-crystalline anisotropy. However, they are usually used for description of the MCE in the region of the paraprocess, which is characterized by a simple relation between M and H . By paraprocess we mean the magnetization in the field region, where the processes of domain wall displacement and magnetization vector rotation are completed and the field acts against thermal agitation and exchange interactions (in antiferromagnetic and ferrimagnetic materials) aligning the magnetic moments along its direction.

At the same time it is necessary to note that along with the above-mentioned contributions the following processes, which could impact on the resulting MCE value, should also be taken into account: the contribution

from magnetoelastic energy change, the contribution related to destruction of the magnetic metastable states, the contribution from nonreversible processes etc. There is also some contribution from domain processes, but it is usually negligible. Different kinds of metastable processes, which could arise during first-order phase transitions, especially simultaneous magnetic and crystal structure transformation processes, have a significant influence on magnetocaloric behaviour in the corresponding temperature range.

In this section we consider the magnetocaloric effect in relation to a reversible process of magnetization. Nonreversible magnetothermal effects are caused by such magnetization processes as displacement of domain walls and nonreversible rotation of the saturation magnetization, or to first-order magnetic phase transitions. These effects are characterized by a hysteresis in the magnetization cycle. The net magnetic work applied on the magnetic material in this case, proportional to $\oint H dM$, is dissipated as a heat which leads to the additional rise in temperature. One more source of additional heating is the Foucault (eddy) currents, which are induced in metals during application of the magnetic field. Tishin (1988) estimated that the currents can give a remarkable contribution (of about 0.1–0.3 K for rapid change of the field from 0 to 60 kOe) only in the low-temperature region. The nonreversible effects can decrease the sample cooling under adiabatic demagnetization.

2.2 Magnetocaloric effect in the frames of the theory of second-order phase transitions

Belov (1961a) adopted the Landau theory of second-order phase transitions (Landau and Lifshitz 1958) to the second-order magnetic phase transitions. In particular, such a transition takes place in a ferromagnet at the Curie point T_C . According to Belov's theory, near the Curie point the potential Φ of a ferromagnet can be expanded in a power series of an order parameter, the latter becoming zero at the Curie point. In magnetic systems the order parameter is the magnetization and, for a single domain, isotropic ferromagnet. In the absence of a magnetic field, the expansion takes the form

$$\Phi = \Phi_0 + \frac{\alpha}{2} I^2 + \frac{\beta}{4} I^4 + \dots \quad (2.26)$$

where Φ_0 is the part of the potential not connected with the magnetization, I is the magnetization ($I = M/V$), and α and β are thermodynamic coefficients.

In the vicinity of the Curie point, where α becomes zero, it can be presented as

$$\alpha = \alpha_\Theta(T - T_C) + \dots \quad (2.27)$$

The coefficient α is positive above T_C and negative below T_C . Near T_C , β is not dependent on T : $\beta = \beta(T_C)$. From the condition of potential Φ minimum ($\partial\Phi/\partial I = 0$) we can obtain the equilibrium value of spontaneous magnetization I_s :

$$I_s^2 = -\frac{\alpha}{\beta} = -\frac{\alpha_\Theta(T - T_C)}{\beta}. \quad (2.28)$$

Substituting I_s into equation (2.26) we obtain the equilibrium value of the thermodynamic potential Φ .

Taking into account the magnetoelastic interaction, we can write down the potential Φ for a ferromagnet in a magnetic field H :

$$\Phi = \Phi_0 + \frac{\alpha}{2}I^2 + \frac{\beta}{4}I^4 + \frac{1}{2}\gamma I^2 p - HI. \quad (2.29)$$

Minimization of equation (2.29) with respect to I gives the equation describing the magnetization near the Curie point (Belov 1961a):

$$(\alpha + \gamma p)I + \beta I^3 = H. \quad (2.30)$$

Coefficient γ describes the magnetoelastic interaction and is related to the Curie temperature displacement under pressure by (following from the condition $(\alpha + \gamma p) = 0$ at T_C)

$$\frac{\Delta T_C}{\Delta p} = -\frac{\gamma}{\alpha_\Theta}. \quad (2.31)$$

Using equation (2.30) we can calculate the derivative $(\partial H/\partial T)_I$ and substitute it into equation (2.23), which gives the value of the MCE near the Curie temperature:

$$dT = \frac{1}{2} \frac{\alpha_\Theta T}{C_{M,p}} dI^2. \quad (2.32a)$$

As can be seen from equation (2.32), the temperature change due to the change of magnetization is proportional to the squared magnetization: $\Delta T = k\Delta I^2$, where k is a coefficient of proportionality. Using this result and equation (2.30), one can obtain an equation describing the MCE field dependence near the Curie temperature in a ferromagnet (Belov 1961a):

$$\frac{\alpha + \gamma p}{k^{1/2}} + \frac{\beta}{k^{3/2}} \Delta T = \frac{H}{\Delta T^{1/2}}. \quad (2.32b)$$

2.3 Statistical and mean-field model of a magnetic material

The statistical sum (or partition function) of a system can be determined as (Smart 1966, Kittel 1958, 1969)

$$Z = \sum_n \exp[-E_n/(k_B T)] = Sp(\exp[-\hat{H}/(k_B T)])$$

where \hat{H} is the Hamiltonian of the system, E_n are its eigenvalues and k_B is the Boltzmann constant. Knowing Z , one can calculate free energy of the system (Smart 1966, Kittel 1958, 1969):

$$F = -k_B T \ln Z \quad (2.33)$$

and, using equations (2.7), the internal parameters of the system.

If the magnetic system is a paramagnet, the Hamiltonian for one atom has the form

$$\hat{H} = -\hat{M}_J \vec{H} \quad (2.34)$$

where \vec{H} is the vector of magnetic field, $\hat{M}_J = g_J \mu_B \hat{\mathbf{J}}$ —the atom magnetic moment operator. The partition function for one atom in this case has the form

$$Z_J(x) = \sum_{m=-J}^J \exp \left[\frac{mx}{J} \right] \quad (2.35a)$$

where x is determined as

$$x = \frac{M_J H}{k_B T} \quad (2.35b)$$

g_J is the g -factor of the atom, J is the total angular momentum quantum number, $m = J, J-1, \dots, -J$, and $M_J = g\mu_B J$ is the magnetic moment of an atom.

Summation of equation (2.35a) gives

$$Z_J(x) = \sinh \left(\frac{2J+1}{2J} x \right) / \sinh \left(\frac{1}{2J} x \right). \quad (2.36)$$

The magnetic free energy (the part of free energy related to the magnetic subsystem of a material) of the system, consisting of N magnetic atoms, has the form

$$F_M = -k_B T \ln(Z_J(x))^N. \quad (2.37)$$

Using this equation we can calculate the magnetic moment of the system by equation (2.7b):

$$M = NM_J B_J(x) \quad (2.38)$$

where $B_J(x)$ is the Brillouin function:

$$B_J(x) = \frac{2J+1}{2J} \coth \left(\frac{2J+1}{2J} x \right) - \frac{1}{2J} \coth \left(\frac{x}{2J} \right). \quad (2.39)$$

For $x \ll 1$ (this condition is characteristic for the high-temperature region and, in particular, is usually realized near the temperature of transition

from magnetically ordered to paramagnetic state) $B_J(x)$ can be expanded as

$$B_J(x) = \frac{J+1}{3J}x - \frac{((J+1)^2 + J^2)(J+1)}{90J^2}x^3 + \dots \quad (2.40)$$

This expansion of paramagnets leads to the Curie law:

$$M = \frac{C_J}{T}H \quad (2.41)$$

where $C_J = N\mu_B^2 g_J^2 J(J+1)/3k_B$ is the Curie constant.

From equation (2.16) one can obtain the MCE of a paramagnet:

$$dT = \frac{T}{2C_{H,p}C_J} \delta(M^2)_{T,p} \quad (2.42)$$

where $\delta(M^2)_{T,p} = (\partial M^2 / \partial H)_{T,p} dH$ is the isothermobaric variation of squared magnetization.

The Hamiltonian of an isotropic ferromagnet has the form

$$\hat{H} = - \sum_{i>j} I_{ij} (\hat{J}_i \hat{J}_j) - \sum_i \hat{M}_{i,j} \vec{H} \quad (2.43)$$

where I_{ij} is the exchange integral for the interaction between the i and j ions, and J_i is the total angular momentum operator of the ion. In the mean field approximation (MFA) equation (2.43) becomes

$$\hat{H} = - \sum_{i>j} I_{\text{ex}} z J (\hat{J}_j \vec{n}) - \sum_i \hat{M}_{i,j} \vec{H} \quad (2.44)$$

where z is the number of nearest-neighbour magnetic ions, J is the quantum number of the total angular momentum, \vec{n} is the unit vector determining the orientation of the total magnetic moment of the ion, and I_{ex} is the exchange integral (it is supposed in MFA that the exchange interaction for every pair of nearest neighbours has the same value I_{ex}). In MFA the exchange interaction is replaced by an effective exchange field H_m (molecular field):

$$H_m = wM \quad (2.45)$$

where w is the molecular field coefficient, related to the exchange integral. The molecular field is added to the external magnetic field so equation (2.35b) becomes

$$x = \frac{M_J(H + wM)}{k_B T}. \quad (2.46)$$

The field and temperature dependences of spontaneous magnetization M_s can be obtained by a simultaneous solution of equations (2.38) and (2.46).

For $T > T_C$ and $H = 0$ the equations have only one stable solution, $M_s = 0$. For the temperature below T_C a stable nonzero solution appears,

corresponding to the spontaneous magnetic moment:

$$M_s^2 = M_{s0}^2 \frac{10(J+1)^2}{3((J+1)^2 + J^2)} \left(1 - \frac{T}{T_C}\right) \quad (2.47)$$

where $M_{s0} = NM_J$ is the spontaneous magnetic moment at $T = 0$ K.

In the paramagnetic region, where $x \ll 1$, only the first term in equation (2.40) may be taken into account and the magnetization equation takes the form of the Curie–Weiss law:

$$M = \frac{C_J H}{T - T_C} \quad (2.48)$$

where the Curie temperature T_C can be expressed as

$$T_C = \frac{NM_{\text{eff}}^2 w}{3k_B} = \frac{2(J+1)}{3Jk_B} z I_{\text{ex}} \quad (2.49)$$

where $M_{\text{eff}} = g_J(J(J+1))^{1/2} \mu_B$ is the effective magnetic moment of an atom. Using equation (2.16), one can obtain for the MCE of a ferromagnet in the paramagnetic region ($T > T_C$) the equation which has the same form as equation (2.42).

For a ferromagnet at $T < T_C$ and in a nonzero magnetic field, a somewhat more complicated analysis than that yielded to equation (2.42) gives (Kuz'min and Tishin 1992)

$$dT = \frac{T_C}{2C_{H,p}C_J} \delta(M^2)_{T,p}. \quad (2.50)$$

Above, the quantum mechanical consideration of the magnetic system was made. In the classical case a magnetic material is regarded as consisting of particles with a magnetic moment μ , which can have an arbitrary orientation in space. The magnetic moment of such a system is given by the formula (Smart 1966)

$$M = N\mu L(x) \quad (2.51)$$

where

$$L(x) = \coth x - \frac{1}{x} \quad (2.52)$$

is the Langevin function,

$$x = \frac{\mu H}{k_B T} \quad (2.53)$$

for paramagnets, and

$$x = \frac{\mu(H + wM)}{k_B T} \quad (2.54)$$

for ferromagnets.

For $x \ll 1$, $L(x)$ can be expanded as

$$L(x) = \frac{x}{3} - \frac{x^3}{45} - \dots \quad (2.55)$$

Equations (2.41), (2.42), (2.48) and (2.50) in this case are valid with the Curie constant

$$C_J = \frac{N\mu^2}{3k_B} \quad (2.56)$$

and the Curie temperature

$$T_C = \frac{N\mu^2 w}{3k_B}. \quad (2.57)$$

2.4 Entropy, its change and magnetocaloric effect

Important characteristics of a magnetic material are its total entropy S and the entropy of its magnetic subsystem S_M (magnetic entropy). Entropy can be changed by variation of the magnetic field, temperature and other thermodynamic parameters. The magnetic entropy and its change are closely related to the MCE value and the magnetic contribution to the heat capacity. The magnetic entropy change is also used to determine the characteristics of magnetic refrigerators, such as the refrigerant capacity and some others (see section 11).

The total entropy of a magnetic material can in general, at constant pressure, be presented as (Tishin 1990a)

$$S(H, T) = S_M(H, T) + S_l(H, T) + S_e(H, T) \quad (2.58)$$

where S_M is the magnetic entropy, S_l is the lattice and S_e is the electron contributions to the total entropy. This formula is correct for rare earth magnetic materials, but in the case of 3d transition materials, where magnetic 3d-electrons have an itinerant nature, their contribution to the conductivity is comparable with p- and s-electron contributions. Separation of the lattice entropy in this case is possible only if electron–phonon interaction is not taken into account.

In general, all three contributions depend on temperature and magnetic field and cannot be clearly separated. The situation is especially difficult in the case of the low-temperature region, where the value of electronic heat capacity coefficient, a_e , can change a few times under the influence of a magnetic field or in the case of coexisting magnetic, structure and electronic phase transitions. For example, in materials with high values of a_e , such as Sc (Ikeda *et al* 1982), CeB₆ and CeCu₂Si₂ (Grewe and Steglich 1991), and UBe₁₃ (Stewart 1984), below about 10 K the electronic entropy and electronic heat

capacity exhibit strong nonlinear dependences on both temperature and magnetic field. However, in the first approximation we can believe that lattice and electronic parts of entropy depend only on temperature, and all contributions depending on magnetic field (from any changes of magnetic subsystem) are presented in total value of entropy in equation (2.58) by $S_M(H, T)$.

The lattice entropy can be represented by the Debye interpolation formula (Gopal 1966):

$$S_l = n_a R \left[-3 \ln(1 - e^{T_D/T}) + 12 \left(\frac{T}{T_D} \right)^3 \int_0^{T_D/T} \frac{x^3 dx}{e^x - 1} \right] \quad (2.59)$$

where R is the gas constant, T_D is the Debye temperature and n_a is the number of atoms per molecule in a substance. As follows from equation (2.59), S_l decreases when T_D increases.

The electron entropy can be obtained by the standard relation

$$S_e = a_e T \quad (2.60)$$

where a_e is the electronic heat capacity coefficient.

Using equation (2.58) and (2.12), one can represent the total heat capacity of a magnetic material in the form

$$C_H = C'_H + C_l + C_e \quad (2.61)$$

where C'_H , C_l and C_e are the magnetic, lattice and electron contributions, respectively.

The heat capacity of a magnetic subsystem (magnetic heat capacity) $C'_H(T, H)$ can be defined using equation (2.12) as

$$C'_H(T, H) = T \left(\frac{\partial S_M(T, H)}{\partial T} \right)_H \quad (2.62)$$

where index H means that the heat capacity is calculated at constant magnetic field.

It should be noted that the contributions to the total heat capacity from the lattice and conduction electron subsystems act as an additional heat load, reducing the MCE (see equation (2.16)).

Using equations (2.37) and (2.7a), one can obtain the expression for the magnetic entropy S_M for a system consisting of N magnetic atoms with the quantum number of the total angular momentum of an atom J (Smart 1966):

$$S_M(T, H) = Nk_B \left[\ln \frac{\sinh \left(\frac{2J+1}{2J} x \right)}{\sinh \left(\frac{1}{2J} x \right)} - x B_J(x) \right]. \quad (2.63)$$

In the case of high temperature and low field ($x \ll 1$) the statistical sum in equation (2.37) can be expanded in a power series of x . This gives the following formula for S_M of a paramagnet (Vonsovskii 1974):

$$S_M(T, H) = Nk_B \left[\ln(2J + 1) - \frac{1}{2} \frac{C_J H^2}{T^2} \right] \quad (2.64)$$

where C_J is the Curie constant, and the formula for S_M of a ferromagnet above the Curie temperature is

$$S_M(T, H) = Nk_B \left[\ln(2J + 1) - \frac{1}{2} \frac{C_J H^2}{(T - T_C)^2} \right]. \quad (2.65)$$

The maximum magnetic entropy value is reached in a completely disordered state, which is realized, in particular, for conditions $T \rightarrow \infty$ and $H = 0$. According to equations (2.64) and (2.65), the maximum magnetic entropy value per mole of magnetic atoms with the quantum number of the total angular momentum of an atom J is equal to

$$S_M = N_A k_B \ln(2J + 1) \equiv R \ln(2J + 1) \quad (2.66)$$

where N_A is Avogadro's number. Consider the total entropy $S(H, T)$ change of a magnetic material caused by the change of magnetic field and temperature under isobaric condition. According to equations (2.58), (2.12) and our suggestion about the independence of S_l and S_e on a magnetic field, we can write the total differential of $S(H, T)$ as

$$dS(H, T) = \frac{C_l(T)}{T} dT + \frac{C_e(T)}{T} dT + \frac{C'_H(H, T)}{T} dT + \left(\frac{\partial S_M(H, T)}{\partial H} \right)_T dH. \quad (2.67)$$

The last two terms in equation (2.67) represent the total differential of the magnetic entropy S_M :

$$dS_M(H, T) = \frac{C'_H(H, T)}{T} dT + \left(\frac{\partial S_M(H, T)}{\partial H} \right)_T dH \quad (2.68)$$

or, using Maxwell equation (2.9a),

$$dS_M(H, T) = \frac{C'_H(H, T)}{T} dT + \left(\frac{\partial M(H, T)}{\partial T} \right)_T dH. \quad (2.68a)$$

As can be seen, dS_M consists of two parts, one related to the change of temperature (field constant part) and another due to the change of the magnetic field (isothermal part). To distinguish them let us denote the first part as dS_{MH} and the second as dS_{MT} .

The finite change of the total magnetic entropy under change of T on $\Delta T = T_2 - T_1$ (T_2 is the final and T_1 is the initial temperature of the sample) and H on $\Delta H = H_2 - H_1$ (H_2 is the final and H_1 is the initial

magnetic field) can be calculated as

$$\begin{aligned}\Delta S_{M\text{tot}}(H, T) &= S_M(H + \Delta H, T + \Delta T) - S_M(H, T) \\ &= \int_H^{H+\Delta H} \left(\frac{\partial M(H, T + \Delta T)}{\partial T} \right)_H dH + \int_T^{T+\Delta T} \frac{C'_H(H, T)}{T} dT.\end{aligned}\quad (2.69)$$

The finite isothermal magnetic entropy change under change of magnetic field (the first integral in equation (2.69)) $\Delta H = H_2 - H_1$ can be calculated from the Maxwell relation (2.9a) on the basis of magnetization data and can be defined as

$$\begin{aligned}\Delta S_{MT}(H, T) &= S_M(H_1, T) - S_M(H_2, T) = \int_{H_1}^{H_2} \left(\frac{\partial S_M(H, T)}{\partial H} \right)_T dH \\ &= \int_{H_1}^{H_2} \left(\frac{\partial M(H, T)}{\partial T} \right)_H dH = S(H_2, T) - S(H_1, T) \\ &= \Delta S(H, T).\end{aligned}\quad (2.70)$$

It should be noted that ΔS_{MT} is equal to the finite isothermal change of the total entropy ΔS . This is valid if S_l and S_e do not depend on H (this suggestion was made earlier).

The second integral in equation (2.69) represents the finite isofield change of the magnetic entropy ΔS_{MH} . The contributions ΔS_{MT} and ΔS_{MH} are illustrated by figure 2.1, where the characteristic temperature dependences of the magnetic entropy S_M at the magnetic field $H_1 = 0$ and $H_2 > 0$ for a ferromagnetic material under isobaric–adiabatic magnetization process are schematically shown. As is known, the magnetic entropy of ferromagnets or paramagnets decreases in the magnetic field, so $S_M(T)$ dependence at $H \neq 0$ in figure 2.1 lies below $S_M(T)$ dependence at $H = 0$. The total entropy change in this process is equal to zero ($S(T, H) = \text{const}$) and the initial temperature of the material T varies due to the magnetocaloric effect by the value ΔT .

The result of the process can be imagined as a sum of two sequential processes of entropy change: isothermal $T = \text{const}$ change of magnetic field $H_1 \rightarrow H_1 + \Delta H = H_2$ (process 1 → 2 in figure 2.1, corresponding to the isothermal entropy change ΔS_{MT}) and temperature change ($T \rightarrow T + \Delta T$) under the constant magnetic field $H = \text{const}$ (process 2 → 3 in figure 2.1, corresponding to the isofield entropy change ΔS_{MH}). Here ΔT is a finite value of the magnetocaloric effect caused by the finite field change $\Delta H = H_2 - H_1$. Both the isothermal and the isofield parts contribute to a total change of magnetic entropy under adiabatic magnetization (or demagnetization). The increase of the isofield contribution $\Delta S_{MH}(T, H)$ leads to a reduction of the total value of $\Delta S_{M\text{tot}}(T, H)$ and to an increase of

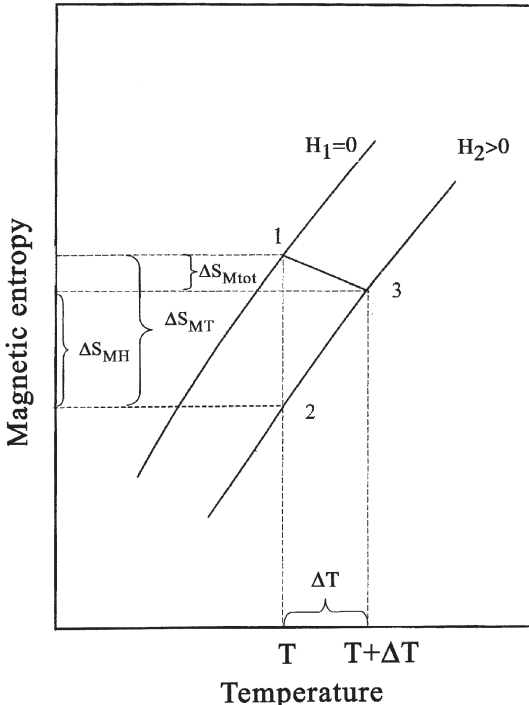


Figure 2.1. Temperature dependences of the magnetic entropy S_M at two different fields H_1 and H_2 ($H_2 > H_1$) in a ferromagnetic material.

the value of magnetocaloric effect (large distance between points 2 and 3). In this case a total adiabatic change of magnetic entropy, $\Delta S_{M\text{tot}}(T, H)$, and isothermal change of magnetic entropy, $\Delta S_{MT}(T, H)$, may differ significantly (see Figure 2.1) and cannot be assumed to be equal. Values of $\Delta S_{M\text{tot}}$ and ΔS_{MT} may be close to each other only at small values of C'_H/T (i.e. small values of magnetic contribution, C'_H , to the total value of heat capacity and/or high temperatures) and/or small value of ΔT (when points 2 and 3 are close; see Figure 2.1). The value of the MCE (the distance between points 2 and 3 on the T axis) is determined by the value of ΔS_{MH} and the value of ΔS_{MT} influence ΔT by displacing the initial $S_M(T)$ curve.

It should be noted above that we consider the equilibrium adiabatic process at which the temperature of electronic, lattice and magnetic subsystems vary simultaneously under magnetic field change and the temperature of the magnetic subsystem is permanently equal to the temperature of the lattice. In the room-temperature range the spin-lattice relaxation time in solids is about 10^{-12} s (Kittel 1969) and according to Ahiezer and Pomeranchuk

(1944) at 10^{-4} K this value is about 1 s. This can be described by the equation, following from equation (2.67),

$$\frac{C_l(T)}{T} dT + \frac{C_e(T)}{T} dT = - \left[\left(\frac{\partial S_M(T, H)}{\partial H} \right)_T dH + \frac{C'_H(T, H)}{T} dT \right]. \quad (2.71)$$

Usually the exact temperature of the lattice is measured in MCE experiments. However, in some special cases under nonequilibrium conditions (for example, due to the absence of possibility of energy exchange between magnetic and electronic and lattice subsystems) the temperatures of electronic and lattice subsystems may differ, which can lead to the hysteresis on the MCE field and temperature dependences.

From equation (2.71) one can obtain for the adiabatic–isobaric process the expression for the magnitude of MCE:

$$\begin{aligned} dT(T, H) &= - \frac{T}{C_H(T, H)} \left(\frac{\partial S_M(T, H)}{\partial H} \right)_T dH = - \frac{T}{C_H(T, H)} dS_{MT}(T, H) \\ &= - \frac{T}{C_H(T, H)} \left(\frac{\partial M(T, H)}{\partial T} \right)_H dH. \end{aligned} \quad (2.72)$$

From equation (2.72) it can be concluded that the value of dT is directly proportional to the isothermal change of S_M , which can be calculated by Maxwell relation (2.9a), and magnetic entropy change due to a temperature change affects the MCE indirectly through an additional term (C'_H) in the total heat capacity. However, the finite value of the MCE (ΔT) in the isobaric–adiabatic process is determined by isofield adiabatic change ΔS_{MH} —see Figure 2.1. To reach the maximum MCE value one should provide such conditions at which $\Delta S_{M\text{tot}}$ should be equal to zero—in this case $\Delta S_{MH} = \Delta S_{MT}$. Under such a ‘magnetic adiabatic’ condition the MCE has the value which, according to equation (2.68), can be calculated by the formula

$$\begin{aligned} dT(T, H) &= - \frac{T}{C'_H(T, H)} \left(\frac{\partial S_M(T, H)}{\partial H} \right)_T dH \\ &= - \frac{T}{C'_H(T, H)} \left(\frac{\partial M(T, H)}{\partial T} \right)_H dH. \end{aligned} \quad (2.73)$$

It should be noted that in equation (2.73) magnetic heat capacity C'_H is used instead of total heat capacity C_H , which includes lattice and electron contributions, in equation (2.72). Analogous conclusions can be made from the consideration of the case when $S(H_2, T)$ lies above $S(H_1, T)$ for $H_2 > H_1$, as takes place in antiferromagnets.

In literature devoted to the MCE, the value of isothermal magnetic entropy change ΔS_{MT} is usually determined and used in various calculations. Because of that, from now on we will omit index T in the symbol of magnetic

entropy change and will use just ΔS_M or dS_M , keeping in mind that this is isothermal magnetic entropy change, unless specially stated.

The infinitesimal change of magnetic entropy dS_M can be written down as

$$dS_M = \frac{C_H}{T} dT. \quad (2.74)$$

Integrating equations (2.74) and taking into account that according to the third law of thermodynamics the entropy at $T = 0$ is assumed to be zero, one can calculate finite entropy change $\Delta S(T)$ and magnetic entropy change $\Delta S_M(T)$ on the basis of data on heat capacity temperature dependences $C_H(T)$:

$$\Delta S_M(T) = \Delta S(T) = \int_0^T \frac{[C_H(H_2, T) - C_H(H_1, T)]}{T} dT. \quad (2.75)$$

It follows from equation (2.75) that large $\Delta S(T)$ and $\Delta S_M(T)$ can be expected for the large difference between heat capacities at H_1 and H_2 and in the low-temperature region. Applying conditions of extremum and maximum or minimum of a function to equation (2.75), it is possible to determine the position of $\Delta S_M(T)$ (or $\Delta S(T)$) maximum and minimum. According to the results of Pecharsky *et al* (2001), the maximum in $\Delta S_M(T)$ is observed for

$$C_H(H_1, T) = C_H(H_2, T) \quad \text{and} \quad \frac{\partial C_H(H_2, T)}{\partial T} < \frac{\partial C_H(H_1, T)}{\partial T} \quad (2.76a)$$

and the minimum in $\Delta S_M(T)$ is observed for

$$C_H(H_1, T) = C_H(H_2, T) \quad \text{and} \quad \frac{\partial C_H(H_2, T)}{\partial T} > \frac{\partial C_H(H_1, T)}{\partial T}. \quad (2.76b)$$

Conditions (2.76) are illustrated by figure 2.2(a) and (b), where heat capacity experimental data of ErAgGa at $H = 0$, 53.2 and 98.5 kOe are shown, together with magnetic entropy change temperature dependences calculated by equation (2.75) (Pecharsky *et al* 2001). As can be seen from figure 2.2, for ErAgGa the condition (2.76b) is fulfilled and accordingly there is a minimum in $\Delta S_M(T)$ dependence. The temperature positions of the minima are determined by intersections between the $C(T)$ curve at $H = 0$ and the corresponding $C(T)$ curve at $H \neq 0$ (the intersections are marked by bold dots in figure 2.2(a)). The minima and maxima on $\Delta S_M(T, H)$ dependence are usually observed near the points of magnetic phase transformations.

The adiabatic change of magnetic field from H_1 to H_2 causes not only a finite change of the magnetic entropy ΔS_M , but also the finite change of sample temperature from T_1 to T_2 (the magnetocaloric effect $\Delta T = T_2 - T_1$). The process is illustrated by figure 2.3, where the total entropy temperature dependences of a typical ferromagnet at $H = 0$ and $H \neq 0$ are shown. According to this diagram, the MCE ΔT at the given

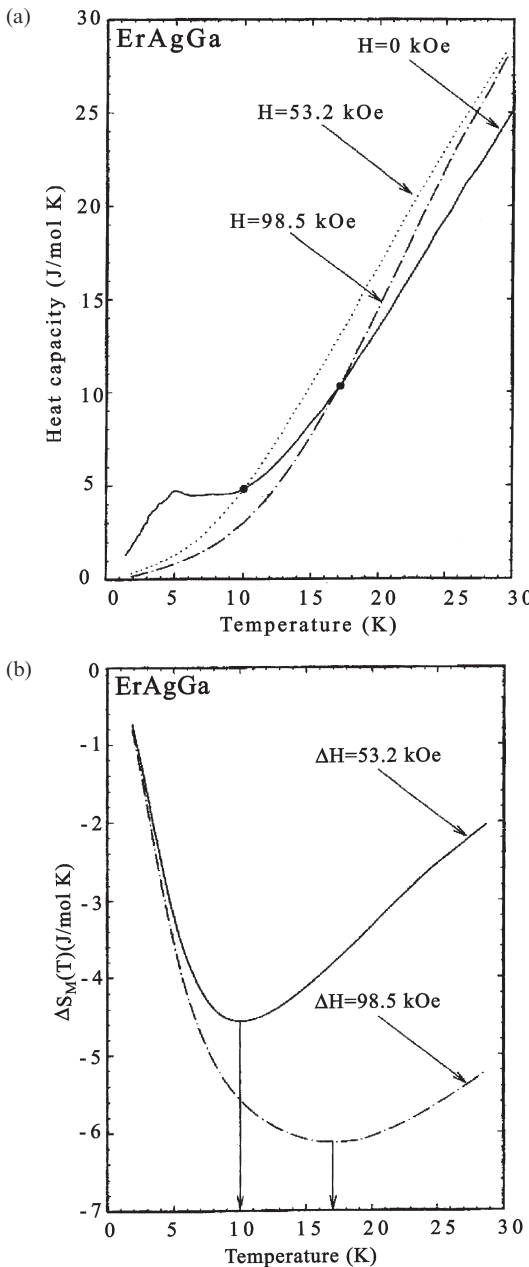


Figure 2.2. Heat capacity (a) and magnetic entropy change temperature dependences (b) of ErAgGa for $H = 0$; 53.2 and 98.5 kOe. Equation (2.76b) holds at the points in (a). At the corresponding temperatures the minima on $\Delta S_M(T)$ takes place—see (b) (Pecharsky *et al* 2001). (Copyright 2001 by the American Physical Society.)

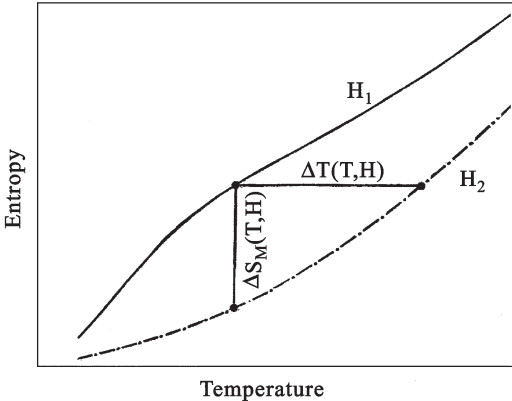


Figure 2.3. The temperature dependences of the total entropy $S(T)$ of a simple ferromagnet in zero and nonzero magnetic fields.

temperature T can be determined by the adiabatic condition $S(T, H_1) = S(T + \Delta T, H_2)$. Integration of equation (2.72) yields the equation for magnetocaloric effect ΔT :

$$\begin{aligned}\Delta T(T, \Delta H) &= T \left\{ \exp \left[- \int_{H_1}^{H_2} \frac{dS_M}{C_H(T, H)} \right] - 1 \right\} \\ &= T \left\{ \exp \left[- \int_{H_1}^{H_2} \frac{\partial M(T, H)/\partial T}{C_H(T, H)} dH \right] - 1 \right\}. \quad (2.77)\end{aligned}$$

Assuming that the heat capacity does not depend on the magnetic field, one can simplify equation (2.77) to

$$\Delta T(T, \Delta H) = T \left\{ \exp \left[- \frac{\Delta S_M(T, \Delta H)}{C_H(T)} \right] - 1 \right\}. \quad (2.78)$$

Equation (2.78) allows some conclusions to be drawn about $\Delta T(T, H)$ behaviour and its relation to ΔS_M . First, ΔT is positive for negative ΔS_M and changes its sign at $\Delta S_M = 0$. It should be noted that the expression in curly braces increases exponentially with ΔS_M absolute value increasing for $\Delta S_M < 0$. If $\Delta S_M(T)$ has a maximum in absolute value, ΔT should also have a maximum. For positive ΔS_M (as takes place in antiferromagnets) the expression in curly braces has small negative values for small $\Delta S_M/C_H$ and rapidly decreases with its increasing, reaching the value of -1 for large $\Delta S_M/C_H$. So, in this case $\Delta T \approx -T$ and does not depend on ΔS_M for large $\Delta S_M/C_H$.

Further simplification of equation (2.77) can be done assuming that $\Delta S_M/C_H$ is small, expanding the exponent function. As was noted by Tishin (1997), these suppositions are valid only in the region far from the transition point and/or in relatively weak fields. The resulting equation has

the form

$$\Delta T = -\frac{T \Delta S_M}{C_H}. \quad (2.79)$$

From equation (2.77) it can also be seen that the value of ΔT increases with increasing temperature (for the same ΔS_M and C_H) and that larger ΔT can be expected for materials with lower total heat capacity. It should be noted that above the Debye temperature T_D the lattice contribution to the heat capacity of solids approaches the value of $3R$ (the DuLong–Petit limit), and this factor can play a role in ΔT increasing in the high-temperature region above T_D . The Debye temperature can have an essential influence on the MCE, which is considered in section 8.1.8.

According to the above, the highest MCE value can be reached in ferromagnets and paramagnets with high absolute values of negative ΔS_M , and low contribution to the total heat capacity from lattice and conduction electron subsystems. The latter condition can be reached in the low-temperature region, where C_e and C_l approach zero. Note also that the value of the MCE is directly proportional to temperature (see equation (2.77)).

Pecharsky *et al* (2001) analysed the temperature behaviour of ΔT by investigation of equation (2.79) on the extremum and showed that in general the maximum (or minimum) $\Delta T(T)$ should not coincide with the temperature of the corresponding minimum (or maximum) in $\Delta S_M(T)$. The conditions of the maximum $\Delta T(T)$ are

$$C(T, H_2) \geq C(T, H_1) \quad \text{and} \quad \frac{\partial}{\partial T} \left(\frac{T}{C(T, H_2)} \right) \geq 0 \quad (2.80a)$$

or

$$C(T, H_2) \leq C(T, H_1) \quad \text{and} \quad \frac{\partial}{\partial T} \left(\frac{T}{C(T, H_2)} \right) \leq 0. \quad (2.80b)$$

This is illustrated in figure 2.4(a) and (b), where the temperature dependences of $T/C(H, T)$ and $\Delta T(T)$ of ErAgGa are shown (Pecharsky *et al* 2001). Here $\partial/\partial T(T/C(H, T)) < 0$ at low temperatures and the peak of $\Delta T(T)$ should be observed for $C(T, H_2) \leq C(T, H_1)$, which holds below 10 K (figure 2.2(a)). $\Delta T(T)$ maxima in ErAgGa are observed at about 7 K (figure 2.4(b)), which is lower than the temperatures of $\Delta S_M(T)$ maxima positions (figure 2.2(b)).

ΔS_M for a paramagnet and a ferromagnet above T_C can be obtained from equations (2.41), (2.48) and (2.70):

$$\Delta S_M = -\frac{1}{2} \frac{C_J \Delta(H)^2}{T^2} \quad (2.81)$$

$$\Delta S_M = -\frac{1}{2} \frac{C_J \Delta(H)^2}{(T - T_C)^2} \quad (2.82)$$

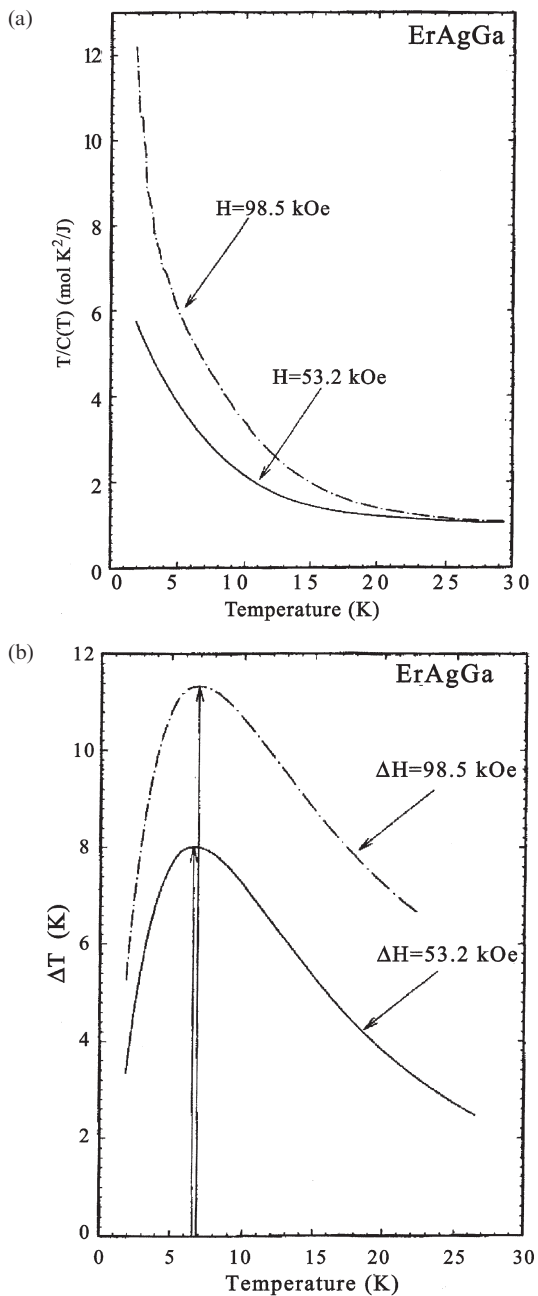


Figure 2.4. The temperature dependences of the $T/C(T, H)$ (a) and $\Delta T(T)$ (b) of ErAgGa in magnetic fields 53.2 and 98.5 kOe (Pecharsky *et al* 2001). (Copyright 2001 by the American Physical Society.)

where $\Delta(H)^2 = H_2^2 - H_1^2$. It is clear from equations (2.81) and (2.82) that large values of ΔS_M are expected in magnetic materials with large M_{eff} and in a temperature range close to 0 K for paramagnets, close to T_C for ferromagnets.

The following expression, describing the field dependence of ΔS_M in a ferromagnet near T_C , was derived by Oesterreicher and Parker (1984) in the frames of MFA:

$$\Delta S_M = -1.07Nk_B \left(\frac{g_J\mu_B JH}{k_B T_C} \right)^{2/3}. \quad (2.83)$$

It follows from this equation that $\Delta T \approx H^{2/3}$ in the vicinity of T_C (see equation (2.79) above).

Figure 2.5 illustrates the typical behaviour of total entropy $S(T, H)$, magnetic entropy $S_M(T, H)$ and magnetic entropy change $\Delta S_M(T, H)$ in a typical ferromagnet EuS. At high temperatures $S_M(T, H)$ approaches its upper limit $R \ln(2J + 1)$ —see equation (2.65)—and $\Delta S_M(T, H)$ has a maximum near T_C . The total entropy increase, observed in the high-temperature region, is due to the increase of the lattice and conduction electron entropies.

In some experiments there were attempts to take into account effects of magnetocrystalline anisotropy in calculations of magnetic entropy S_M . Bennett *et al* (1993) considered the magnetic entropy of a ferromagnet with an axial anisotropy using the total Hamiltonian of the form

$$\hat{H} = - \sum_{i>j} I_{ij} \hat{s}_i \hat{s}_j - \mu_B \sum_i (\hat{s}_i \vec{H} + a \hat{s}_{zi}^2) \quad (2.84)$$

where \hat{s}_i is the spin angular momentum operator and the magnetic field is directed along the z axis. If $a > 0$, the preferred directions of the spins are $\pm z$ (uniaxial anisotropy) and for $a < 0$ the spins lie in the plane perpendicular to the z axis (in-plane anisotropy). The total magnetic moment of the $20 \times 20 \times 20$ fcc lattice was calculated by the Monte Carlo method using the Hamiltonian (2.84), and then ΔS_M was determined by equation (2.70) for $H_1 = 0$ and $H_2 = 10$ kOe. It was shown that for the case of uniaxial anisotropy, an increase of a led to sharpening and an increase of the ΔS_M peak height near T_C , but in the rest of the temperature range the curves were almost identical. For in-plane anisotropy, ΔS_M essentially increased in the vicinity of T_C and decreased above T_C in the paramagnetic region, with increasing of a in the absolute value.

Druzhinin *et al* (1975, 1977, 1979) took into account in Hamiltonian (2.43) the single-ion hexagonal magnetocrystalline anisotropy in the form of

$$\hat{H}_a = - \sum_i \left(a \hat{J}_z^2 + b \hat{J}_z^4 + c \hat{J}_z^6 + \frac{d}{2} (\hat{J}_+^6 + \hat{J}_-^6) \right) \quad (2.85)$$

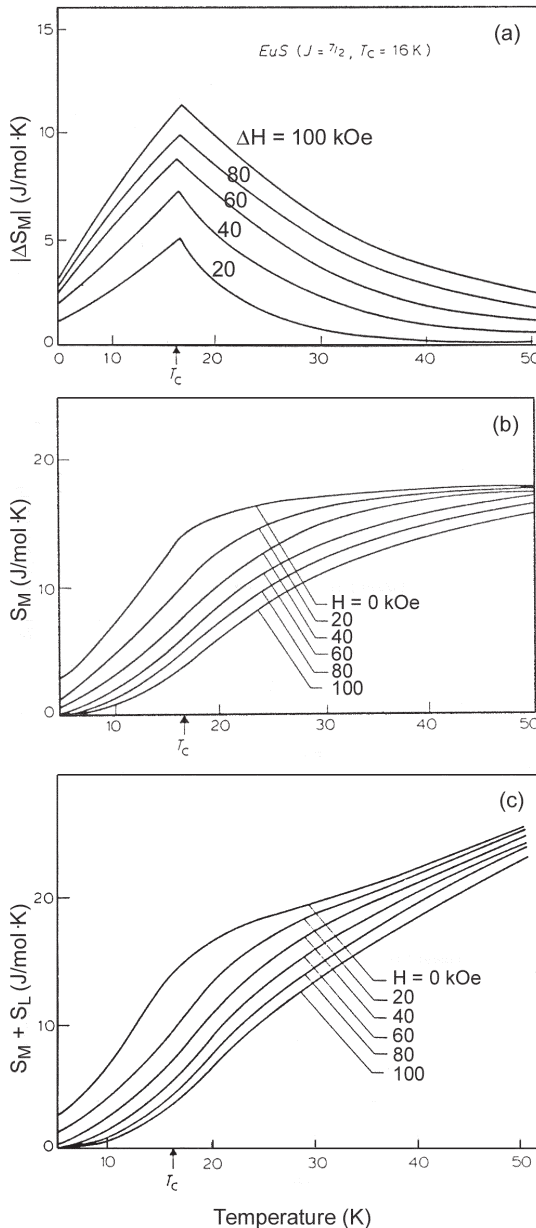


Figure 2.5. The temperature dependences of the magnetic entropy change $\Delta S_M(T, H)$ (a) induced by a magnetic field change ΔH , magnetic entropy $S_M(T, H)$ (b) at different magnetic fields H and total entropy $S(T, H)$ (c) in a typical ferromagnet EuS (Hashimoto *et al* 1981). (Reprinted from Hashimoto *et al* 1981, copyright 1981, with permission from Elsevier.)

(here the coefficients a, b, c and d are related to the crystal field coefficients A_l^m (Taylor and Darby 1972)) and calculated the magnetic entropy S_M by the Boltzmann equation:

$$S_M = -k_B N \sum_n \frac{\exp(-E_n/k_B T)}{Z} \ln \left[\frac{\exp(-E_n/k_B T)}{Z} \right]. \quad (2.86)$$

The calculations of S_M were performed for Tb and Dy for $H = 0$ (Druzhinin *et al* 1977). The results show some better agreement with experimental data than calculations made on the basis of isotropic Hamiltonian (2.43) in the framework of the MFA.

The partition function, free energy and magnetic entropy of the system consisting of N particles with magnetic moments μ have in the classical limit the form (McMichael *et al* 1992)

$$Z_\infty = 4\pi \frac{\sinh x}{x} \quad (2.87)$$

$$F = -k_B T \ln(Z_\infty(x))^N \quad (2.88)$$

$$\begin{aligned} S_M &= Nk_B \left[\ln \left(4\pi \frac{\sinh x}{x} \right) - x \ln(x) \right] \\ &= Nk_B \left[1 - x \coth x + \ln \left(4\pi \frac{\sinh x}{x} \right) \right] \end{aligned} \quad (2.89)$$

where x is determined by equations (2.53) and (2.54).

As in the quantum case, the magnetic entropy change under magnetization in magnetic fields from H_1 to H_2 in the classical limit can be calculated by equation (2.70):

$$\Delta S_M = \int_{H_1}^{H_2} \left(\frac{\partial M}{\partial T} \right)_H dH = -\frac{N\mu^2}{6k_B} \frac{\Delta(H)^2}{T^2} \quad (2.90)$$

for a paramagnet; and

$$\Delta S_M = -\frac{N\mu^2}{6k_B} \frac{\Delta(H)^2}{(T - T_C)^2} \quad (2.91)$$

for a ferromagnet at $T > T_C$.

A more general consideration yields the following expression for ΔS_M caused by a magnetic field increase from zero to H in the classical limit:

$$\Delta S_M = S_M(T, H) - S_M(T, 0) = Nk_B \left[1 - x \coth x + \ln \frac{\sinh x}{x} \right]. \quad (2.92)$$

The magnetic entropy change caused by the occurrence of the spontaneous magnetization in a ferromagnet below ordering temperature T_C in the absence of a magnetic field can be described by means of the Landau theory of the second-order phase transitions (Landau 1958). Using equation

(2.26) for thermodynamic potential Φ , equation (2.28) for equilibrium spontaneous magnetization and equation $S = -\partial\Phi/\partial T$, one can obtain the following formula for the entropy change (Belov 1961a):

$$\Delta S_M = -\frac{\alpha_\Theta}{2} I_s^2 = -\frac{(\alpha_\Theta)^2}{2\beta} (T - T_C). \quad (2.93)$$

2.5 MCE at the first-order transitions

It was assumed in section 2.4, under consideration of the magnetocaloric effect and the entropy change caused by the magnetic field, that the magnetic phase transition is a phase transition of the second-order type. As is known, in the point of the second-order transition the first derivatives on temperature or generalized force (pressure, magnetic field etc.) of the thermodynamic potential are continuous functions and the second derivatives undergo a discontinuous change (jump). The entropy and such generalized coordinates of a system as volume and magnetization are the first-order derivative of the thermodynamic potentials—see equations (2.8). Because of that there are no jumps in entropy, thermal expansion, or magnetization, and there is no latent heat ($\Delta Q = T\Delta S$) in the point of the second-order transition. Such behaviour can be explained by indistinguishability of old and new phases in the second-order transition points. The phases have in the point of the transition the same physical characteristics, which become different only far from the transition. However, the parameters determined as the second derivatives of the thermodynamic potential, such as heat capacity, should undergo at the point of the second-order phase transition a finite discontinuous change—see section 2.11.

If a material undergoes the transition of a first-order type, then the first-order derivatives of the thermodynamic potential changes discontinuously, and such values as entropy, volume and magnetization displays a jump at the point of transition. The heat capacity in the point of the first-order transition should be infinite. The analysis of the magnetic entropy change and MCE behaviour at the first-order magnetic transition was made by Pecharsky *et al* (2001). Figure 2.6 shows an $S-T$ diagram of the magnetic system undergoing first-order transition at the transition point $T_{pt}(H)$, which is displaced in the magnetic field (in this case $T_{pt}(H_2) > T_{pt}(H_1)$). The enthalpy of the first-order transformation is $\Delta E(H)$, which results in discontinuous total entropy change of the value of $\Delta E(H)/T_{pt}(H)$. It is assumed that below $T_{pt}(H_1)$ and above $T_{pt}(H_2)$ a magnetic field has little effect on the entropy, and its main change takes place between $T_{sp}(H_1)$ and $T_{sp}(H_2)$. The consideration was made for the case $H_2 > H_1$, but analogous results with inverse signs of ΔS_M and ΔT can be obtained for the case of $H_2 < H_1$. The total entropy of the system

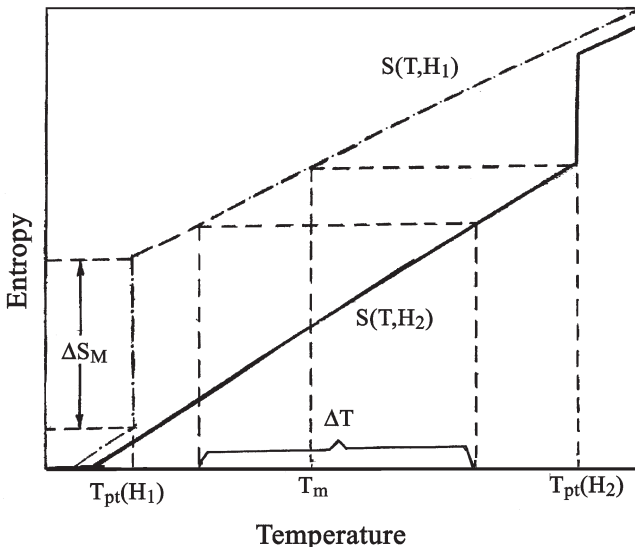


Figure 2.6. A schematic S - T diagram of a magnetic material in two magnetic fields H_1 and H_2 near the first-order transition (Pecharsky *et al* 2001). (Copyright 2001 by the American Physical Society.)

can be represented as

$$S(T, H) = \int_0^{T_{\text{pt}}(H)} \frac{C_H^l(T, H)}{T} dT + \int_{T_{\text{pt}}(H)}^T \frac{C_H^h(T, H)}{T} dT + \frac{\Delta E(H)}{T_{\text{pt}}(H)} \quad (2.94)$$

where $C_H^l(T, H)$ and $C_H^h(T, H)$ are the heat capacities of the phases stable below and above $T_{\text{pt}}(H)$, respectively. Assuming that constant magnetic field capacities of these phases are approximately the same, $C_H^l(T, H) \approx C_H^h(T, H) = C_H(T)$, the total and magnetic entropy change caused by the magnetic field change in the temperature ranges $T < T_{\text{pt}}(H_1)$, $T_{\text{pt}}(H_1) < T < T_{\text{pt}}(H_2)$ and $T > T_{\text{pt}}(H_2)$, respectively, can be written down as follows:

$$\Delta S_M(T, \Delta H) = \Delta S(T, \Delta H) \cong \int_0^T \frac{(C_H(T, H_2) - C_H(T, H_1))}{T} dT \quad (2.95a)$$

$$\begin{aligned} \Delta S_M(T, \Delta H) = \Delta S(T, \Delta H) \cong & \int_0^T \frac{(C_H(T, H_2) - C_H(T, H_1))}{T} dT \\ & - \frac{\Delta E(H_1)}{T_{\text{pt}}(H_1)} \end{aligned} \quad (2.95b)$$

$$\Delta S_M(T, \Delta H) = \Delta S(T, \Delta H) \cong \int_0^T \frac{(C_H(T, H_2) - C_H(T, H_1))}{T} dT - \left(\frac{\Delta E(H_1)}{T_{pt}(H_1)} - \frac{\Delta E(H_2)}{T_{pt}(H_2)} \right). \quad (2.95c)$$

Since $\Delta E(H)/T_{pt}(H)$ is a temperature-independent value, then conditions of minimum and maximum ΔS_M are also valid in the case of the first-order transitions. Because, according to the experimental data (Pecharsky and Gschneidner 1997a, Tishin *et al* 1999a), in materials with first-order magnetic phase transitions the magnetic field has small influence on the heat capacity below $T_{pt}(H_1)$ and above $T_{pt}(H_2)$, it is possible to assume that $C_H(T, H_1) \approx C_H(T, H_2)$ in these temperature ranges. Based on this simplification one can conclude that the magnetic entropy change under first-order transition should have approximately constant and large values between $T_{pt}(H_1)$ and $T_{pt}(H_2)$:

$$\Delta S_M(T, \Delta H) \cong -\frac{\Delta E(H_1)}{T_{pt}(H_1)} \cong -\frac{\Delta E(H_2)}{T_{pt}(H_2)} \quad (2.96)$$

and small values below $T_{pt}(H_1)$ and above $T_{pt}(H_2)$. So, the magnetic entropy change during first-order magnetic phase transition is mainly due to enthalpy of the phase transformation.

Since the largest magnetic entropy change occurs between $T_{pt}(H_1)$ and $T_{pt}(H_2)$, it is natural to expect the largest MCE values in this interval. One can distinguish two different temperature intervals between $T_{pt}(H_1)$ and $T_{pt}(H_2)$, separated by characteristic temperature T_m —see figure 2.6. If the initial temperature lies in the temperature region from $T_{pt}(H_1)$ to T_m , then the material cannot reach $T_{pt}(H_2)$ due to the temperature change caused by the magnetocaloric effect $\Delta T(\Delta H)$. When the initial temperature is situated between T_m and $T_{pt}(H_2)$, the temperature of the material rises up to $T_{pt}(H_2)$ before the magnetic field reaches H_2 due to the MCE. According to Pecharsky *et al* (2001), the further temperature rise (above $T_{pt}(H_2)$) will not happen because the heat capacity of the material has infinite value (extremely large, in practice) in the point of the first-order transition. The temperature T_m can be defined as the temperature where the total entropy $S(T_m, H_1)$ equals the total entropy $S(T_{pt}, H_2)$.

Pecharsky *et al* (2001) considered the simplest case when the magnetic field had an essential effect on the magnetic transition temperature T_{pt} , but did not affect the heat capacity below $T_{pt}(H_1)$ and above $T_{pt}(H_2)$. In this case the MCE has nonzero values only in the interval from $T_{pt}(H_1)$ to $T_{pt}(H_2)$ and can be determined from equations (2.79) and (2.96):

$$\Delta T(T, \Delta H) = -\frac{T}{C_H(H, T)} \Delta S_M(T, \Delta H) \cong \frac{T}{C_H(H, T)} \frac{\Delta E(H_1)}{T_{pt}(H_1)}. \quad (2.97)$$

Since the value of $\Delta E(H_1)/T_{\text{pt}}(H_1)$ is constant, then the MCE temperature dependence is determined by the behaviour of $T/C_H(H, T)$. As was concluded by Pecharsky *et al* (2001) on the basis of experimental data, T/C_H should decrease with increasing temperature in the low-temperature range and increase when the temperature exceeds 20–100 K (depending on the value of the Debye temperature). That is why the MCE is expected to rise proportionally between $T_{\text{pt}}(H_1)$ and T_m . In the temperature range from T_m to $T_{\text{pt}}(H_2)$ the MCE is limited by $T_{\text{pt}}(H_2)$ and its value is just the difference between $T_{\text{pt}}(H_2)$ and initial temperature T :

$$\Delta T(T, \Delta H) = T_{\text{pt}}(H_2) - T. \quad (2.98)$$

So, above T_m the value of the MCE begins to decrease rapidly with temperature. If the magnetic field change or its effect on the magnetic phase transition is small, then it can be assumed that $T_m = T_{\text{pt}}(H_1)$ and equation (2.98) becomes

$$\Delta T(T, \Delta H) \cong T_{\text{pt}}(H_2) - T_{\text{pt}}(H_1) \quad (2.99)$$

indicating that the MCE in this case is determined as just a difference between the temperatures corresponding to the points of the first-order transitions in the fields H_2 and H_1 .

For first-order magnetic phase transitions the magnetic Clausius–Clapeyron equation is valid:

$$\frac{dH}{dT} = -\frac{\Delta S_M}{\Delta M} \quad (2.100)$$

where $\Delta S_M = S_{M(2)} - S_{M(1)}$ and $\Delta M = M_2 - M_1$ are the differences in magnetic part of the entropy and the magnetic moment between the magnetic states 2 and 1 at the temperature of the transition. Using this equation one can calculate the entropy change (and consequently the MCE) at the transition on the basis of magnetization data and the magnetic phase diagram H – T . Using equations (2.79) and (2.100) it is possible to obtain the formula for the MCE at the first-order transition (see, for example, Tishin 1994):

$$\Delta T = \frac{T}{C_H} \left(\frac{\partial H}{\partial T} \right) \Delta M. \quad (2.101)$$

It should be noted that because magnetization changes at the first-order transition theoretically by a jump and usually very fast in real materials, the magnetocaloric effect— ΔS_M and ΔT —at this transition can achieve essential values, much higher than at the second-order transitions for the same values of magnetization. First-order transitions usually take place at magnetic order–order transitions. The effects of short-range order in paramagnetic state and spin fluctuations, which smear magnetic order–disorder transitions and reduces by this MCE, are absent at the first order–order transitions. The order–order magnetic transitions are often accompanied

by the structural transitions (see sections 5 and 7.2.2), which also enforces the magnetization change and makes it sharper and, consequently, causes the MCE strengthening.

2.6 MCE in ferrimagnetic and antiferromagnetic materials

In ferromagnets the magnetic entropy change caused by positive magnetic field change ($\Delta H > 0$) always has a negative sign, and the MCE has a positive sign. Materials with antiferromagnetic or ferrimagnetic structures can display in some field and temperature intervals positive ΔS_M values for positive ΔH (and, correspondingly, negative MCE). Such behaviour is illustrated by figure 2.7(a) and (b), where the temperature dependences of the MCE in polycrystalline iron garnets $\text{Gd}_3\text{Fe}_5\text{O}_{12}$ and $\text{Y}_3\text{Fe}_5\text{O}_{12}$ induced by $\Delta H = 16 \text{ kOe}$ are shown (Belov *et al* 1969). One can see that in certain temperature intervals,

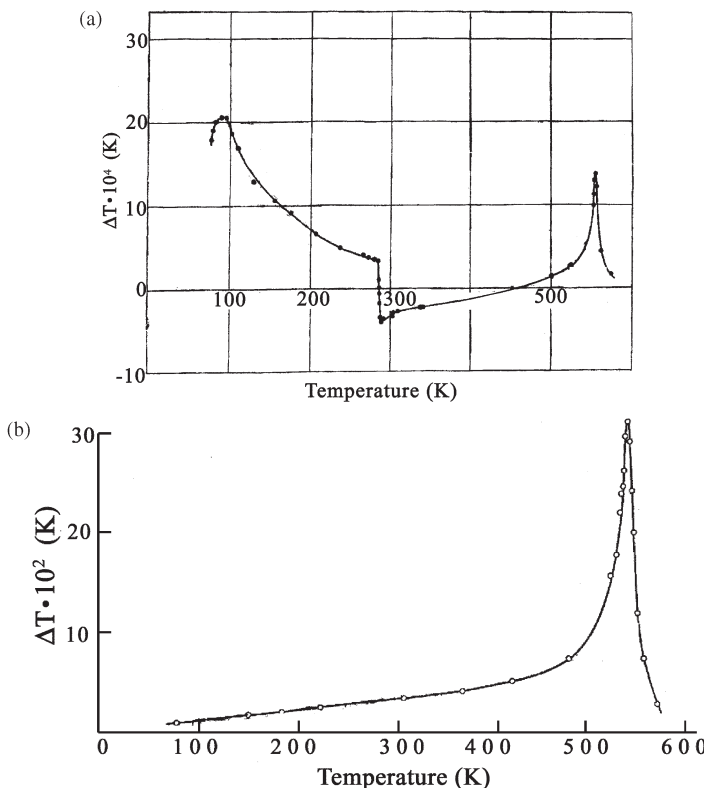


Figure 2.7. Temperature dependences of the MCE in polycrystalline rare earth iron garnets $\text{Gd}_3\text{Fe}_5\text{O}_{12}$ (a) and $\text{Y}_3\text{Fe}_5\text{O}_{12}$ (b) induced by $\Delta H = 16 \text{ kOe}$ (Belov *et al* 1972, 1973).

negative MCE is observed in $\text{Gd}_3\text{Fe}_5\text{O}_{12}$, where ferrimagnetic structures arise below the Curie point. In contrast, in ferromagnetic $\text{Y}_3\text{Fe}_5\text{O}_{12}$ there is only a positive MCE with a characteristic peak near the Curie temperature. The negative MCE is related to the ferrimagnetic structure of $\text{Gd}_3\text{Fe}_5\text{O}_{12}$ garnet and peculiarities of its transformation in the magnetic field.

According to the Néel model (Néel 1954) ferrimagnetic rare earth iron garnets $\text{R}_3\text{Fe}_5\text{O}_{12}$ have a magnetic structure consisting of three sublattices. The R^{3+} ions occupy dodecahedral sites (c-sublattice) and the Fe^{3+} ions occupy octahedral (a-sublattice) and tetragonal (d-sublattice) sites. The a- and d-sublattices are connected by strong antiferromagnetic exchange interactions. The weaker antiferromagnetic interaction occurs between d- and c-sublattices and the c-c and a-c interactions are weak and positive (Anderson 1964). Such exchange field distribution leads to a strong paraprocess in the c-sublattice in the whole temperature range below the Curie point, T_C , which displays itself in a strong temperature and field dependence of the c-sublattice magnetic moment. An intensive paraprocess in the a- and d-sublattices is possible only near T_C and the total magnetic moments of the d- and a-sublattices have weak field and temperature dependence at low temperatures. According to the estimations, made by Belov and Nikitin (1965, 1970a) in the framework of mean field approximation (MFA), the values of effective fields acting in the rare earth (RE) magnetic sublattice ($H_{2\text{eff}}$) and in the iron a-d magnetic sublattices ($H_{1\text{eff}}$) in iron garnets with heavy rare earths are approximately 3×10^5 Oe and 1.7×10^6 Oe, respectively, i.e. $H_{1\text{eff}} \gg H_{2\text{eff}}$.

Due to the difference in temperature dependences of the c-, a- and d-sublattice magnetizations, the compensation temperature T_{comp} , characteristic for ferrimagnets, appears in the garnets containing heavy rare earth metals. Above T_{comp} the magnetic moment of the c-sublattice \vec{M}_R is lower than the total magnetic moment of the a- and d-sublattices \vec{M}_{Fe} , and below T_{comp} the inverse situation takes place. The resultant magnetic moment of the rare earth iron garnet is $\vec{M} = \vec{M}_{\text{Re}} + \vec{M}_{\text{Fe}}$ and is oriented along the field direction. This leads to a change of the \vec{M}_R and \vec{M}_{Fe} orientations relative to the field at $T = T_{\text{comp}}$. This effect was observed by neutron diffraction measurements (Bertran *et al* 1956, Herpin and Meriel 1957, Prince 1957).

Consider the MCE in rare earth iron garnets using the MFA model and following the work of Belov and Nikitin (1970a). The MCE can be determined by formula (2.16), which can be written down in vector form:

$$dT = -\frac{T}{C_H} \left(\frac{\partial \vec{M}}{\partial T} \right) d\vec{H}. \quad (2.102)$$

The total value of the MCE can be presented as the sum

$$\Delta T = \Delta T_{\text{Fe}} + \Delta T_R. \quad (2.103)$$

Taking into account that in the rare earth garnets $|\partial M_R / \partial T| \gg |\partial M_{\text{Fe}} / \partial T|$ and $|\partial M_R / \partial H| \gg |\partial M_{\text{Fe}} / \partial H|$ below T_C , one can conclude that the main

contribution to the MCE in the low-temperature region far enough from the Curie point is provided by the rare earth c-sublattice and can be presented as follows:

$$\Delta T = \frac{I_2^0}{C_H k_B T} \frac{\partial B_J(x_2)}{\partial x_2} \vec{H} \left(\frac{I_2^0}{2n\nu_2} \vec{H} + 2\mu_B s_2 \vec{H}_{2\text{eff}} \right) \quad (2.104a)$$

where I_2^0 is the magnetization of the RE sublattice at $T = 0$ K, ν_2 is the number of the RE atoms in the molecule, s_2 is the spin of the RE atom, n is the number of molecules in the unit volume, and B_J is the Brillouin function. The value of the molecular field acting on the RE sublattice from iron a-d sublattice $\vec{H}_{2\text{eff}}$ is determined by the equation

$$H_{2\text{eff}} = \frac{z_{21} I_{21}}{\mu_B} \frac{I_1}{I_1^0} \quad (2.104b)$$

where I_{21} is the exchange integral describing the interaction between RE and Fe sublattices; z_{21} is the number of the nearest neighbours of the a-d sublattice to an atom of the RE sublattice; I_1 is the magnetization of the a-d sublattices; I_1^0 is I_1 at $T = 0$ K;

$$x_2 = \frac{I_2^0}{n\nu_2 k_B T} H + \frac{2\mu_B s_2}{k_B T} H_{2\text{eff}}. \quad (2.104c)$$

Equations (2.104) allow one to explain negative MCE values in iron garnets with heavy rare earths in the low-temperature region—see figure 2.7. It can be seen from equations (2.104) that if the directions of the external magnetic field \vec{H} and the internal molecular field $\vec{H}_{2\text{eff}}$ coincide, then $\Delta T > 0$. In this case the external magnetic field increases the magnetic order in the c-sublattice and decreases the magnetic entropy ($\Delta S_M < 0$), which leads to sample heating. If \vec{H} and $\vec{H}_{2\text{eff}}$ are aligned in opposite directions, then $\Delta T < 0$. The external magnetic field acts in this case against $\vec{H}_{2\text{eff}}$ and decreases the magnetic order in the c-sublattice. This process is accompanied by the magnetic entropy increase ($\Delta S_M > 0$) and a corresponding sample cooling. The paraprocesses of these two types were called ferromagnetic (it causes $\Delta S_M < 0$ and $\Delta T > 0$ for $\Delta H > 0$) and antiferromagnetic (it causes $\Delta S_M > 0$ and $\Delta T < 0$ for $\Delta H > 0$) ones, respectively (Belov 1968, Belov *et al* 1968, 1969, 1972).

The ferro- and antiferromagnetic paraprocesses can take place in the same magnetic sublattice at various temperature and field ranges, but in the rare earth iron garnets the MCE below the Curie point is determined by the paraprocess in the c-sublattice. Near T_C the ferromagnetic paraprocess in the iron a-d sublattice overcomes the antiferromagnetic one in the c-sublattice, and the MCE becomes positive at some temperature, reaching a maximum near T_C .

Near the compensation temperature a sudden change of the MCE sign is observed in the rare earth iron garnets containing heavy rare earths—see the

$\Delta T(T)$ curve for $\text{Gd}_3\text{Fe}_5\text{O}_{12}$ in figure 2.7(a), for which the change happens at 285 K. The ΔT sign change near T_{comp} is related to the change of the \vec{M}_{Fe} orientation (and, consequently, the $\vec{H}_{2\text{eff}}$ orientation) relative to the magnetic field direction and should be inversely proportional to T_{comp} , as follows from equations (2.104). The latter statement was confirmed experimentally in rare earth iron garnets by Belov *et al* (1969). As was noted by Belov and Nikitin (1970), the existence of ΔT jumps at T_{comp} points to a first-order character of this magnetic phase transition.

Below T_{comp} at $T \approx 90$ K the MCE in $\text{Gd}_3\text{Fe}_5\text{O}_{12}$ displays an additional maximum which is higher than that near T_C —figure 2.7(a). An increase of the MCE below T_{comp} was also observed in the garnets with Ho, Dy and Tb ions (see section 5.1). This behaviour was related to a sharp change of the long-range magnetic order, which took place in the RE sublattice in this temperature range (Belov 1961b, Belov and Nikitin 1970b). The low temperature of this ordering is due to the weakness of the effective field acting on the RE sublattice from the a-d iron sublattice.

If the magnetic c-sublattice in the garnet is absent, as is the case for $R = Y$, one can observe a $\Delta T(T)$ curve with one maximum near the Curie point, caused by the paraprocess in the a-d sublattice (although a- and d-sublattices are connected by negative exchange interaction, the ferromagnetic paraprocess in the d-sublattice prevails in the whole temperature range)—see figure 2.7(b). Further consideration of the rare earth iron garnets' magnetothermal properties will be made in section 5.1.

The magnetic field can decrease the antiferromagnetic order and finally convert it to the ferromagnetic one. This process is accompanied by field-induced MCE (and ΔS_M) sign change. The typical example of such behaviour is shown in figure 2.8, where field dependences of the MCE in Dy are shown. As is known, the helicoidal antiferromagnetic (HAFM) structure arises in Dy between $T_N \cong 180$ K and $T_C \cong 90$ K (Taylor and Darby 1972, McEwen 1991). HAFM structure can be destroyed by the critical magnetic field H_{cr} , which reaches its maximum value of 11 kOe at $T_K = 165$ K (Bykhover *et al* 1990). In the fields above H_{cr} a ‘fan’ structure arises, in which the magnetic moments in the basal planes form fan-type ordering around the field direction. A further increase of the field leads to the establishment of complete ferromagnetic ordering at a field about $2H_{\text{cr}}$ (Greenough and Hettiarachchi 1983, Drillat *et al* 1984, Bagguley and Howe 1986). In the temperature interval from T_K to T_N the field-induced transition fan-HAFM is the second-order phase transition, in which the field continuously deforms the HAFM structure until a fan structure is formed. On the first stage the process leads to decreasing of the antiferromagnetic order with a corresponding increase of the magnetic entropy. On $\Delta T(T)$ curves it corresponds to the field intervals where $\Delta T < 0$ —see the curves for $T = 170$ and 175 K in figure 2.8. At a further magnetic field, an increasing ferromagnetic paraprocess appears and the MCE changes its sign from negative to positive at some value of the magnetic

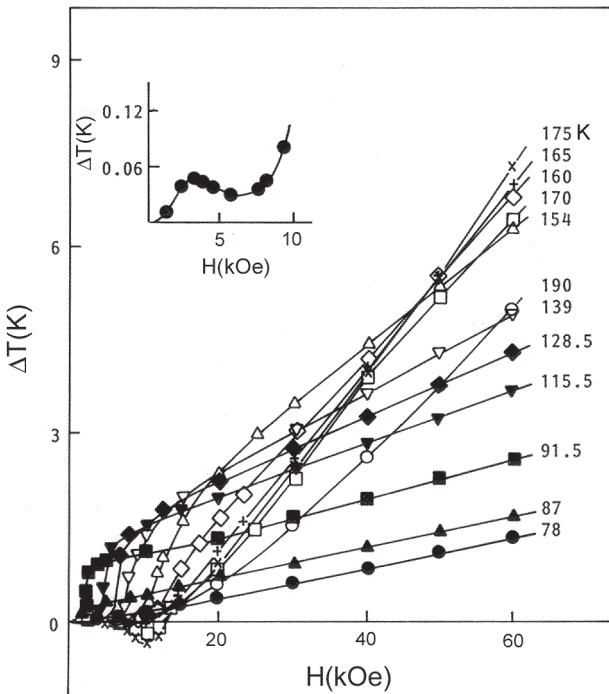


Figure 2.8. MCE dependences in a Dy single crystal on a magnetic field directed along the a -axis (the field is changed from 0 to H). The numbers near curves are temperatures in kelvins (Tishin 1988, Nikitin *et al* 1991b). (Reprinted from Nikitin *et al* 1991b, copyright 1991, with permission from Elsevier.)

field—see figure 2.8. Subsequent magnetization leads to an increase of the ferromagnetic order, and the system behaves just as a ferromagnet with positive MCE caused by positive magnetic field change. It should be noted that ΔS_M behaviour in a magnetic field in such magnetic systems as Dy, which exhibits first-order transition at H_{cr} , can be described by the thermodynamic Clausius–Clapeyron equation (2.100).

2.7 MCE in the vicinity of magnetic phase transitions

Tishin *et al* (1999a) investigated the magnetic field and temperature dependences of ΔT in the vicinity of magnetic phase transitions. The consideration was made on the basis of a reversible closed thermodynamic cycle in the (S , T) coordinates. It was shown that the MCE can be presented by the equation

$$\Delta T(T_0, H) = -T_0 \left[\Delta C(T, H) - \frac{\partial \Delta T(T_0, H)}{\partial T} \frac{C(T, H)}{C(T_0, H)} \right] \quad (2.105a)$$

where

$$\Delta C(T, H) = \frac{C(T_0, 0) - C(T, H)}{C(T_0, 0)} \quad (2.105b)$$

and T_0 and T are the initial and final temperatures, respectively ($\Delta T = T_0 - T$). Recalling that at the temperature where the MCE has its maximum or minimum the condition $\partial\Delta T/\partial T = 0$ should be fulfilled, one can obtain for the peak MCE value:

$$\Delta T(H, T_0)_{\text{peak}} = -T_0 \Delta C(T, H). \quad (2.106)$$

From equation (2.106) it is straightforward that the MCE peak value is positive (maximum of the MCE) if $\Delta C(H, T) < 0$ and is negative (minimum of the MCE) if $\Delta C(H, T) > 0$. Experimental results on the heat capacity of ferromagnets in various magnetic fields show that $\Delta C(H, T) > 0$ at temperatures below and just above the zero magnetic field heat capacity peak. $\Delta C(H, T)$ changes sign and becomes positive at slightly higher temperatures, so the MCE maximum in a ferromagnet should be expected above the temperature corresponding to the zero magnetic field heat capacity peak. This is illustrated by figure 2.9(a), where heat capacity temperature dependences of GdPd at various magnetic fields are presented. According to the magnetic investigations, the binary intermetallic compound orders ferromagnetically below ~ 38 K (Zimm *et al* 1992).

For small ΔT and/or for relatively high temperatures ($\Delta T/T_0 \approx 0$) it follows from equation (2.106) that at temperature T_{peak} , where the peak MCE occurs, the following condition is satisfied:

$$C(0, T_{\text{peak}}) \approx C(H, T). \quad (2.107)$$

So, the heat capacity of the material should be practically independent of the magnetic field at the temperature of the MCE peak. The temperature of the MCE peak (maximum or minimum) should be located close to a characteristic temperature T_{eq} , where the values of $C(0, T)$ and $C(H, T)$ are equal. It should be noted that where the initial magnetic field is not equal to zero, equations (2.105–2.107) are also valid, and in this case the MCE peak temperature must be located close to the temperature where $C(H_1, T)$ and $C(H_2, T)$ are the same.

In general case, when the relation $\Delta T/T_0$ is not negligible, equation (2.106) can be rewritten as follows:

$$C(0, T_{\text{peak}}) \frac{T}{T_M} = C(H, T). \quad (2.108)$$

Since for a ferromagnet the MCE is positive and the T/T_{peak} is always larger than 1, the MCE maximum occurs at a temperature higher than T_{eq} . Experimental data show that zero magnetic field heat capacity in ferromagnets changes sharply with the temperature immediately above its peak (see, for

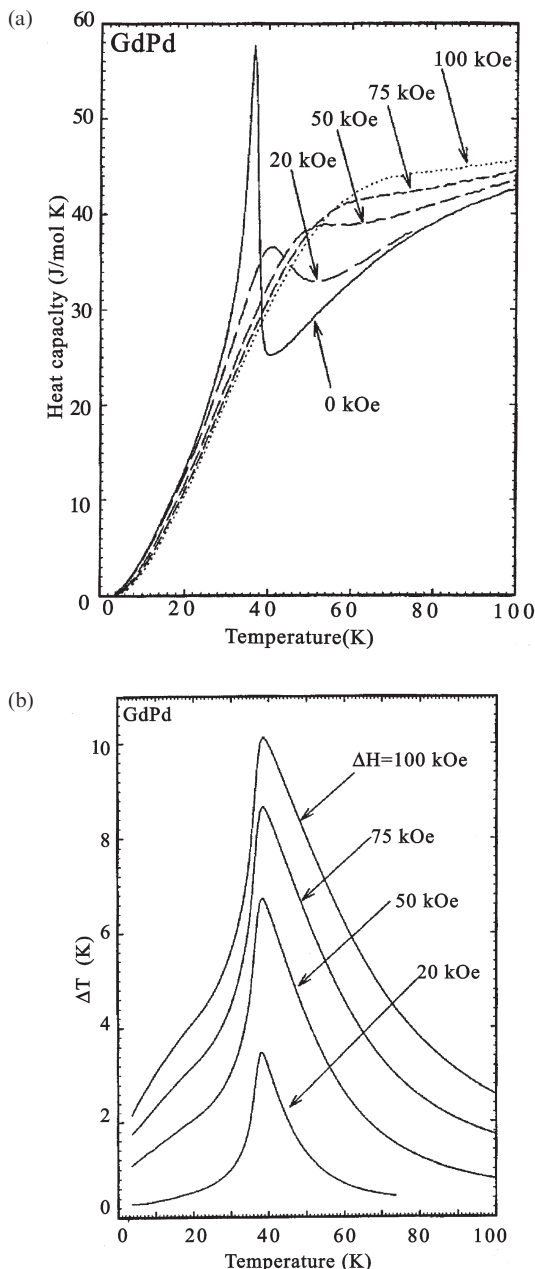


Figure 2.9. The heat capacity of polycrystalline GdPd measured at 0, 20, 50 and 75 kOe (a); and the magnetocaloric effect for a magnetic field change of 20 kOe, 50 kOe and 100 kOe, determined from the heat capacity data (b) (Tishin *et al* 1999a). (Copyright 1999 by the American Physical Society.)

example, figure 2.9(a)) and, therefore, temperatures T_{peak} and T_{eq} are almost equal to each other. For small ΔT (which can take place, for example, for small magnetic fields), T_{peak} approaches T_{eq} , and since $[\partial M(H, T)/\partial T]_H$ has in ferromagnets a maximum at $T \rightarrow T_C$ when $H \rightarrow 0$, and $T/C_H(H, T)$ is weakly dependent on temperature near the transition to the magnetically ordered state, then according to equation (2.72) the position of the MCE maximum in weak fields also approaches the Curie temperature.

From the analysis of equations (2.105) it can be shown that the MCE in a ferromagnet is lowered below and above T_{eq} , and that $\Delta T(T)$ dependence exhibits a typical caret-like shape with a single maximum for any material which orders ferromagnetically. Such behaviour is illustrated in figure 2.9(b), where $\Delta T(T)$ dependences for different ΔH for GdPd are shown. It was established experimentally that T_{eq} is almost independent of a magnetic field and practically coincides with T_{peak} .

A simple antiferromagnetic material should display a reverse caret-like behaviour with a single minimum in the MCE for magnetic fields not strong enough to destroy antiferromagnetism and to flip the magnetic spins to a field-induced ferromagnetism. In a more general case, when magnetic order is more complex than simple ferromagnetism or antiferromagnetism, the ΔT temperature behaviour becomes more complicated, exhibiting features corresponding to the positions of characteristic points T_{eq} . As an example, the temperature behaviour of heat capacity and MCE in rare earth metal dysprosium can be considered—figure 2.10. As is known, upon cooling at $H = 0$, Dy undergoes a transition from a paramagnet to a helicoidal antiferromagnetic state at about 180 K and then from this state to a ferromagnetic state at about 90 K (Taylor and Darby 1972, McEwen 1991). As one can see from figure 2.10(a), at $H = 1$ T there are three characteristic temperatures: $T_{\text{eq}1} = 91.9$ K due to the shifting of a first-order antiferromagnetic–ferromagnetic transition to higher temperature in the magnetic field; and $T_{\text{eq}2} = 178.8$ K and $T_{\text{eq}3} = 181.3$ K, which appear because of the shift of an antiferromagnetic–paramagnetic transition to a lower temperature in the magnetic field. The magnetic field of 2 T is high enough to destroy antiferromagnetic structure and induce noncollinear magnetic structure. This process yields $T_{\text{eq}1} = 126.9$ K at 2 T. Since 2 T is not enough to destroy the noncollinear structure, the upper heat capacity maximum is still shifting to the lower temperature range, which gives $T_{\text{eq}2} = 173.9$ K and $T_{\text{eq}3} = 181.2$ K at 2 T. In the field of 5 T the noncollinear magnetic structure is completely suppressed and there is only field-induced ferromagnetic structure in Dy. So, at 5 T only one characteristic temperature $T_{\text{eq}} = 181$ K remains. All three characteristic temperatures persist on the $\Delta T(T)$ dependences of Dy, for a magnetic field changes from 0 to 1 T and from 0 to 2 T—see figure 2.10(b). The MCE in these fields displays one minimum and two maxima, respectively. For the field change from 0 to 5 T there is only one maximum on the MCE temperature dependence in

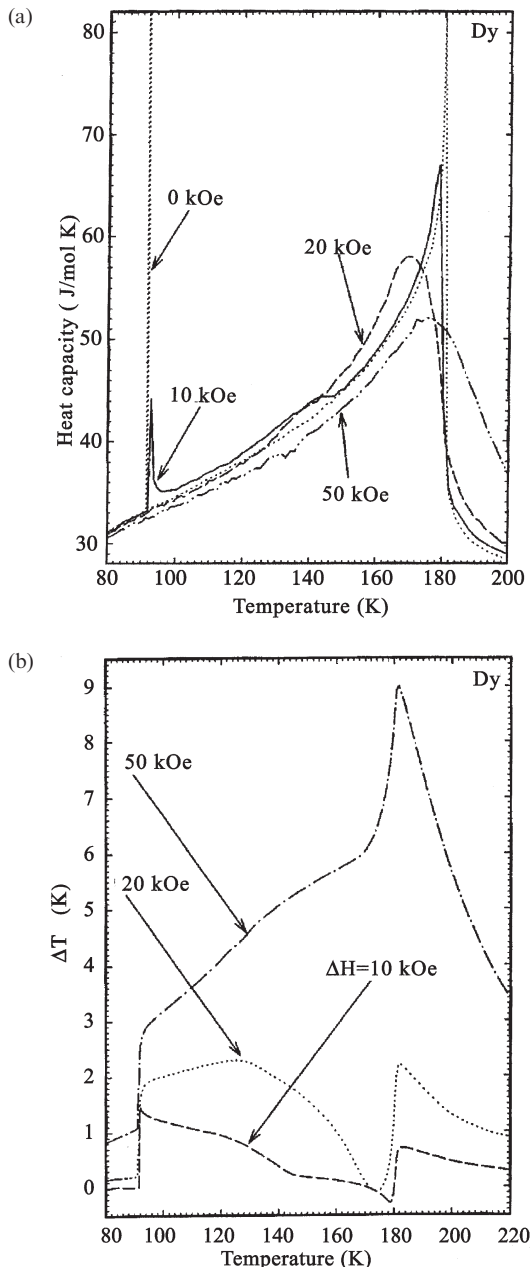


Figure 2.10. The heat capacity temperature dependences of polycrystalline Dy at $H = 0$, 10, 20 and 50 kOe (a); and the MCE temperature dependences for a magnetic field change of 10, 20 and 50 kOe (b) (Tishin *et al* 1999a). (Copyright 1999 by the American Physical Society.)

Dy. The experimental results show that in Dy the characteristic temperatures T_{eq} also practically coincide with the corresponding temperatures T_{peak} .

In the work of Tishin (1998a) the behaviour of magnetic phase transitions under the influence of the heat evolving due to the MCE was discussed. As characteristic examples the transition paramagnetism (PM)—ferromagnetism (FM) in gadolinium and paramagnetism—antiferromagnetism (AFM) and antiferromagnetism—ferromagnetism in dysprosium were considered. In practice, experimental magnetic and heat experimental measurements are conducted under either isothermal or adiabatic conditions. The former conditions can be easily achieved by static and/or quasi-static magnetic field measurements. For example, this is the case for a very slowly increasing field in a situation where a material has the possibility of keeping its zero field temperature due to heat exchange with the surroundings. On the other hand, under adiabatic conditions, the temperature of the magnetic material being measured could be changed by the MCE. For experimental measurements this situation is often realized, for example, in pulsed field studies. According to the data of Levitin *et al* (1997) the transition between isothermal and quasi-adiabatic circumstances occurs in a range of fields increasing with rates from 200 to 2 MOe/sec (for situations where the sample is located in liquid nitrogen or helium). As was shown by Dan'kov *et al* (1997), in a nitrogen gas surrounding a field, a sweep rate of about 900 kOe/sec clearly corresponds to the adiabatic condition.

If we consider the $H-T$ phase diagram of a magnetic material under atmospheric pressure and isothermal conditions, then the concrete magnetic state is determined by the values of the zero field temperature and the applied magnetic field. As is known, the magnetic phase transition temperatures are affected by the magnetic field—in ferromagnets the Curie temperature shifts in the presence of magnetic field towards the high temperature range, and in antiferromagnets the Néel temperature shifts in the opposite direction. In the case of adiabatic conditions the initial temperature in a magnetization process can be changed due to the MCE, so determination of the real $H-T$ coordinates also requires taking into account the value of the MCE. Simultaneous action of these two factors (the MCE and the magnetic transition temperatures shift) can make the question about the real magnetic state of the sample quite complicated—for example, if the point corresponding to the magnetic material state can cross the curve of a first-order phase transition and/or if the rate of increase of the field is too large (for example, 650 MOe/sec as in the report of Nojiri *et al* 1995).

Dan'kov *et al* (1998) measured the position of T_C in different magnetic fields and the MCE in Gd. The value of T_C was determined to be 294 K at $H = 0$ and 339 K at 75 kOe, while the MCE value at 293 K (1 K below T_C) was 15.5 K for $\Delta H = 75$ kOe. Thus, the initial temperature of 293 K shifts in Gd to 308.5 K due to the MCE, which is still lower than $T_C = 339$ K at

75 kOe. It is possible to assume that, first, the value of the MCE in the vicinity of T_C is limited by the position of the Curie temperature $T_C(H)$ and, second, that under adiabatic conditions Gd cannot change its initial magnetic state. Since the magnetic behaviour of rare earth metal Gd is characteristic ferromagnetic behaviour, these assumptions can be extended to other ferromagnets. The first assumption implies that the value of the magnetic transition temperature shift under the action of the magnetic field can be regarded as the upper limit of the specific MCE value per ΔH ($\Delta T/\Delta H$). This suggests a very easy and quick experimental method for the searching of magnetic materials with a large MCE. It is necessary only to measure a shift of T_C value under the action of a magnetic field using a standard experimental method of measuring of initial susceptibility. If this shift of the Curie point has a value larger than 0.6 K/kOe (this is the $\Delta T_C/\Delta H$ value for Gd (Tishin *et al* 2002)) then it is natural to suppose that the MCE value in this material will be more than in Gd. Thus, it can be concluded that the value of the MCE in the vicinity of the magnetic transition point from the paramagnetic to ferromagnetic state is determined by the behaviour of the phase transition line.

An analogous consideration with the same conclusions was made for magnetic phase transitions PM–HAFM and HAFM–FM in Dy on the basis of experimental data on magnetization and MCE (Herz and Kronmüller 1978, Nikitin *et al* 1991b, Alkhafaji and Ali 1997). Tishin (1998a) concluded that FM or AFM states of a magnetic material could not be changed, under adiabatic magnetization conditions, by the MCE that leads to the additional shift of the initial temperature. The MCE cannot exert any influence on the initial magnetic phase state, which can be transformed by applying a magnetic field.

The question about influence of the MCE on the first-order magnetic phase transition was considered by Pecharsky *et al* (2001)—see section 2.5. It was shown that the value of the MCE near the transition is limited by the position of the transition temperature, which is determined by the magnetic field. The heat evolved due to the MCE cannot warm the material above the temperature of transition because the heat capacity at the transition point becomes infinite.

2.8 MCE in inhomogeneous ferromagnets

Belov (1961a) considered spatially inhomogeneous ferromagnets in the framework of the Landau theory of the second-order phase transitions (see section 2.2). It was shown that the inhomogeneity is one of the reasons for the appearance of magnetization ‘tails’ above the Curie temperature. The main idea of Belov’s model was that the local value of the Curie temperature has spatially inhomogeneous distribution $T(\vec{r})$.

Wagner *et al* (1996) and Silin *et al* (1995) used this model for calculation of the mean magnetization $\langle I \rangle$ as a function of the magnetic field and temperature in the region of the magnetic phase transition. The thermodynamic potential (its magnetic part) was chosen in the form

$$\Phi_M(T, M) = \int_0^1 ds W(s) \left\{ \frac{d_0}{2} (T - T_C(s)) M^2 + \frac{\beta}{4} M^4 \right\} \quad (2.109)$$

where s is the parameter responsible for the value of the local Curie temperature, $W(s)$ is the distribution function of the s parameter, I is the local magnetization and $T_C(s)$ was determined as $T_C(s) = T_C - s\Delta T_C$. Using the potential (2.109) the equation for the local magnetization was obtained as

$$H = \alpha_\Theta(T - T_C - s\Delta T_C)I + \beta I^3 \quad (2.110)$$

on the basis of which the mean magnetization was then calculated as

$$\langle I \rangle = \int_0^1 ds W(s)I(s). \quad (2.111)$$

With the help of the results of Wagner *et al* (1996) for $\langle I \rangle$, Romanov and Silin (1997) calculated by equation (2.16) (the dependence of heat capacity on H and T was neglected) the temperature and field dependences of the MCE in the region of the magnetic phase transition for an inhomogeneous ferromagnet. Because the obtained equations were rather complex, we only show in figure 2.11 the results of numerical calculations made under assumptions that $W(s) = 1$ and ΔT_C , characterizing the distribution of T_C values and the length of magnetization tails, is equal to $0.1T_C$. Figure 2.11 shows the dependence of the quantity $\Delta T\beta 10^2/(\alpha^2 T_C)$, which is proportional to the MCE, on T/T_C , and the strength of the magnetic field is characterized by the dimensionless parameter $t_0 = [3\beta/(\alpha\Delta T_C)](H/2\beta)^{2/3}$. The curves marked 1 were calculated by the simple Landau theory and the curves marked 2 for an inhomogeneous ferromagnet in the framework of the model described above.

It was established that near the Curie point $\Delta T(T)$ dependences for an inhomogeneous ferromagnet were more gradual and the MCE was weaker than for a homogeneous one—see figure 2.11. In the first case the ΔT peak is observed in the temperature region of the magnetization tail and in the second case at the Curie temperature, so the inhomogeneity shifts the temperature of the MCE peak from the Curie temperature. An increase in the magnetic field leads to a shift of the MCE maximum to higher temperatures and increases the difference in the $\Delta T(T)$ behaviour. Calculations showed that the nature of the $W(s)$ function had a minor effect on the $\Delta T(T)$ behaviour for the case of strong fields, but had a stronger effect for relatively weak fields.

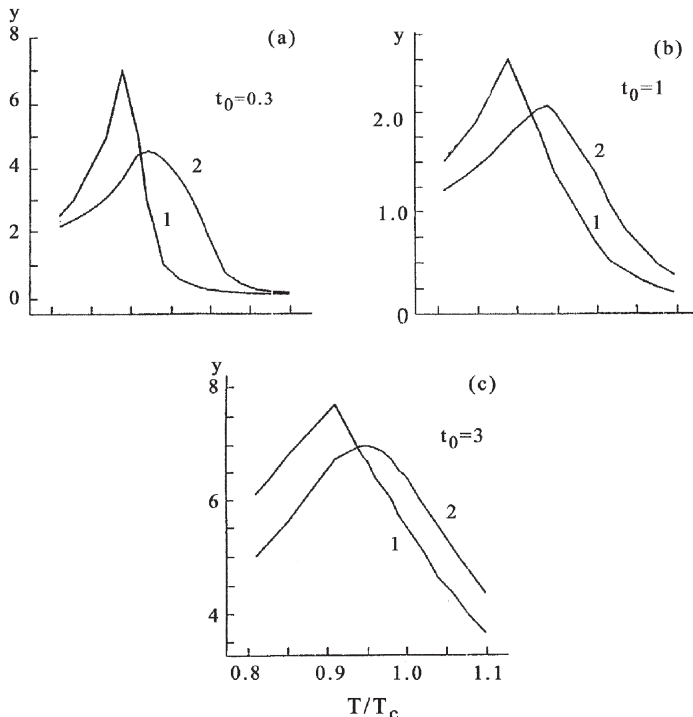


Figure 2.11. Dependence of the dimensionless magnetocaloric effect $y = \Delta T \beta 10^2 / (\alpha^2 T_C)$ on reduced temperature T/T_C for different values of the parameter $t_0 = [3\beta/(\alpha\Delta T_C)] \times (H/2\beta)^{2/3}$ characterizing the strength of magnetic field: (a) $t_0 = 0.3$; (b) $t_0 = 1$; (c) $t_0 = 3$. Curves 1 correspond to the homogeneous ferromagnet and curves 2 to the inhomogeneous ferromagnet (Romanov and Silin 1997).

2.9 MCE in superparamagnetic systems

The MCE enhancement was observed experimentally in nanocomposite magnetic materials containing nanosize particles or crystallites—see Kokorin *et al* (1984), McMichael *et al* (1993b), Shull *et al* (1993), Shull (1993a,b), Shao *et al* (1996a,b) and section 10. This effect was discussed in the frameworks of the mean field approximation in the classical limit.

In the works of McMichael *et al* (1992) and Shull (1993a,b) a superparamagnetic system was taken to consist of monodispersed and noninteracting magnetic clusters (particles) uniformly dispersed in a nonmagnetic matrix. Each cluster contains a certain number of magnetic atoms. The magnetic entropy change of a classical system due to the change of an external magnetic field from zero to H can be calculated by equation (2.92) and

for weak fields and high temperatures ($x \ll 1$) by equation (2.90):

$$\Delta S_M = -\frac{N\mu^2}{6k_B} \frac{H^2}{T^2} \quad (2.112)$$

where N is the number of magnetic moments in the system and μ is the size of magnetic moment. As is seen from equation (2.112), ΔS_M (and consequently the MCE) can be made larger if μ is made larger and N is simultaneously made smaller (to keep the saturation magnetic moment $M_0 = N\mu$ constant), because of the squared dependence of ΔS_M on μ and only a linear dependence on N . For a superparamagnet it can be written (Shull 1993a) as

$$\Delta S_M = -\frac{n((N/n)\mu)^2}{6k_B} \frac{H^2}{T^2} \quad (2.113)$$

where n is the number of particles and $(N/n)\mu = \mu_c$ is the magnetic moment of the particle. The factor $n((N/n)\mu)^2$ in equation (2.113) may be much larger than $N\mu^2$ in equation (2.112).

The optimum value of the particle magnetic moment at given T and H can be obtained from consideration of the function $\Delta S_M/x$, where ΔS_M is determined by equation (2.92) (McMichael *et al* (1992)). This function has a maximum at

$$x_{\max} = \frac{\mu_c H}{k_B T} \approx 3.5 \quad (2.114)$$

where ΔS_M is given by

$$\Delta S_M = -0.272 \frac{M_0 H}{T} \quad (2.115)$$

where $M_0 = \mu_c N$. Equation (2.114) determines an optimal particle size at given H and T . For typical values $T = 300$ K and $H = 10\text{--}50$ kOe it lies in the nanometer range (Chen *et al* 1994).

Integrating the Maxwell relation (2.9a) from zero to H and from $T = 0$ to $T = \infty$ (where $M = 0$), one can derive a sum rule:

$$\int_0^\infty \Delta S_M dT = -M_0 H. \quad (2.116)$$

Equation (2.116) determines the form of the $\Delta S_M(T)$ curve and implies that for materials with the same saturation magnetic moment M_0 , those with higher ΔS_M at a particular temperature will have lower ΔS_M in the rest of the temperature range (McMichael *et al* 1992).

McMichael *et al* (1992) calculated the magnetic entropy change caused by the removal of a magnetic field of 10 kOe for different arrangements of Gd atoms (spin equal to 7/2). For the calculations the mean field quantum mechanical expression (see equation (2.63)) was used. The results for systems consisting of individual atoms and of magnetic clusters of various sizes (10, 30 and 100 atoms) are presented in figure 2.12. The accuracy of

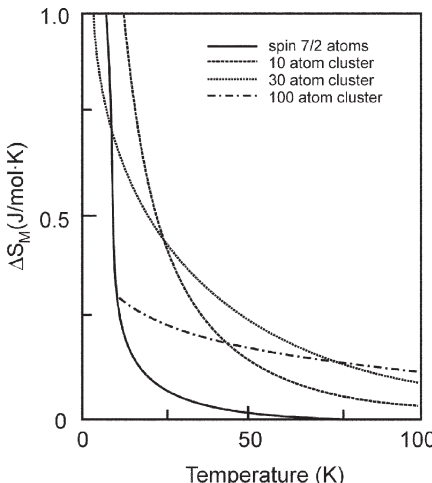


Figure 2.12. Temperature dependences of the magnetic entropy change induced by the removal of a magnetic field of 10 kOe, calculated for systems with different arrangements of 7/2 spin atoms (Shull *et al* 1993). (Reprinted from Shull *et al* 1993, copyright 1993 with permission from Elsevier.)

the calculations is confirmed by the closeness of the calculated curve for the individual atoms to the experimental one measured on gadolinium gallium garnet (Shull *et al* 1993). One can see an obvious enhancement of ΔS_M at high temperatures in clustered systems. The behaviour of $\Delta S_M(T)$ dependences is in accordance with the sum rule (2.116).

It should be noted that the difference between the magnetic entropy changes calculated in quantum and classical approaches is determined by the expression (McMichael *et al* 1992)

$$\Delta(\Delta S_M) = Nk_B \left[1 - \frac{g_J\mu_B H}{2k_B T} \coth \frac{g_J\mu_B H}{2k_B T} + \ln \left(\frac{\sinh \left(\frac{g_J\mu_B H}{2k_B T} \right)}{\left(\frac{g_J\mu_B H}{2k_B T} \right)} \right) \right]. \quad (2.117)$$

For example, for $H = 50$ kOe, $g_J = 2$ and $T = 4.2$ K, the value of $\Delta(\Delta S_M)$ is approximately $0.8 \text{ J mol}^{-1} \text{ K}^{-1}$.

Equation (2.113) was obtained for the case of cluster magnetic moments independent of temperature. In the opposite case, if $\mu_c = \mu_c(T)$, equation (2.113) becomes (Kokorin *et al* 1984)

$$\Delta S_M = - \frac{n\mu_c^2 H^2}{6k_B T^2} \left(1 - \frac{T}{\mu_c} \frac{\partial \mu_c}{\partial T} \right). \quad (2.118)$$

The second term in the parentheses in equation (2.118) can have essential value in the vicinity of the Curie point of magnetic cluster material and lead to an additional contribution to ΔS_M in this region.

Chen *et al* (1994) considered the process of nanocomposite system formation by deposition of magnetic and nonmagnetic particles on a substrate. The possibility of formation of chains, consisting of magnetic particles (clusters) touching each other, in the nonmagnetic matrix was taken into account. These chains increase the effective magnetic cluster size, causing a deviation from the optimum value and a reduction of ΔS_M . The number and length of the chains forming in a nanocomposite during the random deposition process was numerically simulated by a simple computer model. On the basis of these data the magnetic entropy change was calculated by the equation

$$\frac{T\Delta S_M}{M_0 H} = \sum_i \frac{n_i}{n} \frac{1}{x} \left[1 - m_i x \coth(m_i x) + \ln \frac{\sinh(m_i x)}{m_i x} \right] \quad (2.119)$$

where m_i is the number of clusters per chain, n_i is the number of m_i type chains and $n = \sum_i n_i m_i$ is the total number of clusters.

As was shown, the chain formation reduces ΔS_M . The value of this reduction depends on the degree of dilution of the nanocomposite by the nonmagnetic particles, which is determined by the ratio of the number of nonmagnetic particles in the composite to the number of magnetic particles. The general dependence is such that for large clusters ΔS_M increases with increasing dilution and vice versa for small clusters. The cluster size (and the value of x), corresponding to the maximum magnetic entropy change, increases with increasing dilution. Figure 2.13 illustrates these results.

Later Chen *et al* (1995) took into account the ability of particles to migrate to the substrate during the deposition and considered the influence of the substrate temperature on the chain formation. To simulate the process of nanocomposite fabrication, Chen *et al* (1995) used the event-driven Monte Carlo technique. It was shown that a low substrate temperature

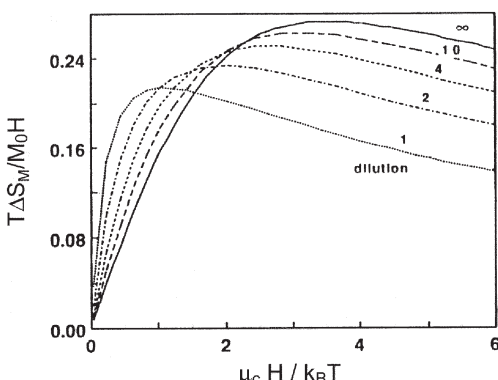


Figure 2.13. Calculated dependence of the reduced magnetic entropy change (the field varies from H to 0) on $x = \mu_c H / k_B T$ at a different dilution degree (numbers near the curves) (Chen *et al* 1994). (Reprinted from Chen *et al* 1994, copyright 1994, with permission from Elsevier.)

impedes chain formation, thus leading to larger values of ΔS_M for a given value of dilution. Chen *et al* (1995) also proposed the way to reduce the effect of chain formation, by using unipolar electrostatic charging of the magnetic particles. The calculation results showed that this method could substantially reduce the decrease of ΔS_M caused by chain formation.

If there is some interaction between particles (dipole and/or exchange interaction) it displays behaviour similar to that of ferromagnets, with an effective interaction temperature T_I , analogous to the Curie temperature T_C . Mørup *et al* (1983) called such systems ‘superferromagnets’. Above T_I the material is superparamagnetic and below T_I long-range order between the clusters occurs. In the superparamagnetic region, ΔS_M induced by a field change from 0 to H can be obtained, analogous to equation (2.91) (Shull, 1993) by the equation

$$\Delta S_M = \frac{n((N/n)\mu)^2 H^2}{6k_B(T - T_I)^2}. \quad (2.120)$$

T_I was defined by Mørup and Christiansen (1993) as

$$T_I = \frac{I_M I^2}{3k_B} \quad (2.121)$$

where I_M is the mean coupling constant. According to Shao *et al* (1996a), T_I should be less than the T_C of the particle material since I_M and magnetization I have reduced values in this state. Analogous to the superparamagnetic case, the factor $n((N/n)\mu)^2$ in equation (2.121) may become much larger than $N\mu^2$ in equation (2.91). The latter is valid for a ferromagnet consisting of single magnetic atoms. This implies that ΔS_M above T_I in a system with magnetically interacting clusters can become substantially larger than in a simple ferromagnet above T_C . The condition of maximum ΔS_M (2.114) is also valid in the case of superferromagnet.

MFA calculations (Bennett *et al.* 1992, McMichael *et al* 1993a,b) show that, at T_I and below T_I , ΔS_M is smaller in clustered systems than in simple ferromagnets. Bennett *et al* (1992) made calculations in the framework of the Monte Carlo method, which is more correct near the Curie temperature than the MFA. Figure 2.14 shows the theoretical results of ΔS_M induced by the removal of a magnetic field of 10 kOe. ΔS_M was calculated for a ferromagnetic system consisting of individual moments of $8\mu_B$ and for interacting magnetic clusters of 30 and 100 atoms. MFA and Monte Carlo results are in good agreement, although in the MFA an adjustment of the ordering temperature was needed. ΔS_M near the ordering temperature in the 100-atom cluster system was about 3.6 times lower than in a simple ferromagnet. In the paramagnetic region ΔS_M in the clustered system was much larger than that in the ferromagnet, as was predicted by the sum rule (2.116). A broader maximum in the ΔS_M curve is observed for the systems with

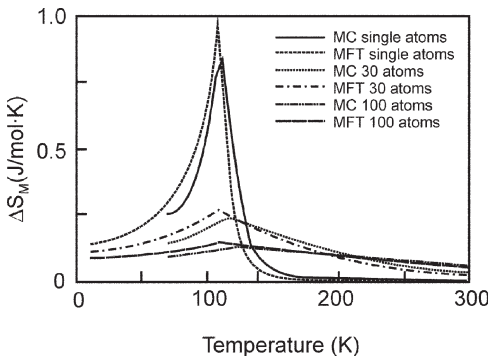


Figure 2.14. Temperature dependences of the magnetic entropy change induced by the removal of a magnetic field of 10 kOe, calculated by mean-field theory (MFT) and the Monte Carlo (MC) method for a ferromagnetic material, and for systems with interacting clusters, which have the same ordering temperature of 108 K (Bennett *et al* 1992).

larger clusters. Experimental results on the MCE in superparamagnetic systems will be considered in chapter 10.

2.10 Anisotropic and magnetoelastic contributions to the MCE

Above we considered the MCE mainly related to the paraprocess. To calculate the magnetocrystalline contribution to the MCE displaying itself in the region of magnetization vector rotation, it is necessary to take into account in the Gibbs energy the anisotropic part, which can be written as

$$G_a = \sum_i K_i \psi_i \quad (2.122)$$

where K_i is the anisotropy constant (it is assumed that it does not depend on magnetic field) and ψ is a function of the orientation of the spontaneous magnetization vector. From equation (2.8a) it follows that the infinitesimal anisotropic magnetic entropy change caused by the rotation of the spontaneous magnetization vector in the magnetic field can be presented as

$$dS_{Ma} = - \sum_i \left(\frac{\partial K_i}{\partial T} \right)_H d\psi_i. \quad (2.123)$$

The corresponding MCE can be calculated from equation (2.74) as follows:

$$dT_a = \frac{T}{C_H} \sum_i \left(\frac{\partial K_i}{\partial T} \right)_H d\psi_i. \quad (2.124)$$

For a cubic crystal the energy of magnetocrystalline anisotropy can be presented by the formula

$$G_a(T, H) = K_1(T) \sum_{i \neq j} \alpha_i^2 \alpha_j^2 + K_2(T) \prod_i \alpha_i^2 \quad (2.125)$$

where α_i are the direction cosines of the spontaneous magnetization vector \vec{I}_s with respect to the crystal axes, and K_1 and K_2 are the magnetocrystalline anisotropy constants. For a hexagonal crystal the anisotropic part of the Gibbs free energy can be expressed as

$$G_a = K_1 \sin^2 \Theta + K_2 \sin^4 \Theta + K_3 \sin^6 \Theta + K_6 \sin^6 \Theta \cos 6\phi \quad (2.126)$$

where Θ is the angle between the spontaneous magnetization vector \vec{I}_s and the c-axis, ϕ is the angle between the basal-plane component of \vec{I}_s and the a-axis, and K_i are the anisotropy constants. The last term in equation (2.126) describes the basal-plane anisotropy, which is usually small, and can be neglected.

Calculations of ΔS_{ma} and ΔT_a on the basis of equations (2.122)–(2.126) were made by Akulov and Kirensky (1940), Ivanovskii (1959), Ivanovskii and Denisov (1966a,b), Pakhomov (1962) and Nikitin *et al* (1978). The magnetocrystalline contribution to the MCE has the following forms for cubic and hexagonal crystals respectively:

$$dT_a = \frac{T}{C_H} \left[\left(\frac{\partial K_1}{\partial T} \right)_H d \sum_{i \neq j} \alpha_i^2 \alpha_j^2 + \left(\frac{\partial K_2}{\partial T} \right)_H d \prod_i \alpha_i^2 \right] \quad (2.127)$$

$$dT_a = \frac{T}{C_H} \left[\left(\frac{\partial K_1}{\partial T} \right)_H d \sin^2 \Theta + \left(\frac{\partial K_2}{\partial T} \right)_H d \sin^4 \Theta + \left(\frac{\partial K_3}{\partial T} \right)_H d \sin^6 \Theta \right]. \quad (2.128)$$

Akulov and Kirensky (1940) integrated equation (2.127), taking into account the first term in the brackets and considering the value T/C_H constant, and obtained the formula for the MCE caused by change of direction cosines on $\Delta \sum_{i \neq j} \alpha_i^2 \alpha_j^2$:

$$\Delta T_a = \frac{T}{C_H} \left(\frac{\partial K_1}{\partial T} \right)_H \Delta \sum_{i \neq j} \alpha_i^2 \alpha_j^2. \quad (2.129)$$

To calculate the field dependence of ΔT_a it is necessary to calculate the field dependence of $d\psi_i$. The equilibrium direction of I_s in a magnetic field is determined by the minimum of the total energy of a crystal. Using this condition Ivanovski (1959, 1960) calculated the field dependence of ΔT_a in cubic and hexagonal crystals, taking into account in the total energy of a crystal the anisotropy and the magnetic field energies. The formulae describing the dependence of dT_a on H in cubic and hexagonal crystals, respectively,

have the form

$$dT_a = \frac{T}{C_H} \left(\frac{\partial K_1}{\partial T} \right)_H \frac{4K_1}{I_s} P(\psi) \frac{dH}{H^2} \quad (2.130)$$

$$dT_a = \frac{T}{C_p I_s} \left[\left(\frac{\partial K_1}{\partial T} \right)_H (P_1 K_1 + P_2 K_2) + \left(\frac{\partial K_2}{\partial T} \right)_H (R_1 K_1 + R_2 K_2) \right] \frac{dH}{H^2} \quad (2.131)$$

where

$$P_1 = 4 \sin^2 \Theta_1 \cos^2 \Theta_1, \quad P_2 = 8 \sin^4 \Theta_1 \cos^2 \Theta_1$$

$$R_1 = 8 \sin^4 \Theta_1 \cos^2 \Theta_1, \quad R_2 = 16 \sin^6 \Theta_1 \cos^2 \Theta_1.$$

$P(\psi)$ is a complex function of I_s orientation; Θ_1 is the angle between the hexagonal axis and the magnetic field direction. Under derivation of equations (2.130) and (2.131) it was supposed that the anisotropy energy of a cubic crystal contains only a term with K_1 and that of a hexagonal crystal—terms with K_1 and K_2 .

To obtain ΔT_a in polycrystals, equations (2.130) and (2.131) were averaged over uniform space distribution of the crystallite axes, which gave the equations for cubic and hexagonal materials (Ivanovskii 1960, Pakhomov 1962):

$$\Delta T_a = -\frac{T}{C_H I_s} \frac{16}{105} K_1 \left(\frac{\partial K_1}{\partial T} \right) \left(\frac{1}{H} - \frac{1}{H_0} \right) \quad (2.132)$$

$$\begin{aligned} \Delta T_a = & -\frac{T}{C_H I_s} \left[\left(\frac{8}{15} K_1 + \frac{64}{105} K_2 \right) \left(\frac{\partial K_1}{\partial T} \right)_H \right. \\ & \left. + \left(\frac{64}{105} K_1 + \frac{256}{315} K_2 \right) \left(\frac{\partial K_2}{\partial T} \right)_H \right] \left(\frac{1}{H} - \frac{1}{H_0} \right) \end{aligned} \quad (2.133)$$

where H_0 is the initial magnetic field value in the region of magnetization vector rotation.

Pakhomov (1962) took into account, in the anisotropic energy of a cubic crystal, the term with K_2 and also included the total energy of the crystal magnetoelastic energy in the form

$$G_{me} = -\frac{3}{2} p_\sigma \lambda_{100} \sum_i (\alpha_i^2 \gamma_i^2 - \frac{1}{3}) - 3p_\sigma \lambda_{111} \sum_{i \neq j} \alpha_i \alpha_j \gamma_i \gamma_j \quad (2.134)$$

where p_σ is the linear mechanical strain applied in the direction with the direction cosines γ_i , and λ_{100} and λ_{111} are magnetostriction constants. If the direction of the strain coincides with that of a magnetic field then the equation for the MCE in the region of magnetization vector rotation has the form (Pakhomov 1962)

$$\Delta T_r = -\frac{T}{C_H I_s} (A + Bp_\sigma + Cp_\sigma^2) \left(\frac{1}{H} - \frac{1}{H_0} \right) \quad (2.135)$$

where

$$\begin{aligned} A &= \left(\frac{\partial K_1}{\partial T} \right)_H \left(\frac{16}{105} K_1 + \frac{32}{1155} K_2 \right) + \left(\frac{\partial K_2}{\partial T} \right)_H \left(\frac{16}{1155} K_1 + \frac{16}{5005} K_2 \right) \\ B &= \frac{8}{35} \left(\frac{\partial K_1}{\partial T} \right)_H (\lambda_{100} - \lambda_{111}) + \frac{8}{385} \left(\frac{\partial K_2}{\partial T} \right)_H (\lambda_{100} - 2\lambda_{111}) \\ &\quad + \frac{3}{2} \left(\frac{\partial \lambda_{100}}{\partial T} \right) \left(\frac{16}{105} K_1 + \frac{16}{1155} K_2 \right) - 3 \left(\frac{\partial \lambda_{111}}{\partial T} \right) \left(\frac{8}{105} K_1 + \frac{8}{1155} K_2 \right) \\ C &= \frac{3}{2} \left(\frac{\partial \lambda_{100}}{\partial T} \right) \left(\frac{8}{35} \lambda_{100} - \frac{2}{5} \lambda_{111} \right) - 3 \left(\frac{\partial \lambda_{111}}{\partial T} \right) \left(\frac{4}{35} \lambda_{100} - \frac{16}{315} \lambda_{111} \right). \end{aligned}$$

ΔT_r consists of two contributions, one of which represents the anisotropic part of the MCE considered above (note that for $K_2 = 0$ and $p_\sigma = 0$ equation (2.135) transforms to equation (2.132)) and the strain dependent part with coefficients B and C .

2.11 Heat capacity

The heat capacity C_x at constant parameter x is defined by equations (2.10) and (2.12). Let us first consider a nonmagnetic material. In this case there are two principal heat capacities— C_p (at constant pressure) and C_V (at constant volume) (Swalin 1962, Bazarov 1964):

$$C_p = \left(\frac{\delta Q}{dT} \right)_p = T \left(\frac{\partial S}{\partial T} \right)_p \quad (2.136a)$$

$$C_p = \left(\frac{\delta Q}{dT} \right)_V = T \left(\frac{\partial S}{\partial T} \right)_V. \quad (2.136b)$$

As one can see from equation (2.2), heat capacity at constant volume can also be calculated as

$$C_V = \frac{dU}{dT}. \quad (2.137)$$

With the help of thermodynamic relations it can be shown that the difference between C_p (which is usually measured in experiment) and C_V is determined by the equation

$$C_p - C_V = T \left(\frac{\partial P}{\partial T} \right)_V \left(\frac{\partial V}{\partial T} \right)_p. \quad (2.138)$$

For solids it is more convenient to present equation (2.138) in the form where the difference is expressed through the coefficient of thermal expansion α_T

and isothermal compressibility κ (Swalin 1962, Kittel 1986):

$$C_p - C_V = \frac{9\alpha_T^2}{\kappa} VT. \quad (2.139)$$

This difference is small in most solids (about 5% at room temperature) and it rapidly decreases as the temperature is lowered. It should be noted that in ideal gas $C_p - C_V = R$, where R is the gas constant.

From the statistical theory point of view the heat capacity of a system consisting of N particles can be calculated from equations (2.7a), (2.12) and (2.33) (Swalin 1962, Kittel 1986) as

$$C_V = k_B N T \left(\frac{\partial^2 (T \ln Z)}{\partial T^2} \right)_V \quad (2.140)$$

where Z is a partition function of the system.

In the general case the total heat capacity of a matter can be presented as a sum of three contributions (see equation (2.61)), namely lattice C_l , electronic C_e and magnetic C_H contributions.

In the framework of Debye's model the mole lattice heat capacity of a solid body (with one atom in a molecule) at constant volume C_l can be presented as (Swalin 1962, Kittel 1986)

$$C_l = 9n_a R \left[\frac{4T^3}{T_D} \int_0^{T_D/T} \frac{x^3 dx}{e^x - 1} - \frac{T_D/T}{e^{T_D/T} - 1} \right] \quad (2.141)$$

where T_D is the Debye temperature and n_a is a number of atoms in a molecular of a substance. Equation (2.141) describes quite well experimental temperature heat capacity behaviour of a variety of substances. At high temperature ($T \gg T_D$) equation (2.141) becomes

$$C_l = 3nR \left[1 - \frac{1}{20} \left(\frac{T_D}{T} \right)^2 + \dots \right] \quad (2.142)$$

and at low temperatures ($T < 0.1 T_D$) it follows from equation (2.141) that

$$C_l = \frac{12\pi^4}{5} n_a R \left(\frac{T}{T_D} \right)^3. \quad (2.143)$$

As one can see from equation (2.142), at high temperatures C_l approaches the value of $3nR$ (the DuLong–Petit limit). For estimation of the heat capacity of alloys and compounds it is possible to use the law of Neumann and Kopp, according to which the molar heat capacity of a compound $A_x B_y$ can be presented as $C_{A_x B_y} = xC_A + yC_B$, where C_A and C_B are the molar heat capacities of the constituent elements (Swalin 1962).

Above room temperature the lattice heat capacity at constant pressure can be represented by the empirical equation (Swalin 1962)

$$C_p = a + bT + cT^{-2} \quad (2.144)$$

where a , b and c are empirical coefficients. For example, for Ag, $a = 21.31 \text{ J/mol K}$, $b = 8.54 \times 10^{-3} \text{ J/mol K}$ and $c = 1.51 \times 10^{-5} \text{ J/mol K}$ (Swalin 1962).

It should be noted that there are some difficulties in describing experimental data by Debye's model, in particular the observed temperature dependence of T_D , which should be constant. The main deficiency of Debye's model is related to neglecting the dispersive character of the solid medium, which is related to discreteness of atomic arrangements in the crystal. These effects are taken into account in the more accurate Born–von Karman model.

The electronic heat capacity is related to the conduction electron subsystem and displays itself in metals at low temperatures. Taking into account Fermi–Dirac statistics of electrons in metals and their band energetic structure, one can obtain the expression for electronic heat capacity (Chikazumi 1964, Gopal 1966, Kittel 1986):

$$C_e = a_e T \quad (2.145a)$$

where coefficient a_e is defined as

$$a_e = \frac{2}{3} \pi^2 k_B^2 V N(E_F) \quad (2.145b)$$

where $N(E_F)$ is the electron density of states at the Fermi level E_F and V is the molar volume. For the model of free electrons (Gopal 1966),

$$a_e = \frac{4\pi^3 m_e k_B^2}{3h^2} \left(\frac{3NV^2}{\pi} \right)^{1/3} = 1.36 \times 10^{-4} V^{2/3} n_e^{1/3} \frac{\text{J}}{\text{mol K}} \quad (2.145c)$$

where m_e is the mass of an electron, h is Plank's constant and n_e is the number of free electrons per atom. Kittel (1986) presented the values of a_e calculated by the free electrons model: for Cu and Ag they are 0.505 and 0.645 mJ/mol K², respectively. The experimental values of a_e were determined to be 0.69–0.92 mJ/mol K² for Cu (Estermann *et al* 1952, Corak *et al* 1955), 0.61–0.68 mJ/mol K² for Ag (Rayne 1954, Corak *et al* 1955), 6.7 mJ/mol K² (Parkinson *et al* 1951), 0.85–1.46 mJ/mol K² (Kok and Keesom 1937), 3.0–3.64 mJ/mol K² (Horowitz *et al* 1952, Clement and Quinell 1952), 13.8 mJ/mol K² for Mn (Guthrie *et al* 1955), 5.0 mJ/mol K² for Fe (Duyckaerts 1939a), 5.0 mJ/mol K² for Co (Duyckaerts 1939b), 7.6 mJ/mol K² for Ni (Busey *et al* 1952), 10.9 mJ/mol K² for Gd (Oesterreicher and Parker 1984), 77 mJ/mol K² for ErCo₂ (Giguere *et al* 1999a), 36.5 mJ/mol K² for YCo₂ and 37 mJ/mol K² for HoCo₂ (Hilschler *et al* 1988), 10.6 mJ/mol K² for LaAl₂ and 4.8 mJ/mol K² for LaNi₂ (von Ranke *et al* 1998a) and 30.6 mJ/mol K² for Pr_{0.7}Ca_{0.3}MnO₃ (Smolyaninova *et al* 2000). Using, for example, experimental values of a_e for Cu and Fe, it is possible to estimate the electronic heat capacity for these metals, which are, at 300 K, ~ 0.2 –0.28 J/mol K and ~ 1.5 J/mol K, respectively. These values are much less than the lattice heat capacity, which can be calculated by equation (2.148): $\sim 1\%$ for Cu and $\sim 7\%$ for Fe. However, because $C_l \approx T^3$ and

$C_e \approx T$, in the low-temperature region C_e becomes greater than C_1 at some temperatures. Equation (2.145a) is valid for $T \ll T_F$, where T_F is the Fermi temperature. For $T > T_F$, the electronic heat capacity C_e approaches the limit of $\frac{3}{2}R$. It should be noted that the typical value of T_F for gas of free electrons in metals is about 10^5 K.

For a magnetic substance the heat capacities related to a magnetic subsystem can be introduced by analogy with C_p and C_V :

$$C_H = \left(\frac{\delta Q}{dT} \right)_H = T \left(\frac{\partial S}{\partial T} \right)_H \quad (2.146a)$$

$$C_M = \left(\frac{\delta Q}{dT} \right)_M = T \left(\frac{\partial S}{\partial T} \right)_M \quad (2.146b)$$

where C_H and C_M are the heat capacities at constant magnetic field and magnetization (magnetic moment), respectively. The difference between C_H and C_M is described by the following equation:

$$C_H - C_M = -T \left(\frac{\partial H}{\partial T} \right)_M \left(\frac{\partial M}{\partial T} \right)_H \quad (2.147)$$

which is analogous to equation (2.138). It should be noted that there is a correspondence between the variables P and V and H and $-M$, respectively.

As shown by Kohlhaas *et al* (1966), the influence of magnetic field on the heat capacity can be determined by means of the relation

$$C_H(T, H) = C_H(T_0, 0) \frac{T}{T_0} \left[1 - \frac{\partial \Delta T}{\partial T} \right] \quad (2.148)$$

where $\Delta T = T - T_0$ is the MCE caused by the magnetic field change. Using equation (2.148), the MCE and zero-field heat capacity data, one could determine the heat capacity in a magnetic field. However, this formula cannot be used for real calculations because the (H, T) coordinates of a point of calculation of the derivation of the MCE are unknown.

The ideal magnetic order (in which, for example, in a ferromagnet all spins are aligned strictly parallel to each other) can exist only in the absence of thermal agitation. At a finite temperature spins decline from their ideal directions, which can be described as an excitation of spin waves. The spin waves can be quantized into magnons and the magnetic excitations can be considered with the help of statistical methods.

For ferromagnets the heat capacity C_M related to the excitation of spin waves (the spin wave heat capacity) can at low temperatures be expressed as (Kittel 1986, Gopal 1966)

$$C_M = c_f N k_B \left(\frac{k_B T}{2I_{ex} S} \right)^{3/2} \quad (2.149)$$

where c_f is a constant defined by a crystal structure type (lattice constant), I_{ex} is the exchange integral, S is the spin of the magnetic atom, and N is the number of the magnetic atoms. So, at low temperatures magnetic contribution to the total heat capacity in ferro- and ferrimagnets is proportional to $T^{3/2}$. For antiferromagnets, the spin wave specific heat is described by the equation (Gopal 1966)

$$C_M = c_a N k_B \left(\frac{k_B T}{2 I_{\text{ex}} S} \right)^3 \quad (2.150)$$

where c_a is the lattice constant. It follows from equation (2.150) that the magnetic contribution to the specific heat in antiferromagnets obeys the T^3 law at low temperatures. The dependence (2.150) is fulfilled in the three-dimensional case, for the case of a two-dimensional antiferromagnet $C_M \approx T^2$ (Ahiezer *et al* 1967).

In the framework of mean field approximation the internal energy U_M related to the magnetic subsystem in the absence of an external magnetic field can be calculated as

$$U_M = - \int_0^{I_s} H_m dI = - \frac{1}{2} w I_s^2 \quad (2.151)$$

where H_m is a molecular field and w is a molecular field coefficient. Magnetic contribution to the heat capacity in a molecular field approximation follows from equations (2.137) and (2.151) (Chikazumi 1964):

$$C_M = - \frac{1}{2} w \frac{dI_s^2}{dT} \quad (2.152)$$

Mean field calculations show that C_M steadily increases from $C_M = 0$ at $T = 0$ K to the maximum value at the Curie temperature T_C . At $T = T_C$ there is a discontinuous drop to zero value of C_M in the temperature range above T_C . The magnetic phase transition in mean field approximation is the second-order phase transition. According to the mean field approximation, the heat capacity change at $T = T_C$, ΔC_M , can be presented as (Foldeaki *et al* 1995)

$$\Delta C_M = N k_B T \frac{5(J+1)}{J^2 + (J+1)^2} \quad (2.153)$$

where N is the number of magnetic atoms. From equation (2.153) it follows that ΔC_M rapidly increases with J increasing, approaching the upper limit of $5Nk_B/2$ (for example, the ΔC_M maximum value amounts to 128 J/kg K for Gd) (Foldeaki *et al* 1995).

According to the Landau theory of the second-order phase transitions (Landau 1958) the magnetic entropy changes due to the occurrence of the spontaneous magnetization below T_C in the absence of a magnetic field can be expressed by formula (2.87). The corresponding change in magnetic

heat capacity can be calculated by equation (2.12) and has the form (Belov 1961a)

$$\Delta C_M = T \alpha_\Theta \frac{\partial I_s^2}{\partial T} = T \frac{(\alpha_\Theta)^2}{2\beta}. \quad (2.154)$$

The experimental behaviour of C_M in ferromagnetic materials near T_C has essential deviations from that predicted by mean field approximation. Among them, the heat capacity ‘tails’ above T_C and the maximum values of C_M at T_C much higher than theoretical should be mentioned.

Statistical models give better results in the description of the C_M behaviour near the transition from paramagnetic to magnetically ordered state. These models involve the calculation of the partition function (see equation (2.32)) on the basis of Heisenberg or Ising magnetic Hamiltonians. For example, in the framework of the two-dimensional Ising lattice the temperature dependence of C_M in the vicinity of T_C has a logarithmic character.

Another heat capacity anomaly displaying itself in the low-temperature region is related to the Schottky effect. Let us suggest that the energy spectrum of a system includes two energy levels separated by the energy ΔE . At the temperature $T \gg \Delta E/k_B$ both energy levels are nearly equally populated, and for $T \ll \Delta E/k_B$ the upper level is almost empty. At $T \approx \Delta E/k_B$ the transitions from lower to upper level will take place in considerable amounts, which will give rise to the internal energy of the system and, consequently, will lead to the appearance of the heat capacity maximum. This peculiarity is superimposed on the other contributions to the heat capacity (lattice, electronic etc.).

In the general case of a system consisting of N particles with energy levels E_1, E_2, \dots, E_m with degeneracies g_1, g_2, \dots, g_m , the Schottky heat capacity C_{Sh} can be calculated by the equation analogous to equation (2.140) (Gopal 1966):

$$C_{Sh} = T \frac{d^2(Nk_B T \ln z)}{dT^2} \quad (2.155)$$

with

$$z = \sum_m g_m \exp\left(-\frac{E_m}{k_B T}\right). \quad (2.155a)$$

For temperatures above the Schottky heat capacity maximum, $C_{Sh}(T)$ behaves like T^{-2} , which allows separation of this contribution from the others.

The Schottky effect can be observed in magnetic materials. A magnetic atom with a total angular momentum quantum number J has $2J + 1$ possible momentum orientations. In the presence of magnetic or any other effective field this degeneracy is removed and the atom has $2J + 1$ discrete energy levels. Magnetic dipole and exchange interactions and crystalline electric

field effects can cause such energy splitting in solids with a magnetic ion energy level separation of about 1 K.

For paramagnets the splitting is caused by an external magnetic field. Paramagnetic salt $\alpha\text{-NiSO}_4\cdot6\text{H}_2\text{O}$ exhibits a heat capacity maximum of $\sim 6.3 \text{ J/mol K}$, related to the Schottky effect, at about 3 K (Stout and Hadley 1964). The experimental results in this compound have good agreement with theoretical calculations.

It should be noted that the Shottky heat capacity peak could arise not only due to the effects related to the electronic system of the atom. Energy splitting (and connected with it the Schottky effect) analogous to that described above can take place for atomic nuclei if they are magnetic. In this case the splitting can be caused by the effective field of interaction between electrons of an atom and the nucleus and by crystalline field effects. Because the nuclear moments are small compared with the electronic moments, the nuclear Schottky anomalies are positioned at much lower temperatures (in the region of 10^{-2} K) than electronic anomalies (in the region 1–10 K). For example, in holmium, the nuclear Schottky heat capacity peak of 7 J/mol K was observed at about 0.03 K (Lounasmaa 1962).

2.12 MCE and elastocaloric effect

An elastocaloric effect (ECE) can be determined as a heat emission or absorption at a constant magnetic field (in a simple case at zero field) and changing external pressure p (Tishin 1998b). If a pressure change takes place under adiabatic conditions then the ECE (like MCE) manifests itself as heating or cooling of a magnetic material by a temperature $\Delta T_{\text{ECE}}(p, T)$. In the case of ECE, equation (2.14) for adiabatic processes and constant H takes the form

$$\frac{C_{H,p}}{T} dT - \left(\frac{\partial V}{\partial T} \right)_{H,p} dp = 0 \quad (2.156)$$

where V is the volume. Thus, for the ECE we can write (Tishin, 1998b)

$$dT_{\text{ECE}} = \frac{T}{C_{H,p}} \left(\frac{\partial V}{\partial T} \right)_{H,p} dp. \quad (2.157)$$

The general form of this formula is close to the thermodynamic equation for a temperature change of a gas in a reversible adiabatic expansion process. Because each real gas has a positive value for $(\partial V / \partial T)_p$, the gases may cool down under adiabatic expansion ($dT < 0$ at $dp < 0$). Using the bulk thermal expansion coefficient, $\alpha_T(T, H, p)$, equation (2.157) can be transformed into

$$dT_{\text{ECE}} = \frac{\alpha_T VT}{C_{H,p}} dp. \quad (2.158)$$

The sign of the ECE is determined by the coefficient α_T . In regular solids the value of α_T is positive and lies in the range 10^{-3} – 10^{-6} K^{-1} . A negative value of α_T occurs, for example, in water at temperatures up to 4°C . In accordance with equation (2.158), it means that in this temperature interval water should cool down under adiabatic stress. For example, this effect, in principle, could lead to freezing of water in micropores of road surfaces under quick pressing of this water (at temperature close to zero) by vehicle tyres.

As is clear from equation (2.157) the ECE value is proportional to the temperature derivative of the volume, and to the pressure change. Thus, a non-zero value of the ECE could be found in any materials for which $(\partial V/\partial T)_p \neq 0$ (with the exception of a case when $T = 0$). From this point of view, the ECE could have a non-zero value in materials without any magnetic structure. This is the first and main difference between the ECE and the MCE.

The second distinction is the sign of the ECE. The volume of most materials increases with increasing temperature ($(\partial V/\partial T)_p > 0$). Thus, under pressure ($dp > 0$) the sign of the ECE should be positive in most cases, in accordance with equation (2.157). It is well known that nonmagnetic solids without electronic or magnetic phase transitions have an almost constant value of $(\partial V/\partial T)_p$ in the temperature region above the Debye temperature T_D . Therefore, at $T > T_D$ the value of the dT_{ECE} is proportional to the temperature T . Obviously, the ECE will have a small absolute value in temperature regions, where $(\partial V/\partial T)_p$ is close to zero. In accordance with equation (2.158), an irregular behaviour of the ECE could be found in the vicinity of temperatures where marked changes of $\alpha_T(T)$ and $C_{H,p}(T)$ take place. Near phase transition the ECE could change its sign, for example, from negative to positive, which could result from the variation of the sign of the coefficient $\alpha_T(T)$ (Tishin 1998b).

Up to the present, the ECE has not been widely studied in different materials. However, simplified thermodynamic equations for the ECE in the case of a steel bar have been obtained by Sychev (1986). It was shown that in first approximation the value of the ECE in the bar does not depend on its length and cross section. However, in a steel wire an ECE value of -0.16 K was reached under a rapidly applied stress up to $2 \times 10^8\text{ Pa}$ (Sychev 1986).

An experimental investigation of the ECE has been made in the work of Annaorazov *et al* (1996). The heat generation measurements in $\text{Fe}_{49}\text{Rh}_{51}$ were conducted under pulsed linear stress applied to the ingot by a couple of hawsers that were attached via two holes to the sample. It was shown that at the temperature corresponding to the AFM–FM phase transition, $T_{\text{AFM–FM}} \approx 315\text{ K}$, the cooling of the ingot was about 5 K under a tensile stress of $5.29 \times 10^8\text{ Pa}$ (Annaorazov *et al* 1996). However, the nature of the negative sign of the ECE has not been explained. The duration of the stress pulses (adiabaticity of the process) and total accuracy of these

measurements are unknown. The results of the work of Annaorazov *et al* (1996) have mostly a fundamental meaning because the compound $\text{Fe}_{49}\text{Rh}_{51}$ cannot be used in any commercial applications due to the extremely high price of Rh. So, the search for other compounds with a large elastocaloric effect is a significant task. From this point of view, lanthanide metals and compounds are of great interest.

In rare earth metals the coefficient $\alpha_T(T)$ has a large value in the vicinity of structural or magnetic phase transitions. In holmium the phase transition from the ferromagnetic conical phase to the antiferromagnetic spiral structure occurs at about 19 K. The specific volume change, dV/V , at this transition is equal to -2.2×10^{-4} in a temperature interval of ~ 0.5 K (Steinitz *et al* 1987). The atomic volume of La changes by 0.5% and 4% at the transitions from dhcp to fcc and from fcc to bcc structures, respectively. The thermal expansion coefficients of Eu and Yb are three times larger than in other rare earth elements (Taylor and Darby 1972). The fcc crystalline form of Sm transforms to dhcp by applying 7×10^8 Pa at room temperature. This structure transformation is accompanied by a volume decrease of about 8% (Jayaraman 1991). The thermodynamic data for structural transitions of lanthanide metals are summarized in table 9.2 of the report of Jayaraman (1991). Thus, the rare earth elements could be considered as a favourable basis for creating materials with large ECE values (Tishin 1998b).

Let us estimate the ECE value in rare earth metals gadolinium and holmium in the vicinity of magnetic phase transitions. According to the experimental data of Dan'kov *et al* (1998) the transition from the paramagnetic to the ferromagnetic phase occurs in Gd at $T_C = 294$ K. Below the spin reorientation temperature, $T_{SR} = 227$ K, the easy magnetization vector departs from the [0001] crystallographic axis. The temperature dependence of the atomic volume in Gd has been studied by Finkel *et al* (1971) and Finkel (1978). Near these magnetic phase transitions the value of the bulk thermal expansion coefficient is close to zero. Thus, the ECE value at the Curie point T_C , as well as around T_{SR} , should be approximately equal to zero. (It is necessary to note that the MCE reaches its maximum value at the Curie point of Gd.) At the same time, the gadolinium has a negative value of $\alpha_T(T)$ (and, therefore, a negative ECE value) in the temperature region between T_C and T_{SR} . Based on the data of Finkel *et al* (1971), Finkel (1978) and Dan'kov *et al* (1998), it is possible to estimate that at $T = 285$ K and $dp = 10^8$ Pa the value of the ECE is negative and approximately close to -0.61 K (Tishin 1998b). Thus, the estimated dT_{ECE} value of Gd has the same order as the ECE value of $\text{Fe}_{49}\text{Rh}_{51}$, $dT_{ECE} \approx -1.7$ K, at pressure $\sim 10^8$ Pa (Annaorazov *et al* 1996).

The experimental data concerning the heat capacity and bulk thermal expansion at the ferromagnetic–antiferromagnetic phase transition at about 19.5 K in holmium can be found in the reports of Lounasmaa and Sundstrom (1966), Steinitz *et al* (1987), Stewart and Collocott (1989) and

White (1989). However, experimental values of the heat capacity presented by Lounasmaa and Sundstrom (1966), Stewart and Collocott (1989) and White (1989) are different at this phase transition. Taking $C_{H,p} \approx 14\text{ J/mol K}$ and $\alpha_T(T) \approx -4.4 \times 10^{-4}\text{ K}^{-1}$, we could obtain a value of the ECE close to -1.1×10^{-2} or -1.2 K at pressure values of $9.8 \times 10^5\text{ Pa}$ ($\sim 10\text{ bar}$) and 10^8 Pa ($\sim 1\text{ kbar}$), respectively (Tishin 1998b). The pressure 10^8 Pa could be compared with a pressure generated by the weight of a middleweight man acting on a magnetic material with a cross section about of $7\text{--}8\text{ mm}^2$. However, it is necessary to note that, according to data of the work of Baazov and Manjavidze (1983), this pressure is close to the value of $\sim 1.7 \times 10^8\text{ Pa}$ (17 kg/mm^2) which determines a breaking point of the rare earth metals under tensile strain.

In these estimations we neglected any influence of pressure on the values of $\alpha_T(T)$ and $C_{H,p}$. Actually, due to the effect of pressure on the elastic and magnetic properties of the rare earth metals (see Jayaraman 1991), the ECE values calculated above should be considered as a first approximation only. In rare earth elements the shifts of magnetic phase transition temperatures reach a few Kelvin under a pressure of $5 \times 10^8\text{ Pa}$ (Jayaraman 1991). However, at present, experimental information about the values of $\alpha_T(T)$ and $C_{H,p}$ at different pressures is unavailable, and therefore more accurate calculations of the ECE are impossible.

As shown above, in accordance with thermodynamics a heat generation and/or absorption in magnets can arise at $dp = 0$ (MCE) as well as at $dH = 0$ (ECE). We have estimated the value of the ECE for the magnetic phase transitions in Gd and Ho. However, it is possible to reach a large value of the ECE and MCE in cases where magnetic and structural phase transitions coexist. For example, the crystal structure of Dy transforms at about 90 K from the $P6_3/mmc$ to the $Cmcm$ type. This transition involves large changes of the interatomic distances and accompanies the transition from HAFM to FM magnetic structures (Taylor and Darby 1972). If in an adiabatic process the pressure and the magnetic field change simultaneously, the total heat evolution can be written down as (Tishin 1998b)

$$dT = dT_{\text{MCE}} + dT_{\text{ECE}} = -\frac{T}{C_{H,p}} \left[\left(\frac{\partial I}{\partial T} \right)_{H,p} dH - \left(\frac{\partial V}{\partial T} \right)_{H,p} dT \right]. \quad (2.159)$$

The MCE and ECE can have positive as well as negative signs. So, the general behaviour of the temperature dependences of the MECE could be complicated. The nature of the ECE is close to that of the MCE in the adiabatic-isochoric process, which was considered by Kuz'min and Tishin (1992).

The influence of pressure on the entropy and temperature of magnetic systems with structural and magnetic first-order transitions was considered by Müller *et al* (1998) and Strässle *et al* (2000a,b). They called this effect the ‘barocaloric effect’. In systems with a structural phase transition, the point

symmetry change is observed which can be induced by temperature change or, for example, by the change of such external parameters as pressure. The point symmetry change leads to the change of a local crystalline electric field, which causes lifting of the $(2J + 1)$ degeneracy of an anisotropic ion (such as, for example, rare earth ions). Due to this effect, in one structural phase an ion can have a nondegenerate ground state and in the other a degenerate one (such as a spin system in an external magnetic field and without it), which causes the system entropy difference in these two phases. The pressure can induce the structural transition and, consequently, the entropy change. The processes described can lead to the temperature change under adiabatic pressuring.

Another manifestation of the barocaloric effect can be observed near the magnetic first-order transition. Here the pressure can cause the magnetic transition temperature shift—the same as is observed in the magnetic field (see figure 2.6) and with the same entropy change. The nature of the temperature change in the adiabatic process in this case is not different from that caused by the magnetic entropy change and considered in section 2.5.

Currently, in various magnetic refrigerator designs only the MCE is utilized. The effects related to crystal lattice expansion or contraction are neglected. However, it is possible to propose, for example, a design of magnetic cryocooler in which a working body is affected by both a magnetic field and by a contraction or expansion due to the magnetostriction (Tishin and Kuz'min 1991, Tishin 1997).

2.13 Adiabatic demagnetization

Although the magnetocaloric effect was discovered in iron (Warburg 1881), historically the main part of experiments on the MCE and magnetic cooling was made at an early stage of the investigations on various paramagnetic salts. This is related to the possibility of achieving temperatures below 1 K with the help of adiabatic demagnetization of these compounds. This question was elucidated in detail in the books and reviews of Garrett (1954), Ambler and Hudson (1955), de Klerk (1955), Vonsovskii (1974), Kittel (1986) etc; here we will only mention it briefly.

The method of achieving temperatures below 1 K with the help of demagnetization of the paramagnetic salts was proposed by Debye (1926) and Giauque (1927). The process of magnetic cooling can be illustrated by figure 2.15, where the total entropy temperature dependences for a paramagnet in zero and nonzero magnetic fields are shown, and fulfilled in two stages. On the first isothermal magnetization stage at the initial temperature T_1 the magnetic field increases isothermally and the system entropy decreases from S_1 to S_2 (the isotherm $a \rightarrow b$), owing to a decrease of the magnetic entropy (the entropy related to the temperature of the system remains

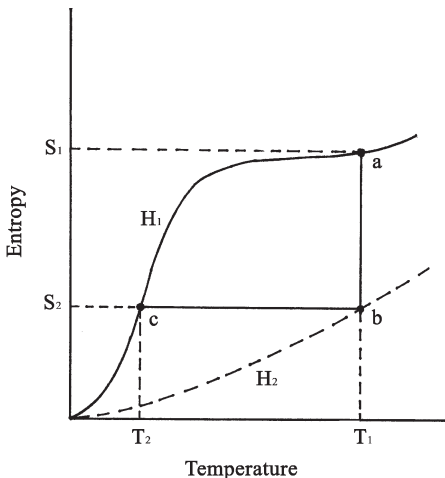


Figure 2.15. The total entropy temperature dependences of a paramagnet in zero ($H_1 = 0$) and nonzero ($H_2 \neq 0$) magnetic fields.

constant). At this time the heat $\Delta Q = T_1(S_2 - S_1) = T_1\Delta S$ is removed from the system in the reversible process. On the second adiabatic demagnetization stage the magnetic field is turned off adiabatically, so that the total entropy remains constant, but the magnetic entropy increases and the entropy determined by the system temperature correspondingly decreases. This means that the system is cooled and passes to the state with new temperature T_2 (the adiabat $b \rightarrow c$ on figure 2.15) and the magnetocaloric effect is $\Delta T = T_2 - T_1$.

It should be noted that the entropies related to the lattice and electronic subsystems are very low in the temperature range where the adiabatic demagnetization of the paramagnetic salts is used, and the entropy of the material is mainly determined by the magnetic entropy. In this case, under adiabatic demagnetization the following condition is valid: $S_M(H_1, T_1) \approx S_M(H_2, T_2)$, where $S_M(H, T)$ is defined by equation (2.64) and H_1 , T_1 and H_2 , T_2 are initial and final values of the magnetic field and temperature. Then from this condition it follows that the final temperature under adiabatic demagnetization of a paramagnetic matter in the low-temperature region (where lattice and electronic contributions to the total entropies are negligible) can be defined by the relation (Kittel 1969, 1986, Vonsovskii 1974)

$$T_2 = T_1 \frac{H_2}{H_1}. \quad (2.160)$$

In real paramagnetic materials there are several factors acting on the magnetic ion, which cause its energy levels to split even in zero external magnetic field—among them the magnetic dipole–dipole and exchange

interactions between the ion magnetic moments, electrostatic fields of the ligands (the crystal field) and interaction of the ion electronic magnetic moment with ion nuclear magnetic moment (hyperfine splitting) should be mentioned (Ambler and Hudson 1955, Vonsovskii 1974). The influence of these factors can be taken into account by consideration of the effective magnetic field, so that H_2 in equation (2.160) will never be equal to zero. This effective magnetic field determines the lower temperature limit, which can be reached by the adiabatic demagnetization and which is about 10^{-2} – 10^{-3} K (Ambler and Hudson 1955, Vonsovskii 1974, Kittel 1986).

The first experiments on the adiabatic demagnetization were made by Giauque and MacDougall (1933), de Haas *et al* (1933a–c) and Kurti and Simon (1934). Giauque and MacDougall (1933) used in their experiments 61 g of gadolinium sulfate ($\text{Gd}_2(\text{SO}_4)_3 \cdot 8\text{H}_2\text{O}$) and reached the minimal temperature of 0.25 K from the initial temperature of 1.5 K with a magnetic field change of 8 kOe. De Haas *et al* (1933a–c) conducted the experiments with cerium fluoride (CeF_3), dysprosium ethylsulfate ($\text{Dy}(\text{C}_2\text{H}_5\text{SO}_4)_3 \cdot 9\text{H}_2\text{O}$) and cerium ethylsulfate ($\text{Ce}(\text{C}_2\text{H}_5\text{SO}_4)_3 \cdot 9\text{H}_2\text{O}$). The lowest temperature achieved was 0.08 K for the last compound (183 mg, the initial temperature 1.35 K, the magnetic field change from 27.6 kOe down to 0.85 kOe). Kurti and Simon (1934) used manganese ammonium sulfate ($\text{MnSO}_4(\text{NH}_4)_2\text{SO}_4 \cdot 6\text{H}_2\text{O}$) and reached 0.1 K from the initial temperature 1 K with the magnetic field change of 6 kOe. The temperature below 1 K in these experiments was determined with the help of magnetic susceptibility measurements and the Curie law extrapolation. In the experiments of de Haas *et al* (1933a–c) the susceptibility was measured by the force-balance method. This method requires the presence of a magnetic field, which is why the final external field was not equal to zero, and which reduced the value of the adiabatic temperature change. In the works of Giauque and MacDougall (1933) and Kurti and Simon (1934) the magnetic susceptibility was measured by the inductance method.

A typical apparatus for experiments on adiabatic demagnetization of the paramagnetic salts is analogous to the apparatus shown in figure 3.14, which is intended for the measurements of the heat capacity temperature dependences. The sample of a paramagnetic salt (1) is in this case secured on a holder with low thermal conductivity in a vacuum chamber (4) (for example, suspended on nylon threads). The sample can be in the form of a single crystal, powder or pressed powder. The vacuum chamber is placed into a cryostat (5) filled with liquid helium, whose temperature is lowered down to ~ 1 K by pumping off the vapour. The electric heater (2), leads (3), thermometer (6) and adiabatic shield (7) in the adiabatic demagnetization apparatus are absent. The heat $\Delta Q = T_1(S_2 - S_1) = T_1\Delta S$, evolved in the sample under magnetization, is taken off to the liquid helium with the help of a heat-exchanging gas (gaseous helium at $\sim 10^{-2}$ – 10^{-3} torr), which fills the vacuum chamber at this stage of the process. After finishing of the

magnetization heat take-off, the heat-exchanging gas is pumped out and the sample is demagnetized adiabatically. It is possible to say that the process described of heat exchanging is fulfilled with the help of a ‘gas heat (thermal) switch’. The heat exchange can also be realized via a metallic heat conductor connecting the sample and liquid helium bath. The heat contact in this case can be disconnected mechanically or by a superconducting thermal switch (Heer and Daunt 1949, Collins and Zimmerman 1953). The operational principle of the last device is based on the fact that the heat conductivity of a superconductor in the low-temperature range in the normal state is much higher than in the superconducting one. The superconducting heat switch itself consists of a piece of superconducting wire and is turned on by application of a magnetic field with a value above the threshold one.

It is also possible to cool down other substances with the help of the paramagnetic salts. Kurti and Simon (1934) used mechanical contact between the salt and the cooling substance, cadmium. They pressed out a tablet consisting of equal volumes of cadmium and manganese ammonium sulfate. Kurti *et al* (1936) proposed to provide the thermal contact between the paramagnetic salt and the cooling substance with the help of liquid helium. In this method a capsule with the salt and the cooling substance is filled with a helium gas at room temperature under high pressure and then soldered. Then the capsule is cooled, helium is condensed, and the salt and the substance become covered by liquid helium, which provides thermal contact between them.

Daunt and Heer (1949) proposed a method of magnetic cooling, in which the process of adiabatic demagnetization was fulfilled cyclically. Essentially, it was a magnetic refrigerator working on the Carnot thermodynamic cycle. Magnetic refrigerators are regarded in detail in chapter 11 and those working on the Carnot cycle in section 11.2.6. A schematic drawing of the method of Daunt and Heer (1949) is presented in figure 11.19. In this method a magnetic working body (paramagnetic salt) is cyclically magnetized and demagnetized with appropriate switching of the thermal switches, connecting by turns the working body to the cooling substance (heat source) and to the liquid helium bath (heat reservoir). The working cycle of such a cooling apparatus is described in detail in section 11.2.6. The method of Daunt and Heer (1949) was realized in the works of Heer *et al* (1953, 1954), where the construction of the magnetic refrigerator operating below 1 K was presented. The authors used the superconducting thermal switches with Pb links, 15 g of paramagnetic iron ammonium alum as a working body and 15 g of chrome alum as the refrigerated heat reservoir (Heer *et al* 1954). The maximum magnetic field was 7 kOe, the operational cycle was 2 min, and the temperature of heat reservoir (helium bath) was 1 K. In the experiments a minimal no-load temperature of ~ 0.2 K was achieved and the refrigeration capacity was 1.2×10^{-5} W at 0.3 K.

Darby *et al* (1951) developed a two-stage adiabatic demagnetization apparatus. In the upper (first) temperature stage iron ammonium alum and in the low (second) temperature stage dilute mixed crystals of potassium aluminum alum and potassium chrome alum (5%) were used. The salts were compressed into two cylinders of diameter 16 mm and length 5.7 cm and of diameter 9 mm and length 2.3 cm in the first and the second stages, respectively. Between the stages there was the superconducting thermal switch with its lead wire. The cylinders were suspended in a thin germanium silver frame on an axial cotton thread. The frame was inserted into the vacuum helium cryostat. The process of cooling was as follows: first the temperature in the cryostat was reduced to ~ 1 K and both stages were magnetized; the heat of magnetization was removed with the help of helium exchange gas. Then the helium gas was pumped away and the first stage was demagnetized by turning on the thermal switch. As a result the heat from the magnetized second stage was transferred to the first stage. On the final stage the thermal switch was turned off and the second stage was demagnetized. The temperature was determined by susceptibility, which was measured by the inductance method. With the magnetic field of 4.2 kOe, Darby *et al* (1951) achieved a temperature of ~ 0.003 K in the second stage. On the first stage the lowest temperature was 0.25 K.

A three-stage adiabatic demagnetization apparatus was used in the works of Peshkov (1964, 1965). It included the high-temperature stage with 60 g of iron ammonium alum, the second stage with 24 g single crystal plates of cerium magnesium nitrate, and the low-temperature stage with 14.1 g of cerium manganese nitrate. The stages were connected by the superconducting (tin) thermal switches. The cooling was accomplished from 0.3 K (obtained by pumping off liquid He³) with a magnetic field of 11 kOe. The lowest achieved temperature measured by the inductance method was 0.0032 K.

As was noted above, the lowest temperature which can be reached by the adiabatic demagnetization of a paramagnetic salt is determined by interactions between the magnetic moments of ions and other internal interactions. In order to take these interactions into account, equation (2.160) can be rewritten in the form (Kurti 1960)

$$T_2 = T_1 \frac{\sqrt{H_2^2 + H_{\text{int}}^2}}{H_1} \quad (2.161)$$

where H_{int} is the field characterizing the energy of the above-mentioned interactions. The value of this field for a diluted paramagnetic substance with dipole interaction between the magnetic moments can be estimated with the help of (Kurti 1960, Vonsovskii 1974)

$$H_{\text{int}} \approx \frac{\mu}{(10r)^3} \quad (2.162)$$

where μ is the magnetic moment of the interacting particles and r is the distance between the particles (it is of the order of an atomic dimension, $\sim 10^{-8}$ cm). H_{int} can be reduced in two ways. The first is the dilution of magnetic atoms, which increases the distance between them. However, this method also decreases the value of the magnetic entropy change per unit of the substance quantity and, consequently, reduces the value of the heat which the substance can absorb ($T\Delta S_M$), or its refrigeration capacity. The other method of decreasing H_{int} is based on decreasing μ . It can be done if instead of the Bohr magneton ($\mu_B \approx 9.27 \times 10^{-21}$ erg/G), which should be used in equation (2.162) in the case of adiabatic demagnetization of the paramagnetic salts, where the magnetic moment of an ion forming by its electronic shells is involved, so one can use a smaller magnetic moment. This can be the nuclear magnetic moment, which is ~ 1000 times smaller than the magnetic moment of an ion (nuclear magneton $\mu_n \approx 5.05 \times 10^{-24}$ erg/G). Using such a ‘nuclear’ paramagnet it is possible to achieve temperatures 1000 times lower than with an ‘electronic’ paramagnet.

However, there are two main difficulties in application of the nuclear adiabatic demagnetization. The first follows from the requirement that the energy of the magnetic moment in the magnetic field should be at least an order of magnitude of the thermal agitation energy at the temperature of the adiabatic demagnetization process realization (i.e. $\mu H \approx k_B T$). Only in this case will the magnetic field be able to cause essential entropy change. For the nuclear paramagnet it means that enormously high magnetic fields should be used if the initial temperature is ~ 1 K ($H \approx k_B T / \mu_n \approx 10^7$ T). That is why to have the possibility of applying the magnetic fields achievable in a laboratory (~ 100 kOe) the preliminary cooling down to at least 10^{-2} K is needed (Simon 1939). The second difficulty is related to slow heat exchange between the nuclear magnetic spin system and the crystal lattice, which in dielectrics in the low-temperature range (at $\sim 10^{-2}$ K) can take about a week (Vonsovskii 1974). In metals the heat transfer is realized via conduction electrons, and thermal relaxation times in the temperature interval 0.01–1 K are much smaller—from the order of seconds to about minutes (Simon 1939, Bloembergen 1949, Kurti *et al* 1956).

The idea of using nuclear paramagnets in the adiabatic demagnetization was proposed by Gorter (1934) and Kurti and Simon (1935). The first experiment on the nuclear demagnetization was carried out by Hatton and Rolling (1949) on the crystal of calcium fluoride. The initial temperature was 1.2 K and the magnetic field was changed from 4 kOe to 0.5 kOe. The final temperature measured by the strength of the nuclear resonance signal was 0.17 K. Further nuclear demagnetization cooling experiments were conducted on copper by Kurti *et al* (1956), Hobden and Kurti (1959) and Kurti (1960). A typical specimen used in these experiments represented a bundle of fine insulated copper wires (~ 35 cm long), with the lower end serving as the nuclear cooling stage and the upper end embedded into the

chrome potassium alum, which was used as a high-temperature electronic stage. So the copper wires acted both as the thermal link and the nuclear stage. The specimen was surrounded by a thermal shield maintained at 0.35 K with the help of a He³ cryostat. The temperature on both stages was determined from the magnetic susceptibility measurements made by the inductance method. The initial temperature of 0.012 K was obtained by means of the electronic stage. The nuclear demagnetization was carried out from the magnetic field with a value up to 30.4 kOe. The lowest temperature reached in the experiments was 1.2×10^{-6} K. The value of H_{int} in the copper nuclear system was determined to be 3.1 Oe (Hobden and Kurti 1959).

Such are the general features of the adiabatic demagnetization experiments, where the magnetocaloric effect first found practical application. More detailed consideration of this question can be found in the books and reviews mentioned at the beginning of this section.

Chapter 3

Methods of magnetocaloric properties investigation

Methods of MCE measurements can be divided into two main groups: direct and indirect techniques. In the direct methods the material is subjected to a magnetic field change and its temperature change is directly measured by some technique. In the indirect methods the MCE and magnetic entropy change is determined on the basis of heat capacity and/or magnetization data.

3.1 Direct methods

3.1.1 Measurements in changing magnetic field

In direct methods the initial sample temperature $T_i(H_i)$ and the final one $T_f(H_f)$ at the end of the magnetization is measured, and the MCE at T_i is determined as the difference between T_f and T_i . The field application to or removal from the sample is usually accomplished using pulsed or ramped magnetic fields changing with a rate of about 10 kOe/s.

The method of direct measurements of the material temperature change during the application or removal of a magnetic field by an electromagnet (switch-on technique) was proposed by Weiss and Forer (1926). Clark and Callen (1969), using this method, made the first measurements in strong magnetic fields (up to 110 kOe) on yttrium iron garnet. The temperature of the sample, in the works of Weiss and Forer (1926) and Clark and Callen (1969), was measured by a thermocouple.

Green *et al* (1988) used the switch-on technique for MCE measurements in a superconducting solenoid. Their apparatus employed a superconducting solenoid 12.13 cm in diameter, 25.4 cm long and 8.54 cm bore, which could produce a field up to 70 kOe. The temperature was measured, after achieving the maximum field value, by five thermocouples placed on the sample, which took 10 s. The overall measurement process duration was about 40 s, together

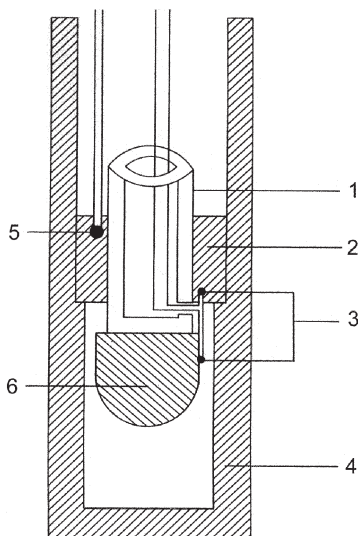


Figure 3.1. Schematic drawing of the insert for MCE measurements using a differential thermocouple: (1) insulating Plexiglas tube; (2) copper ring; (3) differential thermocouple for ΔT measurements; (4) copper screen; (5) thermocouple measuring the average sample temperature T ; (6) the sample (Kuhrt *et al* 1985).

with the field rise time of about 30 s. This method was used to measure MCE in rare earth metals at temperatures above 180 K.

Kuhrt *et al* (1985) proposed a differential thermocouple, which gave more accurate results for the MCE measurement. Its schematic drawing is shown in figure 3.1, where the differential thermocouple (3) measures the temperature difference between a massive copper body (2), (4) and the sample (6), which is the MCE value. The average sample temperature is measured by thermocouple (5). However, it was found that it is better to place the thermocouple inside the specimen (for example, into a drilled hole) because of the temperature gradient between its inner part and the surface (Kuhrt *et al* (1985)).

Borovikov *et al* (1981) measured the MCE in siderite FeCO_3 using pulsed magnetic fields. The sample had a parallelepiped form and linear dimensions of several millimeters. The pulsed field produced by a compact solenoid had a maximum value of 270 kOe, a pulse duration of 2 ms, and a working space 5.5 mm in diameter and 20 mm long. The MCE was measured by a thermocouple or by a magneto-optical technique, allowing instant temperature measurement (Litvinenko *et al* 1973). The latter method is based on the observation of the absorption band series at a wavelength of $24\,000\,\text{cm}^{-1}$ and can be used for sample temperature measurements above 21 K with an accuracy of 0.5 K.

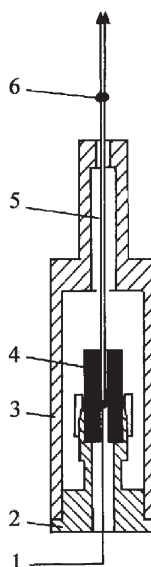


Figure 3.2. Schematic drawing of the insert for MCE measurements in pulsed magnetic fields: (1) thermocouple working junction; (2) collet; (3) insert frame; (4) sample; (5) thermocouple (Ponomarev 1983).

Ponomarev (1983, 1986) made a further development of the pulsed-field method. He measured the MCE in polycrystalline gadolinium in pulsed fields up to 80 kOe (the total pulse length was 0.5 s) in the temperature range 80–350 K. The schematic drawing of the insert used in the measurements is shown in figure 3.2. The MCE was measured by a copper–constantan differential thermocouple (5) made of strips $\sim 20\text{ }\mu\text{m}$ thick and 1 mm wide. Its working junction, 60 μm thick, made of tin (1) was placed inside the sample (4) consisting of two pieces 15 mm long and with total diameter of 6 mm, and chucked at the sample centre by a collet (2). The solenoid used had a length of 200 mm and a bore diameter of 50 mm. It was shown that, for the given pulse duration, sample dimensions and thermocouple configuration any errors due to the heat exchange between the sample, thermocouple and environment can be neglected. The sample temperature change during measurement due to Foucault currents was estimated to be $\sim 10^{-3}$ K. The apparatus sensitivity to the temperature change caused by the MCE was 0.1 K.

Let us consider more thoroughly the pulsed field apparatus, as described by Dan'kov *et al* (1997). Figures 3.3 and 3.4 show the principal scheme of the apparatus and the scheme of its low temperature part, respectively.

To measure the changes of the sample temperature caused by the MCE a differential copper–constantan thermocouple made of small diameter wires (~ 0.05 mm) was used. Application of such a small-mass thermocouple

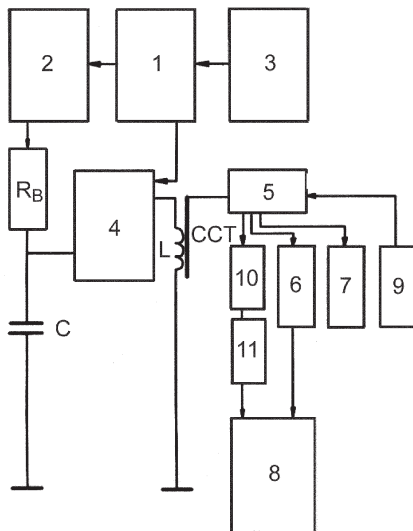


Figure 3.3. Experimental pulsed-field apparatus principal scheme: (1) operation block; (2) high voltage source; (3) rectifier; (4) discharge block; (5) measurement block; (6) integrator; (7) microvoltmeter; (8) memory oscilloscope; (9) heat feeding block; (10) thermocouple signal amplifier; (11) compensation block; C, battery of capacitors; CCT, copper-constantan thermocouple; L, pulse solenoid; R_B , ballast resistor (Dan'kov *et al* 1997).

(typical weight of the sample was about 1 g) provided a negligible heat load, which significantly reduced the heat leaks through the electrical wires.

Similarly as was done by Ponomarev (1983), the sample of Gd was shaped as a parallelepiped (with dimensions $4 \times 4 \times 10$ mm) and cut into two equal parts along the long axis. The thermocouple was placed between the parts in the centre of the sample. The sample was not insulated by a vacuum layer. According to the experimental tests, during the period of time required by the magnetic field to reach its maximum value (0.08 s) the heat exchange with the environment lowers the sample temperature by less than 2%.

The low-temperature insert of the apparatus (figure 3.4) was assembled from thin-walled tubes made of nonmagnetic stainless steel. The sample temperature was regulated by simultaneous work of the electric heater (3) (figure 3.4) controlled by a feeding block (figure 3.3) and cooled by flowing of nitrogen or helium gas through the insert.

Discharge of the capacity battery C created the magnetic field inside the solenoid L. The battery had a total capacity of 0.035 F and was charged up to 1000 V, which provided total pulse duration of 0.2 s. The discharge block (4) included a thyristor driven by a starting signal from the control desk (1) (figure 3.3), which was used as a power switch for the battery discharge. Simultaneously with discharging the battery, the starting signal triggered

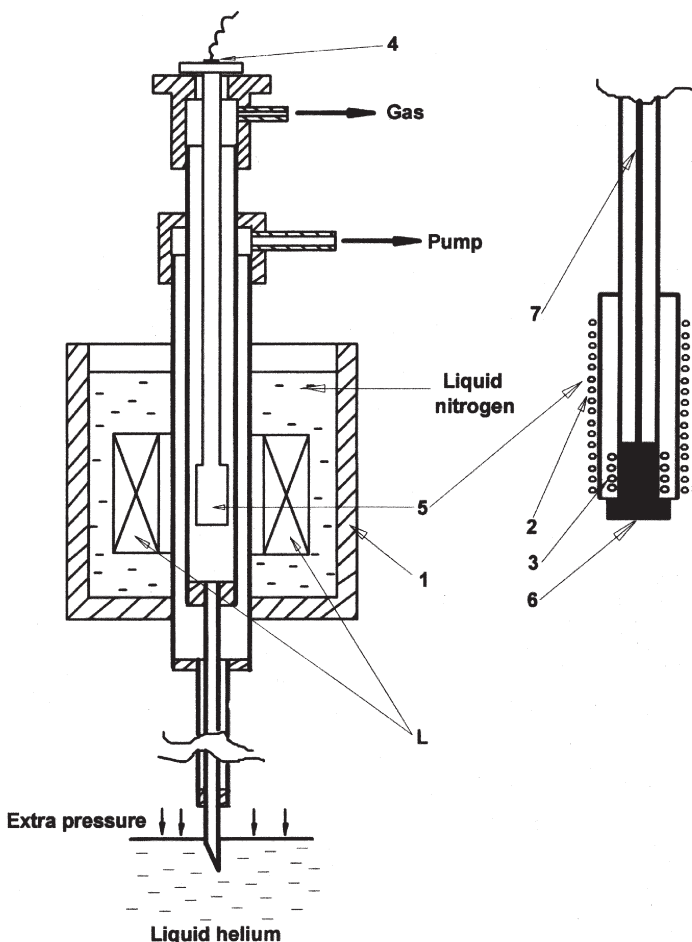


Figure 3.4. Schematic drawing of the low-temperature part of the experimental pulsed-field apparatus (liquid nitrogen cryostat): (2) sample heater; (3) field measuring coil; (4) vacuum-tight feed through connector; (5) sample holder; (6) sample inside the holder; (7) electrical wiring; L, pulsed solenoid (Dan'kov *et al* 1997).

the pulse memory oscilloscope (8). The signal from the thermocouple was fed into one channel of the oscilloscope. Into the second channel was fed the signal from the measuring coil (3) (figure 3.4) integrated in the integrator (6) (figure 3.3). This technique allowed determination of the sample temperature change due to the change of the magnetic field, i.e. the MCE at a given field and temperature. The measurement block (5) (figure 3.3) was used to achieve communications between other apparatus blocks.

It was found that during the measurements a parasitic signal might be induced in the thermocouple wiring. To prevent the influence of this

interference, which can decrease the accuracy of the measurement, a compensation scheme (11) (figure 3.3) was employed. In this scheme a signal from the measuring coil (3) (figure 3.4) was added as a compensation signal to the signal from the thermocouple. Such a scheme almost completely excluded the influence of the interferences on the experimental results.

The solenoid L had a bore diameter of 23 mm and was wound from copper wire with a diameter of 1.3 mm. It was cooled directly by liquid nitrogen, which made it possible to obtain a maximum magnetic field value of 80 kOe. Tests show that the solenoid possessed a small field inhomogeneity: the axial inhomogeneity was less than 5% within the range of ± 1 cm from the solenoid centre, and the radial inhomogeneity was one order of magnitude smaller.

Dan'kov *et al* (1997) considered various sources of random, and systematic errors arose during the measurement process. It was concluded that the pulse field apparatus enabled measurement of the magnetocaloric effect with an accuracy of 8–15%, depending on the MCE value and the temperature range.

3.1.2 Measurements in static magnetic field

A superconducting solenoid can produce magnetic fields with high intensity (at least up to 100 kOe). When the field is produced by a nonsuperconducting electromagnet (typical maximum values of the field intensity up to 20 kOe) the field rising time in a switch-on technique has a maximum value of about a few seconds. However, for a superconducting solenoid it can reach the value of several minutes. During the field rise a dissipation of the heat released in the sample due to the MCE can occur. According to the estimation made by Tishin (1988) the field rising time must not be greater than 10 s for temperatures above 30 K. In the temperature region 10–20 K this time must be several times smaller because of the increase of the heat leakage through the thermocouple. Because of these limitations the MCE measurements by a switch-on technique are difficult and even impossible in the case of the use of a superconducting solenoid.

To overcome the difficulties related to the field rising time a method was proposed in which the sample was brought quickly into the static magnetic field of a superconducting solenoid (Nikitin *et al* 1985a, 1985b, Tishin 1988, Gopal *et al* 1997). The measurement is done in the following sequence. Initially the sample is placed outside the solenoid. When the field in the solenoid has reached the required value, the sample is rapidly (at about 1 s) brought inside the solenoid. After the sample is fixed at the centre of the solenoid, its temperature is measured.

Figure 3.5 shows the scheme of the experimental apparatus, allowing the MCE measurements in the temperature range from 4.2 to 300 K in fields up to 66 kOe (Tishin 1988). The sample holder (15) made of Teflon with the

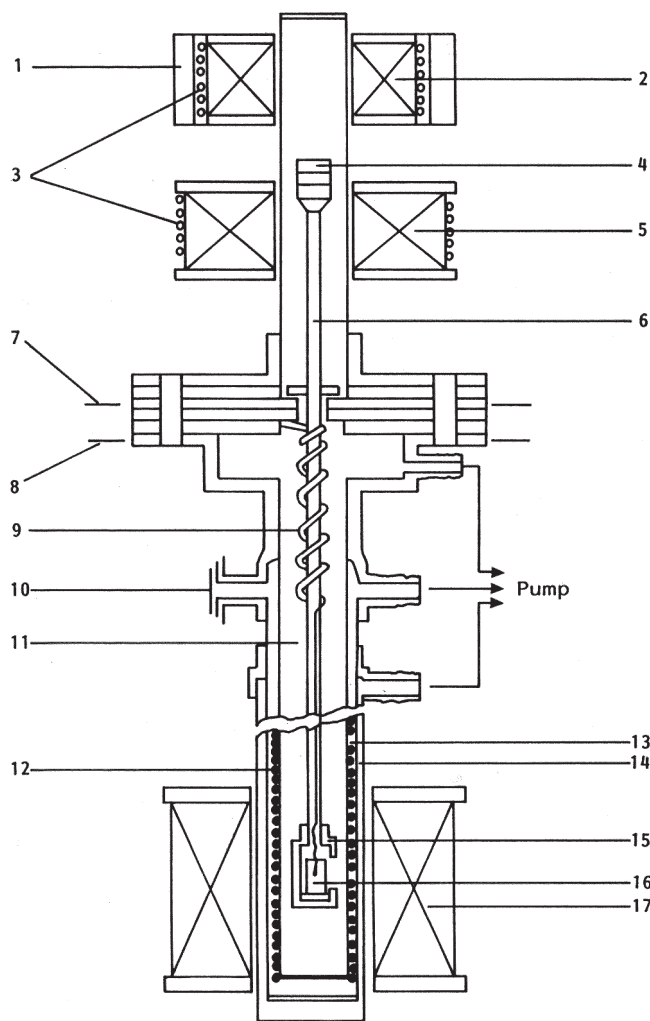


Figure 3.5. The scheme of the experimental apparatus for MCE measurements in a superconducting solenoid: (1) ferrite permanent magnet; (2) coil; (3) cooling system; (4) SmCo₅ permanent magnet; (5) coil; (6) rod; (7) Teflon gasket; (8) flange; (9) leads; (10) heater connector; (11) evacuated tube; (12) electric heater; (13), (14) vacuum jackets; (15) sample holder; (16) sample; (17) superconducting solenoid (Tishin 1988).

sample (16) was fixed at the end of the rod (6). A mica gasket was glued on the bottom of the holder in order to minimize the heat leakage between the sample and the holder. The rod with the holder was placed into a tube (11) evacuated to a pressure of ~ 1 Pa in order to provide adiabatic conditions for the measurements. Vacuum jackets (13) and (14) were used to prevent helium evaporation caused by sample heating by the electric heater (12).

The heater was connected to the temperature control block through a connector (10). The superconducting solenoid created magnetic fields up to 66 kOe. The whole apparatus was placed into helium cryostat.

A permanent SmCo₅ magnet (4) and the special coil (5) were used to prevent the sample from being pulled into the solenoid (the pulling force is the product of the field gradient and the sample magnetic moment). The coil (5) was also used to return the sample to its initial position. The sample is fixed in the upper position (out of the solenoid) by a ferrite permanent magnet (1). Then the magnetic field of the ferrite magnet is compensated by a coil (2) and the sample begins to move in the lower position (inside the solenoid). A Teflon gasket (7) on a flange (8) fixes the sample at the centre of the solenoid. At this time the copper washer on the rod closes the contacts on the gasket (7), leading to the turning off of the coil (5). Coils (2) and (5) were water-cooled.

Tishin (1988) made an estimation of the accuracy of the MCE determination for the apparatus described above. The main sources of the errors are: heat losses in the contact between thermocouple and the sample, the losses through the thermocouple contacting leads and heat emission losses, and heating by eddy currents. It was shown that eddy currents could cause a noticeable value (above 0.1 K) in the temperature region below 10 K. The total error in the MCE measurement was estimated to be about 10%.

Gopal *et al* (1997) reported about the apparatus for automated MCE measurements, which operated in an analogous way to that described above. The apparatus is capable of measuring the MCE in the temperature range from 10 to 325 K in applied magnetic fields up to 90 kOe. As the host platform for the MCE measurement insert, a commercially available Quantum Design Physical Property Measurement System including magnet system with a temperature-controlled bore was used. The sample in the insert (about 3–10 g weight) was moved in and out of the superconducting solenoid by a pneumatic linear actuator. The compressed air feed to the actuator, guiding direction and speed of its movement, was controlled by two solenoid valves. The speed of the sample movement was about 60 cm/s, which provided a magnetic field rising rate of 90 kOe/s.

The measuring chamber was evacuated to 10^{-4} torr during measurements. To measure temperature and its change caused by the MCE, a low magnetic field dependence resistance temperature device (Cernox) was used. It exhibited magnetic-field-induced errors of less than $\pm 0.3\%$ at 5 K. The errors become negligibly small at temperatures above 30 K in magnetic fields up to 100 kOe. A thermal response time of the temperature sensor was 135 ms at 273 K and 1.5 ms at 4.2 K. The device had a very small size in comparison with that of the sample. In order to prevent self heating, the sensor was excited by a precision low-level programmable a.c. source with amplitude in the range 10–100 μ A and amplitude stability better than ± 50 ppm/h. To detect voltage on the device, a lock-in amplifier was

employed. The measured voltage was converted to the corresponding resistance value and the temperature was calculated using the sensor's Chebyshev calibration coefficients. The sensor leads were directed axially to the magnetic field in order to minimize errors related to stray induction by the changing magnetic field. The lock-in amplifier time constant ranged between 30 and 100 ms to further suppress this interference. It was shown that the heating caused by eddy currents induced during sample motion in and out of the magnetic field was about 1 K. This effect was taken into account using the fact that the MCE changes its sign at field reversal and the eddy current contribution does not.

The apparatus worked automatically under the control of the PC-compatible computer. The tests made on Gd and Ho showed that the results obtained on the MCE temperature dependence agree well with the literature data.

3.1.3 Thermoacoustic method

This technique proposed by Gopal *et al* (1995) can be attributed to the non-contact methods of the MCE measurements. It should be noted that this method is also an indirect method because the MCE ΔT in the given magnetic field H is calculated on the basis of the obtained experimental values. However, the measured value is the response of the sample under investigation arising in the alternating magnetic field due to the MCE. That is why this method is considered in this section.

Figure 3.6 shows the scheme of the experimental apparatus. The measuring cell with the sample under investigation is placed between the

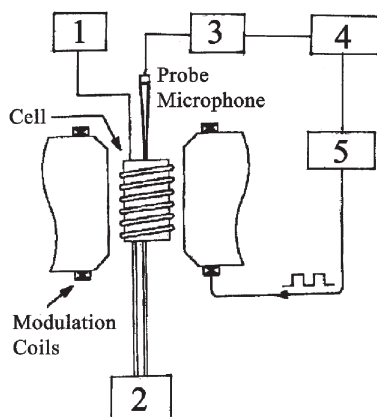


Figure 3.6. The scheme of the experimental apparatus used in the thermoacoustic method: (1) thermometer; (2) temperature control system; (3) preamplifier; (4) lock-in amplifier; (5) field modulation unit (Gopal *et al* 1995).

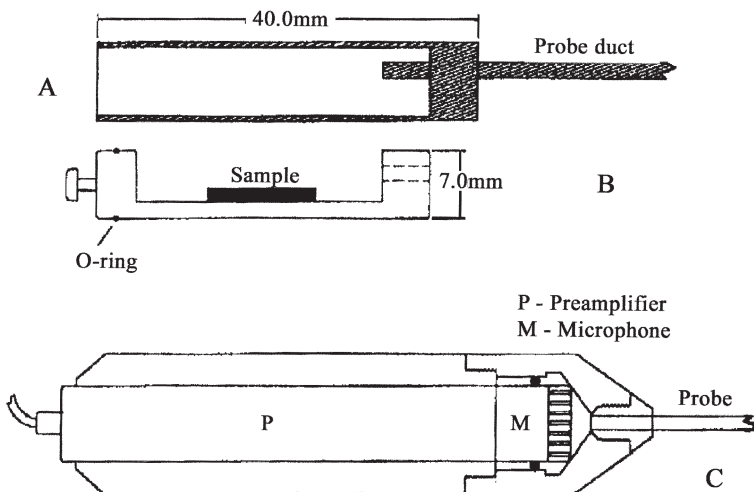


Figure 3.7. The schematic drawing of the measuring cell and microphone probe used in the thermoacoustic method: (A) the cell; (B) the sample holder; (C) the microphone probe (Gopal *et al* 1995).

pole faces of an electromagnet capable of producing magnetic fields up to 4.5 kOe. The field modulation coils on the electromagnet poles produce an a.c. magnetic field parallel to the d.c. field of the magnet. The coils were fed by an a.c. current of 1 A and a square waveform from the field modulation unit (class C amplifier) (5). The signal to the field modulation unit was received from the TTL reference output of a lock-in amplifier. The value of the a.c. field was up to 250 Oe and its frequency was 4 Hz. The cell was surrounded by a temperature-controlling fluid jacket providing control stability of ± 1 K. The cell temperature was measured by a thermistor placed on its wall.

The sample with dimensions of about $12\text{ mm} \times 4\text{ mm} \times 0.5\text{ mm}$ was placed inside the measuring cell made of thin-wall brass tubing of 9 mm diameter and 40 mm length (see figure 3.7). The sample holder was made of Teflon and was set inside the cell. The cell was closed but had an orifice with 1.5 mm diameter for a microphone probe duct, which connected the probe with the cell. The microphone probe consisted of a capacitive-type pressure-response microphone, and a preamplifier was placed outside the magnetic field area in order to minimize the stray induced by the magnetic field. The system measuring cell-microphone probe was gas tight and filled by a gas.

An a.c. magnetic field caused the infinitesimal periodic temperature changes δT induced in the sample due to the MCE. These temperature variations cause periodic heating of the neighbouring gas layer, which begins to expand and contract, producing thermoacoustic waves within the

measuring cell. The waves are propagated through the duct and are received by the microphone probe. Then the signal is amplified by the preamplifier (3) and detected by the lock-in amplifier (4). As shown by Gopal *et al* (1995) the voltage v from the microphone probe is proportional to the temperature change δT :

$$\delta T = C_{\text{sys}} v \quad (3.1)$$

where C_{sys} is the calibration constant. The system was calibrated using Gd. The calibration was made on the basis of equation (2.16) and known data for Gd magnetization and heat capacity.

The measurable quantity in this method is $\delta T/\delta H$ in the corresponding d.c. magnetic field H , where δH is an amplitude of the a.c. magnetic field cases infinitesimal periodic temperature changes δT induced in the sample due to the MCE. As follows from the mean field model (see equations 2.42 and 2.50), at a given temperature the MCE is a linear function of the square magnetization δI^2 . On the basis of independent magnetization measurements one can convert measured $\delta T/\delta H$ into $\delta T/\delta I^2$ for $I \geq I_s$ and obtain the slope of the total magnetocaloric effect ΔT dependence on magnetization I^2 for the given magnetic field H . Knowing this value it is possible to determine ΔT at any desired magnetization, i.e. $\Delta T(I^2)$ dependence, and then convert it into $\Delta T(H)$ dependence.

The method was first proved using a.c. excitation of a 10Ω chip resistor placed in the measuring cell. It was shown that at 25°C the system is capable of detecting input power levels of $320\mu\text{W}$. The dependence of the response microphone voltage on the input power is linear up to 130mW , i.e. in the range of about 3 orders of magnitude. It was also verified that the signal from a magnetic sample is due to the MCE. The contributions to the output signal from eddy currents, hysteresis losses and magnetostriction vibrations were found to be negligible.

Gopal *et al* (1995) made measurements of the MCE for Gd and $\text{Gd}_{91.8}\text{Dy}_{8.2}$ and $\text{Gd}_{89.9}\text{Er}_{10.1}$ alloys. Figure 3.8(a) shows experimental temperature dependences of the temperature change δT caused by an a.c. magnetic field of 200Oe at external magnetic fields of $2.5, 3, 3.5, 4$ and 4.5kOe in Gd, measured by the thermoacoustic method in the region of the Curie temperature. The $\delta T(T)$ behaviour is consistent with equation (2.16). The lower values of δT for higher H are related to $\partial M/\partial T$ decreasing with magnetic field increasing. Figure 3.8(b) represents the $\Delta T(T)$ dependences at different magnetic fields determined on the basis of the magnetization data and δT data from figure 3.8(a).

It should be noted that an alternating magnetic field was also used to direct measurements of the MCE by Fischer *et al* (1991). In this work the alternating modulation magnetic field with a frequency of 0.05Hz and an amplitude of 600Oe was superimposed on the direct field, in which the measurement was conducted. The corresponding alternating temperature

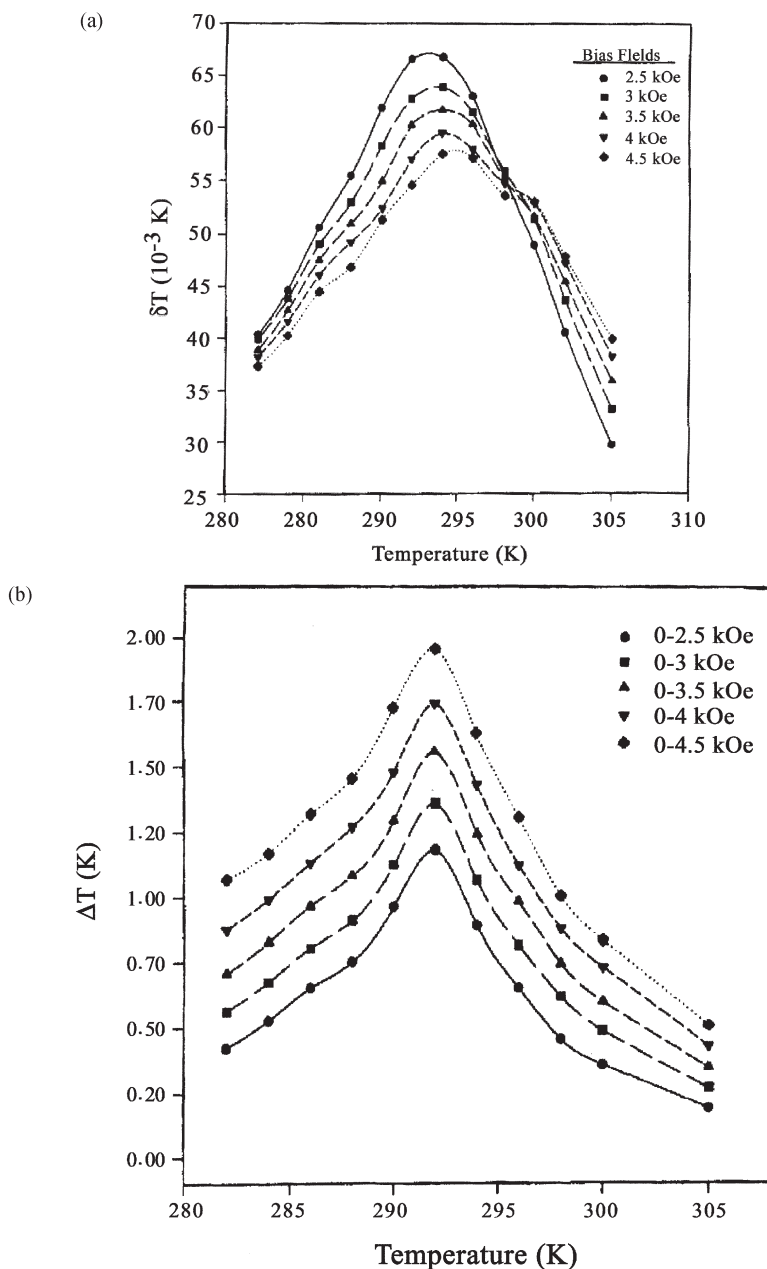


Figure 3.8. Temperature dependences of: (a) the temperature change δT caused by the a.c. field of 200 Oe at different external magnetic fields H in gadolinium; and (b) the magnetocaloric effect ΔT at the different magnetic fields determined on the basis of $\delta T/\delta H$ data (Gopal *et al* 1995).

signal with an amplitude proportional to the MCE was measured directly by a resistor thermometer. The MCE was extracted from the measured signal by Fourier analysis.

3.2 Indirect methods

3.2.1 Magnetization measurements

3.2.1.1 Isothermal magnetization measurements

Experimental data on magnetization isotherms $I(H)$ can be used to calculate magnetic entropy change ΔS_M by means of equation (2.70):

$$\Delta S_M = \int_{H_1}^{H_2} \left(\frac{\partial I}{\partial T} \right)_H dH \quad (3.2a)$$

or, if the field is varied from 0 to H ,

$$\Delta S_M = \int_0^H \left(\frac{\partial I}{\partial T} \right)_H dH. \quad (3.2b)$$

Equations (3.2) can be integrated numerically in the desired range of temperatures and magnetic fields on the basis of the set of experimental magnetization isotherms $I(H)$ at different temperatures T_1, T_2, \dots . The derivative $\partial I / \partial T$ can also be calculated numerically. McMichael *et al* (1993b) proposed the following simple formula for numerical calculations of ΔS_M :

$$|\Delta S_M| = \sum_i \frac{1}{T_{i+1} - T_i} (I_i - I_{i+1}) \Delta H_i. \quad (3.3)$$

Numerical calculations of ΔS_M in rare earth metals on the basis of magnetization isotherms were made by McMichael *et al* (1993b), Foldeaki *et al* (1995), Dan'kov *et al* (1996), Pecharsky and Gschneidner (1999a) and other authors.

Strictly speaking, equation (3.2) can be used for calculations of the magnetic entropy change from the magnetization data only for systems of second-order magnetic phase transitions, because at the first-order transition the derivative $\partial M / \partial T$ becomes infinite. The magnetic entropy change related to the first-order magnetic phase transition can be determined using the Clapeyron–Clausius equation (2.100). However, the infinite $\partial M / \partial T$ can arise only in ideal first-order phase transitions and in real materials it is usually finite, which allows the use of equation (3.2) in this case. However, it is necessary to use caution when using equation (3.2) for the first-order transition, because in some cases the obtained ΔS_M values can be overestimated. The discussion about the possibility of using equation (3.2) in the materials displaying a first-order magnetic transition can be found in

the works of Giguere *et al* (1999c), Sun *et al* (2000a), Gschneidner *et al* (2000c) and Wada *et al* (2001).

To calculate the value ΔT of the MCE from experimental data on magnetization and heat capacity, equation (2.16) can also be used (Tishin 1997):

$$\Delta T(T, H) = \int_{T(H=0)}^{T(H)} dT = - \int_0^H \frac{T}{C_{p,H}} \left(\frac{\partial I(H, T)}{\partial T} \right)_H dH \quad (3.4)$$

where $\Delta T(T, H) = T(H) - T(H = 0)$. It is important to note that because T is permanently changing during magnetic field action and $C_{p,H}$ can strongly depend on H , in a general case neither T nor $C_{p,H}$ can be moved out of the integral in equation (3.4). In an experiment the field usually changes from $H = 0$ to H . In the case where the values of the magnetic field are changed from a value of H_1 to the H_2 , these values should be taken as the limits of the integration in equation (3.4). With the help of the integration by parts it is possible to present equation (3.4) in the form (Foldeaki 1995, 1997a)

$$\begin{aligned} \int_0^{H_0} \frac{T}{C_{p,H}} \left(\frac{\partial I}{\partial T} \right)_H dH &= \left[\frac{T}{C_{p,H}} \int_0^H \left(\frac{\partial I}{\partial T} \right)_{H'} dH' \right]_0^{H_0} \\ &\quad - \int_0^{H_0} \left\{ \frac{d}{dH} \left(\frac{T}{C_{p,H}} \right) \left[\int_0^H \left(\frac{\partial I}{\partial H} \right)_{H'} dH' \right] \right\} dH. \end{aligned} \quad (3.5)$$

If the value $T/C_{p,H}$ varies with H much more slowly than the derivative $(\partial I/\partial T)_H$ which can be assumed in the region of magnetic phase transitions, then the second integral in equation (3.5) is negligible and the MCE can be calculated as

$$\Delta T(T, H) = - \frac{T}{C_{p,H}(T, H)} \Delta S_M(T, H) \quad (3.6)$$

(see also equation (2.79)). According to Foldeaki *et al* (1997a) both ΔS_M and $C_{p,H}$ should be introduced in equation (3.6) at the same field and temperature values. The heat capacity in the given magnetic field H can be determined on the basis of the zero field heat capacity measured experimentally, and equation (2.12) allows calculation of the heat capacity change caused by the magnetic field from ΔS_M data as

$$\Delta C_p = C_p(H) - C_p(0) = T \left(\frac{\partial \Delta S_M}{\partial T} \right)_p \quad (3.7)$$

where $\Delta S_M = S_M(H) - S_M(0)$. As was pointed out by Pecharsky and Gschneidner (1999a), equation (3.6) is valid only under assumption that heat capacity does not depend on magnetic field, i.e. $C_p(0, T) = C_p(H, T)$.

According to estimations of Foldeaki *et al* (1995), an error in the values of ΔS_M calculated numerically from the magnetization data measured with

the accuracy of less than 0.5% in the fields up to 60 kOe is $\pm 7.5\%$. Pecharsky and Gschneidner (1999a) thoroughly analysed the errors in ΔS_M determined by the method described above. It was assumed that ΔS_M was calculated using the trapezoidal rule as

$$\Delta S_M(T_{av}) = \frac{\delta H}{2\delta T} \left(\delta I_1 + 2 \sum_{k=2}^{n-1} \delta I_k + \delta I_n \right). \quad (3.8)$$

It was assumed that the magnetization on each isotherm is measured at the n field points situated on the curve with step $\delta H = \Delta H/(n - 1)$, where ΔH is the value of magnetic field changing. In equation (3.8), $\delta T = T_u - T_l$ is the temperature difference between the two isotherms measured at T_u and T_l , $T_{av} = (T_u + T_l)/2$ —an average temperature for which ΔS_M is calculated, $\delta I_k = [I(T_u)_k - I(T_l)_k]$ is the difference in the magnetizations on the isotherms measured at T_u and T_l at each magnetic field point from 1 to n .

The errors arising from inaccuracies related to magnetization, magnetic field and temperature measurements were taken into account. The following equation was obtained for the total error in ΔS_M (Pecharsky and Gschneidner 1999a):

$$\begin{aligned} \sigma |\Delta S_M(T_{av}, \Delta H)| &= \frac{1}{2|\delta T|} \left\{ |\delta H| \left(\sigma I_1 + 2 \sum_{k=2}^{n-1} \sigma I_k + \sigma I_n \right) \right. \\ &\quad + \left(|\delta I_1| \sigma H_1 + 2 \sum_{k=2}^{n-1} (|\delta I_k| \sigma I_k) + |\sigma I_n| \right) \\ &\quad \left. + 2 |\Delta S_M(T_{av}, \Delta H)| (\sigma T_u + \sigma T_l) \right\} \end{aligned} \quad (3.9)$$

where σT are errors in the temperature measurements, $\sigma I_k = [\sigma I(T_u)_k + \sigma I(T_l)_k]$ is the sum of errors in the magnetization measured at T_u and T_l in the magnetic field H_k , and $\sigma H_k = [\sigma H(T_u)_k + \sigma H(T_l)_k]$ is the sum of errors in the magnetic field at the temperatures T_u and T_l . The first term in equation (3.9) represents the contribution related to the magnetization inaccuracies, the second term relates to the field inaccuracies, and the third term relates to the temperature inaccuracies. Analysis of equation (3.9) shows that the total error in the magnetic entropy increases as δT and δH decrease. It should be noted that these values cannot be made too large because then equation (3.8) becomes invalid.

Figure 3.9 shows $\Delta S_M(T)$ dependences (for $\Delta H = 50$ kOe) calculated by equation (3.8) on the basis of experimental magnetization data for polycrystalline ErAl_2 and single crystal Gd (the field was directed along the [0001] axis), and also temperature dependences of the corresponding total error $\sigma |\Delta S_M(T)|$ estimated by equation (3.9). The measurements were done in the region of the Curie points with temperature steps δT of 2 K below and

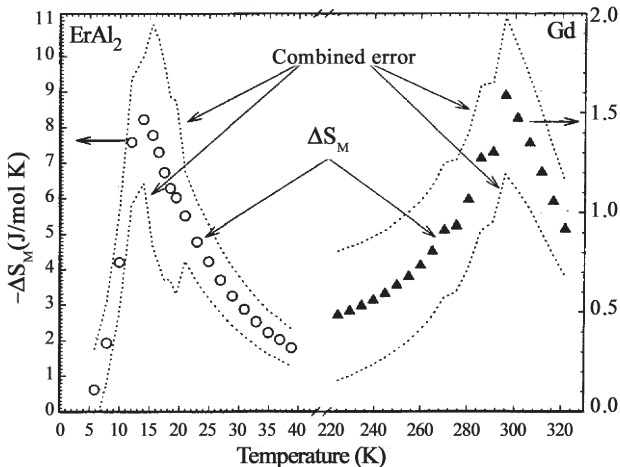


Figure 3.9. Magnetic entropy change $\Delta S_M(T)$ at $\Delta H = 50$ kOe in ErAl₂ and Gd calculated on the basis of magnetization data by equation (3.8)—the open circles and solid triangles. The dotted lines are the margins of the total error calculated by equation (3.9) (Pecharsky and Gschneidner 1999a).

above T_C , 1 K near T_C for ErAl₂, and 5 K in the whole temperature range for Gd. The magnetic field step δH was 1 kOe for ErAl₂ and 2 kOe for Gd. The accuracy of the magnetization measurements was assumed to be 0.5% and for the magnetic field 0.1%. The temperature accuracy was calculated as $\sigma T = 0.1 \text{ K} + 0.001T$.

Figure 3.10 shows temperature dependences of relative total error in ΔS_M and the contributions from different inaccuracies according to equation (3.9) for ErAl₂ and Gd. As can be seen, a twofold increase of δH in Gd compared with ErAl₂ causes a twofold reduction of the corresponding magnetic field contribution to the total error. The twofold reduction of δT in ErAl₂ (the temperature region from 15 to 20 K) gave a step-like increase in the contributions from magnetization and temperature errors. The relative error also depends on the value ΔH —it is low for lower ΔH provided δH is constant. The total relative error in ΔS_M essentially increased below the Curie temperature due to the increase in the magnetization contribution. The errors from magnetic field and temperature were small and temperature dependent. The total relative error near the Curie temperature was about 25% in ErAl₂ and Gd and rapidly deteriorated in a low-temperature region.

3.2.1.2 Adiabatic magnetization measurements

Levitin *et al* (1997) proposed another method for MCE determination from magnetization measurements. The method is based on comparison of the magnetization field dependences measured under isothermal and adiabatic

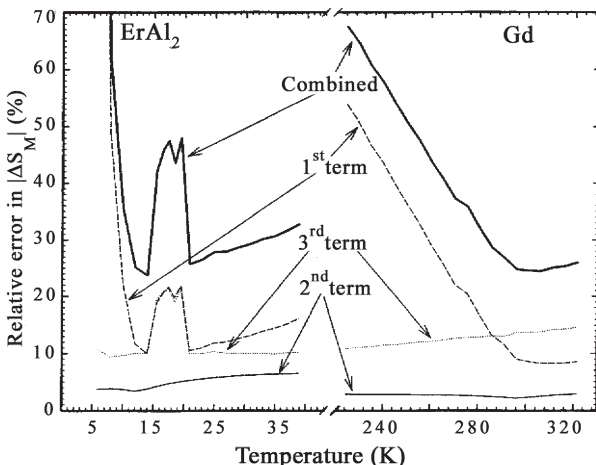


Figure 3.10. Temperature dependence of the total relative error in ΔS_M (full line) in ErAl_2 and Gd calculated using equation (3.9) and (1) the magnetic contribution from the first term in equation (3.9)), (2) the temperature (contribution from the third term in equation (3.9)) and (3) the magnetic field (contribution from the second term in equation (3.9)) errors (Pecharsky and Gschneidner 1999a).

conditions. Due to the MCE the initial temperature of ferro- and paramagnets increases during adiabatic magnetization. Because of that the adiabatic magnetization curve measured at some initial temperature will intersect the isothermal magnetization curves obtained at higher temperatures. The intersection points (T, H) determine the field dependence of the sample temperature under adiabatic magnetization, i.e. $\Delta T(H)$.

The adiabatic magnetization conditions can be provided by the pulse magnetization measurements. It was established that the adiabatic magnetization took place for a field rising rate of about 10^4 kOe/s and higher for the samples with dimensions of several mm. A decrease of the rate to $10\text{--}100$ kOe/s leads to a practically isothermal magnetization process.

Levitin *et al* (1997) demonstrated the capability of this method on paramagnetic single crystal $\text{Gd}_3\text{Ga}_5\text{O}_{12}$. The magnetization measurements were made in pulsed fields up to 400 kOe with a field rising rate of 2–150 MOe/s. Figure 3.11 shows an experimental magnetization curve measured at an initial temperature of 4.2 K (thick line) at the field rising rate of 50 MOe/s, together with isothermal magnetization curves (thin lines) calculated in the frameworks of mean field approximation (it was shown that there was good coincidence between theoretical and experimental isothermal curves in $\text{Gd}_3\text{Ga}_5\text{O}_{12}$). As predicted, intersections between the adiabatic and isothermal curves are observed. The $\Delta T(H)$ curve obtained by this method for $\text{Gd}_3\text{Ga}_5\text{O}_{12}$ gave $\Delta T = 46$ K for $\Delta H = 400$ kOe and an initial temperature of 4.2 K.

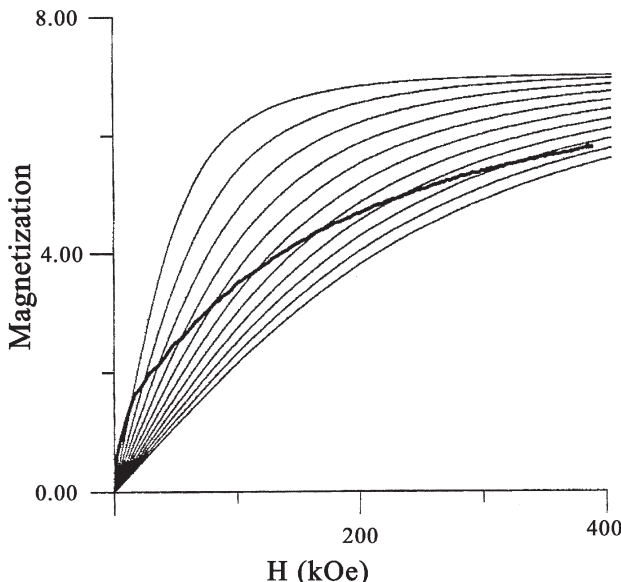


Figure 3.11. Adiabatic magnetization curve (thick line) measured in $\text{Gd}_3\text{Ga}_5\text{O}_{12}$ single crystal in a pulsed magnetic field at an initial temperature of 4.2 K with the average field rising rate of 50 MOe/s. Thin lines represent isotherm magnetization curves calculated in the frameworks of mean-field approximation starting from 5 K (the top curve) with temperature steps of 5 K (Levitin *et al* 1997). (Reprinted from Levitin *et al* 1997, copyright 1997, with permission from Elsevier.)

3.2.2 Heat capacity measurements

The MCE and the magnetic entropy change can be determined from the heat capacity temperature dependences measured in different magnetic fields. This method was used by Brown (1976) and Gschneidner and co-workers (see, for example, Pecharsky and Gschneidner 1996, 1999a). It allows a complete set of parameters required for magnetic refrigerator design to be obtained: heat capacity, total entropy and magnetic entropy change, MCE field and temperature dependences.

The total entropy of a material in a magnetic field $S(T, H)$ can be calculated if the experimental dependence of its heat capacity $C(T, H)$ is known on the basis of the equation following from equation (2.12):

$$S(T, H) = \int_0^T \frac{C(T, H)}{T} dT + S_0 \quad (3.10)$$

where S_0 is the entropy at $T = 0$ K (zero temperature entropy), which is usually assumed to be zero (Foldeaki *et al* 1997a, Pecharsky and Gschneidner 1999a). It should be noted that real measurements are always started not from 0 K but from some temperature T_1 . The contribution to S below T_1 can be

presented as $C(T_1, H)$ because for $T \rightarrow 0$ heat capacity approaches zero and temperature change between 0 K and T_1 is equal to T_1 .

Pecharsky and Gschneidner (1999a) proposed the following equation for the entropy calculation from heat capacity data:

$$S(T, H) = 0.5 \left\{ C(T_1, H) + \sum_{i=1}^{n-1} \left[\left(\frac{C(T_i, H)}{T_i} + \frac{C(T_{i+1}, H)}{T_{i+1}} \right) (T_{i+1} - T_i) \right] \right\} \quad (3.11)$$

where n is the number of measured heat capacity data points between T_1 and T , $C(T_1, H)$ is the contribution in S from the heat capacity data below the temperature of the beginning of the experiment T_1 . On the basis of equation (3.11), Pecharsky and Gschneidner (1999a) obtained the following equation for the errors in the total entropy calculated from the heat capacity:

$$\sigma S(H, T) \cong 0.5 \left\{ \sigma C(T_1, H) + \sum_{i=1}^{n-1} \left[\left(\frac{\sigma C(T_i, H)}{T_i} + \frac{\sigma C(T_{i+1}, H)}{T_{i+1}} \right) (T_{i+1} - T_i) \right] \right\} \quad (3.12)$$

where $\sigma C(T, H)$ is the uncertainty in the measured heat capacity value. The errors in temperature were not taken into account in equation (3.12) because in the method of heat capacity measurements used by Pecharsky and Gschneidner (1999a) (adiabatic heat pulse calorimeter—see section 3.2.2.1) their contribution to the total error did not exceed a few percent. The error in heat capacity in the method using an adiabatic heat pulse calorimeter was $\sim 0.5\%$ in the major temperature interval except at the lowest temperature and above 300 K. The estimated relative error in total entropy for Gd and ErAl₂ measured in a zero magnetic field and in 50 kOe was about 0.5%, except below 10 K, where it reached several percent.

From the calculated total entropy temperature dependences in zero magnetic field $S(0, T)$ (or any other initial field) and in final magnetic field $S(H, T)$, the isothermal magnetic entropy change $\Delta S_M(H, T)$ can be determined (see equation (2.70)) at any temperature T as

$$\Delta S_M(H, T) = \Delta S(H, T) = S(H, T) - S(0, T) \quad (3.13)$$

and adiabatic temperature change caused by the magnetic field change, i.e. magnetocaloric effect, can be obtained as

$$\Delta T(H, T) = T(S, H) - T(S, 0) \quad (3.14)$$

where $T(S, H)$ and $T(S, 0)$ are the temperatures in the field H and $H = 0$ at constant total entropy S . The method of $\Delta S_M(H, T)$ and $\Delta T(H, T)$ determination from $S(H, T)$ curves is illustrated by figure 2.3. Zero temperature entropy S_0 can affect the determined ΔS_M and ΔT values giving additional

error. Pecharsky and Gschneidner (1999a) showed that S_0 has no effect on ΔS_M and its influence on ΔT is negligibly small.

The error in $\Delta S_M(H, T)$ determined from $S(H, T)$ curves is determined as the sum of errors in $S(T, H)$ (Pecharsky and Gschneidner 1996, 1999a):

$$\sigma|\Delta S_M(H, T)| = \sigma S(0, T) + \sigma S(H, T). \quad (3.15)$$

The error in $\Delta T(H, T)$ was presented (Pecharsky and Gschneidner 1996, 1999a) as

$$\begin{aligned} \sigma|\Delta T(H, T)| &= \left(\frac{dT(S, H)}{dS} \right) \sigma S(H, T) + \left(\frac{dT(S, 0)}{dS} \right) \sigma S(0, T) \\ &= \sigma S(H, T) \frac{T}{C(H, T)} + \sigma S(0, T) \frac{T}{C(0, T)}. \end{aligned} \quad (3.16)$$

It can be seen from equation (3.16) that the error in ΔT is directly proportional to $\sigma S(T, H)$ and T/C and inversely proportional to dS/dT . In a ferromagnetic material the error in ΔT increases above T_C because of heat capacity decreasing. Figure 3.12 shows the $\Delta T(T)$ for $\Delta H = 50$ kOe in ErAl_2 and Gd, determined from the heat capacity measurements together with the errors estimated on the basis of equation (3.16). It is seen that the error becomes larger for higher temperatures. The error will strongly

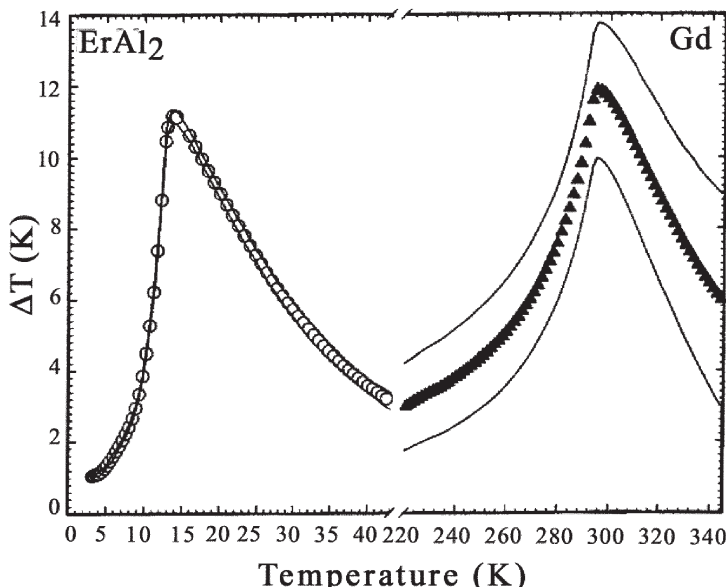


Figure 3.12. MCE temperature dependences for $\Delta H = 50$ kOe in ErAl_2 (open circles) and Gd (solid triangles) determined on the basis of the heat capacity measurements. The solid lines show the margins of the error in ΔT calculated by equation (3.16) (Pecharsky and Gschneidner 1999a).

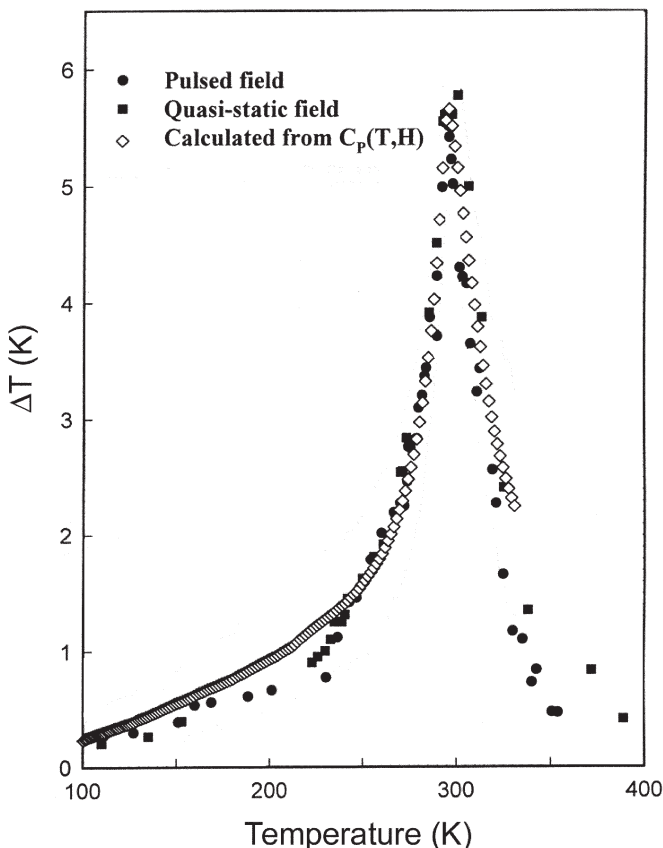


Figure 3.13. $\Delta T(T)$ dependences of high-purity polycrystalline Gd measured directly by pulsed and quasistatic techniques (solid symbols) and those determined from the heat capacity (open symbols) for $\Delta H = 20$ kOe (Dan'kov *et al* 1998). (Copyright 1998 by the American Physical Society.)

depend on the influence of the magnetic field on the heat capacity. If this influence is small (which usually takes place far from the magnetic phase transitions) the error can be considerable.

Figure 3.13 shows the MCE temperature dependences measured on high-purity polycrystalline Gd by the direct method in pulsed and quasistatic (switch-on technique) fields and determined from the heat capacity data for a magnetic field change from 0 to 20 kOe. Quite good agreement can be seen between the results obtained by these three methods, especially in the temperature range from 220 to 330 K. The $\Delta S_M(T)$ curves of Gd and ErAl₂ determined for $\Delta H = 50$ kOe from the magnetization measurements are also in good accordance with those calculated from the heat capacity data (Dan'kov *et al* 1998, Pecharsky and Gschneidner 1999a).

3.2.2.1 Heat pulse calorimetry

In this widely used method a heat pulse introduces into an adiabatically isolated sample the amount of heat ΔQ at the initial temperature T_i . As a result the sample temperature changes on the value of $\Delta T = T_f - T_i$, where T_f is the final temperature of the sample. The heat capacity at the temperature T_i can be calculated (see the heat capacity definition equation (2.10)) as

$$C \cong \frac{\Delta Q}{\Delta T}. \quad (3.17)$$

Figure 3.14 shows a schematic drawing of the vacuum calorimeter by which this method is realized. The calorimeter includes the sample (1) over which the electric heater (2) is wound. The sample is suspended by the leads (3) in the vacuum tight chamber (4), which is put in a cryostat (5). Vacuum in the camera provides thermal isolation of the sample. During the measurement process a known amount of heat ΔQ is introduced into the sample by passing a known current for a definite time interval, and the temperature change is measured by a thermometer (6). The sample initial temperature is also measured by the thermometer (6). To prevent heat transfer by radiation, which is significant at temperatures above about 20 K, an adiabatic shield (7) is

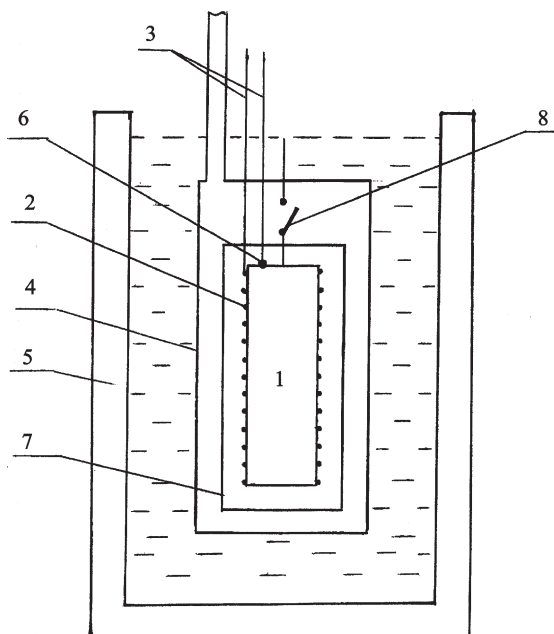


Figure 3.14. Schematic drawing of the vacuum heat pulse calorimeter: (1) sample; (2) electric heater; (3) leads; (4) vacuum-tight chamber; (5) cryostat; (6) thermometer; (7) adiabatic shield; (8) heat switch.

used. It contains a separate heater in order to follow the temperature of the sample (1) precisely, which makes a temperature gradient and thus heat exchange between the sample and the shield minimal. To provide cooling down to the lowest temperatures a heat switch (8) is used. It connects the sample inside the chamber (4) with the liquid gas in the cryostat during cooling. It should be noted that the real measurements always take place in semiadiabatic conditions, where some heat exchange between the sample and the surroundings occurs.

Consider, as an example, design and operation of the automatic heat pulse calorimeter proposed by Pecharsky *et al* (1997b). This apparatus works in the temperature range from ~ 3 to ~ 350 K and in magnetic fields from 0 to 100 kOe. An insert with the calorimeter and a low-temperature liquid helium pot is put into a cryostat, including a 120 kOe superconducting magnet with a room temperature vacuum-insulated 2.5 cm gap inside the magnet bore. The electronic hardware includes current sources, voltmeters and cryocontroller, and is guided by an IBM PC-compatible desktop computer with an IEEE-488 general-purpose interface board. The whole system is pumped by a high-speed vacuum pumping system capable of attaining a vacuum level of about 10^{-7} torr in order to obtain thermal insulation of the sample. The sample is placed inside the sample holder made of low-oxygen pure copper, for which the design is shown in figure 3.15. The sample (7) is clamped by the holding screw (6) on the top plate (4). Between the sample and the plate the mixture (3) of Apiezon-X grease and fine silver powder is

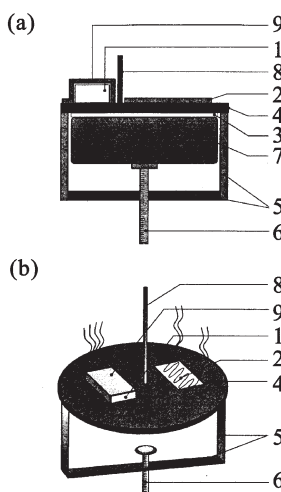


Figure 3.15. Design of the sample holder: its back (a) and three-dimensional (b) views. (1) Cernox temperature sensor; (2) heater; (3) mixture of Apiezon-N grease and silver powder; (4) top plate; (5) sample holder frame; (6) holding screw; (7) sample; (8) heat switch; (9) temperature sensor holding clamp (Pecharsky *et al* 1997b).

placed, which improves the thermal contact between them. A Cernox temperature sensor (1) in a copper clamp (9) is fixed by GE 7031 varnish. The sensor is characterized by low magnetic field dependence, fast response time and high accuracy. As a heater (2) a $350\text{-}\Omega$ thin film strain gauge is used. It is held in place by silver epoxy. A short copper wire (8) of 0.5 mm diameter is a part of mechanical heat switch. Besides the wire (8) it includes a modified alligator clamp constantly thermally shorted to the low-temperature helium pot above the sample holder. The sample holder is suspended on four nylon threads inside a massive copper frame, which is attached to the bottom of the helium pot. These three parts form the removable insert placed inside the room-temperature vacuum-insulated gap in the superconducting magnet bore. The insert is pumped by the vacuum system. Three concentric copper adiabatic shields (the inner shield contains a heater) provide for the sample conditions very close to adiabatic.

The calorimeter was calibrated using a high-purity copper sample, because its heat capacity is well known with an accuracy of 0.5%. The calibration allowed the heat capacity of the empty calorimeter to be obtained (sample holder and addenda), which were further subtracted from the measured total heat capacity in order to obtain the heat capacity of the sample under investigation.

Figure 3.16 illustrates the characteristic temperature–time dependence observed during a measurement in the calorimeter described above. Because the conditions inside the calorimeter were semiadiabatic (some

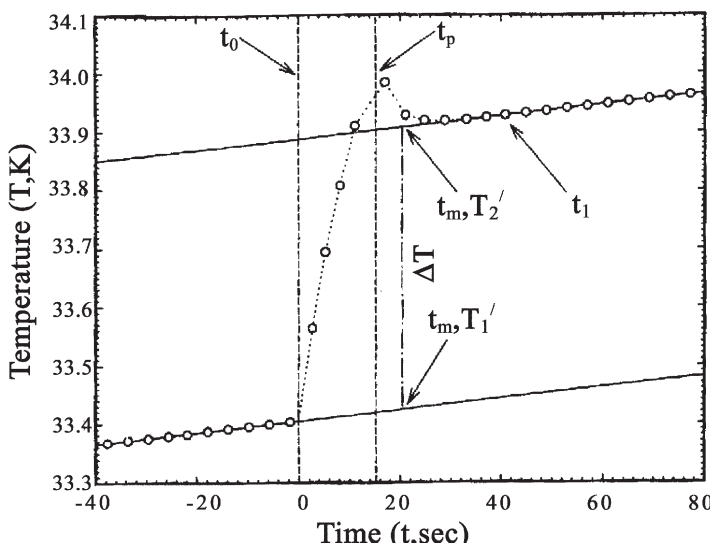


Figure 3.16. The characteristic temperature–time dependence observed during a measurement in the heat pulse calorimeter of Pecharsky *et al* (1997b).

heat exchange between the sample and surroundings existed) the temperature varied during the measurement. Pecharsky *et al* (1997b) distinguished four time periods in the measurement: ‘foredrift’ is the time just preceding the heat pulse (up to t_0); the ‘heat pulse period’ is when the heater is switched on, and starts at t_0 ($t = 0$) and ends at t_p ; ‘the relaxation period’ begins at t_p and ends at t_1 when the heat ΔQ introduced in the heat pulse period is distributed inside the calorimeter; and ‘afterdrift’ starts from t_1 when the calorimeter again reaches the state of thermal equilibrium. The temperature rise ΔT caused by introduction of the heat ΔQ is calculated as $\Delta T = T'_2 - T'_1$, where T'_2 and T'_1 are before- and after-pulse temperatures determined at median time $t_m = (t_0 + t_1)/2$ by extrapolation of the observed linear temperature time dependences. It is supposed that heat capacity is measured at the median temperature $T_m = (T'_2 - T'_1)/2$.

Thermal equilibrium of the calorimeter is considered to be reached when the calorimeter time dependence becomes linear with constant slope, i.e. the derivative $dT/dt = \text{const}$. In general, dT/dt is described by the linear function of time: $dT/dt = a + bt$. The formal criterion of the equilibrium was chosen as $b \approx 0$ then $|b| \leq 2 \times \sigma b$, where σb is the uncertainty in b .

The measurement was made in the following sequence. On the first stage the presence of the equilibrium state in the foredrift is established on the basis of 10 consecutive temperature readouts and the equilibrium criterion described above. When thermal equilibrium is achieved the heater is switched on automatically for a definite time, introducing a known value of the heat ΔQ . After the heat pulse it is necessary to detect the beginning of the afterdrift. It was supposed to begin when after-pulse values of dT/dt began to fall within the interval determined as $a \pm 2(\sigma a + \sigma b \times t)$, where σa and σb are the uncertainties in a and b coefficients of $dT/dt(t)$ dependence determined in the foredrift. If the afterdrift criterion is satisfied, 10 more temperature readouts are taken (the first reading corresponds to t_1) and the measurement is finished.

The particular feature of the apparatus under consideration is the method of adiabatic shield temperature controlling. Usually a special temperature sensor (or several sensors) is placed on the shield. The temperature data from the sensor are used by the control circuit to maintain the shield temperature equal to the median temperature of the calorimeter or to its temperature before the heat pulse. In such a method the power of the shield heater is determined by the readings from the temperature sensor on the shield and does not display the real heat transfer between the calorimeter and the surroundings. In the apparatus of Pecharsky *et al* (1997b) there is no temperature sensors on the adiabatic shield. The heat transfer state is determined from the measured $T(t)$ dependence. If the heat transfer is absent, the sample temperature does not change and the $T(t)$ curve slope is equal to zero. The slope differs from zero if the heat transfer is present—it is positive if the sample warms up and it is negative when the sample cools down. In the case

of zero slope no shield heater adjustment is necessary. In the case of sample heating or cooling data collection, software changes the heater power in order to minimize the heat transfer.

The errors in the considered heat pulse calorimeter arise from the errors related to heat and temperature measurements. Because the electronic equipment used in the apparatus allow highly precise determination of the input heat (estimation showed that the uncertainty in ΔQ is no more than 0.1%), the main source of errors is the measurement of the temperature of the calorimeter. It was shown that the total error in heat capacity is generally of the order of 0.5% except at the lowest temperatures and in the temperature range above 300 K (Pecharsky *et al* 1997b, Pecharsky and Gschneidner 1999a).

3.2.3 Other methods

Bready and Seyfert (1988) investigated entropy changes in EuS caused by a magnetic field with the help of a system consisting of a temperature control circuit and thermal resistor.

The temperature control circuit, including a carbon thermometer, electric heater and electronic system, allowed the sample temperature constant to be maintained independently of the magnetic field variation. Magnetic fields up to 30 kOe were created by the superconducting solenoid. A brass thermal resistor linked the sample holder to a liquid helium bath. The heat flux dQ/dt , flowing through the thermal resistor, determined the sample temperature. At constant magnetic field the flux is determined by the heat power W_0 , generated by the sample heater. When the magnetic field is changed, additional heat Q_{magn} is released in the sample due to the magnetocaloric effect and the electronic circuit increases or decreases the heater power W_x in order to keep the temperature of the sample constant. The process described can be represented by the following system of equations:

$$\frac{dQ(T)}{dt} = W_0, \quad \frac{dQ(T)}{dt} = W_x + \frac{dQ_{\text{magn}}}{dt}. \quad (3.18)$$

On the basis of this system it is possible to obtain the following equation after integration:

$$T\Delta S = T[S(H_2) - S(H_1)] = \int \left(\frac{dQ_{\text{magn}}}{dt} \right) dt = \int_{H_1}^{H_2} (W_x - W_0) dt \quad (3.19)$$

where $H_2 = H(t_2)$ and $H_1 = H(t_1)$. Measuring W_0 and W_x and integrating these values over time it is possible to determine the entropy change induced by the magnetic field change, mainly related to the magnetic entropy change.

Abramovich *et al* (2001) proposed to determine MCE from measurements of thermal expansion and magnetostriction in adiabatic and isothermal

regimes. Under adiabatic conditions of the forced magnetostriction measurements, the temperature change generated by the MCE causes a corresponding additional change of the sample dimensions. The total sample dimension change is a sum of this additional thermal expansion change and the magnetostriction. In general, the change of relative elongation of the sample $\lambda = \Delta l/l$ caused by the change of magnetic field H and temperature T can be written as

$$d\lambda = \left(\frac{\partial \lambda}{\partial H} \right)_T dH + \left(\frac{\partial \lambda}{\partial T} \right)_H dT. \quad (3.20)$$

From equation (3.20) the following equation which is allowed to determine the MCE can be obtained:

$$\frac{dT}{dH} = \frac{1}{\alpha_l} \left[\left(\frac{d\lambda}{dH} \right)_{ad} - \left(\frac{d\lambda}{dH} \right)_H \right] \quad (3.21)$$

where $\alpha_l = (d\lambda/dT)_H$ is the linear thermal expansion coefficient, $(d\lambda/dH)_{ad}$ and $(d\lambda/dH)_T$ are adiabatic and isothermal forced magnetostrictions, respectively. Using equation (3.21) and experimental data on α_l and on the magnetostriction measured in adiabatic and isothermal conditions, Abramovich *et al* (2001) obtained $\Delta T(T)$ dependence for $\text{Sm}_{0.6}\text{Sr}_{0.4}\text{MnO}_3$. However possible errors and limitations which could arise during utilization of this method are unknown.

Chapter 4

Magnetocaloric effect in 3d metals, alloys and compounds

3d metals were the first objects in which the MCE was investigated. Contributions to the MCE related to magnetic crystalline anisotropy were studied for the first time in Ni and Co. The Curie temperatures of magnetic 3d metals Fe, Co and Ni lie in the high-temperature region and the MCE near room temperature and below is not large. However, the magnetocaloric properties of alloys and compounds based on 3d metals have attracted much attention in recent times. This is due to various crystal and magnetic phases and corresponding phase transformations existing in some of them, and high magnetic entropy change values related to these transformations. In this section we consider the magnetocaloric properties of 3d metals (including thin Ni films), alloys and compounds based on 3d metals.

4.1 Ferromagnetic 3d metals

3d metals Fe, Co and Ni have high Curie temperatures: 1043, 1394 and 636 K (Bozorth 1978). For the first time the MCE maximum in the vicinity of the Curie temperature was observed in Ni by Weiss and Piccard (1918). This and further investigations of the MCE made in Fe, Co and Ni in the fields up to 30 kOe showed that the magnetocaloric effect near T_C was well described by equation (2.16) and is governed by the paraprocess (Weiss and Piccard 1918, Weiss and Forrer 1924, 1926, Potter 1934, Hirschler and Rocker 1966, Kohlhaas *et al* 1966, Kohlhaas 1967, Rocker and Kohlhaas 1967).

Weiss and Forrer (1926) showed experimentally that $\Delta T(I^2)$ dependences in ferromagnets are linear in the paraprocess region in accordance with equations (2.42) and (2.50). Extrapolating the linear part of $\Delta T(I^2)$ to the I^2 axis, Weiss and Forrer (1926) determined a value of spontaneous magnetization I_s^2 at various temperatures. This method was used to determine $I_s(T)$ dependence in Fe, Ni and Co by Weiss and Forrer (1926),

Table 4.1. Parameters of 3d ferromagnets used in theoretical calculations, the results of the calculations of the maximum possible values of the MCE (ΔT_{\max}) at T_C and the values of the magnetic field H_{\max} (the field varies from 0 to H_{\max}), in which the MCE differs from ΔT_{\max} by at most 1% (Tishin 1990a).

3d ferromagnet	J	T_C (K)	T_D (K)	ΔT_{\max} (K)	H_{\max} ($\times 10^4$ kOe)
Fe	1.4	1043	420	350	6
Ni	0.3045	631	385	84	2.9
Co	0.95	1403	375	348	6.5

Potter (1934) and Rocker and Kohlhaas (1967). Belov (1961a,b) observed in Ni in the temperature range from 618 to 627 K the linear dependence of $H/\Delta T^{1/2}$ on ΔT predicted by the Landau theory (see equation (2.32b)).

It is known that the mean field approximation satisfactorily describes the temperature dependence of the spontaneous magnetization in 3d ferromagnets. Based on this, Tishin (1990a) used the MFA to determine the MCE in Fe, Co and Ni. First, by means of equations (2.58)–(2.60) and (2.63), the temperature dependences of the total entropy of a material in zero and nonzero magnetic fields were calculated and then $\Delta T(T)$ dependences were obtained by the method described in section 3.2.2 (see equation (3.14)). In the calculations $g_J = 2$ was used and the values of J were determined from comparison of the experimental temperature dependences of the spontaneous magnetization in the vicinity of the Curie temperature with the results of calculations made by MFA. Table 4.1 shows the values of J , T_C and Debye temperature T_D used in the calculations.

The results of $\Delta T(T)$ theoretical calculations for Fe, Co and Ni made by Tishin (1990a), together with experimental curves of Weiss and Forrer (1924), Potter (1934) and Kohlhaas (1967), are presented in figures 4.1–4.3. It is seen that they are in good agreement. In Fe the MCE near the Curie temperature for $\Delta H = 60$ kOe is 9.5 K. According to the measurements of Hirschler and Rocker (1966) and Kohlhaas (1967) near the Curie temperature ΔT in Ni is ~ 1.8 K and ~ 5.1 K in Fe for $\Delta H = 30$ kOe and in Co $\Delta T \approx 3.3$ for $\Delta H = 21.6$ kOe (this corresponds to $\Delta T/\Delta H$ of 0.06, 0.17 and 0.153 K/kOe, respectively). In Gd and Tb, having the largest MCE values among rare earth metals, the MCE is about 12 and 10.5 K in the same field, respectively (Brown 1976, Nikitin *et al* 1985a,b). So, the values of magnetocaloric effect in 3d ferromagnets in strong magnetic fields have magnitudes comparable with those observed in rare earth metals. This result can be easily understood by taking into account that in accordance with equation (2.16) the value of MCE is directly proportional to the value of initial temperature T . Thus in the high-temperature region it is natural to expect elevated MCE values even for the magnetic materials with medium values of magnetic moments.

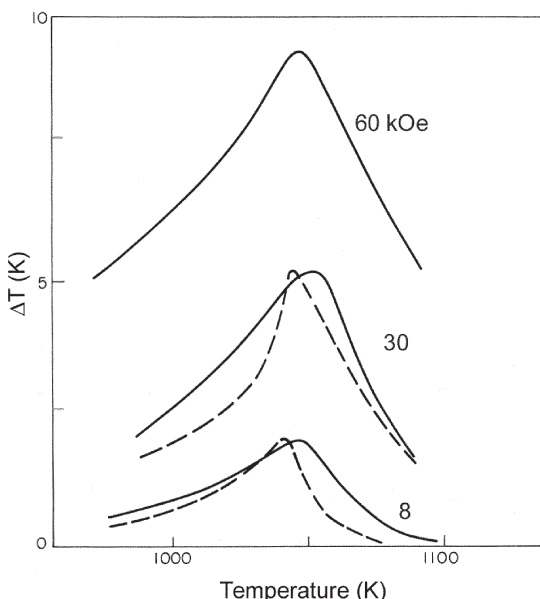


Figure 4.1. Theoretical (—) and experimental (---) MCE temperature dependence for various magnetic field changes ΔH (specified near the curves) in Fe (Potter 1934, Tishin 1990a). (Reprinted from Tishin 1990a, copyright 1990, with permission from Elsevier.)

The calculated MCE field dependences in Fe, Co and Ni in the vicinity of the Curie temperature are shown in figure 4.4. The linear MCE increase with the field is observed only in weak magnetic fields. The obtained dependences describe well the MCE experimental values (see figure 4.4).

The calculated MCE temperature dependences induced by the magnetic fields of 6×10^3 kOe are presented in figure 4.5. Unlike rare earth metals, in 3d ferromagnets in this field the MCE maximum is quite sharp. The MCE in Fe and Co exceeds that of Ni by several times. Tishin (1990a) also calculated the maximum possible MCE (ΔT_{\max}) in Fe, Co and Ni at the Curie temperature using equation (2.79). The maximum possible ΔS_M value was determined by equation (2.66) for the corresponding J value and the heat capacity was assumed to be equal to the DuLong–Petit limit $3R$. The values of $\Delta H_{\max}(T_C)$ in which the MCE is different from ΔT_{\max} by at most 1% were calculated in the framework of MFA. The results are shown in table 4.1. ΔT_{\max} in Fe and Co is larger than in rare earth metals (see table 8.3).

Hashimoto *et al* (1981) made analogous mean field calculations of MCE at low magnetic field. They were found to be in good agreement with experimental results for Ni obtained by Weiss and Forrer (1926). According to their measurements in Ni, $\Delta T \approx 1.3$ K at $T_C = 628$ K and $\Delta H = 17.8$ kOe. Noakes and Arrott (1973) studied the MCE of a nickel single crystal in the

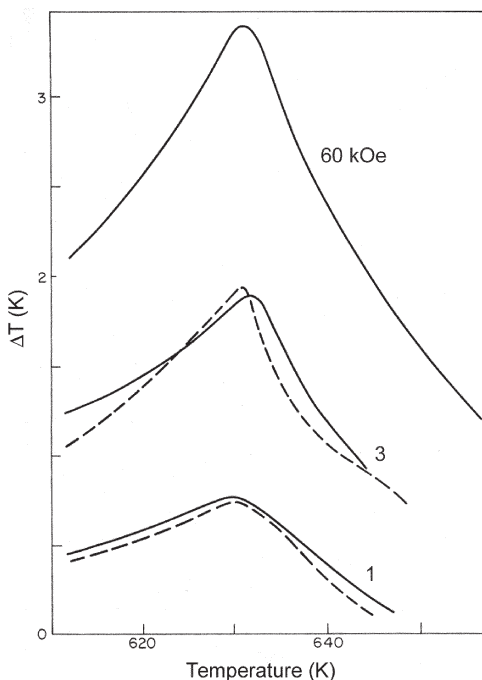


Figure 4.2. Theoretical (—) and experimental (---) MCE temperature dependence for various magnetic field changes ΔH (specified near the curves) in Ni (Weiss and Forrer 1924, Tishin 1990a). (Reprinted from Tishin 1990a, copyright 1990, with permission from Elsevier.)

vicinity of T_C in weak fields up to 900 Oe. They found for $\Delta H = 900$ Oe the maximum MCE value of 0.15 K.

Akulov and Kirensky (1940) investigated the MCE caused by the process of saturation magnetization vector rotation in Ni single crystal. The crystal was magnetized in the (110) plane and the spontaneous magnetization vector orientation in this plane was determined by an angle φ from [100] direction. The direction cosines α_i of the spontaneous magnetization vector in this case have the form

$$\alpha_1 = \frac{1}{\sqrt{2}} \sin \varphi, \quad \alpha_2 = \frac{1}{\sqrt{2}} \sin \varphi, \quad \alpha_3 = \cos \varphi. \quad (4.1)$$

Using equations (2.136), (4.1) and the temperature dependence of anisotropy constant K_1 in the form

$$K_1 = K_{10} \exp(-aT^2) \quad (4.2)$$

where K_{10} and a are constants, Akulov and Kirensky (1940) obtained the following equation for the angle dependence of the MCE under the given

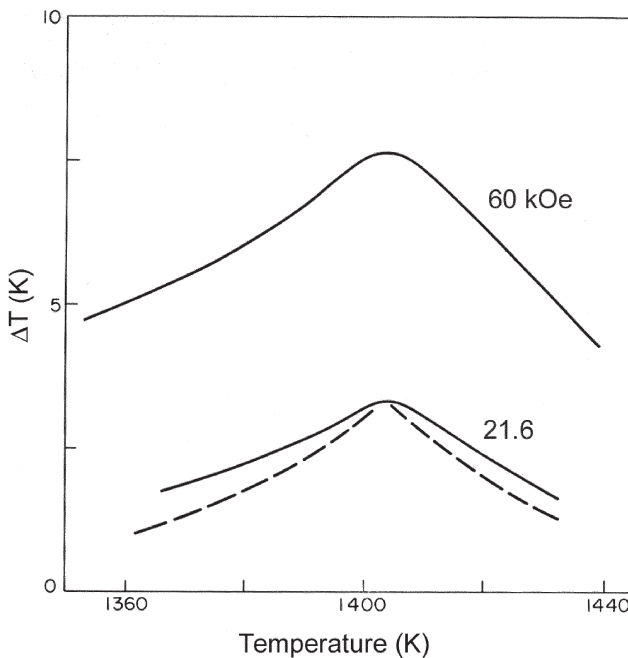


Figure 4.3. Theoretical (—) and experimental (---) MCE temperature dependence for various magnetic field changes ΔH (specified near the curves) in Co (Kohlhaas 1967, Tishin 1990a). (Reprinted from Tishin 1990a, copyright 1990, with permission from Elsevier.)

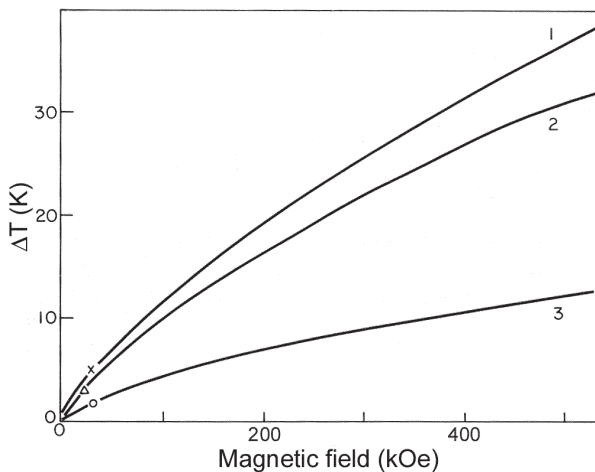


Figure 4.4. Theoretical MCE dependences on the magnetic field (the magnetic field is changed from 0 to H) at T_C for Fe (1), Co (2) and Ni (3) (Tishin 1990a). Experimental values are taken from Weiss and Piccard (1918), Potter (1934) and Kohlhaas (1967). (Reprinted from Tishin 1990a, copyright 1990, with permission from Elsevier.)

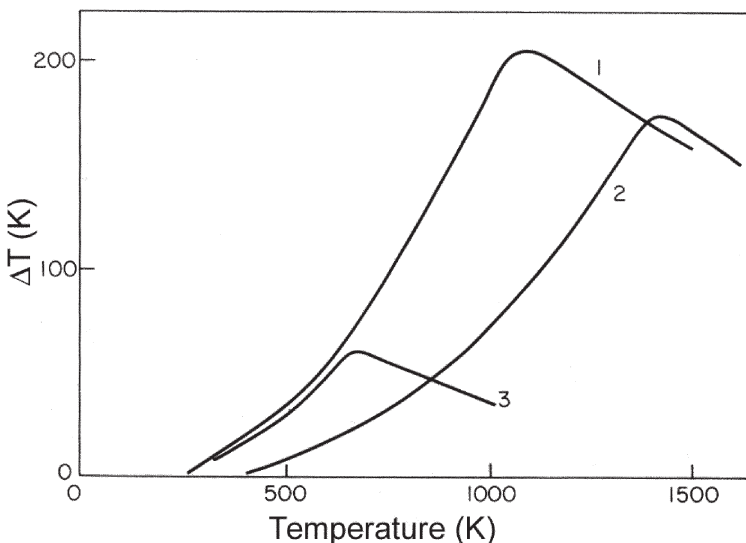


Figure 4.5. Theoretical MCE temperature dependences calculated for $\Delta H = 6 \times 10^3$ kOe in Fe (1), Co (2) and Ni (3) (Tishin 1990a). (Reprinted from Tishin 1990a, copyright 1990, with permission from Elsevier.)

conditions:

$$\Delta T_a = \frac{4aK_{10}}{C_H} T^2 (1 - \frac{3}{4} \sin^2 \varphi) \sin^2 \varphi. \quad (4.3)$$

Figure 4.6 shows experimental MCE dependence on the angle φ obtained in Ni single crystal magnetized by rotation of the magnetization vector in the (110) plane (circles), together with the theoretical curve (solid line) calculated by equation (4.3) (the values of K_{10} , a and C_H were determined experimentally in separate measurements). As can be seen the experimental MCE values display periodical dependence on the spontaneous magnetization vector direction, which is well described by theoretical dependence (4.3). Analogous measurements were made by Ivanovskii and Denisov (1966a,b) on Co single crystal. In this case the angle φ was an angle between a hexagonal axis and a spontaneous magnetization vector. The observed periodical MCE dependence on φ was explained by the formula derived on the basis of equation (2.135).

The MCE magnetic field dependence in Co polycrystal in the region of magnetization vector rotation was studied by Ivanovskii (1959). The measurements were made in the temperature interval from 78 to 812 K in the following way: First the initial magnetic field H_0 was imposed on the sample. The value of H_0 was reduced for higher temperatures because magnetocrystalline anisotropy decreased with temperature. When the temperature of the sample relaxed to the temperature of its surroundings the magnetic field changed

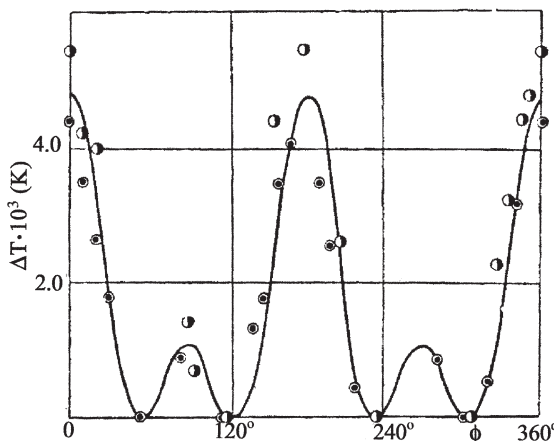


Figure 4.6. Experimental MCE dependence on the angle φ obtained in Ni single crystal magnetized by rotation of the magnetization vector in (110) plane (\circ) and the theoretical curve (—) calculated by equation (4.3) (Akulov and Kirensky 1940).

from H_0 to H . The MCE dependences obtained for Co polycrystal in this way at different temperatures are shown in figure 4.7. Experiments showed that below 500 K the MCE caused by magnetic field increase had a negative sign and above 600 K it is positive. It was shown that the ΔT sign change took place near 565 K. In the interval between 500 and 600 K, first sample cooling was observed in low fields, and heating in more intensive fields (see the curve for 542 K in figure 4.7). The obtained results were interpreted on the basis of equation (2.140). The results were corrected on the value of the

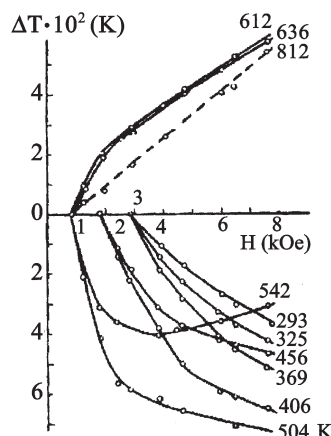


Figure 4.7. MCE field dependences obtained for Co polycrystal at different temperatures (Ivanovskii 1959).

MCE of the paraprocess, which is described by equation (2.16) and can have some contribution to the MCE, especially in the high-temperature region. The observed behaviour was related to sign change of the value in brackets in equation (2.140), which in turn was explained by the temperature behaviour of the anisotropy constant K_1 in Co: near 535 K, K_1 changed its sign from positive in the low-temperature region to negative at higher temperatures.

Pakhomov (1962), with the help of equation (2.142), estimated the influence of mechanical strain on the MCE in the region of spontaneous magnetization vector rotation in Fe and Ni, using experimentally determined data on anisotropy and magnetostriction constants. It was shown that the strain-dependent part in the MCE under strains in the limit of elasticity ($\sim 5 \text{ kg/mm}^2$ for Fe and $\sim 9 \text{ kg/mm}^2$ for Ni) is about 13% of the anisotropic part in Fe and about 100% of the anisotropic part in Ni.

Kohlhaas *et al* (1966) used equation (2.155) to obtain the heat capacity of Fe in a magnetic field from the data on zero-field heat capacity. As can be seen from figure 4.8, where the experimental results and the results of calculations are shown, the $C_{H,p}(T)$ curve near the Curie temperature becomes smooth and the heat capacity maximum becomes significantly lower in the

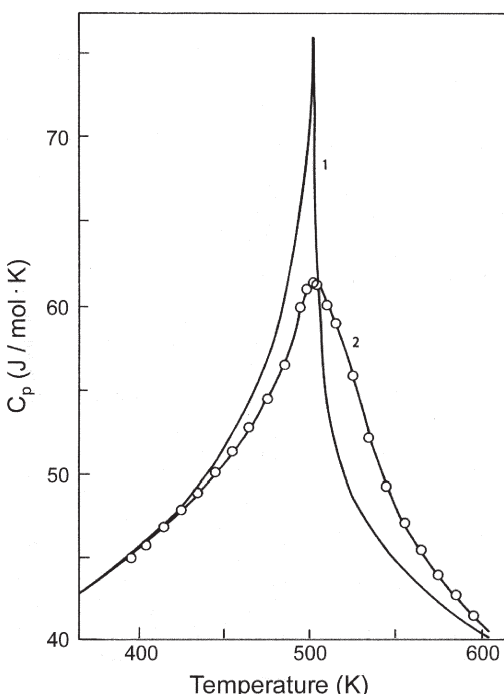


Figure 4.8. Heat capacity temperature dependences of Fe in zero magnetic field (curve 1: experimental data) and $H = 30 \text{ kOe}$ (curve 2: —, result of calculations; ○, experimental data) (Kohlhaas *et al* 1966).

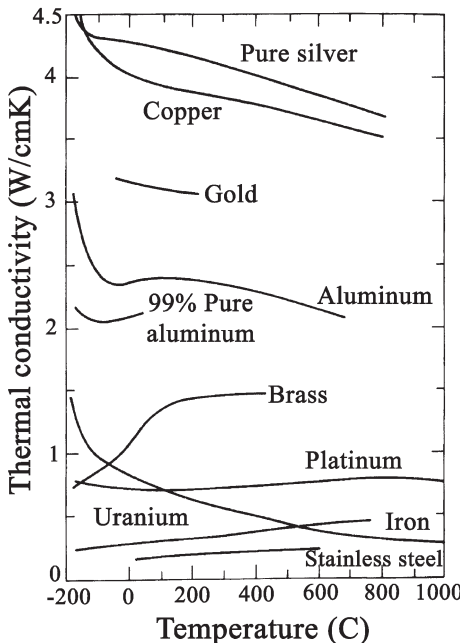


Figure 4.9. Thermal conductivity temperature dependences for some metals (Lienhard *et al* 2002).

magnetic field. Analogous behaviour was observed in Ni, Co and Fe–Si alloys (Hirschler and Rocker 1966, Rocker and Kohlhaas 1967, Korn and Kohlhaas 1969). The numerical heat capacity data for Fe, Ni and some other metals are presented in table A2.1 in appendix 2.

The data about thermal conductivity of various metals including Fe and Ni can be found in the book by Lienhard *et al* (2002); some of them are presented in table A2.1 in appendix 2. Figure 4.9 shows temperature dependences of the thermal conductivity for various metals. As can be seen, in most cases it increases with temperature decreasing in the interval from high temperatures down to liquid nitrogen temperature. The highest thermal conductivity values are observed in high conductivity metals—silver and copper—which are nonmagnetic. In general, thermal conductivity of nonmagnetic metals can be presented as a sum of electronic and phonon (lattice) contributions (Hume-Rothery 1961, Kittel 1986). In the case of a pure electron heat conduction mechanism, the thermal conductivity at not very low temperatures obeys the Wiedemann–Franz law, which states that (Hume-Rothery 1961, Kittel 1986)

$$\frac{\lambda}{\sigma} = L_0 T \quad (4.4)$$

where λ is the thermal conductivity, T is the temperature, σ is the electrical conductivity and L_0 is a constant (Lorentz number). From the pure electron heat conduction model it follows that L_0 is equal to $2.45 \times 10^{-8} \text{ V}^2/\text{K}^2$. Using equation (4.4) it is possible to estimate the thermal conductivity of a metal, knowing its electrical conductivity. At low temperatures the electronic thermal conductivity of a pure metal has two contributions, one of which is proportional to T (related to electron scattering on various structural defects) and another to T^{-2} (related to electron scattering on phonons) (Hume-Rothery 1961). Such temperature dependence of the contributions causes the appearance of a maximum on the thermal conductivity temperature dependence of a metal in the low-temperature range, which was observed experimentally, for example, in Cu at $\sim 18 \text{ K}$ by Berman and MacDonald (1952). In magnetic metals the additional magnon mechanism can also make a contribution to the thermal conductivity and make it dependent on the magnetic field.

4.2 Alloys and compounds

Hashimoto *et al* (1981) investigated MCE in ferromagnetic Cr_3Te_4 experimentally and theoretically with the help of MFA. Figure 4.10 shows experimental and theoretical MCE temperature dependences in Cr_3Te_4 for $\Delta H = 20 \text{ kOe}$. One can see a fairly good agreement between the calculations and experiment. At $T_C = 316 \text{ K}$ the MCE in Cr_3Te_4 reaches a value of about 1.1 K for $\Delta H = 20 \text{ kOe}$. The peak values of ΔS_M in ferromagnets MnAs, MnP and CrTe near T_C are presented in table 4.2. MFA was also successfully

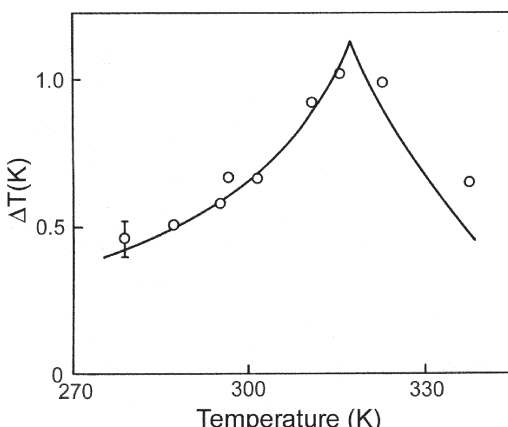


Figure 4.10. The MCE temperature dependence in Cr_3Te_4 for $\Delta H = 20 \text{ kOe}$. Open circles are the experimental points and the solid curve is the MFA calculations (Hashimoto *et al* 1981). (Reprinted from Hashimoto *et al* 1981, copyright 1981, with permission from Elsevier.)

Table 4.2. Peak values of the magnetocaloric effect ΔT and magnetic entropy change ΔS_M near the temperature of the magnetic phase transition T_{pt} induced by a magnetic field change ΔH and $\Delta T/\Delta H$ and $-\Delta S_M/\Delta H$ values for 3d metal-based compounds and alloys. (T_{pt} is T_C for MnAs, MnP, CrTe, Mn_5Ge_3 , MnFeP_{1-x}As_x, $Fe_{0.966}Si_{0.0334}$, $Mn_5Ge_{3-x}S_{x}$ ($x = 3-5$), $Mn_5Ge_{3-x}S_{x}$ ($x = 0-3$); T_N for $Mn_{0.95}V_{0.05}As$, $Mn_{0.228}Ch_{0.772}$; T_{AFM-FM} for $Fe_{0.49}Rh_{0.51}$, $Mn_{1.95}Cr_{0.05}Sb$; noncollinear AFM-collinear AFM for Mn_5Si_3 ; martensitic-austenitic transition for $Ni_{0.515}Mn_{0.227}Ga_{0.258}$, $Ni_{0.501}Mn_{0.207}Ga_{0.296}$, $Ni_{0.526}Mn_{0.231}Ga_{0.243}$, $Ni_{0.53}Mn_{0.22}Ga_{0.25}$). References are in square brackets.

Substance	T_{pt} (K)	Peak MCE			Peak – ΔS_M		
		ΔT (K)	ΔH (kOe)	$\Delta T/\Delta H \times 10^2$ (K/kOe)	$-\Delta S_M$ (J/kg K)	ΔH (kOe)	$-\Delta S_M/\Delta H \times 10^2$ (J/kg K kOe)
MnAs	318 [1]	–	–	–	2.9 [1]	10	29
	312 [2]	–	–	–	11.4 [1]	80	14.3
		13 [7]	50	26	32 [7]	50	64
		5 [7]	20	25			
$MnAs_{0.9}Sb_{0.05}$	310 [7]	–	–	–	30 [7]	50	60
$MnAs_{0.9}Sb_{0.1}$	283 [7]	–	–	–	30 [7]	50	60
$MnAs_{0.85}Sb_{0.15}$	262 [15]	–	–	–	30 [5]	50	60
$MnAs_{0.75}Sb_{0.25}$	230 [15]	–	–	–	26 [15]	50	52
$MnAs_{0.7}Sb_{0.3}$	220 [15]	–	–	–	27 [15]	50	54
$MnAs_{0.6}Sb_{0.4}$	210 [15]	–	–	–	14 [15]	50	28
$Mn_{0.95}V_{0.05}As$	203 [8]	5.5 [8]	250	2.2	–	–	–
MnP	298 [1]	–	–	–	2.9 [1]	10	29
CrTe	333 [1]	–	–	–	11.4 [1]	80	14.3
		–	–	–	1.7 [1]	10	17
		–	–	–	6.8 [1]	80	8.5
Mn_5Ge_3	298 [3]	1.7 [3]	20	–	–	–	–
$Fe_{0.49}Rh_{0.51}$ (quenched)	313 [4, 5]	–12.9 [4]	19.5	–66.2	–22 [5]	19.5	–112.8
		–4.6 [4]	6.5	–70.8	–16 [5]	6.5	–246.2

$\text{Fe}_{0.49}\text{Rh}_{0.51}$ (annealed)	342 [4, 5]	-3.8 [4] -1.2 [4]	19.5 6.5	-19.5 -18.5	-6.5 [5] -2 [5]	9.5 6.5	-33.3 -30.8
$\text{Fe}_{0.49}\text{Rh}_{0.51}$	315.6 [6]	-8.5 [6] -2.5 [6]	25 3	-34 -83.3	-	-	-
$\text{MnFeP}_{0.75}\text{As}_{0.25}$	168 [9]	-	-	-	27 [9] 11 [9] 33 [9] 12 [9]	50 20 50 20	54 55 66 60
$\text{MnFeP}_{0.65}\text{As}_{0.35}$	~212 [9]	-	-	-	24 [9] 20 [9] 20 [9]	50 20 50	48 100 40
$\text{MnFeP}_{0.55}\text{As}_{0.45}$	~244 [9]	-	-	-	16 [9] 18 [9] 14 [9]	20 50 20	80 36 70
$\text{MnFeP}_{0.5}\text{As}_{0.5}$	~287 [9]	-	-	-	15 [9]	50	30
$\text{MnFeP}_{0.45}\text{As}_{0.55}$	~308 [9]	-	-	-	11 [9]	20	55
$\text{MnFeP}_{0.35}\text{As}_{0.65}$	332 [9]	-	-	-	-	-	-
$\text{Mn}_{0.228}\text{Cu}_{0.772}$	94 [10]	0.14	13.8	1	-	-	-
$\text{Ni}_{0.515}\text{Mn}_{0.227}\text{Ga}_{0.258}$	197 [11]	-	-	-	-4.1 [11] -6 [12] 6 [12]	9 8 50	-46 -75 12
$\text{Ni}_{0.501}\text{Mn}_{0.207}\text{Ga}_{0.296}$	219 [12]	-	-	-	18 [13] -1.1 [9] -2.5 [9]	50 20 10	36 -5.5 -25
$\text{Ni}_{0.526}\text{Mn}_{0.231}\text{Ga}_{0.243}$	297 [13]	-	-	-	-	-	-
$\text{Ni}_{0.53}\text{Mn}_{0.22}\text{Ga}_{0.25}$	220 [9]	-	-	-	-	-	-
$\text{Fe}_{0.9666}\text{Si}_{0.0334}$	1013 [14]	5	30	16.7	-4 [9] -1 [9]	50 10	-8 -10
Mn_5Si_3	66 [9]	-	-	-	-	-	-

Table 4.2. Continued.

Substance	T_{pt} (K)	Peak MCE			Peak $-\Delta S_M$		
		ΔT (K)	ΔH (kOe)	$\Delta T/\Delta H \times 10^2$ (K/kOe)	$-\Delta S_M$ (J/kg K)	ΔH (kOe)	$-\Delta S_M/\Delta H \times 10^2$ (J/kg K kOe)
Mn ₂ Fe ₃ Si ₃	250 [16]	—	—	—	1.7 [16]	50	3.4
Mn ₁ Fe ₄ Si ₃	310 [16]	—	—	—	0.5 [16]	20	2.5
Fe ₅ Si ₃	363 [16]	—	—	—	4 [16]	50	8
Mn ₅ Ge ₃	298 [17]	—	—	—	2 [16]	20	10
Mn ₅ Ge _{2.9} Sb _{0.1}	304 [17]	—	—	—	2.7 [16]	50	5.4
Mn ₅ Ge _{2.8} Sb _{0.2}	307 [17]	—	—	—	1 [16]	20	5
Mn ₅ Ge _{2.7} Sb _{0.3}	312 [17]	—	—	—	9.3 [17]	50	18.6
Mn _{1.95} Cr _{0.05} Sb	198 [9]	—	—	—	3.8 [17]	20	19

1. Hashimoto *et al.* (1981); 2. Adachi (1961); 3. Hashimoto *et al.* (1990); 4. Nikitin *et al.* (1982); 5. Annaorazov *et al.* (1992); 6. Annaorazov *et al.* (1996); 7. Wada and Tanabe (2001); 8. Selle *et al.* (1977); 9. Tegus *et al.* (2002b); 10. Znamenskii and Fakidov (1962); 11. Hu *et al.* (2000a); 12. Hu *et al.* (2001d); 13. Hu *et al.* (2001c); 14. Hirschler and Rocker (1966); 15. Wada *et al.* (2002); 16. Songlin *et al.* (2002b); 17. Songlin *et al.* (2002a).

used by Hashimoto *et al* (1982) to describe the MCE in ferromagnetic compound Mn_5Ge_3 , which had $\Delta T \approx 1.7$ K for $\Delta H = 20$ kOe at $T_C = 298$ K.

The MCE at the first-order order–order transition (for example, from ferrimagnetic (FI) or ferromagnetic to antiferromagnetic (AFM) state) was studied in FeRh (Fe concentration of 0.48–0.50) (Ponomarev 1972, Nikitin *et al* 1990, Annaorazov *et al* 1992), $\text{Mn}_{2-x}\text{Cr}_x\text{Sb}$ ($x = 0.03$ –0.16), Mn_3Ge_2 , $\text{CrS}_{1.17}$, $\text{Li}_{0.1}\text{Mn}_{0.9}\text{Se}$, $\text{Mn}_{0.95}\text{V}_{0.05}\text{As}$, Mn_5Si_3 and $\text{Mn}_{1.95}\text{Cr}_{0.05}\text{Sb}$ (Flippen and Darnell 1963, Seltz *et al* 1977, Baranov *et al* 1992, Engelhardt *et al* 1999, Tegus *et al* 2002b).

In Fe–Rh alloys the AFM–FM phase transition happens near room temperature within the concentration range 47–53% of Rh (Kouvel and Hartelius 1962, Zaharov *et al* 1964). The first direct MCE measurements of quenched and annealed $\text{Fe}_{0.49}\text{Rh}_{0.51}$ alloys in magnetic fields up to 19.5 kOe were made in the works of Nikitin *et al* (1990), Annaorazov *et al* (1991) and Annaorazov *et al* (1992) with participation of one of the authors of this book. The samples prepared by induction melting were homogeneously annealed at 1300 K in vacuum for 72 h. After annealing, one of the samples was quenched in water from 1300 to 278 K. In the region of AFM–FM transition at about 310 K the magnetic field induced the transition from the AFM state to the ferromagnetic one. The maximum MCE reached 12.9 K in the quenched sample and 3.8 K in the annealed sample in a field of 19.5 kOe near the temperature of the first-order transition of 313 and 342 K, respectively (the Curie temperature of the alloy obtained from initial permeability measurements was 633 K)—see figure 4.11. It should be noted that the MCE induced under application of a magnetic field was negative. On the basis of the experimental MCE values it is possible to determine the value of the MCE per kOe ($\Delta T/\Delta H$): for the quenched sample it is 0.662 K/kOe and 0.708 K/kOe for $\Delta H = 19.5$ and 6.5 kOe; and for the annealed sample it is 0.195 K/kOe and 0.185 K/kOe for $H = 19.5$ and 6.5 kOe, respectively. The values of $\Delta T/\Delta H$ in the quenched $\text{Fe}_{0.49}\text{Rh}_{0.51}$ sample are the highest found so far among the magnetocaloric materials in the room-temperature range. It should also be mentioned that such high $\Delta T/\Delta H$ values were obtained in the fields that can be created by permanent magnets. However, as was noted by Annaorazov *et al* (1996) there is the influence of thermomagnetic cycling caused by repeatable induction of the transition by a magnetic field on the parameters of AFM–FM transition, which manifests itself in an irreversible decrease of the MCE value. The authors related this behaviour to the appearance of the part of the sample stable in the FM or AMF phase, which did not contribute to the MCE under further magnetic cycling. The magnetic entropy change in $\text{Fe}_{0.49}\text{Rh}_{0.51}$ was determined on the basis of the heat capacity and magnetocaloric effect data. Figure 4.12 shows the entropy change temperature dependences for $\Delta H = 6.5$ and 19.5 kOe in the annealed and quenched $\text{Fe}_{0.49}\text{Rh}_{0.51}$ alloy. As one can see, the entropy change in the quenched sample reaches about 22 J/kg K in the field of 19.5 kOe—this corresponds to

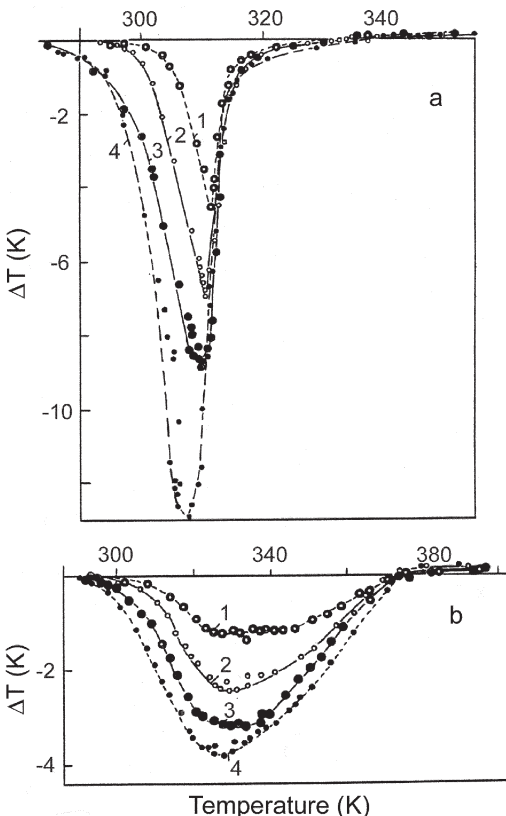


Figure 4.11. MCE temperature dependences for quenched (a) and annealed (b) samples of $\text{Fe}_{0.49}\text{Rh}_{0.51}$ induced by a magnetic field: (1) $\Delta H = 6.5 \text{ kOe}$, (2) 12.5 kOe , (3) 17 kOe , (4) 19.5 kOe (Nikitin *et al* 1990, Annaorazov *et al* 1992). (Reprinted from Annaorazov *et al* 1992, copyright 1992, with permission from Elsevier.)

$\Delta S_M/\Delta H = 1.128 \text{ J/kg K kOe}$, which is much higher than that in Gd and is at the level of $\text{Gd}_5(\text{Si}-\text{Ge})_4$ and LaFeSi alloys—see tables 8.2, 7.2 and 6.4. The even higher value of $\Delta S_M/\Delta H = 2.462 \text{ J/kg K kOe}$ was obtained for $\Delta H = 6.5 \text{ kOe}$ for the quenched sample.

Annaorazov *et al* (1996) demonstrated the higher value of $\Delta T/\Delta H = 0.833 \text{ K/kOe}$ in $\text{Fe}_{0.49}\text{Rh}_{0.51}$ alloy for $\Delta H = 3 \text{ kOe}$ and $T_{\text{AFM-FM}} = 315.6 \text{ K}$. It should be noted that the properties of Fe–Rh alloys are sensitive to thermal treatment and composition. Based on the fact that the value of the magnetic phase transition of the alloy investigated by Annaorazov *et al* (1996) is different from that obtained in the works of Nikitin *et al* (1990), Annaorazov *et al* (1991) and Annaorazov *et al* (1992), it is possible to suggest that the thermal treatment and the exact composition of the sample studied by Annaorazov *et al* (1996) are not the same as in the earlier works.

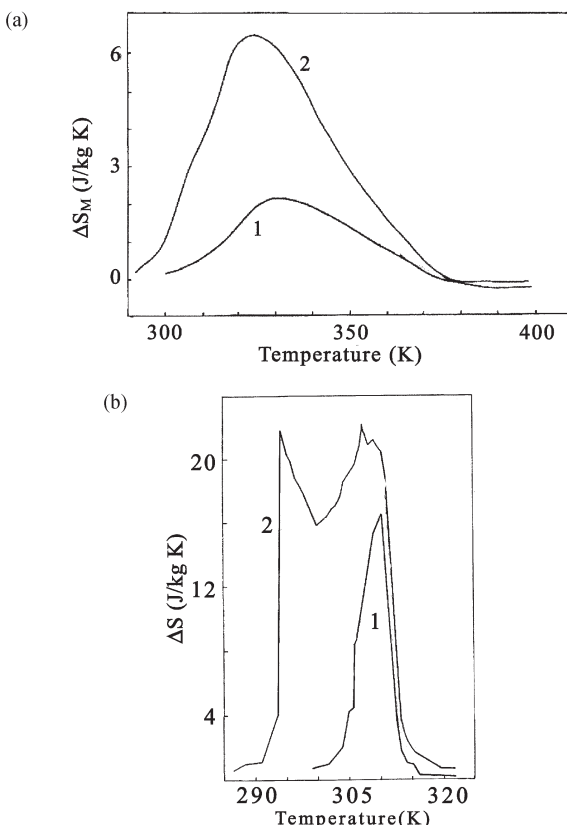


Figure 4.12. Magnetic entropy change temperature dependences in the annealed (a) and quenched (b) $\text{Fe}_{0.49}\text{Rh}_{0.51}$ samples induced by $\Delta H = 6.5\text{ kOe}$ (1) and 19.5 kOe (2) (Nikitin *et al* 1990, Annaorazov *et al* 1992). (Reprinted from Annaorazov *et al* 1992, copyright 1992, with permission from Elsevier.)

Annaorazov *et al* (1996) conducted the analysis of various contributions to the magnetic entropy change under the transition on the basis of the model of the first-order magnetic phase transition proposed by Kittel (1960). They concluded that the change of the electronic part of the entropy (11.82 J/kg K) gave the major contribution and that the contribution from the change of the lattice entropy is much lower (0.76 J/kg K). According to the results of Annaorazov *et al* (1996) the change in electronic structure (the change in Fermi surface topology) is the determining factor of the transition.

According to Ibarra and Algarabel (1994) the Fe–Rh alloy is characterized by large crystal lattice volume change (0.82%) at the first-order transition. Using the data about crystal lattice volume change and $dT_C/dP = 3.08\text{ K/kbar}$ from the work of Bean and Rodbell (1962) for dP/dT , Tishin *et al* (2002) calculated with the help of equation (6.3) the

lattice entropy change in $\text{Fe}_{0.49}\text{Rh}_{0.51}$ at the transition. The value of change was determined to be 27 J/kg K , which is close to the experimentally obtained value of $\sim 21 \text{ J/kg K}$ for $\Delta H = 19.5 \text{ kOe}$. It was concluded that high magnetocaloric properties of $\text{Fe}_{0.49}\text{Rh}_{0.51}$ are determined by the strong coupling of magnetic and lattice systems and essential change of crystal lattice dimensions at the first-order transition.

Ponomarev (1972) measured magnetization of $\text{Fe}_{0.48}\text{Rh}_{0.52}$ in pulsed fields up to 300 kOe in the temperature range from 77 to 320 K (saturation magnetization at 77 K was determined to be 128 emu/g). He constructed the magnetic phase diagram $H_{\text{cr}}(T)$ (here $H_{\text{cr}}(T)$ is the field of the AFM structure destruction) and determined specific magnetization change $\Delta\sigma$ ($\sigma = M/m$, where m is a mass) under the transition. On the basis of these data and the Clausius–Clapeyron equation (2.100) the magnetic entropy change ΔS_M at the transition temperature $T_{\text{AFM–FM}} = 333 \text{ K}$ was calculated to be 18.3 J/kg K . Then the magnetocaloric effect $\Delta T \approx 200 \text{ K}$ was determined with the help of equation (2.79). Tishin *et al* (2002) also estimated the magnetic entropy change under first-order AFM–FM transition in $\text{Fe}_{0.49}\text{Rh}_{0.51}$ alloy using equation (2.100) and magnetic phase diagram data from the work of Ibarra and Algarabel (1994), and obtained the value of 12.9 J/kg K .

Analogous calculations of the entropy change ΔS on the basis of magnetization measurements were made by Baranov *et al* (1992) for $\text{Mn}_{1.9}\text{Cr}_{0.1}\text{Sb}$ and by Flippin and Darnell (1963) for $\text{Fe}_{0.5}\text{Rh}_{0.5}$, $\text{Mn}_{2-x}\text{Cr}_x\text{Sb}$, Mn_3Ge_2 , $\text{CrS}_{1.17}$ and $\text{Li}_{0.1}\text{Mn}_{0.9}\text{Se}$. Engelhardt *et al* (1999) constructed a magnetic phase diagram of the $\text{Mn}_{2-x}\text{Cr}_x\text{Sb}$ ($x = 0.10, 0.05, 0.03$) system and also determined the entropy change of the first-order transition from heat capacity measurements in various magnetic fields. The results are summarized in table 4.3. Direct MCE measurements in $\text{Mn}_{1.90}\text{Cr}_{0.10}\text{Sb}$ made by Baranov *et al* (1992) gave a maximum value of $\Delta T = -2.7 \text{ K}$ for $\Delta H = 60 \text{ kOe}$ at $T \approx 245$ in the vicinity of the magnetic transition point. Theoretical estimations of Engelhardt *et al* (1999) showed that the main contribution into ΔS in $\text{Mn}_{2-x}\text{Cr}_x\text{Sb}$ had magnetic nature. They also revealed a maximum on the entropy change concentration dependence at about $x = 0.10$ (T_s about 250 K).

Bouchaud *et al* (1966) measured $I(H)$ dependences for Mn_3GaC compound and constructed its magnetic phase diagram. This compound has perovskite-type crystal structure, orders ferromagnetically below $T_C = 246 \text{ K}$, and displays ferromagnetic–antiferromagnetic first-order transition at about 150 K . Magnetic entropy change at the first-order transition determined by the Clausius–Clapeyron equation (2.100) on the basis of the data of Bouchaud *et al* (1966) is presented in table 4.3.

Magnetothermal properties of the systems based on MnAs and MnP were investigated by Selte *et al* (1977), Krokoszinski *et al* (1982), Kuhrt *et al* (1985) and Wada and Tanabe (2001). These compounds order

Table 4.3. Change of the specific magnetization ($\Delta\sigma$) and the entropy change (ΔS), and temperature derivative ($-\partial H_{\text{cr}}/\partial T$) of the critical field at the first-order transition T_s (at T_C for MnAs) in magnetic materials based on 3d metals.

Substance	T_C (K)	T_s (K)	$\Delta\sigma$ (emu/g)	$-\partial H_{\text{cr}}/\partial T$ (kOe/K)	ΔS (J/kg K)	Ref.
$\text{Mn}_{1.97}\text{Cr}_{0.03}\text{Sb}$	127	39.6	1.08	4.28	[1]	
	551	154	1.8	3.6	[2]	
$\text{Mn}_{1.95}\text{Cr}_{0.05}\text{Sb}$	211	32.8	1.97	6.5	[1]	
	547	212	2.5	5.25	[2]	
$\text{Mn}_{1.90}\text{Cr}_{0.10}\text{Sb}$	305	24.3	2.43	5.9	[1]	
	524	298	2.8	5.69	[2]	
	264	≈26	2.6	≈6.8	[3]	
$\text{Mn}_{1.84}\text{Cr}_{0.16}\text{Sb}$	373	13.7	2.33	3.19	[1]	
Mn_3Ge_2	164	3.5	2.08	0.72	[1]	
$\text{CrS}_{1.17}$	160	1.85	2.29	0.42	[1]	
$\text{Fe}_{0.5}\text{Rh}_{0.5}$	355	117	0.925	10.8	[1]	
$\text{Fe}_{0.48}\text{Rh}_{0.52}$	333	104	1.75	18.3	[4]	
$\text{Fe}_{0.49}\text{Rh}_{0.51}$	633	308.2	102	0.74	[7,8]	
$\text{Li}_{0.10}\text{Mn}_{0.9}\text{Se}$	72	26.4	5.3	14	[1]	
MnAs	312	—	95	2.57	24.2	[5]
Mn_3GaC	246	150	85	3.3	28.5	[6]

1. Flippin and Darnell (1963); 2. Engelhardt *et al* (1999); 3. Baranov *et al* (1992); 4. Ponomarev (1972); 5. de Blois and Rodbell (1963); 6. Bouchaud *et al* (1966); 7. Tishin *et al* (2002); 8. Annaorazov *et al* (1992).

ferromagnetically below the Curie temperature, which is 298 K for MnP (saturation magnetic moment μ_s is $1.2 \mu_B$ per atom Mn) and 312 K ($\mu_s = 3.4$ and $\mu_{\text{eff}} = 4.95 \mu_B$ per atom Mn) for MnAs (Adachi 1961). The transition from paramagnetic to ferromagnetic state in MnAs is first-order transition accompanied by crystallographic structure change from MnP (orthorhombic) type to NiAs (hexagonal) type (Selte *et al* 1977). Such transition was explained by Kittel (1960) and Bean and Rodbell (1962) by the strong dependence of exchange interaction on the interatomic distance and inversion of the exchange parameter sign due to the crystal lattice deformation. Figure 4.13 shows the temperature dependence of the magnetic moment in a field of 4 kOe and ΔT for $\Delta H = 6.5$ kOe in the MnAs compound measured by Kuhrt *et al* (1985). The temperature hysteresis characteristic for the magnetic first-order transition is observed on the $\Delta T(T)$ curve. The experimental magnetic entropy change for MnAs and MnP determined by Hashimoto *et al* (1982) for $\Delta H = 10$ and 80 kOe are shown in table 4.2, and ΔS_M of the first-order magnetic transition at T_C in MnAs estimated by the Clausius–Clapeyron equation (2.100) from the magnetization data of de Blois and Rodbell (1963) are shown in table 4.3.

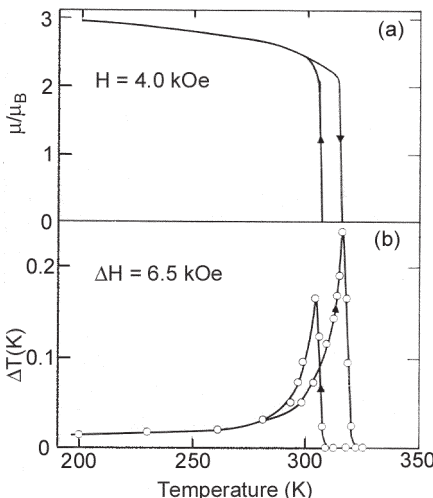


Figure 4.13. Temperature dependences of the magnetic moment in the field of 4 kOe and MCE ($\Delta H = 6.5$ kOe) in MnAs compound (Kuhrt *et al* 1985).

Schünemann *et al* (1992), from the heat capacity measurements, determined the magnetic entropy jump in MnAs at T_C to be 4.1 J/mol K (31.6 J/kg K). Zieba *et al* (1982) obtained that T_C in MnAs increases in magnetic field at the rate of 0.4 K/kOe . Based on these data in the works of Wada and Tanabe (2001) and Wada *et al* (2002) it was suggested that the MCE data of Kuhrt *et al* (1985) are underestimated and the MCE in this compound should be higher. They determined $\Delta S_M(T)$ dependences for various ΔH from magnetization measurements and $\Delta T(T)$ curves on the basis of $\Delta S_M(T)$ and heat capacity data. According to the magnetization measurements of Wada *et al* (2002) above 320 K in MnAs there is a sharp metamagnetic field-induced transition from the paramagnetic to the ferromagnetic state on $M(H)$ curves. The maximum magnetic entropy change in MnAs near T_C has high values (the absolute value about 32 J/kg K for $\Delta H = 50 \text{ kOe}$), $\Delta S_M(T)$ is rather wide and its width increases linearly with magnetic field change (for $\Delta H = 50 \text{ kOe}$ the full width of $\Delta S_M(T)$ at half maximum is $\sim 20 \text{ K}$) (Wada and Tanabe 2001, Wada *et al* 2002). This is typical for first-order transition behaviour. Analogous field dependence demonstrated $\Delta T(T)$ curves (for $\Delta H = 50 \text{ kOe}$ the full width of $\Delta T(T)$ at half maximum was $\sim 13 \text{ K}$). The peak ΔT value for $\Delta H = 50 \text{ kOe}$ in MnAs was $\sim 13 \text{ K}$. The obtained peak ΔT and ΔS_M correspond to rather high $\Delta T/\Delta H$ and $\Delta S_M/H$ values—see table 4.2—which are comparable with those in the $\text{Gd}_5(\text{Si}-\text{Ge})_4$ system. It should be noted that the maximum absolute ΔS_M value in MnAs was weakly sensitive to the ΔH value, the latter mainly determined from $\Delta S_M(T)$ curve width.

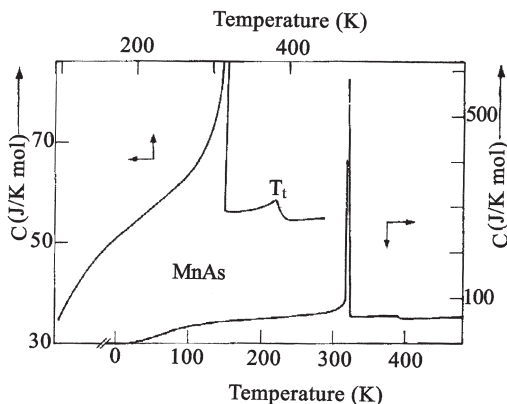


Figure 4.14. Heat capacity temperature dependence for MnAs (Krokszinski *et al* 1982).

Figure 4.14 shows the heat capacity temperature dependence of MnAs measured by Krokszinski *et al* (1982). The anomaly observed in the paramagnetic region at $T_t \approx 390$ K is related to the crystal structure transition from an MnP-type structure to an NiAs-type one (high-temperature region). The heat capacity temperature behaviour of the system $\text{MnAs}_{1-x}\text{P}_x$ ($x = 0.03\text{--}0.13$), where arsenic is substituted by phosphorus, was studied by Krokszinski *et al* (1982). First-order phase transition at T_C persists for x up to 0.03, and for higher phosphorus concentration there are three anomalies on $C(T)$ —see figure 4.15. The high-temperature anomaly at T_t is the structural transition analogous to that observed in

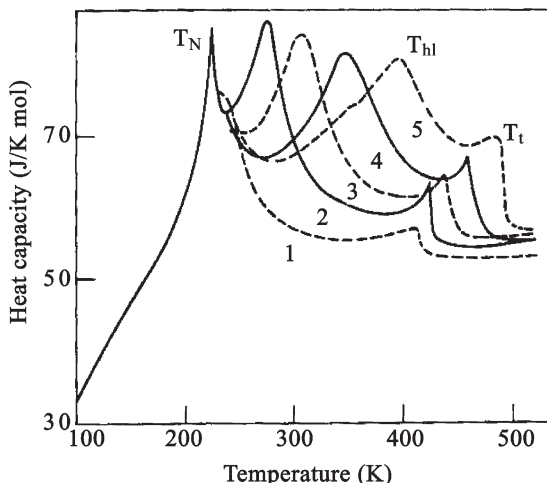


Figure 4.15. Heat capacity temperature dependences for the $\text{MnAs}_{1-x}\text{P}_x$ system: (1) $x = 0.04$; (2) 0.085; (3) 0.09; (4) 0.11; (5) 0.13 (Krokszinski *et al* 1982).

MnAs. Anomaly at the Néel-type temperature T_N corresponds to the transition from paramagnetic to magnetically ordered state. The anomaly between T_N and T_C is related to high spin–low spin transition, at which the magnetic moment of the Mn atom is changed from a high value above the transition temperature T_{hl} to the low value below T_{hl} . Based on the heat capacity data, Krokoszinski *et al* (1982) constructed phase diagram temperature–concentration for the $\text{MnAs}_{1-x}\text{P}_x$ system.

The influence of substitution of Mn by V, Cr, Fe and Co in MnAs (the concentration of substituted metal was up to 10%) on its magnetic properties was studied by Selte *et al* (1977). It was established that the first-order magnetic transition from paramagnetic to ferromagnetic state analogous to that observed in MnAs persisted in the $\text{Mn}_{1-x}\text{Fe}_x\text{As}$ system for $x < 0.3$ and in the $\text{Mn}_{1-x}\text{V}_x\text{As}$ system for $x < 0.05$. For higher x the systems ordered from paramagnetic to helimagnetic state below the ordering temperature T_N . It should be noted that the transition at T_N was not accompanied by the structural transition—the crystal structure was MnP-type for paramagnetic and magnetically ordered states. However, in the $\text{Mn}_{1-x}\text{V}_x\text{As}$ system with $x > 0.05$ a strong magnetic field induced a magneto-structural transition to ferromagnetic NiAs-type state (in the $\text{Mn}_{1-x}\text{Fe}_x\text{As}$ system under such magnetic transition, change of crystal structure type was not observed). Figure 4.16 shows the MCE temperature dependence for $\text{Mn}_{0.95}\text{V}_{0.05}\text{As}$ induced by the magnetic field change of

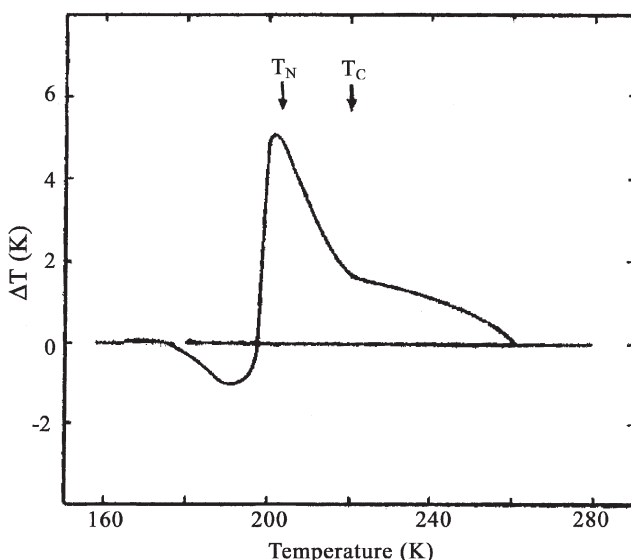


Figure 4.16. Temperature dependence of the MCE induced in $\text{Mn}_{0.95}\text{V}_{0.05}\text{As}$ by a magnetic field change of 210 kOe (Selte *et al* 1977). (Reprinted from Selte *et al* 1977, copyright 1977, with permission from Elsevier.)

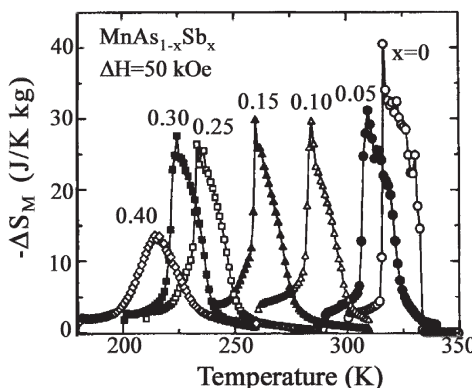


Figure 4.17. The temperature dependences of ΔS_M in $MnAs_{1-x}Sb_x$ compounds for $\Delta H = 50$ kOe (Wada *et al* 2002).

210 kOe. In this composition two magnetic transitions exist, from paramagnetic state to ferromagnetic at $T_C = 220$ K and from ferromagnetic to helicoidal state at $T_N = 203$ K. The maximum MCE of about 5.5 K is observed near T_N .

Wada and Tanabe (2001) and Wada *et al* (2002) investigated magnetic entropy change in the $MnAs_{1-x}Sb_x$ system ($0 \leq x \leq 0.4$) on the basis of magnetization measurements. They found that temperature hysteresis observed in MnAs (see figure 4.13) disappeared for $x \geq 0.05$ and the $M(T)$ curve became smoother under substitution of Sb. The first-order magnetic phase transition disappears for $x > 0.1$. In this concentration range NiAs-type crystal structure is stable and no structural transition was observed. However, some features of the first-order transition (such as metamagnetic transition above the Curie temperature and rather sharp magnetization changing with temperature near T_C) remain for x up to 0.3. These properties are reflected on the magnetic entropy change and its dependence on temperature, which is shown in figure 4.17 for $\Delta H = 50$ kOe. For x up to 0.3 the $\Delta S_M(T)$ curves are quite similar and have asymmetric form, while for $x = 0.4$ the $\Delta S_M(T)$ curve changes and becomes symmetrical, which is typical for the second-order magnetic phase transitions. The ΔS_M and $\Delta S_M/\Delta H$ values also decrease above $x = 0.3$ (see table 4.2), although they remain rather large—on the level of those in Gd (see table 8.2).

Tegus *et al* (2002a,b) reported results about investigation of the magnetic and magnetocaloric properties of the $MnFeP_{1-x}As_x$ ($x = 0.25, 0.35, 0.45, 0.5, 0.55$ and 0.65) system. The Curie temperatures were found to be between 168 K for $x = 0.25$ and 332 K for $x = 0.65$. According to magnetization measurements the alloys with $x > 0.25$ in this system undergo under heating a sharp temperature-induced transition from ferromagnetic to paramagnetic state. Magnetization isotherm measurements

made in $\text{MnFeP}_{0.45}\text{As}_{0.55}$ above T_C showed the presence of the field-induced magnetic phase transition from paramagnetic to ferromagnetic state with field hysteresis typical for the first-order transitions. However, the first-order transitions at T_C in the $\text{MnFeP}_{1-x}\text{As}_x$ system are not accompanied by crystal structure transitions. Magnetization measurements made by Zach *et al* (1990) on $\text{MnFeP}_{0.5}\text{As}_{0.5}$ showed that it was ordered ferromagnetically below 270 K. Between 270 and 310 K some disordered magnetic phase exists, which can be transformed to ferromagnetic by a magnetic field through first-order transition. Above 310 K the magnetization curves had paramagnetic character. X-ray studies showed that a and c lattice parameters changed at T_C stepwise, although the unit cell remained almost unchanged (c increased and a decreased). It can be concluded that the magnetic phase transition near T_C for the composition around $x = 0.5$ has first-order character.

Temperature dependences of the magnetic entropy change in this system determined from magnetization data are shown in figure 4.18. First-order magnetic phase transitions with rapid magnetization change in their vicinity causes large ΔS_M values in the $\text{MnFeP}_{1-x}\text{As}_x$ system. The maximum peak absolute ΔS_M value of 33 J/kg K for $\Delta H = 50$ kOe was observed for $x = 0.35$. For the alloy with $x = 0.45$, $-\Delta S_M = 20$ J/kg K for the magnetic field change of 20 kOe, which can be obtained with the help of a permanent magnet. In previously reported $\text{MnFeP}_{0.45}\text{As}_{0.55}$ (Tegus *et al* 2002a) the

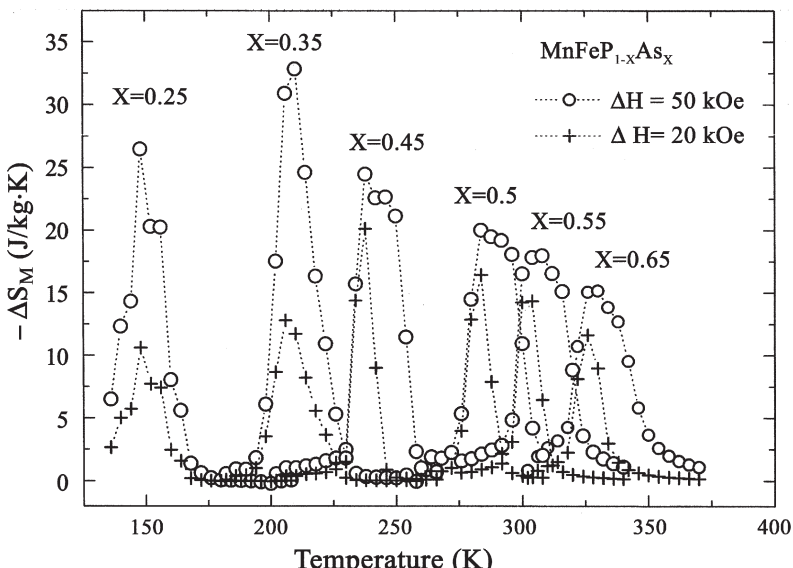


Figure 4.18. Temperature dependence of magnetic entropy change in $\text{MnFeP}_{1-x}\text{As}_x$ compounds for $\Delta H = 20$ kOe (\times) and 50 kOe (\circ) (Tegus *et al* 2002b). (Reprinted from Tegus *et al* 2002b, copyright 2002, with permission from Elsevier.)

absolute maximum value of ΔS_M near the magnetic ordering temperature in $\text{MnFeP}_{0.45}\text{As}_{0.55}$ for $\Delta H = 50 \text{ kOe}$ was about 18 J/kg K , which is more than two times higher than that measured by the authors in Gd (about 8 J/kg K for $\Delta H = 50 \text{ kOe}$). It should be noted that the saturation magnetic moment in $\text{MnFeP}_{0.45}\text{As}_{0.55}$ is about two times lower than in Gd ($3.9 \mu_B$ per formula unit in $\text{MnFeP}_{0.45}\text{As}_{0.55}$ versus $7.55 \mu_B$ in Gd) (Tegus *et al* 2002a). $\Delta S_M(T)$ curves in the $\text{MnFeP}_{1-x}\text{As}_x$ system are rather wide (for example, full width at half maximum for the compound with $x = 0.45$ is about 25 K for $\Delta H = 50 \text{ kOe}$) and increase with ΔH increasing as it usually is in the materials with the first-order magnetic phase transition. The observed high absolute $\Delta S_M/\Delta H$ values for $\Delta H = 20 \text{ kOe}$ should be noted (see table 4.2)—they are in some cases higher than the values observed in $\text{Gd}_5(\text{Si}-\text{Ge})_4$ compounds (table 7.2).

The MCE in ferromagnetic Ni–Mn alloys (66–83% of Ni) characterized by partial atomic disorder in the crystalline structure was studied by Okazaki *et al* (1993). The order degree was changed by annealing of the sample. The MCE peak was observed in the Curie temperature region and had a maximum value of about 0.5 K for $\Delta H = 6.4 \text{ kOe}$ in the ordered $\text{Mn}_{0.17}\text{Ni}_{0.83}$ alloy—see figure 4.19. Linear $\Delta T(I^2)$ dependence was observed in these alloys, which allowed determination of $I_s(T)$ curves.

Sucksmith *et al* (1953) and Znamenskii and Fakidov (1962) studied the MCE in alloys of copper with nickel and manganese, respectively. Sucksmith *et al* (1953) established linear behaviour of ΔT on I^2 in $\text{Ni}_{0.725}\text{Cu}_{0.275}$ near the Curie temperature of about 368 K . Znamenskii and Fakidov (1962) investigated the MCE in $\text{Mn}_{0.228}\text{Cu}_{0.772}$ alloy with fcc crystal structure. According

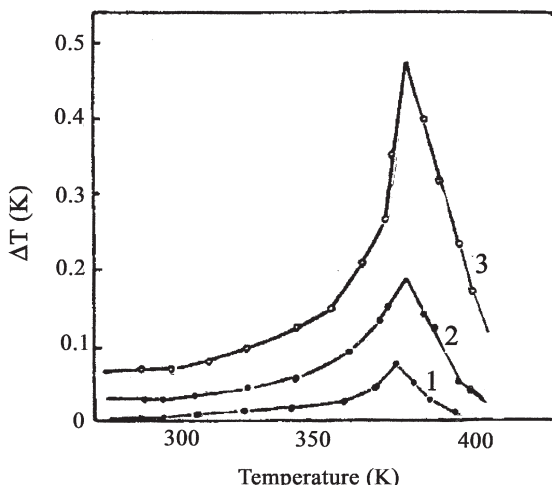


Figure 4.19. Temperature dependences of the MCE in the $\text{Mn}_{0.17}\text{Ni}_{0.83}$ alloy induced by the magnetic field change: $\Delta H = 624 \text{ Oe}$ (1); 2412 Oe (2); 6393 Oe (3) (Okazaki *et al* 1993).

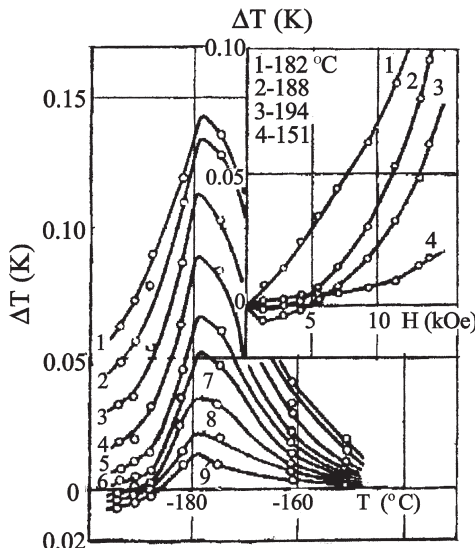


Figure 4.20. The MCE temperature and magnetic field dependences for $Mn_{0.228}Cu_{0.772}$ alloy: $\Delta H = 13.8$ kOe (1); 13.1 kOe (2); 11.25 kOe (3); 9.25 kOe (4); 7 kOe (5); 5.5 kOe (6); 4.15 kOe (7); 2.8 kOe (8); 1.3 kOe (9). The insert shows MCE magnetic field dependence at different temperatures (Znamenskii and Fakidov 1962).

to the magnetic measurements at the temperature of 94 K, this alloy exhibited the transition from paramagnetic to antiferromagnetic state. Paramagnetic Curie temperature is positive and has a value of 153 K, and the effective magnetic moment of the Mn atom is $3.75 \mu_B$. The critical magnetic field of antiferromagnetic state destruction is about 4 kOe at 56 K. The MCE has its maximum near the ordering temperature (see figure 4.20) with the value of 0.14 K for $\Delta H = 13.8$ kOe. Under cooling below about 88 K for ΔH less than the critical field the negative MCE is observed, which can be related to an antiferromagnetic-type paraprocess. The insert in figure 4.20 shows $\Delta T(H)$ dependences at various temperatures.

Hu *et al* (2000a, 2001c,d) and Tegus *et al* (2002b) determined the magnetic entropy change in nonstoichiometric Heusler alloys $Ni_{0.515}Mn_{0.227}Ga_{0.258}$, $Ni_{0.501}Mn_{0.207}Ga_{0.296}$, $Ni_{0.526}Mn_{0.231}Ga_{0.243}$ and $Ni_{0.53}Mn_{0.22}Ga_{0.25}$ (the last three compositions were single crystals). These alloys first order ferromagnetically (the Curie temperatures were 351, 342, 345 and 329 K for $Ni_{0.515}Mn_{0.227}Ga_{0.258}$, $Ni_{0.501}Mn_{0.207}Ga_{0.296}$, $Ni_{0.526}Mn_{0.231}Ga_{0.243}$ and $Ni_{0.53}Mn_{0.22}Ga_{0.25}$, respectively), and then at lower temperatures undergo first-order magnetic phase transition corresponding to the reversible structural transition from the high-temperature cubic austenite phase to the low-temperature tetragonal martensite phase. The transition is accompanied by a considerable magnetization jump, which causes essential magnetic entropy

change. The nonstoichiometric composition was chosen in order to get the temperature of the first-order transition close to the room-temperature range. The transition to martensitic phase causes distortion of the crystal lattice structure, leading to increasing of the magnetocrystalline anisotropy and hardening of the magnetic saturation process. Because of that, magnetization in the martensitic phase in the low-field range becomes lower than that in austenitic phase. The field of $M(H)$ curves corresponding to the phases intersects at some field above which the magnetization in the martensitic phase is higher than in the austenitic one (the saturation magnetization of the martensitic phase is higher than that in the austenitic phase by up to 20%). Such behaviour was observed, in particular, in $\text{Ni}_{0.501}\text{Mn}_{0.207}\text{Ga}_{0.296}$ (the temperature of martensitic–austenitic transition measured under heating of 219 K), where the magnetic entropy change was determined from magnetization measured along the [001] axis. The intersection field was about 8 kOe. Below this field ΔS_M was positive with a peak value of 6 J/kg K for $\Delta H = 8$ kOe at about 219 K (this corresponds to $\Delta S_M/\Delta H = 0.75$ J/kg K kOe, which is higher than that in Gd and is on the level of $\text{Gd}_5(\text{Si–Ge})_4$ compounds (see tables 7.2 and 8.2)). With further ΔH increasing ΔS_M decreases, then becomes negative and increases in absolute value reaching -6 J/kg K for $\Delta H = 50$ kOe. Analogous behaviour was observed in an $\text{Ni}_{0.526}\text{Mn}_{0.231}\text{Ga}_{0.243}$ single crystal with a martensitic–austenitic transition temperature of 297 K (measured under heating), magnetization of which was also measured along the [001] axis. The intersection field in this sample was low (2.3 kOe) and positive magnetic entropy change observed in the fields below 4.5 kOe was also not high. The peak $-\Delta S_M$ value was 18 J/kg K for $\Delta H = 50$ kOe at 300 K. It was found that the absolute ΔS_M value increased linearly with magnetic field at the rate of about 0.4 J/kg K kOe, which is a rather high value. Polycrystalline $\text{Ni}_{0.515}\text{Mn}_{0.227}\text{Ga}_{0.258}$ alloy exhibited transition from austenitic to martensitic crystal structure at 187 K under cooling and reverse transition at 197 K under heating. The maximum value of ΔS_M near the martensitic–austenitic transition determined from magnetization is about 4.1 J/kg K for $\Delta H = 9$ kOe at 197 K (this corresponds to $\Delta S_M/\Delta H = 0.46$ J/kg K kOe). Tegus *et al* (2002b) determined magnetic entropy change in $\text{Ni}_{0.53}\text{Mn}_{0.22}\text{Ga}_{0.25}$ not only near the austenitic–martensitic transition (220 K measured on heating), but also near the Curie point. It was found that the peak absolute value of ΔS_M near T_C is essentially lower than near the austenitic–martensitic transition: 2.5 J/kg K and 1 J/kg K, respectively, for $\Delta H = 10$ kOe. Besides, these values have opposite sign in this field range: ΔS_M is negative near T_C and positive near the austenitic–martensitic transition. An advantage of the investigated alloys from the point of view of their possible application in a working body of magnetic refrigerators is that one can attribute their weak magnetic field hysteretic properties (although the martensitic–austenitic transition temperature hysteresis is large—more than 10 K)—the materials are magnetically soft. However,

it should be noted that the peaks on the $\Delta S_M(T)$ curves corresponding to the martensitic–austenitic transition in the alloys are rather narrow—for example, in $\text{Ni}_{0.515}\text{Mn}_{0.227}\text{Ga}_{0.258}$ alloy full width at half maximum is about 3 K.

The MCE in $\text{Fe}_{0.9666}\text{Si}_{0.0334}$ was measured directly by Hirschler and Rocker (1966). The MCE maximum of about 5 K was observed near the temperature 1013 K for $\Delta H = 30$ kOe (for Fe the MCE maximum value is about 5.1 K near 1042 K).

Magnetic entropy change in compounds $\text{Mn}_5\text{Ge}_{3-x}\text{Sb}_x$ and $\text{Mn}_{5-x}\text{Fe}_x\text{Si}_3$ with Mn_5Si_3 -type crystal structure was investigated by Songlin *et al* (2002a,b) and Tegus *et al* (2002b). According to magnetic studies, Mn_5Si_3 exhibits two first-order magnetic phase transitions—one at 66 K (between noncollinear and collinear antiferromagnetic states) and another at 99 K (from magnetically ordered to paramagnetic state) (Kappel *et al* 1976). The anomaly (positive peak) on the $\Delta S_M(T)$ curve was found only near the low-temperature transition (Tegus *et al* 2002b, Songlin *et al* 2002a,b). Its value increased with ΔH increasing, which was related to destruction by the field of the magnetic structure consisting of anti-ferromagnetically coupled Mn spins in various crystallographic sites (i.e. antiferromagnetic-type paraprocess). The positive ΔS_M peak value (see table 4.2) was not too high in this compound. With further temperature increase, ΔS_M in Mn_5Si_3 becomes positive. In contrast to Mn_5Si_3 , Fe_5Si_3 has ferromagnetic ordering with a Curie temperature of 363 K. The $\text{Mn}_{5-x}\text{Fe}_x\text{Si}_3$ system with $x = 0, 1, 2, 3, 4$ and 5 was investigated by Songlin *et al* (2002b). It was found that compositions with $x = 1$ and 2 are antiferromagnets and that with $x = 4$ is a ferromagnet. In the compounds with $x = 3, 4$ and 5, $-\Delta S_M(T)$ dependence revealed maxima near the magnetic ordering temperatures. The maximum peak absolute ΔS_M value in the $\text{Mn}_{5-x}\text{Fe}_x\text{Si}_3$ system was observed for $x = 4$. The system $\text{Mn}_5\text{Ge}_{3-x}\text{Sb}_x$ ($x = 0, 0.1, 0.2$ and 0.3) was ferromagnetic with soft magnetic properties (Songlin *et al* 2002a). Its $-\Delta S_M(T)$ curves revealed the usual ferromagnetic-type maxima near T_C , with the absolute peak value decreasing and the Sb content increasing. As one can see from table 4.2, the magnetic entropy change in $\text{Mn}_5\text{Ge}_{3-x}\text{Sb}_x$ is essentially higher than in the $\text{Mn}_{5-x}\text{Fe}_x\text{Si}_x$ system.

Positive magnetic entropy change was observed by Tegus *et al* (2002b) in $\text{Mn}_{1.95}\text{Cr}_{0.05}\text{Sb}$. According to magnetic measurements under heating at 198 K, a first-order magnetic phase transition accompanied by rapid and essential increasing of magnetization occurs, which was suggested by the authors to be an AFM to FM transition. On $M(H)$ curves below the transition point, jumps at critical fields typical for destruction of AFM structure were observed. The maximum ΔS_M values near the transition temperature were 7 and 5.7 J/kg K for $\Delta H = 20$ and 50 kOe, respectively. The positive ΔS_M values and ΔS_M increasing with magnetic field change increasing the

authors explained by the same reason as in Mn_5Si_3 . The $\Delta S_M(T)$ curves were rather wide (the full width at half maximum of about 21 K for $\Delta H = 50$ kOe) and their width increased for higher ΔH . The compound is also characterized by high $\Delta S_M/\Delta H$ in low fields (see table 4.2).

The ΔS_M temperature dependences for alloy systems $\text{Ni}_2(\text{Mn}_{1-x}\text{M}_x)\text{Sn}$ with $\text{M} = \text{V}$ and Nb ($x = 0.1, 0.2, 0.3, 0.4$) and $\text{Mn}_{3-y-z}\text{Cr}_y\text{AlC}_{1+z}$ (y and $z = -0.16, -0.08, 0$, $z = 0.1$, and $y = 0, 0.06, 0.15, 0.26$) have been determined by Maeda *et al* (1983) on the basis of magnetization measurements. It was established that the Curie temperature of the alloys linearly decreased from room temperature down to about 200 K as x or ($y + z$) increased. In the Curie temperature region a peak usual for ferromagnets was observed on $\Delta S_M(T)$ curves. For $\text{Ni}_2(\text{Mn}_{1-x}\text{V}_x)\text{Sn}$ alloys the peak ΔS_M induced by $\Delta H = 14$ kOe had an absolute value of $13 \text{ kJ/m}^3 \text{ K}$ for $x = 0.1$ ($T_C \approx 300$ K) and decreased down to $7 \text{ kJ/m}^3 \text{ K}$ for $x = 0.4$ ($T_C \approx 170$ K). According to the measurements made by the authors on Gd, the absolute ΔS_M value was about $30 \text{ kJ/m}^3 \text{ K}$ for $\Delta H = 14$ kOe, which is about two times higher than that for the alloy with $x = 0.1$. The field change of 70 kOe caused absolute magnetic entropy change of about $36 \text{ kJ/m}^3 \text{ K}$ in $\text{Ni}_2(\text{Mn}_{0.8}\text{V}_{0.2})\text{Sn}$ alloy. In $\text{Mn}_{3-y-z}\text{Cr}_y\text{AlC}_{1+z}$ alloys the maximum absolute peak value induced by $\Delta H = 14$ kOe was about $14 \text{ kJ/m}^3 \text{ K}$ for $x = 0$ and $y = 0.1$ ($T_C \approx 270$ K), and decreased with increasing of x or y .

Pérez *et al* (1998) studied the heat capacity and the MCE of the distorted triangular crystal lattice antiferromagnet RbMnBr_3 in order to determine its magnetic phase diagram. The Néel temperature obtained from the heat capacity peak is 8.54 K. The value of $\Delta T/\Delta H$ measured in the basal plane at 3 K and in magnetic field of 40 kOe was about $2.3 \times 10^{-2} \text{ K/kOe}$, and decreased to $0.6 \times 10^{-2} \text{ K/kOe}$ at 6.4 K.

4.3 3d thin films

Babkin and Urinov (1987, 1989) investigated the MCE induced by a magnetic field in thin films on the basis of 3d metals.

The MCE caused by the uniform rotation of the spontaneous magnetization vector in thin films was considered in the work of Babkin and Urinov (1989). The magnetic free energy of the film was presented in the form

$$F_M = K \sin^2 \Theta - IH \cos(\phi - \Theta) \quad (4.5)$$

where K is the film anisotropy constant including the form anisotropy and induced magnetic anisotropy, ϕ and Θ are the angles between the surface and the \vec{H} and \vec{I} vectors, respectively.

The value of the MCE was determined with the help of equations (2.7a) and (2.21) and the expression for the equilibrium magnetic free energy obtained from equation (4.5). As a result the following formula for the

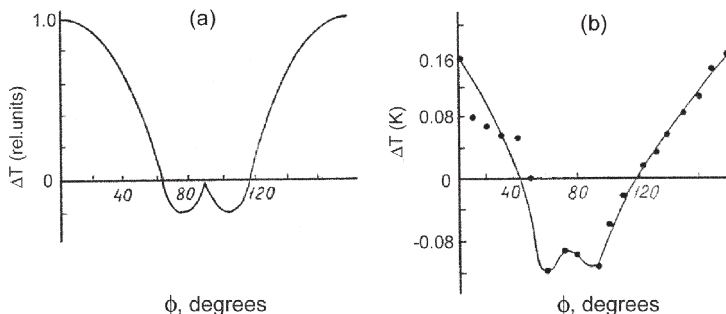


Figure 4.21. The MCE dependence on the angle ϕ between the film surface and the magnetic field H : (a) theoretical calculations by equation (4.5) for $H = 4\pi I$ and $K = 2\pi I^2$; (b) experimental data for the polycrystalline Ni film, $H = 3.4$ kOe (Babkin and Urinov 1989).

MCE was derived (Babkin and Urinov 1989):

$$\left(\frac{\Delta T}{\Delta H} \right)_S = \left\{ \frac{T}{C_H} \frac{K \sin^2 2\Theta}{IH[2K \cos 2\Theta + IH \cos(\phi - \Theta)]} \left[I \frac{\partial K}{\partial T} - K \frac{\partial I}{\partial T} \right] - \frac{T}{C_H} \frac{\partial I}{\partial H} \cos(\phi - \Theta) \right\}. \quad (4.6)$$

The first term in equation (4.6) gives a positive or negative contribution to the MCE depending on the relation between $I(T)$ and $K(T)$. If the anisotropy is absent ($K = 0$, $\phi = 0$), equation (4.6) transforms into equation (2.16). If the film anisotropy is determined only by the form anisotropy ($K = 2\pi I^2$) the first term in equation (4.6) is always negative. The results of calculations made by equation (4.5) for the case of $H = 4\pi I$ and $K = 2\pi I^2$ are shown in figure 4.21(a).

Experimental MCE measurements were done on polycrystalline ferromagnetic Ni and single crystalline ferromagnetic γ -Fe₂O₃ films with thickness of 0.15–0.30 μm . As a temperature-sensitive element a vanadium dioxide 0.1–0.5 μm thick film was used (its resistance decreased drastically under heating near ~ 330 K).

The experimental results for the Ni film for $H = 3.4$ kOe are shown in figure 4.21(b) (analogous, although some more complex, behaviour was observed for the γ -Fe₂O₃ film). With increasing magnetic field the MCE maximum near the hard magnetization axis ($\phi = 0$) disappeared. The proposed theory contradicted the experimental results obtained in the region of the hard axis direction (the negative MCE). The authors connected such behaviour with the presence of defects and surface anisotropy in the films violating the condition of uniform rotation of the magnetization vector.

In conclusion, in this chapter we have considered the MCE and related properties of 3d metals, their alloys and compounds. The MCE in Fe, Co and Ni near T_C is rather high, which can be related to their high Curie

temperatures. In spite of the itinerant nature of 3d magnetism, the MCE in 3d metals and compounds in the region of a paraprocess can be successfully described by MFA. The contribution to the MCE from the magnetization vector rotation in Ni and Co was low compared with the contribution from the paraprocess. Among the alloys and compounds on the basis of 3d metals the highest MCE and magnetic entropy change values were found experimentally in those with first-order magnetic transition. It can be the transition from magnetically ordered to paramagnetic state, between various magnetic structures, or the transition related to change of crystal structure, such as martensitic-austenitic transition in nonstoichiometric Heusler Ni_2MnGa alloys. This is related to a sharp change of magnetization near the first-order transition. Experimental data show that as a rule the materials with large magnetoelastic interaction display essential MCE. It should be noted that the main amount of results on 3d compounds with high MCE properties appeared in recent times and this class of materials can be recognized as promising for MCE practical applications.

Chapter 5

Magnetocaloric effect in oxides

Magnetothermal and magnetocaloric properties were investigated in various oxide compounds: garnets, orthoaluminates, vanadites, manganites and ferrites. Rare earth iron garnets ($R_3Fe_5O_{12}$) and various ferrites can have several different magnetic sublattices with antiferromagnetic or more complex noncollinear ordering and exhibit various magnetic transitions and transformations typical for ferrimagnets, in particular such as compensation points. The transformations of their magnetic structure by temperature and magnetic field should be reflected on magnetocaloric properties. Gallium and aluminium rare earth garnets ($R_3Ga_5O_{12}$ and $R_3Al_5O_{12}$) are characterized by low magnetic ordering temperatures (usually several K) and are paramagnetic in the rest of the temperature interval. Analogous behaviour displays orthoaluminates ($RAIO_3$) and vanadites (RVO_4). Due to the presence of rare earth ions the above-mentioned oxide compounds can have an essential magnetic entropy change. The orthoaluminates and vanadites also have a higher percentage content of RE ion per mole in comparison with garnets, which can provide higher specific MCE per mole and cm^3 —an important parameter for practical applications. Perovskite-type manganites ($RMnO_3$) with various dopants and related compounds attract the attention of investigators because of their interesting and complex magnetic and electrical properties, such as colossal magnetoresistance effect, charge and orbital ordering and electronic phase separation. Such compounds can reveal first-order magnetic phase transitions with a sharp change of magnetization and, because of that, high magnetocaloric properties. This circumstance, together with the ability to change in wide range the magnetic phase transition temperatures by variation of their composition (Curie temperatures of some compositions lie in room temperature range), makes the manganites attractive for applications in magnetic refrigerators.

5.1 Garnets

5.1.1 Rare earth iron garnets

The MCE in polycrystalline rare earth garnets $R_3Fe_5O_{12}$ ($R = \text{Gd}, \text{Tb}, \text{Dy}, \text{Ho}, \text{Er}, \text{Tm}, \text{Yb}$ and Y) was studied by Belov *et al* (1968, 1969, 1970,

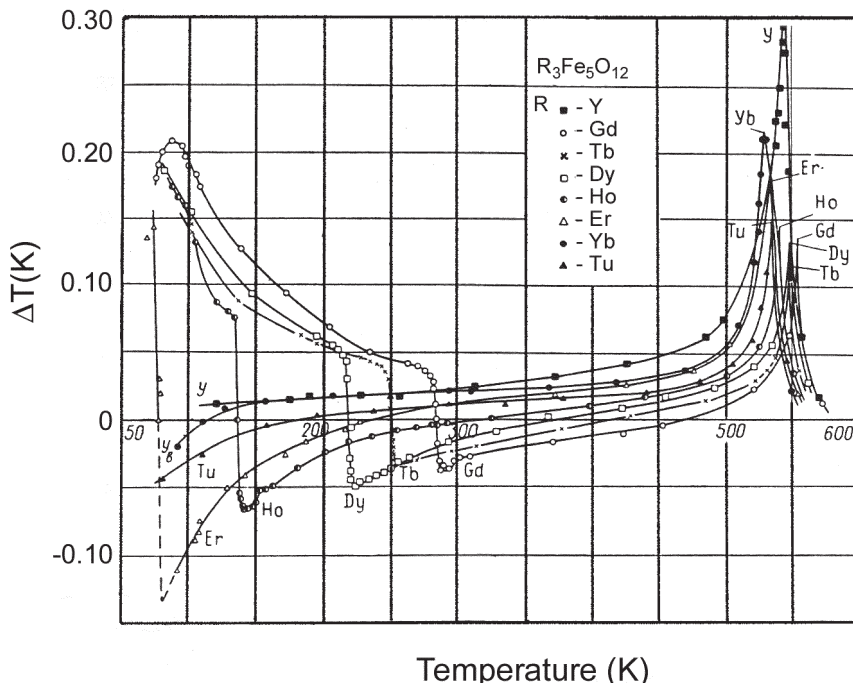


Figure 5.1. The MCE temperature dependences in $R_3Fe_5O_{12}$ for $\Delta H = 16$ kOe (Belov *et al* 1969).

1971, 1972, 1973), Clark and Callen (1969), Clark and Alben (1970), Belov and Nikitin (1970a,b), and Kamilov *et al* (1975).

The temperature dependences of MCE induced by the magnetic field change of 16 kOe in polycrystalline $R_3Fe_5O_{12}$ ($R = Gd, Tb, Dy, Ho, Er, Tm, Yb$ and Y) are shown in figure 5.1 (Belov *et al* 1969). As one can see for $Y_3Fe_5O_{12}$ the MCE is positive in the whole temperature range and has a maximum near the Curie temperature. For the garnets containing rare earth elements the MCE displays more complicated temperature behaviour. The MCE also has a positive maximum near T_C , but with cooling it becomes negative. Then at some temperature a jump occurs, which reverts the MCE to positive values. At further cooling, the MCE continues to increase (see the curves for $R = Gd, Tb, Dy, Ho$ in figure 5.1). The observed behaviour is related to transformation of the ferromagnetic structure of garnets and anti-ferromagnetic- and ferromagnetic-type paraprocesses in RE and iron magnetic sublattices. It was considered in section 2.6 for $Gd_3Fe_5O_{12}$ as an example.

The influence of the replacement of Fe in the garnets by nonmagnetic Ga ions was studied by Belov *et al* (1972). The results of the MCE measurements in a system of $Gd_3Ga_xFe_{5-x}O_{12}$ ($0 \leq x \leq 1.5$) alloys are presented in

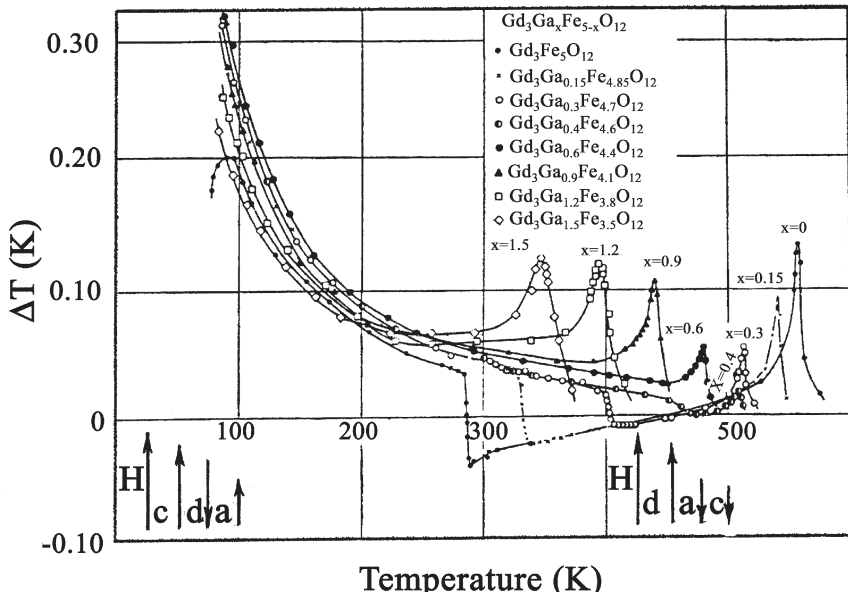


Figure 5.2. The MCE temperature dependences in $\text{Gd}_3\text{Ga}_x\text{Fe}_{5-x}\text{O}_{12}$ ($0 \leq x \leq 1.5$) for $\Delta H = 16$ kOe (Belov *et al* 1972).

figure 5.2. As one can see for $x = 0.15$ and 0.3 the Curie temperature decreases and compensation temperature increases. Simultaneously, the maximum MCE value near the Curie point decreases and the MCE does not reach its maximum in the low-temperature region (it has a maximum at about 90 K in $\text{Gd}_3\text{Fe}_5\text{O}_{12}$). The former effect is observed for all investigated compositions and can be explained by decreasing of effective field H_{eff} acting from an a-d iron sublattice on an RE c-sublattice due to dilution of Fe ions by nonmagnetic Ga ions. This decrease causes increasing of the RE sublattice paraprocess and the MCE in the low-temperature region and a shift of the low-temperature MCE peak to lower temperatures.

Relative values and orientations of iron a- and d-sublattices, and the RE c-sublattice in the rare earth iron garnets in external magnetic field H below the compensation point, are shown in the left lower corner in figure 5.2. A ferromagnetic-type paraprocess is observed in c- and a-sublattices and an antiferromagnetic-type paraprocess in the iron d-sublattice. In $\text{R}_2\text{Fe}_5\text{O}_{12}$ garnets, iron a- and d-sublattices in the low-temperature region are coupled via strong antiferromagnetic exchange interactions and the paraprocess in these magnetic sublattices is small. So, the MCE in the rare earth iron garnets below the compensation point is governed by a ferromagnetic-type paraprocess in the RE c-sublattice.

The observed decreasing of the maximum MCE value at the Curie point for x up to 0.4 in $\text{Gd}_3\text{Ga}_x\text{Fe}_{5-x}\text{O}_{12}$ is the consequence of weakening of the

d-sublattice due to dilution by the nonmagnetic element. For composition with x greater than 0.4 the compensation point is absent (Curie and compensation temperatures merge at about $x = 0.4$)—the magnetic moment of the c-sublattice is higher than the total magnetic moment of the iron sublattices in the whole investigated temperature range. The MCE in these compositions is mainly determined by a ferromagnetic-type paraprocess in c- and a-sublattices.

Belov *et al* (1973) investigated the influence of iron sublattices on the MCE in the system $(Y_{3-x/2}Na_{x/2})Fe_{5-x}Ge_xO_{12}$ ($x = 0, 0.5, 1, 1.5, 2, 2.5$), where iron in the d-sublattice is substituted by nonmagnetic Ge. In this alloy system, the magnetic RE c-sublattice is absent and magnetic properties of the material are governed by iron a- and d-sublattices. For $x < 1$, the magnetic moment of the d-sublattice is higher than that of the a-sublattice because the quantity of magnetic ions in the d-sublattice in this case is higher. For $x = 1$, the magnetic moments of the d- and a-sublattices are equal to each other and the total spontaneous magnetic moment of the material is zero because a- and d-sublattices are coupled antiferromagnetically. For x from 1 to 2 the magnetic moment of the a-sublattice is higher than that of the d-sublattice. Finally, for x from 2 to 3 the intersublattice a-d exchange is essentially weakened and the antiferromagnetic exchange interactions inside the a-sublattice prevail, which causes antiferromagnetic ordering of the a-sublattice. Magnetocaloric effect temperature dependences measured by Belov *et al* (1973) (shown in figure 5.3) confirm this picture. For $x = 0$ there is only one large MCE peak near the Curie temperature, which is

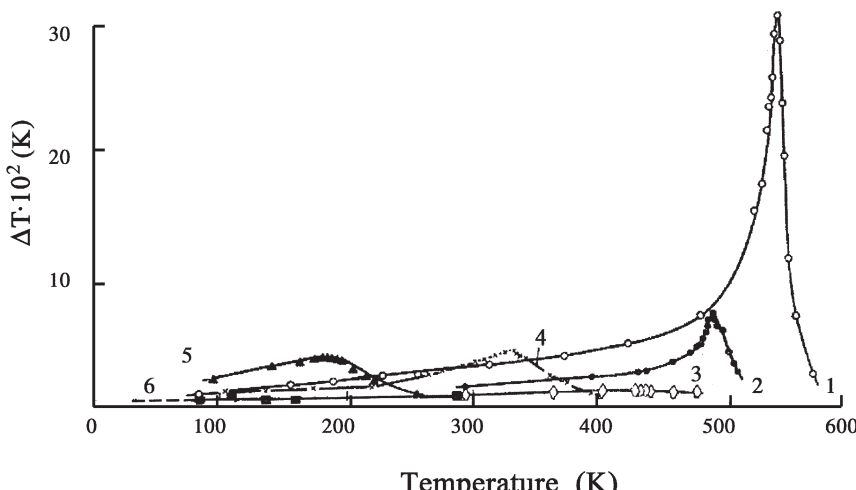


Figure 5.3. Temperature dependences of the MCE induced by 16 kOe in $(Y_{3-x/2}Na_{x/2})Fe_{5-x}Ge_xO_{12}$: (1) $x = 0$; (2) 0.5; (3) 1; (4) 1.5; (5) 2; (6) 2.5 (Belov *et al* 1973).

related to a strong ferromagnetic-type paraprocess in the d-sublattice prevailing antiferromagnetic-type paraprocess in the a-sublattice. Substitution of Ge reduces the value of the MCE peak and the Curie temperature due to decreasing of the magnetic ion quantity in the d-sublattice and weakening of the a-d exchange interaction. The latter factor causes increasing of the antiferromagnetic-type paraprocess in the a-sublattice. For composition with $x = 1$, where a spontaneous total magnetic moment is equal to zero, the MCE is vanishingly small. For x in the range from 1 to 2 the MCE increases, which can be explained by a ferromagnetic-type paraprocess in the a-sublattice (the magnetic moment of the a-sublattice is directed now along the magnetic field direction, and the d-sublattice is essentially weakened, its magnetic moment is small and directed opposite to the magnetic field). For the composition with $x = 2.5$, the a-sublattice is ordered antiferromagnetically and the MCE again approaches zero.

The MCE measurement near the Curie point (548 K) on $\text{Y}_3\text{Fe}_5\text{O}_{12}$ single crystal was made by Kamilov *et al* (1975). The peak MCE value for $\Delta H = 15 \text{ kOe}$ was determined to be about 0.38 K.

Belov *et al* (1970) studied the field dependences of the MCE near the compensation point T_{comp} in $\text{R}_3\text{Fe}_5\text{O}_{12}$ ($\text{R} = \text{Gd}, \text{Dy}$ and Ho). As was shown in a series of works, in ferrimagnets in some temperature and field intervals ($H_{c1} < H < H_{c2}$) a noncollinear magnetic structure can appear as a result of competition between the external magnetic field and the negative intersublattice exchange interactions (Tiablikov 1956, Pahomov and Gusev 1964, and Clark and Callen 1968). H_{c1} and H_{c2} can achieve essential values but near T_{comp} they should abruptly decrease.

The noncollinear magnetic structure in ferrimagnets is characterized by practically temperature independent total magnetic moment ($\partial M / \partial T = 0$) which, according to equation (2.16), leads to $dT/dH = 0$. Consequently, the $\Delta T(H)$ dependence should have the following form in the noncollinear ferromagnetic phase: an increase of ΔT with H for $H < H_{c1}$ with subsequent saturation for $H > H_{c1}$. Such saturation behaviour was observed in $\text{R}_3\text{Fe}_5\text{O}_{12}$ ($\text{R} = \text{Gd}, \text{Dy}$ and Ho) near T_{comp} by Belov *et al* (1970). For $\text{R} = \text{Dy}$ and Ho some field dependence persisted in saturation field region, which was related by the authors to the anisotropy of rare earth ions.

Analogous MCE behaviour was observed by Clark and Callen (1969) and Clark and Alben (1970) in polycrystalline $\text{Yb}_3\text{Fe}_5\text{O}_{12}$, $\text{Yb}_{0.9}\text{Y}_{2.1}\text{Fe}_5\text{O}_{12}$ and $\text{Gd}_{0.6}\text{Y}_{2.4}\text{Fe}_5\text{O}_{12}$ in the temperature region below 30 K and in high magnetic fields (up to 110 kOe). Figure 5.4 presents an $H-T$ diagram measured in the low-temperature range for $\text{Yb}_3\text{Fe}_5\text{O}_{12}$, which shows the change in the sample temperature as a function of an applied magnetic field in adiabatic conditions. For example, for an initial temperature of 21 K the sample cools down to 16 K ($\Delta T = 5 \text{ K}$) for magnetic fields up to 61 kOe. For the fields above this value no additional cooling occurs and the sample temperature remains almost constant (the saturation state). The solid line in figure 5.4

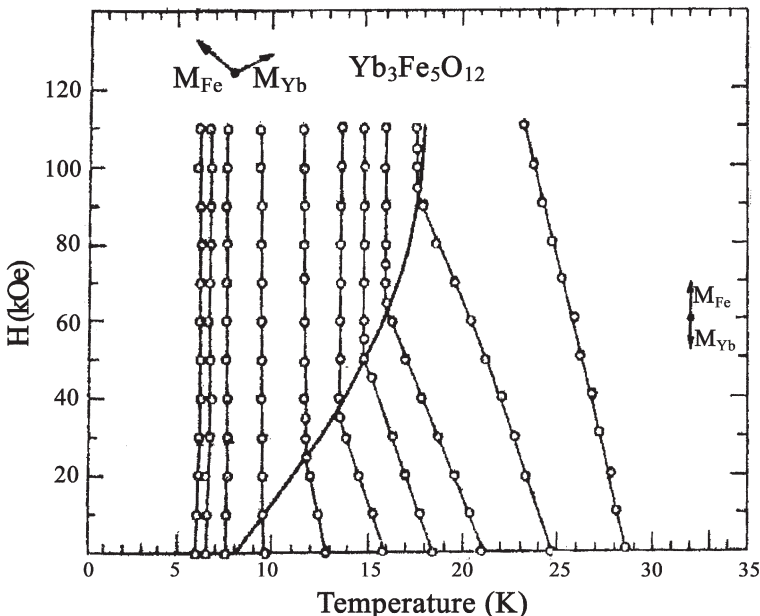


Figure 5.4. H - T diagram measured on $\text{Yb}_3\text{Fe}_5\text{O}_{12}$ in the low-temperature region (Clark and Alben 1970).

marks the boundary between collinear and noncollinear magnetic phases. The cooling rate in the collinear phase in $\text{Yb}_3\text{Fe}_5\text{O}_{12}$ is about 0.1 K/kOe . Dilution of Yb^{3+} ions by Y caused the collinear–noncollinear transition to move to lower temperatures and higher fields, so that no phase boundary was observed in $\text{Yb}_{0.9}\text{Y}_{2.1}\text{Fe}_5\text{O}_{12}$ for $H < 110 \text{ kOe}$. In diluted gadolinium iron garnet $\text{Gd}_{0.6}\text{Y}_{2.4}\text{Fe}_5\text{O}_{12}$ the phase boundary was detected for the fields below 110 kOe with the phase boundary field at 0 K of about 55 kOe .

5.1.2 Rare earth gallium and aluminium garnets

In a series of works the magnetothermal properties of gadolinium gallium garnet $\text{Gd}_3\text{Ga}_5\text{O}_{12}$ (GGG), dysprosium gallium garnet $\text{Dy}_3\text{Ga}_5\text{O}_{12}$ (DGG), dysprosium aluminium garnet $\text{Dy}_3\text{Al}_5\text{O}_{12}$ (DAG) and Er-doped yttrium aluminium garnet were studied (Ball *et al* 1963, Onn *et al* 1967, Fisher *et al* 1973, Filippi *et al* 1977, Barclay and Steyert 1982a, Daudin *et al* 1982a,b, Numazawa *et al* 1983, Antyukhov *et al* 1984, Hashimoto 1986, Li *et al* 1986, Dai *et al* 1988, Kimura *et al* 1988, Kuz'min and Tishin 1993a,b, Kushino *et al* 2001, 2002).

According to Dai *et al* (1988) the magnetic susceptibility measurements on GGG shows that it is characterized by a paramagnetic Curie temperature of -2.3 K , which implies antiferromagnetic ordering. However, specific heat

results indicate no evidence of long-range magnetic order down to 0.35 K and a broad Schottky-type anomaly at about 0.8 K (Onn *et al* 1967, Fisher *et al* 1973, Daudin *et al* 1982b, Dai *et al* 1988). Dai *et al* (1988) proposed the model describing magnetic and magnetothermal properties of GGG without involving magnetic ordering. It was supposed that the ground state of the Gd^{3+} ion in GGG is not a pure $^8\text{S}_{7/2}$ state, but is mixed with the excited $^6\text{P}_{7/2}$ state. Because of that, the *g*-factor is 1.992 and the ground state splits by crystal field into four Kramer doublets. The energy levels of the Gd^{3+} and their magnetic field dependence were determined by fitting the theoretically calculated magnetization to the experimental one. Then using these data, the internal magnetic energy was calculated and by equation (2.144) the magnetic heat capacity was obtained. The total heat capacity was calculated by summing the magnetic and lattice theoretical contributions. The obtained heat capacity temperature dependences were in good agreement with those measured experimentally on a sintered GGG sample by Dai *et al* (1988) and on a GGG single crystal by Fisher *et al* (1973) and Daudin *et al* (1982b) in the temperature interval from 0.2 to 50 K. The experimental $C(T)$ curves measured on the sintered sample coincide with an accuracy of 5% with the heat capacity measured on single crystal samples. Figure 5.5 shows the total entropy temperature dependences of GGG in different magnetic fields obtained by Dai *et al* (1988) from the experimental heat capacity data. The broken curve in figure 5.5 shows the lattice entropy contribution and the dash-and-dot straight line marks the expected saturation entropy for the system of Gd^{3+} ions with $J = 7/2$: $3R \ln(2(7/2) + 1) = 6.24R$. Analogous $S(T)$ curves were obtained by Daudin *et al* (1982a) on single crystal GGG.

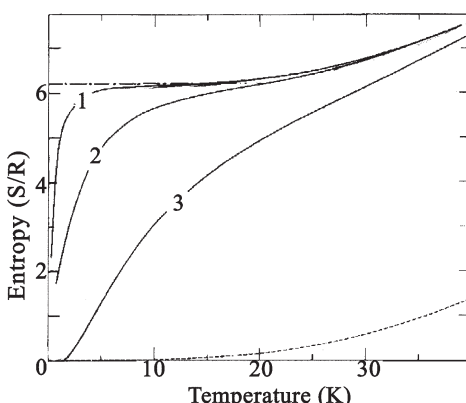


Figure 5.5. Total entropy temperature dependences for different magnetic fields for $\text{Gd}_3\text{Ga}_5\text{O}_{12}$: (1) $H = 0$ kOe; (2) 25 kOe; (3) 90 kOe. The broken curve shows the lattice entropy contribution and the dash-and-dot straight line marks the expected saturation entropy for the system of Gd^{3+} ions (Dai *et al* 1988).

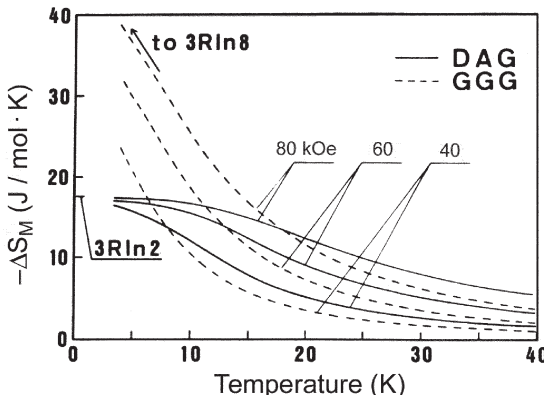


Figure 5.6. ΔS_M temperature dependences in DAG and GGG induced by the magnetic field change $\Delta H = 40, 60$ and 80 kOe (Hashimoto 1986).

According to the results obtained by Landau *et al* (1971) and Li *et al* (1986), $\text{Dy}_3\text{Al}_5\text{O}_{12}$ is antiferromagnet with a Néel temperature T_N of 2.54 K, a paramagnetic Curie temperature of -1.1 K and an effective magnetic moment $\mu_{\text{eff}} = 5.25 \mu_B$. Measurements on dilute samples of Dy^{3+} in $\text{Y}_3\text{Al}_5\text{O}_{12}$ and $\text{Lu}_3\text{Al}_5\text{O}_{12}$ showed that dysprosium ions can be characterized by $S = 1/2$ and $g_J \approx 17.7$ (Ball *et al* 1963). Heat capacity measurements revealed a sharp peak (with the height of ~ 44.1 J/mol K) on $C(T)$ dependence of DAG at 2.49 K (Ball *et al* 1963). $\text{Dy}_3\text{Ga}_5\text{O}_{12}$ displays antiferromagnetic properties with $T_N = 0.373$ K, and an average paramagnetic Curie temperature and effective magnetic moment of -0.26 K and $0.373 \mu_B$, respectively (Filippi *et al* 1977, Kimura *et al* 1988). The maximum value of the g-factor of 8.5 for the [110] direction and the minimum value of 8.0 for the [111] direction were obtained for DGG single crystal by Kimura *et al* (1988).

In DGG and DAG, the population of all energy levels except ground Kramer doublets of the Dy ions in the low-temperature region (below 20 K) can be neglected since the energy of the excited state is larger than the thermal agitation energy due to the crystal field splitting. Therefore, the total angular momentum quantum number for Dy ions in the garnets is $J = 1/2$. However, they are characterized by an essentially higher than Gd^{3+} ion in GGG g-factor values. Figure 5.6 illustrates the ΔS_M increase in GGG in comparison with DAG in the low-temperature region caused by the effect of crystal field splitting.

Hashimoto (1986), by means of MFA, studied the influence of g-factor and J quantum number values on the $\Delta S_M(T)$ curves. The calculations were made for an antiferromagnetic system with $T_N = 1$ K for $g_J = 2$ (J varied) and $J = 1/2$ (g_J varied) and for $\Delta H = 60$ kOe. The results of calculations are presented in figure 5.7(a,b). As one can see, the value of the magnetic entropy change increased with J and g_J increasing. For $J = 7/2$ and $g_J = 2$

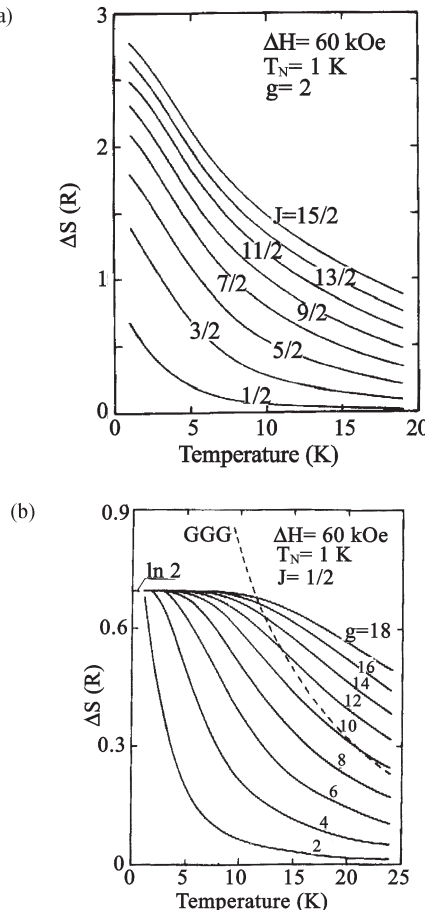


Figure 5.7. Calculated $\Delta S_M(T)$ curves for an antiferromagnet with $T_N = 1 \text{ K}$ induced by removal of the field of 60 kOe: (a) $g_J = 2$, J being varied; (b) $J = 1/2$, g_J being varied. The broken curve presents the data for GGG (Hashimoto 1986).

the Hashimoto (1986) value is smaller than that for $J = 1/2$ and $g_J \geq 10$ in the temperature region above 20 K. This means that GGG is more effective for magnetic cooling below 20 K, and DGG and DAG is more effective above 20 K.

Kimura *et al* (1988) investigated the MCE and magnetic entropy change in DGG single crystal. ΔS_M was determined from magnetization measurements and the MCE was measured by a direct method. Figure 5.8 shows the experimental $\Delta S_M(T)$ curves obtained for different ΔH when the field was applied along the [111] direction. The solid lines are results of MFA calculations for $J = 1/2$ and $g_J = 13$. From experimental $\Delta S_M(T)$ dependences and the lattice entropy determined on the basis of heat capacity

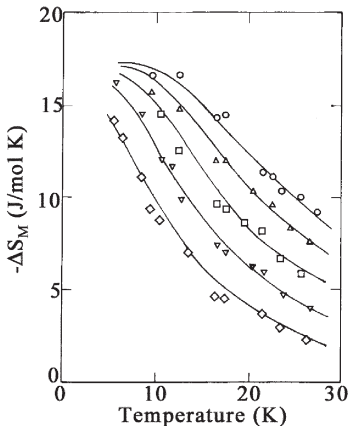


Figure 5.8. The magnetic entropy change temperature dependences for DGG single crystal determined for various ΔH with a magnetic field applied along the [111] direction: 30 kOe (\diamond); 40 kOe (∇); 50 kOe (\square); 60 kOe (\triangle) and 70 kOe (\circ) (Kimura *et al* 1988).

data in zero magnetic field, the total entropy temperature dependences were calculated. The latter allow $\Delta T(T)$ curves to be obtained by the method described in section 3.2.2, which are represented by solid lines in figure 5.9 together with directly measured points. As one can see, the peak ΔT values are observed at about 12–14 K and are ~ 12 and ~ 9 K for $\Delta H = 50$ and 30 kOe, corresponding to $\Delta T/\Delta H = 0.24$ and 0.3 K/kOe, which are high values (such $\Delta T/\Delta H$ values were observed in the $\text{Gd}_5(\text{Si}-\text{Ge})_4$ system—see table 7.2). Earlier, similar $\Delta T(T)$ curves for DGG were obtained by Tomokyo *et al* (1985) from the heat capacity measurements. The magnetic entropy change in DGG is also high—near 12 K, where a ΔT peak at $\Delta H = 30$ kOe is observed, $-\Delta S_M/\Delta H \approx 0.27$ J/mol K kOe for $\Delta H = 30$ kOe (see figure 5.8).

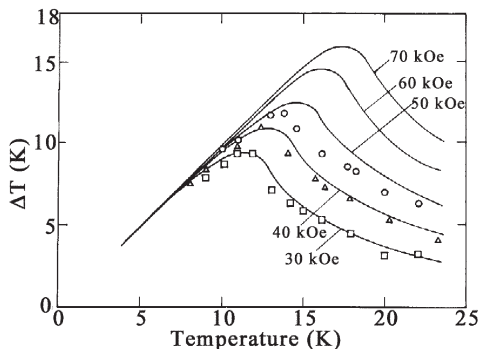


Figure 5.9. MCE temperature dependences for DGG single crystal for a magnetic field applied along the [111] direction (Kimura *et al* 1988).

Kushino *et al* (2001, 2002) investigated heat capacity, magnetization and magnetic entropy of erbium-doped yttrium aluminium garnet ($(\text{Er}_{0.317}\text{Y}_{0.683})_3\text{Al}_5\text{O}_{12}$) single crystal. This compound was prepared in order to obtain the material suitable for use as a magnetic refrigerant below 1 K. In the garnets discussed above (GGG, DGG and DAG) the interaction between RE ions lifts the ground-state degeneracy at low temperatures, decreasing magnetic entropy change and increasing the temperature where the garnets can be effectively used as refrigerants. Dilution of Er by Y in $(\text{Er}_{0.317}\text{Y}_{0.683})_3\text{Al}_5\text{O}_{12}$ should weaken such interactions. From magnetization and heat capacity measurements it was confirmed that the ground state of Er^{3+} ion in the considered compound is a doublet (as in the case of DAG and DGG) and $g = 6.46$. Magnetic entropy temperature dependences in various magnetic fields were constructed on the basis of magnetization and heat capacity data. It was established that for $H = 0$ the magnetic entropy per RE ion decreased below 2 K, reaching half the high-temperature value of $R \ln 2$ at about 160 mK. Based on these data the authors suggested that the operational temperature of $(\text{Er}_{0.317}\text{Y}_{0.683})_3\text{Al}_5\text{O}_{12}$ can be around 100 mK. The magnetic entropy change for the material determined from magnetization was about -6.1 J/K mol per R ion for $\Delta H = 55 \text{ kOe}$ at 4 K (this was the minimum temperature at which ΔS_M values were reported by the authors).

The thermal conductivity of GGG was investigated by Slack and Oliver (1971) and Numazawa *et al* (1983, 1996). According to their data it has a maximum at about 20 K. Numazawa *et al* (1983) studied single crystals and polycrystals. The highest maximum thermal conductivity value revealed the single crystal with a low density of dislocation, $\sim 5 \text{ W/cm K}$. An increase of the dislocation density caused some decrease of the maximum thermal conductivity value. In polycrystalline samples much lower maximum values of the thermal conductivity were observed by Numazawa *et al* (1983)—about 0.5 W/cm K . The results of Slack and Oliver (1971) obtained on a single crystal were almost the same as that of Numazawa *et al* (1983). For comparison with GGG, Slack and Oliver (1971) and Numazawa *et al* (1983) gave the thermal conductivity temperature dependence of Cu, which also has a round maximum at $\sim 20 \text{ K}$ with the value of $\sim 15 \text{ W/cm K}$. Numazawa *et al* (1996) also presented thermal conductivity data for DGG in the temperature range from 2 to 10 K. The curve displays a round maximum at $\sim 4.5 \text{ K}$ with the value of $\sim 0.3 \text{ W/cm K}$. The thermal conductivity of $\text{Dy}_3\text{Al}_5\text{O}_{12}$ single crystal along the [111] axis was measured by Kimura *et al* (1997b) in the temperature interval from 8 to 20 K. The maximum with the value of $\sim 1.5 \text{ W/cm K}$ was found at $\sim 11 \text{ K}$. Some numerical values of the thermal conductivity of GGG, DGG and DAG are presented in table A2.1 in appendix 2.

The heat capacity of DGG and GGG was investigated by Onn *et al* (1967), Fisher *et al* (1973), Filippi *et al* (1977), Daudin *et al* (1982b),

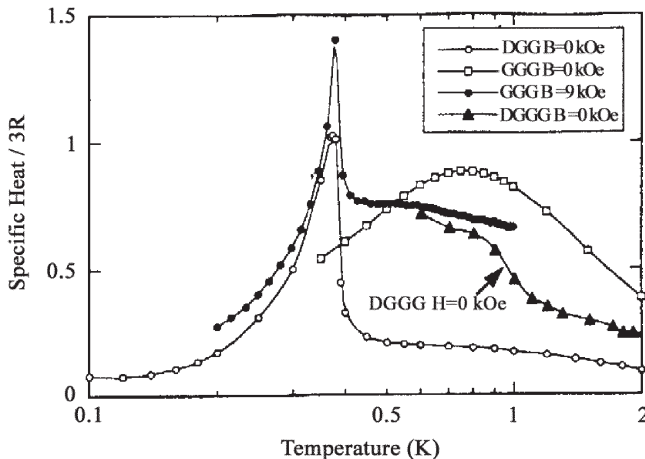


Figure 5.10. Heat capacity temperature dependences for GGG (Fisher *et al* 1973, Schiffer *et al* 1994), DGG (Filippi *et al* 1977) and $(\text{Dy}_{0.5}\text{Gd}_{0.5})_3\text{Ga}_5\text{O}_{12}$ (Numazawa *et al* 1996).

Tomokiyo *et al* (1985), Dai *et al* (1988), Schiffer *et al* (1994) and Numazawa *et al* (1996). DGG displays a sharp λ -type heat capacity anomaly (with a height of about $3R$) at $T_N = 0.35$ K. Tomokiyo *et al* (1985) measured the heat capacity of DGG in the fields up to 49.1 kOe. GGG shows a broad maximum near 0.8 K. According to the data of Schiffer *et al* (1994) this peak corresponds to the formation of antiferromagnetic short-range order. Application of the magnetic field causes the appearance of another peak in the low-temperature region, whose position for $H = 9$ kOe is about 0.4 K. The authors related this peak with a new low-temperature antiferromagnetic phase existing in the field of 10 kOe. Figure 5.10 shows heat capacity temperature dependences for GGG and DGG from Fisher *et al* (1973), Filippi *et al* (1977) and Schiffer *et al* (1994), and for $(\text{Dy}_{0.5}\text{Gd}_{0.5})_3\text{Ga}_5\text{O}_{12}$ single crystal measured by Numazawa *et al* (1996). Dai *et al* (1988) measured the heat capacity of sintered GGG in the temperature range from 1 to 300 K. The heat capacity minimum of 0.92 J/mol K was found at 10 K. With further heating the heat capacity increased, reaching 376.34 J/mol K at 300 K.

5.2 Perovskites

5.2.1 Rare earth orthoaluminates

Rare earth orthoaluminates (REOA)s RAIO_3 have an orthorhombically distorted perovskite-type structure (Geller and Bala 1956). REOA with $\text{R} = \text{Gd}, \text{Dy}, \text{Er}$ display an antiferromagnetic order below the Néel temperature T_N and paramagnetic behaviour above T_N (Schuchert *et al* 1969, Blazey

Table 5.1. Magnetic parameters and the magnetic entropy change determined along easy magnetization directions in RAIO_3 ($\text{R} = \text{Gd}, \text{Dy}, \text{Ho}$ and Er) and in $\text{Dy}_{0.9}\text{Er}_{0.1}\text{AlO}_3$.

Compound	T_N (K)	T_p (K)	μ_{eff} (μ_B)	$-\Delta S_M$ ($\text{J}/\text{cm}^3 \cdot \text{K}$) ($T = 5 \text{ K}$)	$-\Delta S_M$ ($\text{J}/\text{cm}^3 \cdot \text{K}$) ($T = 20 \text{ K}$)	Ref.*
GdAlO_3	3.875	-4.4	4.58	~0.43 ($\Delta H = 60 \text{ kOe}$, calc.)	~0.075 ($\Delta H = 60 \text{ kOe}$, calc.)	1, 2
DyAlO_3	3.52	-1.5	6.88 (b-axes)	~0.19 ($\Delta H = 60 \text{ kOe}$, calc.) ~0.16 ($\Delta H = 50 \text{ kOe}$, exp.)	~0.12 ($\Delta H = 60 \text{ kOe}$, calc.) ~0.16 ($\Delta H = 50 \text{ kOe}$, exp.)	3-6
HoAlO_3	12			~0.06 ($\Delta H = 50 \text{ kOe}$, exp., b-axis)	~0.055 ($\Delta H = 50 \text{ kOe}$, exp., b-axis)	6, 7
ErAlO_3	0.6		4.35 (c-axis)	~0.19 ($\Delta H = 50 \text{ kOe}$, exp.)	~0.07 ($\Delta H = 50 \text{ kOe}$, exp.)	6, 8, 9
$\text{Dy}_{0.9}\text{Er}_{0.1}\text{AlO}_3$	2.86	-1.0	6.62 (b-axis)	~0.19 ($\Delta H = 50 \text{ kOe}$, calc.)	~0.1 ($\Delta H = 50 \text{ kOe}$, calc.)	10

* 1. Blazey *et al.* (1971); 2. Kuz'min and Tishin (1991); 3. Schuchert *et al.* (1969); 4. Kolmakova *et al.* (1990); 5. Kuz'min and Tishin (1993b); 6. Kimura *et al.* (1997a); 7. Kimura *et al.* (1995); 8. Sivardière and Quezel-Ambrunaz (1971); 9. Bonville *et al.* (1980); 10. Tishin and Bozkova (1997).

et al 1971, Sivardi  re and Quezel-Ambrunaz 1971, Bonville *et al* 1980, Kolmakova *et al* 1990, Kimura *et al* 1995). DyAlO_3 and ErAlO_3 are characterized by a substantial magnetic anisotropy (for $\text{DyAlO}_3 \mu_{\text{eff}} = 6.88 \mu_B$ along the b-axis ([010]) and $0.8 \mu_B$ along the c-axis ([001])) and GdAlO_3 is almost magnetically isotropic. According to Kimura *et al* (1995, 1997a,b) magnetization in DyAlO_3 and ErAlO_3 decreased, with temperature increasing for all crystal axes. The same behaviour was observed in HoAlO_3 along the a- and b-axes, but along c-axes its magnetization remained almost constant. It should be noted that, for HoAlO_3 , inverse magnetic susceptibility did not obey the Curie-Weiss law and its T_N was established by a small peak on magnetization temperature dependence (Kimura 1995). The easy magnetization axes in DyAlO_3 and ErAlO_3 are the b- and c-axis, respectively (see Kuz'min and Tishin 1991). Magnetic characteristics of RAIO_3 compounds with $R = \text{Gd}, \text{Dy}, \text{Ho}$ and Er are summarized in table 5.1.

Kuz'min and Tishin (1991, 1993a,b) calculated the magnetic entropy change ΔS_M induced by a magnetic field in GdAlO_3 and DyAlO_3 using the MFA (J was taken to be 7/2 and 1/2, for Gd and Dy perovskites, respectively). The results are presented in figure 5.11. Kimura *et al* (1995, 1997a,b) determined ΔS_M for RAIO_3 ($R = \text{Dy}, \text{Ho}, \text{Er}$) on the basis of the magnetization measurements along various crystal axes. The obtained experimental ΔS_M results are presented in figure 5.12(a). One can see a substantial dependence of $\Delta S_M(T)$ character on the direction of a measurement. The experimental results for DyAlO_3 and ErAlO_3 along the easy axes are in good agreement with the calculations of Kuz'min and Tishin (1991). Kimura *et al* (1995) compared ΔS_M induced by a magnetic field of 50 kOe aligned along the easy magnetization direction in ErAlO_3 and DyAlO_3 with that in $\text{Dy}_3\text{Al}_5\text{O}_{12}$ and $\text{Gd}_3\text{Al}_5\text{O}_{12}$ (the easy directions are c- and b-axes in ErAlO_3 and DyAlO_3 , respectively, and the [111] axis in $\text{Dy}_3\text{Al}_5\text{O}_{12}$ and $\text{Gd}_3\text{Al}_5\text{O}_{12}$) (see figure 5.12(b)). It is evident that ΔS_M for ErAlO_3 and DyAlO_3 is superior to that of $\text{Dy}_3\text{Al}_5\text{O}_{12}$ and $\text{Gd}_3\text{Al}_5\text{O}_{12}$. This is in agreement with the conclusion that ErAlO_3 and DyAlO_3 are promising materials for magnetic refrigeration below 20 K, made by Kuz'min and Tishin (1991) on the basis of theoretical calculations. Tishin and Bozkova (1997) in the frames of MFA calculated the $\Delta S_M(T)$ dependences for different ΔH in $\text{Dy}_{0.9}\text{Er}_{0.1}\text{AlO}_3$ along the b-axis—see figure 5.13. The experimental and theoretical ΔS_M values for RAIO_3 ($R = \text{Gd}, \text{Dy}, \text{Ho}$ and Er) and $\text{Dy}_{0.9}\text{Er}_{0.1}\text{AlO}_3$ at 5 and 20 K are summarized in table 5.1.

Thermal conductivity of DyAlO_3 , HoAlO_3 and ErAlO_3 single crystals along the c-axis was measured by Kimura *et al* (1997b) in the temperature interval from 4.2 to 25 K. As was noted by Kimura *et al* (1997b), all of them have thermal conductivity higher than $\text{Dy}_3\text{Al}_5\text{O}_{12}$, which is used in magnetic refrigerators. The maximum thermal conductivity values were observed in ErAlO_3 ($\sim 12 \text{ W/cm K}$ at $\sim 18 \text{ K}$). DyAlO_3 are characterized by lower thermal conductivity (maximum of $\sim 4 \text{ W/cm K}$ at $\sim 11 \text{ K}$) and

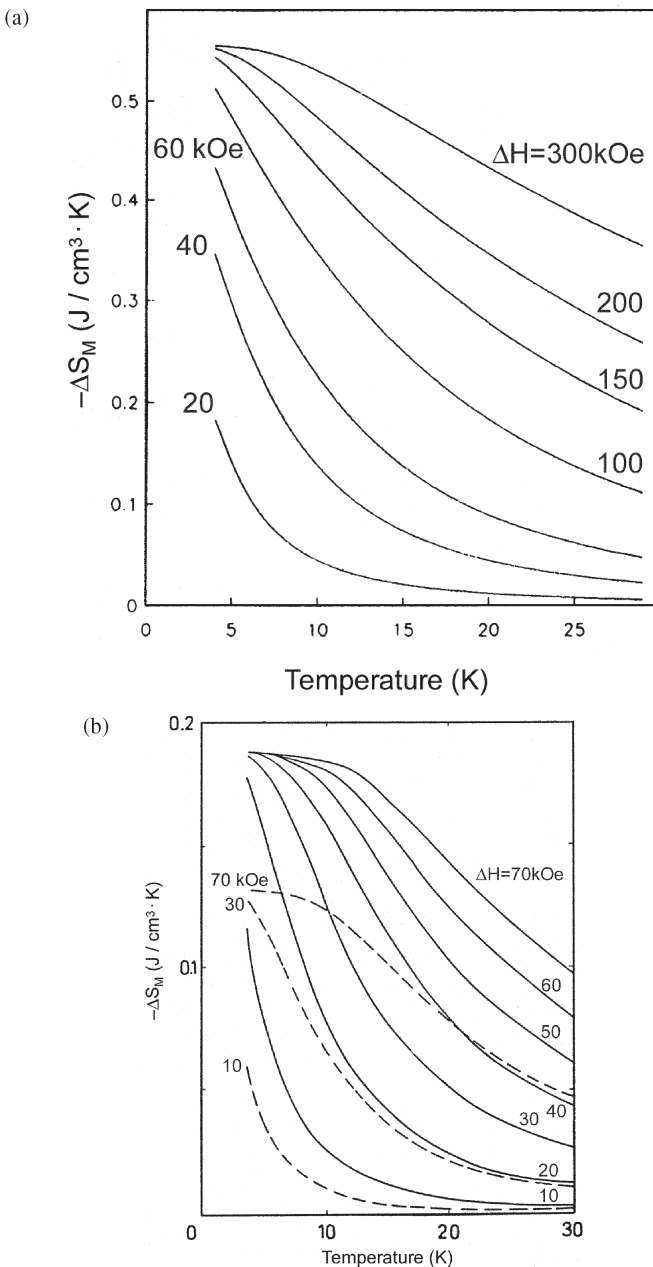


Figure 5.11. Temperature dependences of the magnetic entropy change ΔS_M induced by a magnetic field in (a) GdAlO_3 and (b) DyAlO_3 with H along the b-axis [010]. The dashed lines are the same for $\text{Dy}_3\text{Al}_5\text{O}_{12}$ with H along the [111] direction (Kuz'min and Tishin 1991, 1993b).

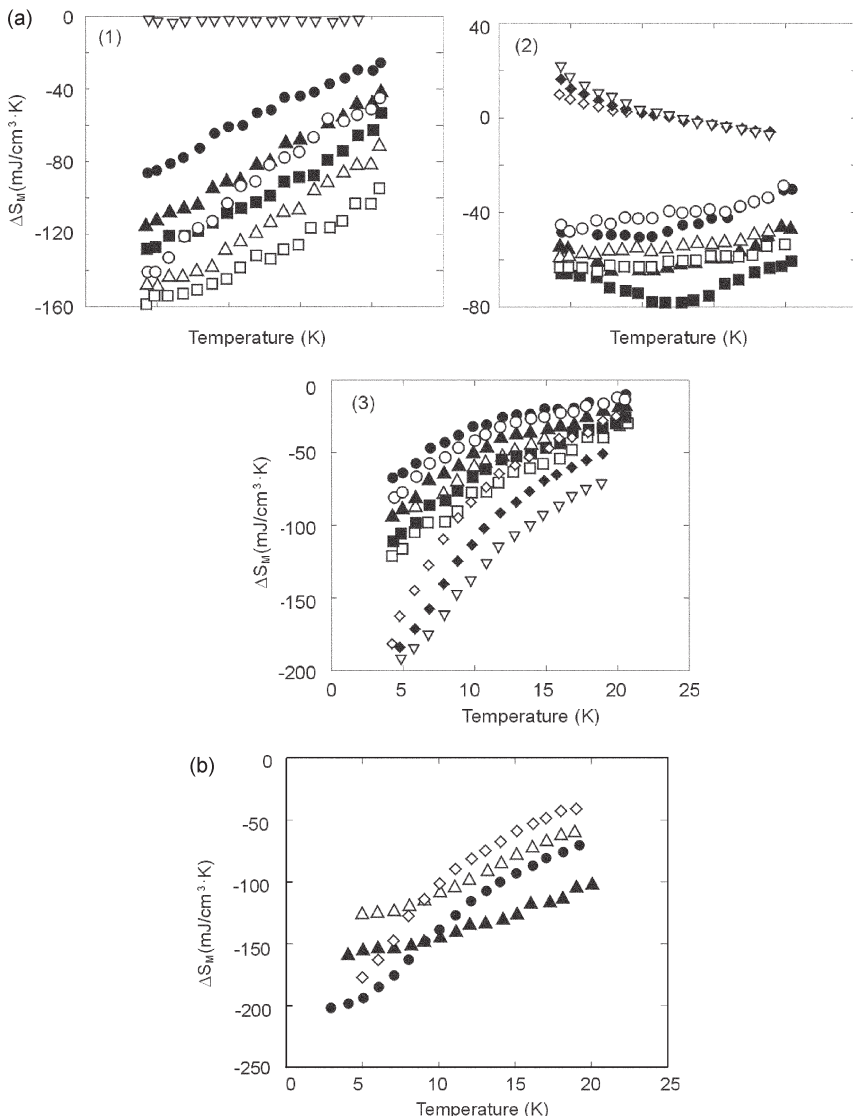


Figure 5.12. (a) Temperature dependences of the magnetic entropy change ΔS_M induced by various ΔH in (1) DyAlO₃, (2) HoAlO₃ and (3) ErAlO₃ single crystals. The magnetic field was applied along the a-axis (● ($\Delta H = 30$ kOe); ▲ ($\Delta H = 40$ kOe); ■ ($\Delta H = 50$ kOe)), the b-axis (○ ($\Delta H = 30$ kOe); △ ($\Delta H = 40$ kOe); □ ($\Delta H = 50$ kOe)), and the c-axis (◇ ($\Delta H = 30$ kOe); ♦ ($\Delta H = 40$ kOe); ∇ ($\Delta H = 50$ kOe)). The ΔS_M was calculated from experimental magnetization data. (b) Comparison of ΔS_M temperature dependences in DyAlO₃ (▲) measured along the b-axis and in ErAlO₃ (●) along the c-axis with that in Gd₃Ga₅O₁₂ (◇) and Dy₃Ga₅O₁₂ (△) measured along the [111] direction for $\Delta H = 50$ kOe (Kimura *et al* 1997a).

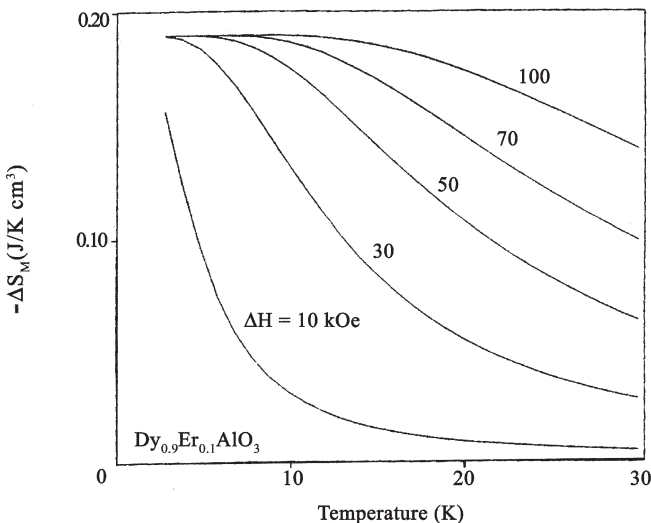


Figure 5.13. Temperature dependences of the magnetic entropy change ΔS_M in $\text{Dy}_{0.9}\text{Er}_{0.1}\text{AlO}_3$ (Tishin and Bozkova 1997).

HoAlO_3 has $\sim 1.8 \text{ W/cm K}$ at $\sim 14 \text{ K}$ (Kimura *et al* 1997b). Schnelle *et al* (2001) measured the thermal conductivity of LaAlO_3 single crystal along the [110] axis. Some numerical values of the thermal conductivity of ErAlO_3 , DyAlO_3 and LaAlO_3 are presented in table A2.1 in appendix 2.

5.2.2 Other RMeO₃ perovskites

The heat capacity of rare earth orthoferrites RFeO_3 ($\text{R} = \text{Yb, Er and Tm}$) was studied by Moldover *et al* (1971) and Saito *et al* (2001). The magnetic ordering in the orthoferrites takes place below about 600 K, where the Fe sublattice orders antiferromagnetically. The RE sublattice orders in the liquid helium temperature range. Under cooling many orthoferrites display spin reorientation transition and compensation points. ErFeO_3 and TmFeO_3 undergo spin reorientation transitions near 90 K and compensation points at about 45 and 20 K, respectively (see Saito *et al* 2001). According to the data of Saito *et al* (2001), heat capacity temperature dependences of ErFeO_3 and TmFeO_3 reveal the anomalies corresponding to the spin reorientation transitions at about 90 K and show no peculiarities at the compensation temperatures. In ErFeO_3 a heat capacity peak was found near 3.6 K, which was attributed by the authors to ordering in the RE sublattice. In YbFeO_3 , a spin-reorientation anomaly (peak) was observed on heat capacity temperature dependence at $\sim 7 \text{ K}$ by Moldover *et al* (1971).

The heat capacity of neodymium gallate NdGaO_3 was studied experimentally and theoretically in the works of Bartolomé *et al* (1994) and Luis

et al (1998). According to the magnetic measurements, this compound reveals under cooling a transition from the paramagnetic to the antiferromagnetic state at $T_N = 1$ K (Luis *et al* 1998). The experimental heat capacity temperature dependence displays a sharp λ -type anomaly at 0.97 K (Bartolomé *et al* 1994). The experimental heat capacity and magnetization data were described by Luis *et al* (1998) in the framework of the Ising model on the simple tetragonal lattice in the quasi-two-dimensional regime in supposition that intralayer exchange is strong and antiferromagnetic, and that the interlayer exchange is an order of magnitude weaker and ferromagnetic.

Thermal conductivity of $\text{Sr}_{1-x}\text{Ca}_x\text{RuO}_3$ ($x = 0, 0.25, 0.5, 1$) single crystals was studied by Shepard *et al* (1998). SrRuO_3 is a ferromagnet with $T_C = 160$ K, and CaRuO_3 remains paramagnetic down to 30 mK (Shepard *et al* 1998). The thermal conductivity temperature dependences were measured up to 250 K. At 250 K the maximum thermal conductivity value has CaRuO_3 (~ 0.085 W/cm K) and the minimum has $\text{Sr}_{0.75}\text{Ca}_{0.25}\text{RuO}_3$ (~ 0.01 W/cm K), which is close to the value for LaMnO_3 (about 0.012 W/cm K) obtained by Cohn *et al* (1997). Thermal conductivities of SrRuO_3 and CaRuO_3 have a maximum of about 60 K (peak values ~ 0.13 and ~ 0.075 W/cm K, respectively) and decrease with heating.

5.2.3 Manganites and related compounds

Doped perovskite-type manganese oxides $\text{La}_{1-x}\text{A}_x\text{MnO}_3$ (manganites), where A is a divalent metal such as Ca, Ba, Sr, attract the attention of researchers due to their unusual magnetic and electric properties (see reviews by Nagaev 1996, Gorkov 1998, Coey *et al* 1999). In particular, the doped manganites with a dopant concentration of about 0.15–0.4 undergo a transition from the paramagnetic isolator state to the ferromagnetic state with high conductivity. This causes a so-called colossal magnetoresistance effect, which can also be induced by application of a magnetic field (Ju and Sohn 1977, Jin *et al* 1994, Schiffer *et al* 1995, Nagaev 1996, Coey *et al* 1999, Tokura and Tomioka 1999). The Curie temperatures of the manganites lie in the room-temperature range. Among other interesting effects phase separation, charge and orbital ordering should be mentioned. Analogous properties are observed in the manganites with other rare earth metals instead of La. In general, the doped manganites can be represented by the formula $\text{R}_{1-x}\text{A}_x\text{MnO}_3$, where R is an R^{3+} rare earth ion. In the extreme compounds RMnO_3 and AMnO_3 the Mn ions are trivalent Mn^{3+} with four electrons in 3d shell ($3d^4$) or tetravalent Mn^{4+} with three 3d electrons ($3d^3$).

An ideal perovskite ABO_3 has a cubic structure. The crystal lattice of real perovskite-type compounds is distorted due to cation size mismatch and the Jahn–Teller effect. Such distorted structures are usually

orthorhombic. In LaMnO_3 the Mn^{3+} ions having four electrons in the 3d shell are located in the centre of octahedrons formed of O^{2-} anions. The crystal field of the ligands determines the following structure of 3d shells of the ions: three electrons in the low-lying t_{2g} states (t_{2g}^3) and one electron in higher-lying e_g states (e_g^1) for Mn^{3+} ions and t_{2g}^3 configuration for Mn^{4+} ions. The t_{2g} electrons are mainly localized and have minor hybridization with 2p electrons of oxygen. They form local 3/2 spins. The e_g electrons in the extreme compounds RMnO_3 and AMnO_3 are strongly hybridized with the 2p oxygen states and are also localized, causing isolating properties of the extreme compounds. The magnetic ordering in the compounds is antiferromagnetic (LaMnO_3 undergoes a transition from paramagnetic to antiferromagnetic state at 141 K (Matsumoto 1970)) and is realized by the superexchange Mn–O–Mn interaction. In doped mixed-valence compounds $(\text{R}_{1-x}\text{A}_x)^{3+}(\text{Mn}_{1-x}^{3+}\text{Mn}_x^{4+})\text{O}_3$ holes are created in the e_g states and e_g electrons become itinerant and mobile, providing high conduction properties of such materials. The ferromagnetic interaction between localized t_{2g}^3 spins in such states is mediated via e_g electrons and can be described in terms of the so-called double exchange interactions model (Zener 1951, De Gennes 1960). The e_g electrons can easily hop between Mn ions through the oxygen orbitals, with the condition that the Hund rule requiring high spin state should not be violated. In this case the e_g electrons energetically prefer to align the spins in their vicinity, providing ferromagnetic ordering in the material. If Mn spins are ordered ferromagnetically the e_g electrons hop between Mn ions with minimum scattering and their kinetic energy is optimal. The lack of long-range magnetic order or antiferromagnetic ordering in the Mn subsystem or bending of Mn–O–Mn bonds reduces the mobility of e_g electrons and the system can become insulating. The large magnetoresistive effect is observed near the Curie temperature since the localized Mn spins can easily be aligned here by an external magnetic field. The considered mechanism shows interrelation between electric and magnetic properties in the manganites, which allows a change of resistivity of the materials by changing their magnetic ordering. It was found that the optimum divalent element concentration for the colossal magnetoresistance effect in $\text{R}_{1-x}\text{A}_x\text{MnO}_3$ manganites is $x = 0.33$ and $x > 0.5$. No long-range ferromagnetic order is observed (see Nagaev 1996, Coey *et al* 1999, Moreo *et al* 1999).

However, the double exchange model discussed above cannot explain all experimentally observed phenomena in the manganites related to colossal magnetoresistance and magnetic behaviour. The shortcomings of the double exchange model were discussed by Millis *et al* (1995) and Edwards *et al* (1999). There are other important interactions, which are not taken into account in the double exchange model: crystal lattice–electron interactions, superexchange interactions (negative and positive) between Mn ions, exchange and Coulomb repulsion interactions between e_g electrons

etc. The listed interactions compete with the ferromagnetic double exchange interaction, leading to formation of various electronic phases and to high sensitivity of magnetic and other properties of the materials to a magnetic field.

Among other important effects found in the doped manganites, charge ordering and phase separation should be mentioned (Goodenough 1955, Mizokawa and Fujimori 1977, Nagaev 1996). The models of charge ordering and phase separation can be used to explain colossal magnetoresistance in the doped manganites. Yunoki *et al* (1998) made a computational analysis of the double exchange model using the Monte Carlo technique and obtained a phase diagram of temperature–concentration, which is consistent with experimental data. It was shown that the ground state of a system with double exchange interaction is not homogeneous, but consists of two phases with different electron densities—the phenomenon called phase separation. It was shown by Gorkov and Sokol (1987) that such phases can exist in the form of a ‘foggy’ state with the dimension of ‘droplets’ determined by Coulomb energy. The droplets with high electron concentration are ferromagnetic and highly conductive (Nagaev 1996). Under low concentration of the charge carriers, the ferromagnetic droplets are separated by an antiferromagnetic isolator matrix and the material is an isolator at $T = 0$. Increasing of the charge carriers concentration, as a result of doping or the ordering action of an external magnetic field, causes increasing of the droplets volume, their overlapping and the appearance of a high conductive state in the material. Various experimental data show that in the doped manganites, on the concentration and temperature borders of the ferromagnetic phase, there are nonhomogeneous states with high electron concentration ferromagnetic clusters. As an example, the elastic neutron scattering experiments on antiferromagnetic $\text{La}_{1-x}\text{A}_x\text{MnO}_3$ with $x = 0.05$ and 0.08 can be mentioned (Hennion *et al* 1998). According to interpretation of the obtained results, metallic ferromagnetic droplets with dimensions of less than 10 \AA exist in the antiferromagnetic matrix of these materials.

The charge-ordered state can arise in some doped manganites when x is a rational fraction, such as $1/8$, $1/3$, $1/2$ etc. In this state the mobile d electrons are localized on certain manganese ions (because the interelectronic Coulomb interaction overcomes the kinetic energy of the electrons) and Mn^{3+} and Mn^{4+} ions show a real space ordering commensurate with the crystal lattice. The localization of the d electrons leads to weakening of the ferromagnetic double exchange interaction. As a result, antiferromagnetic superexchange interaction between Mn ions becomes dominant and antiferromagnetic ordering arises in the material. The transition to the charge ordered state is accompanied by the first-order transition from the metallic ferromagnetic state to the insulating antiferromagnetic state (for $x = 0.5$ the AFM state in most manganites is of the so-called CE type). The characteristic feature of the charge-ordered state in the manganites is the possibility

of its magnetic field-induced destruction (melting) with transition from AFM insulating to FM metal state. The charge-ordered behaviour was found experimentally in $\text{Pr}_{0.5}\text{Sr}_{0.5}\text{MnO}_3$, $\text{Nd}_{0.5}\text{Sr}_{0.5}\text{MnO}_3$ and $\text{Pr}_{0.63}\text{Ca}_{0.37}\text{MnO}_3$ (Kuwahara *et al* 1995, Tomioka *et al* 1995, Tokura *et al* 1996, Raychaudhuri *et al* 2001).

The doped manganites display strong coupling between magnetic and structural subsystems. Anomalous thermal expansion and discontinuous volume variation was observed in $(\text{NdSm})_{1/2}\text{Sr}_{1/2}\text{MnO}_3$, $\text{La}_{0.75}\text{Ca}_{0.25}\text{MnO}_3$, $\text{La}_{0.6}\text{Y}_{0.07}\text{Ca}_{0.33}\text{MnO}_3$ and $\text{La}_{0.875}\text{Sr}_{0.125}\text{MnO}_3$ compounds at the Curie temperature (Radaelli *et al* 1995, Ibarra *et al* 1995, 2000, Argyriou *et al* 1996, Dai *et al* 1996, Kuwahara *et al* 1996). Discontinuous lattice parameter change is accompanied by sharp change in magnetization due to the variation in interatomic distance and Mn–O–Mn bond angles (Radaelli *et al* 1995, Ibarra *et al* 1995). Asamitsu *et al* (1995) observed structural (orthorhombic–rhombohedral) transition in $\text{La}_{0.83}\text{Sr}_{0.17}\text{MnO}_3$ driven by a magnetic field.

The electronic and crystal lattice transformations in the doped manganites described above have an essential influence on the magnetization and the rate of its variation under magnetic field and temperature-induced transitions. Mira *et al* (1999) studied the magnetic transitions at the Curie temperature in the compound system $\text{La}_{2/3}(\text{Ca}_{1-x}\text{Sr}_x)_{1/3}\text{MnO}_3$. The type of the transition was established on the basis of $H/M(M^2)$ plots and the criterion proposed by Banerjee (1964), according to which the slope of $H/M(M^2)$ isotherms should be positive for second-order transitions and can be negative for some temperatures in the case of second-order transitions. It was found that in $\text{La}_{2/3}\text{Ca}_{1/3}\text{MnO}_3$ the magnetic phase transition is of first-order type and changes to second-order under substitution of Sr at $x = 0.05\text{--}0.15$. In $\text{La}_{2/3}\text{Sr}_{1/3}\text{MnO}_3$ the transition is of first-order type. It was also established by Mira *et al* (2001) that in this concentration range the crystal structure changes from an orthorhombic type to a rhombohedral one.

The magnetization change under the transitions described above is rather sharp, which should cause essential values of magnetic entropy change and, possibly, magnetocaloric effect. Because of that a vast quantity of experimental work was devoted to investigation of the magnetic entropy change in the manganites with substitution of rare earth metal and Mn by various elements. It should be noted that in spite of theoretical and experimental investigations of the nature of the magnetic phase transitions in manganites, data are not yet clear.

The main quantity of the experimental investigations was made on the system prepared on the basis of an LaMnO_3 compound. Morelli *et al* (1996) was the first to measure the magnetic entropy change in the doped manganites. The investigations were conducted on $2.4\ \mu\text{m}$ thick polycrystalline films of $\text{La}_{0.67}\text{A}_{0.33}\text{MnO}_3$ ($\text{A} = \text{Ca}, \text{Ba}$ or Sr), which displayed an FM–PM transition at 250, 300 and 350 K, respectively. The films were fabricated by a

metal-organic deposition technique. The $\Delta S_M(T)$ dependences were calculated on the basis of magnetization data. Near the Curie temperatures, wide maxima of ΔS_M were observed with the following values (for $\Delta H = 50$ kOe applied parallel to the film plane): 2 J/kg K for A = Ca, 1.4 J/kg K for Ba, and 1.5 J/kg K for Sr. The maximum $-\Delta S_M/\Delta H$ value of 0.04 J/kg K kOe observed by Morelli *et al* (1996) for A = Ca was not high.

Larger ΔS_M values were observed later in ceramic bulk (La–Ca)MnO₃ samples. As a rule ΔS_M was determined from magnetization measurements. First Zhang *et al* (1996) obtained the $-\Delta S_M$ peak value of 2.75 J/kg K for $\Delta H = 30$ kOe in ceramic La_{0.67}Ca_{0.33}MnO_δ (this corresponds to $-\Delta S_M/\Delta H = 9.2$ J/kg K kOe) near $T_C = 260$ K. Substitution of La by Y in this composition reduced T_C (to 230 K) and saturation magnetization, which caused the reduction of the ΔS_M absolute value (see table 5.2). The reduction in the magnetization and T_C were attributed by the authors to a decrease of the ferromagnetic coupling due to the contraction of the crystal lattice under substitution. Several times higher $-\Delta S_M/\Delta H$ value equal to 36.7 J/kg K kOe ($\Delta H = 15$ kOe) was found in polycrystalline La_{0.8}Ca_{0.2}MnO₃ ($T_C = 230$ K) by Guo *et al* (1997a). With Ca concentration increasing, the absolute value of $\Delta S_M/\Delta H$ decreased. The $\Delta S_M(T)$ curves for La_{0.8}Ca_{0.2}MnO₃ and La_{0.67}Ca_{0.33}MnO₃ display relatively narrow peaks near T_C (see figure 5.14)—for La_{0.67}Ca_{0.33}MnO₃, full width at half maximum was about 15 K for $\Delta H = 15$ kOe. In La_{0.55}Ca_{0.45}MnO₃ the ΔS_M maximum was broader and lower, which is consistent with a less sharp change of the magnetization at T_C in this sample compared with lower Ca content compositions.

Further investigations of the MCE in Ca-doped ceramic La manganites were made by Bohigas *et al* (1998, 2000), Sun *et al* (2000b) and Xu *et al* (2001, 2002). The results are listed in table 5.2, where all available data on the MCE in manganites and related compounds are summarized. The ΔS_M was determined from magnetization and ΔT in La_{0.6}Ca_{0.4}MnO₃ (Bohigas *et al* 2000) was obtained from heat capacity measurements. The data of Xu *et al* (2002) show highly absolute $\Delta S_M/\Delta H$ values for La_{0.67}Ca_{0.33}MnO₃ and La_{0.67}Sr_{0.33}MnO₃ (66 and 54 J/kg K kOe) for low magnetic field change values (0.5 kOe). At higher ΔH the absolute value of $\Delta S_M/\Delta H$ in La_{0.67}Ca_{0.33}MnO₃ became much lower (17 J/kg K kOe for $\Delta H = 20$ kOe). Such behaviour can be related to essential smoothing of the magnetization change near the Curie temperature in high magnetic fields.

Bohigas *et al* (2000) measured temperature dependences of magnetization of La_{0.6}Ca_{0.4}MnO₃ in low field (50 Oe) in two different conditions. The first one was cooled in the presence of the field from the paramagnetic temperatures down to 4.2 K (field cooled (FC) regime). In the second regime the sample was first cooled from the paramagnetic region down to 4.2 K without external field and then warmed in the field (zero field cooled (ZFC) regime). Below the Curie temperature (260 K) the sample revealed

Table 5.2. The Curie temperature T_C , saturation magnetization I_s at 4.2 K, the absolute value of the magnetic entropy change $|\Delta S_M|$ induced by the magnetic field change ΔH , $|\Delta S_M|/\Delta H$, the magnetocaloric effect ΔT induced by ΔH for manganites and related compounds. The values for Gd is given for comparison.

Compound	T_C (K)	I_s (emu/g)	$ \Delta S_M $ (J/kg K)	ΔH (kOe)	$ \Delta S_M /\Delta H \times 10^2$ (J/kg K kOe)	ΔT (K)	ΔH (kOe)	$\Delta T/\Delta H \times 10^2$ (K/kOe)	Ref.*
$\text{La}_{0.67}\text{Ca}_{0.33}\text{MnO}_3$	250		2	50	4	-	-	-	1
$\text{La}_{0.67}\text{Ca}_{0.33}\text{MnO}_\delta$	260		2.75	30	9.2	-	-	-	2
$\text{La}_{0.6}Y_{0.07}\text{Ca}_{0.33}\text{MnO}_\delta$	230		1.55	30	5.2	-	-	-	
$\text{La}_{0.8}\text{Ca}_{0.2}\text{MnO}_3$	230		5.5	15	36.7	-	-	-	3
$\text{La}_{0.67}\text{Ca}_{0.33}\text{MnO}_3$	257		4.3	15	28.7	-	-	-	
$\text{La}_{0.55}\text{Ca}_{0.45}\text{MnO}_3$	234		2.0	15	13.3	-	-	-	
$\text{La}_{0.75}\text{Ca}_{0.25}\text{MnO}_3$ (120 nm)	177		2	15	13.3	-	-	-	4
$\text{La}_{0.67}\text{Ca}_{0.33}\text{MnO}_3$ (300 nm)	224		4.7	15	31.3	-	-	-	
$\text{La}_{0.67}\text{Ca}_{0.33}\text{MnO}_{3-\delta}$ (60 nm)	258		62	1.75	10	17.5	-	-	
$\text{La}_{0.67}\text{Ca}_{0.33}\text{MnO}_{3-\delta}$ (500 nm)	265		83	5	10	50	-	-	
$\text{La}_{2/3}\text{Ca}_{1/3}\text{MnO}_3$	267		6.4	30	21.3	-	-	-	5
$\text{La}_{0.6}\text{Ca}_{0.4}\text{MnO}_3$	263		5.0	30	16.6	-	-	-	6
$\text{La}_{0.65}\text{Ca}_{0.35}\text{Ti}_{0.4}\text{Mn}_{0.6}\text{O}_3$	42		30	0.6	30	2	-	-	
$\text{La}_{0.65}\text{Ca}_{0.35}\text{Ti}_{0.2}\text{Mn}_{0.8}\text{O}_3$	87		60	0.9	30	3	-	-	
$\text{La}_{0.65}\text{Ca}_{0.35}\text{Ti}_{0.1}\text{Mn}_{0.9}\text{O}_3$	103		70	1.3	30	4.3	-	-	
$\text{La}_{0.83}\text{Li}_{0.1}\text{Ti}_{0.4}\text{Mn}_{0.6}\text{O}_3$	35		30	0.9	30	3	-	-	
$\text{La}_{0.85}\text{Li}_{0.15}\text{Ti}_{0.3}\text{Mn}_{0.7}\text{O}_3$	60		43	1.1	30	3.7	-	-	
$\text{La}_{0.917}\text{Li}_{0.05}\text{Ti}_{0.2}\text{Mn}_{0.8}\text{O}_3$	77		60	1.7	30	5.7	-	-	
$\text{La}_{0.938}\text{Li}_{0.025}\text{Ti}_{0.1}\text{Mn}_{0.9}\text{O}_3$	90		64	2.0	30	6.7	-	-	

$\text{La}_{0.65}\text{Nd}_{0.05}\text{Ca}_{0.3}\text{MnO}_3$	260	1.7	10	17	-	-	-	-	28
$\text{La}_{0.65}\text{Nd}_{0.05}\text{Ca}_{0.3}\text{Mn}_{0.9}\text{Cr}_{0.1}\text{O}_3$	200	0.95	10	9.5	-	-	-	-	
$\text{La}_{0.65}\text{Nd}_{0.05}\text{Ca}_{0.3}\text{Mn}_{0.9}\text{Fe}_{0.1}\text{O}_3$	120	0.45	10	4.5	-	-	-	-	
$\text{La}_{0.6}\text{Ca}_{0.4}\text{MnO}_3$	260	100	5.0	30	16.6	2.1	30	7	7
			2.5	10	25	1.1	10	11	
$\text{La}_{0.75}\text{Ca}_{0.25}\text{MnO}_3$	230	4.8	15	32	-	-	-	-	8
$\text{La}_{0.75}\text{Ca}_{0.125}\text{Sr}_{0.125}\text{MnO}_3$	280	1.5	15	10	-	-	-	-	
$\text{La}_{0.75}\text{Ca}_{0.1}\text{Sr}_{0.15}\text{MnO}_3$	330	2.9	15	19.3	-	-	-	-	
$\text{La}_{0.75}\text{Ca}_{0.075}\text{Sr}_{0.175}\text{MnO}_3$	335	2.8	15	18.7	-	-	-	-	
$\text{La}_{0.75}\text{Sr}_{0.25}\text{MnO}_3$	345	1.5	15	10	-	-	-	-	
$\text{La}_{2/3}\text{Ca}_{1/3}\text{MnO}_3$	260	3.7	10	37	-	-	-	-	26
$\text{La}_{2/3}(\text{Ca}_{0.95}\text{Sr}_{0.05})_{1/3}\text{MnO}_3$	275	3.3	10	33	-	-	-	-	
$\text{La}_{2/3}(\text{Ca}_{0.85}\text{Sr}_{0.15})_{1/3}\text{MnO}_3$	287	1.9	10	19	-	-	-	-	
$\text{La}_{2/3}(\text{Ca}_{0.75}\text{Sr}_{0.25})_{1/3}\text{MnO}_3$	300	1.85	10	18.5	-	-	-	-	
$\text{La}_{2/3}(\text{Ca}_{0.5}\text{Sr}_{0.5})_{1/3}\text{MnO}_3$	337	1.7	10	17	-	-	-	-	
$\text{La}_{2/3}(\text{Ca}_{0.25}\text{Sr}_{0.75})_{1/3}\text{MnO}_3$	360	1.65	10	16.5	-	-	-	-	
$\text{La}_{2/3}\text{Sr}_{1/3}\text{MnO}_3$	375	1.6	10	16	-	-	-	-	
$\text{La}_{0.67}\text{Ca}_{0.33}\text{MnO}_3$	275	3.4	20	17	-	-	-	-	23
			0.33	0.5	66	-	-	-	
$\text{La}_{0.67}\text{Sr}_{0.33}\text{MnO}_3$	368	0.27	0.5	54	-	-	-	-	
$\text{La}_{0.67}\text{Ba}_{0.33}\text{MnO}_3$	345	0.12	0.5	24	-	-	-	-	
$\text{La}_{0.54}\text{Ca}_{0.32}\text{MnO}_{3-\delta}$	272	2.9	9	32	-	-	-	-	25
$\text{La}_{0.55}\text{Er}_{0.05}\text{Ca}_{0.4}\text{MnO}_3$	180	2.7	18	15	-	-	-	-	9
(solid state method)					-	-	-	-	
$\text{La}_{0.55}\text{Er}_{0.05}\text{Ca}_{0.4}\text{MnO}_3$ (sol-gel method)	180	2.3	18	12.8	-	-	-	-	

Table 5.2. Continued.

Compound	T_C (K)	I_s (emu/g)	$ \Delta S_M $ (1/kg K)	ΔH (kOe)	$ \Delta S_M / \Delta H \times 10^2 $ (J/kg K kOe)	ΔT (K)	ΔH (kOe)	$\Delta T/\Delta H \times 10^2$ (K/kOe)	Ref.*
$\text{La}_{0.7}\text{Ca}_{0.3}\text{MnO}_3$	256		1.38	10	13.8	—	—	—	27
$\text{La}_{0.65}\text{Nd}_{0.05}\text{Ca}_{0.3}\text{MnO}_3$	247		1.68	10	16.8	—	—	—	
$\text{La}_{0.60}\text{Nd}_{0.10}\text{Ca}_{0.3}\text{MnO}_3$	233		1.95	10	19.5	—	—	—	
$\text{La}_{0.55}\text{Nd}_{0.15}\text{Ca}_{0.3}\text{MnO}_3$	224		2.15	10	21.5	—	—	—	
$\text{La}_{0.50}\text{Nd}_{0.20}\text{Ca}_{0.3}\text{MnO}_3$	213		2.31	10	23.1	—	—	—	
$\text{La}_{2/3}(\text{Ca},\text{Pb})_{1/3}\text{MnO}_3$	296		7.5	70	10.7	5.7	70	8.1	33
			2	10	20	2.5	20	12.5	
$\text{La}_{0.75}\text{Sr}_{0.075}\text{Ca}_{0.175}\text{MnO}_3$	295		—	—	—	0.78	14	5.6	10
$\text{La}_{0.75}\text{Sr}_{0.1}\text{Ca}_{0.15}\text{MnO}_3$	300		—	—	—	0.49	14	3.5	
$\text{La}_{0.87}\text{Sr}_{0.13}\text{MnO}_3$	196.5		2.9	15	19.3	—	—	—	11
			4.2	30	14	—	—	—	
$\text{La}_{0.84}\text{Sr}_{0.16}\text{MnO}_3$	243.5		7.5	80	9.4	—	—	—	
			2.7	15	18	—	—	—	
			4.2	30	14	—	—	—	
			7.9	80	9.9	—	—	—	
$\text{La}_{0.65}\text{Y}_{0.05}\text{Sr}_{0.3}\text{MnO}_3$	~325		4.9	60	8.2	—	—	—	12
$\text{La}_{0.6}\text{Y}_{0.1}\text{Sr}_{0.3}\text{MnO}_3$	~270		4.3	60	7.2	1.8	60	3	
$\text{La}_{0.55}\text{Y}_{0.15}\text{Sr}_{0.3}\text{MnO}_3$	~220		3.4	60	5.7	1.3	60	2.2	
$\text{La}_{0.5}\text{Y}_{0.2}\text{Sr}_{0.3}\text{MnO}_3$	~190		4	60	6.7	1.4	60	2.3	
$\text{La}_{0.5}\text{Gd}_{0.2}\text{Sr}_{0.3}\text{MnO}_3$	270.5		8.8	80	11	—	—	—	30
			1.6	10	16	—	—	—	

$\text{La}_{0.67}\text{Sr}_{0.33}\text{Mn}_{0.9}\text{Cr}_{0.1}\text{O}_3$	328	5	50	10	13
$\text{La}_{0.925}\text{Na}_{0.075}\text{MnO}_3$	193	~1.4	10	14	
$\text{La}_{0.9}\text{Na}_{0.1}\text{MnO}_3$	220	1.3	10	13	
$\text{La}_{0.835}\text{Na}_{0.165}\text{MnO}_3$	343	1.5	10	15	
$\text{La}_{0.8}\text{Na}_{0.2}\text{MnO}_3$	334	2.1	10	21	
$\text{La}_{0.898}\text{Na}_{0.072}\text{Mn}_{0.971}\text{O}_{3.00}$	193	1.9	10	19	
$\text{La}_{0.880}\text{Na}_{0.099}\text{Mn}_{0.977}\text{O}_{3.00}$	220	1.32	10	13.2	
$\text{La}_{0.834}\text{Na}_{0.163}\text{Mn}_{1.000}\text{O}_{2.99}$	343	1.53	10	15.3	
$\text{La}_{0.799}\text{Na}_{0.199}\text{Mn}_{1.000}\text{O}_{2.97}$	334	2.11	10	21.1	
$\text{La}_{0.893}\text{K}_{0.070}\text{Mn}_{0.965}\text{O}_{3.00}$	230	1.96	10	19.6	
$\text{La}_{0.877}\text{K}_{0.096}\text{Mn}_{0.974}\text{O}_{3.00}$	283	1.19	15	7.9	
$\text{La}_{0.813}\text{K}_{0.160}\text{Mn}_{0.987}\text{O}_{3.00}$	338	0.78	10	7.8	
$\text{La}_{0.796}\text{K}_{0.196}\text{Mn}_{0.993}\text{O}_{3.00}$	344	1.47	15	9.8	
$\text{La}_{0.95}\text{Ag}_{0.05}\text{MnO}_3$	214	1.10	10	11	
$\text{La}_{0.80}\text{Ag}_{0.20}\text{MnO}_3$	278	2.11	15	14.1	
$\text{La}_{0.75}\text{Ag}_{0.25}\text{MnO}_3$	306	1.53	10	15.3	
$\text{La}_{0.70}\text{Ag}_{0.30}\text{MnO}_3$	306	~1.3	10	13	
$\text{La}_{0.78}\text{Ag}_{0.22}\text{MnO}_3$ (film)	295	2.22	10	22.2	
$\text{Pr}_{0.7}\text{Sr}_{0.3}\text{MnO}_3$	260(T_C)	1.75	10	17.5	
$\text{Pr}_{0.6}\text{Sr}_{0.4}\text{MnO}_3$	243(T_C)	1.97	10	19.7	
$\text{Pr}_{0.5}\text{Sr}_{0.5}\text{MnO}_3$	205(T_C)	2.63	10	26.3	
	161(T_{CO})	-7.1	10	-71	

Table 5.2. Continued.

Compound	T_C (K)	I_s (emu/g)	$ \Delta S_M $ (J/kg K)	ΔH (kOe)	$ \Delta S_M /\Delta H \times 10^2$ (J/kg K kOe)	ΔT (K)	ΔH (kOe)	$\Delta T/\Delta H \times 10^2$ (K/kOe)	Ref.*
(Pr _{0.7} Nd _{0.3}) _{0.5} Sr _{0.5} MnO ₃	215(T_C) 164(T_{CO})	— -6.8	— 10	— -68	—	—	—	—	19
(Pr _{0.5} Nd _{0.5}) _{0.5} Sr _{0.5} MnO ₃	225(T_C) 168(T_{CO})	— -7.9	— 10	— -79	—	—	—	—	—
(Pr _{0.3} Nd _{0.7}) _{0.5} Sr _{0.5} MnO ₃	243(T_C) 175(T_{CO})	— -6.5	— 10	— -65	—	—	—	—	—
Nd _{0.5} Sr _{0.5} MnO ₃	268(T_C) 183(T_{CO})	— -7.3	— 10	— -73	—	—	—	—	—
Nd _{0.5} Sr _{0.5} MnO ₃	240(T_C) 155(T_{CO})	0.9 -2.8 -0.4	10 10 2.5	9 -28 -16	—	—	—	—	32
Sm _{0.6} Sr _{0.4} MnO ₃	110	—	—	—	4.6	8.4	54.8	20	
Nd _{0.299} Tb _{0.251} Sr _{0.45} MnO ₃	90	—	—	—	1.4	14	10	10	21
Nd _{0.153} Eu _{0.397} Sr _{0.45} MnO ₃	127	—	—	—	1.4	14	10	10	
Sm _{0.55} Sr _{0.45} MnO ₃	131	—	—	—	2.0	14	14.3	14.3	
La _{1.6} Ca _{1.4} Mn ₂ O ₇	171	3.8	15	25.3	—	—	—	—	22
La _{1.4} Ca _{1.6} Mn ₂ O ₇	246	2.75	20	13.75	—	—	—	—	29
La _{1.2} Y _{0.2} Ca _{1.6} Mn ₂ O ₇	211	2.1	20	10.5	—	—	—	—	

$\text{La}_{0.95}\text{Sr}_{0.05}\text{CoO}_3$	235	0.07	15	0.46	—	—	—	34
$\text{La}_{0.85}\text{Sr}_{0.15}\text{CoO}_3$		0.15	15	1	—	—	—	
$\text{La}_{0.8}\text{Sr}_{0.2}\text{CoO}_3$		0.65	15	4.3	—	—	—	
$\text{La}_{0.7}\text{Sr}_{0.3}\text{CoO}_3$		1.2	15	8	—	—	—	
$\text{La}_{0.6}\text{Sr}_{0.4}\text{CoO}_3$		1.45	15	9.7	—	—	—	
$\text{La}_{0.8}\text{Sr}_{0.2}\text{CoO}_3$	240	0.56	13.5	4.1	—	—	—	35
$\text{La}_{0.7}\text{Sr}_{0.3}\text{CoO}_3$	250	0.79	13.5	5.6	—	—	—	
$\text{La}_{0.6}\text{Sr}_{0.4}\text{CoO}_3$	253	0.94	13.5	6.9	—	—	—	
$\text{La}_{0.55}\text{Sr}_{0.45}\text{CoO}_3$	255	29	1.04	13.5	7.7	—	—	
$\text{La}_{0.5}\text{Sr}_{0.5}\text{CoO}_3$	252	18	0.87	13.5	6.4	—	—	

* 1. Morelli *et al* (1996); 2. Zhang *et al* (1997a); 3. Guo *et al* (1997b); 4. Guo *et al* (1997); 5. Sun *et al* (2000b); 6. Boligas *et al* (2000); 8. Guo *et al* (1998); 9. Gu *et al* (1998); 10. Zhang *et al* (2000a); 11. Szewczyk *et al* (2000); 12. Bose *et al* (1998); 13. Sun *et al* (2001); 14. Zhong *et al* (1998a); 15. Zhong *et al* (1998b); 16. Zhong *et al* (1999); 17. Tang *et al* (2000); 18. Chen *et al* (2000); 19. Chen and Du (2001); 20. Abramovich *et al* (2001); 21. Chernyshov *et al* (2001); 22. Zhou *et al* (1999); 23. Xu *et al* (2002); 24. Hueso *et al* (2002); 25. Xu *et al* (2001); 26. Mira *et al* (2001a); 27. Wang *et al* (2002); 28. Wang *et al* (2001b); 29. Hincinschi *et al* (2001); 30. Sun *et al* (2002a); 31. Wang *et al* (2002); 32. Sande *et al* (2001); 33. Sun *et al* (2002b); 34. Sande *et al* (2002); 35. Chaudhary *et al* (1999); 35. Luong *et al* (2002).

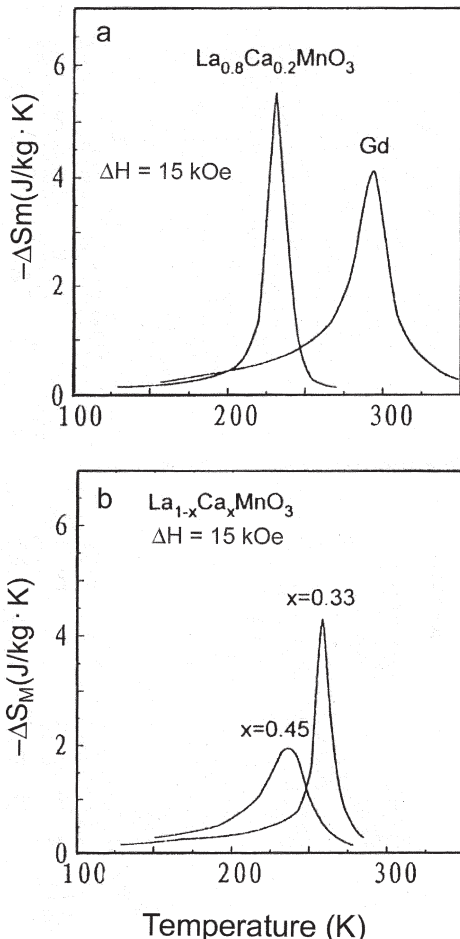


Figure 5.14. Temperature dependences of the magnetic entropy change ΔS_M for $\Delta H = 15$ kOe in $\text{La}_{1-x}\text{Ca}_x\text{MnO}_3$: (a) $x = 0.2$ and Gd; (b) $x = 0.33$ and 0.45 (Guo *et al* 1997a). (Copyright 1997 by the American Physical Society.)

temperature ZFC–FC hysteresis, which is typical for spin freezing in spin glass systems or for such systems as superparamagnets in the blocking state. Such behaviour was also observed in oxygen-depleted $\text{R}_{0.67}\text{Sr}_{0.33}\text{MnO}_\delta$ ($\text{R} = \text{Nd}, \text{Pr}$) (Nagaev 1996), $\text{La}_{0.8}\text{Ca}_{0.2}\text{MnO}_{2.96}$ (Ju and Sohn 1997), $\text{R}_{0.55}\text{Ba}_{0.45}\text{MnO}_{3-\delta}$ ($\text{R} = \text{La}, \text{Nd}, \text{Sm}, \text{Gd}; \delta \leq 0.37$) (Troyanchuk *et al* 2000) and in $(\text{LaBa})\text{MnO}_3$ (Ju *et al* 2000). It was related to the existence in the sample of the phase separation state discussed above with small ferromagnetic regions (droplets) imbedded in a nonferromagnetic (for example, antiferromagnetic) surrounding.

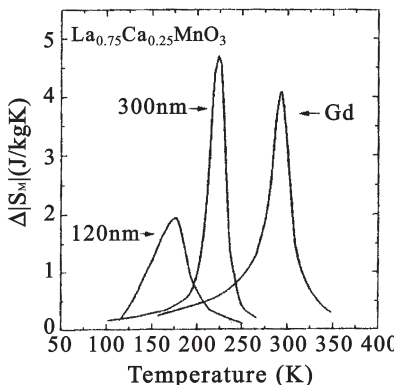


Figure 5.15. Temperature dependences of the magnetic entropy change ΔS_M for $\Delta H = 15$ kOe in $\text{La}_{0.75}\text{Ca}_{0.25}\text{MnO}_3$ samples with different grain sizes (Guo *et al* 1997b).

The influence of grain size on the magnetocaloric properties of the manganites was studied by Guo *et al* (1997b) and Hueso *et al* (2002). Usually the grain size in ceramic manganites lies in the range of several microns. Different T_C values (177 and 224 K, respectively) were found by Guo *et al* (1997b) for ceramic $\text{La}_{0.75}\text{Ca}_{0.25}\text{MnO}_3$ samples with grain sizes of 120 and 300 nm. The lowering of T_C was accompanied by a broadening of the magnetic phase transition in the $M(T)$ curve. This leads to the broadening of the ΔS_M peak and its decrease in the sample with 120 nm grain size—see figure 5.15. Analogous results were obtained by Hueso *et al* (2002) on $\text{La}_{0.67}\text{Ca}_{0.33}\text{MnO}_{3-\delta}$ samples with grain sizes from 60 to 500 nm—Curie temperature, saturation magnetization and the maximum magnetic entropy change increased with the grain size increasing. The latter value increased: for $\Delta H = 10$ kOe $|\Delta S_M|$ reached 5 J/kg K, which corresponded to $|\Delta S_M|/\Delta H = 0.5$ J/kg K kOe. Hueso *et al* (2002) explained the observed dependence of magnetic and magnetocaloric properties on the grain size by the presence of a ‘dead’ magnetically disordered layer on the grains’ surface. With grain size decreasing, the role of this layer in formation of the magnetic properties of the sample increases. On the basis of magnetization measurements and Arrot plot behaviour near the Curie temperature, the authors concluded that with grain size increasing the magnetic phase transition at T_C gets the features of the first-order transition with sharp changing of magnetization. In the sample with the small grains, the magnetic phase transition is of second-order with smooth magnetization variation and, consequently, lower magnetic entropy change values. It should be noted that the magnetoresistance follows the same dependence on the grain size as ΔS_M (Hueso *et al* 2002).

The magnetocaloric properties of $(\text{La}-\text{Ca})\text{MnO}_3$ manganites in which La, Ca and Mn were substituted by various elements were studied by Guo *et al*

(1998), Bohigas *et al* (1998, 1999), Zhang *et al* (2000a), Wang (2001a,b), Mira *et al* (2002) and Sun *et al* (2002b). According to magnetic studies by Mira *et al* (1999), in a manganite system $\text{La}_{2/3}(\text{Ca}_{1-x}\text{Sr}_x)_{1/3}\text{MnO}_3$ there is a change of magnetic phase transition type from first-order in $\text{La}_{2/3}\text{Ca}_{1/3}\text{MnO}_3$ to second-order in $\text{La}_{2/3}\text{Sr}_{1/3}\text{MnO}_3$, which takes place between $x = 0.05$ and 0.15 and is accompanied by transformation of crystal structure type from orthorhombic to rhombohedral, respectively. The nature of the magnetic phase transition type changing was related by Mira *et al* (2002) with modification of magnetic coupling due to the lack of the Jahn–Teller effect in rhombohedral structure, thus explaining the steep decrease (by a factor of two) of the peak absolute values of $|\Delta S_M|$ in the $\text{La}_{2/3}(\text{Ca}_{1-x}\text{Sr}_x)_{1/3}\text{MnO}_3$ system experimentally observed in the range of x between 0.05 and 0.15 . Analogous behaviour was observed earlier by Guo *et al* (1998) in $\text{La}_{0.75}\text{Ca}_{0.25-x}\text{Sr}_x\text{MnO}_3$ compounds, where crystal structure transition from orthorhombic to rhombohedral type takes place at about $x = 0.12$ – 0.15 with increasing of Sr content. Guo *et al* (1998) related lower $|\Delta S_M|$ values in $\text{La}_{0.75}\text{Ca}_{0.25-x}\text{Sr}_x\text{MnO}_3$ compared with Ca-doped La manganites with weaker magnetoelastic coupling in the Sr-doped La manganites. They concluded that, for obtaining large $|\Delta S_M|$ in a fixed crystal structure, La in the manganites should be substituted by ions with smaller ionic radius (the ionic radius of Ca is $\sim 1.06 \text{ \AA}$, and that of Sr is $\sim 1.27 \text{ \AA}$), because smaller internal pressure created by such ions can provide larger magnetoelastic effects (e.g. thermal expansion) and, consequently, sharper changing of magnetization near the Curie temperature. The temperature dependence of electrical resistivity was also measured at $H = 0$ for the sample with $x = 0.125$. It was found that a ferromagnetic metal to paramagnetic insulator transition happened at the Curie temperature ($\sim 280 \text{ K}$), where the magnetic entropy peak is observed.

Gu *et al* (1998) and Wang *et al* (2001a) investigated the magnetic entropy change in $(\text{La–Ca})\text{MnO}_3$ compounds in which La was substituted by RE elements. In the work of Gu *et al* (1998) two $\text{La}_{0.55}\text{Er}_{0.05}\text{Ca}_{0.4}\text{MnO}_3$ samples were prepared by different methods—the solid-state reaction and sol–gel method. Scanning electron microscopy studies showed that in the samples prepared by solid-state reaction the grains were connected loosely and were structurally inhomogeneous. The sol–gel method gave more compact samples with bigger (1 – $5 \mu\text{m}$) grains. The peak values of $|\Delta S_M|$ near the Curie point of 180 K were not essentially different: ~ 2.7 and 2.3 J/kg K for the solid state and sol–gel samples, respectively, for $\Delta H = 18 \text{ kOe}$. The authors also measured electrical resistivity and found ferromagnetic metal–paramagnetic insulator transition at T_C in these compounds. In the $\text{La}_{0.7-x}\text{Nd}_x\text{Ca}_{0.3}\text{MnO}_3$ system the Curie temperature decreased and $|\Delta S_M|$ increased with Nd concentration increasing (Wang *et al* 2001a)—see table 5.2. The authors related this to weakening of ferromagnetic interactions due to distortion of Mn–O bond length and Mn–O–Mn bond angle and interaction between Mn and Nd magnetic subsystems.

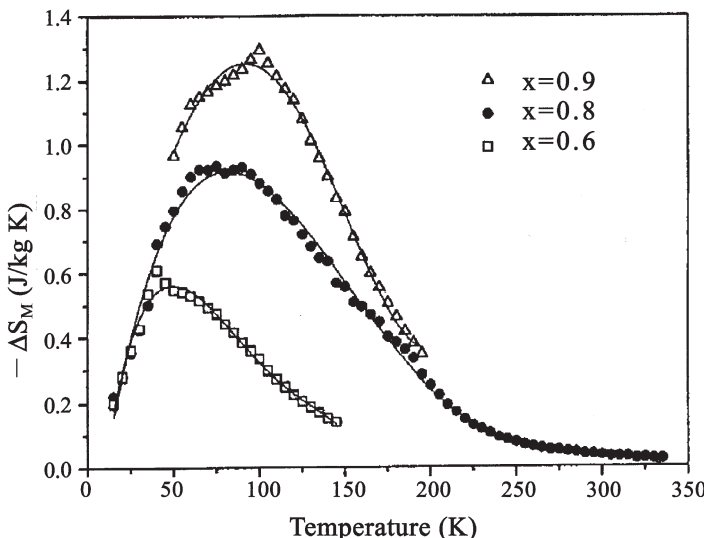


Figure 5.16. Magnetic entropy change temperature dependences of $\text{La}_{0.65}\text{Ca}_{0.35}\text{Ti}_{1-x}\text{Mn}_x\text{O}_3$ for $\Delta H = 30 \text{ kOe}$ (Bohigas *et al* 1998).

Heat capacity and magnetic entropy, and adiabatic temperature change and temperature dependences, were determined in $\text{La}_{2/3}(\text{Ca},\text{Pb})_{1/3}\text{MnO}_3$ single crystal by Sun *et al* (2002b). The magnetic field was applied in the a–b plane. The MCE was calculated on the basis of the zero field heat capacity data and $\Delta S_M(T)$ by equation (2.79). The obtained peak ΔS_M and ΔT values are presented in table 5.2. $\Delta S_M(T)$ and $\Delta T(T)$ curves in this compound are rather wide—their full width at half maximum is about 35 K for $\Delta H = 40 \text{ kOe}$.

Ceramic La manganites with substitution of La by Li and Mn by Ti were investigated by Bohigas *et al* (1998, 1999). They display ferromagnetic ordering below the Curie temperature with different saturation magnetization, which can be changed in a wide range by changing the concentration of the doping element and oxygen stoichiometry. The ΔS_M temperature dependences calculated from magnetization data for $\text{La}_{0.65}\text{Ca}_{0.35}\text{Ti}_{1-x}\text{Mn}_x\text{O}_3$ and $\text{La}_{0.5+x+y}\text{Li}_{0.5-3y}\text{Ti}_{1-3x}\text{Mn}_{3x}\text{O}_3$ are shown in figures 5.16 and 5.17. The peak $|\Delta S_M|$ values for all studied samples are lower than that observed in $(\text{LaCa})\text{MnO}_3$ compounds with the analogous concentration of Ca (see table 5.2), although $\Delta S_M(T)$ curves in the compounds were essentially wider than in $(\text{La}-\text{Ca})\text{MnO}_3$: the full width at half maximum for $\text{La}_{0.958}\text{Li}_{0.026}\text{Ti}_{0.1}\text{Mn}_{0.9}\text{O}_3$ is $\sim 70 \text{ K}$ and for $\text{La}_{0.65}\text{Ca}_{0.35}\text{Ti}_{0.1}\text{Mn}_{0.9}\text{O}_3$ is $\sim 150 \text{ K}$ in comparison with $\sim 30 \text{ K}$ for $\text{La}_{0.6}\text{Ca}_{0.4}\text{MnO}_3$ ($\Delta H = 30 \text{ kOe}$). A wide $\Delta S_M(T)$ curve was also found for $\text{La}_{0.65}\text{Nd}_{0.05}\text{Ca}_{0.3}\text{Mn}_{0.9}\text{Cr}_{0.1}\text{O}_3$ (the full width at half maximum here is $\sim 110 \text{ K}$ for $\Delta H = 10 \text{ kOe}$) by Wang *et al*

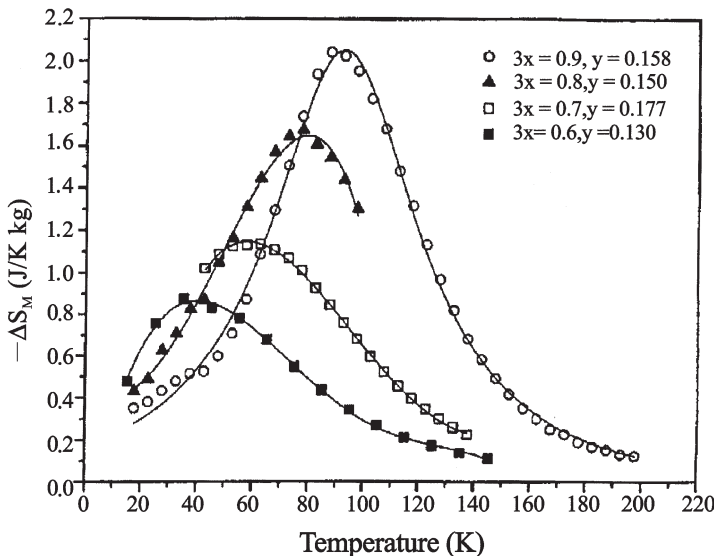


Figure 5.17. Magnetic entropy change temperature dependences of $\text{La}_{0.5+x+y}\text{Li}_{0.5-3y} \cdot \text{Ti}_{1-3x}\text{Mn}_{3x}\text{O}_3$ for $\Delta H = 30$ kOe (Bohigas *et al* 1998).

(2001b), who studied the ceramic $\text{La}_{0.65}\text{Nd}_{0.05}\text{Ca}_{0.3}\text{Mn}_{0.9}\text{B}_{0.1}\text{O}_3$ system with $\text{B} = \text{Mn, Cr, Fe}$. The composition $\text{La}_{0.65}\text{Nd}_{0.05}\text{Ca}_{0.3}\text{MnO}_3$ was characterized by essentially narrower $\Delta S_M(T)$ dependence (the full width at half maximum ~ 50 K for $\Delta H = 10$ kOe). The peak $|\Delta S_M|$ values and T_C in the system decreased with the substitution of Mn by other elements—see table 5.2. The authors related this effect with strengthening of AFM superexchange and weakening of FM double exchange interactions in the material due to decreasing of movable 3d electrons under substitution of Mn by Cr or Fe. The sharpness of the magnetic phase transition in the system decreased with the addition of Cr and Fe and the magnetization change in $\text{La}_{0.65}\text{Nd}_{0.05}\text{Ca}_{0.3}\text{Mn}_{0.9}\text{Fe}_{0.1}\text{O}_3$ was characterized by maximum smoothness in comparison with the other two compositions.

Zhou *et al* (1999) studied magnetic entropy change in ceramic $\text{La}_{1.6}\text{Ca}_{1.4}\text{Mn}_2\text{O}_7$, which the authors called a layered variant of $\text{La}_{0.8}\text{Ca}_{0.2}\text{MnO}_3$. It has layered a $\text{Sr}_3\text{Ti}_2\text{O}_7$ -type perovskite crystal structure and the same ratio of Mn^{3+} and Mn^{4+} ions as $\text{La}_{0.8}\text{Ca}_{0.2}\text{MnO}_3$. The magnetic entropy change of $\text{La}_{1.6}\text{Ca}_{1.4}\text{Mn}_2\text{O}_7$ was calculated from the magnetization and its peak absolute value was found to be 3.8 J/kg K for $\Delta H = 15$ kOe at 166 K ($T_C = 171$ K), which is lower than that in $\text{La}_{0.8}\text{Ca}_{0.2}\text{MnO}_3$ (5.3 J/kg K according to the measurements of Zhou *et al* (1999)), but comparable with the value in Gd. The $\Delta S_M(T)$ curve of $\text{La}_{1.6}\text{Ca}_{1.4}\text{Mn}_2\text{O}_7$ is also broader than that for $\text{La}_{0.8}\text{Ca}_{0.2}\text{MnO}_3$ —its full width at half maximum is about 40 K for $\Delta H = 15$ kOe. Himcinschi *et al* (2001) studied another two

compounds with $\text{Sr}_3\text{Ti}_2\text{O}_7$ -type crystal structure: $\text{La}_{1.4}\text{Ca}_{1.6}\text{Mn}_2\text{O}_7$ and $\text{La}_{1.2}\text{Yb}_{0.2}\text{Ca}_{1.6}\text{Mn}_2\text{O}_7$. Curie temperature and $|\Delta S_M|$ peak values in these compounds decreased with adding of Yb, which was related to structural distortions induced by smaller-than-lanthanum Yb^{3+} ions resulting in weaker Mn–Mn ferromagnetic exchange interactions.

The values of $|\Delta S_M|/\Delta H$ for $\text{La}_{2/3}\text{Sr}_{1/3}\text{MnO}_3$ compound measured by various authors lie in the wide interval from 0.1 to 0.54 J/kg K kOe (see table 5.2), which complicates their comparison with $|\Delta S_M|/\Delta H$ values for $\text{La}_{2/3}\text{Ca}_{1/3}\text{MnO}_3$. However, if the comparison is made inside the group of materials presented in the same work the general tendency is that $|\Delta S_M|/\Delta H$ values are higher in $\text{La}_{2/3}\text{Ca}_{1/3}\text{MnO}_3$ than in $\text{La}_{2/3}\text{Sr}_{1/3}\text{MnO}_3$. This is consistent with the result of Mira *et al* (1999) about the second-order character of the magnetic transition at T_C in $\text{La}_{2/3}\text{Sr}_{1/3}\text{MnO}_3$. However, in the (La–Sr)MnO₃ system, colossal magnetoresistance effect, charge ordering and structural orthorhombic–rhombohedral crystal phase transition take place (Amaitsu *et al* 1995, Gorkov 1998, Coey *et al* 1999, Moreo *et al* 1999) and the values of magnetic entropy change are also rather high.

The magnetic entropy change in the $\text{La}_{1-x}\text{Sr}_x\text{MnO}_3$ system with $x = 0.13$ and 0.16 was determined by Szewczyk *et al* (2000)—see table 5.2. The authors also made theoretical calculations of the entropy change in the framework of mean field approximation and obtained good agreement between experimental and calculated $\Delta S_M(T)$ curves, especially for $\Delta H \leq 50$ kOe.

The MCE behaviour in $\text{La}_{0.7-x}\text{Y}_x\text{Sr}_{0.3}\text{MnO}_3$ ceramics ($x = 0, 0.05, 0.10, 0.15, 0.10$) was investigated by Bose *et al* (1998). In accordance with the authors' idea, if La is substituted by a nonmagnetic trivalent element, this does not change the balance of valances in the manganites and that is why the magnetization of such compositions can remain constant. However, the magnetic transition temperature can change due to the change of interatomic distances if the ionic radius of the doped element is different from that of La, and the corresponding violation of the AFM and FM interactions balance. The experimental $\Delta S_M(T)$ (calculated from magnetization) and $\Delta T(T)$ (measured directly) curves are shown in figure 5.18. As one can see, Y substitution essentially changes T_C and has only a minor influence on the magnetic entropy change. However, it should be noted that according to the results of Zhang *et al* (1996), $|\Delta S_M|$ in Y-substituted $\text{La}_{0.6}\text{Y}_{0.07}\text{Ca}_{0.33}\text{MnO}_\delta$ is essentially lower than in the initial $\text{La}_{0.67}\text{Ca}_{0.33}\text{MnO}_\delta$ —see table 5.2. The $\Delta S_M(H)$ curves in the $\text{La}_{0.7-x}\text{Y}_x\text{Sr}_{0.3}\text{MnO}_3$ system reveal a tendency to saturation in the high-field region. Higher magnetic entropy change was observed by Sun *et al* (2002a) in Gd-doped $\text{La}_{0.5}\text{Gd}_{0.2}\text{Sr}_{0.3}\text{MnO}_3$. The authors reported this with the introduction of an additional carrier of magnetic moments—Gd in the material. The peak absolute ΔS_M value in this material showed near T_C

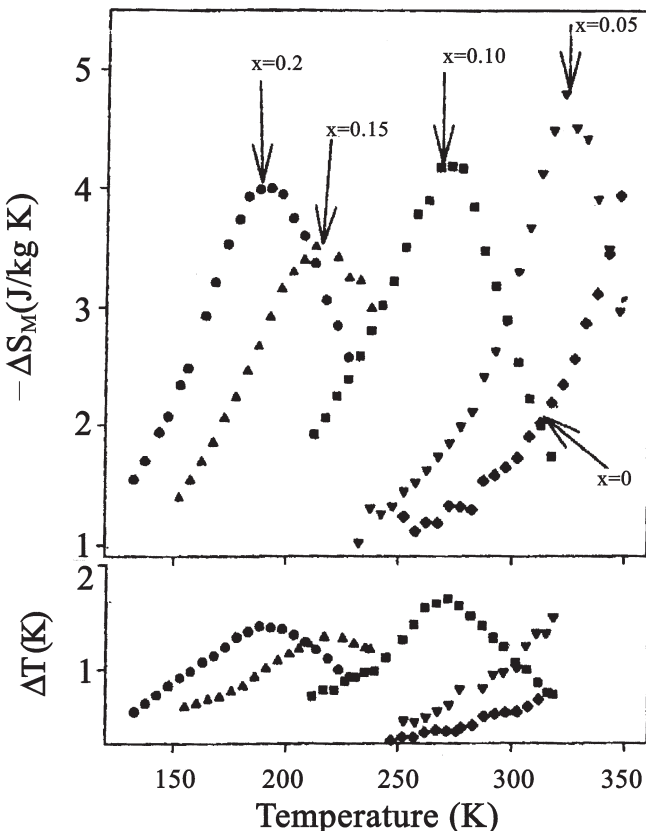


Figure 5.18. The temperature dependences of $|\Delta S_M|$ and ΔT induced by $\Delta H = 60$ kOe in the $\text{La}_{0.7-x}\text{Y}_x\text{Sr}_{0.3}\text{MnO}_3$ system (Bose *et al* 1998).

almost linear dependence on magnetic field up to 80 kOe with no saturation. Besides, the $\Delta S_M(T)$ curve in this compound was rather wide—for $\Delta H = 10$ kOe its full width at half maximum was ~ 30 K.

$\text{La}_{0.67}\text{Sr}_{0.33}\text{Mn}_{0.9}\text{Cr}_{0.1}\text{O}_3$ compound, where Mn was substituted by Cr, was studied by Sun *et al* (2001). The maximum value of $|\Delta S_M| = 5.8$ J/kg K was found for $\Delta H = 60$ kOe near T_C . On high-field $\Delta S_M(T)$ curves a second shoulder maximum on about 10 K higher than the maximum corresponding to the Curie temperature was observed.

Zhong *et al* (1998a,b, 1999) substituted La in the manganites by monovalent alkali metals K and Na. The results obtained for magnetic entropy change in these systems are shown in figure 5.19 and table 5.2. The doping causes Curie temperature increase accompanied by an increase of the $|\Delta S_M|$ peak value. However, the $|\Delta S_M|$ values are lower than that in $(\text{LaCa})\text{MnO}_3$ compounds.

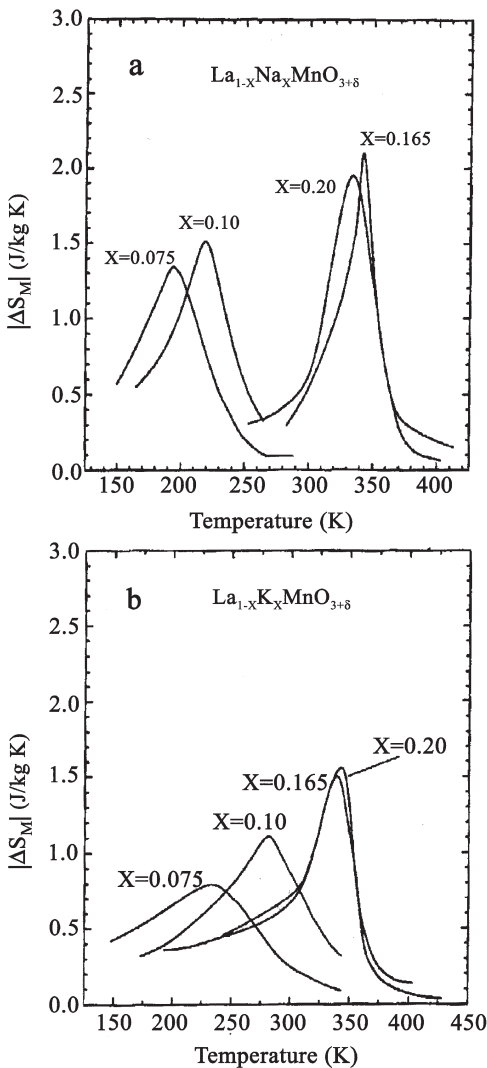


Figure 5.19. The temperature dependence of $|\Delta S_M|$ induced by $\Delta H = 10$ kOe in (a) $\text{La}_{1-x}\text{Na}_x\text{MnO}_3$ and (b) $\text{La}_{1-x}\text{K}_x\text{MnO}_3$ systems (Zhong *et al* 1998b). (Reprinted from Zhong *et al* 1998b, copyright 1988 by Springer Verlag.)

The ceramic system $\text{La}_{1-x}\text{Ag}_x\text{MnO}_3$ ($x = 0.05, 0.20, 0.25, 0.30$) also showed T_C increase with adding of Ag^+ ions, which was reported by Tang *et al* (2000) with enhancement of the double exchange interactions due to increasing of Mn^{4+} ions concentration. The $\Delta S_M(T)$ curves for $\text{La}_{1-x}\text{Ag}_x\text{MnO}_3$ obtained from the magnetization measurements are shown in figure 5.20. The peak value of $|\Delta S_M|$ for $\text{La}_{0.8}\text{Ag}_{0.2}\text{MnO}_3$

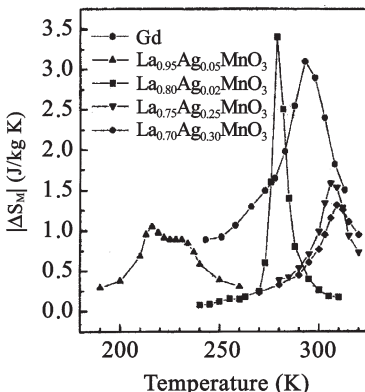


Figure 5.20. The temperature dependence of $|\Delta S_M|$ induced by $\Delta H = 10$ kOe in the $\text{La}_{1-x}\text{Ag}_x\text{MnO}_3$ system (Tang *et al* 2000). (Reprinted from Tang *et al* 2000, copyright 2000, with permission from Elsevier.)

($T_C = 278$ K) is higher than that for Gd and is at the level of ΔS_M values observed in the $(\text{LaCa})\text{MnO}_3$ system. Magnetization measurements showed that the $\text{La}_{1-x}\text{Ag}_x\text{MnO}_3$ compounds investigated are magnetically soft near room temperature with a coercive force value below 10 Oe. A high ΔS_M value was obtained on $\text{La}_{0.78}\text{Ag}_{0.22}\text{MnO}_3$ film with giant magnetoresistance properties (Wang *et al* 2002a).

The magnetic entropy change under charge-ordering transition accompanied by transition from the ferromagnetic to the antiferromagnetic state was investigated in polycrystalline $\text{Pr}_{0.5}\text{Sr}_{0.5}\text{MnO}_3$ and $(\text{Pr}_{1-x}\text{Nd}_x)_{0.5}\text{Sr}_{0.5}\text{MnO}_3$ ($x = 0, 0.3, 0.5, 0.7$ and 1) compounds by Chen *et al* (2000), Chen and Du (2001) and Sande *et al* (2001). The $I(T)$ curves for the compounds $\text{Pr}_{1-x}\text{Sr}_x\text{MnO}_3$ ($x = 0.3, 0.4, 0.5$) measured by Chen *et al* (2000) are shown in figure 5.21. Two of them (for $x = 0.3$ and 0.4) display typical ferromagnetic behaviour. The $\text{Pr}_{0.5}\text{Sr}_{0.5}\text{MnO}_3$ compound first orders ferromagnetically at about 205 K, but then at $T_{CO} = 161$ K turns into a charge-ordered antiferromagnetic state, which is accompanied by an abrupt decrease of magnetization. Near the Curie temperature, all the samples reveal negative ΔS_M peaks. In $\text{Pr}_{0.5}\text{Sr}_{0.5}\text{MnO}_3$ near 161 K, an additional positive peak is observed (see figure 5.22) at which $\Delta S_M = 7.1$ J/kg K for $\Delta H = 10$ kOe. This is about three times higher than the ΔS_M peak value near T_C and corresponds to the high value of $\Delta S_M/\Delta H = 0.71$ J/kg K kOe. This peak can be related to a sharp magnetization change near 161 K caused by field-induced collapse of the antiferromagnetic charge-ordered state. It is necessary to note that the charge ordering transition in $\text{Pr}_{0.5}\text{Sr}_{0.5}\text{MnO}_3$ is accompanied by an abrupt change of lattice parameters in orthorhombic crystal structure (Knizek 1992), which can give an additional change in magnetization.

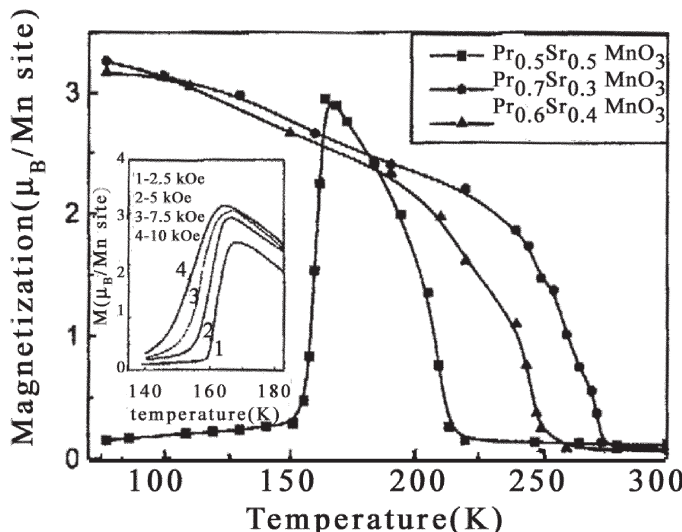


Figure 5.21. The temperature dependence of the magnetization for the $\text{Pr}_{1-x}\text{Sr}_x\text{MnO}_3$ system in the magnetic field of 5 kOe (Chen *et al* 2000).

An analogous large positive ΔS_M was observed at charge-ordering transitions in the ceramic system $(\text{Pr}_{1-x}\text{Nd}_x)_{0.5}\text{Sr}_{0.5}\text{MnO}_3$ ($x = 0, 0.3, 0.5, 0.7, 1$) (Chen and Du 2001). These oxides undergo the transition paramagnetism–ferromagnetism at the Curie temperatures lying in the range of 205 K ($x = 0$) to 268 K ($x = 1$)—see table 5.2. The charge-ordering transition occurs in the lower temperature range at T_{CO} , ranging from 161 K ($x = 0$) to 183 K ($x = 1$). The magnetic entropy changes at the charge-ordering transitions are listed in table 5.2. As one can see its mean value is about 7 J/kg K. Magnetization on field dependences measured by Chen and Du (2001) showed that the magnetic field of metamagnetic transition corresponding to destruction of the antiferromagnetic charge-ordered state in

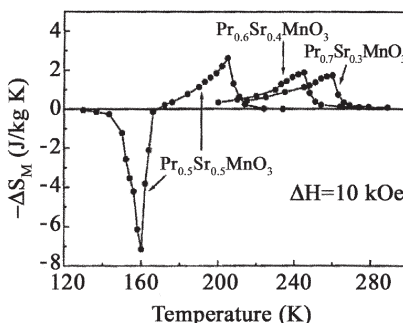


Figure 5.22. Temperature dependences of the magnetic entropy change ΔS_M induced by $\Delta H = 10$ kOe in $\text{Pr}_{1-x}\text{Sr}_x\text{MnO}_3$ (Chen *et al* 2000).

the field is about 2–4 kOe (the maximum value of 4 kOe was in $(\text{Pr}_{0.5}\text{Nd}_{0.5})_{0.5}\text{Sr}_{0.5}\text{MnO}_3$), just below T_{CO} . The $\text{Pr}_{0.5}\text{Sr}_{0.5}\text{MnO}_3$ compound was also studied by Sande *et al* (2001). The values obtained of T_{C} , T_{CO} and magnetic entropy change at the charge-ordering transition were somewhat lower than those of Chen and Du (2001). It was also found out that ΔS_{M} monotonically increased with the field up to 10 kOe near T_{CO} in this compound. It should be noted that $\Delta S_{\text{M}}(T)$ peaks near T_{CO} for the investigated compounds were rather narrow—about 10 K for $\Delta H = 10$ kOe.

In the $\text{Pr}_{0.63}\text{Ca}_{0.37}\text{MnO}_3$ compound at $H = 0$ the charge ordering takes place at $T_{\text{CO}} \approx 235$ K, then the material orders antiferromagnetically at $T_{\text{N}} \approx 170$ K, and finally a transition to the AFM canting state with small ferromagnetic component occurs at about 30 K (Raychaudhuri *et al* 2001). Application of the magnetic field causes the appearance below T_{CO} of a mixed state consisting of charge-ordered insulating and ferromagnetic metallic phases. Heat capacity measurements were made on $\text{Pr}_{0.63}\text{Ca}_{0.73}\text{MnO}_3$ single crystal in a zero magnetic field and 80 kOe by Raychaudhuri *et al* (2001). The heat capacity anomalies were observed near T_{CO} and T_{N} . A sharp heat capacity peak was found at T_{CO} for $H = 0$. It persisted in 80 kOe but shifted to lower temperatures with a rate of -0.1 K/kOe. On the basis of the heat capacity data, the temperature dependence of a total entropy was determined with jumps at T_{CO} of 1.8 J/mol K for $H = 0$ and 1.5 J/mol K for $H = 80$ kOe. This implies that the ferromagnetic state has lower entropy than the charge-ordered one.

Ceramic lanthanum cobaltate $\text{La}_{1-x}\text{Sr}_x\text{CoO}_3$ with perovskite structure and Sr concentration from 0.05 to 0.40 was investigated by Chaudhary *et al* (1999). According to the magnetization measurements, the $\text{La}_{1-x}\text{Sr}_x\text{CoO}_3$ system displays spin-glass-like behaviour for $x < 0.2$ and cluster-glass-like behaviour with short-range ferromagnetic ordering for $x > 0.2$ (Itoh *et al* 1994). The Curie temperature in this system was found to be nearly independent of Sr concentration (within 2.5 K) and equals about 235 K. The samples revealed typical ferromagnetic $\Delta S_{\text{M}}(T)$ curves with a peak near T_{C} . The peak absolute ΔS_{M} values were small for $0.2 < x$ and increase up to 1.45 J/kg K for $\Delta H = 15$ kOe in $\text{La}_{0.6}\text{Sr}_{0.4}\text{CoO}_3$. The system $\text{La}_{1-x}\text{Sr}_x\text{CoO}_3$ with higher Sr concentration ($0.2 < x < 0.5$) was studied by Luong *et al* (2002). X-ray measurements showed that the crystal structure of the compounds for $x = 0.20$ –0.45 is rhombohedral and is cubic for $x = 0.5$. This crystal structure transformation was accompanied by magnetization and magnetic entropy change decrease in $\text{La}_{0.5}\text{Sr}_{0.5}\text{CoO}_3$. The absolute $\Delta S_{\text{M}}/\Delta H$ values obtained by Luong *et al* (2002) was close to those of Chaudhary *et al* (1999), although the Curie temperature was changed from 240 to 255 K.

The adiabatic temperature change in the doped manganites was determined by Bose *et al* (1998), Bohigas *et al* (2000), Zhang *et al* (2000a), Abramovich *et al* (2001), Chernyshov *et al* (2001) and Sun *et al* (2002b).

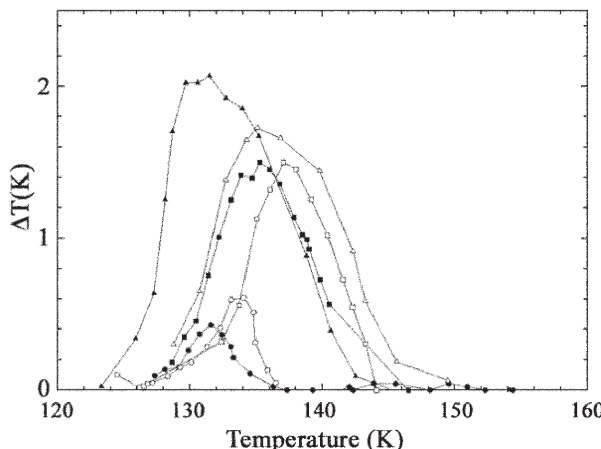


Figure 5.23. Magnetocaloric effect of $\text{Sm}_{0.55}\text{Sr}_{0.45}\text{MnO}_3$ as a function of temperature: $\Delta H = 5\text{ kOe}$ (\circ), 10 kOe (\square) and 14 kOe (\triangle). Data are collected on the heated sample (open symbols) and the cooled sample (closed symbols) (Chernishov *et al* 2001).

Figure 5.23 shows temperature dependences of ΔT for $\text{Sm}_{0.55}\text{Sr}_{0.45}\text{MnO}_3$ measured by Chernishov *et al* (2001) near T_C by a direct method for $\Delta H = 5, 10$ and 14 kOe . One can see some temperature hysteresis of ΔT , characteristic of first-order transitions, for the curves measured under cooling and under heating. Direct MCE measurements were also made by Bose *et al* (1998) and Zhang *et al* (2000a).

One can see from table 5.2 that excluding the value of $\Delta T/\Delta H = 0.548\text{ K/kOe}$ of Abramovich *et al* (2001), which is obviously overestimated because of uncertainties of the MCE determination method (it was obtained indirectly on the basis of thermal expansion and magnetostriction measurements—see section 3), the values of $\Delta T/\Delta H$ in the investigated manganites lie in the interval from 0.023 to 0.143 K/kOe , which is essentially lower than in Gd where $\Delta T/\Delta H = 0.195\text{--}0.29\text{ K/kOe}$ (see table 8.2). At the same time $\Delta S_M/\Delta H$ in the manganites reach substantial values (in units of J/kg K kOe)—at the level of those in Gd. So high magnetic entropy change in the manganites does not provide high adiabatic temperature change. This circumstance was discussed by Pecharsky and Gschneidner (2001b) on the basis of equation (2.79). It was shown that low ΔT in the manganites is related to their high heat capacity (which is about two times higher than in Gd), because in accordance with equation (2.79) ΔT is inversely proportional to the heat capacity.

Heat capacity of the Ca-, Sr- and Ba-doped manganites was studied by Tanaka and Mitsuhashi (1984), Coey *et al* (1995), Ramirez *et al* (1996), Woodfield *et al* (1997), Chivelder *et al* (1998), Bohigas *et al* (2000), Hlopkin *et al* (2000) and Raychaudhuri *et al* (2001). Low temperature heat capacity

measurements (in the temperature range up to 20 K) on $R_{0.7}A_{0.3}MnO_3$ ($R = Y, La; A = Sr, Ba, Ca$), $Nd_{0.7}Ba_{0.3}MnO_3$ and $La_{1-x}Sr_xMnO_{3+\delta}$ were undertaken by Coey *et al* (1995) and Woodfield *et al* (1997). It was shown that the heat capacity of ferromagnetic $R_{0.7}A_{0.3}MnO_3$ ($R = Y, La; A = Sr, Ba, Ca$) obeyed the temperature dependence $C = a_e T + bT^3$. For $Nd_{0.7}Ba_{0.3}MnO_3$ the heat capacity exhibited the Schottky-type anomaly in the low-temperature region. Woodfield *et al* (1997) revealed in $LaMnO_3$ in $C(T)$ dependence in the low-temperature region term proportional to T^2 , which is typical of spin-wave excitations in a layered antiferromagnet. Ferromagnetic sample $La_{0.7}Mn_{0.3}MnO_3$ had the heat capacity term $C \approx T^{3/2}$ typical of ferromagnetic spin waves. However, Hlopkin *et al* (2000) did not find in $LaMnO_3$, $La_{0.8}Sr_{0.2}MnO_3$ and $La_{0.7}Sr_{0.3}MnO_3$ heat capacity terms proportional to $T^{3/2}$ or T^2 . The low-temperature heat capacity of the ferromagnetic insulator $La_{0.9}Ca_{0.1}MnO_3$, ferromagnetic metal $La_{0.67}Ca_{0.33}MnO_3$ and antiferromagnetic insulator $La_{0.38}Ca_{0.62}MnO_3$ was studied by Chivelder *et al* (1998). In the first sample there was no electronic heat capacity term and the experimental data were best fitted by the expression $C = aT^3 + bT^5 + cT^{3/2}$. For $La_{0.67}Ca_{0.33}MnO_3$ the experimental data could be approximated by electronic and lattice heat capacity terms. The $La_{0.38}Ca_{0.62}MnO_3$ low-temperature specific heat data were fitted by T^3 and T^2 terms.

Tanaka and Mitsuhashi (1984) found in $C(T)$ dependence of $La_{0.8}Ca_{0.2}MnO_3$ an anomaly, related to the Curie temperature, at 206 K. Chivelder *et al* (1998) measured $C(T)$ dependences for $La_{0.9}Ca_{0.1}MnO_3$, $La_{0.67}Ca_{0.33}MnO_3$ and $La_{0.38}Ca_{0.62}MnO_3$ in the temperature range from 50 to 300 K in a zero magnetic field. The $C(T)$ curve of $La_{0.9}Ca_{0.1}MnO_3$ did not show a well-defined heat capacity anomaly near the Curie temperature (180 K) and had a peak value of ~ 73.5 J/mol K (~ 317 J/kg K). Such behaviour was also observed for the sample with this composition by Ramirez *et al* (1996). The authors related it to a wide magnetic ordering transition in this composition. In $La_{0.67}Ca_{0.33}MnO_3$ a sharp anomaly was found on the $C(T)$ curve near the Curie temperature at 263 K (the peak value of ~ 195 J/mol K (~ 930 J/kg K)). A well defined but rather wide peak on the $C(T)$ curve was also observed in $La_{0.38}Ca_{0.62}MnO_3$ at 270 K (the peak value of ~ 142 J/mol K (~ 785 J/kg K)). The zero field $C(T)$ dependences for temperatures up to 400 K were measured for ceramic $LaMnO_3$, $La_{0.8}Sr_{0.2}MnO_3$ and $La_{0.7}Sr_{0.3}MnO_3$ by Hlopkin *et al* (2000). The heat capacity anomalies (peaks) in these samples were observed at the magnetic phase transitions from paramagnetic to magnetically ordered states (AFM for $LaMnO_3$ and FM for $La_{0.8}Sr_{0.2}MnO_3$ and $La_{0.7}Sr_{0.3}MnO_3$). The peak heat capacity values for $La_{0.8}Sr_{0.2}MnO_3$ (at 296 K) and $La_{0.7}Sr_{0.3}MnO_3$ (at 345 K) were ~ 605 J/kg K and 660 J/kg K, respectively. Bohigas *et al* (2000) measured heat capacity temperature dependence on $La_{0.6}Ca_{0.4}MnO_3$ in the temperature range up to 300 K and in the fields up to 30 kOe. The $C(T)$ curve displayed an anomaly typical for second-order transitions in a zero

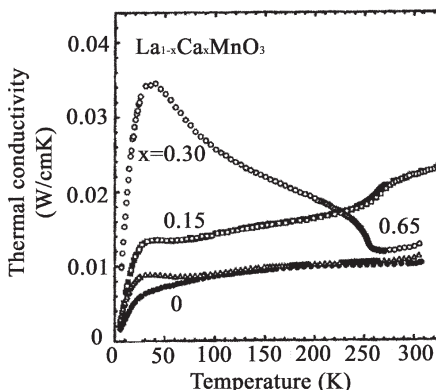


Figure 5.24. Temperature dependences of the thermal conductivity of $\text{La}_{1-x}\text{Ca}_x\text{MnO}_3$ polycrystals (Cohn *et al* 1997). (Copyright 1997 by the American Physical Society.)

field at 260 K (the anomaly peak value was $\sim 640 \text{ J/kg K}$). In magnetic field the anomaly became smoother and for $H = 30 \text{ kOe}$ the peak heat capacity value near T_C was $\sim 570 \text{ J/kg K}$. In connection with the analysis of Pecharsky and Gschneidner (2001b) it should be mentioned that, in Gd, zero field peak heat capacity near T_C is $\sim 382 \text{ J/kg K}$ and drops to 268 J/kg K in a magnetic field of 50 kOe (see figure 8.1).

The thermal conductivity of polycrystalline $\text{La}_{1-x}\text{Ca}_x\text{MnO}_3$ compounds ($x = 0, 0.1, 0.15, 0.3, 0.65$) was studied by Cohn *et al* (1997) and Visser *et al* (1997). The values of thermal conductivity of these materials were rather low. At 300 K the thermal conductivity of LaMnO_3 is $\sim 0.01 \text{ W/cm K}$ and monotonically decreases with cooling. Figure 5.24 shows temperature dependences of the thermal conductivity of $\text{La}_{1-x}\text{Ca}_x\text{MnO}_3$ polycrystals measured by Cohn *et al* (1997). Addition of Ca caused an increase of the thermal conductivity values. As one can see above T_C (255 K) in $\text{La}_{0.7}\text{Ca}_{0.3}\text{MnO}_3$, the thermal conductivity decreases with cooling, and below T_C it increases, reaching a maximum of 0.035 W/cm K at about 30 K. Analogous behaviour of the thermal conductivity for $\text{La}_{0.7}\text{Ca}_{0.3}\text{MnO}_3$ was found by Visser *et al* (1997). Charge-ordering transition was observed at $T_{\text{CO}} = 275 \text{ K}$ in $\text{La}_{0.35}\text{Ca}_{0.65}\text{MnO}_3$. In this sample the thermal conductivity decrease was observed in the whole temperature range with an anomaly corresponding to T_{CO} and a rapid decrease below $\sim 30 \text{ K}$ (Cohn *et al* 1997). However, no anomalies at $T_C = 170 \text{ K}$ were observed on the thermal conductivity temperature dependence of $\text{La}_{0.9}\text{Ca}_{0.1}\text{MnO}_3$, which almost linearly decreased with cooling from the value of $\sim 1.2 \text{ W/cm K}$ at 350 K (Visser *et al* 1997). Visser *et al* (1997) also measured the temperature dependences of thermal conductivity on $\text{La}_{0.6}\text{Pb}_{0.4}\text{MnO}_3$ and $\text{La}_{0.2}\text{Nd}_{0.4}\text{Pb}_{0.4}\text{MnO}_3$ single crystals. They displayed behaviour analogous with that of $\text{La}_{0.7}\text{Ca}_{0.3}\text{MnO}_3$. At 350 K the thermal

conductivity of $\text{La}_{0.6}\text{Pb}_{0.4}\text{MnO}_3$ and $\text{La}_{0.2}\text{Nd}_{0.4}\text{Pb}_{0.4}\text{MnO}_3$ was 0.025 W/cm K and 0.01 W/cm K , respectively. With cooling the thermal conductivity first decreased and then below T_C (350 K for $\text{La}_{0.6}\text{Pb}_{0.4}\text{MnO}_3$ and 270 K for $\text{La}_{0.2}\text{Nd}_{0.4}\text{Pb}_{0.4}\text{MnO}_3$) it increased, reaching the maximum values of $\sim 0.05 \text{ W/cm K}$ for $\text{La}_{0.6}\text{Pb}_{0.4}\text{MnO}_3$ at $\sim 40 \text{ K}$ and $\sim 0.01 \text{ W/cm K}$ for $\text{La}_{0.2}\text{Nd}_{0.4}\text{Pb}_{0.4}\text{MnO}_3$ at $\sim 170 \text{ K}$. Similar thermal conductivity temperature dependences were observed in $\text{La}_{0.83}\text{Sr}_{0.17}\text{MnO}_3$ and $\text{Pr}_{0.5}\text{Sr}_{0.5}\text{MnO}_3$ polycrystals by Cohn *et al* (1997). The maximum thermal conductivity below T_C (275 K for $\text{La}_{0.83}\text{Sr}_{0.17}\text{MnO}_3$ and 265 K for $\text{Pr}_{0.5}\text{Sr}_{0.5}\text{MnO}_3$) in $\text{La}_{0.83}\text{Sr}_{0.17}\text{MnO}_3$ was found to be $\sim 0.04 \text{ W/cm K}$ (at $\sim 120 \text{ K}$) and in $\text{Pr}_{0.5}\text{Sr}_{0.5}\text{MnO}_3$ was $\sim 0.028 \text{ W/cm K}$ (at $\sim 160 \text{ K}$). At 300 K both compounds displayed the thermal conductivity of $\sim 0.022 \text{ W/cm K}$. The influence of a magnetic field on the thermal conductivity was studied for $\text{La}_{0.2}\text{Nd}_{0.4}\text{Pb}_{0.4}\text{MnO}_3$, $\text{La}_{0.83}\text{Sr}_{0.17}\text{MnO}_3$ and $\text{Pr}_{0.5}\text{Sr}_{0.5}\text{MnO}_3$ (Cohn *et al* 1997, Visser *et al* 1997). It was found that application of a magnetic field caused an increase in thermal conductivity. Near T_C in $\text{La}_{0.2}\text{Nd}_{0.4}\text{Pb}_{0.4}\text{MnO}_3$ thermal conductivity increased from a zero-field value of $\sim 0.0075 \text{ W/cm K}$ to $\sim 0.01 \text{ W/cm K}$. Some numerical values of LaMnO_3 and $\text{La}_{0.7}\text{Ca}_{0.3}\text{MnO}_3$ thermal conductivity are presented in table A2.1 in appendix 2.

5.3 3d oxide compounds

The MCE in manganese spinel ferrites–chromites $\text{MnFe}_{2-x}\text{Cr}_x\text{O}_4$ ($0 \leq x \leq 1.6$) was measured by Belov *et al* (1974)—see figure 5.25. The samples with $x = 0$ and 0.125 display a typical ferromagnetic behaviour in the whole investigated temperature range, with a maximum of ΔT near the Curie point. The maximum MCE value in MnFe_2O_4 is $\Delta T \approx 0.48 \text{ K}$ for $\Delta H = 16 \text{ kOe}$ near $T_C \approx 570 \text{ K}$. For the samples with $x > 0.125$ the MCE changed its sign in the low-temperature region. This change corresponds to the specific compensation point, arising due to noncollinear Fe^{3+} and Cr^{3+} ions' spin alignment in the octahedral B-sublattice characterized by local slant angles. Due to the temperature dependence of the local slant angles the total magnetic moment of the B-sublattice can become equal to the total magnetic moment of the tetrahedral A-sublattice. Such a compensation point is difficult to disclose from magnetization measurements, but it is clearly seen on the $\Delta T(T)$ curves. For example, this compensation point is observed in the sample with $x = 1.085$, where the total magnetic moment of the A-sublattice is higher than that of B-sublattice in the low-temperature region, and is directed along the magnetic field causing a ferromagnetic paraprocess in A-sublattice. Above $\sim 150 \text{ K}$ the B-sublattice becomes stronger and is aligned along the field direction. Such change of the sublattice magnetization directions is accompanied by the MCE sign change—see figure 5.25—and is confirmed by the magnetization measurements. The

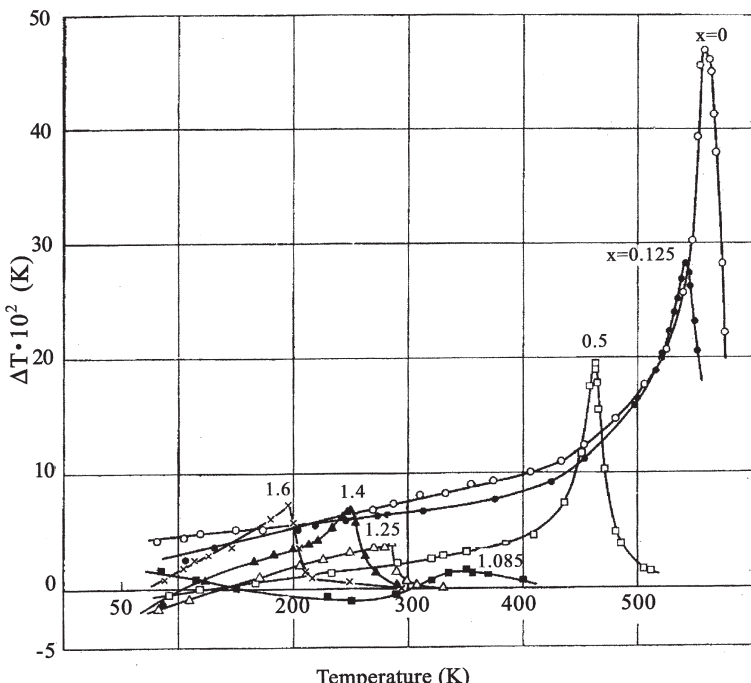


Figure 5.25. Temperature dependence of the MCE in $\text{MnFe}_{2-x}\text{Cr}_x\text{O}_4$ induced by $\Delta H = 16 \text{ kOe}$ (Belov *et al* 1974).

negative sign of the MCE in the temperature interval from 150 to 300 K is explained by the more intensive antiferromagnetic paraprocess in the A-sublattice than the ferromagnetic paraprocess in the B-sublattice in this temperature range. At about 305 K the antiferromagnetic and ferromagnetic contributions to the MCE become equal to each other, but above 305 K and near the Curie temperature the ferromagnetic contribution prevails. The fuzziness of the MCE maximum near T_C in the sample with $x = 1.085$ is related to the weakness of the intersublattice exchange interaction caused by substitution of Fe^{3+} ions in the B-sublattice by Cr^{3+} ions.

Nikolaev *et al* (1966) found a change of sign of the MCE in the nickel-chromite NiFeCrO_4 at the magnetic compensation point ($T_{\text{comp}} = 333 \text{ K}$). The observed effect can be explained on the basis of antiferromagnetic and ferromagnetic paraprocess conception (see section 2.6).

The MCE in the spinel $\text{Li}_2\text{Fe}_5\text{Cr}_5\text{O}_{16}$ was measured by Belov *et al* (1968). A sign change of the MCE was also observed at the compensation point in this compound—see figure 5.26. In the low-temperature region the MCE was not high and decreased with temperature decreasing, which was different from the low-temperature MCE in $\text{Gd}_3\text{Fe}_5\text{O}_{12}$ —see figures 5.1 and 5.2. Such behaviour

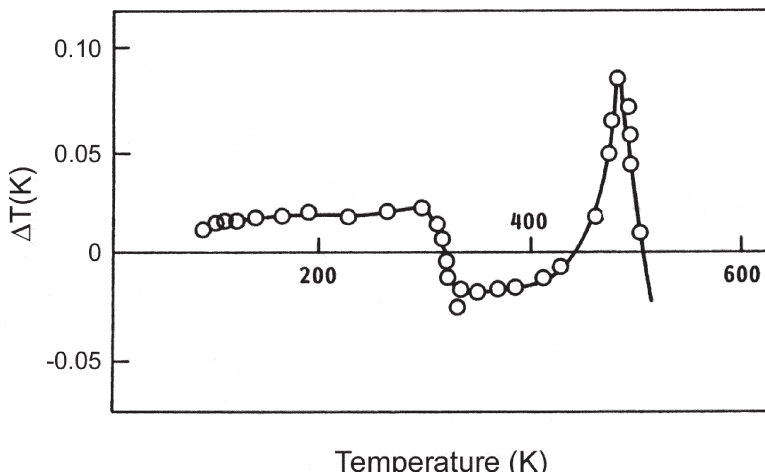


Figure 5.26. The temperature dependence of the MCE induced by $\Delta H = 16$ kOe in the spinel $\text{Li}_2\text{Fe}_5\text{Cr}_5\text{O}_{16}$ (Belov *et al* 1968).

was related to the low intensity of the paraprocess in the A- and B-sublattices due to the strong intersublattice exchange interactions.

Sucksmith *et al* (1953) used experimental magnetocaloric data to obtain the $I_s(T)$ curve of the mixed magnesium–zinc ferrite $\text{MgOZnO}\cdot 2\text{Fe}_2\text{O}_3$ from ΔT on I^2 dependences.

Belov *et al* (1977), Zhilyakov *et al* (1993, 1994) and Naiden and Zhilyakov (1997), investigated the MCE in hexagonal ferrites. The MCE in polycrystalline $\text{BaFe}_{12-x}\text{Co}_x\text{Ti}_x\text{O}_{19}$ (CoTi-M structure $x = 0\text{--}3$) and $\text{BaCa}_{2-x}\text{Zn}_x\text{Fe}_{16}\text{O}_{27}$ (CoZn-W structure $x = 0\text{--}3$) was measured below the Curie temperature in the temperature range from 150 to 500 K (Zhilyakov *et al* 1993, 1994). In these ferrimagnets, warming causes a set of spin-reorientation transitions—from easy cone to easy plane (at T_1), from easy plane to easy cone (T_2) and from easy cone to easy axis (T_3). Which magnetic state (easy plane, easy cone or easy axis) will be realized in the hexagonal ferrite sample is determined by the ratio of the magnetic anisotropy constant of different orders. Temperatures T_1 , T_2 and T_3 depend on x and for $\text{BaCo}_{0.62}\text{Zn}_{1.38}\text{Fe}_{16}\text{O}_{27}$ are 115, 220 and 260 K, and for $\text{BaCo}_{0.7}\text{Zn}_{1.3}\text{Fe}_{16}\text{O}_{27}$ are 120, 250 and 300 K, respectively.

Differential thermal analysis of the CoZn-W ferrite at $H = 0$ showed that there was a peak of about 0.1 K near 310 K, where the spin-reorientation transition from easy plane to easy cone takes place. In the presence of a magnetic field in CoTi-M ($x = 1.2$) and CoZn-W ($x = 1.0$) ferrites, the maxima at the spin-reorientation transitions and sign changes of the MCE from negative to positive at ~ 300 K and from positive to negative at ~ 420 K with warming were observed. The maximum absolute value of the

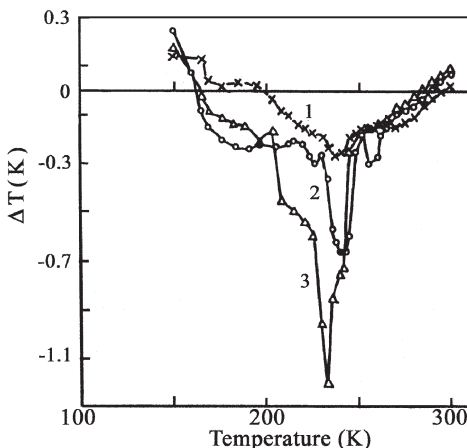


Figure 5.27. Temperature dependence of the MCE in the textured CoZn–W hexaferrite with $x = 1.3$ for various ΔH : (1) 2 kOe; (2) 8 kOe; (3) 12 kOe (Zhilyakov *et al* 1994).

negative MCE was about 0.2 K at $T \approx 150$ K in CoZn–W ferrite and the value of the positive MCE was about 0.1 K at $T \approx 340$ K in CoTi–M ($x = 1.2$) for $\Delta H = 7$ kOe. The MCE temperature behaviour was reported by the authors with competition between the anisotropy constants determining the magnetocrystalline anisotropy along the hexagonal axis. Results of Zhilyakov *et al* (1993, 1994) show that the absolute values of the MCE in the polycrystalline hexagonal ferrites are small in the temperature range from 150 to 450 K.

Much higher MCE values were induced in the basal plane textured samples of CoZn–W hexaferrites ($0 \leq x \leq 2.0$) by the magnetic field directed along the hard magnetization axis (Zhilyakov *et al* 1994). For the samples with $x = 1.1$ – 1.5 the first-order spin-reorientation transitions are observed in the presence of a magnetic field in the temperature interval between T_1 and T_3 . Figure 5.27 shows the MCE near such a transition at $T_2 = 250$ K in the textured CoZn–W hexaferrite for the field aligned perpendicular to the texture plane. When $\Delta H = 2$ kOe, which is lower than the critical field of the transition (about 9 kOe), the absolute MCE value has a weak peak near ~ 250 K. For $\Delta H = 12$ kOe this MCE peak is much higher and pronounced and is shifted towards the low-temperature region. The peak absolute value of the MCE for $\Delta H = 12$ kOe is comparable with the MCE value in rare earth materials (see section 8). The estimations made by the authors showed that the main contribution to the MCE at $T = T_2$ is related to the field-induced spin-reorientation transitions.

Naiden and Zhiliakov (1997) calculated the MCE in a CoZn–W ($x = 1.38$) hexaferrite single crystal for a magnetic field directed along the hexagonal axis and in the basal plane. The calculations were made on the

basis of the formula

$$dT = \left[\frac{TDB}{C_H HIA} - \left(\frac{T}{C_H} \right) \left(\frac{\partial I}{\partial T} \right) \cos(\Theta - \psi) \right] dH \quad (5.1)$$

where A , B and D are the values related to magnetocrystalline anisotropy constants K_1 , K_2 and K_3 , Θ is the angle between magnetization and the c-axis, ψ is the angle between the magnetic field direction and the c-axis. The first term in square brackets in equation (5.1) corresponds to the anisotropic part of the MCE and the second term is related to the MCE of the para-process. Experimental data on temperature dependences of magnetization, anisotropy constants and heat capacity, as well as previously determined equilibrium values of Θ , were used in the calculations. Peaks of negative (approximately -0.65 K) and positive (~ 1.5 K) MCE were presented on the calculated $\Delta T(T)$ dependences for the field applied along the c-axis and in the basal plane ($\Delta H = 8$ kOe) at 210 and 230 K, respectively (T_2 for this compound is 220 K). According to the Naiden-Zhiliakov data, these temperatures correspond to the most intensive transformation of the magnetic phase diagram of the investigated compound by a magnetic field.

The hexagonal ferrite with Co_xW structure and composition $\text{BaCo}_{1.65}\text{Fe}_{0.35}^{2+}\text{Fe}_{16}^{3+}\text{O}_{27}$ was investigated by Belov *et al* (1977) in the temperature range from 200 to 800 K. This compound is characterized by the dependence of the orientation of the magnetic moments on temperature. At room-temperature, spins lie in the basal plane and the c-axis is the hard magnetization axis. With temperature increasing, spins turn from the basal plane towards the c-axis, forming a cone of easy magnetization axes. In the high-temperature region the c-axis becomes the easy magnetization axis. There are two maxima on the $\Delta T(T)$ curve measured in the basal plane for $\Delta H = 10$ kOe: the first at about 400 K ($\Delta T \approx 0.05$ K) and the second at ~ 0.16 K near the Curie temperature (750 K). The first anomaly corresponds to the second-order transition—spin reorientation from the basal plane to the c-axis. On the $\Delta T(T)$ curve measured along the c-axis there is an MCE sign change near this temperature.

Belov *et al* (1977) considered the MCE in $\text{BaCo}_{1.65}\text{Fe}_{0.35}^{2+}\text{Fe}_{16}^{3+}\text{O}_{27}$ related to the rotation of the spontaneous magnetization vector \vec{I}_s by the magnetic field H in strong magnetic fields. This contribution to the total MCE (ΔT_r) can be calculated by integration of equation (2.135) from Θ_0 (the angle between the c-axis and \vec{I}_s) to Θ_H (the angle between the c-axis and the magnetic field) and has the form

$$\begin{aligned} \Delta T_r = & \frac{T}{C_H} \left[\frac{\partial K_1}{\partial T} (\sin^2 \Theta_H - \sin^2 \Theta_0) + \frac{\partial K_2}{\partial T} (\sin^4 \Theta_H - \sin^4 \Theta_0) \right. \\ & \left. + \frac{\partial K_3}{\partial T} (\sin^6 \Theta_H - \sin^6 \Theta_0) \right]. \end{aligned} \quad (5.2)$$

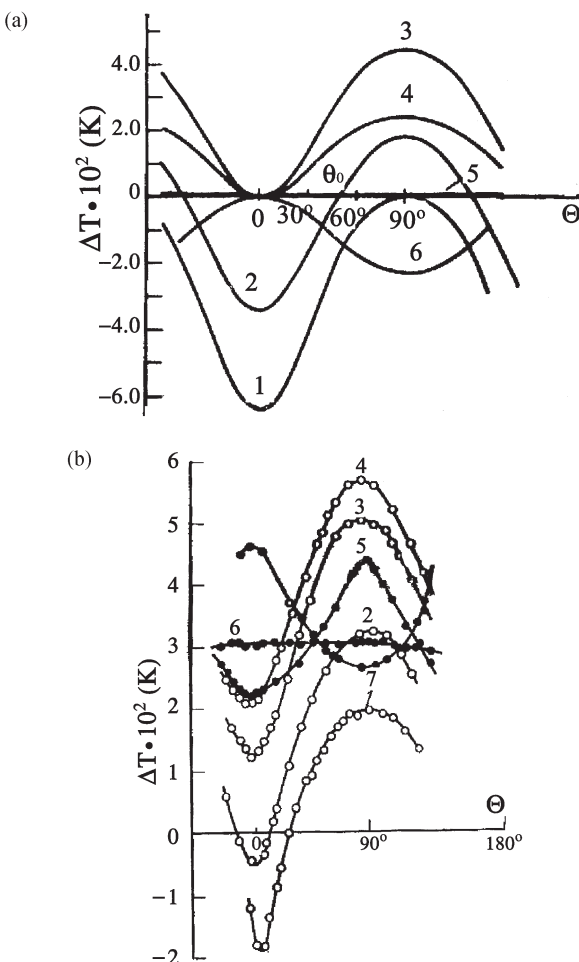


Figure 5.28. Calculated dependences of ΔT_r (a) and experimental dependence of the MCE (b) in $\text{BaCo}_{1.65}\text{Fe}^{2+}_{0.35}\text{Fe}^{3+}_{16}\text{O}_{27}$ on the angle between the c-axis and magnetic field at different temperatures: (a) curve 1 (296.7 K), 2 (329.5 K), 3 (398 K), 4 (438 K), 5 (545 K), 6 (637 K); (b) curve 1 (291.8 K), 2 (343.2 K), 3 (368 K), 4 (387 K), 5 (452 K), 6 (545 K), 7 (641.5 K) (Belov *et al* 1977).

In the compound studied, the constant K_3 turns to zero above 200 K and K_2 above 430 K, which simplifies calculations by equation (5.2). The results of calculations made on the basis of the experimental $K_1(T)$, $K_2(T)$ and $\Theta_0(T)$ dependences in the temperature range above 290 K are shown in figure 5.28(a). There is an oscillation of the ΔT with Θ_H changing. Curve 1 corresponds to 296.7 K, where the magnetic moments lie in the basal plane ($\Theta_0 = 0$). ΔT for this temperature is negative for all Θ_H and has

maximum absolute value when the field is directed along hard magnetization c-axis ($\Theta_H = 0$) and minimum absolute value when the field is directed in the basal plane ($\Theta_H = 90^\circ$). Curve 3 (398 K) corresponds to the case when the spins are aligned along the c-axis (now the easy magnetization axis) and ΔT here is positive for all Θ_H . At 545 K (curve 5) the constant K_2 becomes zero and $\partial K_1 / \partial T \approx 0$, which implies independence of ΔT on Θ_H . The results of the experimental measurements are shown in figure 5.28(b). As one can see they conform in general to the calculated $\Delta T(\Theta_H)$ curves. The observed shift of the curves upwards is related to the presence of the contribution from the magnetocaloric effect caused by the paraprocess (this contribution increases with temperature).

Druzhinin *et al* (1979) calculated the dependences $\Delta T(T)$ for various values of the angle formed by the field and the threefold axis in corundum (Al_2O_3) with 0.13% of V^{3+} . The calculations were made allowing for uniaxial magnetic anisotropy and uniaxial g -tensor anisotropy on the basis of a spin Hamiltonian with the parameters known from the experiment. The sign and the value of the MCE were shown to depend on the angle between the field and the threefold axis. The single crystal $\text{Al}_2\text{O}_3\text{-V}^{3+}$ revolved rapidly in the magnetic field of 93.4 kOe display oscillations of the MCE in the temperature range from 0 to 8 K—see figure 5.29.

Litvinenko *et al* (1973) and Borovikov *et al* (1981) explored the MCE in an antiferromagnetic ($T_N = 32$ K) single crystal siderite FeCO_3 in a pulsed

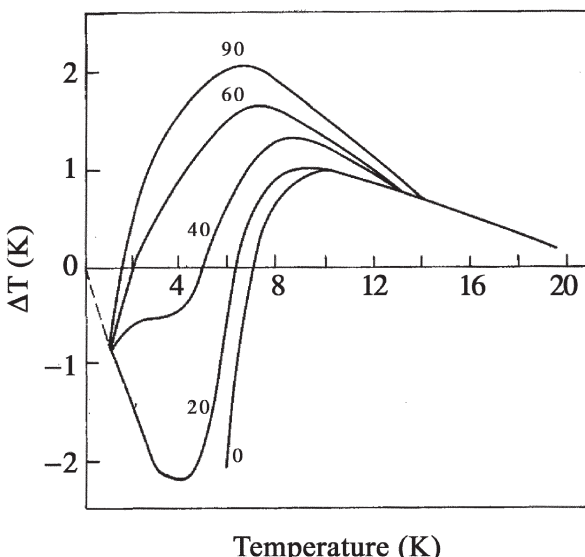


Figure 5.29. The MCE temperature dependences in $\text{Al}_2\text{O}_3\text{-V}^{3+}$ for $H = 93.4$ kOe and different values of the angle between the magnetic field and the threefold crystal axis (Druzhinin *et al* 1979).

magnetic field of 300 kOe. The sample displayed essential field hysteresis at the metamagnetic transition from the antiferromagnetic to ferromagnetic state. The value of the MCE at 4.2 K in a field of 300 kOe was 24 K. Some features of phase transitions in antiferromagnets under adiabatic conditions were studied theoretically by Borovikov *et al* (1981), and it was shown that adiabaticity could be violated in some cases. This effect can lead to non-stationary phenomena.

5.4 RXO₄ compounds

Rare earth compounds RXO₄ (where X = V, As, P, and R is the rare earth ion) have tetragonal zircon-type crystal structure. Some of them display a low-temperature crystallographic transition caused by the cooperative Jahn-Teller effect, which gives an additional contribution to the entropy change. A magnetic field can also influence this transition.

DyVO₄ exhibits a crystallographic transition at 14.3 K and an antiferromagnetic one at 3 K. Figure 5.30 shows temperature dependences of the total entropy in DyVO₄ in various magnetic fields determined from the heat capacity data of Daudin *et al* (1982a). The shoulders near 3 and 15 K in the entropy curve corresponding to $H = 0$ are related to antiferromagnetic and structural phase transitions, respectively.

Kimura *et al* (1998) studied magnetization of single crystals of Dy_{1-x}Gd_xVO₄ ($x = 0, 0.25, 0.5$ and 1) in the temperature range from 3 to

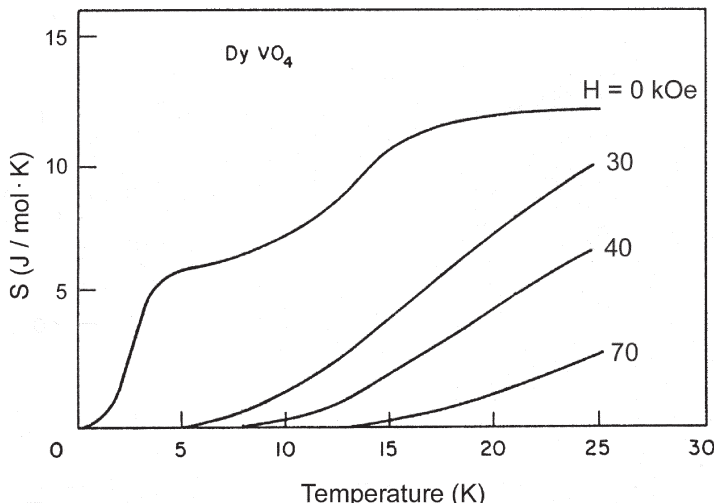


Figure 5.30. Temperature dependences of the total entropy in DyVO₄ for various values of the external magnetic field (Daudin *et al* 1982a). (Reprinted from Daudin *et al* 1982a, copyright 1982, with permission from Elsevier.)

20 K. X-ray measurements confirmed that all crystals had zircon-type tetragonal structure. It was found that the easy magnetization axis is the a-axis, and the crystals are paramagnetic in the investigated temperature range. On the $I(T)$ curve measured in 50 kOe along the c-axis for DyVO_4 the peak corresponding to the Jahn–Teller crystallographic transition was observed at 14 K. For other investigated crystals this peak was not found. The inverse d.c. magnetic susceptibility of the samples with $x = 0.5$ and 1 obeyed the Curie–Weiss law and that of DyVO_4 and $\text{Dy}_{0.75}\text{Gd}_{0.25}\text{VO}_4$ had deviations due to the Jahn–Teller effect. In particular, the positive paramagnetic Curie temperatures were found for the latter samples (for others they were negative). The anisotropy of the crystals was weakened by adding Gd. Figure 5.31 shows magnetic entropy change temperature dependences for the investigated crystals calculated from the magnetization measurements. One can see the anomalies related to the Jahn–Teller effect at 14 K.

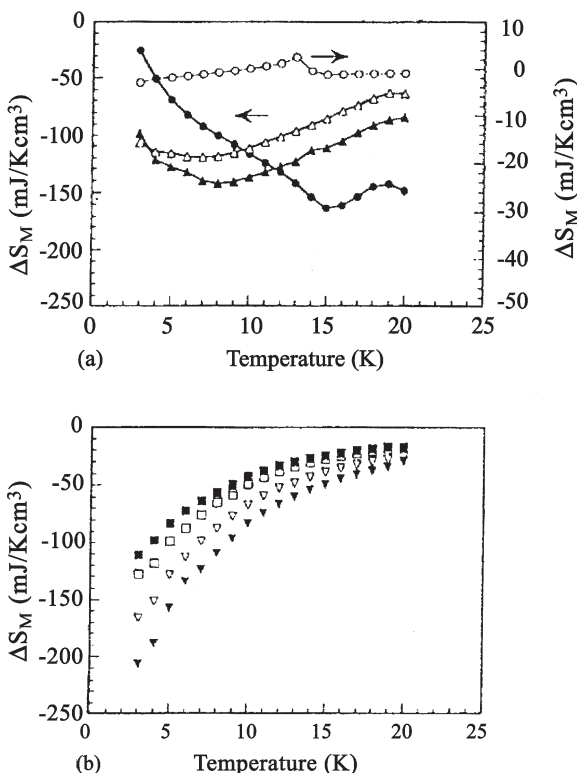


Figure 5.31. Temperature dependences of the magnetic entropy change in $\text{Dy}_{1-x}\text{Gd}_x\text{VO}_4$ single crystals induced by $\Delta H = 50$ kOe: (a) $x = 0$ (\circ) and $x = 0.25$ (\triangle); (b) $x = 0.5$ (\square) and $x = 1$ (∇). The open symbols correspond to the measurements along the c-axis and the solid symbols correspond to those along the a-axis (Kimura *et al* 1998).

in DyVO₄ and at about 8 K at Dy_{0.75}Gd_{0.25}VO₄. The absolute values of ΔS_M in Dy_{0.75}Gd_{0.25}VO₄ are superior to those in DyAlO₃, Dy₃Al₅O₁₂ and Gd₃Ga₅O₁₂. It should also be noted that, in Dy_{0.75}Gd_{0.25}VO₄ single crystal, Jahn-Teller stresses are small and cannot cause crystal cracking.

Kimura *et al* (1998) also measured the thermal conductivity of DyVO₄ and GdVO₄ single crystals along the c-axis in the temperature range from 5 K to 28 K. In both compounds the thermal conductivity had a general trend to decrease with cooling, although GdVO₄ had essentially larger thermal conductivity values than DyVO₄. Some numerical values of the thermal conductivity of GdVO₄ and DyVO₄ are presented in table A2.1 in appendix 2.

In the work of Fischer *et al* (1991) the results of temperature change in magnetic field GdVO₄ at the initial temperature of 1.1 K were cited. According to them the MCE for $\Delta H = 23$ kOe is negative and has the maximum absolute value of about 0.7 K.

In high magnetic fields the effect called ‘crossover’ is observed in RVO₄ compounds (Kazei *et al* 1998, 2000, 2001). Crossover consists of crossing of the magnetic ion ground energy level by a higher energy level in a magnetic field due to the Zeeman effect. It is accompanied by a sharp increase of the magnetization and a peak in differential magnetic susceptibility dI/dH. The susceptibility peaks related to the crossover were observed experimentally in YbPO₄ (at ~ 2500 kOe at 4.2 K) and PrVO₄ (at ~ 450 kOe in the temperature range below 24 K) (Kazei *et al* 1998, 2000, 2001). The magnetocaloric effect in YbPO₄ and PrVO₄ related to the crossover was calculated by Kazei *et al* (1998, 2000, 2001). $T(H)$ dependences were determined by equation (2.16) and magnetization calculated using numerical diagonalizations of the system Hamiltonian. The results of calculations for PrVO₄ for the case when the magnetic field is directed along the [001] axis are presented in figure 5.32, where adiabatic magnetization and $T(H)$ curves for temperatures below 24 K are shown. As one can see near the field corresponding to the crossover, there are magnetization jumps and maximal temperature change. The form and depth of the minimum in $T(H)$ curves depends on the initial sample temperature. The maximum absolute temperature change related to the crossover (about 20 K) is observed for the initial temperature of 22 K. The $T(H)$ curve calculated for YbPO₄ magnetized along the [001] crystallographic direction for the initial temperature of 4.2 K shows that the sample is first heated by about 25 K, and then near the crossover field is cooled by 25 K with subsequent heating. Experimental investigation of the $T(H)$ curve can give information about the crystal field, since it determines the energy structure of the rare earth ion and $T(H)$ behaviour.

To summarize, in this section we have considered magnetocaloric properties of various oxides. Rare earth garnets and ferrites do not display an essential magnetocaloric effect. However, the MCE studies in this case allow us to get information about magnetic structure transformations and magnetic phase transitions, which is difficult or even impossible to obtain

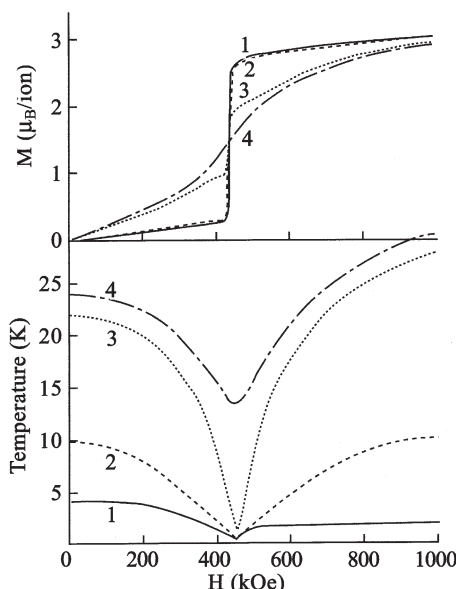


Figure 5.32. Calculated adiabatic magnetization and temperature field dependences in PrVO_4 (a magnetic field is directed along the [001] axis) for different initial temperatures: (1) 4.2 K; (2) 10 K; (3) 22 K; (4) 24 K (Kazei *et al* 2000).

by other methods. Substituting magnetic ions by various elements, investigators determine the details of magnetic structure and magnetic interactions in these compounds on the basis of the MCE data. Gallium and aluminium rare earth garnets, rare earth orthoaluminates and vanadites reveal essential magnetic entropy and adiabatic temperature change in the low-temperature range. Because of that they can be considered as appropriate materials for magnetic cryocoolers. Such interesting effects as the crossover observed in high magnetic fields in rare earth vanadites, accompanied by magnetocaloric effect, should also be mentioned. The doped perovskite-type manganites are characterized by essential magnetic entropy change near the Curie temperatures (insulator-conductor transition) and especially near first-order FM–AFM transition at the transition to the charge-ordered state. However, the adiabatic temperature change in these compounds is not high. According to consideration of Pecharsky and Gschneidner (2001b) this experimentally observed fact is related to high heat capacity in the manganites. This can make difficult their application in magnetic cooling devices.

Chapter 6

Magnetocaloric effect in intermetallic compounds

In this chapter we consider intermetallic magnetic compounds containing rare earth elements. Among them, two large groups of the materials where the magnetocaloric properties were studied can be singled out—alloys and compounds between rare earth and nonmagnetic elements and those between rare earth and 3d metal elements. In the first group RE ions are the only carriers of the magnetic moment (to this group the compounds R–Ni can also be attributed because Ni in them does not have a magnetic moment). These materials can display not only ferromagnetic but also more complex types of magnetic ordering, in particular due to the crystalline field effects. In RE–Fe compounds there are two magnetic sublattices, Fe and RE, ordered ferrimagnetically, and they exhibit magnetic behaviour analogous to that observed in rare earth iron garnets. The magnetic moment of Co in RE–Co compounds has an itinerant nature and according to the existing models is induced by a molecular field acting from an RE sublattice. The transition to magnetically ordered state in some of these materials is of the first order. There is also a metamagnetic transition induced by an external magnetic field related to the itinerant behaviour of the Co moment. Because of that it is possible to expect essential values of the magnetocaloric effect in RE–Co compounds.

6.1 Rare earth–nonmagnetic element compounds

6.1.1 Rare earth–aluminium compounds

RAI_2 compounds have the cubic Laves phase (Cu_2Mg -type) structure and display magnetic phase transition from the paramagnetic to the ferromagnetic state at the Curie temperature T_C (Taylor and Darby 1972). Magnetocaloric properties of RAI_2 series are the most thoroughly studied among the rare earth–nonmagnetic element compounds.

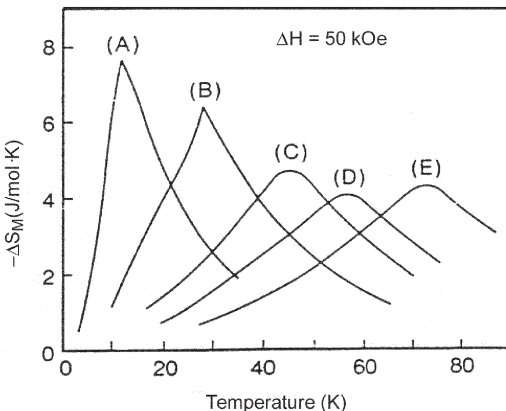


Figure 6.1. Temperature dependences of ΔS_M induced by $\Delta H = 50$ kOe in RAl_2 alloys: (A) $ErAl_2$; (B) $HoAl_2$; (C) $(Dy_{0.5}Ho_{0.5})Al_2$; (D) $DyAl_2$; (E) $(Gd_{0.1}Dy_{0.9})Al_2$ (Hashimoto 1991).

Hashimoto *et al* (1986) and Hashimoto (1991) measured the heat capacity and the magnetization of the RAl_2 compounds with $R = Er$, Ho and Dy , and of $(Gd_{0.1}Dy_{0.9})Al_2$ and $(Dy_{0.5}Ho_{0.5})Al_2$. The $\Delta S_M(T)$ curves determined from the magnetization data are shown in figure 6.1. The analogous peaks were observed on $\Delta S_M(T)$ curves near T_C in other RAl_2 compounds investigated.

Gschneidner *et al* (1994a,b, 1996a,b) determined the magnetic entropy S_M in RAl_2 compounds on the basis of the magnetic heat capacity data and the formula obtained on the basis of equation (2.62):

$$S_M(H, T) = \int_0^T \frac{C'_H(T)}{T} dT \quad (6.1)$$

where C'_H is the magnetic heat capacity contribution to the total heat capacity, which approaches zero at temperatures far from the temperature of transition from paramagnetic to magnetically-ordered state. The prorated zero-field heat capacities of $LaAl_2$ and $LuAl_2$ were used to evaluate the lattice contributions needed for C_M determination of the $(Dy_{1-x}Er_x)Al_2$ system. The magnetic entropy change ΔS_M , induced by field change ΔH , was obtained from the heat capacity measurements at various magnetic fields (see section 3.2.2).

The experimental data on S_M , ΔS_M and ΔT in various polycrystalline RAl_2 alloys are presented in table 6.1. The majority of the results on rare earth–nonmagnetic element alloys was summarized in the reports of Gschneidner *et al* (1996a,b). The amount of the magnetic entropy S_M utilized in the magnetic ordering process (see table 6.1) was determined on the basis of the values of the theoretically available maximum entropy

Table 6.1. The Curie temperatures (T_C), temperature of the maximum in the $\Delta T(T)$ curves (T_{\max}), magnetic entropy S_M , peak magnetic entropy change ΔS_M near the Curie temperature induced by the magnetic field change ΔH , peak MCE value ΔT at $T = T_{\max}$ induced by ΔH , $\Delta T/\Delta H$ and $\Delta S_M/\Delta H$ of polycrystalline RE–nonmagnetic element alloys. The values of S_M are in J/mol K per RE atom (J/molRK).

Compound	T_C (K)	T_{\max} (K)	ΔT (K)	ΔH (kOe)	$\Delta T/\Delta H$ ($\times 10^2$)	Experimental value (J/moIRK)	% of theoretical value	S_M		ΔS_M peak		Ref.*
								ΔS_M (J/kg K)	ΔH (kOe)	$\Delta H \times 10^2$ (J/kg K) Ref.*		
GdAl ₂	167	167	5.2	75	6.93	15.3	91.4	7.6	50	15.2	1	
TbAl ₂	105	—	2.1	20	10.5	—	—	4.2	20	21	2, 3	4
	108	—	—	—	—	—	—	14	50	28		
	—	—	4.4	50	8.8	—	—	7.5	20	37.5		
	—	—	2.2	20	11	—	—	11.4	50	22.8	23	
DyAl ₂	63.3	63.9	9.18	75	12.24	20.6	89.4	18.5	50	37	1, 2	5, 6
	—	3.6	3.6	20	1.8	—	—	9.7	20	48.5		
	—	—	—	—	—	—	—	18.9	50	37.8		
HoAl ₂	55.9	—	—	—	—	—	—	28.8	50	57.6	6	23
	28.6	—	4.6	20	23	—	—	25.6	50	51.3		
ErAl ₂	31	—	—	—	—	—	—	12.8	20	64.1		
	13	13.6	14.2	75	18.93	21.8	94.6	36.15	50	72.3	1, 2	
	—	—	—	—	—	—	—	22.6	20	113	5, 6	
ErAl _{2.20}	11.7	22	9	50	1.8	—	—	34.3	50	68.6	7	
HoAl _{2.24}	11	—	—	—	—	—	—	27.3	50	54.6	7	
DyAl _{2.22}	25	—	—	—	—	—	—	22.2	50	44.4	7	
	50	—	—	—	—	—	—	19.3	50	38.6	7	

Table 6.1. Continued.

Er ₃ AlC _{0.25}	9	8	75.3	10.62	—	—	—	—	—	—	12
Er ₃ AlC _{0.5}	7	9.2	98.5	9.75	—	—	—	—	—	—	12
Gd ₃ Al ₂	281	—	—	—	—	—	—	—	—	—	—
	279.2	273	4.6	55	8.36	—	—	—	—	—	10
	281	260	7	100	7	—	—	7.2	100	7.2	14
GdPd	38	38	2.4	20	12	—	—	2.3	20	11.6	15
Gd ₃ Pd ₄	323	18(<i>T_N</i>)	5.2	30	7.47	—	16.41	95	1.3	98.5	16
Gd ₇ Pd ₃	328	—	8.5	50	17	—	—	—	6.4	50	22
GdRh	19.93	—	3.4	20	17	—	17.4	100	2.6	20	17
TmCu	20	7.8(<i>T_N</i>)	9	7	80	8.75	—	—	15	80	18
TmAg	270	9.2(<i>T_N</i>)	10	7.3	80	9.13	—	—	15.5	80	19
GdZn	270	—	10.6	100	10.6	—	—	—	11.2	100	20
Gd _{0.70} Zn _{0.30}	295	295	9	75	12	—	—	—	3.4	20	17
Gd ₃ In	191	210	7.3	100	7.3	—	—	—	9.4	75	20
	200	2	20	10	10	—	—	2.7	100	2.7	21
						—	—	0.8	20	4	—

*1. Gschneidner *et al.* (1996b); 2. Gschneidner *et al.* (1996a); 3. Dan'kov *et al.* (2000); 4. Wang *et al.* (2000); 5. von Ranke *et al.* (1998a); 6. Hashimoto *et al.* (1986); 7. Sahashi *et al.* (1987); 8. Johansson *et al.* (1988); 9. Zimm *et al.* (1992); 10. Korte *et al.* (1998a); 11. Sill and Esau (1984); 12. Pecharsky *et al.* (1996); 13. Tokai *et al.* (1992a); 14. Nikitin *et al.* (1999); 15. Pecharsky *et al.* (1989a); 16. Tanoue *et al.* (1992); 17. Azhar *et al.* (1985); 18. Buschow *et al.* (1975); 19. Rawat and Das (2001a); 20. Pecharsky and Gschneidner (1999b); 21. Ilyn *et al.* (2002); 22. Canepa *et al.* (2000); 23. Ilyn *et al.* (2001).

Table 6.2. Maximum value of the magnetic entropy and total angular momentum S_M in RE metals.

Element	J	S_M (J/mol K)	S_M (J/kg K)
La	0	0	0
Ce	5/2	14.9	106.34
Pr	4	16.2	114.96
Nd	9/2	19.2	133.11
Pm	4	18.3	126.28
Sm	5/2	19.2	127.69
Eu	0	0	0
Gd	7/2	17.3	110.02
Tb	6	21.3	134.02
Dy	15/2	23.1	142.15
Ho	8	23.6	143.09
Er	15/2	23.1	138.11
Tm	6	21.3	126.09
Yb	7/2	17.3	99.98
Lu	0	0	0

related to the R ion, calculated by means of equation (2.66) using J for the corresponding RE element (see table 6.2). As one can see from tables 6.1 and 6.2, the experimental S_M is about 10–20% lower than the theoretical value. The residuary part of the magnetic entropy is related to magnetic spin fluctuations above T_C (Gschneidner *et al* 1996b). The values of ΔT in table 6.1 are taken at the temperature T_{\max} corresponding to the maximum at the temperature dependence of the MCE. The Curie temperatures were determined from a.c. susceptibility and magnetization measurements.

The $\Delta S_M(T)$ and $\Delta T(T)$ curves for GdAl_2 were obtained by Dan'kov *et al* (2000) from heat capacity, magnetization and direct pulse-field measurements. The results of the different methods are in good agreement with each other—see figure 6.2. The magnetic field dependence of the MCE effect value at T_C showed behaviour typical of ferromagnets—a rapid increase for low fields and more moderate and almost linear increase for the fields higher than 20 kOe. ΔS_M and ΔT for RAl_2 ($\text{R}=\text{Tb}, \text{Dy}, \text{Er}$ and Ho) were defined from heat capacity, magnetization and by a direct method by von Ranke *et al* (1998a), Wang *et al* (2000) and Ilyn *et al* (2001). The peak ΔS_M and ΔT values near the Curie temperatures for these compounds are presented in table 6.1. HoAl_2 has high magnetocaloric properties, but its $\Delta S_M(T)$ and $\Delta T(T)$ curves are rather narrow—full width at half maximum about 15 K for $\Delta H = 20$ K.

Von Ranke *et al* (1998a) considered theoretically the MCE in DyAl_2 and ErAl_2 , using a Hamiltonian consisting of contributions from a crystalline

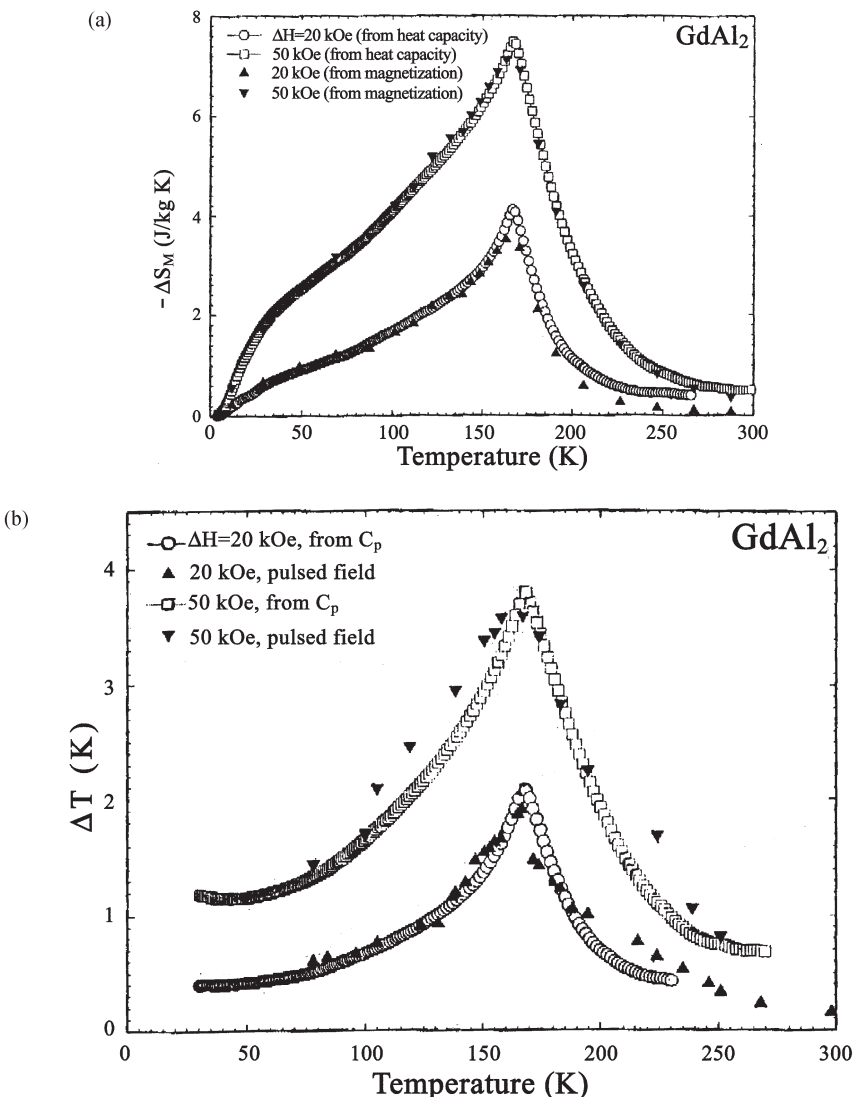


Figure 6.2. Temperature dependences of (a) ΔS_M and (b) ΔT in GdAl_2 determined by different experimental methods (Dan'kov *et al* 2000).

electric field acting on the anisotropic Dy ion and exchange interactions. The latter were regarded in the framework of one-dimensional mean field approximation. The crystalline field parameters from inelastic neutron scattering were used in the calculations. The calculated $\Delta S_M(T)$ and $\Delta T(T)$ dependences were in good agreement with the experimental ones obtained from the heat capacity measurements. Analogous calculations were made for

RAI_2 with $\text{R} = \text{Pr}, \text{Nd}, \text{Tb}, \text{Ho}, \text{Tm}$, and for $\text{Dy}_{1-x}\text{Er}_x\text{Al}_2$ ($0.15 < x < 0.5$) compounds (von Ranke *et al* 2001b, Lima *et al* 2002). The calculation for the RAI_2 compound $\Delta S_M(T)$ curves display typical ferromagnetic behaviour near T_C with the following peak $-\Delta S_M$ values for $\Delta H = 50 \text{ kOe}$: 21.6 J/kg K for PrAl_2 ($-\Delta S_M$ maximum near 34 K), 11.1 J/kg K for NdAl_2 ($-\Delta S_M$ maximum near 63 K), 16.4 J/kg K for TbAl_2 , 29.7 J/kg K for HoAl_2 and 31.4 J/kg K for TmAl_2 (ΔS_M maximum near 9 K). The peak ΔS_M values for TbAl_2 and HoAl_2 are consistent with those obtained earlier experimentally—see table 6.1. Lima *et al* (2002) determined $\Delta T(T)$ for $\text{Dy}_{1-x}\text{Er}_x\text{Al}_2$ ($0.15 < x < 0.5$) on the basis of the calculated total entropy in various magnetic fields. The results of calculations agree with experimental measurements obtained by Gschneidner *et al* (1996b)—they reproduce a peak near T_C and low-temperature anomalies (lower maxima) in the alloys with $x = 0.3$ and 0.5 . The latter were related by the authors to crystal field effects.

Further theoretical consideration of DyAl_2 magnetocaloric properties were made in the work of von Ranke *et al* (2000a), where two-dimensional and three-dimensional mean field approximations with the exchange-Zeeman term in the Hamiltonian, including three components of the magnetization vector, were used to describe the magnetic interactions. This allowed magnetization and ΔS_M field and temperature dependences to be obtained along the [100], [110] and [111] crystal axes in DyAl_2 . The calculated magnetization field dependences for different crystallographic axes and $T = 4.2 \text{ K}$ are shown in figure 6.3. As one can see they display different behaviours. For [100] (the easy axis in DyAl_2), the magnetic saturation is achieved in the low-field region and the [110] curve displays a steady increase in the whole temperature range. On the [110] curve, the jump in magnetization is

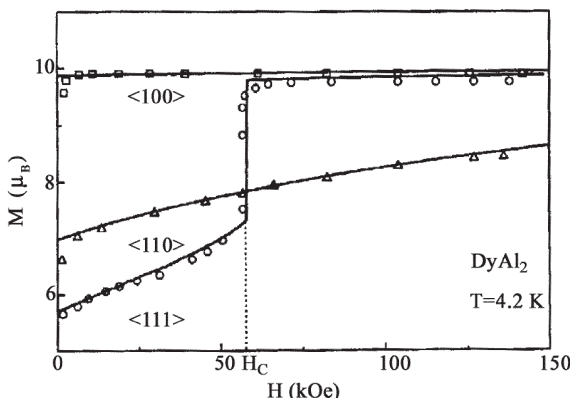


Figure 6.3. Magnetization field dependences for DyAl_2 at 4.2 K . Solid lines show results of calculations. Experimental points are represented by squares for the [100] direction of the magnetic field, by triangles for the [110] direction and by circles for the [111] direction (von Ranke *et al* 2000a). (Copyright 2000 by the American Physical Society.)

observed at 58 kOe, which corresponds to the first-order transition when Dy magnetic moments are aligned in the [110] direction. The experimental measurements are in good accord with the theoretically calculated $I(H)$ curves. Correspondingly, there were two different magnetic entropy behaviours. If magnetization is made along the [100] and [110] axes the magnetic entropy decreases under application of the magnetic field in all temperature intervals in the manner usual for ferromagnets. For [111] directions in the low-temperature region, positive values of ΔS_M values were observed—see figure 6.4. For $\Delta H = 20$ kOe the temperature where ΔS_M changes its sign is 40.7 K. It is worth noting that there is an inflection at about 40 K on the experimental $\Delta S_M(T)$ and $\Delta T(T)$ curves measured on polycrystalline $DyAl_2$ for $\Delta H = 20$ kOe in the work of von Ranke *et al* (1998a).

Sahashi *et al* (1987) measured the heat capacity temperature dependences for Al-rich $ErAl_{2.20}$, $HoAl_{2.24}$, $DyAl_{2.22}$ and $Ho_{0.5}Dy_{0.5}Al_{2.25}$ high-density sintered compounds. To prepare the samples the metallurgical powder route was used. From the ingots of arc-melted RAI_2 ($R = Dy$, Ho , Er and $Ho_{0.5}Er_{0.5}$), 3 μm sized powder was ball milled in ethanol. The milled powder was pressed under 10^3 kg/cm² and then sintered in an argon atmosphere for 1.5 h at 1105 °C. According to X-ray analysis the samples have specific structure: the Laves phase RAI_2 is surrounded by the RAI_3 phase with cubic Cu₃Au structure. The Curie temperatures of the $ErAl_{2.20}$, $HoAl_{2.24}$, $(Ho_{0.5}Dy_{0.5})Al_{2.25}$ and $DyAl_{2.22}$ alloys prepared by this method

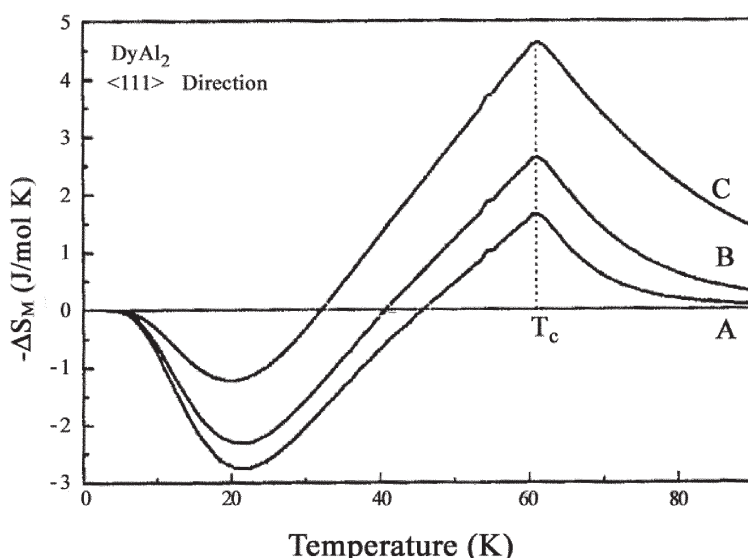


Figure 6.4. Calculated ΔS_M temperature dependences for $DyAl_2$ magnetized along the [111] axis for (A) $\Delta H = 10$ kOe, (B) 20 kOe and (C) 50 kOe (von Ranke *et al* 2000a). (Copyright 2000 by the American Physical Society.)

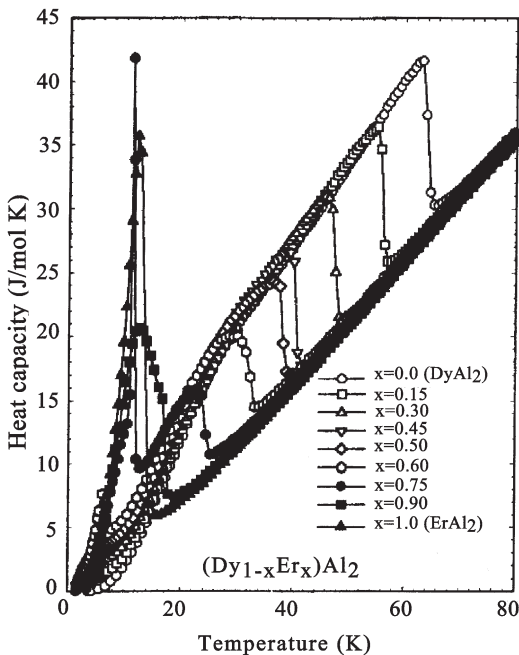


Figure 6.5. The zero-field heat capacity temperature dependences of the $(\text{Dy}_{1-x}\text{Er}_x)\text{Al}_2$ alloys (Gschneidner *et al* 1996b).

were obtained from $C(T)$ curves and are somewhat lower than that in the corresponding stoichiometric compounds—see table 6.1. The maxima on $\Delta S_M(T)$ curves in the sintered compounds were broader than in the corresponding RAl_2 compounds.

The heat capacity measurements of $(\text{Dy}_{1-x}\text{Er}_x)\text{Al}_2$ alloys made by Gschneidner *et al* (1994a,b, 1996a,b) for x from 0.6 to 1.0 revealed a sharp peak below 14 K—see figure 6.5. Its position on the temperature scale remained almost constant and its height decreased with increasing Dy content. For x from 0 to 0.75 the heat capacity showed a broad λ -type anomaly at the Curie temperature. For $x = 0.6, 0.75$ and 0.9 both anomalies were observed. The low-temperature peak was related by the authors to the Schottky anomaly caused by the splitting of the ground states of the RE ions with $L \neq 0$ by the crystalline electric field. Earlier, Inoue *et al* (1977) found the Schottky anomaly at about 23 K in the heat capacity of ErAl_2 .

Figure 6.6 shows the temperature dependences of the MCE in the $(\text{Dy}_{1-x}\text{Er}_x)\text{Al}_2$ alloy system determined from the heat capacity data. The curves have caret-like character with broad maxima, which can be due to the possible spin-reorientation transitions. The maximum MCE is observed in ErAl_2 and the lowest in DyAl_2 . According to the magnetization measurements, the hysteresis in $(\text{Dy}_{0.5}\text{Er}_{0.5})\text{Al}_2$ alloy was about 340 Oe at 2 K and

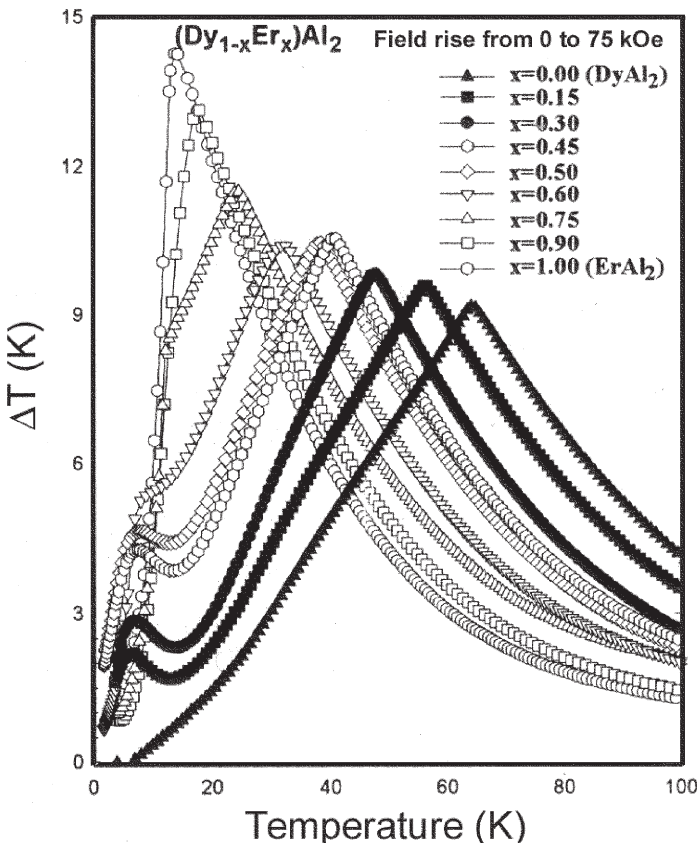


Figure 6.6. Temperature dependences of the MCE induced by $\Delta H = 75$ kOe for the $(\text{Dy}_{1-x}\text{Er}_x)\text{Al}_2$ alloy system (Gschneidner *et al* 1996b).

vanished at 17 K (Gschneidner *et al* 1994b). The low-temperature anomalies in the $\Delta T(T)$ curves in the $(\text{Dy}_{1-x}\text{Er}_x)\text{Al}_2$ alloy system were related by the authors to the effects of the crystalline field. An analogous low-temperature anomaly in calculated $\Delta S_M(T)$ and $\Delta T(T)$ curves of HoNi_2 was found by von Ranke *et al* (2001a). They explained it by a high density of states on the two lowest energy levels that exist in this compound at low temperatures—see section 6.2.

Zimm *et al* (1992) studied the heat capacity and measured directly the MCE in $(\text{Gd}_{0.14}\text{Er}_{0.86})\text{Al}_2$ alloy (see table 6.1). The $\Delta T(T)$ curves obtained for various magnetic fields had broad maxima at $T_{\max} \approx 25$ K, although the magnetic susceptibility measurements give $T_C \approx 40$ K. The authors related the broad ΔT maximum with random distribution of Er and Gd atoms on the RE sites, which leads to the local magnetic environment changing. The heat capacity of $\text{Gd}_{0.06}\text{Er}_{0.94}\text{Al}_2$ alloy was measured by

Johanson *et al* (1988). The Curie temperature and the MCE defined from the obtained data were 13 K for $\Delta H = 80$ kOe.

Bauer *et al* (1986) measured thermal conductivity of RAl_2 , where $R = Y$, La, Ce, Pr, Nd, Sm, Gd, Tb, Ho, Er, Tm and Lu, in the temperature range from 4.2 to 395 K. Among the compounds with nonmagnetic elements Y, La and Lu the thermal conductivity revealed a maximum in the low-temperature range in $LaAl_2$ (with a height of ~ 0.22 W/cm K at 20 K). The thermal conductivity of YAl_2 and $LuAl_2$ monotonically (although nonlinearly) decreased from room temperature values of ~ 0.23 and ~ 0.22 W/cm K, respectively, down to ~ 0.026 and ~ 0.018 W/cm K at 10 K, respectively. $LaLu_2$ has a lower room-temperature thermal conductivity, ~ 0.165 W/cm K. $CeAl_2$ (antiferromagnet with $T_N = 3.8$ K (Barbara *et al* 1977)) has almost linear temperature dependence of the thermal conductivity, which decreases from the room-temperature value ~ 0.12 W/cm K to ~ 0.01 W/cm K at 10 K. Analogous thermal conductivity temperature dependence is observed for $SmAl_2$. $NdAl_2$ and $PrAl_2$ display thermal conductivity maxima (~ 0.11 W/cm K at ~ 22 K and ~ 0.12 W/cm K at ~ 14 K, respectively) at low temperatures in the magnetically-ordered state ($T_C = 65$ K for $NdAl_2$ and 33 K for $PrAl_2$ (Taylor and Darby 1972)). At room temperature the thermal conductivity of $NdAl_2$ and $PrAl_2$ is ~ 0.17 W/cm K. The thermal conductivity of RAl_2 compounds with heavy rare earth elements has a general trend to decrease with temperature with change of the curvature of the curve near T_C (Bauer *et al* 1986). The thermal conductivity of $ErAl_2$ was also studied by Zimm *et al* (1988a), whose data was quite different from that of Bauer *et al* (1986). According to Bauer *et al* (1986) the thermal conductivity of $ErAl_2$ at 170 K is 0.15 W/cm K and monotonically decreased down to liquid helium temperature (~ 0.04 W/cm K at 25 K). Zimm *et al* (1988a) reported the higher values (~ 0.3 W/cm K at 170 K) and more complex temperature behaviour—near T_C (at ~ 12 K) the temperature dependence of the thermal conductivity reveals a wide minimum, with a minimal value of about 0.07 W/cm K with a subsequent rise at lower temperatures. Application of a magnetic field of 70 kOe caused an increase in the thermal conductivity near T_C —from a minimal value of ~ 0.07 W/cm K up to 0.11 W/cm K (Zimm *et al* 1988a). Below T_C the magnetic field decreased the thermal conductivity and above T_C its influence on the thermal conductivity was weak. Some numerical values of the thermal conductivity of RAl_2 compounds are presented in table A2.1 in appendix 2.

Summarizing the data presented in table 6.1 for RAl_2 , one should note that these compounds are characterized by essential magnetic entropy change (the absolute values of $\Delta S_M/\Delta H$ lie in the interval from 0.21 J/kg K kOe (($Tb_{0.4}Gd_{0.6}$) Al_2) to 113 J/kg K kOe ($ErAl_2$) and magnetocaloric effect (maximum $\Delta T/\Delta H$ value is 0.23 K/kOe in $HoAl_2$). At the same time the width of the $\Delta S_M(T)$ and $\Delta T(T)$ curves can be large—for

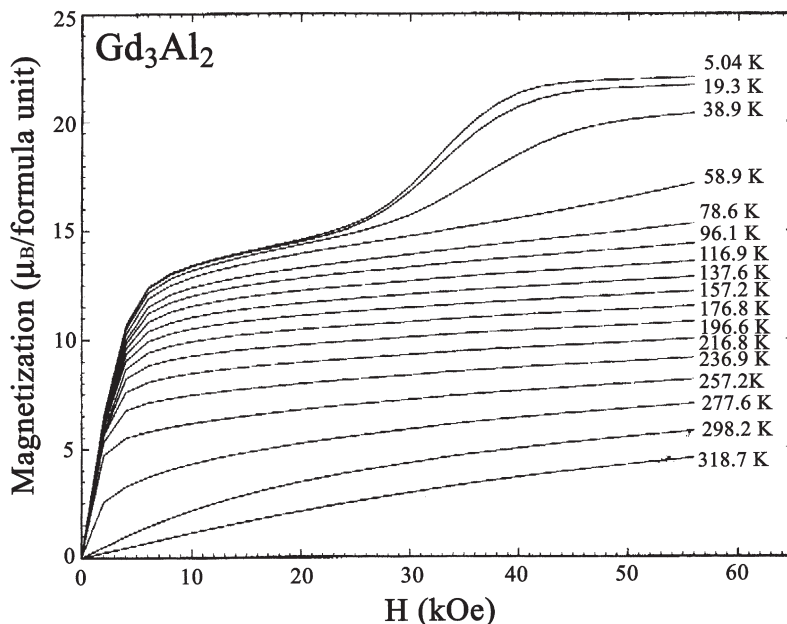


Figure 6.7. Magnetization isotherms for Gd₃Al₂ at different temperatures (Pecharsky *et al* 1999).

example, in DyAl₂ the full width of $\Delta T(T)$ dependence at the half maximum is ~ 65 K for $\Delta H = 75$ kOe (see figure 6.6).

The MCE in Gd₃Al₂ was studied by Nikitin *et al* (1989a) and Pecharsky *et al* (1999). The direct measurements of Nikitin *et al* (1989a) made near the Curie point, determined from the Arrott plots to be 279.2 K, gave a peak value of the MCE of 4.6 K for $\Delta H = 55$ kOe. Heat capacity, magnetization and MCE of Gd₃Al₂ were measured by Pecharsky *et al* (1999) by pulse field and switch-on direct methods. The λ -type anomaly on the heat capacity temperature dependence corresponding to the Curie point was found at 281 K. Magnetization on field dependences for Gd₃Al₂ at various temperatures are shown in figure 6.7. They have ferromagnetic character Gd₃Al₂ below the Curie point. However, the saturation magnetic moment per Gd atom in the temperature range down to about 60 K was two-thirds of that for the case where the magnetic moments are ordered ferromagnetically. This indicates probable ferrimagnetic structure below the Curie temperature. The crystal structure of Gd₃Al₂ is complex, with three nonequivalent crystallographic sites. It is possible that part of the magnetic moments in different sites is ordered antiferromagnetically. Below 60 K in the fields of about 25 kOe a metamagnetic transition takes place, which leads to the saturation magnetization value corresponding to the fully ferromagnetically aligned Gd magnetic moments. The magnetic structure changes are reflected on the

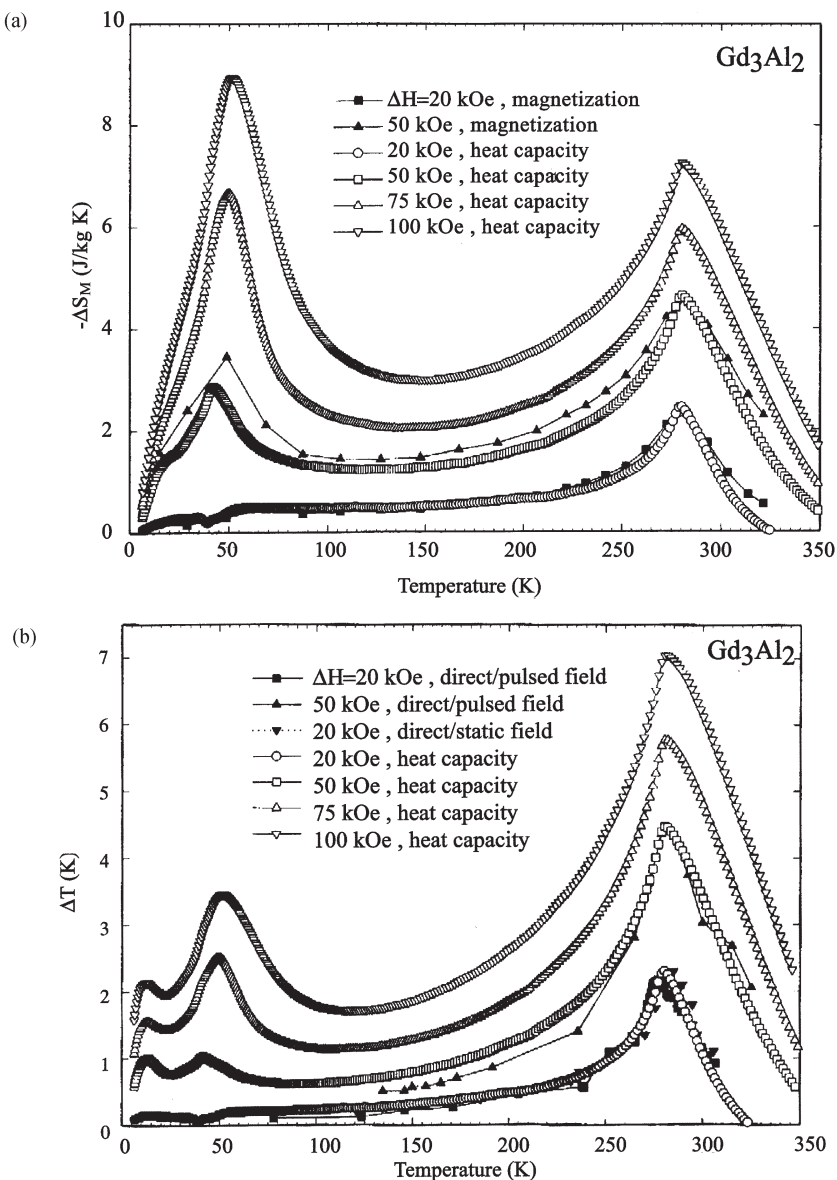


Figure 6.8. Temperature dependences of (a) ΔS_M and (b) ΔT in Gd_3Al_2 measured by different methods (Pecharsky *et al* 1999).

$\Delta S_M(T)$ and $\Delta T(T)$ curves—see figure 6.8, where one can see two peaks, corresponding to the magnetic ordering at T_C and to the low-temperature field-induced metamagnetic transition. The total magnetic entropy defined by equation (2.66) is distributed in Gd_3Al_2 between two magnetic transitions,

which reduces the possible peak values of ΔS_M . However, the presence of two separate magnetic phase transitions gives noticeable ΔS_M and ΔT in the temperature range between 100 and 250 K.

Pecharsky *et al* (1996) and Gschneidner *et al* (1996a,b) investigated the heat capacity of the carbide alloys Er_3AlC_x ($x = 0.1, 0.25, 0.5, 1$). Er_3AlC has an antiperovskite-type crystal structure and, according to the measurements of Tokai *et al* (1992a), orders magnetically at 2.8 K showing a λ -type heat capacity anomaly. An analogous anomaly was observed by Pecharski *et al* (1996) at 3.1 K. The a.c. susceptibility measurements of Pecharsky *et al* (1996) revealed in the Er_3AlC alloy a negative paramagnetic Curie temperature (-1.6 K), which was regarded as evidence of antiferromagnetic ordering. As proposed by the latter authors, this antiferromagnetic order transforms to a ferromagnetic one by a magnetic field of about 24.6 kOe.

For the other carbide phases two heat capacity maxima were found, one at about 3 K and another one at approximately 8 K. X-ray diffraction studies made by Pecharsky *et al* (1996) on Er_3AlC_x ($x = 0.1, 0.25, 0.5$) showed that these compounds contain two phases, Er_3AlC and Er_2Al . The high-temperature heat capacity maximum in Er_3AlC_x was attributed by the authors to the antiferromagnetic ordering of Er_2Al (~ 6 K).

The MCE of Er_3AlC_x ($x = 0.1, 0.25, 0.5$), determined from heat capacity data, displays a wide maximum due to the presence of two phases with slightly different magnetic-ordering temperatures. One can see from table 6.1 a gradual decrease of the MCE in Er_3AlC_x with increasing x . This was related by the authors to a reduction of Er_3AlC phase content and an increase of the amount of the antiferromagnetic Er_2Al phase.

6.1.2 Rare earth–Cu, Zn, Ga, Rh, Pd, Ag, In

According to the data of Sill and Esau (1984), an $ErAgGa$ compound with $CeCu_2$ -type crystal structure orders ferromagnetically at about 3 K. The zero field heat capacity temperature dependences display two overlapping maxima at about 3 and 5 K (Pecharsky *et al* 1996). The a.c. susceptibility measurements showed considerable frequency dependence below 8 K, which was explained by Pecharsky *et al* (1996) by the existence of a spin-glass state. The additional maximum in the temperature dependence $C(T)$ measured in zero field was related to the Schottky anomaly caused by the crystalline electric field splitting of low-lying energy levels of Er ions. The $\Delta T(T)$ curves of $ErAgGa$ obtained from heat capacity show a broad maximum at about 6 K with peak MCE value of ~ 11.2 K for $\Delta H = 98.5$ kOe.

Tanoue *et al* (1992) investigated the heat capacity, magnetic susceptibility and magnetization of the Gd_3Pd_4 compound that has the rhombohedral Pu_3Pd_4 -type structure. It was found that at 18 K in Gd_3Pd_4 the magnetic phase transition from paramagnetic to antiferromagnetic state took place. At about 6 K the compound displays another transition of ferromagnetic

nature. The antiferromagnetic transition shows on the $C(T)$ curve as a maximum. In the presence of a magnetic field up to 98.5 kOe an additional heat capacity peak at about 13 K developed, which was attributed to a spin-reorientation transition. The magnetic entropy S_M calculated from the heat capacity measurements was equal to 16.41 J/mol Gd K, which is in good agreement with theoretical data on Gd (see table 6.2). The temperature dependences of $-\Delta S_M$ of Gd_3Pd_4 determined from the heat capacity for ΔH up to 98.5 kOe have a maximum at about 20 K. Zimm *et al* (1992) measured directly $\Delta T(T)$ curves for GdPd. This compound has the orthorhombic CrB-type structure and orders ferromagnetically below $T_C = 38$ K. The $\Delta T(T)$ curves obtained for various magnetic field change have sharp peaks near the Curie temperatures. Another compound studied with Pd is ferromagnetic Gd_7Pd_3 with Th_7Fe_3 -type crystal structure and $T_C = 323$ K (Canepa *et al* 2002). $\Delta S_M(T)$ and $\Delta T(T)$ curves for this compound were calculated on the basis of the heat capacity data. The peak ΔT and ΔS_M values of the listed Gd–Pd compounds are presented in table 6.1. As one can see, $\Delta T/\Delta H$ in Gd_7Pd_3 is rather high: 17 K/kOe retains this value in high fields.

The heat capacity of ferromagnetic intermetallic compound GdRh with CsCl-type crystal structure was studied by Buschow *et al* (1975) and Azhar *et al* (1985). Curie temperature values of 19.93 and 20 K were defined from the temperature dependences of the heat capacity by Buschow *et al* (1975) and Azhar *et al* (1985), respectively. From magnetization measurements $T_C = 24$ K was found (Buschow *et al* 1975). The volumetric peak heat capacity value at T_C was found by Buschow *et al* (1975) to be ~ 0.9 J/cm³ K. The magnetic entropy S_M , determined from the heat capacity data, was obtained to be 17.4 J/mol K, very close to the theoretical value for Gd (see table 6.2).

Pecharsky and Gschneidner (1999b) measured heat capacity, and determined magnetocaloric properties of the GdZn compound and $\text{Gd}_{0.75}\text{Zn}_{0.25}$ and $\text{Gd}_{0.70}\text{Zn}_{0.30}$ alloys. GdZn compound has cubic CsCl-type crystal structure and is ferromagnetic with a Curie temperature of 270 K. Its heat capacity temperature dependence displays a λ -type anomaly at 268 K. The $-\Delta S_M(T)$ and $\Delta T(T)$ curves determined from the magnetic and heat capacity measurements has caret-type peaks near T_C (ΔS_M and ΔT peak values are presented in table 6.1). Eutectic compositions $\text{Gd}_{0.75}\text{Zn}_{0.25}$ and $\text{Gd}_{0.70}\text{Zn}_{0.30}$ contain two phases (Gd and GdZn) and have two λ -anomalies at about 270 and 292 K, corresponding to the Curie temperatures of GdZn and Gd. $\text{Gd}_{0.75}\text{Zn}_{0.25}$ reveals a constant ΔS_M in the temperature interval from 270 to 293 K and its ΔT increases almost linearly over this temperature interval. In $\text{Gd}_{0.70}\text{Zn}_{0.30}$ alloy the linear decrease of ΔS_M and increase of ΔT is observed between 270 and 293 K. Below 270 K and above 293 K, $-\Delta S_M$ and ΔT decrease and increase as in a simple ferromagnet.

Rawat and Das (2001a) measured heat capacity in TmCu and TmAg compounds. These compounds crystallize in CsCl-type cubic structure.

TmCu exhibits first-order transition from a paramagnetic to an antiferromagnetic state at 7.7 K. TmAg orders antiferromagnetically at 9.5 K and the transition is a second-order transition. The first-order character of the magnetic phase transition in TmCu is related to strong quadrupolar interactions in this compound. The $C(T)$ curves show corresponding anomalies at the transition temperatures—a sharp first-order character anomaly at 7.8 K in TmCu and a λ -type anomaly at 9.2 K in TmAg. The $\Delta S_M(T)$ and $\Delta T(T)$ dependences for TmCu obtained from heat capacity are shown in figure 6.9. Around 10 K there is a maximum on $-\Delta S_M(T)$ and $\Delta T(T)$ curves corresponding to the magnetic ordering transition. Below ~ 7 K, ΔS_M becomes positive and ΔT becomes negative, which can be related to the prevailing of an antiferromagnetic-type paraprocess in this temperature region. TmAg reveal analogous $\Delta S_M(T)$ and $\Delta T(T)$ dependences, which are typical for antiferromagnets. It should be noted that the values of $-\Delta S_M$ and ΔT maxima in TmCu and TmAg were not essentially different in spite of the different character of magnetic ordering transitions in these compounds. The field dependence of ΔS_M and ΔT in the paramagnetic region was found to be proportional to H^2 (see equations (2.81), (2.82)). Dörr *et al* (1999) investigated heat capacity temperature dependences $C(T)$ in orthorhombic $DyCu_2$ single crystal and their transformations under the influence of the magnetic field up to 40 kOe applied along the a-axis. This compound is characterized by strong magnetic anisotropy, and several magnetic phases (commensurate and incommensurate) appear in it below the transition from paramagnetic to antiferromagnetic state at 26.5 K. The anomalies corresponding to these transitions were found on $C(T)$ curves in different magnetic fields.

The heat capacity of Er_xAg_{1-x} ($x = 0.4, 0.5, 0.6, 0.7$) and $(PrNd)Ag$ systems with cubic CsCl-type crystal structure was investigated by Biwa *et al* (1996) and Yagi *et al* (1997). These alloys order antiferromagnetically below 30 K and are characterized by essential volumetric peak heat capacity values. The heat capacity peak value for NdAg is $\sim 1.5 \text{ J/cm}^3 \text{ K}$ ($T_N = 22 \text{ K}$), for PrAg is $\sim 1 \text{ J/cm}^3 \text{ K}$ (at 10 K) and ErAg is $\sim 0.7 \text{ J/cm}^3 \text{ K}$ (at 15 K) (for comparison, the volumetric heat capacity peak value in GdRh is $\sim 0.9 \text{ J/cm}^3 \text{ K}$ at 24 K). The observed high magnetic contributions to the heat capacity in the $(PrNd)Ag$ system were explained by the authors by high degeneracy of RE ion ground states. The Schottky anomaly was responsible for the essential heat capacity above T_N in PrAg.

Biwa *et al* (1996) and Yagi *et al* (1997) also investigated thermal conductivity of Er_xAg_{1-x} and $(PrNd)Ag$ systems in the temperature range below 20 K. It was found that the thermal conductivity monotonically decreased with cooling in the temperature range under investigation. The values of the thermal conductivity of Er_xAg_{1-x} and $(PrNd)Ag$ alloys lie in the range from 0.01 to 0.1 W/K cm, which is higher than that of Er_3Ni . Some numerical values of the thermal conductivity obtained by Biwa *et al* (1996) and Yagi *et al* (1997) are presented in table A2.1 in appendix 2.

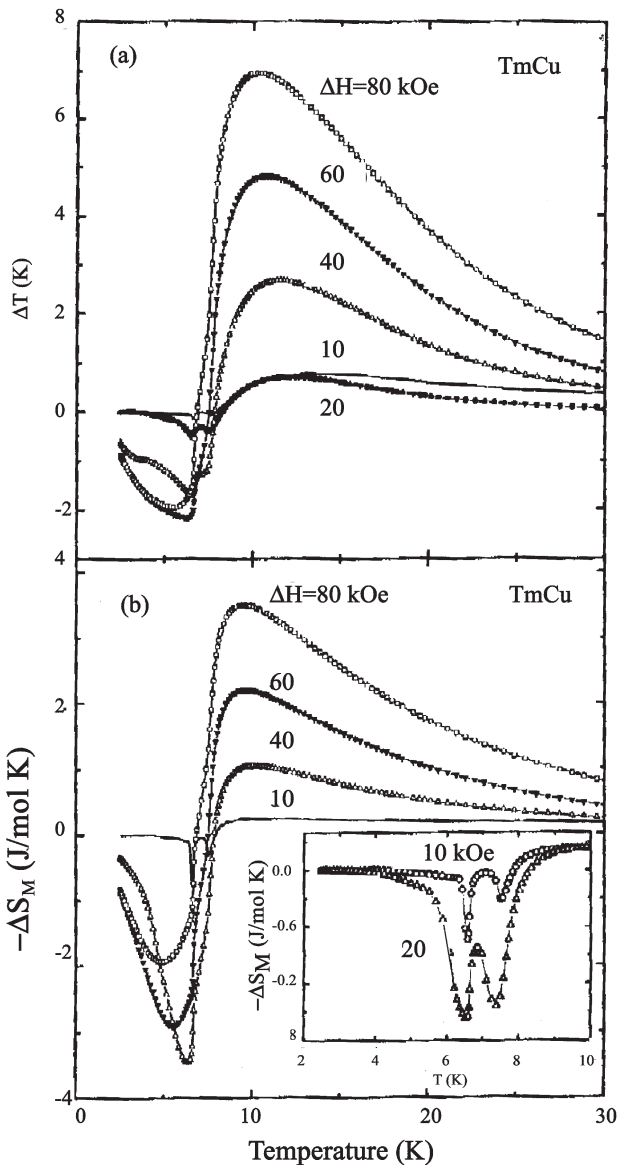


Figure 6.9. (a) $\Delta T(T)$ and (b) $\Delta S_M(T)$ curves for TmCu for different values of the magnetic field change ΔH (Rawat and Das 2001a).

The heat capacity of RGa_2 ($\text{R} = \text{Pr}, \text{Nd}, \text{Gd}, \text{Tb}, \text{Dy}, \text{Ho}, \text{Er}$) compounds and the $\text{Dy}_{1-x}\text{Ho}_x\text{Ga}_2$ ($0 < x < 1$) system was investigated by Yagi *et al* (1998) for the temperature region below 20 K. RGa_2 compounds have hexagonal AlB_2 -type crystal structure with alternate R and Ga atomic

layers. It was found that DyGa_2 displayed a pair of sharp peaks at 6.5 and 9 K with high values of volumetric heat capacity (1.45 and 1 J/K cm^3). Two peaks with high volumetric heat capacity values were also observed in HoGa_2 (0.6 and 0.5 J/K cm^3 at 7 and 8.1 K, respectively). The authors related the peaks with magnetic ordering and magnetic structure transformations. The peak volumetric heat capacity values of ErGa_2 , PrGa_2 and NdGa_2 at the Néel temperatures of transition from paramagnetic to magnetically-ordered state (7 K, 7 K and 9 K) lay below 0.4 J/K cm^3 . The heat capacity of GdGa_2 monotonically increased with temperature in the investigated temperature range, consistent with its Néel temperature value of 22 K. TbGa_2 revealed the heat capacity peak of about 0.7 J/K cm^3 at the Néel temperature of 17 K. In $\text{Dy}_{1-x}\text{Ho}_x\text{Ga}_2$ the double-peak $C(T)$ curve structure characteristic for DyGa_2 and HoGa_2 compounds is suppressed for $x > 0.2$ and a broad plateau on the $C(T)$ curves appears in the magnetically ordered state (all $\text{Dy}_{1-x}\text{Ho}_x\text{Ga}_2$ alloys were ordered below 10 K). The magnetic entropy calculated from the heat capacity data for DyGa_2 and HoGa_2 compounds reached the values of $R \ln 5.9$ and $R \ln 6.1 \text{ J/mol K}$, respectively, at the Néel temperatures. This result points to the six-fold degeneracy of the ground state of RE ions in these compounds above T_N . The observed large heat capacity in DyGa_2 and HoGa_2 was related by the authors to lifting of this degeneracy upon the antiferromagnetic transition. Yagi *et al* (1998) also measured thermal conductivity of the DyGa_2 , which was found to increase from about $4 \times 10^{-3} \text{ W/K cm}$ at 5 K up to $1.1 \times 10^{-2} \text{ W/K cm}$ at 20 K. In connection with high heat capacity values in DyGa_2 , HoGa_2 and $\text{Dy}_{1-x}\text{Ho}_x\text{Ga}_2$ compounds, Yagi *et al* (1998) pointed to their possible use in low-temperature (below 10 K) regenerators.

Aoki *et al* (2000) undertook a systematic study of HoGa_2 single crystal in the magnetic fields up to 80 kOe applied along the [100] crystallographic axis. The magnetic structure of this compound is complex and determined by competition between RKKI-type exchange interactions and uniaxial magnetic anisotropy acting on the RE ion. With temperature decreasing, HoGa_2 undergoes a transition from paramagnetic to antiferromagnetic phase I_2 at $T_N = 7.6 \text{ K}$ and then to a second magnetic phase I_0 at $T_t = 6.5 \text{ K}$ (Aoki *et al* 2000). According to the neutron scattering experiments, phase I_0 is a simple collinear antiferromagnetic phase. Between T_N and T_t phases, I_0 and I_2 coexist. The easy magnetization axis in HoGa_2 is [100]. Magnetization isotherm $I(H)$ measured at 2 K display two magnetization jumps, at 20 and 26 kOe, indicating the presence of the intermediate magnetic phase I_1 and final transition to the ferromagnetic state. The heat capacity temperature dependences in HoGa_2 were measured in different magnetic fields directed along the [100] axis. On the zero field $C(T)$ curve, besides anomalies at T_N (inflection at 8.3 K) and T_t (sharp maximum at 6.6 K), an additional anomaly (wide maximum) was observed at $\sim 0.27 \text{ K}$. The latter was not influenced by the magnetic field and was attributed to

the nuclear Schottky contribution. Taking into account this Schottky contribution, the electronic ($\sim T$) and lattice ($\sim T^3$) heat capacity contributions, the authors singled out the magnetic heat capacity contribution, which had $T^{2.8}$ temperature dependence. The obtained exponent (2.8) is close to 3, which is typical of the spin wave excitations in a three-dimensional antiferromagnet (see section 2.11). The magnetic entropy calculated from the magnetic heat capacity temperature dependence was 13 J/mol K at T_N , which is lower than that for the Ho^{3+} ion (see table 6.2). At T_t a rapid increase on the $S_M(T)$ curve was observed, indicating a first-order character of this transition. The $S_M(T)$ curves calculated for nonzero magnetic fields lie above the zero field curve for the fields lower than 30 kOe for temperatures ~ 6 K. According to the magnetic phase diagram of HoGa_2 , this implies that magnetic entropy rises under application of the magnetic field in phases I_1 and I_2 . The MCE of the HoGa_2 single crystal was measured by Aoki *et al* (2000) directly, and magnetic entropy change ΔS_M was calculated on the basis of these data by integration of the equation

$$\left(\frac{\partial S}{\partial H} \right)_T = - \frac{C_{H,p}}{T} \left(\frac{dT}{dH} \right)_S \quad (6.2)$$

following from equation (2.14). The dT/dH and ΔS_M field dependences obtained at 3.5 and 1.5 K are shown in figure 6.10. As one can see, there are anomalies at the fields corresponding to the transitions between different

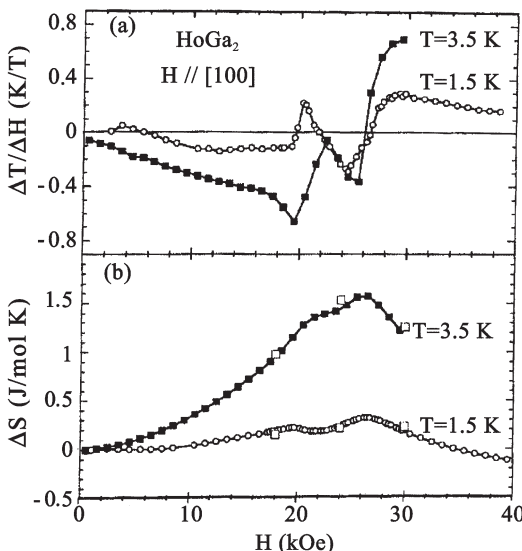


Figure 6.10. Magnetic field dependences of dT/dH and ΔS_M at 1.5 and 3.5 K in HoGa_2 single crystal for the magnetic field directed along the [100] axis (Aoki *et al* 2000). (Copyright 2000 by the American Physical Society.)

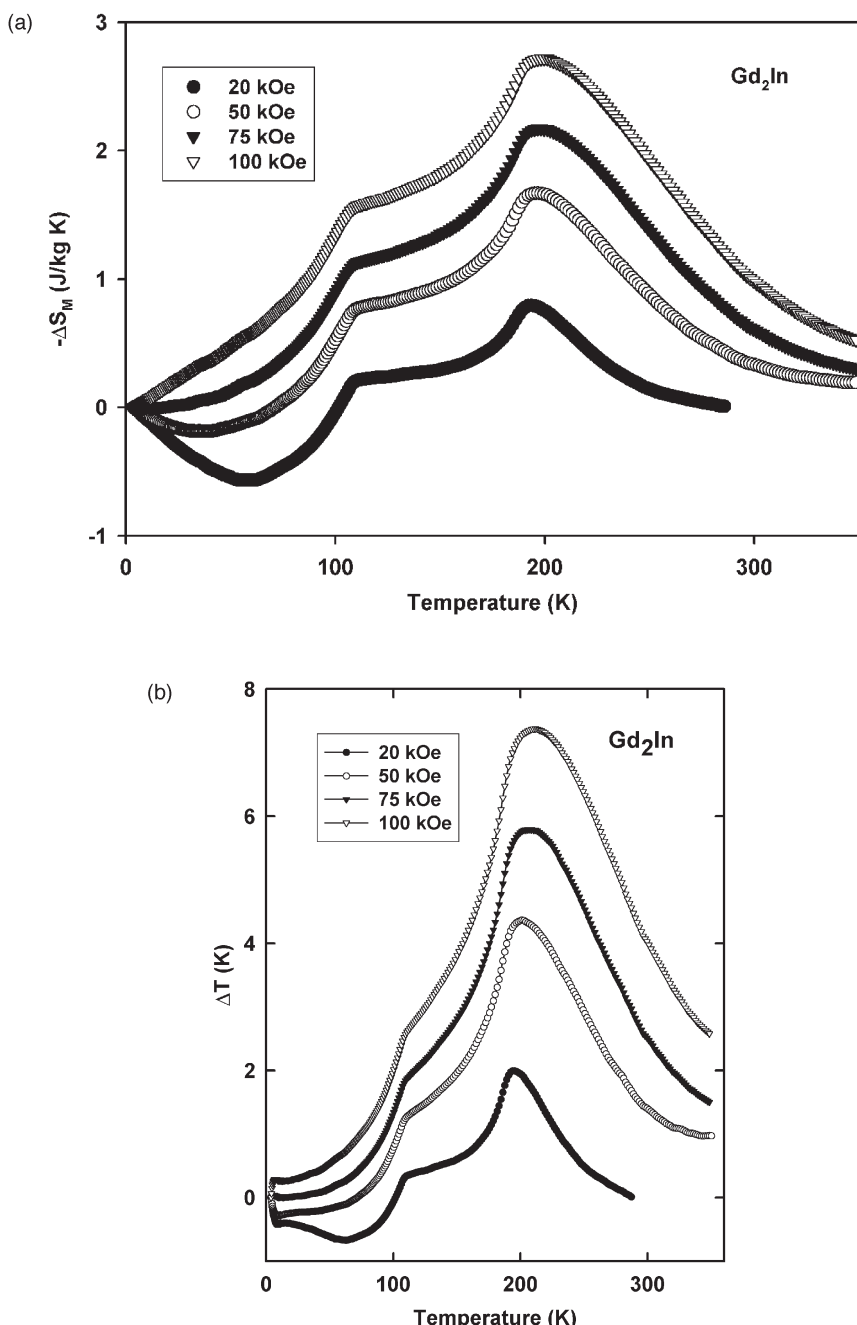


Figure 6.11. Temperature dependences (a) ΔS_M and (b) ΔT induced by different ΔH in Gd_2In (Ilyn *et al* 2001).

magnetic phases. Above 26 kOe, where the ferromagnetic state arises, dT/dH becomes positive. Magnetic entropy temperature dependence was also calculated with the help of a crystalline electric field model and was shown to be in reasonable agreement with the experiment.

Ilyn *et al* (2000, 2001) investigated heat capacity, magnetic entropy change and magnetocaloric effect in Gd_2In , which has a hexagonal Ni_2In -type crystal structure. According to the previous magnetization measurements this compound orders ferromagnetically below 109 K (from paramagnetic state) and then antiferromagnetically below 99.5 K (Gamari-Seale *et al* 1979, McAlister 1984, Jee *et al* 1996). It undergoes metamagnetic transition from antiferromagnetic to ferromagnetic structure in magnetic fields. McAlister (1984) suggested that antiferromagnetic structure is a spiral structure with an axis along the crystal c-axis. Magnetization measurements made by Ilyn *et al* (2000, 2001) showed that $T_C = 191$ K and $T_N = 91$ K. The critical field of metamagnetic transition reached its maximum of 8.4 kOe at 4.2 K and became zero at T_N . The heat capacity temperature dependence revealed two distinct anomalies—at T_C and T_N with the shape typical of second-order transitions. From the magnetization data the ΔS_M temperature dependences were obtained—see figure 6.11(a). $\Delta S_M(T)$ curves display two anomalies—at T_C and T_N and below T_N , ΔS_M became positive for fields less than 40 kOe, which can be related to the antiferromagnetic-type paraprocess in this temperature range. Analogous behaviour showed the MCE, determined from the heat capacity data—see figure 6.11(b). The values of ΔS_M and ΔT are presented in table 6.1.

6.2 Rare earth–nickel

In this section we consider the magnetothermal properties of R_3Ni , RNi , RNi_2 and RNi_5 compounds and some alloys based on them. According to the magnetic investigations, Ni in these compounds does not have a magnetic moment (Taylor and Darby 1972, Kirchmayer and Poldy 1978).

The heat capacity of RNi ($\text{R} = \text{Gd}, \text{Ho}, \text{Er}$) was measured by Sato *et al* (1990), Hashimoto *et al* (1990, 1992) and Zimm *et al* (1992). GdNi is a simple ferromagnet, while in HoNi and ErNi a noncollinear magnetic structure due to crystalline field effects arises. Heat capacity anomalies typical of ferromagnets were revealed at the Curie temperature T_C : 70 K for GdNi and 10 K for ErNi . The heat capacity temperature dependence of HoNi displayed an anomaly at the temperature of the spin-reorientation transition equal to 13 K ($T_C = 37$ K from the magnetic susceptibility measurements of Sato *et al* (1982)). The magnetic entropy in ErNi , determined by Sato *et al* (1990) from the heat capacity temperature dependences and equation (6.1) in the temperature interval from 0 to 15 K, was equal to 15 J/mol K. This is lower than the value calculated by equation (2.66) for the Er^{3+} ionic

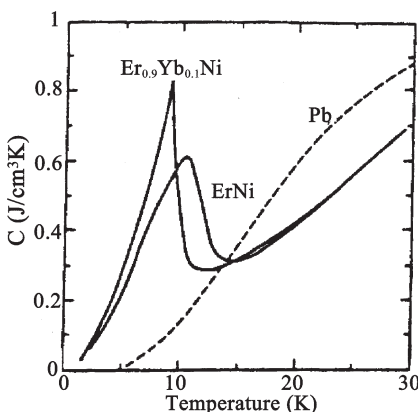


Figure 6.12. Heat capacity temperature dependences of ErNi , $\text{Er}_{0.9}\text{Yb}_{0.1}\text{Ni}$ and Pb (Hashimoto *et al* 1992).

state (see table 6.2). The authors attributed this difference to the crystalline field splitting of the Er ion ground state. The magnetic entropy due to the crystalline field effect was calculated by Sato *et al* (1990) on the basis of the point charge model to be 11 J/mol K at 15 K.

The heat capacity temperature dependences of ErNi and $\text{Er}_{0.9}\text{Yb}_{0.1}\text{Ni}$ measured by Hashimoto *et al* (1992) are presented in figure 6.12. Addition of Yb reduces the Curie temperature to about 4 K and increases the value of the heat capacity peak. The $C(T)$ curve for the lead metal is given for comparison—this material is usually used as a material for regenerators in cryocoolers. The question of using magnetic materials in regenerators in the low-temperature range will be discussed in section 11.1.

Zimm *et al* (1992) measured the temperature dependences of the MCE in GdNi_2 directly. A relatively sharp peak (with a height of 7.5 K for $\Delta H = 70$ kOe) was observed near T_C . Gschneidner *et al* (1996b) determined the MCE in GdNi_2 from the heat capacity. The peak value of 7.4 K was found near T_C for $\Delta H = 70$ kOe, which is in good agreement with the value of Zimm *et al* (1992).

The heat capacity of the Laves phase compounds RNi_2 ($\text{R} = \text{Pr}, \text{Gd}, \text{Tb}, \text{Dy}, \text{Ho}, \text{Er}$) and $(\text{RR}')\text{Ni}_2$ alloys was studied by Tomokiyo *et al* (1986), Yayama *et al* (1987), Hashimoto *et al* (1990, 1992), Melero *et al* (1995), Gschneidner *et al* (1996a) and Ranke *et al* (1998a). The Curie temperatures of these materials lie in the temperature range below 40 K (except GdNi_2)—see table 6.3. Melero *et al* (1995) measured the heat capacity of PrNi_2 , GdNi_2 and ErNi_2 in the temperature range from 2 to 300 K. The GdNi_2 compound revealed λ -type anomaly at 75.3 K with the magnetic entropy of the transition corresponding to $J = 7/2$ of the Gd ion. PrNi_2 did not demonstrate magnetic ordering down to 4 K. ErNi_2 showed a magnetic ordering

Table 6.3. The Curie temperatures (T_C), temperature of the maximum in the $\Delta T(T)$ curves (T_{\max}), magnetic entropy change ΔS_M near the Curie temperature induced by the magnetic field change ΔH , peak MCE value ΔT at $T = T_{\max}$ induced by ΔH , $\Delta T/\Delta H$ and $\Delta S_M/\Delta H$ of polycrystalline RE–Ni alloys. The values of S_M are in J/molR K.

Compound	T_C (K)	T_{\max} (K)	ΔT (K)	ΔH (kOe)	$\Delta T/\Delta H \times 10^2$ (K/kOe)	MCE peak		S_M		ΔS_M peak	
						Experimental value (J/molRK)	% of theoretical value	$-\Delta S_M$ (J/kg K)	ΔH (kOe)	$\Delta H \times 10^2$ (J/kg K kOe)	Ref.*
GdNi	70	70	7.5	70	10.7	—	—	—	—	—	1, 2
ErNi	10	—	—	—	—	15	65	—	—	—	3
GdNi ₂	75	75	5.9	70	8.4	—	—	—	—	—	1
			3.2	30	10.7	—	—	—	—	—	2
			74	5.8	70	8.3	—	—	—	—	4
				3.1 [†]	50	6.2	—	12.8 [†]	50	25.6	
TbNi ₂	37	38	11	75.3	14.6	12.1	56.3	—	14	70	5
DyNi ₂	20	—	8.1 [†]	50	16.2	—	62.9	—	—	—	6
			—	—	—	14.5	—	25.3 [†]	50	50.6	
			21	8.5	50	17	—	21.4	50	42.8	7
				4	20	20	—	10.7	20	53.5	8
HoNi ₂	13	—	—	13.8 [†]	50	27.6	—	—	—	—	5
ErNi ₂	6	—	—	—	—	14.9	64.6	—	24.2	50	48.4
	6.6	—	—	—	—	—	—	22.3	50	44.6	7
	8	8	8	50	16	—	—	—	20.4	50	40.8
				10.4 [†]	50	20.8	—	30.8 [†]	50	61.6	4
								—	—	—	6
								21.8 [†]	50	43.6	7

1. J. Zimm *et al.* (1992); 2. Gschneidner *et al.* (1996b); 3. Sato *et al.* (1990); 4. Von Ranke *et al.* (2001a); 5. Foldeaki *et al.* (1998a); 6. Gschneidner *et al.* (1996a); 7. Tomokyo *et al.* (1986); 8. Von Ranke *et al.* (1998a); 9. Gschneidner *et al.* (1994b); 10. Gschneidner *et al.* (1995); 11. Korte *et al.* (1998a); 12. Korte *et al.* (1998b); 13. Canepa *et al.* (1999).

Theoretical values.

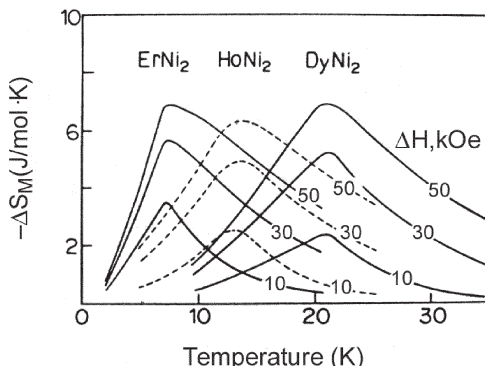


Figure 6.13. $\Delta S_M(T)$ curves for different ΔH for DyNi_2 , HoNi_2 and ErNi_2 (Tomokiyo *et al* 1986).

anomaly at 6.5 K. The magnetic contribution to the heat capacity was obtained by subtraction of the lattice heat capacity calculated on the basis of experimental LuNi_2 and LaNi_2 heat capacities. It was shown that PrNi_2 and ErNi_2 made an essential contribution to the heat capacity related to crystalline field effects.

The heat capacity measurements allowed Gschneidner *et al* (1996a) to determine the magnetic entropy S_M in compounds TbNi_2 , DyNi_2 and ErNi_2 —see table 6.3. As one can see from tables 6.2 and 6.3, in the Ni-based compounds approximately 60% of the theoretically available magnetic entropy is utilized in the magnetic ordering process, while in the Al-based compounds (RAI_2) this value is about 90%. The authors attributed this difference to the crystalline field effects. The results on ΔS_M of Tomokiyo *et al* (1986) are shown in figure 6.13. The $\Delta S_M(T)$ curves for DyNi_2 and ErNi_2 were evaluated from heat capacity, and that of HoNi_2 was obtained from the magnetization data.

Foldeaki *et al* (1998a) obtained $\Delta S_M(T)$ curves for GdNi_2 and DyNi_2 from magnetization measurements. The peak $-\Delta S_M(T)$ values at $T = T_C$ were obtained to be $\sim 28 \text{ J/kg K}$ for DyNi_2 and $\sim 14 \text{ J/kg K}$ for GdNi_2 at $\Delta H = 70 \text{ kOe}$. It is seen that ΔS_M in DyNi_2 is two times larger than in GdNi_2 . The low field (100 Oe) temperature dependence of the magnetic susceptibility in DyNi_2 showed irreversible behaviour—there was a substantial hysteresis for the field-cooled and zero-field-cooled curves. The Arrot plots of the DyNi_2 compound did not display linear sections in the temperature range from 5 to 50 K (T_C for DyNi_2 is 37 K). The authors related this behaviour to the complex nature of a magnetic transition at the Curie temperature and a noncollinear magnetic structure below T_C due to the presence of crystalline field effects. The irreversible magnetic behaviour was not observed in GdNi_2 . The temperature dependences of ΔT for GdNi_2 were obtained by a direct method by Zimm *et al* (1992) and for TbNi_2 from magnetization by

Gschneidner *et al* (1994b). MCE peaks were observed near T_C and the maximum ΔT values are presented in table 6.3. Yayama *et al* (1987) measured heat capacity temperature dependences of $\text{Er}_{0.5}\text{Dy}_{0.5}\text{Ni}_2$ and $\text{Er}_{0.75}\text{Dy}_{0.25}\text{Ni}_2$ alloys in various magnetic fields. It was found that the Curie temperature linearly decreased with a decrease in Er concentration (for $\text{Er}_{0.5}\text{Dy}_{0.5}\text{Ni}_2$, $T_C \approx 13.5\text{ K}$ and for $\text{Er}_{0.75}\text{Dy}_{0.25}\text{Ni}_2$, $T_C \approx 10.5\text{ K}$) and heat capacity had a λ -type anomaly near T_C . On the basis of the heat capacity data, $S(T)$ curves for these compounds were constructed.

Tishin *et al* (1990g) by means of MFA calculated the field dependences of magnetic entropy change $-\Delta S_M(H)$ (the magnetic field varied from 0 to H with a maximum magnetic field of 100 kOe) at $T = T_C$ for GdNi , GdNi_2 and GdNi_5 (as in GdNi and GdNi_2 , nickel in GdNi_5 is nonmagnetic). The nonlinear character of $-\Delta S_M(H)$ curves was found for H to be less than 50 kOe. At $H = 100\text{ kOe}$ the value of $-\Delta S_M$ was found to be about 12.5 J/kg K for GdNi , 6.2 J/kg K for GdNi_2 and 2.9 J/kg K for GdNi_5 .

Theoretical consideration of the MCE in RNi_2 ($\text{R} = \text{Pr}, \text{Nd}, \text{Gd}, \text{Tb}, \text{Ho}, \text{Er}$) single crystals was made by von Ranke *et al* (2001a). The calculations of the magnetic entropy $S_M(T)$ for the magnetic field applied along the easy magnetization axis ([111] crystal axis for TbNi_2 and [001] for others) were carried out using a Hamiltonian, taking into account the contributions from the crystalline electric field acting on the R ion and exchange interactions. The latter were regarded in the framework of three-dimensional mean field approximation. The total entropy was determined as a sum of magnetic, lattice and electronic contributions. The calculations were fulfilled on the basis of the proper model parameters found in the literature. From the obtained $S(T)$ curves at different magnetic fields the $\Delta T(T)$ and $\Delta S_M(T)$ curves were determined in the way described in section 3.2.2. The resultant curves are shown in figure 6.14. All the considered compounds are ferromagnets except PrNi_2 , which is paramagnetic in all temperature ranges. PrNi_5 displays a wide smooth maximum at about 18 K due to the Schottky anomaly related to the crystalline electric field splitting of Pr ion energy levels. Other investigated RNi_2 compounds had a caret-like maximum on $\Delta T(T)$ and $\Delta S_M(T)$ curves typical of ferromagnets. The theoretical results for ErNi_2 were compared with experimental data and good agreement was obtained in both magnetic entropy change and the MCE. The experimental $\Delta T(T)$ and $\Delta S_M(T)$ curves do not have sharp peaks, because the magnetic short range order effects above the Curie temperature smooth the magnetic order transition. There is a low-temperature anomaly (additional peak at ~ 1.5) on $\Delta T(T)$ and $\Delta S_M(T)$ curves of HoNi_2 . The authors showed that it arises due to the high density of states at the two lowest levels at low temperatures in HoNi_2 .

Analogous calculations were made by von Ranke *et al* (1998a) for polycrystalline DyNi_2 . In this case one-dimensional mean field approximation was used. The crystalline field parameters necessary for calculations were

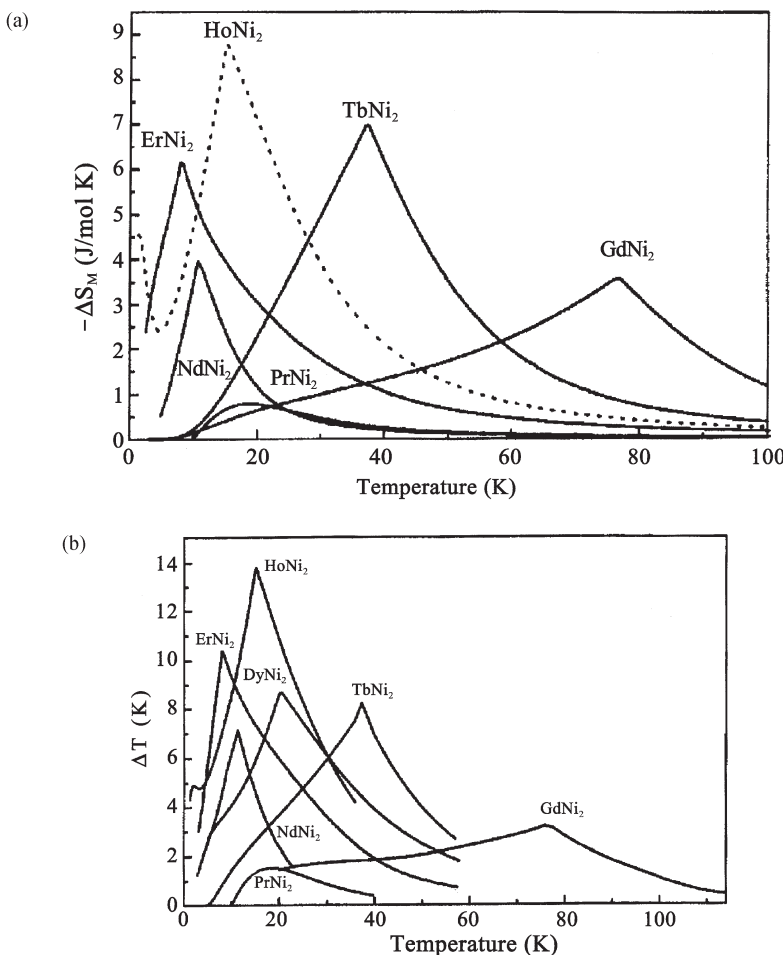


Figure 6.14. Calculated temperature dependences of (a) ΔS_M and (b) ΔT for RNi_2 compounds for $\Delta H = 50$ kOe. The magnetic field is supposed to be applied along the easy magnetization axis (von Ranke *et al* 2001a). (Copyright 2001 by the American Physical Society.)

determined by fitting of the experimental zero-field magnetic heat capacity temperature dependence to the theoretical one. This method provided good accordance between theoretical and experimental $\Delta T(T)$ and $\Delta S_M(T)$ curves.

It should be noted that RNi_2 compounds are characterized by rather high magnetic entropy change and magnetocaloric effect values. According to table 6.3, for example, the experimental absolute value of $\Delta S_M/\Delta H$ is 0.535 J/kg K kOe and $\Delta T/\Delta H$ is 0.2 K/kOe in $DyNi_2$ for $\Delta H = 20$ kOe, which is on the level of these parameters in Gd.

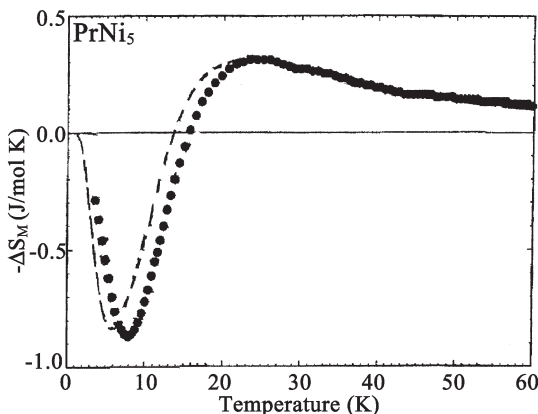


Figure 6.15. Experimental (●) and theoretical (—) temperature dependences of the $-\Delta S_M$ induced by the magnetic field change $\Delta H = 70$ kOe in polycrystalline PrNi₅ (von Ranke *et al* 1998b). (Copyright 1998 by the American Physical Society.)

An interesting magnetocaloric behaviour reveals PrNi₅. This compound, with a hexagonal crystal structure, is paramagnetic in the whole temperature range, and that is why its magnetic entropy should decrease under application of the magnetic field. However, in the temperature range below about 14 K von Ranke *et al* (1998b) found a region of positive ΔS_M on the $\Delta S_M(T)$ curve—see figure 6.15. The experimental ΔS_M values were obtained from the heat capacity measurements. The results were explained by the authors by crossover (see section 5.4) of lowest Γ_4 and Γ_1 energy levels of the Pr³⁺ ion caused by the effect of the magnetic field. The calculations of the magnetization and magnetic entropy were conducted in a way analogous to that discussed above for RNi₂ with Hamiltonian containing contributions from the crystalline electric field of hexagonal symmetry and the exchange interactions. The $\Delta S_M(T)$ curve calculated using the crystalline field parameters obtained from experimental inelastic neutron scattering measurements is shown in figure 6.15 by the broken line. One can see good agreement between the calculated and experimental curves. The magnetic entropy increase under intersection of the energy levels in crossover was reported by the authors, with an increase of the density of states and the number of available states of the magnetic system at this moment. The calculations showed that the crossover should take place at the magnetic field of 16 kOe at 0.3 K if the magnetic field is applied along the easy magnetization crystallographic a-axis.

The heat capacity of R₃Ni (R = Pr, Nd, Er) was investigated by Sahashi *et al* (1990), Hashimoto *et al* (1992), Tokai *et al* (1992), Hershberg *et al* (1994), Gschneidner *et al* (1995, 1997b) and Pecharsky *et al* (1997a). It was found that these compounds have substantial heat capacity values in the

low-temperature region that make them useful for application in low-temperature regenerators. The R_3Ni compounds investigated order anti-ferromagnetically and their ordering temperatures determined from $C(T)$ curves are listed in table 6.3. The total heat capacity peak at the ordering temperature is of the λ -type.

Especial attention was paid by investigators for Er_3Ni , because of its high heat capacity in the low-temperature region and the possibility of its application in low-temperature regenerators working in cryocoolers below 10 K—see section 11.1. This compound, according to magnetization measurements, undergoes a transition from the paramagnetic to the anti-ferromagnetic state at $T_N = 7.7$ K (Buschow 1968, 1977). The volumetric heat capacity temperature dependence of Er_3Ni has a broad maximum (the maximum value about $0.4 \text{ J/cm}^3 \text{ K}$) near ~ 7 K (the heat capacity of Pb at this temperature is about $0.02 \text{ J/cm}^3 \text{ K}$), and above 15 K its heat capacity becomes comparable with that of Pb (Sahashi *et al* 1990, Hashimoto *et al* 1992, Gschneidner *et al* 1995). Above T_N in Er_3Ni there is an additional Schottky heat capacity maximum that is superimposed on the magnetic ordering peak and which provides a wide heat capacity maximum below 10 K. These properties make Er_3Ni suitable for low-temperature regenerator applications.

A broad heat capacity peak was also observed in Pr_3Ni . Nd_3Ni revealed the sharp heat capacity peak with a height of about $0.7 \text{ J/cm}^3 \text{ K}$. The magnetic entropy of the R_3Ni compounds determined by Gschneidner *et al* (1995) from the heat capacity data are listed in table 6.3. They are in good agreement with the S_M value expected for a ground-state doublet of the Er ions ($J = 1/2$): $R \ln 2 = 5.77 \text{ J/mol K}$. This confirms the presence of strong crystalline field effects in the R_3Ni ($R = Pr, Nd, Er$) compounds.

Heat capacity temperature dependences of the polycrystalline alloys Er_6Ni_2Sn , Er_6Ni_2Pb and $Er_6Ni_2(Sn_{0.75}Ga_{0.25})$ display two maxima at ~ 8 and ~ 18 K (Gschneidner *et al* 1995). The value of heat capacity in these alloys was higher than in Pb below 18 K and higher than in Er_3Ni between 9 and 18 K. X-ray measurements showed that the samples consisted mainly of two phases, Er_6Ni_2X and Er_3Ni . The magnetic measurements revealed that Er_6Ni_2X phases ordered ferrimagnetically at about 18 K. So the high-temperature heat capacity peak can be connected to the Er_6Ni_2X phase and the low-temperature one to Er_3Ni . The influence of heat treatment on the heat capacity of the alloys was also studied by Gschneidner *et al* (1995). It was shown that the annealing at 700 K could essentially increase the height of the high-temperature heat capacity peak.

The influence of the addition of Ti on the Er_3Ni heat capacity properties was investigated by Pecharsky *et al* (1997a). It was shown that in as-cast alloys the effect of substitution of Ni by Ti (alloys $Er_3Ni_{0.98}Ti_{0.02}$ and $Er_3Ni_{0.90}Ti_{0.10}$ were considered) was minimal with a slight increase of magnetic ordering temperature and slight decrease of the heat capacity peak at

the ordering temperature. The addition of Ti allowed partly amorphous alloys to be obtained by the method of melt spinning. Although the heat capacity peak in the amorphous samples was lower than that in the as-cast alloys, its mechanical properties were much better for application in regenerators—the obtained foils were quite flexible.

Korte *et al* (1998a,b) undertook a complex study of the magnetic properties, heat capacity and MCE in $(\text{Gd}_{1-x}\text{Er}_x)\text{NiAl}$ pseudo-ternary alloys ($x = 0, 0.30, 0.46, 0.50, 0.55, 0.60, 0.80, 1.00$). All these alloys have the ZrNiAl-type crystalline structure. From the specific heat and magnetic susceptibility measurements it was shown that ErNiAl orders antiferromagnetically at 6 K. The heat capacity temperature dependences of the other alloys revealed a series of peaks (for example, $(\text{Gd}_{0.54}\text{Er}_{0.46})\text{NiAl}$ at $T = 23, 28 and 58 K). The authors related the low-temperature heat capacity anomalies to antiferromagnetic transitions and the upper anomalies to ferromagnetic ordering. Magnetic susceptibility measurements confirmed these suppositions. The lowest (T_l) and highest (T_h) magnetic ordering temperatures determined from the heat capacity measurements (for $(\text{Gd}_{0.2}\text{Er}_{0.8})\text{NiAl}$ alloy from the a.c. susceptibility data) are shown in table 6.3. The $\Delta S_M(T)$ curves (measured for $\Delta H = 50$ kOe) of ErNiAl and $(\text{Gd}_{0.2}\text{Er}_{0.8})\text{NiAl}$ have single peaks near the antiferromagnetic ordering temperatures. In Gd-rich alloys a broad maximum due to the remaining contribution from the low-temperature antiferromagnetic ordering process was observed. The MCE temperature dependences display analogous behaviour—see figure 6.16. $(\text{Gd}_{0.54}\text{Er}_{0.46})\text{NiAl}$ has a wide temperature range with almost flat ('table-like') $\Delta S_M(T)$ and $\Delta T(T)$ behaviour. The authors related this to the existence of multiple-ordering processes with entropy changes comparable in magnitude to both AFM and FM transitions. Analogous $\Delta S_M(T)$ and $\Delta T(T)$ curves were observed for the alloys with $x = 0.3$ and 0 . The full width of the $\Delta T(T)$ curve at half maximum in GdNiAl is about 65 K for $\Delta H = 50$ kOe. Comparison of the maximum values of ΔS_M and ΔT for $(\text{Gd}_{0.54}\text{Er}_{0.46})\text{NiAl}$, $(\text{Dy}_{0.25}\text{Er}_{0.75})\text{Al}_2$ and $(\text{Dy}_{0.40}\text{Er}_{0.60})\text{Al}_2$ alloys showed that although the values of ΔS_M in these three materials are comparable, the $\Delta T(T_{\max})$ value is larger in the $(\text{RR}')\text{Al}_2$ alloys. This is connected to the large contribution of lattice heat capacity in RNiAl compounds.$

The MCE and magnetic entropy changes in GdNiGa and GdNiIn intermetallic compounds were determined from the heat capacity data by Canepa *et al* (1999). These two compounds order ferromagnetically at 30.5 K (GdNiGa) and 93.5 K (GdNiIn). The peak of $\Delta S_M(T)$ and $\Delta T(T)$ dependences (sharp in GdNiGa and wide and rounded in GdNiIn) was observed near the Curie temperature. The peak values of ΔS_M and ΔT are shown in table 6.3.

Long *et al* (1995a) studied heat capacity temperature dependences of RNiGe (R=Gd, Dy, Er) compounds in the temperature range from 2 to 40 K. These compounds have orthorhombic TiNiSi-type crystal structure

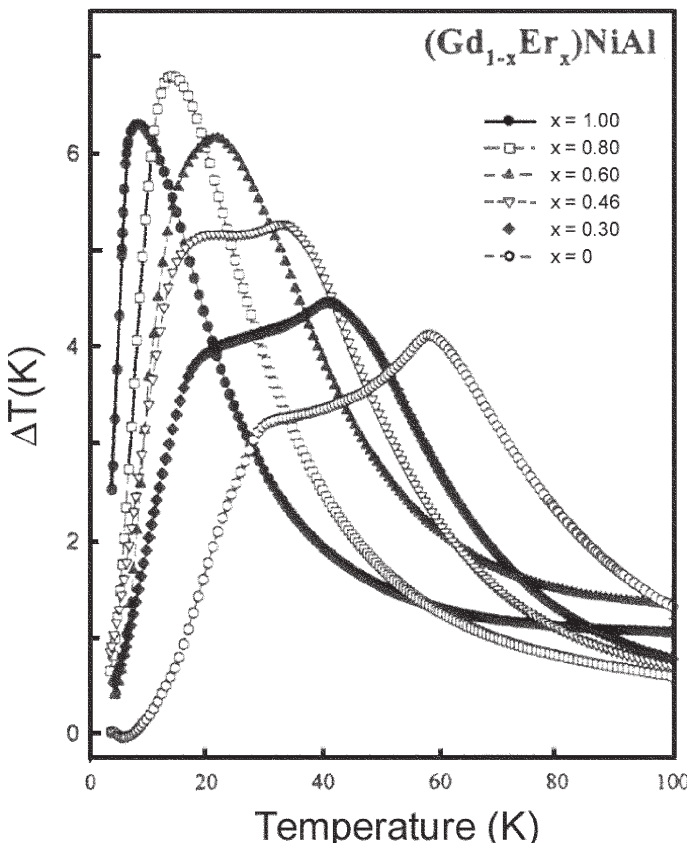


Figure 6.16. Temperature dependences of the MCE induced by $\Delta H = 50$ kOe in the $(\text{Gd}_{1-x}\text{Er}_x)\text{NiAl}$ alloy system (Korte *et al* 1998a).

and are antiferromagnetic below 20 K. As in RNi compounds, Ni here is nonmagnetic. The heat capacity displayed λ -type peaks near T_N , which were found to be 3.3, 7.4 and 10.7 K for R = Er, Dy and Gd, respectively. The heat capacity peak value of about 17 J/mol K was observed in ErNiGe, which had the smallest T_N among the investigated compounds. The magnetic heat capacity was obtained by subtracting the lattice heat capacity. In ErNiGe and DyNiGe compounds the large magnetic heat capacity was also observed above T_N , which was reported by the authors with crystal field effects. The Schottky-type maximum was observed in ErNiGe near 30 K.

The thermal conductivity of polycrystalline Er_3Ni , ErNi , ErNi_2 and DyNi_2 was investigated by Hashimoto *et al* (1990) and Ogawa *et al* (1991). The thermal conductivity of these compounds has a general trend to decrease

with decreasing temperature and changed in the temperature interval between 3 and 50 K in the range from ~ 0.03 to ~ 0.08 W/K cm. Near the transition from paramagnetic to magnetically ordered state there are slight anomalies on the temperature dependences of thermal conductivities of these compounds. Some numerical values of the thermal conductivity for Er_3Ni , ErNi , ErNi_2 and DyNi_2 are presented in table A2.1 in appendix 2.

6.3 Rare earth–iron

6.3.1 RFe_2 , RFe_3 and R_2Fe_{17} compounds

Nikitin *et al* (1973, 1975) measured the MCE in the intermetallic compounds RFe_2 ($\text{R} = \text{Tb}, \text{Er}, \text{Y}$), RFe_3 ($\text{R} = \text{Ho}, \text{Y}$) and $\text{Tb}_x\text{Y}_{1-x}\text{Fe}_2$ ($x = 0, 0.2, 0.33, 0.45, 0.8, 1.0$) alloys by a direct method in the temperature interval from 80 to 700 K. YFe_2 and YFe_3 have only one magnetic sublattice and display $\Delta T(T)$ behaviour typical of a simple ferromagnet with one maximum near the Curie temperature T_C . ErFe_2 and HoFe_3 are ferrimagnets with two magnetic sublattices and compensation temperature T_{comp} of 490 and 389 K, respectively. Their $\Delta T(T)$ have a form analogous to that observed in gadolinium iron garnet: with increasing temperature the MCE suddenly changes its sign from positive to negative near T_{comp} : compare figure 5.1 (for example, the curve for $\text{Gd}_3\text{Fe}_5\text{O}_{12}$) and figure 6.17, where $\Delta T(T)$ curves for YFe_3 and

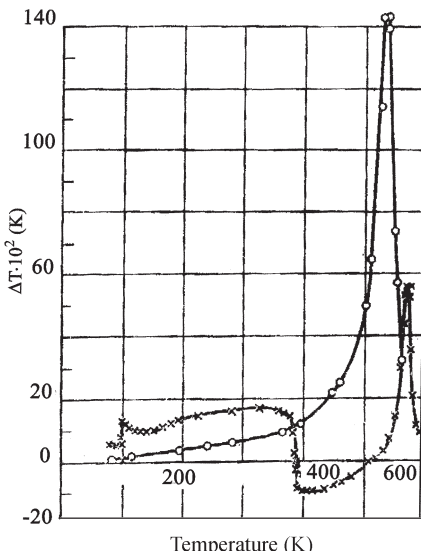


Figure 6.17. Temperature dependences of the MCE induced by $\Delta H = 15.8$ kOe in YFe_3 (○) and HoFe_3 (×) (Nikitin *et al* 1973).

Table 6.4. The Curie temperatures (T_C), temperature of the maximum in the $\Delta T(T)$ curves (T_{\max}), magnetic entropy change ΔS_M near the Curie temperature induced by the magnetic field change ΔH , peak MCE value ΔT at $T = T_{\max}$ induced by ΔH , $\Delta T/\Delta H$ and $\Delta S_M/\Delta H$ of polycrystalline RE–Fe alloys.

Compound	T_C (K)	MCE peak			ΔS_M peak			Ref.*
		T_{\max} (K)	ΔT (K)	ΔH (kOe)	$\Delta T/\Delta H \times 10^2$ (K/kOe)	$-\Delta S_M$ (J/kg K)	ΔH (kOe)	
YFe ₃	535	1.4	15.8	8.9	—	—	—	1, 2
HoFe ₃	567	0.55	15.8	3.5	—	—	—	2, 3
YFe ₂	535	1.25	15.8	7.9	—	—	—	4
Tb _{0.2} Y _{0.8} Fe ₂	570	0.7	15.8	4.4	—	—	—	4
Tb _{0.33} Y _{0.67} Fe ₂	596	0.4	15.8	2.5	—	—	—	4
Tb _{0.45} Y _{0.55} Fe ₂	610	0.25	15.8	1.6	—	—	—	4
Tb _{0.8} Y _{0.2} Fe ₂	670	0.5	15.8	3.2	—	—	—	4
TbFe ₂	695	0.75	15.8	4.7	—	—	—	4
ErFe ₂	575	0.2	15.8	1.3	—	—	—	2
Y ₂ Fe ₁₇ (as cast)	307	305	2.35	20	11.8	5	50	10
Y ₂ Fe ₁₇ (annealed)	303	303	1.9	50	3.8	3.8	20	19
Y ₂ Fe ₁₇ (quenched)	303	303	2.6	50	3.8	3.2	50	6.4
Lu ₂ Fe ₁₇ (annealed)	264	263	0.94	20	4.7	4	50	5
Lu ₂ Fe ₁₇ (quenched)	263	262	2.7	50	5.4	1.5	20	7.5
Y ₂ Fe _{17.1} (quenched)	306	320	0.6	20	1	1	20	5
Nd ₂ Fe ₁₇	320	325	3.1	50	6.2	5.1	50	10.2
La(Fe _{0.98} Co _{0.02}) _{11.7} Al _{1.3}	198	—	1.4	20	—	2.4	20	12
La(Fe _{0.94} Co _{0.06}) _{11.83} Al _{1.17}	273	—	4	50	8	6	50	12

* 1. Kirchmayer and Poldy (1978); 2. Nikitin *et al.* (1975); 3. Taylor and Darby (1972); 4. Nikitin *et al.* (1998); 5. Ivchenko (1998); 6. Danikov *et al.* (2000); 7. Hu *et al.* (2000b); 8. Hu *et al.* (2001a); 9. Zhang *et al.* (2000b); 10. Hu *et al.* (2001b); 11. Hu *et al.* (2003); 12. Hu *et al.* (2002a); 13. Hu *et al.* (2001c); 14. Hu *et al.* (2002b); 15. Wen *et al.* (2002); 16. Fujieda *et al.* (2002).

HoFe_3 are shown. This MCE sign change is related to change of RE (and Fe) sublattice magnetic moment direction relative to the external magnetic field. Below T_{comp} the RE moment is directed along the magnetic field vector and above T_{comp} the reverse situation takes place. Since the paraprocess in RE magnetic sublattice in the low-temperature range is higher than that in the Fe sublattice, and it has antiferromagnetic character above T_{comp} , there is a temperature range with negative MCE on the $\Delta T(T)$ curve above T_{comp} .

The estimations made from MCE and Curie point data by means of MFA (Nikitin and Bisliev 1974) showed that the effective field $H_{2\text{eff}}$ acting in the RE sublattice is about 1.6×10^6 Oe in ErFe_2 and about 10^6 Oe in HoFe_3 (Nikitin *et al* 1973). This is considerably higher than $H_{2\text{eff}}$ in rare earth iron garnets ($\sim 3 \times 10^5$ Oe) and leads to a weaker paraprocess in the RE magnetic sublattice as compared with the garnets and to the MCE temperature behaviour analogous with that observed in the $\text{Li}_2\text{Fe}_5\text{Cr}_5\text{O}_{16}$ spinel below T_{comp} (see figure 5.26)—without the MCE peak in the low-temperature region. In $\text{Tb}_x\text{Y}_{1-x}\text{Fe}_2$ alloys the compensation behaviour of the MCE was observed for $x = 0.33$ and 0.45 . For the other compounds only one maximum near T_C was observed in the $\Delta T(T)$ curves. The peak values of MCE near T_C for the RFe_2 and RFe_3 compounds and $\text{Tb}_x\text{Y}_{1-x}\text{Fe}_2$ alloys investigated by Nikitin *et al* (1973, 1975) are presented in table 6.4. The maximum MCE peak values in the system $\text{Tb}_x\text{Y}_{1-x}\text{Fe}_2$ were observed in YFe_2 and this decreased with Tb concentration increasing. The minimum MCE peak value among $\text{Tb}_x\text{Y}_{1-x}\text{Fe}_2$ alloys was found when $x = 0.5$ (see table 6.4), where T_{comp} coincided with T_C .

Jin *et al* (1991) studied the MCE in as-cast $\text{R}_x\text{Ce}_{2-x}\text{Fe}_{17}$ ($\text{R} = \text{Y}$ or Pr and $x = 0\text{--}2$) by a direct method at room temperature. The Curie temperature of Y_2Fe_{17} is 320 K (Nikitin *et al* 1991a), and that of $\text{Ce}_2\text{Fe}_{17}$ and $\text{Pr}_2\text{Fe}_{17}$ are 270 and 278 K, respectively (Kirchmayr and Poldy 1978). The maxima of the measured (in arbitrary units) MCE for $\Delta H = 8$ kOe were observed at $x = 1.2$ in the $\text{Y}_x\text{Ce}_{2-x}\text{Fe}_{17}$ system and $x = 1.3$ in the $\text{Pr}_x\text{Ce}_{2-x}\text{Fe}_{17}$ system. This implies that the samples with such compositions have T_C near room temperature. Annealing of the samples at 800–1000 °C for several hours had no effect on ΔT in $\text{Y}_x\text{Ce}_{2-x}\text{Fe}_{17}$ alloys and led to its doubling for $x = 1.3$ in $\text{Pr}_x\text{Ce}_{2-x}\text{Fe}_{17}$ alloys. It is stated that the MCE value obtained in the annealed $\text{Pr}_{1.3}\text{Ce}_{1.7}\text{Fe}_{17}$ is one-half of the peak MCE value in Gd, used by the authors as a calibrating material. The strong heat treatment influence on the MCE properties of the $\text{Pr}_x\text{Ce}_{2-x}\text{Fe}_{17}$ system is related to the peculiarities of the Pr–Fe phase diagram, according to which the annealing is necessary to form the $\text{Pr}_2\text{Fe}_{17}$ phase.

Ivtchenko (1998) studied the MCE properties of stoichiometric Y_2Fe_{17} and $\text{Lu}_2\text{Fe}_{17}$ compounds, nonstoichiometric $\text{Y}_{16.9}\text{Fe}_2$ and $\text{Y}_{17.1}\text{Fe}_2$ compositions and the effect of heat treatment on them. The magnetic entropy change, MCE, heat capacity and magnetization were measured on as-cast samples, annealed at 940 °C for 15 days, and slowly cooled down to room temperature

and annealed and quenched in water at 0 °C. R_2Fe_{17} compounds (with R being a heavy rare earth from Tb to Lu or Y) have a hexagonal Th_2Ni_{17} -type structure. According to the neutronographic data, Y_2Fe_{17} has a collinear ferromagnetic structure, magnetic moments of Fe ions being parallel to the basal plane (Givord and Lemaire 1974). Investigations of the magnetic properties of Y_2Fe_{17} also revealed typically ferromagnetic behaviour with a Curie temperature lying between 302.5 and 324 K (Strnat *et al* 1966, Pszczola and Krop 1986, Andreenko *et al* 1991, Nikitin *et al* 1991a).

The heat capacity measurements were made by Ivchenko (1998) on three Y_2Fe_{17} samples: as-cast (sample Y_2Fe_{17} N 1), annealed at 940 °C for 15 days and slowly cooled down to room temperature (sample Y_2Fe_{17} N 2) and annealed at 940 °C for 15 days and quenched in water at 0 °C (sample Y_2Fe_{17} N 3). It should be noted that as-cast Y_2Fe_{17} was found to contain two crystalline phases: hexagonal with Th_2Ni_{17} -type structure and rhombohedral with Th_2Zn_{17} -type structure, and the samples Y_2Fe_{17} N 2 and N 3 had the main crystal phase with hexagonal Th_2Ni_{17} -type structure. The zero field heat capacity temperature dependences of these three samples are shown in figure 6.18. They demonstrate behaviour typical of ferromagnets with a

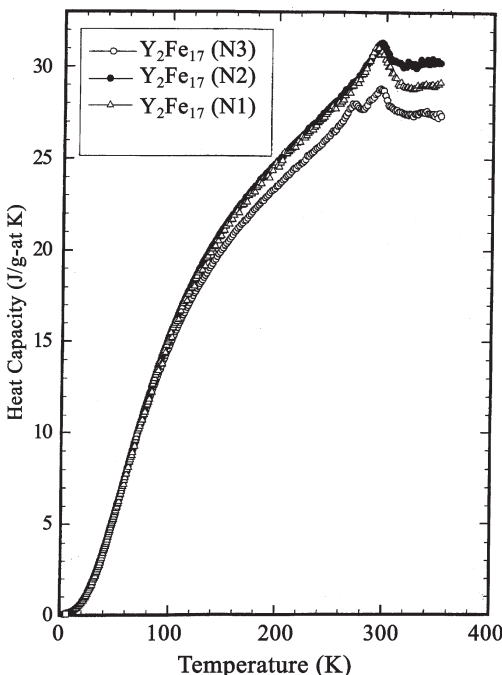


Figure 6.18. Zero-field heat capacity temperature dependences for as-cast Y_2Fe_{17} (sample N 1), Y_2Fe_{17} annealed at 940 °C for 15 days and slowly cooled down to room temperature (sample N 2), and Y_2Fe_{17} annealed at 940 °C for 15 days and quenched in water at 0 °C (sample N 3) (Ivchenko 1998).

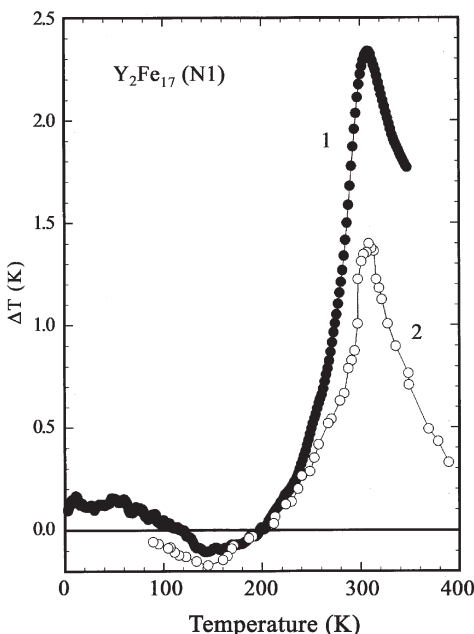


Figure 6.19. Temperature dependences of the MCE induced by $\Delta H = 20$ kOe in the as-cast Y_2Fe_{17} (sample N 1) determined from heat capacity measurements (curve 1) and by a direct method (curve 2) (Ivtchenko 1998).

heat capacity maximum at 291 K for the as-cast sample and 294 K for sample N 2. The quenched sample N 3 displayed two heat capacity maxima, at 273 and 295 K. It is interesting that they disappeared after the sample was held in normal conditions for two months and in this case only one maximum, at 291 K, was observed.

Figure 6.19 shows temperature dependences of the MCE induced by $\Delta H = 20$ kOe in the as-cast Y_2Fe_{17} determined from heat capacity measurements and by a direct method. The $\Delta T(T)$ curves display a maximum near the Curie temperature (at ~ 305 K). There is also a region of negative ΔT values between about 115 and 200 K on both curves. Analogous behaviour (with a positive ΔS_M region) had $\Delta S_M(T)$ curves. The presence of this region can be related to the existence of some kind of noncollinear or antiferromagnetic structure in this temperature range due to mechanical strains in the sample. Earlier, a new magnetic phase in Y_2Fe_{17} under hydrostatic pressure was indicated by Nikitin *et al* (1991a) on the basis of magnetic measurements. There were also anomalies (inflections) on the temperature dependences of a.c. magnetic susceptibility of the as-cast Y_2Fe_{17} sample at about 120 K. The positive region of ΔS_M between 115 and 200 K in the as-cast Y_2Fe_{17} disappeared for ΔH above 30 kOe, although the nonmonotonic

character of the $\Delta S_M(T)$ curve in this temperature range was preserved up to $\Delta H = 50$ kOe.

On the $\Delta T(T)$ and $\Delta S_M(T)$ curves of the annealed Y_2Fe_{17} samples the anomalies described above were not observed. The heat treatment also decreased the peak $-\Delta S_M$ value in Y_2Fe_{17} samples, although it had a minor influence on the Curie temperature. The Curie temperatures (determined from the heat capacity measurements) of the nonstoichiometric $Y_{16.9}Fe_2$ and $Y_{17.1}Fe_2$ compositions were almost the same as in the investigated Y_2Fe_{17} samples. The influence of violation of stoichiometry on the heat capacity, magnetic entropy and the MCE in Y_2Fe_{17} was not significant.

Neutronographic investigations of the magnetic structures of R_2Fe_{17} compounds made by Givord and Lemaire (1974) led to the conclusion that when the rare earth ion radius is small enough (e.g. Ce^{4+} , Tm^{3+} , Lu^{3+}) helimagnetic phases can occur. At low temperatures the stated compounds show transitions either to a fun or to a collinear ferrimagnetic order. In particular, a neutronographic study of Lu_2Fe_{17} showed that at $T_N = 270$ K this compound displayed a transition from paramagnetic to helicoidal anti-ferromagnetic structure, which at 210 K transformed into a fun structure (Gignoux *et al* 1979). The maximum critical field in the range of temperatures from 210 to T_N was 2 kOe at 200 K.

However, the heat capacity measurements of Ivchenko (1998) on Lu_2Fe_{17} did not reveal any anomalies at 210 K—only a weakly pronounced anomaly at 264 K related to the transition from paramagnetic to magnetically ordered state was observed. There were also no negative ΔT or positive ΔS_M temperature ranges on the $\Delta T(T)$ or $\Delta S_M(T)$ curves determined from the heat capacity for positive $\Delta H = 20$ kOe, which had typical ferromagnetic behaviour with a maximum near the magnetic transition point. The results of measurements made on the samples annealed and quenched by the scheme described above for Y_2Fe_{17} are presented in table 6.4. Figure 6.20 summarizes the results on $\Delta S_M(T)$ and $\Delta T(T)$ dependences for $\Delta H = 20$ kOe obtained near the magnetic ordering transitions for Y_2Fe_{17} and Lu_2Fe_{17} compounds by Ivchenko (1998).

The heat capacity and MCE in Nd_2Fe_{17} were investigated by Dan'kov *et al* (2000). The zero-field heat capacity temperature dependence has a λ -type anomaly near 320 K. The $\Delta S_M(T)$ and $\Delta T(T)$ curves determined from the heat capacity show typical ferromagnet maxima near the Curie temperature. The peak values of ΔS_M and ΔT are shown in table 6.4.

Magnetic entropy and heat capacity of $Ce(Fe_{1-x}Co_x)_2$ ($x = 0\text{--}0.3$) alloys were studied by Wada *et al* (1993). The Laves-phase compound $CeFe_2$ is an example of a system which is intermediate between localized and itinerant ferromagnetism. The magnetic measurements showed that $CeFe_2$ is a ferromagnet with $T_C = 230$ K and the magnetic moment per iron atom of about $1.15 \mu_B$, which is lower than for other RFe_2 compounds (Deportes *et al* 1981). The paramagnetic iron moment in $CeFe_2$ was found

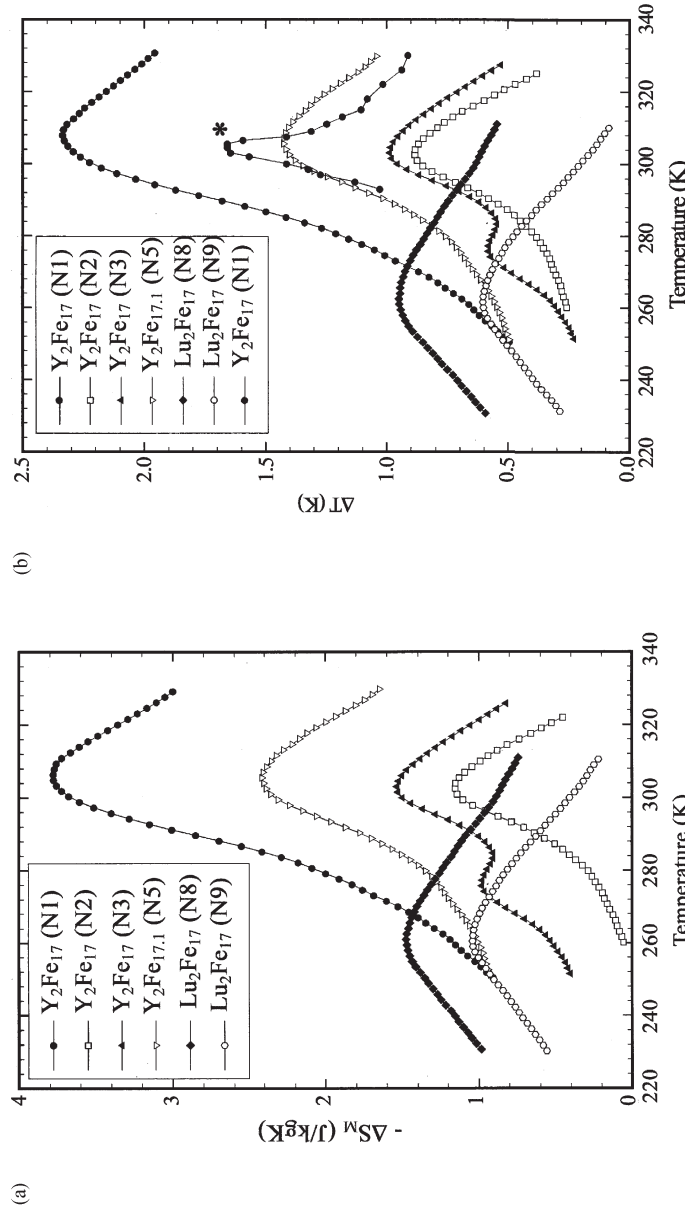


Figure 6.20. Temperature dependences of (a) ΔS_M and (b) ΔT induced by $\Delta H = 20$ kOe in the as-cast Y_2Fe_{17} (sample N1), Y_2Fe_{17} annealed at 940 °C for 15 days and slowly cooled down to room temperature (sample N2), Y_2Fe_{17} quenched after annealing in water at 0 °C (sample N3), quenched after the annealing nonstoichiometric $Y_{17.1}Fe_2$ (sample N5), annealed and quenched after annealing Lu_2Fe_{17} —samples N8 and N9, respectively determined from the heat capacity measurements. The curve marked by (*) in (b) is measured by a direct method (Ivchenko 1998).

from inelastic neutron scattering experiments to be $0.5 \mu_B$ at 300 K (Lindley *et al* 1988). Such a small magnetic moment in CeFe_2 was attributed to substantial hybridization of the iron 3d states with the 4f band states of Ce (Eriksson *et al* 1988). The substitution of a small amount of Co ($0.04 < x < 0.3$) to CeFe_2 caused the appearance of an antiferromagnetic phase at the temperature of AFM–FM phase transition $T_{\text{AFM–FM}}$. Lattice parameter and electrical resistivity temperature dependence measurements showed that the transition at $T_{\text{AFM–FM}}$ was first-order. Magnetization on magnetic field measurements made on the alloys with $x = 0.1$ and 0.2 at 4.2 K in the fields up to 250 kOe revealed a metamagnetic transition at about 80 kOe with a considerable field hysteresis. The compounds with $x = 0$ and $x \geq 0.3$ had typical ferromagnetic behaviour.

Heat capacity temperature dependence measurements carried out on CeFe_2 , $\text{Ce}(\text{Fe}_{0.9}\text{Co}_{0.1})_2$, $\text{Ce}(\text{Fe}_{0.8}\text{Co}_{0.2})_2$ and $\text{Ce}(\text{Fe}_{0.7}\text{Co}_{0.3})_2$ found anomalies at the Curie temperatures of 227, 180, 162, and 156 K, respectively. In the $\text{Ce}(\text{Fe}_{0.9}\text{Co}_{0.1})_2$ alloy an additional sharp heat capacity peak was observed at $T_{\text{AFM–FM}} = 80$ K. A less pronounced heat capacity anomaly at $T_{\text{AFM–FM}} = 68$ K was also found in $\text{Ce}(\text{Fe}_{0.8}\text{Co}_{0.2})_2$. Wada *et al* (1993) calculated the temperature dependences of the magnetic entropy S_M of the $\text{Ce}(\text{Fe}_{1-x}\text{Co}_x)_2$ system for $x = 0, 0.1, 0.2$ and 0.3 using equation (6.1) and the heat capacity data. The data on paramagnetic CeCo_2 were used to evaluate the lattice and electronic contributions to the heat capacity near the transition from the paramagnetic to the ferromagnetic state. For CeFe_2 , S_M started to increase at temperatures above 100 K and above T_C it reached a saturation value of 2.5 J/mol K . The same result (but with a saturation S_M value of about 1 J/mol K) was obtained for $x = 0.3$. According to equation (2.66), which is valid for systems with localized magnetic moments, the magnetic entropy for a system including two iron atoms ($J = 1/2$) should be equal to 11.5 J/mol K . This value is inconsistent with that observed for CeFe_2 of 2.5 J/mol K , which points to the intermediate character of magnetism in CeFe_2 .

More complicated behaviour was shown by the $S_M(T)$ curves of the samples with $x = 0.1$ and 0.2 . At $T = T_{\text{AFM–FM}}$ an entropy jump $\Delta S_{\text{AFM–FM}}$ ($\Delta S_{\text{AFM–FM}} = 1.2$ and 0.8 for $x = 0.1$ and 0.2 , respectively) was observed with a subsequent gradual rise to the saturation S_M values of 2.3 J/mol K for $x = 0.1$ and 1.5 J/mol K for $x = 0.2$ above the Curie temperature. Because it is difficult to separate the magnetic entropy contribution in the compositions with $x = 0.1$ and 0.2 at the AFM–FM magnetic phase transition in the usual way, the magnetic entropy change at the $\Delta S_{\text{AFM–FM}}$ transition was considered by the authors as consisting of the following three contributions: the entropy change due to a difference in the degree of magnetic order in antiferromagnetic and ferromagnetic states, the lattice entropy change and the electronic entropy change. It was shown that the first two contributions in the alloys under consideration were close to zero.

The main contribution to the entropy jump at the AFM–FM transition was due to the electronic entropy change, which arose from the difference between the values of the electronic heat capacity coefficient a_e in ferromagnetic and antiferromagnetic states (see equation (2.60)): 50 and 36.6 mJ/mol K², respectively for $x = 0.1$.

6.3.2 LaFe₁₃ compounds

Among RM₁₃ (R = rare earth element, M = 3d transition metal Fe, Co, Ni) binary compounds with cubic NaZn₁₃-type crystal structure there is only one stable composition, LaCo₁₃, which has a Curie temperature of 1318 K (Buschow 1977). Although the compounds LaFe₁₃ or LaNi₁₃ do not exist, a small amount of Al or Si can stabilize the structure forming the pseudo-binary compounds La(M_{1-x}M'_x)₁₃ (M = Fe, Ni; M' = Si, Al) (Kripyakevich *et al* 1968). Magnetic investigations of these systems were made by Palstra *et al* (1983, 1985), Helmhold *et al* (1986), Tang *et al* (1994), Fujita and Fukamichi (1999) and Fujita *et al* (1999). According to the results obtained, the Curie temperatures of the alloys lie near room temperature or below it. La(Fe_xAl_{1-x})₁₃ alloys with NaZn₁₃-type crystal structure exist for $0.46 \leq x \leq 0.92$ and exhibit mictomagnetic, ferromagnetic and antiferromagnetic ordering with variation of x . For iron concentration $0.62 \leq x \leq 0.86$ the ground magnetic state in the La(Fe_xAl_{1-x})₁₃ system is ferromagnetic and for $0.88 \leq x \leq 0.92$ it is antiferromagnetic. Hu *et al* (2000b, 2001a) found that partial substitution of Fe by Co in this concentration range completely destroys antiferromagnetic ordering and the alloys are ordered ferromagnetically.

Fujita and Fukamichi (1999) and Fujita *et al* (1999) stated that La(Fe_xSi_{1-x})₁₃ alloys are ferromagnetic in the concentration range $0.81 \leq x \leq 0.89$. They display behaviour similar to that observed in Invar and itinerant electron magnetic compounds. In particular, the saturation magnetic moment increased with increasing Fe concentration and the Curie temperature decreased. In the alloys with $x = 0.86$ and 0.88 ($T_C = 207$ and 195 K, respectively) a metamagnetic transition in the paramagnetic temperature region was observed, which the authors identified as the first-order transition from the paramagnetic to the ferromagnetic state. X-ray investigations showed a discontinuous crystalline lattice volume decrease of about 1.2% at the transition from ferromagnetic to paramagnetic state at the Curie temperature in the alloy with $x = 0.88$. Large lattice volume change induced by a magnetic field was observed from thermal expansion measurements in both alloys investigated (in the field of 90 kOe it was 0.9% in La(Fe_{0.86}Si_{0.14})₁₃ and 1.5% in La(Fe_{0.88}Si_{0.12})₁₃). The authors attributed the observed effects to first-order transitions with an itinerant electron nature, analogous to that in compounds based on LuCo₂ and YCo₂ Laves phases.

The magnetic entropy change in $\text{La}(\text{Fe}_{0.98}\text{Co}_{0.02})_{11.7}\text{Al}_{1.3}$ and $\text{La}(\text{Fe}_{1-x}\text{Co}_x)_{11.83}\text{Al}_{1.17}$ ($x = 0.06, 0.08$) was determined by Hu *et al* (2000b, 2001a) from the magnetization measurements. It was found that the alloys have a cubic NaZn_{13} -type crystal structure with a small amount of α -Fe phase in $\text{La}(\text{Fe}_{0.98}\text{Co}_{0.02})_{11.7}\text{Al}_{1.3}$. The Curie temperature of $\text{La}(\text{Fe}_{0.98}\text{Co}_{0.02})_{11.7}\text{Al}_{1.3}$ was 198 K and that of $\text{La}(\text{Fe}_{0.94}\text{Co}_{0.06})_{11.83}\text{Al}_{1.17}$ and $\text{La}(\text{Fe}_{0.92}\text{Co}_{0.08})_{11.83}\text{Al}_{1.17}$ was 273 and 303 K, respectively. The magnetization on magnetic field measurements showed below the Curie temperature typical soft ferromagnetic behaviour with a maximum coercive force of about 20 Oe at 5 K. $\Delta S_M(T)$ curves for the investigated alloys also demonstrated behaviour characteristic of ferromagnets with a maximum near T_C . Qualitative agreement was shown between $\Delta S_M(T)$ curves calculated by mean field approximation and the experimental curves of $\text{La}(\text{Fe}_{1-x}\text{Co}_x)_{11.83}\text{Al}_{1.17}$ alloys. $\Delta S_M(H)$ curves in $\text{La}(\text{Fe}_{1-x}\text{Co}_x)_{11.83}\text{Al}_{1.17}$ had the same form as in Gd without saturation up to 50 kOe. The maximum values of $-\Delta S_M$ induced by $\Delta H = 50$ kOe were 10.6 J/kg K in $\text{La}(\text{Fe}_{0.98}\text{Co}_{0.02})_{11.7}\text{Al}_{1.3}$, 9.5 J/kg K in $\text{La}(\text{Fe}_{0.94}\text{Co}_{0.06})_{11.83}\text{Al}_{1.17}$ and 9.0 J/kg K in $\text{La}(\text{Fe}_{0.92}\text{Co}_{0.08})_{11.83}\text{Al}_{1.17}$, which is at the level of ΔS_M values in Gd (see table 8.2). The observed high ΔS_M values in the alloys investigated were related by the authors to their high saturation magnetization—about $2.0 \mu_B/\text{atom Fe, Co}$. It should be noted that in $\text{La}(\text{Fe}_{0.98}\text{Co}_{0.02})_{11.7}\text{Al}_{1.3}$ a rapid magnetization on temperature change near T_C was observed.

The alloys with higher Al content— $\text{LaFe}_{11.44}\text{Al}_{1.56}$ and $\text{LaFe}_{11.375}\text{Al}_{1.625}$ —revealed two successive magnetic phase transitions under cooling (Hu *et al* 2001e, 2002b). The first, from the paramagnetic to the antiferromagnetic state, took place at T_N (186 K for $\text{LaFe}_{11.44}\text{Al}_{1.56}$ and 181 K for $\text{LaFe}_{11.375}\text{Al}_{1.625}$) and then at T_{A-F} (127 and 140 K, respectively) the first-order transition to the ferromagnetic state occurs. The transition at T_{A-F} is accompanied by temperature hysteresis of magnetization and a large jump of the lattice parameter. Between T_N and T_{AFM-FM} , the AFM state can be converted to the FM state by application of a magnetic field. This transition is accompanied by field hysteresis which, however, does not persist down to zero field. The $S_M(T)$ curve displays two peaks, at T_N and T_{A-F} . The peak at T_{A-F} was asymmetrical and its width essentially increased with increasing ΔH as it usually observed for first-order transitions. The magnetic entropy change is much higher in absolute value at T_{A-F} than at T_N for low ΔH —see table 6.4. However, it rapidly increases in the latter case and two maxima merge at the high-field region forming a wide table-like $\Delta S_M(T)$ curve. This effect is especially pronounced in $\text{LaFe}_{11.375}\text{Al}_{1.625}$, where the full width of the $\Delta S_M(T)$ curve at half maximum is about 60 K for $\Delta H = 40$ kOe. The alloys are also characterized by high magnetic entropy change related to the first-order transition.

$\text{LaFe}_{13-x}\text{Si}_x$ alloys with $x = 2.4-2.8$ exhibited second-order magnetic phase transition from paramagnetic to ferromagnetic state at the Curie

temperature (Zhang *et al* 2000b, Hu *et al* 2001b, Wen *et al* 2002). However, the magnetic entropy change values in these alloys were rather high (see table 6.4), especially for low ΔH . The $\Delta S_M(T)$ dependences in the alloys had the symmetrical form typical of ferromagnets and the peak on the $\Delta S_M(T)$ curve was quite wide (the maximum full width at half maximum of ~ 90 K for $\Delta H = 50$ kOe was observed in the alloy with $x = 2.8$).

In the work of Hu *et al* (2001b) the comparison was made between LaFe_{11.4}Si_{1.6} and LaFe_{10.4}Si_{2.6} alloys, which, as was shown, are characterized by essentially different magnetic behaviour. X-ray diffraction studies showed that both alloys have cubic NaZn₁₃-type crystal structure with small (about 8 wt%) admixture of α -Fe. The temperature dependence of the lattice parameter in LaFe_{11.4}Si_{1.6} demonstrates a sharp decrease (from ~ 11.52 to ~ 11.48 Å, which is about 0.35%) at the transition from the ferromagnetic to the paramagnetic state ($T_C = 208$ K) under heating (the crystal structure type remains unchanged). No such behaviour was observed in LaFe_{10.4}Si_{2.6}—only a small and slow change of the lattice parameter with rather shallow minimum at $T_C = 243$ K. It should be noted that the obtained lattice parameter change corresponds to the relative volume change $\Delta V/V$ of about 1%, which is greater than that in the alloy Gd₅(Si_{1.8}Ge_{2.2}), exhibiting structural phase transition at the Curie temperature and corresponding high ΔS_M , where $\Delta V/V$ is about 0.4% (Morellon *et al* 1998). The magnetization on temperature curves measured in 10 kOe was also strictly different in these alloys—a sharp change of magnetization in LaFe_{11.4}Si_{1.6} near T_C , typical for first-order transition, and the smooth magnetization change in LaFe_{10.4}Si_{2.6}, characteristic of the second-order transition. However the field hysteresis in both alloys was very small in the whole temperature region with a maximum coercive force of 18 Oe in LaFe_{11.4}Si_{1.6} at 5 K. The temperature hysteresis on $M(T)$ curves was also not found. The $M(H)$ curves in LaFe_{11.4}Si_{1.6} above T_C demonstrated a bend, which was attributed to the metamagnetic transition between paramagnetic and ferromagnetic states. The saturation magnetization of LaFe_{11.4}Si_{1.6} and LaFe_{10.4}Si_{2.6} alloys was found to be 2.1 and 1.9 μ_B/Fe . The $\Delta S_M(T)$ curves of the investigated alloys obtained from the magnetization measurements were of ferromagnetic type with peaks near the Curie points—see figure 6.21 (however, as one can see, $\Delta S_M(T)$ curves for LaFe_{11.4}Si_{1.6} demonstrated asymmetrical behaviour with a high-temperature shoulder typical of the first-order transitions). The peak values of $-\Delta S_M$ were essentially different: 14.3 J/kg K for $\Delta H = 20$ kOe and 19.4 J/kg K for $\Delta H = 50$ kOe (this is about two times higher than in Gd) in LaFe_{11.4}Si_{1.6} in comparison with only ~ 2 J/kg K for $\Delta H = 20$ kOe in LaFe_{10.4}Si_{2.6}.

Higher peak ΔS_M values were obtained in the compound with lower Si content—LaFe_{11.7}Si_{1.3} (Hu *et al* 2003). This alloy under heating undergoes first-order ferromagnetic to paramagnetic transition at 188 K. A temperature hysteresis of about 3 K typical of the first-order magnetic phase transition

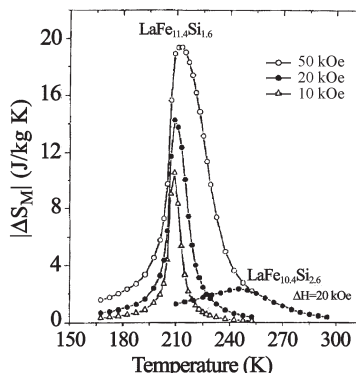


Figure 6.21. Temperature dependences of the magnetic entropy change in $\text{LaFe}_{11.4}\text{Si}_{1.6}$ and $\text{LaFe}_{10.4}\text{Si}_{2.6}$ induced by different ΔH (Hu *et al* 2001b).

was observed on the $M(T)$ curve measured in 100 Oe. As in $\text{LaFe}_{11.4}\text{Si}_{1.6}$, an abrupt lattice parameter change of about 0.6% was observed in $\text{LaFe}_{11.7}\text{Si}_{1.3}$ at the Curie temperature. As one can see from table 6.4, $\Delta S_M/\Delta H$ values in $\text{LaFe}_{13-x}\text{Si}_x$ alloys with first-order magnetic phase transitions essentially decrease for higher ΔH .

At temperatures below T_C , the $M(H)$ isotherms display a characteristic ferromagnetic behaviour. Above T_C a sharp change of the magnetization with a hysteresis appears above a critical field, which means that a field-induced first-order metamagnetic phase transition from the paramagnetic to the ferromagnetic state takes place in the paramagnetic region. The critical fields of the transition were about 7 kOe just above T_C and increased with increasing temperature. However, the width of the hysteresis loop decreased at higher temperatures and magnetic hysteresis did not extend to zero fields in the whole temperature range. Figure 6.22 shows $\Delta S_M(T)$ curves for $\text{LaFe}_{11.7}\text{Si}_{1.3}$ calculated from magnetization. The peak $-\Delta S_M$ value for $\Delta H = 50$ kOe is 29 J/kg K, which is higher than in $\text{LaFe}_{11.4}\text{Si}_{1.6}$. The field-induced metamagnetic transition from the paramagnetic to the ferromagnetic state above T_C results in a significant broadening of the ΔS_M peak to a higher temperature region with increasing field—see figure 6.22. Besides the magnetic entropy change the MCE temperature dependence in $\text{LaFe}_{11.7}\text{Si}_{1.3}$ was also measured by a direct method for $\Delta H = 14$ kOe—see figure 6.23. The peak ΔT value for this ΔH reached 4 K. The observed temperature hysteresis (~ 3 K) of ΔT in the heating and cooling process is in agreement with the hysteresis on the $M(T)$ curves.

Analogous results were obtained by Fujieda *et al* (2002) on the $\text{LaFe}_{13-x}\text{Si}_x$ system with $x = 1.3, 1.43, 1.56$ and 1.6 —see table 6.4. Here magnetic entropy change was determined from magnetization data, and the adiabatic temperature change was determined on the basis of the heat capacity and ΔS_M data. The $\Delta T(T)$ curves had the same asymmetrical

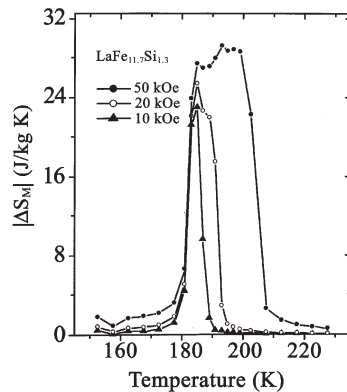


Figure 6.22. Temperature dependences of the magnetic entropy change in $\text{LaFe}_{11.7}\text{Si}_{1.3}$ induced by different ΔH (Hu *et al* 2003).

character as $\Delta S_M(T)$ curves. It should be noted that, in the $\text{LaFe}_{13-x}\text{Si}_x$ alloys with low Si content, not only high ΔS_M values but also high ΔT values were found. For $\text{LaFe}_{11.7}\text{Si}_{1.3}$ direct MCE measurements for $\Delta H = 14 \text{ kOe}$ gave $\Delta T/\Delta H = 0.286 \text{ K/kOe}$ (Hu *et al* 2003) (the highest value for Gd is 0.29 K/kOe—see table 8.2). Fujieda *et al* (2002) found even higher $\Delta T/\Delta H$ value for this composition—0.405 k/kOe.

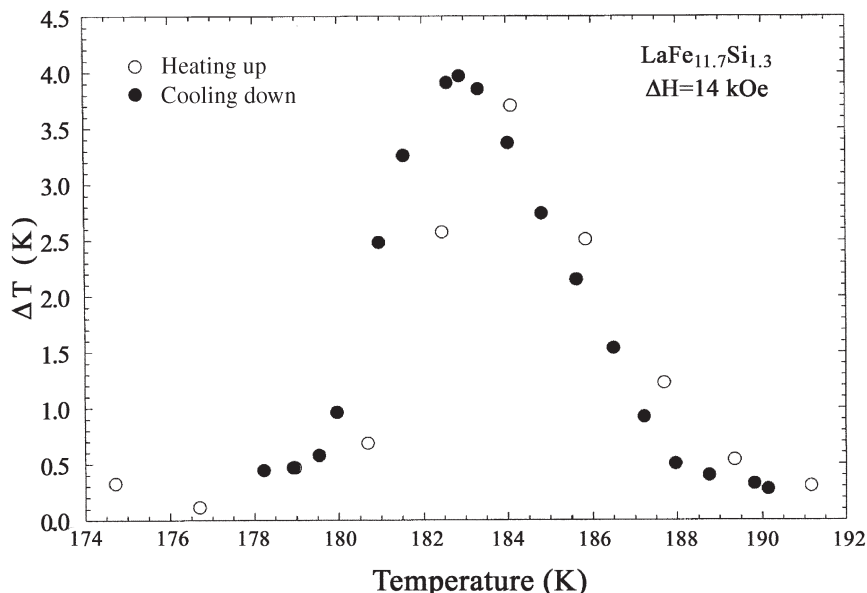


Figure 6.23. Temperature dependences of the MCE in $\text{LaFe}_{11.7}\text{Si}_{1.3}$ for $\Delta H = 14 \text{ kOe}$ measured under cooling and under heating (Hu *et al* 2003).

Fujieda *et al* (2002) also determined magnetocaloric properties of hydrogenated $\text{LaFe}_{13-x}\text{Si}_x$ alloys— $\text{LaFe}_{11.44}\text{Si}_{1.56}\text{H}_{1.0}$ and $\text{LaFe}_{11.57}\text{Si}_{1.43}\text{H}_{1.3}$. They were prepared in order to increase the Curie temperatures of the corresponding initial alloys. Introduction of hydrogen led to a significant increase of T_C with preservation of high magnetocaloric parameters—see table 6.4.

The magnetic entropy change in $\text{LaFe}_{11.2}\text{Co}_{0.7}\text{Si}_{1.1}$ was determined from magnetization by Hu *et al* (2002a). Cobalt was introduced into the alloy in order to increase the Curie temperature with preservation of first-order character of the magnetic phase transition in silicon-doped LaFe_{13} . As in the silicon-containing alloys discussed above, at the Curie temperature of $\text{LaFe}_{11.2}\text{Co}_{0.7}\text{Si}_{1.1}$ ($T_C = 274\text{ K}$) the lattice parameter drops sharply while the crystal structure remains of cubic NaZn_{13} -type. The lattice parameter in the ferromagnetic state was bigger than in the paramagnetic one and its change under transition was $\sim 0.43\%$. The peak on the $\Delta S_M(T)$ curve near the Curie temperature had the same form as in $\text{LaFe}_{11.4}\text{Si}_{1.6}$ with a slightly higher absolute value of 20.3 J/kg K for $\Delta H = 50\text{ kOe}$.

6.3.3 Other rare earth–iron compounds

The heat capacity of ErFe_4Al_8 and YFe_4Al_8 compounds was investigated by Hagmusa *et al* (1999). RFe_4Al_8 compounds have a tetragonal ThMn_{12} -type crystal structure. According to magnetization studies, Fe sublattice orders antiferromagnetically in the temperature range $135\text{--}200\text{ K}$. At the same time rare earth sublattice orders in low-temperature range. Heat capacity measurements of ErFe_4Al_8 and YFe_4Al_8 of Hagmusa *et al* (1999) did not reveal anomalies at the temperatures corresponding to the ordering of iron sublattice. However, a sharp heat capacity maximum was found out in ErFe_4Al_8 at the temperature of 5.5 K , which was related by the authors with ordering of Er magnetic moments. The magnetic heat capacity contribution was obtained by subtracting of YFe_4Al_8 heat capacity data from that of ErFe_4Al_8 with correction for the mass difference. On the basis of the magnetic heat capacity the magnetic entropy temperature dependence of ErFe_4Al_8 was determined. It was established that the magnetic transition at 5.5 K was characterized by the magnetic entropy change of $R \ln 2$. This is in agreement with the energy structure of Er ion in this compound, according to which the ground state is a doublet. The magnetic entropy at 100 K reached the value close to the theoretical magnetic entropy value of Er.

6.4 Rare earth–cobalt

The intermetallic compounds RCO_2 (where R = heavy rare earth Gd, Tb, Dy, Ho and Er) have C15-type cubic Laves-phase crystal structure and exhibit a transition from paramagnetic to ferrimagnetic (FIM) state. The type of

magnetic PM–FIM transition changes from second-order for GdCo_2 ($T_C = 400\text{ K}$) and TbCo_2 (230 K) to first-order for DyCo_2 (140 K), HoCo_2 (75 K) and ErCo_2 (32 K) (Bloch *et al* 1971, Voiron and Bloch 1971, Kamarad *et al* 1995, Duc and Goto 1999).

The magnetic properties of the RCO_2 intermetallic compounds are well described by the s-d model in which the coexistence of rare earth localized spins and itinerant 3d electrons is assumed (Bloch and Lemaire 1970, Inoue and Shimizu 1982). According to this model the rare earth ions have localized magnetic moments and the 3d magnetic moment of Co is induced by the molecular field produced by the rare earth magnetic sublattice ordered ferromagnetically below the Curie temperature. Bloch *et al* (1975) explained the first- and second-order transitions in the RCO_2 compounds with the help of an s-d model and an expansion of the magnetic free energy as a power series of the d-electron magnetization. It was shown by Bloch *et al* (1975) that below 200 K the transition at T_C is of first-order type and above this border point it is of second-order type. Dilution of the rare earth element in HoCo_2 compounds by Y led to a change from the first-order transition to the second-order type (Pillmayr *et al* 1987). According to Gratz (1983), HoCo_2 displays two magnetic-crystallographic transformations upon cooling: a cubic to tetragonal transition at 82.5 K (magnetic phase transition from paramagnetic to ferromagnetic state), and a tetragonal to orthorhombic transition at 18 K (spin-reorientation transition).

Generally, R–Co compounds demonstrate so-called itinerant electron metamagnetic behaviour—under the influence of a magnetic field a transition between nonmagnetic or low magnetic moment state and high magnetic moment state occurs (Duc and Goto 1999). The metamagnetic transition is related to the itinerant nature of the Co magnetic moment and the splitting of the majority and minority 3d subbands of Co in the magnetic field. In RCO_2 compounds with nonmagnetic R ions, such as exchange-enhanced Pauli paramagnets YCo_2 and LuCo_2 , the field of metamagnetic transition reaches high values (about 700 kOe) (Buschow 1977, Kirchmayer and Poldy 1978). However, in the compounds with magnetic R ions the 3d band splitting necessary for the formation of a Co magnetic moment can be provided by a molecular field acting from the R magnetic sublattice. The external magnetic field in this case can induce the metamagnetic transition at much lower magnetic fields by assisting the formation of a Co moment.

Application of the magnetic field can lead in the RCO_2 compounds to a change of the order of the magnetic phase transition from first to second (Gratz *et al* 1993). Hybridization of 5d and 3d electrons is responsible for ferrimagnetic ordering of 3d and 4f magnetic moments in RCO_2 compounds containing heavy rare earth ions (Duc and Goto 1999). At the temperature of the first-order transition from a paramagnetically to a magnetically ordered state, magnetic instability in RCO_2 compounds can lead to a sudden

change of magnetization and resistivity, large spontaneous magnetostriction ($\Delta V/V \approx 0.4\%$), a large change of the electronic heat capacity constant, enhanced magnetic susceptibility and fluctuations of the spin density (Duc and Goto 1999).

Results of investigations of the heat capacity of RCO_2 intermetallic compounds were published in the works of Voiron *et al* (1974), Pillmayr *et al* (1987), Hilscher *et al* (1988), Imai *et al* (1995), Giguere *et al* (1999a) and Wada *et al* (2001). Voiron *et al* (1974) calculated magnetic heat capacity as the difference between the total heat capacity and the lattice plus electronic contributions. It was found that experimental values of the magnetic entropy of $TbCO_2$ and $HoCO_2$ compounds at $T = 200$ K, which were 22 and 24 J/mol K, respectively, were very close to the theoretical values for free rare earth ions (see table 6.2). Voiron *et al* (1974) concluded that the Co moment in these compounds is not permanent but is induced by exchange interactions with rare earths.

The heat capacity of $ErCO_2$ as a function of temperature was measured by Imai *et al* (1995). A sharp anomaly associated with a first-order magnetic phase transition was found at 32 K. The magnetic contribution to the heat capacity, obtained by subtraction of the $LuCO_2$ heat capacity from the $ErCO_2$ experimental data, still persisted above T_C . This was explained by an interaction of the RE magnetic ions with a crystalline electric field. The temperature dependence of the magnetic entropy $S_M(T)$, calculated on the basis of the heat capacity data, displayed a discontinuous increase (of about 9 J/mol K) at the Curie point, and at high temperatures (above 150 K) it reached its saturation value which is close to the value of 23.1 J/mol K calculated by equation (2.66) for Er ions ($J = 15/2$ —see table 6.2). The latter fact indicates that the Co magnetic moments make a small contribution to the total S_M . The magnetic entropy discontinuity at T_C was explained by the authors by the change of the Er ion ground-state degeneracy from a singlet in the magnetically-ordered state to a quadruplet in the paramagnetic state. According to the estimation of Wada *et al* (1999), such change should yield the entropy change of 11.5 J/mol K. The sharp heat capacity peak in $ErCO_2$ (at 32.2 K in zero field with a maximum value of 1794 J/mol K) shifted to the high-temperature region in the presence of the magnetic field at a rate of 0.2 K/kOe (Wada *et al* 1999). The heat capacity peak height decreased but its sharpness persisted up to the field of 80 kOe. Wada *et al* (1999) explained the observed heat capacity peak field behaviour in polycrystalline $ErCO_2$ by strong magnetic anisotropy in this compound aligning the magnetization along the [111] easy direction and its cubic crystalline structure. The heat capacity temperature dependences in various fields analogous to that obtained by Wada *et al* (1999) were observed in $ErCO_2$ by Giguere *et al* (1999a).

The first direct investigation of the magnetocaloric effect in RCO_2 compounds was conducted by Nikitin and Tishin (1991), who measured

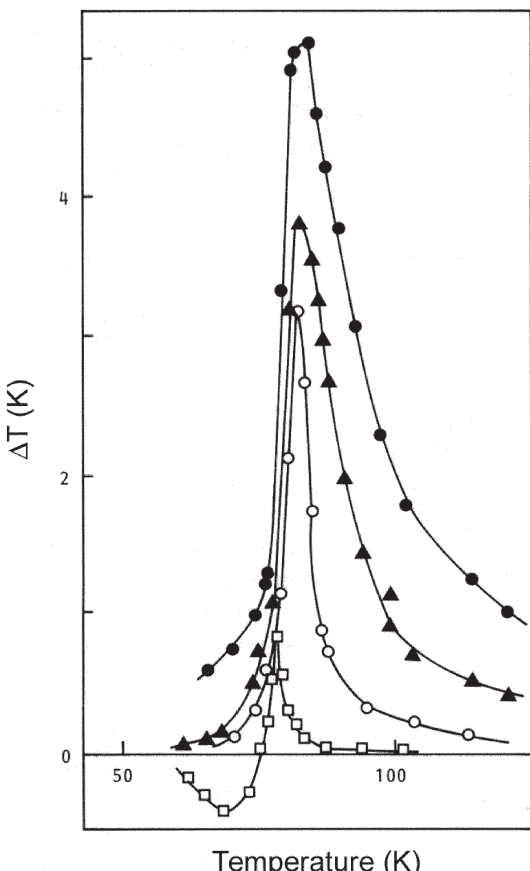


Figure 6.24. Temperature dependences of the MCE in HoCo_2 induced by a magnetic field change $\Delta H = 60 \text{ kOe}$ (●), 40 kOe (Δ), 20 kOe (\circ) and 5 kOe (\square) (Nikitin and Tishin 1991). (Reprinted from Nikitin and Tishin 1991, copyright 1991, with permission from Elsevier.)

$\Delta T(T, H)$ dependences of HoCo_2 . The $\Delta T(T, H)$ curves are shown in figure 6.24. The asymmetrical form of the MCE temperature profile is consistent with the sharp character of the first-order magnetic phase transition. The estimation of ΔS_M made by Nikitin and Tishin (1991) on the basis of heat capacity data of Voiron *et al* (1974) gave the value of -6.4 J/mol K at $T = 82 \text{ K}$ and $\Delta H = 60 \text{ kOe}$. The temperature range of negative MCE should be noted below about 75 K for $\Delta H = 5 \text{ kOe}$. The MCE field dependences measured in the temperature interval from 81 to 120 K were not saturated in the fields up to 60 kOe —see figure 6.25.

Later, the magnetic entropy change and MCE temperature and field dependences in RCo_2 ($\text{R} = \text{Tb}, \text{Dy}, \text{Ho}, \text{Er}$) compounds were determined on

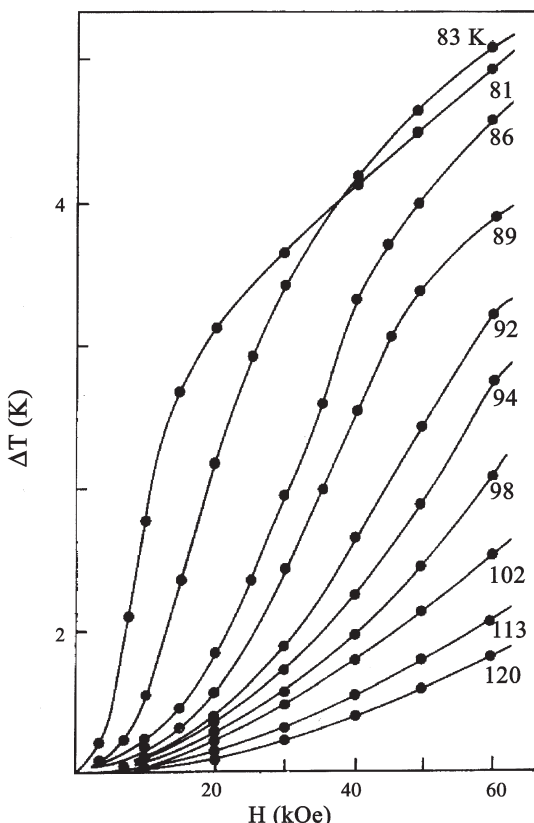


Figure 6.25. Field dependences of the MCE in HoCo_2 (Nikitin and Tishin 1991). (Reprinted from Nikitin and Tishin 1991, copyright 1991, with permission from Elsevier.)

the basis of magnetization and heat capacity measurements by Foldeaki *et al* (1998a), Giguere *et al* (1999a), Wada (1999, 2001), Wang *et al* (2001c, 2002b,c), Duc and Kim Anh (2002), Duc *et al* (2002), Gomes *et al* (2002) and Tishin *et al* (2002). Foldeaki *et al* (1998a) measured the magnetization of RCO_2 ($\text{R} = \text{Dy}$, Ho , Er) compounds and on the basis of these data calculated the magnetic entropy change ΔS_M induced by a field change of 70 kOe. Maxima were observed near the Curie point and the maximum values of $-\Delta S_M$ were about 14.5 J/kg K (at $T \approx 140$ K) for DyCo_2 , about 22 J/kg K (at $T \approx 85$ K) for HoCo_2 and about 28 J/kg K (at $T \approx 42$ K) for ErCo_2 . It should be noted that the maxima on $\Delta S_M(T)$ curves in the investigated compounds had a rather symmetrical form. Two ErCo_2 samples were studied: ‘good’ and ‘wrong’. The first, according to X-ray diffraction analysis, was a homogeneous one. The second had some distortions in crystalline structure and contained an oxide. The wrong ErCo_2 sample displayed $-\Delta S_M$ values 30% smaller than the good one. The Arrott plots of both wrong and good ErCo_2 constructed near

the magnetic phase transition temperature did not show linear ranges predicted by the Landau second-order transitions theory. The Arrott plot of the wrong ErCo₂ showed a behaviour analogous to that observed in Dy-Zr nanocomposites. According to the authors, this indicates a multi-phase nanosize crystalline structure in the wrong ErCo₂.

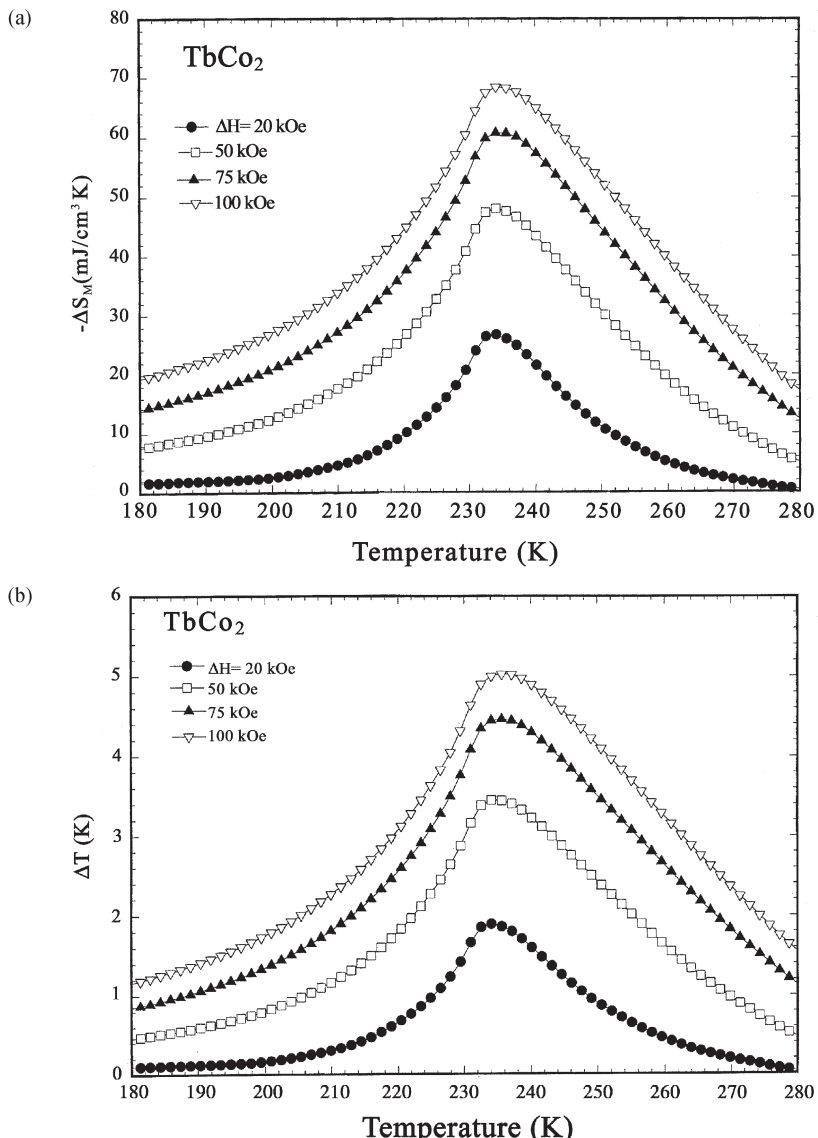


Figure 6.26. Temperature dependences of the magnetic entropy change (a) and MCE (b) in TbCo₂ (Tishin *et al* 2002).

Tishin *et al* (2002) undertook a comprehensive study of magnetic properties, heat capacity and the MCE of polycrystalline RCO_2 ($\text{R} = \text{Tb}, \text{Dy}, \text{Ho}, \text{Er}$). It was found that the heat capacity temperature dependence of TbCo_2 has a (typical for ferromagnets) λ -type anomaly near the Curie temperature, and DyCo_2 , HoCo_2 and ErCo_2 display a sharp δ -function like peaks at T_C . The variation of the heat capacity as a function of the applied magnetic field clearly showed that TbCo_2 undergoes a second-order magnetic phase transition—the λ -type peak observed in zero field changed to a rounded bump under application of the field. For DyCo_2 , HoCo_2 and ErCo_2 the heat capacity peak changed in the magnetic field from the δ -type form to a reasonably sharp but somewhat broader and greatly diminished peak for $H < 20\text{ kOe}$, and to a rounded broad peak for $H > 20\text{ kOe}$. This can imply that application of the magnetic field higher than 20 kOe change the order of the magnetic phase transition from first to second. The zero field $C(T)$ curve of HoCo_2 displayed an additional small maximum at about 18 K, where the spin reorientation transition occurred. Application of the magnetic field washed this peak away and in 100 kOe it completely disappeared.

The $\Delta S_M(T)$ and $\Delta T(T)$ curves of TbCo_2 obtained by Tishin *et al* (2002) from heat capacity had a symmetric shape typical for ferromagnets with a maximum near the Curie temperature and an absence of any other peculiarities—see figure 6.26. Those of DyCo_2 , HoCo_2 and ErCo_2 demonstrated quite different behaviour—they had an asymmetrical ‘half-dome’ shape, similar to the ‘skyscraper’ shape observed in $\text{Gd}_5(\text{Si}_x\text{Ge}_{1-x})_4$ compounds at the first-order magnetic phase transition (Gschneidner and Pecharsky 1999). The $\Delta S_M(T)$ and $\Delta T(T)$ curves for HoCo_2 , ErCo_2 and DyCo_2 are shown in figures 6.27, 6.28 and 6.29. As one can see, a temperature range of negative MCE values in HoCo_2 is below about 80 K, as already observed from the direct measurements (see figure 6.24). This range was not observed in DyCo_2 and ErCo_2 . Near 18 K (magnetic spin-reorientation transition) in HoCo_2 , ΔS_M and MCE change their signs and negative MCE (and positive ΔS_M) typical for the antiferromagnetic-type paraprocess in antiferromagnets and ferrimagnets are observed below this temperature.

Giguere *et al* (1999a), Wada *et al* (1999, 2001), Duc and Kim Anh (2002), Duc *et al* (2002) and Gomes *et al* (2002) obtained $\Delta S_M(T)$ and $\Delta T(T)$ curves for ErCo_2 , HoCo_2 and TbCo_2 analogous to those of Tishin *et al* (2002). The peak values of ΔS_M and ΔT in TbCo_2 were substantially smaller than in other investigated RCO_2 ($\text{R} = \text{Dy}, \text{Ho}, \text{Er}$) compounds (see table 6.5), which can be related to the second-order character of the magnetic transition in this compound. In DyCo_2 , however, Wang *et al* (2001c, 2002b,c) and Duc *et al* (2002) obtained a rather symmetrical $\Delta S_M(T)$ peak near T_C . Wang *et al* (2001c) prepared melt-spun and annealed DyCo_2 alloy samples. Both samples had MgCu_2 -type crystal structure and their Curie temperatures were almost the same, although the magnetization change with temperature

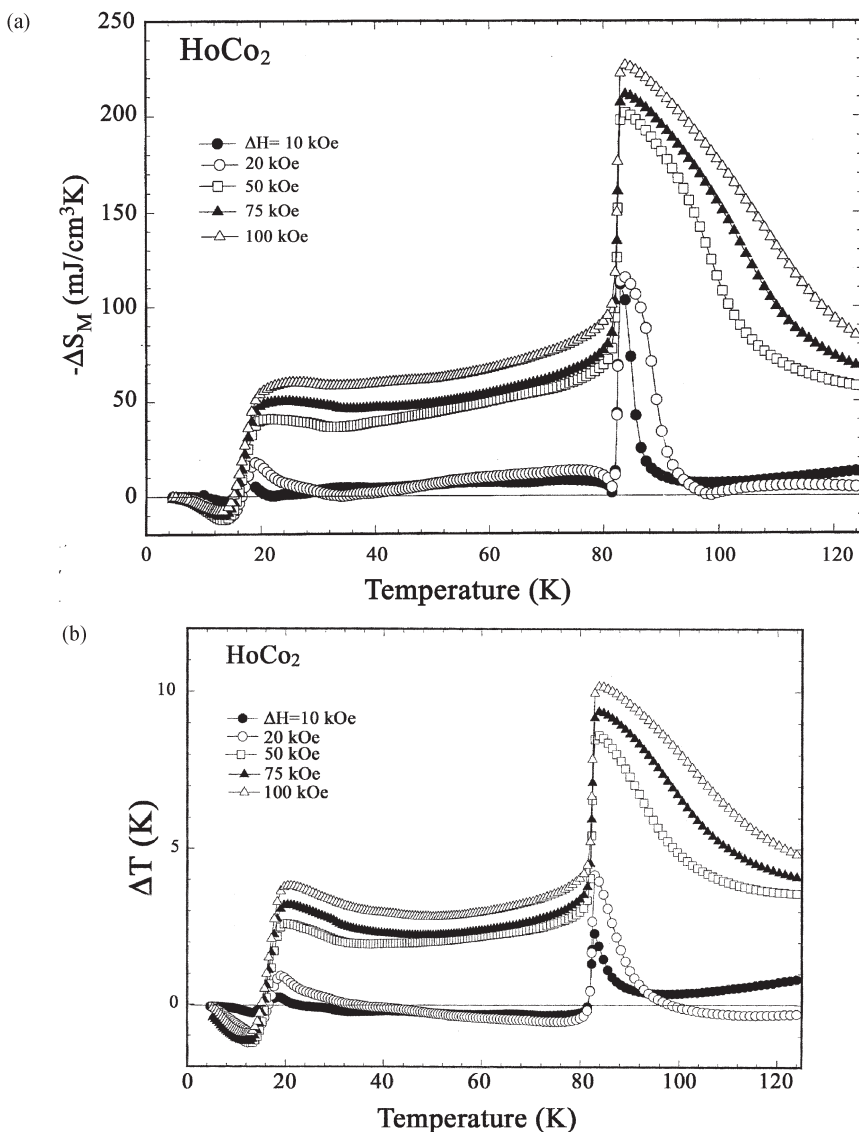


Figure 6.27. Temperature dependences of the magnetic entropy change (a) and MCE (b) in HoCo_2 (Tishin *et al* 2002).

near T_C was much sharper in the annealed sample. The latter circumstance provided the absolute peak ΔS_M value in the annealed sample about two times higher than that in the melt-spun sample.

As one can see from table 6.5, RCO_2 compounds with the first-order magnetic transition are characterized by essential values of $\Delta S_M/\Delta H$ and

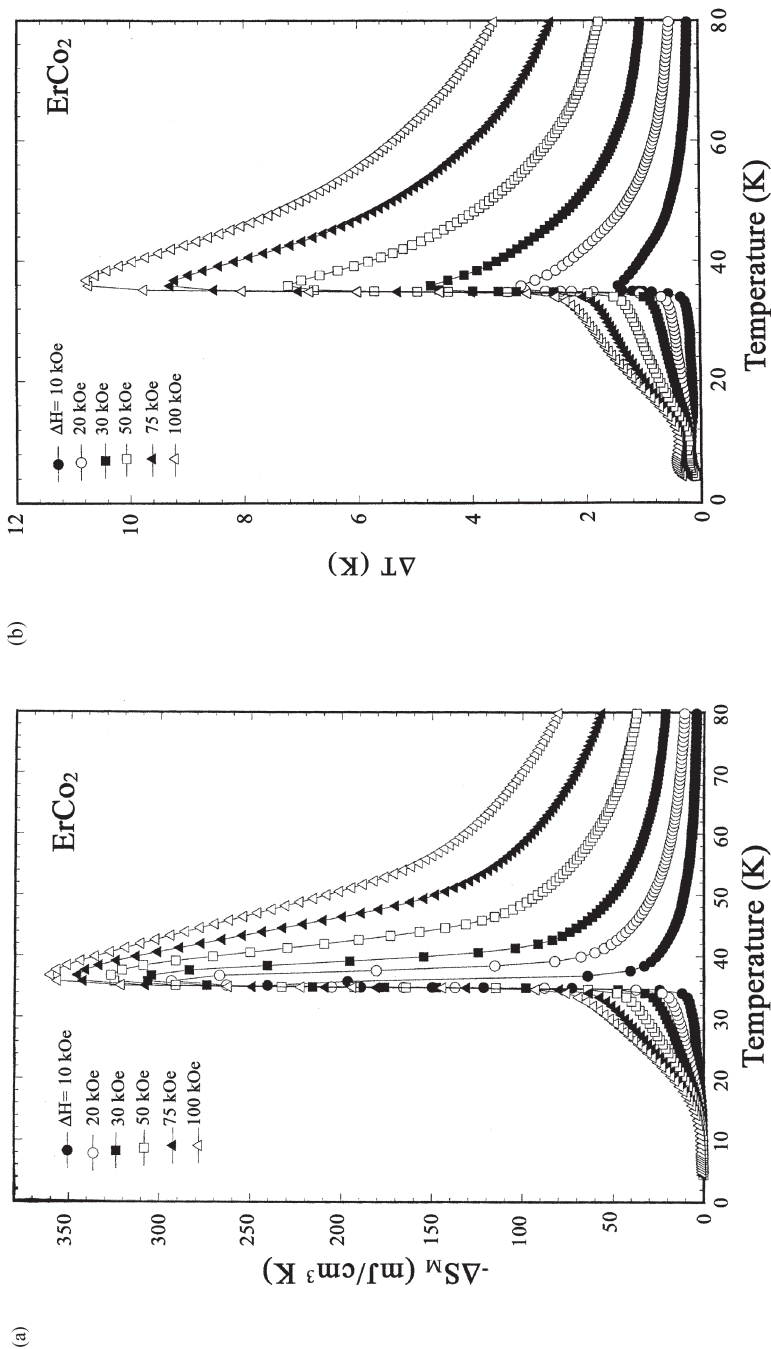


Figure 6.28. Temperature dependences of the magnetic entropy change (a) and MCE (b) in ErCo_2 (Tishin *et al* 2002).

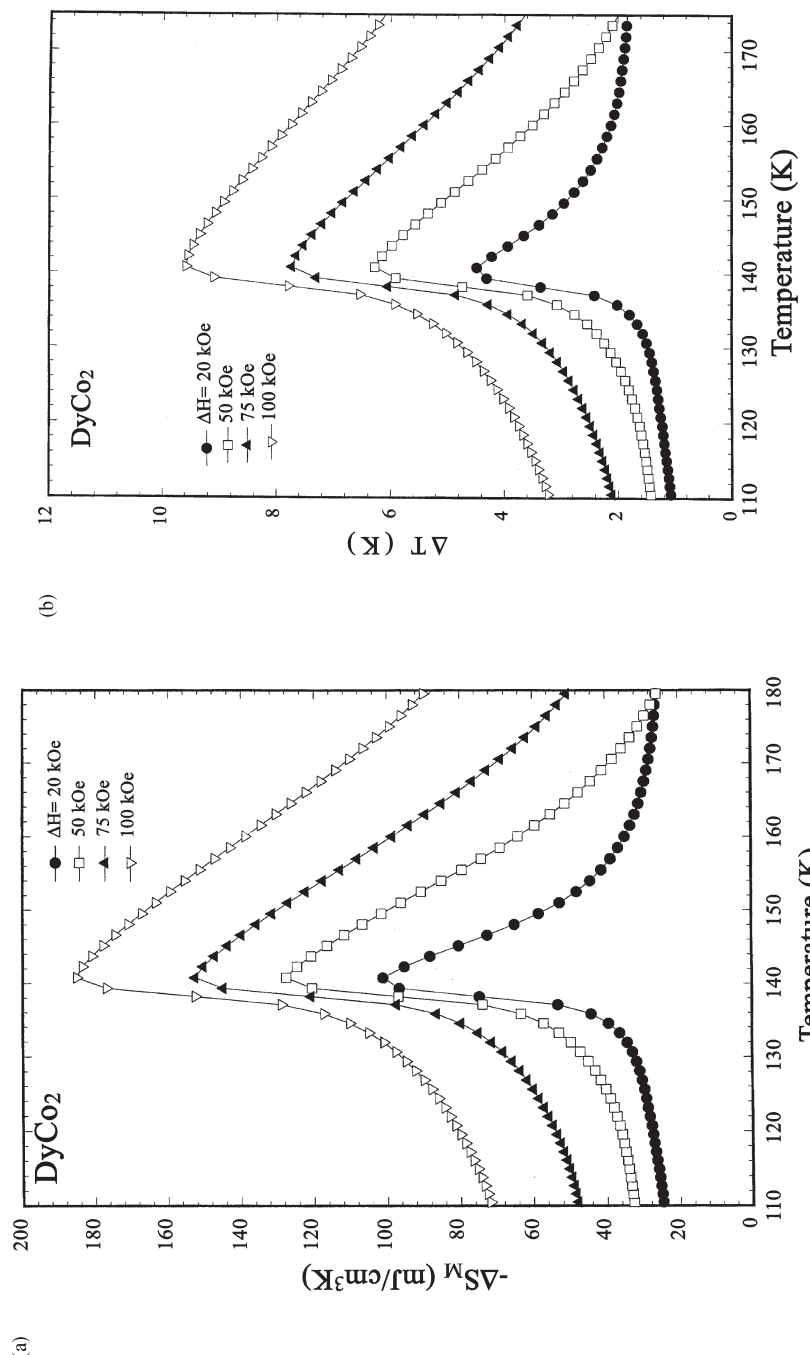


Figure 6.29. Temperature dependences of the magnetic entropy change (a) and MCE (b) in DyCo₂ (Tishin *et al.* 2002).

Table 6.5. The Curie temperatures (T_C), temperature of the maximum in the $\Delta T(T)$ curves (T_{\max}), magnetic entropy S_M , peak magnetic entropy change ΔS_M near the Curie temperature induced by the magnetic field change ΔH , peak MCE value ΔT at $T = T_{\max}$ induced by ΔH , $\Delta T/\Delta H$ and $\Delta S_M/\Delta H$ of polycrystalline RE–Co alloys.

Compound	MCE peak				ΔS_M peak				Ref.*
	T_C (K)	T_{\max} (K)	ΔT (K)	ΔH (kOe)	$\Delta T/\Delta H \times 10^2$ (K/kOe)	ΔS_M (J/kg K)	ΔH (kOe)	$-\Delta S_M/\Delta H \times 10^2$ (J/kg K kOe)	
TbCo ₂	231	235	5	100	5	68 [†]	100	68 [‡]	1
			3.4 1.9	50 20	6.8 9.5	48 [†] 26 [†]	50 20	96 [‡] 130 [‡]	
DyCo ₂	227	138	9.6	100	9.6	183 [†]	100	183 [‡]	1
			6.3 4.4	50 20	12.6 22	12.7 10.2	50 20	25.4 51	
	140					14	70	20	2
						11	50	22	9
	142					9	20	45	
Annealed	141					5.8	10	58	10, 11
Melt-spun	142					5.9	10	59	12
ErCo ₂	35	36	10.8	100	10.8	360 [†]	100	360 [‡]	1
			7.2 3.2	50 20	14.4 16	28.4 31.7	50	63.4	
			—	—	—	2.8	10	28	
	45	40	12.5 8	80 20	15.6 40	49.1 35.1	70 20	41.4 61.3	2 3
	33		14.4	140	10.3	38	140	175.3	
			10	70	14.3	32	35	27.1	4
	33.6					38	50	91.4 76	9

Table 6.5. Continued.

Compound	T_c (K)	MCE peak			ΔS_M peak			Ref.*
		T_{max} (K)	ΔT (K)	ΔH (kOe)	$\Delta T/\Delta H \times 10^2$	$-\Delta S_M$ (J/kg K)	ΔH (kOe)	
HoCo ₂	82.5	84	10	100	10	225 [†]	100	225 [‡]
			8.5	50	17	20	50	40
		4	20	20	—	11	20	55
		—	—	—	—	22	70	31.4
		80	5.2	60	8.7	—	—	—
			3.2	20	16	—	—	—
		75				22.5	40	56.3
						13	30	43.3
Er(Co _{0.9} Ni _{0.05}) ₂	19	20	9	50	18	36.8	50	73.6
Er(Co _{0.9} Ni _{0.1}) ₂	13	16	6.2	30	20.7	33	30	110
			9.5	50	19	29.8	50	59.6
DyCo ₂			6.5	30	21.7	22.8	30	76
DyCo ₂	142	—	—	—	—	5.8	10	58
Dy(Co _{0.99} Si _{0.01}) ₂	152	—	—	—	—	4.1	10	41
Dy(Co _{0.97} Si _{0.03}) ₂	162	—	—	—	—	3.3	10	33
Dy(Co _{0.95} Si _{0.05}) ₂	167	—	—	—	—	3.3	10	33
Dy(Co _{0.93} Si _{0.07}) ₂	168	—	—	—	—	2.6	10	26
DyCo ₂	142	—	—	—	—	5.8	10	58
Dy _{0.92} Gd _{0.05} Co ₂	160	—	—	—	—	3.2	10	32
Dy _{0.9} Gd _{0.1} Co ₂	169	—	—	—	—	2.8	10	28
Dy _{0.8} Gd _{0.2} Co ₂	203	—	—	—	—	2.1	10	21
Dy _{0.7} Gd _{0.3} Co ₂	225	—	—	—	—	1.8	10	18
Dy _{0.6} Gd _{0.4} Co ₂	248	—	—	—	—	1.5	10	15
Dy _{0.45} Gd _{0.55} Co ₂	298	—	—	—	—	1	10	10

Gd _{0.4} Tb _{0.6} Co ₂	306	—	—	—	—	6	60	10
Gd _{0.65} Lu _{0.35} Co ₂	301	—	—	—	—	6	60	10
Gd _{0.65} Y _{0.35} Co ₂	301	—	—	—	—	6	60	10
Tb _{0.8} Er _{0.2} Co ₂	200	—	—	—	—	6.11	47.5	12.9
Er _{0.8} Y _{0.2} Co ₂	24	25	8.8	80	11	9	80	11.3
GdCoAl	100	—	—	—	—	10.4	50	20.8
TbCoAl	70	—	—	—	—	4.9	20	24.5
DyCoAl	37	—	—	—	—	10.5	50	21
HoCoAl	10	—	—	—	—	5.3	20	26.5
(Gd _{0.5} Dy _{0.25} Er _{0.25})CoAl	45	—	—	—	—	16.3	50	32.6
Nd ₇ Co ₆ Al ₇	15.5	16.5	2.7	50	5.4	9.2	20	46
						21.5	50	43
						12.5	20	62.5
						14	50	28
						6.3	20	31.5
						4.6	50	9.3
								8

*1. Tishin *et al.* (2002); 2. Foldeaki *et al.* (1998a); 3. Wada *et al.* (1999); 4. Gignere *et al.* (1999a); 5. Nikitin and Tishin (1991); 6. Wada *et al.* (2001); 7. Zhang *et al.* (2001a); 8. Canepa *et al.* (2000); 9. Duc *et al.* (2002); 10. Wang *et al.* (2002b); 11. Wang *et al.* (2002c); 12. Wang *et al.* (2001c); 13. Gomes *et al.* (2002).

[†]In mJ/cm³ K.

[‡]In mJ/cm³ K kOe.

$\Delta T/\Delta H$. It should be noted that the maximum $\Delta S_M/\Delta H$ and $\Delta T/\Delta H$ values are observed in low magnetic fields and essentially increased with ΔH increasing. This is related to changing of the magnetic transition order from first to second under the action of the magnetic field, which is also reflected on the heat capacity (see above).

Tishin *et al* (2002) also estimated possible contributions to the magnetic entropy change at the first-order transitions in DyCo_2 and ErCo_2 . It was supposed that the entropy change consists of three main parts: $\Delta S_{\text{FM-PM}}$, related to paraprocess, which can be described by equation (2.83); ΔS_{FO} , which is the jump of the magnetic entropy caused by the first-order transition, which can be calculated using the Clausius–Clapeyron equation (2.100); and lattice entropy change ΔS_{LFO} , which is related to the lattice dimension change at the transition. The latter contribution was also estimated from the corresponding Clausius–Clapeyron equation, which in this case had the form

$$\frac{dP}{dT} = \frac{\Delta S_{\text{LFO}}}{\Delta V} \quad (6.3)$$

where ΔV is the crystal lattice volume change at the transition. It was supposed that the point at the phase equilibrium curve on the T – P diagram moves with pressure in a way analogous to the magnetic transition point T_C , so the value of $(dT_C/dP)^{-1}$ was used as dP/dT . The values of dT_C/dP and magnetic moment change ΔM were taken from literature and from experimental measurements, respectively, and the value of ΔV was calculated from the literature data on spontaneous volume magnetostriction of the compounds. The calculated contributions are shown in table 6.6. Gadolinium and $\text{Gd}_5\text{Si}_2\text{Ge}_2$ are also present in table 6.6 for comparison as examples of the system with second-order and first-order transitions (concerning the $\text{Gd}_5(\text{SiGe})_4$ system and its unique properties, see section 7.2.2). To get upper limit of ΔS_{LFO} in Gd the value of $\Delta V/V = 0.01$ was used.

As one can see from table 6.6, $\Delta S_{\text{FM-PM}}$ almost coincides with the experimental value of ΔS_M in Gd. In a relatively weak magnetic field change of 20 kOe the value of $\Delta S_{\text{FM-PM}}$ is lower than experimental ΔS_M values in $\text{Gd}_5\text{Si}_2\text{Ge}_2$, DyCo_2 , HoCo_2 and ErCo_2 . For $\text{Gd}_5\text{Si}_2\text{Ge}_2$, $\Delta S_{\text{FM-PM}}$ is significantly lower than experimental values even for $\Delta H = 100$ kOe, where $-\Delta S_{\text{FM-PM}} = 14.1 \text{ J/kg K}$ and experimental $-\Delta S_M = 23.7 \text{ J/kg K}$. This is not true for DyCo_2 , HoCo_2 and ErCo_2 compounds, where this contribution is close to the experimental values already known for $\Delta H = 50$ kOe.

Due to the absence of the magnetization jump at the second-order transition the contribution ΔS_{FO} is equal to zero. At the same time in $\text{Gd}_5\text{Si}_2\text{Ge}_2$, HoCo_2 and ErCo_2 the values of ΔS_{FO} are very close to the experimental ΔS_M values (especially in $\text{Gd}_5\text{Si}_2\text{Ge}_2$). In DyCo_2 the estimated ΔS_{FO} is about an order of magnitude less than experimentally observed ΔS_M .

Table 6.6. Experimental magnetic entropy change ΔS_M , and calculated contributions to the magnetic entropy change: $\Delta S_{\text{FM-PM}}$, related with paraprocess; ΔS_{FO} , which is the jump of the magnetic entropy caused by the first-order transition; and lattice entropy change ΔS_{LFO} , which is related to the lattice dimensions change at the transition, magnetization change ΔI and relative volume change $\Delta V/V$ at the transition and the shift of the Curie temperature under pressure dT_C/dP in RCO_2 compounds, Gd and $\text{Gd}_5(\text{Si}_2\text{Ge}_2)$ (Tishin *et al.* 2002). References are shown in brackets.

ΔH (kOe)	Gd			$\text{Gd}_5(\text{Si}_2\text{Ge}_2)$			Dy Co_2			Ho Co_2			Er Co_2		
	20	50	20	50	20	50	20	50	20	50	20	50	20	50	
$-\Delta S_M$ (J/kg K)	5.4 [1]	10.5 [1]	16 [3, 4]	19.5 [3, 4]	10.2	12.7	11	20	28.4	31.7					
$T = T_C$ (experimental)	5.8	10.7	4.8	8.9	6.4	11.7	9.1	17	15.2	28.1					
$-\Delta S_{\text{FM-PM}}$ (J/kg K)					<5		30								
$T = T_C$					1.4	1.8	9.1								
ΔI (emu/g)	0 [1]		86 [3, 4]												
$H = H_{\text{cr}}$	0		19.1	15.1											
$-\Delta S_{\text{FO}}$ (J/kg K)					<0.01										
$H = H_{\text{cr}}$					<0.04 [5]										
$\Delta V/V$ (%)															
dT_C/dP (K/kbar)															
$T = T_C, H = 0$															
$-\Delta S_{\text{LFO}}$ (J/kg K)															
$T = T_C, H = 0$															

- Dan'kov *et al.* (1998); 2. Tishin *et al.* (1999b); 3. Pecharsky and Gschneidner (1997d); 4. Pecharsky and Gschneidner (2001a); 5. Morello *et al.* (1998); 6. Minakata *et al.* (1976); 7. Kamarad *et al.* (1995); 8. Duc *et al.* (1992a); 9. Jayaraman (1991); 10. Leontiev (1988); 11. Duc *et al.* (1992b); 12. Lee and Pourarian (1976); 13. Petrich (1969).

It was shown by Tishin *et al* (2002) that the values of ΔS_{LFO} and ΔS_{FO} in $\text{Gd}_5\text{Si}_2\text{Ge}_2$ are close to each other. Because according to the work of Morellon *et al* (1998) the first-order transition volume change in this compound has almost the same value in nonzero magnetic fields as in zero magnetic fields, it can be suggested that ΔS_{LFO} obtained from the zero-field volume change data will preserve its value in higher magnetic fields. However, experimentally observed $-\Delta S_M = 23.7 \text{ J/kg K}$ induced by $\Delta H = 100 \text{ kOe}$ in $\text{Gd}_5\text{Si}_2\text{Ge}_2$ cannot be explained without consideration of the contribution from the paraprocess $\Delta S_{\text{FM-PM}}$. Because of insufficiency of literature data on the magnetostriction it was impossible to determine nonzero-field ΔS_{LFO} in RCO_2 compounds. Due to the large difference of the literature data on zero-field magnetostriction and dT_C/dP in RCO_2 compounds, ΔS_{LFO} was estimated using average values of available data. It should be noted that in DyCo_2 the estimated value of $\Delta S_{\text{LFO}} = 11 \text{ J/kg K}$ is close to the experimental ΔS_M values for $\Delta H = 20$ and 50 kOe . The abnormally large value of ΔS_{LFO} calculated for ErCo_2 and HoCo_2 can be related to erroneous values of dT_C/dP , especially taking into account a significant scattering of the published experimental data. Based on the data presented in table 6.6 the authors made the conclusion that, as in $\text{Gd}_5\text{Si}_2\text{Ge}_2$, the compounds RCO_2 ($R = \text{Dy}, \text{Ho}, \text{Er}$) also had rather large values of ΔS_{LFO} in zero magnetic fields. At least in DyCo_2 this value is close to that in $\text{Gd}_5\text{Si}_2\text{Ge}_2$, but it is about an order of magnitude higher than ΔS_{FO} , which is not observed in $\text{Gd}_5\text{Si}_2\text{Ge}_2$. The analysis of the calculated contributions to the entropy change and its experimental values showed that in low magnetic fields the main contribution to the magnetic entropy change comes from the lattice dimension change related to the first-order transition. However, in the investigated RCO_2 compounds the lattice contribution is suppressed in strong magnetic fields because a large change of volume, which is observed in a zero magnetic field at the first-order transition, disappears in a higher magnetic field. In the case of $\text{Gd}_5\text{Si}_2\text{Ge}_2$ this suppression has not happened, and the lattice contribution preserves its value even in a strong magnetic field, and that is why $\text{Gd}_5\text{Si}_2\text{Ge}_2$ exhibits more advanced magnetocaloric properties (in particular, much higher ΔS_M —see section 7.2.2).

The influence of substitution of Co in ErCo_2 by Ni ($\text{Er}(\text{Co}_{1-x}\text{Ni}_x)_2$ system) on the heat capacity and MCE was studied by Wada *et al* (2001). Under substitution the Curie temperature decreased from 32 K for ErCo_2 to 13 K for $\text{Er}(\text{Co}_{0.9}\text{Ni}_{0.1})_2$. The heat capacity peak retained its first-order sharpness for $x = 0.05$ and was essentially reduced and broadened for $x = 0.1$. It should be noted that the heat capacity peak in the sample with $x = 0.1$ was consistent with two superimposed peaks—a sharp peak near 12.4 K and a broad one centred at 13.5 K. The authors interpreted the observed effect by separation of the magnetic ordering temperatures of Er and Co magnetic subsystems—Er moments ordered at higher temperature

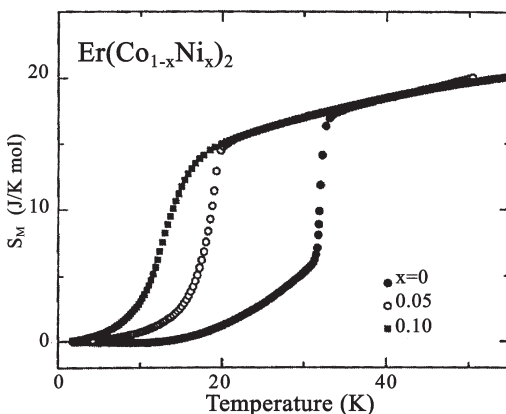


Figure 6.30. Temperature dependences of the magnetic entropy in $\text{Er}(\text{Co}_{1-x}\text{Ni}_x)_2$ alloys (Wada *et al* 2001). (Reprinted from Wada *et al* 2001, copyright 2001, with permission from Elsevier.)

than Co moments. From magnetization measurements it was shown that Ni concentration $x = 0.05$ is the critical concentration for the first-order transition—it disappears in the samples with higher x .

From the experimental heat capacity data Wada *et al* (2001) determined magnetic entropy temperature dependences in the $\text{Er}(\text{Co}_{1-x}\text{Ni}_x)_2$ system, using the heat capacity of LuCo_2 as a nonmagnetic contribution—see figure 6.30. As one can see, in all investigated alloys large magnetic entropy is realized at the Curie temperature in spite of the change of magnetic transition order from first to second with Ni substitution. The magnetic entropy reached about 15 J/mol K just above T_C , which was about 65% of the theoretical value for Er (see table 6.2). The authors related the observed $S_M(T)$ behaviour and the MCE properties described below with preservation of Er ions' magnetic state under Ni substitution. The temperature dependences of the magnetic entropy change ΔS_M were determined from the magnetization data. The MCE was obtained combining $\Delta S_M(T)$ curves with total entropy temperature dependences calculated from the heat capacity. The resultant $\Delta S_M(T)$ and $\Delta T(T)$ curves are shown in figure 6.31. It can be seen that for the compositions containing Ni the forms of $\Delta S_M(T)$ and $\Delta T(T)$ have the features typical for second-order magnetic phase transitions—in particular, more symmetry and width of the peaks near T_C . However, the absolute peak values of ΔS_M and ΔT were not sufficiently changed in comparison to that in ErCo_2 with first-order transition—in particular, in $\text{Er}(\text{Co}_{0.95}\text{Ni}_{0.05})_2$ the peak ΔS_M value is almost the same as in ErCo_2 .

The analogous disappearance of the first-order transition under substitution of Co by Si was observed by Wang *et al* (2002b) in the $\text{Dy}(\text{Co}_{1-x}\text{Si}_x)_2$ system for $x > 0.05$. Si substitution caused an increase of the Curie temperature and decrease of the absolute peak ΔS_M values in the system—

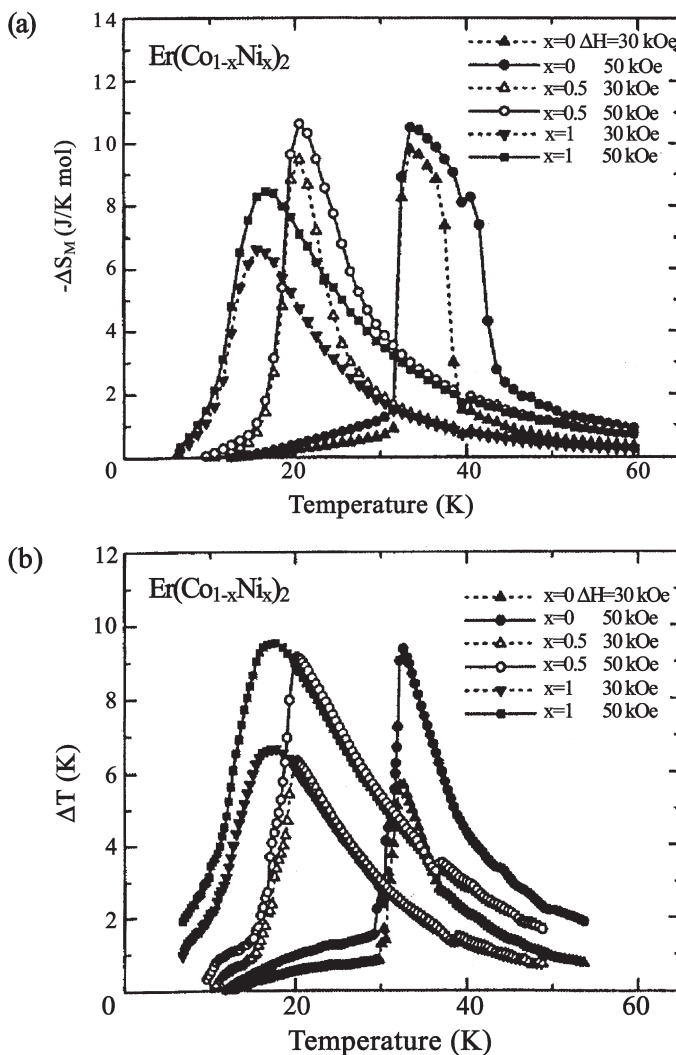


Figure 6.31. The temperature dependences of (a) ΔS_M and (b) ΔT in $\text{Er}(\text{Co}_{1-x}\text{Ni}_x)_2$ (Wada *et al* 2001). (Reprinted from Wada *et al* 2001, copyright 2001, with permission from Elsevier.)

see table 6.5. The authors related the appearance of the second-order magnetic phase transition in the Si-substituted compositions to the stabilization of the Co moment and the absence of metamagnetism in 3d electron subsystems.

In a number of works an influence of substitution of the R element in RCO_2 compounds on their magnetocaloric properties was studied. In the work of Wang *et al* (2002c), Dy in the DyCo_2 compound was substituted

by Gd. For all Gd-containing alloys $Dy_{1-x}Gd_xCo_2$ ($0.05 \leq x \leq 0.55$), the transition at T_C was of second order with low values of ΔS_M (see table 6.5), although for compositions with $x = 0.05$ and 0.1 the Curie temperature was below 200 K , determined by Bloch *et al* (1975) as the upper limit for the first-order transition in the framework of the s-d model. Low absolute peak ΔS_M values were also observed in the Gd- and Tb-based RCo_2 alloys with the second-order transition at T_C : $Gd_{0.4}Tb_{0.6}Co_2$, $Gd_{0.65}Lu_{0.35}Co_2$, $Gd_{0.65}Y_{0.35}Co_2$ and $Tb_{0.8}Er_{0.2}Co_2$ (Duc *et al* 2002, Gomes *et al* 2002).

Wada *et al* (1999) measured the heat capacity of $Er_{0.8}Y_{0.2}Co_2$ alloy and on the basis of these data investigated the influence of Y addition to the MCE in $ErCo_2$. A sharp heat capacity peak was observed at T_C (about 24 K) in the magnetic fields up to 40 kOe . In 80 kOe the peak became rounded. The obtained $\Delta S_M(T)$ and $\Delta T(T)$ curves were similar to that in $ErCo_2$ and preserved first-order transition features; however, the maximum ΔS_M and ΔT values were $20\text{--}30\%$ lower than in $ErCo_2$. De Oliveira *et al* (2002) theoretically considered the magnetocaloric effect in the $Er_{1-x}Y_xCo_2$ system in the framework of the model, where the localized 4f spins of the RE element are coupled by exchange interaction with 3d itinerant electrons and also experience the effect of crystalline electric field. The results of calculations were in good agreement with the experimental data of Wada *et al* (1999). It was also established that the main contribution to ΔS_M in the $Er_{1-x}Y_xCo_2$ system comes from RE magnetic moments and the electronic magnetic entropy is small.

Pillmayr *et al* (1987) and Hilscher *et al* (1988) investigated the heat capacity of the $(R_xY_{1-x})Co_2$ ($R = Ho, Dy$) alloy systems. The sharp peak at T_C in $HoCo_2$ was rounded and decreased with the addition of more than 40% of Y, and its position was shifted to the low-temperature range. However, for $x > 0.6$ the sharpness of the heat capacity peak at T_C remained pointing to the first-order character of this transition in the $(Ho-Y)Co_2$ system in this concentration range. The peak corresponding to the low-temperature spin-reorientation transition was moved to higher temperatures with x decreasing and merged with the Curie temperature peak at $x \approx 0.45$. The magnetic ordering entropy S_M determined from these measurements dropped for $x < 0.2$, and for $x \geq 0.2$ it attained the theoretical values for Ho and Dy (see table 6.2). The magnetic entropy associated with the magnetic moment of Co (for $S = 1/2$ it is equal to 5.76 J/mol K) was not observed above T_C in either alloy system. This was attributed to the itinerant character of the Co magnetic moment (Pillmayr *et al* 1987). According to the authors' opinion the magnetic entropy decrease observed for $x < 0.2$ may point to an instability of the RE magnetic moment in this concentration range (Pillmayr *et al* 1987 and Hilscher *et al* 1988).

Zhang *et al* (2001a) determined the magnetic entropy change in ternary $RCoAl$ compounds ($R = Gd, Tb, Dy, Ho$) from magnetization. These compounds crystallize in a hexagonal $MgZn_2$ structure. General ferromagnet behaviour, with the ΔS_M maximum near the Curie temperature, was obtained

for all investigated RCoAl compounds and $(\text{Gd}_{0.5}\text{Dy}_{0.25}\text{Er}_{0.25})\text{CoAl}$ alloy except for GdCoAl, where the table-like form of the $\Delta S_M(T)$ curve was observed. The plateau was positioned in the temperature range from 70 to 105 K. Earlier analogous $\Delta S_M(T)$ curves with plateaus were observed in the $(\text{GdEr})\text{NiAl}$ system—see section 6.2. In DyCoAl the authors observed at 5 K an essential field hysteresis of magnetization with a coercive force of about 1 kOe. In order to decrease the anisotropy and keep the Curie temperature constant, Zhang *et al* (2001a) fabricated $(\text{Gd}_{0.5}\text{Dy}_{0.25}\text{Er}_{0.25})\text{CoAl}$, where Er was used to cancel anisotropy of Dy, since Stevens' coefficients of these elements have opposite signs. It was found that peak ΔS_M in $(\text{Gd}_{0.5}\text{Dy}_{0.25}\text{Er}_{0.25})\text{CoAl}$ was much lower than in DyCoAl, but the coercive force was essentially decreased—to about 150 Oe at 5 K. The Curie temperatures and peak ΔS_M values for the investigated RCoAl compounds are presented in table 6.5.

The heat capacity of the ternary $\text{Nd}_7\text{Co}_6\text{Al}_7$ intermetallic compound was investigated by Canepa *et al* (2000). This compound has tetragonal $\text{Pr}_7\text{Co}_6\text{Al}_7$ -type crystal structure and was not studied before. According to magnetization measurements it orders magnetically below 16 K with the formation of some type of noncollinear magnetic structure. The coercive force was determined to be 80 Oe at 5 K. The zero-field heat capacity revealed a λ -type anomaly at 15.5 K, which under application of the magnetic field became less pronounced and disappeared in 50 kOe. This behaviour points to the ferromagnetic character of the magnetic ordering in $\text{Nd}_7\text{Co}_6\text{Al}_7$. The $\Delta S_M(T)$ and $\Delta T(T)$ dependences also revealed ferromagnetic-type behaviour with a maximum near the temperature of magnetic ordering. However, the observed ΔS_M and ΔT peak values were lower than in the other RE compounds—see table 6.5.

The heat capacity of the Er_3Co compound, which below $T_C = 13$ K exhibited a noncollinear magnetic structure, was measured by Saito *et al* (1995). Above T_C a large magnetic contribution to the heat capacity was found. It was related to a crystalline electric field effect (Schottky-type) anomaly and was interpreted in the framework of the point-charge model.

The thermal conductivity of ErCo_2 was studied by Ogawa *et al* (1991). As for Er_3Ni , ErNi , ErNi_2 and DyNi_2 , it decreased with decreasing temperature with a slight anomaly near T_C . Some numerical values of the thermal conductivity for ErCo_2 are presented in table A2.1 in appendix 2.

6.5 Rare earth–manganese

The heat capacity of Laves-phase compounds RMn_2 ($\text{R} = \text{Y, Gd, Er}$) was measured by Okamoto *et al* (1987). These compounds display various magnetic ordering and behaviour. YMn_2 is an itinerant antiferromagnet

with a Néel temperature of 100 K. The heat capacity temperature dependence displayed a symmetric anomaly typical for first-order transitions. The magnetic entropy temperature dependence was determined from the magnetic heat capacity obtained by subtracting lattice and electronic contributions from the total heat capacity. The magnetic entropy associated with the transition at T_N was about 3.9 J/mol K, which is much smaller than the theoretical value for $J = 3/2$ corresponding to the magnetic moment of Mn in this compound. This is related to the itinerant nature of the Mn magnetic moment.

In GdMn_2 the Mn subsystem is ordered antiferromagnetically and Gd moments are in a canted state. The heat capacity temperature dependence measured by Okamoto *et al* (1987) revealed a sharp symmetric peak at 110 K (Néel temperature). The magnetic entropy below 50 K was about 9 J/mol K, which is much less than the theoretical value for Gd. ErMn_2 is a simple ferromagnet and its heat capacity displays a λ -type anomaly at the Curie temperature of 15 K. The essential magnetic heat capacity contribution observed above T_C was related to crystalline field effects.

Although there is no research devoted to determination of the magnetic entropy change or MCE in RMn_2 compounds, two of them, namely GdMn_2 and TbMn_2 , seem to be promising from the point of view of high magnetocaloric properties. In these compounds the Mn magnetic moment is unstable and plays an essential role in forming the magnetic properties of the compounds. The transition to a magnetically ordered state in these compounds, which takes place at 109 K for GdMn_2 and 54 K for TbMn_2 , is accompanied by essential spontaneous lattice expansion—in TbMn_2 , $\Delta V/V$ at the transition reaches $\sim 1.4\%$ (Labroo *et al* 1990, Marquina *et al* 1995). Tishin *et al* (2002) estimated the lattice entropy change ΔS_{LFO} arising due to the lattice dimension change at the transition with the help of equation (6.3) and available literature data. It was obtained that, for TbMn_2 , ΔS_{LFO} is $\sim 94 \text{ J/kg K}$ and for GdMn_2 it is $\sim 20.5 \text{ J/kg K}$, which is higher than in $\text{Gd}_5\text{Si}_2\text{Ge}_2$ (see table 6.6), the compound with a huge magnetocaloric effect. The shift of the transition point in magnetic field in TbMn_2 , estimated by Tishin *et al* (2002) on the basis of results of Marquina *et al* (1995), also has a high value of $\sim 0.5 \text{ K/kOe}$.

Duong *et al* (2000) and Hagmausa *et al* (2000) undertook investigations of heat capacity in RMn_4Al_8 ($\text{R} = \text{Y}, \text{Nd}, \text{Gd}, \text{Dy}, \text{Er}$), which has tetragonal ThMn_{12} -type crystal structure. Magnetization measurements showed that there is antiferromagnetic interaction between rare earth magnetic moments. In RMn_4Al_8 ($\text{R} = \text{Nd}, \text{Dy}, \text{Er}$) compounds the heat capacity temperature dependences did not display any anomalies related to magnetic ordering down to 1.5 K. The zero-field heat capacity temperature dependence of GdMn_4Al_8 had an anomaly typical for Schottky anomaly. From behaviour of the anomaly in the magnetic field it was concluded that it is related to short-range antiferromagnetic correlations between Gd magnetic

moments. The magnetic entropy of GdMn_4Al_8 became temperature independent above 20 K with the value close to the theoretical one of Gd.

Finally, based on the consideration made above we can make the following conclusions about magnetocaloric properties of the intermetallic compounds containing RE and 3d metals: RAI_2 and RNi_2 compounds, where the RE ion is the only carrier of the magnetic moment, are characterized by high magnetic entropy change and adiabatic temperature change—the maximum $-\Delta S_M/\Delta H$ and $\Delta T/\Delta H$ values of 0.723 J/kg K kOe and 0.189 K/kOe were observed in ErAl_2 . It should also be noted that a large amount of the magnetic entropy—about 90% of theoretical value—is utilized in the magnetic ordering process in RAI_2 compounds. The ΔS_M and ΔT temperature behaviour in RAI_2 and RNi_2 compounds was successfully described in the framework of the model based on mean field approximation and taking into account crystalline field effects. The compounds with RE and nonmagnetic elements of Ni usually have low magnetic ordering temperatures, which determines their possible magnetocaloric applications in the low-temperature range. Some of the compounds are characterized by essential magnetic and crystalline electric field effect contributions to the heat capacity near magnetic ordering temperatures below 20 K. Such compounds, among which GdRh , Er-Ag , RGa_2 , ErNi and Er_3Ni should be mentioned, can be used in passive magnetic regenerators instead of Pb. $(\text{Gd-Er})\text{NiAl}$ alloys showed multiple magnetic transitions providing wide table-like ΔS_M and ΔT temperature dependences. In the most investigated R–Fe compounds the magnetocaloric properties were not high. However, this was not the case for $\text{LaFe}_{13-x}\text{A}_x$, where A = Si or Al and x is below 1.6, and where first-order magnetic phase transition to the magnetically ordered state is observed. Due to the first-order type of the transition these alloys display essential ΔS_M and ΔT —maximum $-\Delta S_M/\Delta H$ and $\Delta T/\Delta H$ of 2.3 J/kg K kOe and 0.405 K/kOe were found in $\text{LaFe}_{11.7}\text{Si}_{1.3}$ with $T_C = 188$ K. High magnetocaloric properties were also demonstrated by RCO_2 compounds with R = Dy, Ho and Er, where the first-order magnetic phase transition at T_C is also observed. The magnetic phase transitions in the $\text{LaFe}_{13-x}\text{A}_x$ alloys and RCO_2 compounds is accompanied by essential lattice parameter change. In HoCo_2 , even change of crystal structure type from cubic to tetragonal at T_C is observed. It was shown by Tishin *et al* (2002) that in the RCO_2 (R = Dy, Ho, Er) the main contribution to ΔS_M is related to the lattice dimension change at the transition. Based on the data about large magnetovolume effect in TbMn_2 , Tishin *et al* (2002) assumed this compound to have essential magnetocaloric properties. However, it should be noted that high $-\Delta S_M/\Delta H$ and $\Delta T/\Delta H$ values in $\text{LaFe}_{13-x}\text{A}_x$ and RCO_2 decreased in higher magnetic field. This can be related to change of the magnetic transition order from first to second in high magnetic fields.

Chapter 7

Magnetocaloric effect in rare earth–metalloid compounds

Rare earth–metalloid compounds display various types of magnetic ordering and magnetic transitions. The most interesting compounds among this group of magnetic materials are the silicides and germanides. In particular, RMn_2Ge_2 ($R = La, Gd, Tb, Dy$) compounds have layered crystal structure, two magnetic sublattices (Mn and R) ordering at different temperatures and strong dependence of exchange interactions on interatomic distance. All these factors determine complex magnetic structures of the compounds with multiple magnetic phase transitions, including first-order transitions. In recent years attention of investigators was attracted to the system $(RR')_5(Si-Ge)_4$. This is related to unusual magnetic properties discovered in $Gd_5(Si-Ge)_4$ compounds. In a certain concentration range in this system the compounds undergo magnetic first-order transition accompanied by reversible structural transition and essential change in lattice parameters and magnetic properties. This effect causes high magnetocaloric properties of $Gd_5(Si-Ge)_4$ and increased interest for these compounds.

7.1 Compounds with Sb and As

Heat capacity, magnetization and MCE of the $Gd_4(Bi_xSb_{1-x})_3$ ($x = 0, 0.25, 0.5, 0.75, 1$) system was studied by Niu *et al* (2001) in the temperature interval from 3.5 K up to 350 K. The obtained alloys had anti- Th_3P_4 -type crystal structure and were ferromagnets with Curie temperatures increased with x increasing from 264 K (Gd_4Sb_3) to 332 K (Gd_4Bi_3)—see table 7.1. The zero-field heat capacities of the investigated materials exhibited λ -type peaks near the Curie temperatures, which broadened with application of the magnetic field and shifted to the higher-temperature region. The magnetic entropy change and MCE temperature dependences were calculated from the heat capacity. They showed caret-type peaks typical for ferromagnets near the Curie temperatures and were lower than those in

Table 7.1. The Curie temperatures (T_C), temperature of the maximum in the $\Delta T(T)$ curves (T_{\max}), magnetic entropy change ΔS_M near the Curie temperature induced by the magnetic field change ΔH , peak MCE value ΔT at $T = T_{\max}$ induced by ΔH , $\Delta T/\Delta H$ and $\Delta S_M/\Delta H$ in rare earth–metalloid compounds.

Compound	T_C (K)	MCE peak				ΔS_M peak				Ref.*
		T_{\max} (K)	ΔT (K)	ΔH (kOe)	$\Delta T/\Delta H \times 10^2$	$-\Delta S_M$ (J/kg K)	ΔH (kOe)	$-\Delta S_M/\Delta H \times 10^2$		
Gd ₄ Sb ₃	264	278	10.5	100	10.5	81 [†]	100	81 [‡]	1	
		270	3.2	20	16	30 [†]	20	150 [‡]		
Gd ₄ (Bi _{0.25} Sb _{0.75}) ₃	272	285	10.9	100	0.9	80 [†]	100	80 [‡]	1	
Gd ₄ (Bi _{0.5} Sb _{0.5}) ₃	289	298	10.8	100	0.8	75 [†]	100	75 [‡]	1	
Gd ₄ (Bi _{0.75} Sb _{0.25}) ₃	306	314	10.9	100	0.9	72 [†]	100	72 [‡]	1	
Gd ₄ Bi ₃	332	337	11.8	100	11.8	65 [†]	100	65 [‡]	1	
DyMn ₂ Ge ₂	40	45	6.3	50	12.6	12	50	24	2	
			(plateau)							
		42	5	20	25	9.6	20	47.9		
GdRu ₂ Ge ₂	32 (T _N)	—	—	—	—	5	40	12.5	10	
CeCu _{0.86} Ge ₂	17 (T _N)	17	4.5	80	5.6	—	—	8.5	3	
PrCr _{0.76} Ge ₂	23	23	1.25	20	6.3	—	—	—	3	
			5.8	80	7.3	—	—	—		
HoTiGe	90 (T _N)	—	—	—	—	4	50	8	11	
GdFeSi	118	130	4.4	90	4.9	22.4	90	24.9	4	
GdPd ₂ Si	17 (T _N)	17	12	80	15	21.9	80	27.4	5	
PrCo ₂ Si ₂	31 (T _N)	25	3.1	20	15.5	4.5	20	22.5	6	
Pr _{0.8} La _{0.2} Co ₂ Si ₂	26 (T _N)	19	-1.2	80	-1.5	—	—	—	6	
			-1.3	80	-1.63	—	—	—		

Tb_2PdSi_3 (along the [1010] axis)	23 (T_N)	—	—	—	—	—	8.8	50	17.7	7
$Gd_2Pd_2Si_3$	17 (T_N)	22	8.5	80	10.6	13.1	80	16.4	—	8
$NdMn_2Si_2$	32 (FM-PM)	32	~1	10	10	0.82	10	8.2	—	9

* 1. Niu *et al.* (2001); 2. Wada *et al.* (2000); 3. Rawat and Das (2001c); 4. Napoletano *et al.* (2000); 5. Rawat and Das (2001b); 6. Das and Rawat (2000); 7. Majumdar *et al.* (2000); 8. Sampathkumaran (2000); 9. Nikitin *et al.* (1987); 10. Tegus *et al.* (2002c); 11. Tegus *et al.* (2001).

[†] In mJ/cm³K.

[‡] In mJ/cm³K kOe.

Gd. The latter was explained by reduction of the Gd content in the alloys. However the saturation magnetic moment in the alloys at 5 K was about $7.3 \mu_B$ per Gd atom. The absolute values of the MCE increased and ΔS_M decreased with an increase of Bi concentration—see table 7.1.

The heat capacity of $Er_xDy_{1-x}Sb$ pseudobinary compounds was measured in the temperature interval from 2 to 40 K by Long *et al* (1995b). The heat capacity peaks were found at the magnetic ordering transitions at 3.6, 4.1, 4.9, 7.6 and 9.4 K for $x = 1, 0.8, 0.6, 0.2$ and 1, respectively. The maximum heat capacity peak value of about 200 J/mol K was observed for DySb and the minimum value (12.3 J/mol K) in $Er_{0.6}Dy_{0.4}Sb$. The value of the heat capacity peak in the compound with minimal ordering temperature ($ErSb$) was about 60 J/mol K. From the heat capacity data the temperature dependences of the magnetic entropy for the alloys were calculated. The magnetic entropy change associated with transition to the magnetically ordered state was determined to be about $R \ln 2$ for all investigated alloys. This was related by the authors to the doublet ground state of the rare earth ions due to the splitting in crystalline electric field. Above the magnetic transition point the magnetic entropy continued to increase up to 40 K. The maximum magnetic entropy value decreased with increasing Dy concentration.

The magnetic entropy change temperature dependences were theoretically calculated in YbAs by von Ranke *et al* (2000b). This compound is antiferromagnetic with the Néel temperature of 0.49 K and is characterized by strong quadrupolar interactions. The calculations were made for paramagnetic temperature region. In the model Hamiltonian the single-ion crystalline field energy, quadrupolar interaction energy and Zeeman energy were taken into account. The exchange interactions were neglected because of low magnetic ordering temperature. In the compound under investigation the energy levels of Yb ion are split by the crystalline electric field by the following scheme: ground state Γ_6 (doublet), Γ_8 (quartet) and Γ_7 (doublet). In the frameworks of the proposed model it was shown that the Γ_8 level is split by the quadrupolar interaction into two doublets and the magnetic field removes all degeneracy. The magnetic entropy change ΔS_M calculations showed that it is negative for temperatures below 30 K. In the temperature range between 30 and 84 K, ΔS_M was positive for ΔH lower than 23.5 kOe. The temperature interval of positive ΔS_M was narrowed as the value of ΔH increased. The ΔS_M anomalous behaviour was related to the quadrupolar interaction and disappeared if it was not taken into account.

7.2 Silicides and germanides

7.2.1 Ternary compounds of rare earths with Si and Ge

Let us consider first ternary germanides containing rare earth elements. Wada *et al* (1996, 2000) investigated the heat capacity of RMn_2Ge_2

(R = La, Gd, Tb, Dy) compounds in the temperature interval from 4.2 K to 300 K. RMn₂Ge₂ compounds crystallize in the tetragonal ThCr₂Si₂ structure, in which R—Ge—Mn—Ge—R layers are stacked along the crystalline c-axis. According to the magnetic studies, both Mn and R atoms in these compounds possess magnetic moments. The Mn sublattice in the compounds can be ordered ferromagnetically or antiferromagnetically. The Mn magnetic moments lie in the c-plane and have ferromagnetic ordering inside it. The interlayer Mn—Mn interaction is sensitive to the interlayer distance and can be antiferromagnetic or ferromagnetic depending on that distance. So, the type of magnetic ordering in the Mn sublattice depends on the size of the R ion. LaMn₂Ge₂ is a ferromagnet ($T_C = 306$ K) and YMn₂Ge₂ is antiferromagnet (Szytula 1992, Narasimhan *et al* 1975).

If R is a heavy rare earth element, the compounds undergo high-temperature magnetic transition from paramagnetic to antiferromagnetic state in the Mn sublattice at the Néel temperature T_N of 350–450 K (Szytula 1992, Narasimhan *et al* 1975) and the R sublattice remains disordered. The R sublattice orders ferromagnetically at the second low-temperature magnetic phase transition. Below the second magnetic phase transition temperature the ferrimagnetic state arises at which all Mn magnetic moments are aligned antiparallel to the R moments. In GdMn₂Ge₂ and TbMn₂Ge₂ the second magnetic phase transition is first-order and takes place at 96 K and 95 K, respectively. DyMn₂Ge₂ displays double transitions at $T_1 = 40$ K and $T_2 = 36$ K. Neutron diffraction studies showed that below T_2 the compound has the ferrimagnetic structure and above T_1 the antiferromagnetic structure with disordered Dy moments arose (Kobayashi *et al* 1991, Venturini *et al* 1992). Between T_1 and T_2 an intermediate mixed phase existed. DyMn₂Ge₂ is also characterized by strong magnetocrystalline anisotropy in the ferrimagnetic phase with the easy c-axis.

The heat capacity of LaMn₂Ge₂ did not show anomalies in the investigated temperature range from 4.2 to 300 K (Wada *et al* 1996). GdMn₂Ge₂ and TbMn₂Ge₂ displayed sharp first-order character heat capacity peaks at 95 K and 96 K, respectively. The magnetic heat capacity was extracted from the measured heat capacity by subtraction of electronic and lattice contributions. The electronic contribution was calculated by equation (2.60) with $a_e = 14 \text{ mJ/K}^2$ obtained for LaMn₂Ge₂. As the lattice contribution the heat capacity of paramagnetic LaFe₂Ge₂ was taken. From the magnetic heat capacity the temperature dependences of magnetic entropy in the investigated RMn₂Ge₂ compounds were determined. In LaMn₂Ge₂ the magnetic entropy appeared above 50 K and reached 20 J/mol K at 300 K, which is comparable with theoretical value for two magnetic ions with $J = 1$ (18.3 J/mol K) calculated by equation (2.66). In GdMn₂Ge₂ at 95 K a magnetic entropy jump of 3.3 J/mol K was observed and just above the transition the magnetic entropy was about 15.2 J/mol K, close to the theoretical value of Gd (see table 6.2). In TbMn₂Ge₂ the jump was of

7 J/mol K and the entropy just above the low-temperature transition was about 12 J/mol K, which is essentially smaller than the theoretical value for Tb. The results on magnetic entropy were analysed with the help of MFA including crystalline field effects. Good accordance between the calculated and the experimental $S_M(T)$ dependences was obtained. It was shown that the entropy jumps could be completely ascribed to the R sublattice. The observed difference between the magnetic entropy values in GdMn_2Ge_2 and TbMn_2Ge_2 just above the transition was related by the authors to the essential temperature dependence of the Tb sublattice magnetic entropy above the transition temperature due to the crystalline field effects acting on anisotropic Tb ions.

Wada *et al* (2000) made heat capacity and magnetization measurements on poly- and single crystals of DyMn_2Ge_2 . The heat capacity temperature dependences of polycrystalline DyMn_2Ge_2 revealed in zero field two sharp peaks corresponding to T_1 and T_2 , at 40.3 and 37.0 K. Under application of the field of 40 kOe the low-temperature peak remained almost unchanged and at the same temperature, while the high-temperature peak was significantly broadened and shifted in the high-temperature region. The total entropy zero-field and in-field temperature dependences were calculated from the heat capacity data. The entropy jump associated with two successive transitions at T_1 and T_2 was determined to be about 9 J/mol K, which is 36% of the theoretical full entropy of Dy.

The magnetization measurements along the easy c-axis in DyMn_2Ge_2 showed the field-induced metamagnetic transition from the antiferromagnetic state to the intermediate state just above T_1 with a critical field of about 15 kOe at 45 K. With rising temperature, the critical field increased to the values above 50 kOe at 60 K. Just below T_2 the magnetization on field curves demonstrated ferromagnetic behaviour. The magnetization temperature dependences displayed behaviour characteristic of first-order magnetic transition at the temperature of transition from the intermediate phase to the antiferromagnetic phase. It should be noted that the sharpness of the transition persisted even in high magnetic fields up to 40 kOe. The rate of the transition displacement in the field was about 0.3 K/kOe. From the obtained magnetization data the magnetic entropy change ΔS_M temperature dependences were calculated, which are shown in figure 7.1. As one can see above 40 K, $-\Delta S_M$ shows a wide plateau up to 60 K for $\Delta H = 50$ kOe. Its height weakly depends on the magnetic field. The authors related such behaviour to the first-order nature of the transition at T_1 , which preserves its character in high magnetic field. The positive ΔS_M near about 35 K was explained by disordering of ferrimagnetic structure by the magnetic field (i.e. by the antiferromagnetic-type paraprocess, which was discussed earlier—see section 2.6). Analogous temperature behaviour was obtained for the MCE, which was calculated using zero-field entropy (determined from the zero-field heat capacity) and in-field entropy (determined from

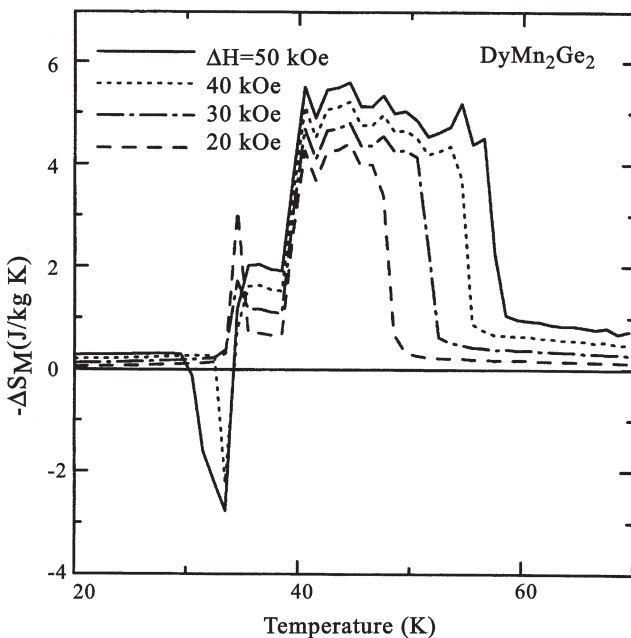


Figure 7.1. Temperature dependences of the magnetic entropy change ΔS_M induced by different ΔH in $DyMn_2Ge_2$ (Wada *et al* 2000). (Reprinted from Wada *et al* 2000, copyright 2000, with permission from Elsevier.)

zero-field entropy and ΔS_M) by the method described in section 3.2.2. The MCE value above 40 K was about 6.3 K for $\Delta H = 50$ kOe—see table 7.1.

The zero-field heat capacity temperature dependence of $GdRu_2Ge_2$ revealed two peaks at 32 and 29 K (Tegus *et al* 2002c). Magnetization measurements showed that the compound orders antiferromagnetically below 32 K and undergoes in the AFM state a field-induced magnetic transition to the ferromagnetic state in relatively low magnetic fields (the critical field of the transition was 10 kOe at 5 K). $\Delta S_M(T)$ curves obtained from magnetization measurements showed a negative maximum near 32 K and a positive region below about 20 K related to the antiferromagnetic-type paraprocess. Absolute peak values of ΔS_M in $GdRu_2Ge_2$ near T_N are presented in table 7.1.

The heat capacity and MCE of nonstoichiometric $CeCu_{0.86}Ge_2$ and $PrCu_{0.76}Ge_2$ compounds with CeNiSi₂-type crystal structure were studied by Rawat and Das (2001c). The heat capacity temperature dependence of $CeCu_{0.86}Ge_2$ reveals a pronounced peak at 15 K, which is related to magnetic ordering and shifts by the magnetic field to the high-temperature region. It should be noted that according to the magnetic measurements this compound is antiferromagnetic with a Néel temperature of 15 K, although its paramagnetic Curie temperature is positive (~ 7 K). At about 4 K there is

an additional small heat capacity anomaly, which shifts by the magnetic field to lower temperatures and was related by the authors to antiferromagnetic ordering. The heat capacity of $\text{PrCu}_{0.76}\text{Ge}_2$ revealed a peak near 23 K and a knee at 16 K, shifted by the magnetic field to higher temperatures. The $\Delta T(H)$ curves showed that the rate of the MCE changing with field for $\text{CeCu}_{0.86}\text{Ge}_2$ and $\text{PrCu}_{0.76}\text{Ge}_2$ compounds is not higher than 0.1 K/kOe for fields up to 20 kOe and decreased with increasing ΔH . The peak values of the MCE in $\text{CeCu}_{0.86}\text{Ge}_2$ and $\text{PrCu}_{0.76}\text{Ge}_2$ are presented in table 7.1.

The MCE temperature dependences for $\text{CeCu}_{0.86}\text{Ge}_2$ and $\text{PrCu}_{0.76}\text{Ge}_2$ in different magnetic fields were determined from the heat capacity data. For $\text{PrCu}_{0.76}\text{Ge}_2$ the MCE was positive in all investigated temperature ranges (4.2–40 K) and in all magnetic fields with a ferromagnetic-type maximum near 23 K and a knee near 16 K. For $\text{CeCu}_{0.86}\text{Ge}_2$ the MCE is positive with a maximum near 23 K for the magnetic field change higher than 10 kOe. In lower field the negative MCE was observed in the temperature range below about 15 K with negative minima at about 14 K. The authors related this behaviour to metamagnetic transition occurring at about 8 kOe, which was also observed on magnetization isotherms and in magnetoresistance measurements.

Tegus *et al* (2001) investigated magnetic properties of HoTiGe , which has a layered CeFeSi-type tetragonal structure with a sequence of R–Ge– Ti_2 –Ge–R layers along the c-axis. The competitive FM and AFM interactions between R ions in this compound provide its complex magnetic structure with ferromagnetic ordering inside R layers and antiferromagnetic interaction between them. At $T_N = 90$ K the compound turns to the antiferromagnetic state, which can be destroyed by an external magnetic field. The critical field of the AFM state destruction increases with decreasing temperature and is about 50 kOe for 5 K. The existence of an AFM structure leads to the appearance of the positive ΔS_M below ~ 80 K for $\Delta H = 50$ kOe and ~ 100 K for $\Delta H = 20$ kOe. The peak of negative ΔS_M (with a rather low absolute ΔS_M value) is observed in this compound above T_N —at ~ 102 K for $\Delta H = 20$ kOe and 91 K for $\Delta H = 50$ kOe.

Napoletano *et al* (2000) studied magnetic properties, heat capacity and magnetocaloric effect in ternary equiatomic compound GdFeSi , which has a Cu₂Sb-type structure. It is ferromagnetic and orders at the Curie temperature of 118 K. Magnetization measurements showed that there is no contribution from iron atoms to the total magnetic moment in this compound and saturation magnetization moment at 5 K in the field of 90 kOe is $6.62 \mu_B$. The zero-field heat capacity temperature dependence demonstrated λ -type anomaly near T_C , which was not observed in the field of 90 kOe. On the temperature dependence of ΔS_M and ΔT the wide asymmetric maximum was found with a shoulder in the low-temperature region. The maximum $-\Delta S_M$ and ΔT values were 5.4 J/mol K and 4.5 K for $\Delta H = 90$ kOe, respectively.

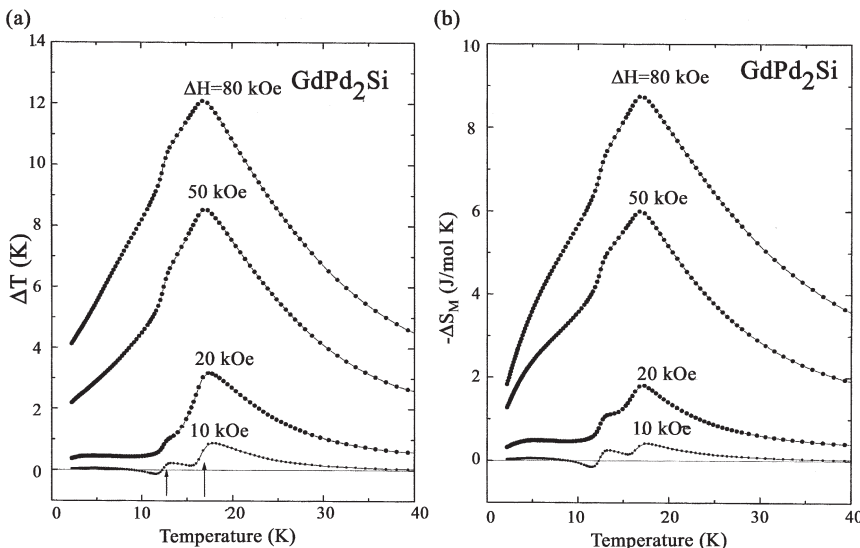


Figure 7.2. Temperature dependences of (a) ΔT and (b) ΔS_M in GdPd₂Si for various ΔH (Rawat and Das 2001b).

The MCE, heat capacity and resistivity of GdPd₂Si were investigated by Rawat and Das (2001b). This compound crystallizes in orthorhombic crystal structure. According to the data of Gignoux *et al* (1984) it is antiferromagnetic with a Néel temperature of 13.5 K, although its positive paramagnetic Curie temperature (14 K) points to the presence of ferromagnetic interactions and possible noncollinear magnetic ordering. The zero field heat capacity temperature dependence displays two peaks, at 17 K and at 13 K. Both peaks are shifted to low temperatures under application of the magnetic field, which points to their antiferromagnetic nature, and disappeared at 80 kOe. On the basis of the heat capacity and field dependence the authors concluded that between 13 K and 17 K a magnetic amplitude-modulated structure exists. Figure 7.2 shows the temperature dependences of the magnetic entropy change and the MCE determined from the heat capacity. One can see two anomalies, near 17 K and 13 K. Besides there is a temperature region of negative ΔT (positive $-\Delta S_M$) near ~ 12 K for the curves corresponding to $\Delta H = 10$ kOe, which disappears for higher ΔH . The authors related this behaviour to the occurrence of metamagnetic transition from antiferromagnetic to ferromagnetic structure above 10 kOe. This conclusion was verified by the field dependence of the MCE peak value, which has a characteristic bend at 10 kOe.

The heat capacity and resistivity of PrCo₂Si₂ and Pr_{0.8}La_{0.2}Co₂Si₂ were measured by Das and Rawat (2000). From the heat capacity data the MCE temperature dependences were determined. PrCo₂Si₂ has a complex crystal

structure consisting of layers of Pr, Co and Si, analogous to that of RMn_2Ge_2 discussed above. The only magnetic element in this compound is Pr and three magnetic phase transitions occur under cooling: paramagnetism–modulated magnetic structure at 30 K with change in propagation vector direction at 17 K; and the modulated magnetic structure–layered antiferromagnetic structure (ferromagnetically ordered layers coupled antiferromagnetically) at 9 K. λ -type anomalies were observed on the heat capacity temperature dependences of PrCo_2Si_2 near these temperatures. For $\text{Pr}_{0.8}\text{La}_{0.2}\text{Co}_2\text{Si}_2$ there were two heat capacity anomalies, at 9 K and 26 K. The MCE of PrCo_2Si_2 was negative for ΔH up to 80 kOe in all investigated temperature (up to 40 K) ranges with three anomalies near magnetic transition temperatures. However the peak absolute values of the MCE were shifted from the transition temperatures to the low-temperature region at a value of about 5 K. The MCE in $\text{Pr}_{0.8}\text{La}_{0.2}\text{Co}_2\text{Si}_2$ was negative for $\Delta H = 20$ kOe down to 12 K and then became positive. For $\Delta H = 80$ kOe the temperature range of negative MCE in $\text{Pr}_{0.8}\text{La}_{0.2}\text{Co}_2\text{Si}_2$ was situated from about 26 K down to 12 K. The authors established correlation between the temperature dependence of MCE and the change of resistivity under magnetic field (magnetoresistive effect). The magnetoresistive effect and MCE temperature dependences were quite different for PrCo_2Si_2 and analogous for $\text{Pr}_{0.8}\text{La}_{0.2}\text{Co}_2\text{Si}_2$. The authors explained this by different mechanisms of the magnetoresistive effect in PrCo_2Si_2 and $\text{Pr}_{0.8}\text{La}_{0.2}\text{Co}_2\text{Si}_2$. In the authors' opinion, in the first case it is related to change of carrier's (conduction electrons) concentration (it does not affect the MCE) and in the second case the resistivity is determined by the scattering of electrons on the magnetic moments. The latter mechanism is directly related to the influence of the magnetic field on magnetic subsystem entropy and, consequently, with the magnetocaloric effect.

The first direct MCE measurement in a rare earth silicide was made on a NdMn_2Si_2 compound by Nikitin *et al* (1987) in the temperature range from 4.2 K to 60 K. This compound has a tetragonal crystal structure with ferromagnetic layers stacked along the tetragonal axis and containing Mn, R and Si atoms in the following sequence: R–Si–Mn–Si–R (it is analogous to the structure of RMn_2Ge_2 compounds discussed above). According to the previous neutron diffraction data, this compound has a magnetic phase transition temperature of 32 K, above which Mn magnetic moments are ordered antiferromagnetically and below are ordered ferromagnetically along the tetragonal axis (Siek *et al* 1981). The Nd sublattice did not reveal the magnetic ordering above 1.8 K. On the basis of the magnetization measurements Nikitin *et al* (1987) made a conclusion that just above 32 K the magnetic field above 10 kOe converts the antiferromagnetic structure to the ferromagnetic one through the metamagnetic first-order transition. The MCE temperature dependences are shown in figure 7.3. Near 32 K (denoted as Θ_1 on the figure) the MCE maximum with the form typical for

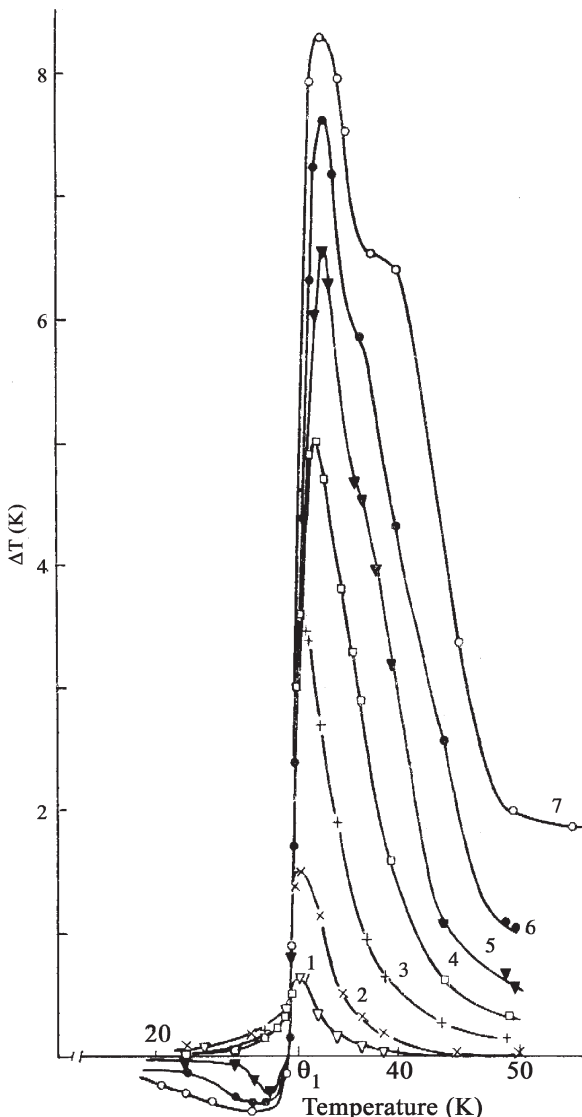


Figure 7.3. Temperature dependences of the MCE in NdMn_2Si_2 for different ΔH . $\Theta_1 = 32$ K (Nikitin *et al* 1987).

first-order transitions is observed. The region of negative MCE below 32 K corresponding to ΔH above 40 kOe was related by the authors to arising of noncollinear magnetic structure in these fields.

Majumdar *et al* (2000) investigated magnetization and determined ΔS_M in single crystalline Tb_2PdSi_3 . This compound has a hexagonal AlB_2 -type

crystal structure and revealed a magnetic phase transition from the paramagnetic state to the antiferromagnetic state at the Néel temperature of 23 K. The magnetization measurements were performed along [0001] and [1010] crystallographic axes. They showed that the compound was easily magnetized along the [1010] axis and hardly magnetized along the [0001] axis. The $-\Delta S_M$ temperature dependence displayed a wide maximum at about 30 K (with a peak $-\Delta S_M$ value of $\sim 8.8 \text{ J/kg K}$ at 25 K for $\Delta H = 50 \text{ kOe}$) if the magnetic field is directed along the [1010] axis. For magnetic field directed along the [0001] axis the magnetic entropy change was small and negative in the temperature range investigated (from 4.2 to 50 K). It should be noted that the paramagnetic Curie temperature is positive (23 K) in the first case and negative (-30 K) in the second case. This implies that magnetic coupling along the [1010] axis is of ferromagnetic character and along the [0001] axis is antiferromagnetic.

The heat capacity and magnetization of the Gd_2PdSi_3 compound were investigated by Sampathkumaran *et al* (2000). This compound is antiferromagnetic with a Néel temperature of 21 K and has a hexagonal AlB_2 -type crystal structure. The zero-field heat capacity had a rounded peak at about 18 K, which under application of the magnetic field shifted to the low-temperature range (with a rate of 0.23 K/kOe) and disappeared in the field of 80 kOe. The $-\Delta S_M(T)$ and $\Delta T(T)$ curves displayed positive wide maxima near T_N . However, for ΔH of 5 kOe and 10 kOe the temperature region of positive ΔS_M (and negative ΔT) existed just below $\sim 13 \text{ K}$, which can be related to an antiferromagnetic-type paraprocess in the magnetic structure of the compound. The peak values of $-\Delta S_M$ and ΔT near T_N are shown in table 7.1.

7.2.2 Magnetocaloric effect in $\text{R}_5(\text{Si}-\text{Ge})_4$ alloys

The $\text{R}_5(\text{Si}-\text{Ge})_4$ alloy system has attracted considerable attention in recent years because of a large magnetic entropy change and other unusual magnetic and structural phenomena observed in this system (see Pecharsky and Gschneidner 1997a–c, 1998, Gschneidner *et al* 2000a, Gschneidner and Pecharsky 2002). Especially high magnetocaloric properties were found in $\text{Gd}_5(\text{Si}-\text{Ge})_4$ alloys. It was shown by Morellon *et al* (1998) and Choe *et al* (2000) that structural and magnetic properties in this system are strongly interrelated. According to earlier structure investigations of Smith *et al* (1967), Holtzberg *et al* (1967) and Iglesias and Steinfink (1972) Gd_5Si_4 and Gd_5Ge_4 at room temperature have Sm_5Ge_4 -type orthorhombic crystal structure. This structure can be considered as a sequence of Ge, Sm and mixed Ge–Sm layers stacked along the crystal b-axis in the following order: $\cdots \text{Ge}, \text{Sm}, \text{Ge-Sm}, \text{Sm}, \text{Ge} \cdots$. Holtzberg *et al* (1967) reported the existence of the solid solution with an orthorhombic structure in the $\text{Gd}_5\text{Si}_x\text{Ge}_{4-x}$ system for $x = 0\text{--}0.8$ and $x = 2\text{--}4$ and an intermediate phase with unidentified crystal structure for $x = 1.2\text{--}2$.

More thorough crystallographic studies of the $\text{Gd}_5\text{Si}_x\text{Ge}_{4-x}$ system were performed by Pecharsky and Gschneidner (1997d) and Choe *et al* (2000). It was established that the intermediate phase exists for $x = 0.96\text{--}2$ and has a monoclinic crystal structure at room temperature; a homogeneous Gd_5Ge_4 -based solid solution extends from $x = 0$ to 0.8 and a second homogeneous Gd_5Si_4 -based solid solution extends from $x = 2$ to 4. The crystal structure of the $\text{Gd}_5\text{Si}_x\text{Ge}_{4-x}$ system was shown to be built from equivalent layers (slabs) that are infinite in the ac crystal plane and are stacked along the b-axis (Choe *et al* 2000). Essential difference was revealed between Gd_5Si_4 and Gd_5Ge_4 compounds. In the former, the slabs at room temperature are connected with each other along the b-axis by covalent-like bonds between pairs of Si atoms. In Gd_5Ge_4 such bonds between Ge atoms are absent at room temperature. The monoclinic phase ($x = 0.96\text{--}2$) is a case intermediate between Gd_5Si_4 and Gd_5Ge_4 compounds: only one half of the covalent-like bonds between the slabs through the metalloid (Si or Ge) atoms is preserved when compared with the Gd_5Si_4 compound. Thus, the monoclinic phase is composed from alternating strongly and weakly interacting slabs.

This description is illustrated by the magnetic and crystallographic phase diagram shown in figure 7.4, where O-1 is the orthorhombic Gd_5Si_4 -type phase with covalent bonds present between all slabs, M is the

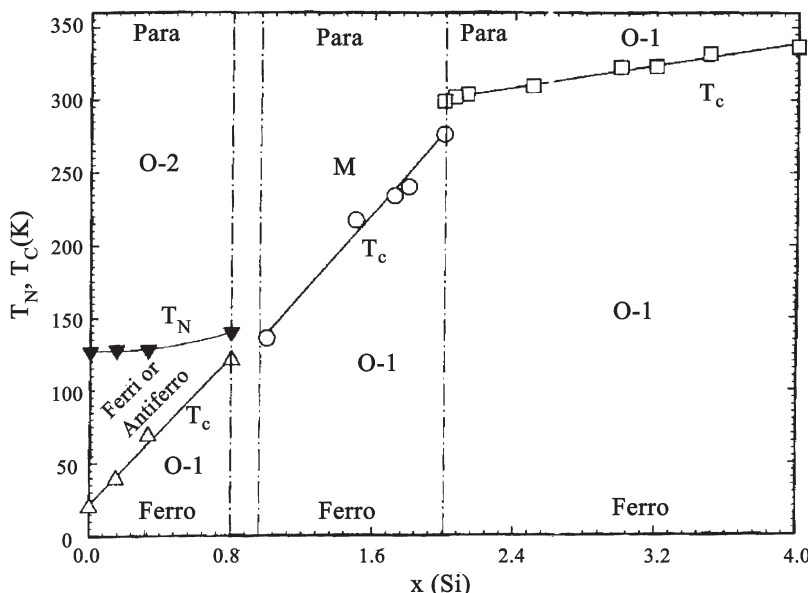


Figure 7.4. The magnetic and crystallographic phase diagram of the $\text{Gd}_5\text{Si}_x\text{Ge}_{4-x}$ alloy system: O-1, orthorhombic Gd_5Si_4 -type crystal structure; O-2, orthorhombic Gd_5Ge_4 -type crystal structure; M, monoclinic crystal structure (Gschneidner and Pecharsky 2002).

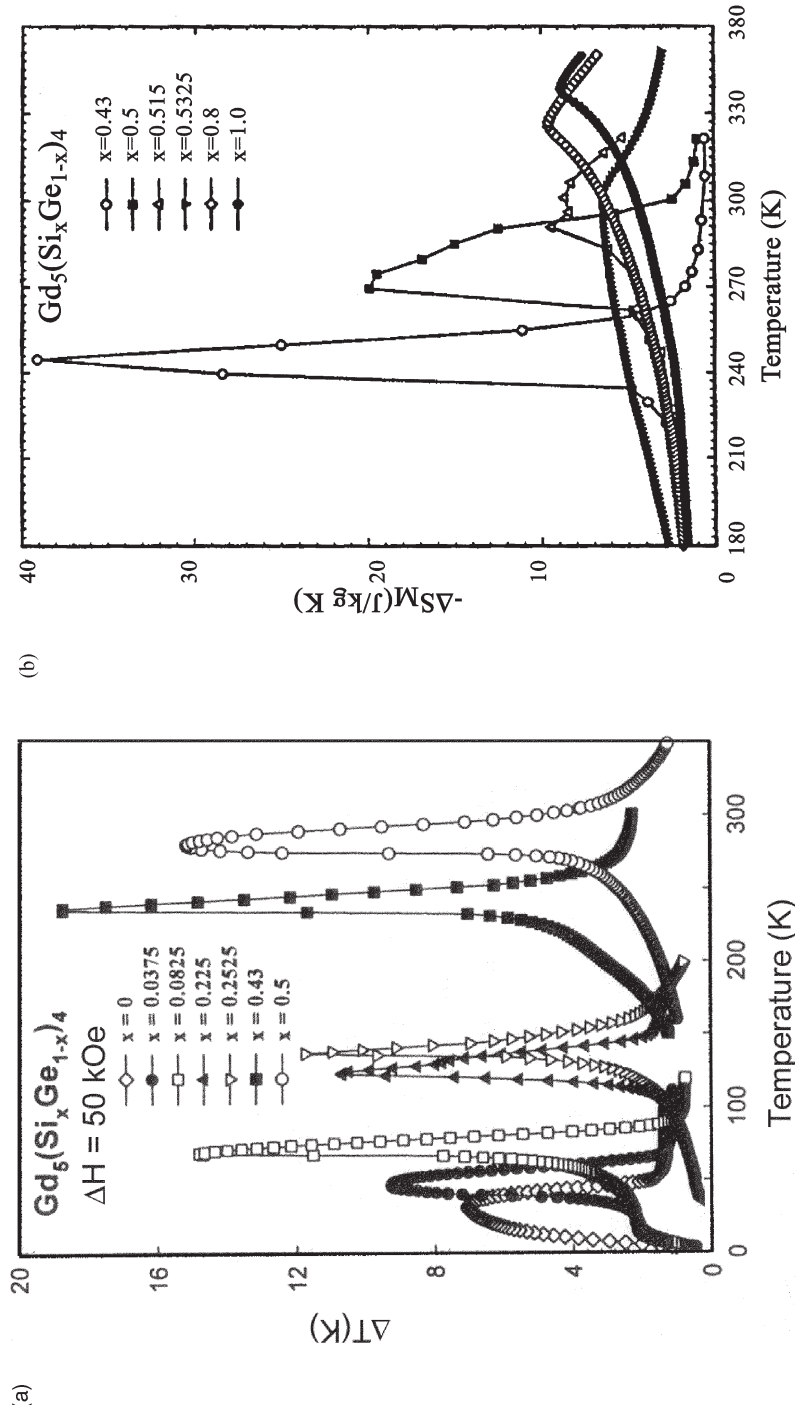


Figure 7.5. Temperature dependences of (a) the MCE and (b) magnetic entropy change ΔS_M for the $\text{Gd}_5(\text{Si}_x\text{Ge}_{1-x})_4$ alloys induced by $\Delta H = 50 \text{ kOe}$ (Pecharsky and Gschneidner 1998, Gschneidner *et al.* 1999).

monoclinic $\text{Gd}_5\text{Si}_2\text{Ge}_2$ -type phase with one half of the covalent bonds formed between the slabs, and O-2 is the orthorhombic Sm_5Ge_4 -type phase without bonds between the slabs. From magnetic and crystallographic studies it was found that magnetic phase transitions in the monoclinic and the Gd_5Ge_4 -type orthorhombic phase are accompanied by crystal structure changes (Pecharsky and Gschneidner 1997a-d, Morellon *et al* 1998, Choe *et al* 2000). Under cooling, the monoclinic phase orders ferromagnetically at the Curie temperature with the simultaneous change of crystal structure from monoclinic to orthorhombic Gd_5Si_4 -type. Thus, additional covalent bonds are created between the slabs. A similar process takes place under magnetic ordering for Gd_5Ge_4 -type solid solutions ($x = 0\text{--}0.8$) where orthorhombic Sm_5Ge_4 -type phase without interslab bonding changes to orthorhombic Gd_5Si_4 -type phase. The ferromagnetic ordering in this case happens through an intermediate ferri- or antiferromagnetic state (see figure 7.4). The ferromagnetic ordering for both the monoclinic $\text{Gd}_5\text{Si}_2\text{Ge}_2$ -type and orthorhombic Gd_5Ge_4 -type phases occurs via first-order magnetic phase transitions accompanied by a sharp change of the magnetization, which leads to high magnetic entropy and MCE values. The alloys with orthorhombic Gd_5Si_4 -type crystal structure ($x = 2\text{--}4$) display second-order magnetic phase transition at the Curie temperature with much lower magnetic entropy change. This behaviour is illustrated by figure 7.5, where the temperature dependences of the MCE and magnetic entropy change for the $\text{Gd}_5\text{Si}_x\text{Ge}_{4-x}$ system determined from the heat capacity measurements are shown. The maximum magnetic entropy change (68.5 J/K kg for $\Delta H = 50 \text{ kOe}$ at 143 K) was found in $\text{Gd}_5\text{Si}_1\text{Ge}_3$ alloy. Peak $-\Delta S_M$ and MCE values for the $\text{Gd}_5\text{Si}_x\text{Ge}_{4-x}$ alloy system are presented in table 7.2. One can see that magnetic entropy change in the alloys with monoclinic room temperature structure is much higher than in Gd in spite of considerable dilution of the magnetic Gd by nonmagnetic Ge and Si. It is worth noting that even when the magnetic entropy change in $\text{Gd}_5\text{Si}_{\sim 2}\text{Ge}_{\sim 2}$ and Gd is compared on a per mole of atoms basis, which is a proper way of comparing different classes of materials as shown by Pecharsky and Gschneidner (2001b), the resulting magnetic entropy change in the former remains larger than that in the latter.

The structural-magnetic phase transition in the $\text{Gd}_5\text{Si}_x\text{Ge}_{4-x}$ alloy system described above can be induced not only by changing temperature, but also by changing the magnetic field or pressure (Pecharsky and Gschneidner 1997a,c, Morellon *et al* 1998). Figure 7.6 shows the magnetization isotherms measured near T_C for the $\text{Gd}_5\text{Si}_2\text{Ge}_2$ alloy, where the crystallographic phase transition from the monoclinic to the orthorhombic structure also takes place (Choe *et al* 2000). One can see the magnetic field hysteresis typical for the first-order transitions induced by the magnetic field. It should be noted that the magnetization returns to zero after the magnetic field is brought back to zero and no remanent magnetization is observed.

Table 7.2. Magnetic ordering temperatures T_N or T_C , temperature of the maximum in the $\Delta T(T)$ curves (T_{\max}^T), temperature of the maximum in the $\Delta S_M(T)$ curves (T_{\max}^S) and maximum values of ΔS_M (at $T = T_{\max}^S$) and ΔT (at $T = T_{\max}^T$) induced by a magnetic field change ΔH and $\Delta T/\Delta H$ and $-\Delta S_M/\Delta H$ for $R_3(Si-Ge)_4$ alloys. References are shown in brackets.

Compound	T_C, T_N (K)	T_{\max}^T (K)	ΔT (K)	ΔH (kOe)	MCE peak		$-\Delta S_M$ peak		
					$\Delta T/\Delta H \times 10^2$ (K/kOe)	T_{\max}^S (K)	$-\Delta S_M$ (J/kg K)	ΔH (kOe)	$-\Delta S_M/\Delta H \times 10^2$ (J/kg K kOe)
Gd_5Si_4	336 [1] 345.7 [8]		8.8 [1]	50	17.6	339 [2] 340 [8]	9 [2] 8.2 [8]	50 50	18 16.4
$Gd_5Si_3Ge_1$	323 [1]		8.6 [1]	50	17.2	—	—	—	—
$Gd_5Si_{2.06}Ge_{1.94}$	306 [1]		8 [1]	50	16	281 [2]	9.5 [2]	50	19
$Gd_5Si_2Ge_2$	276 [1]	280 [3] 274 [3]	15 [3] 7.4 [3]	50 20	30 37	276 [3]	18.5 [3] 14 [3]	50 20	37 70
$Gd_5Si_{1.72}Ge_{2.28}$	246 [1]	235 [4]	18.8 [4]	50	37.6	275 [6]	20 [6]	50	40
$Gd_5Si_1Ge_3$	140 [1]		11.8 [1]	50	23.6	242 [5]	39 [5]	50	78
$Gd_5Si_{0.8}Ge_{3.2}$	121 [1] T_C 135 [1] T_N		9.2 [1]	50	18.4	256 [6]	33 [6]	50	66
$Gd_5Si_{0.33}Ge_{3.67}$	68 [1] T_C 128 [1] T_N	70 [4]	14.8 [4]	50	29.6	143 [5] 149 [6]	68.5 [5] 59 [6]	50 50	137 118
$Gd_5Si_{0.15}Ge_{3.85}$	40 [1] T_C 127 [1] T_N	45	9.2 [4]	50	18.4	—	—	—	—
Gd_5Ge_4	20 [1] T_C 125 [1] T_N	32	7.5 [4]	50	15	40 [5]	26 [5]	50	52

Table 7.2. Continued

Compound	T_C, T_N (K)	T_{max}^T (K)	ΔT (K)	ΔH (kOe)	MCE peak		$-\Delta S_M$ peak	
					$\Delta T/\Delta H \times 10^2$	T_{max}^S (K)	$-\Delta S_M$ (J/kg K)	$-\Delta S_M/\Delta H \times 10^2$
Gd _{4.5} Tb _{0.5} Si ₄	333.6 [8]	—	—	—	—	328 [8]	8.2 [8]	50
Tb ₅ Si ₃ Ge ₁	209.6 [9]	210 [9]	10.4 [9]	100	10.4	328 [8]	4.1 [8]	20
		210 [9]	8.4 [9]	75	11.2	210 [9]	14.8 [9]	20.5
		210 [9]	5.8 [9]	50	11.6	210 [9]	12 [9]	14.8
		210 [9]	2.4 [9]	20	12	210 [9]	8.4 [9]	16
215 [13]	—	—	—	—	—	213 [13]	3.8 [9]	50
		—	—	—	—	213 [13]	10.5 [13]	20
		—	—	—	—	213 [13]	6.7	19
Tb ₅ Si ₂ Ge ₂	100.1 [9]	110 [9]	10.4 [9]	100	10.4	110 [9]	24.8 [9]	90
		110 [9]	8 [9]	75	10.7	110 [9]	20.2 [9]	50
		110 [9]	5.4 [9]	50	10.8	105 [9]	15 [9]	30
		115 [9]	2.2 [9]	20	11	102 [9]	5.5 [9]	30
		—	—	—	—	100 [10]	22.5 [10]	27.5
110 [10]	—	—	—	—	—	102 [12]	36.4 [12]	45
110 [12]	—	—	—	—	—	102 [12]	21.8 [12]	52
116 [13]	—	—	—	—	—	104 [12]	20.3 [13]	22.6
76 [14]	—	—	—	—	—	100 [13]	12.8 [13]	50
Tb ₅ Ge ₄	95 [12] T_N	—	—	—	—	75 [14]	19.5 [14]	25.6
		—	—	—	—	75 [14]	5.5 [14]	39
		—	—	—	—	85 [12]	13.1	50
		—	—	—	—	100 [12]	3.7	10.9
		—	—	—	—	100 [12]	1	7.4
		—	—	—	—	—	—	5

Nd_5Si_4	71 [11]	—	—	—	—	—	8.3 [11]	50	16.6
$\text{Nd}_5\text{Si}_3\text{Ge}_1$	124 [11]	—	—	—	—	—	6.4 [11]	50	12.8
$\text{Nd}_5\text{Si}_2\text{Ge}_2$	65 [11]	—	—	—	—	—	5.6 [11]	50	11.2
	110 [10]	—	—	—	—	115 [10]	6 [10]	50	12
$\text{Nd}_5\text{Si}_1\text{Ge}_3$	61 [11]	—	—	—	—	—	4.2 [11]	50	8.4
Nd_5Ge_4	55 [11]	—	—	—	—	—	6.4 [11]	50	12.8
$\text{Gd}_4\text{Pr}_1\text{Si}_4$	291.5 [8]	—	—	—	—	310 [8]	6.1 [8]	50	12.2
$\text{Gd}_{4.25}\text{Pr}_{0.75}\text{Si}_4$	303.9 [8]	—	—	—	—	308 [8]	3 [8]	20	15
$\text{Gd}_{4.5}\text{Pr}_{0.5}\text{Si}_4$	316.3 [8]	—	—	—	—	304 [8]	7.5 [8]	50	15
						300 [8]	3.6 [8]	20	18
						290 [8]	8 [8]	50	16
						284 [8]	4 [8]	20	20

1. Gschneidner and Pecharsky (2000a); 2. Gschneidner *et al.* (1999); 3. Pecharsky and Gschneidner (1997c); 4. Pecharsky and Gschneidner (1998); 5. Pecharsky and Gschneidner (1997a); 6. Vinh *et al.* (1999); 7. Ivchenko *et al.* (2000); 8. Spichkin *et al.* (2001a); 9. Huang *et al.* (2002); 10. Thuy *et al.* (2000a); 11. Gschneidner *et al.* (2000a); 12. Moreillon *et al.* (2001); 13. Thuy *et al.* (2002); 14. Tegus *et al.* (2002d).

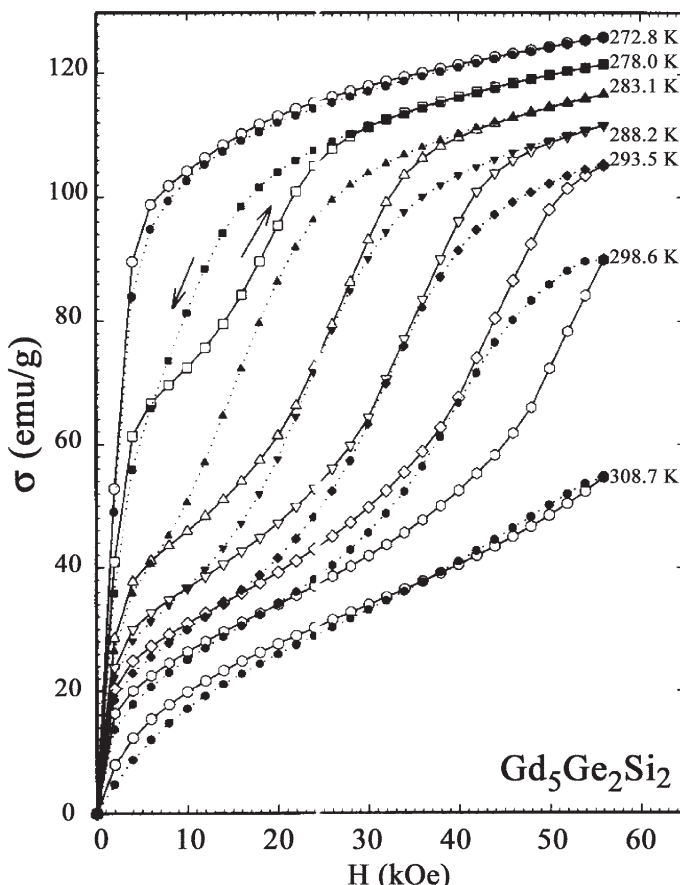


Figure 7.6. Magnetic field dependences of the specific magnetization of $Gd_5Si_2Ge_2$ alloy near the Curie temperature (Pecharsky and Gschneidner 1997c). (Copyright 1997 by the American Physical Society.)

This feature points to a reversible character of the structural transition, at which the structure of the alloy returns to the initial state after switching off the magnetic field. Analogous behaviour was observed by Morellon *et al* (1998) during measurements of the magnetic field dependences of the forced volume magnetostriiction in $Gd_5Si_{1.8}Ge_{2.2}$. A characteristic feature of the structural–magnetic transition in $Gd_5Si_2Ge_2$ is the preservation of its first-order character even in high magnetic fields. This can be seen from the behaviour of the heat capacity as a function of temperature during the transitions in various magnetic fields as illustrated in figure 7.7. No rounding, typical for second-order transitions, is observed in the magnetic field of 100 kOe. This feature is one of the reasons for high magnetic entropy change values in the monoclinic $Gd_5(Si–Ge)_4$ alloys.

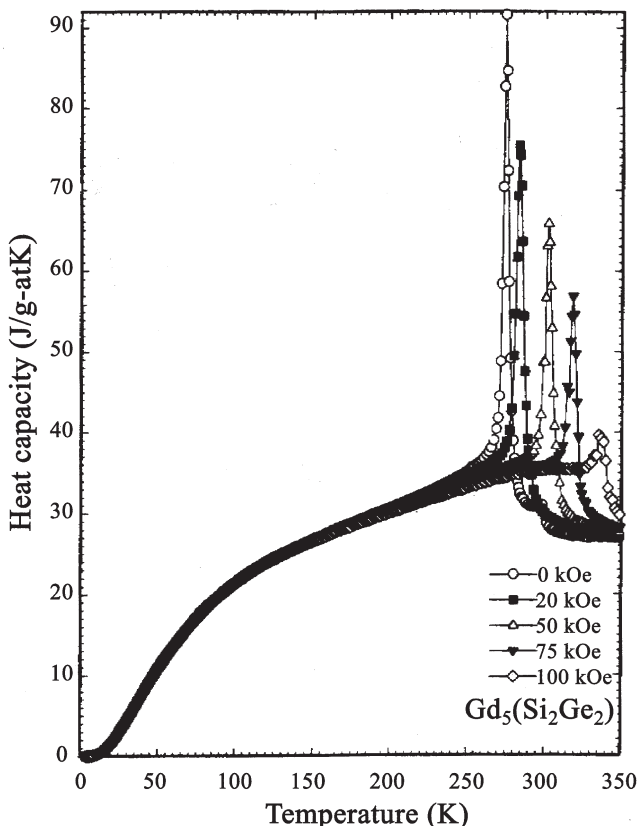


Figure 7.7. Heat capacity temperature dependences in various magnetic fields for $\text{Gd}_5\text{Si}_2\text{Ge}_2$ alloy (Pecharsky and Gschneidner 1997c). (Copyright 1997 by the American Physical Society.)

Vihl *et al* (1999) studied the magnetic entropy change in $\text{Gd}_5\text{Si}_x\text{Ge}_{4-x}$ ($x = 0.33, 1.01, 1.72, 2, 3$) on the basis of magnetization measurements. Two methods of magnetization measurement were used—pulse field (with pulse duration of 15 ms) and SQUID magnetometer. The $\Delta S_M(T)$ curves obtained by both methods were quite consistent and the peak $-\Delta S_M$ values were of the same order as obtained earlier by Pecharsky and Gschneidner (1997a,c). However it was noted that $M(H)$ curves obtained by different methods were quite different near the temperature of the magnetic phase transition: the curves measured by the SQUID magnetometer showed more complex behaviour, more pronounced hysteresis and higher magnetization than the curves measured by pulse magnetometer. In the regions far away from the transition, the correspondence between the curves was much better. The authors related the observed discrepancy to additional heat generated in the samples due to the magnetocaloric effect in the pulse

magnetization measurements, which is especially high near the magnetic phase transition.

The MCE in $R_5(Si-Ge)_4$ alloys with rare earth elements other than Gd, such as Nd, Pr, Tb and Dy, was studied by Gschneidner *et al* (2000a), Thuy *et al* (2000a,b), Ivchenko *et al* (2000), Spichkin *et al* (2001a) and Huang *et al* (2002). The results on the $Dy_5(Si_xGe_{1-x})_4$ alloy system were reported by Ivchenko *et al* (2000) and Gschneidner *et al* (2000a). According to X-ray data, the crystallographic sequence of phases in this system at room temperature is analogous to that in $Gd_5(Si_xGe_{1-x})_4$. A solid solution of Si in Dy_5Ge_4 with orthorhombic Sm_5Ge_4 -type crystal phase exists for $x = 0$ –0.62 and the solid solution of Ge in Dy_5Si_4 of analogous crystal type is stable for $x = 0.82$ –1. For $x = 0.67$ –0.78 the intermediate monoclinic $Gd_5Si_2Ge_2$ -type phase exists. The magnetic ordering temperatures in the system are lower than in $Gd_5(Si_xGe_{1-x})_4$ alloys: they rise from 46 K for Dy_5Ge_4 to 137 K for Dy_5Si_4 with a sharp jump at $x \approx 0.8$ (where the transition from the monoclinic to the orthorhombic phase takes place). The paramagnetic Curie temperatures of all alloys were positive, pointing to the ferromagnetic nature of the magnetic ordering. Figure 7.8 shows temperature dependences of the magnetic entropy change for $\Delta H = 50$ kOe for the investigated alloys determined from magnetization. $-\Delta S_M(T)$ curves for the alloys with $x \leq 0.62$ display a caret-like form typical of ferromagnets with peaks near the

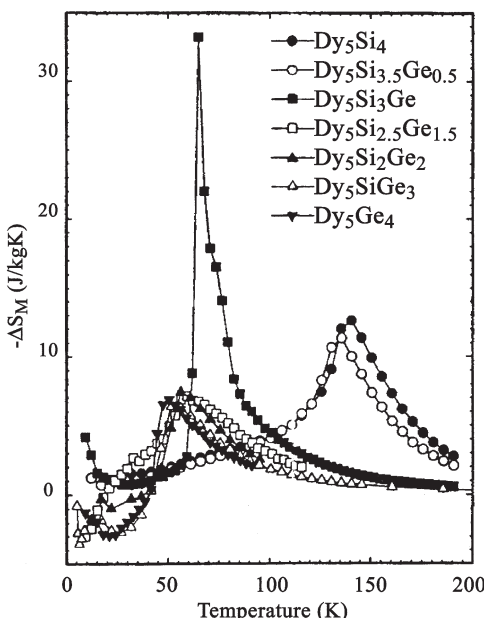


Figure 7.8. Temperature dependences of $-\Delta S_M$ for $Dy_5(Si_xGe_{1-x})_4$ alloys for $\Delta H = 50$ kOe (Ivchenko *et al* 2000).

magnetic transition temperatures. The alloy $Dy_5Si_3Ge_1$ belonging to a monoclinic phase region showed a $-\Delta S_M$ peak much higher than in other alloys investigated in this system (about 33 J/kg K), which points to the first-order character of the transition analogous to that observed in the monoclinic $Gd_5(Si_xGe_{1-x})_4$ alloys. The related Gd-based alloy, $Gd_5Si_{0.33}Ge_{3.67}$, which has the same ordering temperature shows a peak $-\Delta S_M$ value 28% higher than that of $Dy_5Si_3Ge_1$ (Gschneidner *et al* 2000a). ΔS_M behaviour in the Dy_5Ge_4 -based solid solution alloys demonstrated a positive peak in the low-temperature region in addition to a negative peak at the magnetic phase transition. This behaviour can be taken as an indication of noncollinear magnetic structure in these alloys. ΔS_M and MCE peak values for the investigated $Dy_5(Si_xGe_{1-x})_4$ alloys are shown in table 7.2.

MCE properties of the $(Tb-Gd)_5(Si-Ge)_4$ alloy system were studied by Spichkin *et al* (2001a), Huang *et al* (2002) and Thuy *et al* (2000a). Spichkin *et al* (2001) reported the results on the alloys $Gd_xTb_{5-x}Si_4$ ($x = 0, 2.5, 3, 3.5, 4, 4.5, 5$), where Tb is substituted by Gd. From x-ray diffraction measurements, it was established that all alloys had an orthorhombic crystal structure identical to pure Gd_5Si_4 . The lattice parameters increased almost linearly with increasing gadolinium concentration (Gd has metallic radii of 1.801 Å and Tb of 1.783 Å) with no discontinuities, indicating that a continuous solid solution formed over the whole range of the concentration. The magnetization measurements showed that the system is ferromagnetic below the Curie temperature, which varied from 345.7 K (Gd_5Si_4) to 223.2 K (Tb_5Si_4)—see table 7.2. The $M(T)$ and $C(T)$ curves displayed behaviour typical of second-order magnetic phase transitions near T_C . The character of a.c. magnetic susceptibility temperature dependences (existence of additional anomalies just below the Curie temperature peak) for the alloys with $x = 2.5-4.0$ pointed towards the possible existence of a noncollinear spin structure just below the temperature of transition from the paramagnetic to the magnetically ordered state. However no similar anomalies were found in $M(T)$ dependences measured in the magnetic field of 5 kOe, which can be explained by a complete destruction of the noncollinearity by a magnetic field of 5 kOe or less. The temperature dependences of the a.c. magnetic susceptibility and heat capacity of Tb_5Si_4 displayed additional anomaly (maximum) at ~ 85 K. Small peaks in a.c. magnetic susceptibility versus temperature curves were also found for the alloys with $x = 2.5-4.5$ at the temperatures corresponding to the low-temperature anomalies seen on $M(T)$ curves measured in 5 kOe. The authors related these anomalies to spin-reorientation transformations occurring in the alloys with $x = 0-4.5$ in the temperature region below ~ 100 K, and they believe that they are somehow connected to ferromagnetic or noncollinear ordering of the lanthanide magnetic moments located in different lattice sites. The maximum coercive force of 600 Oe at 5 K was observed in the investigated

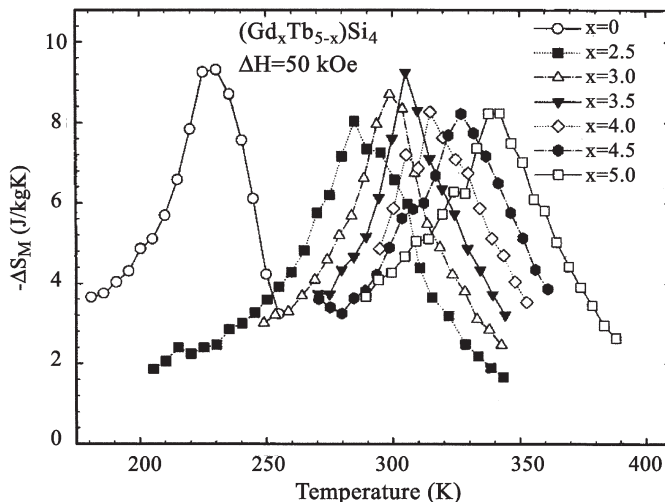


Figure 7.9. Temperature dependences of the magnetic entropy change in $\text{Gd}_x\text{Tb}_{5-x}\text{Si}_4$ alloys for $\Delta H = 50$ kOe (Spichkin *et al* 2001a).

alloy system in Tb_5Si_4 . At higher temperatures the coercive force rapidly decreased and became negligible near the Curie temperature. It should also be noted that the $M(H)$ curves of the alloys containing Tb ions were not saturated at 5 K even in a magnetic field of 90 kOe due to considerable magnetocrystalline anisotropy of Tb ions. The observed linear dependence of the paramagnetic Curie temperature in the investigated alloys on the de Gennes factor pointed to the RKKY character of exchange interaction between the magnetic ions.

The temperature dependences of the magnetic entropy change in the investigated $\text{Gd}_x\text{Tb}_{5-x}\text{Si}_4$ alloys determined from the magnetization measurements are shown in figure 7.9. As one can see, there are relatively narrow peaks of $-\Delta S_M$ near the Curie temperatures. Although the dependence of the peak $-\Delta S_M$ values on gadolinium concentration has irregular character, the general trend is a decrease of peak $-\Delta S_M$ values from Tb_5Si_4 to Gd_5Si_4 . This behaviour is expected since the theoretical magnetic entropy of Tb is greater than that of Gd (see table 6.2). The $-\Delta S_M$ values for $\text{Gd}_x\text{Tb}_{5-x}\text{Si}_4$ alloys are presented in table 7.2. The MCE value for $\text{Gd}_{3.5}\text{Tb}_{1.5}\text{Si}_4$ is obtained from the heat capacity data.

The $\text{Tb}_5\text{Si}_x\text{Ge}_{4-x}$ alloy system was studied by Morellon *et al* (2001), Huang *et al* (2002), Tegus *et al* (2002d) and Thuy *et al* (2000a, 2002). X-ray measurements made by Huang *et al* (2002) for $\text{Tb}_5\text{Si}_x\text{Ge}_{4-x}$ alloys with $x = 2, 3$ and 4 revealed that $\text{Tb}_5\text{Si}_3\text{Ge}_1$ had an orthorhombic Gd_5Si_4 -type crystal structure and $\text{Tb}_5\text{Ge}_2\text{Si}_2$ had a monoclinic $\text{Gd}_5\text{Si}_2\text{Ge}_2$ -type crystal structure at room temperature. Magnetization measurements showed that

all three alloys order ferromagnetically. Substitution of Si by Ge led to the Curie temperature decrease from 225.1 K (Tb_5Si_4) to 100.1 K ($Tb_5Si_2Ge_2$). The heat capacity anomalies at T_C and their behaviour in a magnetic field demonstrated second-order character for Tb_5Si_4 and $Tb_5Si_3Ge_1$ and first-order character for $Tb_5Si_2Ge_2$, analogous to that in $Gd_5Si_2Ge_2$. The low-temperature anomaly on $C(T)$ observed earlier in Tb_5Si_4 at 85 K by Spichkin *et al* (2001a) was also found in $Tb_5Si_3Ge_1$ at ~ 80 K and in $Tb_5Si_2Ge_2$ at ~ 74 K. Figure 7.10 shows $-\Delta S_M(T)$ and $\Delta T(T)$ dependences determined from the heat capacity measurements. The maximum peak $-\Delta S_M$ and ΔT values among the investigated $Tb_5Si_xGe_{4-x}$ alloys occurs for $Tb_5Si_2Ge_2$ alloy. One can see additional anomalies at about 75 K. The peak $-\Delta S_M$ and ΔT values for the $Tb_5Si_xGe_{4-x}$ alloy system are presented in table 7.2. Thuy *et al* (2000a) calculated the magnetic entropy change for $Tb_5Si_2Ge_2$ from the magnetization data obtained by pulse magnetometer. The $-\Delta S_M$ peak value near T_C for $\Delta H = 50$ kOe was determined to be 22.5 J/kg K, which is higher than the value of 15 J/kg K obtained by Huang *et al* (2002). However, static magnetization measurements of Thuy *et al* (2002) gave the peak absolute ΔS_M value in $Tb_5Si_2Ge_2$ of 12.8 J/kg K for $\Delta H = 50$ kOe. Quite different results on $Tb_5Si_2Ge_2$ were obtained by Tegus *et al* (2002d). The Curie temperature of $Tb_5Si_2Ge_2$ in this case was determined to be 76 K and the peak absolute ΔS_M value near this temperature was 19.5 J/kg K. It should be noted that Thuy *et al* (2002) and Tegus *et al* (2002d) observed in $Tb_5Si_2Ge_2$ the metamagnetic field-induced transition analogous to that found out in $Gd_5Si_2Ge_2$ (Thuy *et al* (2002) also reported about the metamagnetic transition in $Tb_5Si_3Ge_1$). At the same time in the earlier measurements of Morellon *et al* (2001) no such behaviour in $Tb_5Si_2Ge_2$ was revealed, although the peak absolute ΔS_M value was also high: 21.8 J/kg K for $\Delta H = 50$ kOe. Morellon *et al* (2001) also determined $-\Delta S_M(T)$ curves for Tb_5Ge_4 , which displayed two peaks—one at the Néel temperature $T_N = 95$ K and other at about 60 K. Both peaks had approximately equal height and the latter was related to transformation of the magnetic structure.

Magnetocaloric properties of $R_5(Si-Ge)_4$ alloy systems with light rare earth elements Pr and Nd were investigated by Spichkin *et al* (2001a), Gschneidner *et al* (2000a) and Thuy *et al* (2000a,b). It should be noted that Nd_5Ge_4 has an orthorhombic Sm_5Ge_4 -type crystal structure but Nd_5Si_4 and Pr_5Si_4 belong to the tetragonal Zr_5Si_4 -type crystal structure (Smith *et al* 1967, Gschneidner *et al* 2000a). X-ray analysis of the $Nd_5Si_xGe_{4-x}$ system at room temperature showed that replacement of a quarter of Si atoms by Ge (Nd_5Si_3Ge) stabilized the orthorhombic Gd_5Si_4 -type structure. Increasing the content of Ge led to the appearance of the monoclinic $Gd_5Si_2Ge_2$ -type structure at the $Nd_5Si_2Ge_2$ composition. In the $Nd_5Si_1Ge_3$ alloy both the monoclinic and orthorhombic phases coexist. The magnetization measurements revealed positive paramagnetic

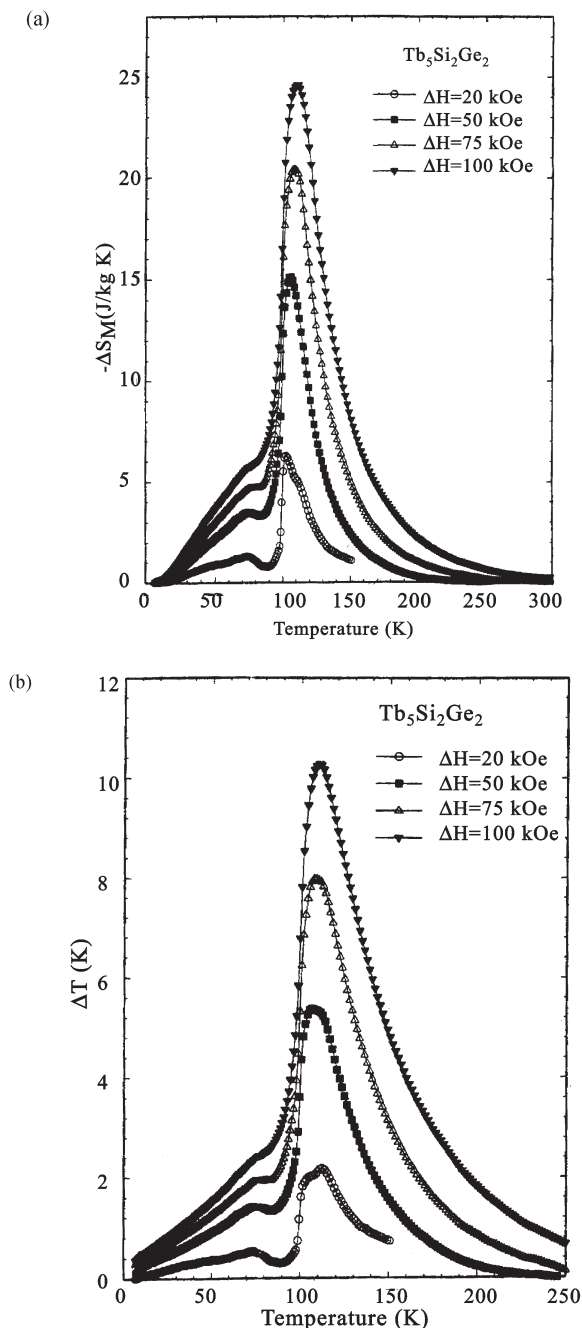


Figure 7.10. Temperature dependences of (a) the magnetic entropy change and (b) the MCE for $\text{Tb}_5\text{Si}_2\text{Ge}_2$ alloy (Huang *et al* 2002).

Curie temperatures, pointing to a ferromagnetic character of the magnetic ordering in $\text{Nd}_5\text{Si}_x\text{Ge}_{4-x}$ alloy system. However, as noted by Gschneidner *et al* (2000a), earlier neutron scattering studies by Schobinger-Papamantellos and Niggli (1981) pointed to a canted ferrimagnetic structure of Nd_5Ge_4 . The peak magnetic entropy change $-\Delta S_M$ values for the investigated alloys for $\Delta H = 50 \text{ kOe}$ are presented in table 7.2. They are not especially high, even for the $\text{Nd}_5\text{Si}_2\text{Ge}_2$ composition with a monoclinic crystal structure. The obtained ΔS_M value for $\text{Nd}_5\text{Si}_2\text{Ge}_2$ was rather typical for a material with a second-order magnetic phase transition. The Curie temperature in the $\text{Nd}_5\text{Si}_x\text{Ge}_{4-x}$ alloy system has a general trend to increase from 55 K (Nd_5Ge_4) to 71 K (Nd_5Si_4). The Curie temperature of $\text{Nd}_5\text{Si}_3\text{Ge}_1$ was about 50 K higher than that of the other alloys. The authors related this to the orthorhombic Gd_5Si_4 -type crystal structure of $\text{Nd}_5\text{Si}_3\text{Ge}_1$ alloy, where all metalloid–metalloid bonds between the slabs exist. Such magnetic ordering temperature increase in comparison of the monoclinic crystal phase was also observed in the $\text{Gd}_5(\text{Si}-\text{Ge})_4$ alloy system. Thuy *et al* (2000a,b) calculated $\Delta S_M(T)$ dependence near T_C in $\text{Nd}_5\text{Si}_2\text{Ge}_2$ from magnetization data obtained by pulse magnetometer. The obtained peak $-\Delta S_M$ value in $\text{Nd}_5\text{Si}_2\text{Ge}_2$ is consistent with that of Gschneidner *et al* (2000a).

The influence of Pr addition on the MCE properties of the Gd_5Si_4 compound was studied by Spichkin *et al* (2001a). From X-ray analysis it was found that $\text{Gd}_x\text{Pr}_{5-x}\text{Si}_4$ alloys with $x = 4, 4.25$ and 4.5 had an orthorhombic crystal structure of Gd_5Si_4 -type. The magnetization measurements showed that the alloys have ferromagnetic-type behaviour just below the Curie temperature. An additional anomaly was found in the temperature region below 100 K on $M(T)$ curves measured in 5 kOe. For $x = 4$ and 4.25 the anomaly manifested itself as a decrease of the magnetization, which for higher gadolinium concentration ($x = 4.5$) was transformed into an increase of the magnetization on cooling. The authors related the anomalies to complex ordering on different magnetic lanthanide sublattices (there are three nonequivalent crystallographic positions occupied by lanthanide atoms in Gd_5Si_4 -type compounds (Pecharsky and Gschneidner 1997d, Iglesias and Steinfink 1972), which changes due to the change of average interatomic distances upon substitution of Gd by Pr. The coercive force in $\text{Gd}_x\text{Pr}_{5-x}\text{Si}_4$ alloys for $T = 5 \text{ K}$ was small (maximum value of 110 Oe in $\text{Gd}_4\text{Pr}_1\text{Si}_4$) and disappeared at higher temperatures. As in the $\text{Gd}_x\text{Tb}_{5-x}\text{Si}_4$ alloy system, the linear dependence of the paramagnetic Curie temperature on the de Gennes factor was observed for $\text{Gd}_x\text{Pr}_{5-x}\text{Si}_4$ alloys. Figure 7.11 shows the temperature dependences of $-\Delta S_M$ induced by $\Delta H = 50 \text{ kOe}$ calculated from magnetization data. As one can see, the magnetic entropy change peak is observed near the Curie temperatures and its absolute value increased with increasing gadolinium concentration.

It should be noted that the $\text{Gd}_5(\text{Si}-\text{Ge})_4$ alloys, which display the giant magnetocaloric effect, were prepared from high-purity components: at least

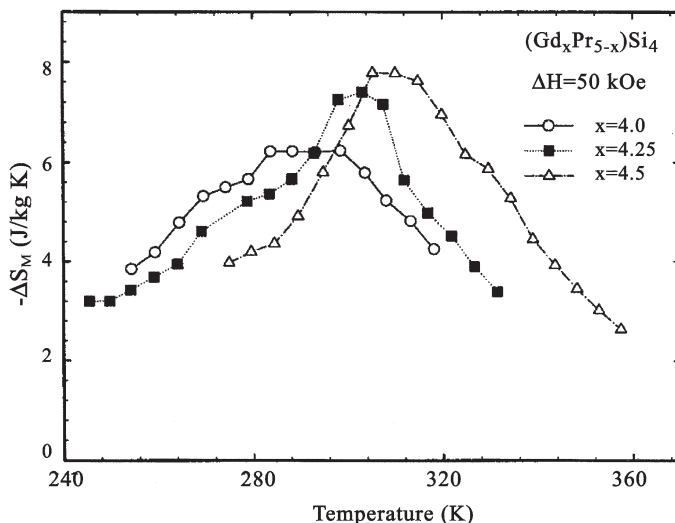


Figure 7.11. Temperature dependences of the magnetic entropy change in the $\text{Gd}_x\text{Pr}_{5-x}\text{Si}_4$ alloy system for $\Delta H = 50$ kOe (Spichkin *et al* 2001a).

99.8 at% Gd and at least 99.99 at% Si and Ge. The effect of substituting small amounts (up to 0.6 at%) of Fe, Co, Ni, Cu, Ga, Al and C on ΔS_M and MCE in $\text{Gd}_5\text{Si}_2\text{Ge}_2$ was investigated by Pecharsky and Gschneidner (1997b). It was found that the substitutions by Fe, Co, Ni and Cu (arc melted alloys) led to a Curie temperature increase with simultaneous $|\Delta S_M|$ reduction. The maximum value of $|\Delta S_M|$ found for $\text{Gd}_5\text{Si}_{1.985}\text{Ge}_{1.985}\text{Ni}_{0.03}$ was $|\Delta S_M| \approx 12.4$ J/kg K for $\Delta H = 50$ kOe at $T \approx 296$ K. This was related by the authors to the loss of the first-order nature of the magnetic phase transition, which was confirmed by magnetization measurements. The addition of carbon and aluminium acted similarly to Fe, Co, Ni and Cu, leading to the destruction of the first-order transition and the disappearance of the giant MCE. Addition of Ga in an amount of ~ 0.33 at% preserved the first-order nature of the magnetic phase transition in $\text{Gd}_5\text{Si}_2\text{Ge}_2$ and increased its temperature from about 276 K to about 286 K. The ΔS_M value for $\text{Gd}_5\text{Si}_{1.985}\text{Ge}_{1.985}\text{Ga}_{0.03}$ was ~ 17.6 J/kg K at $T \approx 286$ K and the maximum ΔT value was about 14.8 K at $T \approx 292$ K for $\Delta H = 50$ kOe, which is almost the same as in $\text{Gd}_5\text{Si}_2\text{Ge}_2$ alloy. The substitution of ~ 0.67 at% Ga shifted the magnetic ordering temperature to higher temperatures to about 300 K, but led to the loss of the high MCE (the maximum value of $|\Delta S_M|$ was about 9.5 J/kg K at $T \approx 300$ K). The results of the investigations showed that impurities have strong effect on the magnetocaloric properties of the $\text{Gd}_5(\text{Si}-\text{Ge})_4$ alloy system.

Recently a process was proposed by Gschneidner *et al* (2000b) to allow the preparation of large quantities of $\text{Gd}_5\text{Si}_2\text{Ge}_2$ -type alloys from commercial

purity (95–98 at% pure) gadolinium. Excellent magnetocaloric properties are preserved despite the presence of numerous impurities in the starting metal. The main feature of the process is holding the alloy in a liquid state at 1800 °C for 1 h in a suitable refractory container in a dynamic vacuum of 10^{-6} torr or better. This time is long enough for C and O, present in the melt, to react and form CO and/or CO_2 , which are then pumped-off from the liquid. This process results in a considerable reduction of carbon content in the alloy. ‘Self-purification’ cannot be achieved during arc melting where the process lasts for a few minutes in an argon atmosphere and both C and O remain in the product. The absolute peak value of the magnetic entropy change near the Curie temperature in the $\text{Gd}_5\text{Si}_2\text{Ge}_2$ prepared from commercial gadolinium using the process described above was 17 J/kg K for $\Delta H = 50$ kOe in comparison with 7 J/kg K for the sample with identical stoichiometry prepared by arc melting using components with identical purity.

In conclusion, in this section we have considered magnetocaloric properties of rare earth–metalloid compounds. In general these compounds (except the $(\text{RR}')_5(\text{Si–Ge})_4$ system) are not characterized by high magnetocaloric properties. However, such compounds as DyMn_2Ge_2 , NdMn_2Si_2 , GdPd_2Si , $\text{Gd}_2\text{Pd}_2\text{Si}_3$ and GdFeSi demonstrated large absolute $\Delta S_M/\Delta H$ and $\Delta T/\Delta H$ values. $(\text{RR}')_5(\text{Si–Ge})_4$ compounds have outstanding magnetocaloric properties. The most investigated system is $\text{Gd}_5\text{Si}_x\text{Ge}_{4-x}$. According to magnetic and structural studies the compositions with $x = 0.96–2$ exhibit first-order transition to magnetically ordered state with simultaneous structural transition from monoclinic to orthorhombic structure. This transition is reversible, can be induced by external magnetic fields and is accompanied by sharp change in the compounds’ magnetization. The sharp character of the magnetic phase transition persists even in high magnetic field (at least up to 100 kOe), which is not observed in other compounds with first-order transition. The described transition provides especially high magnetic entropy change and MCE in these compounds: $-\Delta S_M/\Delta H = 1.37$ J/kg K kOe in $\text{Gd}_5\text{Si}_1\text{Ge}_3$ ($T_C = 140$ K) and $\Delta T/\Delta H = 0.376$ K/kOe in $\text{Gd}_5\text{Si}_{1.72}\text{Ge}_{2.28}$ ($T_C = 246$ K) for $\Delta H = 50$ kOe. Higher $-\Delta S_M/\Delta H$ values were observed in $\text{La}(\text{Fe–Si})_{13}$ alloys in low fields, but they rapidly decreased with ΔH increasing. $\text{Gd}_5\text{Si}_2\text{Ge}_2$ compound with $T_C = 276$ K, which makes it suitable for applications near room temperature, also has $-\Delta S_M/\Delta H$ and $\Delta T/\Delta H$ values higher than in Gd. High magnetocaloric properties observed in the compounds with $R = \text{Dy}$ and Tb can also be related to the magnetostuctural transition at T_C . Taking into account that, by changing composition in $(\text{RR}')_5(\text{Si–Ge})_4$ compounds, the Curie temperature can be tuned in a wide range while retaining the magnetocaloric properties, these compounds should be recognized as the most promising materials for magnetic cooling devices.

Chapter 8

Magnetocaloric effect in rare earth metals and alloys

The rare earth metals and their alloys were the second objects after 3d metals where magnetocaloric properties were intensively investigated. This is related to the existence of different magnetic structures and transitions in these materials, the high values of their magnetization and the localized nature of the rare earth ion magnetic moment. The latter makes rare earth metals and alloys a convenient model object for magnetic investigations. A large variety of magnetic structures are provided by oscillating indirect exchange interactions between localized 4f magnetic moments mediated in the rare earth metals via conduction electrons. Alloying of different rare earth elements allows us to vary magnetic transition temperatures, types of magnetic phase and magnetic transitions.

The heavy rare earth metals (REM) Gd–Lu (except Yb) and Y have hexagonal close-packed (hcp) crystalline structures. In the magnetically ordered state they display complex magnetic structures (Taylor and Darby 1972). In Tb, Dy and Ho a helicoidal antiferromagnetic (HAFM) structure occurs in a certain temperature interval from T_C to T_N . In the HAFM state, the magnetic moments within the same basal plane order ferromagnetically and are turned by some angle with respect to those in the neighbouring basal plane. The axis of such an antiferromagnetic spiral coincides with the six-fold crystallographic c-axis. The HAFM structure can be transformed by a field-induced transition into the fan and then ferromagnetic state if the magnetic field exceeds some critical value H_{cr} . In the magnetic phase diagram $H_{cr}(T)$ one can mark out the temperature T_K , which corresponds to the maximum value of H_{cr} (where $\partial H_{cr}/\partial T = 0$). Below T_K the transition at $H = H_{cr}$ is of first-order and above T_K it has a second-order character. The first-order transition is accompanied by ‘jumps’ and some field hysteresis in the magnetization on field ($I(H)$) curves at $H = H_{cr}$. Below T_C a ferromagnetic basal-plane phase was observed in Tb and Dy and in Ho an HAFM structure with a ferromagnetic component along the c-axis was found.

A more complicated magnetic structure was found in erbium. In the temperature range between $T_N = 85\text{ K}$ and $T_{CY} = 53\text{ K}$ a longitudinal spin wave along the c-axis occurs. Below T_{CY} the structure changed to a cycloid in which the spin wave was superimposed on a basal plane spiral structure. Below $T_C = 18\text{ K}$ the c-axis component ordered ferromagnetically and the basal planes retained the spiral ordering, forming a ferromagnetic cone (conical phase) (Cable *et al* 1965, Habenshuss *et al* 1974, Atoji 1974).

Thulium, below $T_N = 56\text{ K}$, displays an antiferromagnetic longitudinal spin wave phase. Below 32 K it turns into a ferromagnetic-type structure composed of four basal-plane layers with magnetic moments aligned parallel to the c-axis, followed by three layers with moments aligned antiparallel (Brun *et al* 1970).

Neodymium has a double-hcp crystalline structure with two crystallographically inequivalent (hexagonal and cubic) sites and a complicated antiferromagnetic structure. The magnetic moments on the hexagonal sites order at $T_N = 19.2\text{ K}$ and on the cubic sites below 7.8 K (Johansson *et al* 1970).

8.1 Rare earth metals

8.1.1 Gadolinium

Neutron diffraction studies made by Cable and Wollan (1968) showed that Gd exhibits ferromagnetic ordering from liquid helium temperatures up to the Curie temperature $T_C = 293\text{ K}$. The easy magnetization axis is directed along the c-axis from T_C down to the spin-reorientation temperature $T_{SR} \approx 230\text{ K}$, below which the spontaneous magnetization vector departs from the c-axis and the easy cone arises.

The MCE in Gd is studied the most thoroughly in comparison with other magnetic materials—see for example, Brown (1976), Nikitin *et al* (1978), Hashimoto *et al* (1981), Maeda *et al* (1983), Tishin (1990b,c), Burkhanov *et al* (1991), Dan'kov *et al* (1992, 1996, 1998), Foldeaki *et al* (1995) and Gschneidner and Pecharsky (1997). Because gadolinium often serves as some standard of the magnetocaloric effect, and MCE in new materials is usually compared with it, we decided to present its magnetocaloric properties in detail—see figures 8.1–8.4.

In figure 8.1 the temperature dependences of heat capacity of Gd single crystal in different magnetic fields up to 100 kOe are shown. The λ -type anomaly observed on the zero-field $C(T)$ curve (maximum at 291 K, inflection point at 294 K) corresponds to the second-order transition from paramagnetic to ferromagnetic state. The magnetic field had a pronounced effect on the anomaly—it was considerably broadened and shifted to higher temperatures with increasing magnetic field, which is typical for ferromagnets. Near the

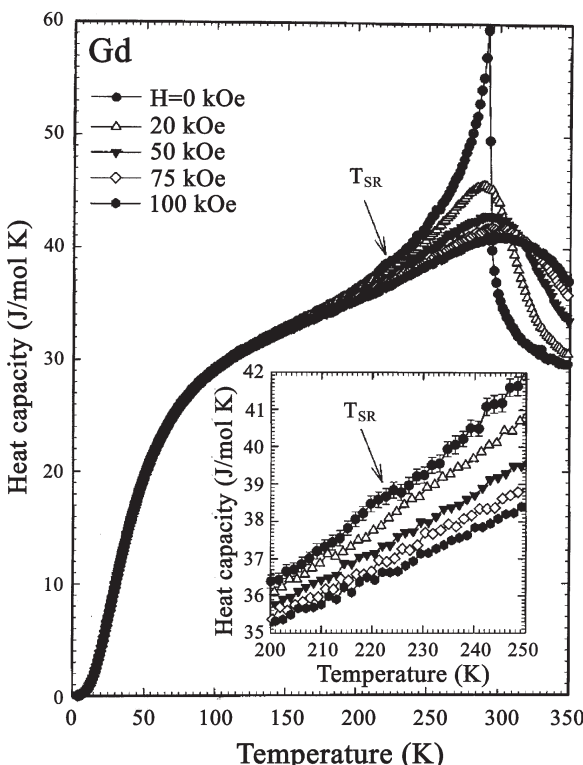


Figure 8.1. The heat capacity temperature dependences of the Gd single crystal in various magnetic fields applied along the [0001] crystal axis. The insert shows the temperature range near the spin-reorientation transition (Dan'kov *et al* 1998). (Copyright 1998 by the American Physical Society.)

temperature of the spin-reorientation transition at $\sim 220\text{--}225\text{ K}$ a small anomaly was observed, which was wiped out by the magnetic field of 20 kOe.

The MCE temperature dependences of polycrystalline Gd near T_C determined by Gschneidner and Pecharsky (1997) from heat capacity measurements are shown in figure 8.2. They demonstrate typical ferromagnetic behaviour with a wide symmetric maximum near the Curie temperature. The full width of the $\Delta T(T)$ curve at half maximum is about 78 K for $\Delta H = 20\text{ kOe}$. The MCE field dependence near T_C is nonlinear and the rate of MCE change with field decreases in high field region—see figure 8.3. However, the MCE field dependence in Gd in the ferromagnetic state at 90 K is almost linear up to 100 kOe.

Nikitin *et al* (1978) found an additional small MCE anomaly in a Gd single crystal near the spin-reorientation temperature for H aligned along c- and a-crystal axes and studied the dependence of the MCE in Gd single crystal on the magnetic field orientation. The analysis was made on the

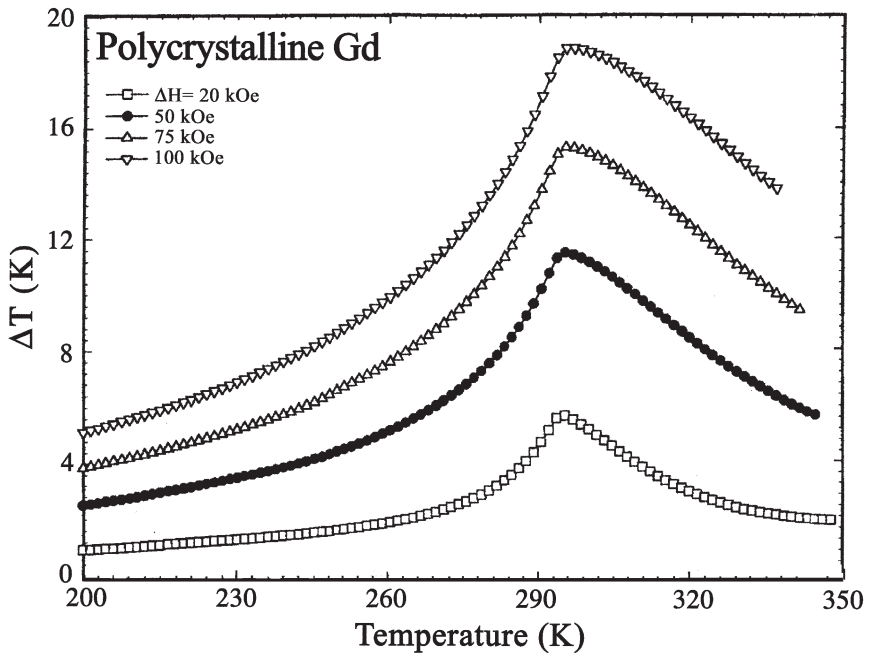


Figure 8.2. The MCE temperature dependences for Gd for different ΔH (Gschneidner and Pecharsky 1997).

basis of equation (5.2), which was considered as a contribution $\Delta S_{A,\Theta}$ to the MCE related to variation of the \vec{I}_s direction from the initial position determined by the angle Θ_0 (relative to the c-axis) to the final angle Θ_H . The anisotropy constants K_i can also depend on H , which leads to a magnetic entropy change $\Delta S_{A,H}$:

$$\begin{aligned} \Delta S_{A,H} = - & \left[\left(\frac{\partial^2 K_1}{\partial H \partial T} \right)_p \sin^2 \Theta_H + \left(\frac{\partial^2 K_2}{\partial H \partial T} \right)_p \sin^4 \Theta_H \right. \\ & \left. + \left(\frac{\partial^2 K_3}{\partial H \partial T} \right)_p \sin^6 \Theta_H \right] \Delta H. \end{aligned} \quad (8.1)$$

The total magnetic entropy change related to the process of magnetization vector rotation is determined as $\Delta S_A = \Delta S_{A,H} + \Delta S_{A,\Theta}$ and causes the anisotropic contribution to the MCE (Nikitin *et al* 1978):

$$\Delta T_A = \Delta T_{A,\Theta} + \Delta T_{A,H} = - \frac{T}{C_p} (\Delta S_{A,\Theta} + \Delta S_{A,H}) \quad (8.2)$$

where $\Delta T_{A,\Theta}$ is the contribution from the rotation of \vec{I}_s against a magnetic anisotropy force and $\Delta T_{A,H}$ is the contribution from the variation of the anisotropy constants in the applied field. The total MCE was obtained as a

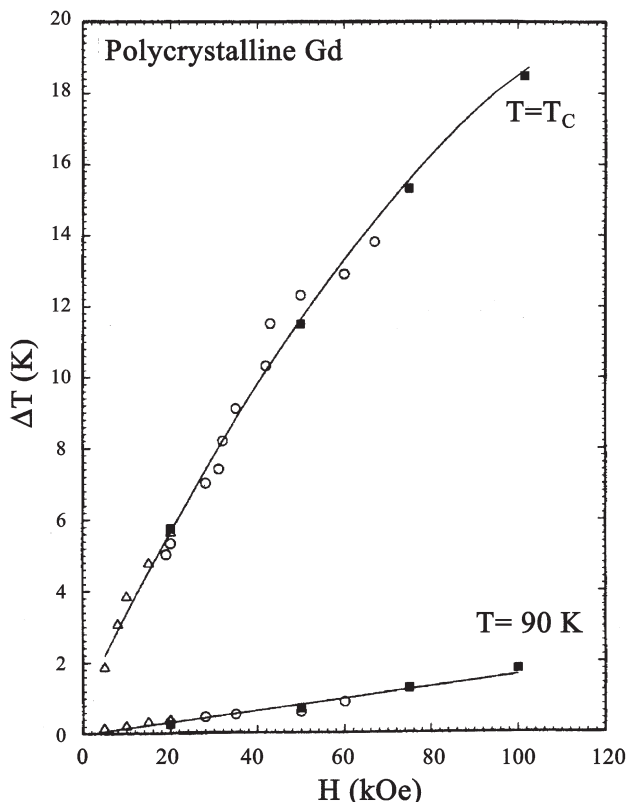


Figure 8.3. The MCE field dependences in Gd at $T = T_C$ and $T = 90$ K (○, direct measurements in pulsed fields; △, direct measurements by switch-on method and ■, indirect determination from the heat capacity (Pecharsky and Gschneidner 1996, Dan'kov *et al* 1997).

sum of the MCE caused by a paraprocess (calculated by equation (2.16)) and ΔT_A . The calculated $\Delta T(T)$ curve was in good agreement with the experimental one.

The ΔT_A values were determined from the experimental $\Delta T(H)$ dependences measured at various T as the intercepts on the ΔT axis by the extrapolation of the linear high-field part of the $\Delta T(H)$ curves. It was shown that near T_C the main contribution to ΔT_A gave the second term in equation (8.2). Below 230 K, the ΔT_A value is determined by the first term. As follows from equations (5.2) and (8.1), in this case $\Delta T_A = 0$ for $\Theta_H = \Theta_0$. This allowed determination of the temperature dependence of the Θ_0 (Nikitin *et al* 1978), which was in good accordance with data obtained by other authors.

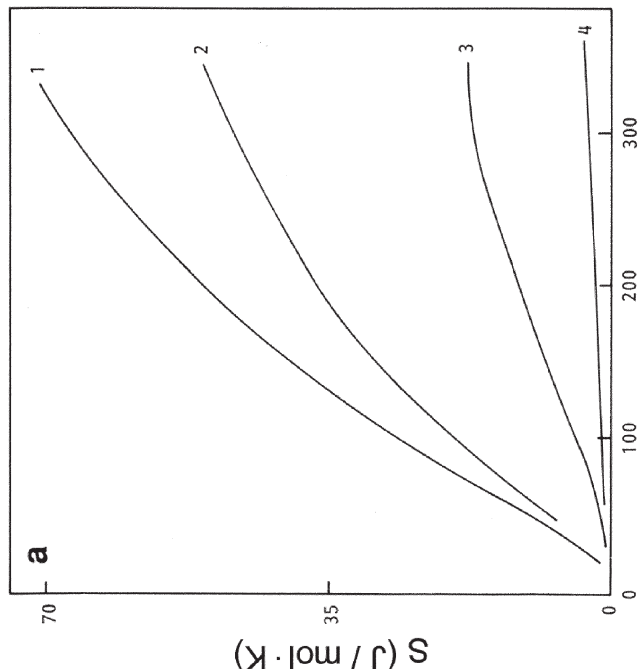
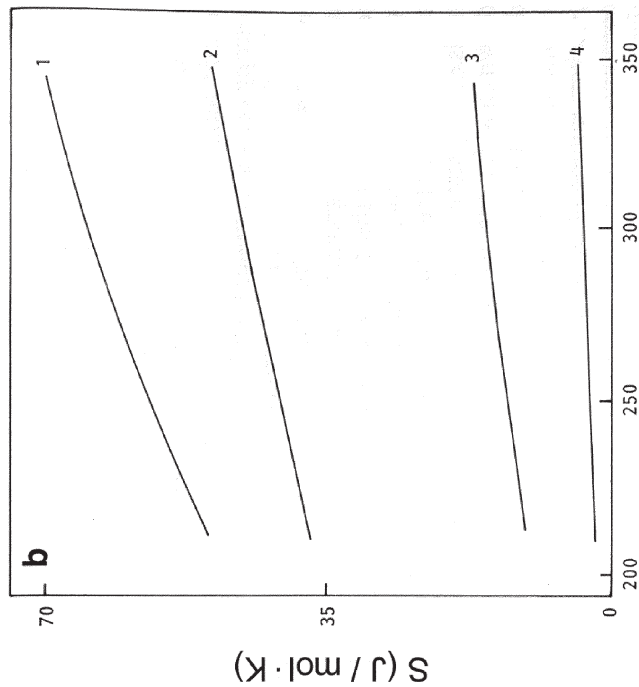
Good agreement was found between the experimental data on MCE and ΔS_M in Gd and those calculated by MFA (Maeda *et al* 1983; Tishin 1990a–c).

Figures 8.4(a) and (b) present various contributions to the entropy of Gd in zero magnetic field and in a field of 70 kOe, calculated by equations (2.59), (2.60), (2.63) by Tishin (1990a). The MCE in Gd for $\Delta H = 70$ kOe determined by the method described in section 4.1 is shown in figure 8.4c (curve 1). This figure also presents experimental values of the MCE in Gd (curve 2) obtained by Brown (1976). It can be seen that the results of the calculations describe the experimental data rather well. The values of g_J , J , T_C , T_N and T_D used in the MFA calculations are presented in table 8.1. Figure 8.4d presents the theoretical and experimental ΔS_M curves for polycrystalline Gd. The values of ΔS_M determined from the results of magnetization and MCE measurements are quite close. The maximum ΔS_M and MCE values near the Curie temperature in Gd obtained by various authors are collected in table 8.2.

The heat capacity of polycrystalline Gd was measured by Griffel *et al* (1954) and Lounasmaa and Sundström (1966), and on single-crystal samples near T_C by Lanchester *et al* (1980) and Glorieux *et al* (1995). Dan'kov *et al* (1998) measured the heat capacity and magnetic field dependences of polycrystalline and single-crystal gadolinium. Three samples were studied: a low-purity (commercial, 93.1 at% pure) polycrystal, a high-purity polycrystal and a high-purity single crystal. As was noted earlier by Gschneidner (1993a) the magnetic properties of RE metals are critically dependent on their purity. In all samples a pronounced λ -type anomaly was observed near T_C on the temperature dependence of the zero-field heat capacity.

The significant reduction of the purity in the commercial Gd sample caused a significant reduction of the maximum of the λ -type anomaly ($\sim 10\%$ as compared with high-purity samples) and its temperature ($\sim 5\%$). An excess heat capacity in the commercial sample appeared in the temperature range between 70 and 286 K and above 300 K. The authors related these features to straining of the crystal lattice and weakening of the exchange interactions due to the interstitial impurities (such as carbon) dissolved in Gd. The interstitial impurities also had a distinct effect on the MCE measured in pulsed fields: the MCE value in the commercially pure Gd was about two times lower than in the high-purity samples (the maximum of ΔT was about 3.2 K at 288 K for $\Delta H = 20$ kOe in the commercial Gd). Earlier heat capacity measurements on polycrystalline Gd made by Lounasmaa and Sundström (1966) revealed a distinct heat capacity maximum with a height of ~ 300 mJ/mole K at about 3 K, which was related to the presence of Gd_2O_3 oxide.

Data about the thermal conductivity of Gd and other heavy rare earth metals can be found in the works of Arajs and Colvin (1964), Powell and Jolliffe (1965), Aliev and Volkenshtein (1965a), Gallo (1965), Nellis and Legvold (1969), Beaudry and Gschneidner (1978) and Gschneidner (1993b). Figure 8.5 shows thermal dependences of thermal conductivity measured on Gd single crystals along c- and a-axes (Nellis and Legvold 1969). As one can



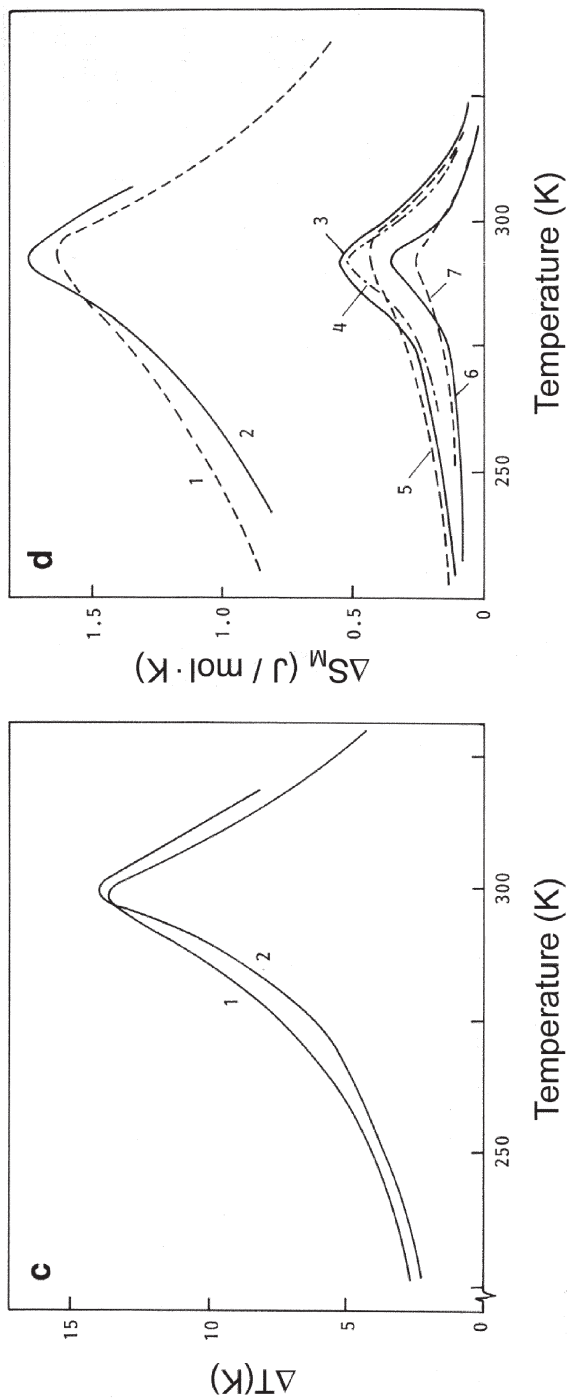


Figure 8.4. Temperature dependences of the calculated MCE and entropy in Gd: (a) $H = 0$; (b) $H = 70$ kOe; (1) lattice entropy; (2) magnetic entropy; (4) electronic entropy. (c) Experimental (curve 1) and calculated (curve 2) dependences of MCE in Gd for $\Delta H = 70$ kOe. (d) Temperature dependence of magnetic entropy ΔS_M in Gd for $\Delta H = 60$ kOe (curves 1, 2); $\Delta H = 10$ kOe (curves 3, 4, 5); $\Delta H = 5$ kOe (curves 6, 7) (calculated values: curves 1, 5 and 7; experimental values obtained from magnetization and MCE data: curves 2, 3, 6, and 4) (Trishin *et al* 1990a).

(Reprinted from Trishin *et al* 1990a, copyright 1990, with permission from Elsevier.)

Table 8.1. Parameters of RE elements used in theoretical MFA calculations by Tishin (1990a).

Parameter	Rare earth metal					
	Gd	Tb	Dy	Ho	Er	Tm
g_J	2	1.5	1.33	1.25	1.2	1.7
J	3.5	6	7.5	8	7.5	6
T_C (K)	293	—	—	—	—	—
T_N (K)	—	230	178	133	85	60
T_D (K)	184	177	179	194	192	190

see, in the paramagnetic region thermal conductivity along the c-axis is higher than that in basal plane. Analogous behaviour was observed in Dy, Er and Tm (Boys and Legvold 1968, Edwards and Legvold 1968). Thermal conductivity of heavy rare earths is rather low and initially decreased with decreasing temperature from the high-temperature region. As was suggested in a number of works, besides electrons magnons and phonons take a part in forming the thermal conductivity of the heavy rare earth metals. In contrast, in nonmagnetic Lu, the thermal conductivity along the c-axis is in good accordance with the value given by the electron heat conduction mechanism (Boys and Legvold 1968). The values of thermal conductivities in Gd and other heavy rare earth metal single and polycrystals are presented in table A2.1 in appendix 2.

8.1.2 Terbium

Terbium displays HAFM ordering in the temperature interval from $T_N = 230$ K to $T_C = 220.6$ K, which is characterized by weak critical fields: maximum $H_{cr} = 190$ Oe at $T_K = 228.5$ K (Bykhover *et al* 1990). In fields above H_{cr} the HAFM structure in Tb and Dy is destroyed and a ‘fan’ structure arises (in the given temperature interval), in which the magnetic moments in the basal planes form fan-type ordering around the field direction. Further increase of the field leads to complete ferromagnetic ordering at a field of about $2H_{cr}$ (Greenough and Hettiarachchi 1983, Drillat *et al* 1984, Bagguley and Howe 1986).

When the HAFM structure is destroyed by a magnetic field, an MCE arises because the entropies of the two phases (HAFM and fan or FM) are not equal. The MCE at the first-order transition at $H = H_{cr}$ applied in the basal plane of Dy and Tb_xY_{1-x} alloys was considered by Nikitin *et al* (1977a,b, 1979a, 1991b) and Nikitin and Andreenko (1981). It was shown that the transition is caused by changes in several energies, namely the energy of exchange interaction between the basal planes, the magnetoelastic

Table 8.2. Magnetic ordering temperatures T_N or T_C , temperature of the maximum in the $\Delta T(T)$ curves (T_{\max}^T), temperature of the maximum in the $\Delta S_M(T)$ curves (T_{\max}^S) and maximum values of ΔS_M (at $T = T_{\max}^S$) and ΔT (at $T = T_{\max}^T$) induced by a magnetic field change ΔH and and $\Delta T/\Delta H$ and $-\Delta S_M/\Delta H$ for heavy rare earth metals. References are shown in brackets.

Element	T_C, T_N (K)	Peak MCE				Peak $-\Delta S_M$			
		T_{\max}^T (K)	ΔT (K)	ΔH (kOe)	$\Delta T/\Delta H \times 10^2$ (K/kOe)	T_{\max}^S (K)	$-\Delta S_M$ (J/kg K)	ΔH (kOe)	$-\Delta S_M/\Delta H \times 10^2$ (J/kg K kOe)
Gd	292 [1]	296 [2]	11.2 [2]	50	22.4	294 [9]	11.1 [9]	60	18.5
	294 [7]	296 [2]	5.6 [2]	20	28	292 [9]	3.5 [9]	10	35
	296 [3]	18.8 [3]	100	18.8	295 [10]	3.2 [10]	10	32	
	292 [4]	10.8 [4]	50	21.6	295 [11] (c)	4.9 [11] (c)	12	41	
	294 [5]	4.8 [5]	20	24	3 [6]	10	30		
	293 [6]	14 [6]	70	20	4.2 [12]	15	28		
	295 [7]	5.8 [7]	20	29	8.8 [5]	40	22		
	296 [7]	19.5 [7] (c)	100	19.5	13.7 [5]	80	17.1		
	294 [8]	2.8 [8] (a, c)	10	28	—	—	—		
	227 [14]	0.23 (b) [14]	0.4	57.5	230 [17]	3.8 [17] (a)	12	31.5	
	231 [15]	5 [15]	20	25	230 [18]	15.7 [18]	60.2	26	
	233 [15]	10.5 [15]	60	17.5	232 [19]	20 [19]	75	26.7	
	231 [15]	10 (b) [15]	60	16.7	232 [19]	9 [19]	20	45	
	230 [16]	60 (bas. plane) [16]	350	17.1	—	—	—		
	230 [16]	43 (bas. plane) [16]	150	28.7	—	—	—		
	180 [20]	2.2 [20]	20	11	178 [18]	14.2 [18]	60.2	23.6	
	179 [15]	8.6 [15]	60	14.3	168 [21]	13.5 [21]	60	22.6	
Dy	180 [13]	7.7 (a) [21]	60	12.8	180 [22]	29 (a) [22]	100	29	

Table 8.2. Continued.

Element	T_C , T_N (K)	T_{\max}^T (K)	Peak MCE				Peak $-\Delta S_M$		
			ΔT (K)	ΔH (kOe)	$\Delta T/\Delta H \times 10^2$ (K/kOe)	T_{\max}^S (K)	$-\Delta S_M$ (J/kg K)	ΔH (kOe)	$-\Delta S_M/\Delta H \times 10^2$ (J/kg K kOe)
Dy	178 [21]	6.5 (b) [21]	60	10.8		180 [22]	3 (a) [22]	20	15
	182 [22]	19.5 (a) [22]	100	19.5		—	—	—	—
	182 [22]	2.9 (a) [22]	20	14.5		—	—	—	—
	180 [23]	12 [23]	70	17.1		—	—	—	—
		2.2 [23]	20	11		—	—	—	—
	182 [24]	9 [24]	50	18		—	—	—	—
Ho	134 [1]	132 [25]	4.6 [25]	60	7.7	130 [18]	1.8 [18]	60.2	3
	136 [26]	6.1 [26]	70	8.7		—	—	—	—
	85 [25]	3.2 [25]	60	5.3		85 [18]	1.2 [18]	60.2	2
Er	86 [28]	4.7 [28]	75	6.3		—	—	—	—
	58 [15]	3 [15]	60.2	5		—	—	—	—
Tm	56 [29]	58 [30]	3.1 [30]	70	4.4	—	—	—	—

1. Nikitin *et al.* (1991d); 2. Pecharsky and Gschneidner (1996); 3. Gschneidner and Pecharsky (1997); 4. Benford and Brown (1981); 5. Hashimoto *et al.* (1981); 6. Brown (1976); 7. Dan'kov *et al.* (1998); 8. Nikitin *et al.* (1978); 9. Tishin *et al.* (1990b); 10. Foldeaki *et al.* (1995); 11. Dan'kov *et al.* (1992); 12. Guo *et al.* (1997a); 13. Bykhov *et al.* (1990); 14. Nikitin *et al.* (1989b); 15. Tishin (1988); 16. Druzhinin *et al.* (1977); 17. Dan'kov *et al.* (1996); 18. Nikitin and Tishin (1988); 19. Chernyshov *et al.* (2002a); 20. Hudgins and Pavlovic (1965); 21. Nikitin *et al.* (1991b); 22. Chernyshov *et al.* (2002b); 23. Benford (1979); 24. Gschneidner and Pecharsky (2000b); 25. Tishin and Martinenko (1995); 26. Green *et al.* (1988); 27. Milton and Scott (1967); 28. Zimm *et al.* (1988b); 29. Brun *et al.* (1970); 30. Zimm *et al.* (1989).

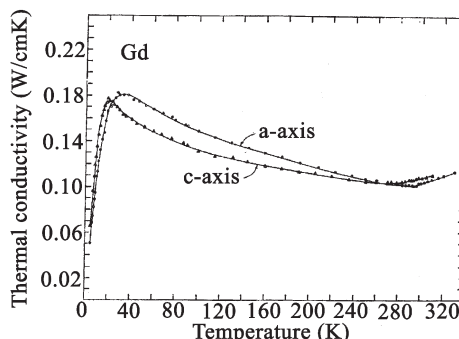


Figure 8.5. Thermal conductivity temperature dependences in Gd single crystal (Nellis and Legvold 1969). (Copyright 1969 by the American Physical Society.)

energy, the Zeeman energy and the in-plane anisotropy energy. The first three contributions were shown to dominate.

Nikitin *et al* (1989b) studied the MCE of Tb by a direct method in the temperature interval from T_C to T_N in magnetic fields up to 400 Oe applied along the easy magnetization direction (b-axis)—see figure 8.6. Between 220.5 and 223.4 K the MCE is small and positive in weak fields and sharply increases above H_{cr} . For temperatures from 223.4 to 226 K the MCE is negative for $\Delta H < 350$ Oe. The negative MCE is typical for anti-ferromagnets, in which the external field reduces the magnetic order, thus increasing the magnetic entropy (antiferromagnetic-type paraprocess). In the case of Tb the external field transforms the HAFM structure into the lower-symmetry fan structure. The magnetic phase diagram $H_{cr}(T)$ constructed on the basis of $\Delta T(H)$ curves (the magnetic field was changed from 0 to H) is in good agreement with that obtained from the magnetization measurements. H_{cr} was defined as the field of the maximum increase of ΔT .

Figure 8.7 shows the temperature dependences of the MCE in a single crystal of Tb induced by fields applied along the b-axis (Tishin 1988). The MCE maximum in Tb is observed near T_N and is caused by a paraprocess, which is known to be strongest near the temperature of the transition to a magnetically ordered state. Due to the complete destruction of the HAFM structure no MCE anomalies were observed near T_C for $\Delta H \geq 10$ kOe. The same results were obtained for measurements in the field applied along the a-axis (hard axis in Tb), which implies a small magnetic anisotropy of Tb in the basal plane in the temperature range near magnetic phase transitions.

Calculations of the MCE in Tb, made by Tishin (1990a) on the basis of the MFA, have shown satisfactory agreement with the experimental data near T_N : for $\Delta H = 20$ kOe the calculation leads to $\Delta T = 6$ K, while the experimental value is 5 K—see figure 8.8. The insert in figure 8.8 shows the calculated MCE in strong magnetic fields. It is seen that for $\Delta H > 2000$ kOe the

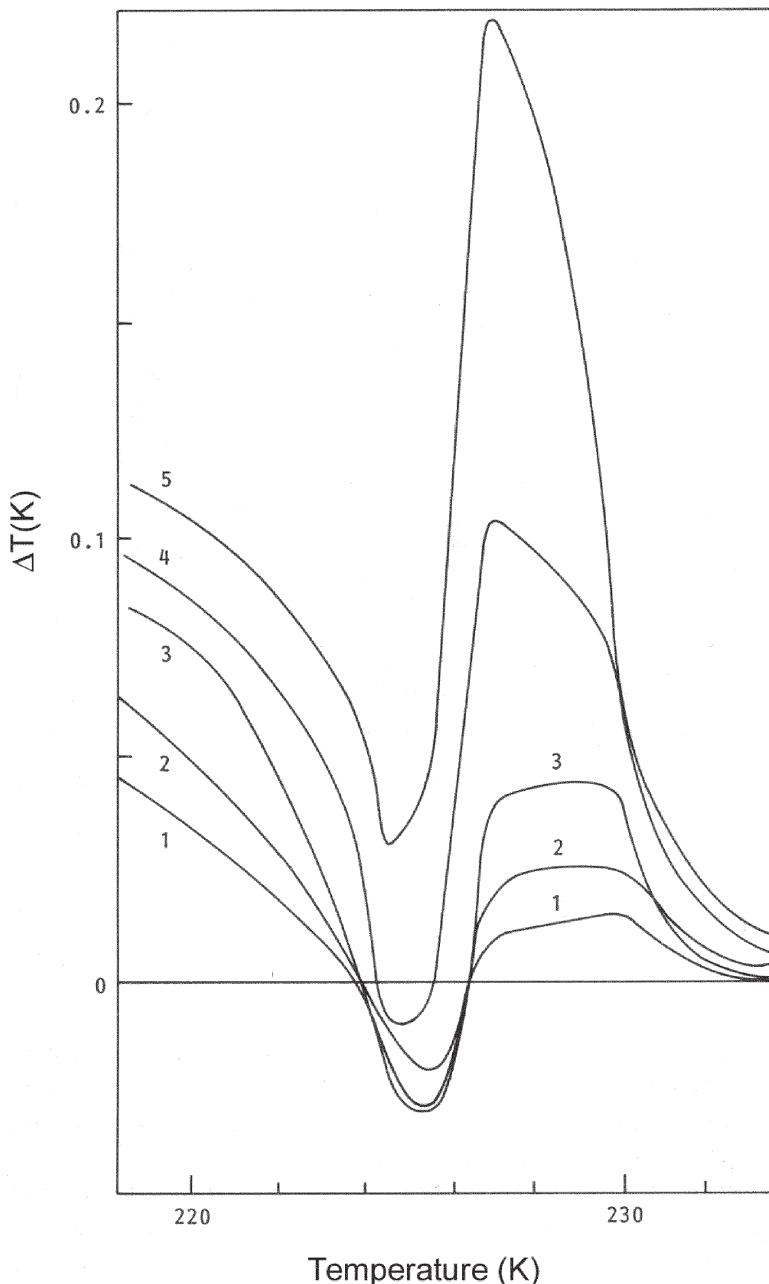


Figure 8.6. Temperature dependences of the MCE in Tb single crystal for the magnetic field applied along the b-axis: $\Delta H = (1) 200$ Oe; (2) 250 Oe; (3) 300 Oe; (4) 350 Oe; (5) 400 Oe (Nikitin *et al* 1989b).

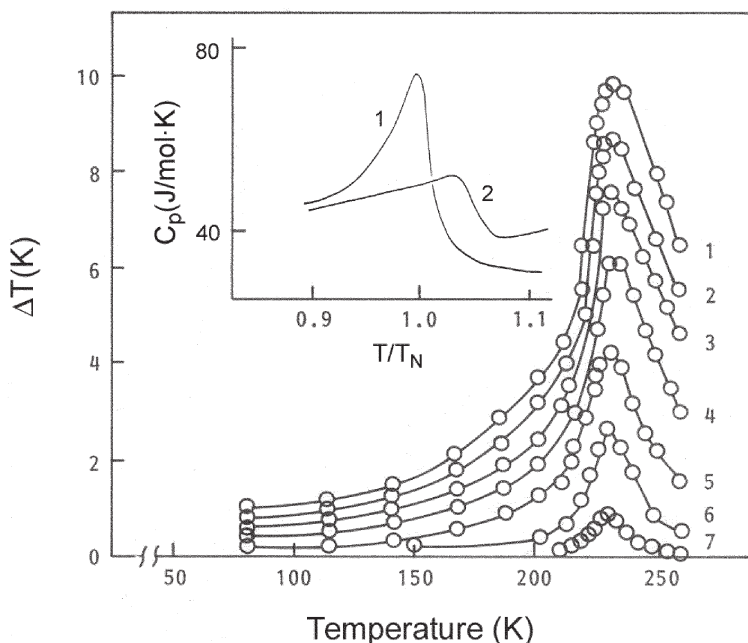


Figure 8.7. Temperature dependences of the MCE in a Tb single crystal for the magnetic field applied along the b-axis: $\Delta H = (1) 60 \text{ kOe}; (2) 50 \text{ kOe}; (3) 40 \text{ kOe}; (4) 30 \text{ kOe}; (5) 20 \text{ kOe}; (6) 10 \text{ kOe}; (7) 2.5 \text{ kOe}$. Temperature dependences of the heat capacity of a Tb single crystal at: (1) zero field; $H = 60.2 \text{ kOe}$ are shown in the insert (Tishin 1988, Nikitin *et al* 1985a).

maximum in the $\Delta T(T)$ curve disappears and for $T > T_N$ the MCE practically does not change. There is disagreement of these results with the MCE value calculated earlier by Druzhinin *et al* (1979) in the framework of MFA (the shape of the $\Delta T(T)$ curves was quite similar): $\Delta T = 120 \text{ K}$ for Tb at $T = T_N$ and $\Delta H = 1500 \text{ kOe}$. According to Tishin (1990a), at $T = T_N$ the MCE value of 120 K can be reached only in a field of 2250 kOe, while for $\Delta H = 1500 \text{ kOe}$ the MCE amounts to 98 K.

Druzhinin *et al* (1977) determined the MCE in a Tb single crystal in fields up to 350 kOe from the experimental adiabatic dependences of the magnetization in the basal plane measured by the pulse method. The MCE was calculated by integration of equation (2.23):

$$\Delta T = T - T_i = T_i \left\{ \exp \left[\int_{I_s(T_i)}^{I_f} \frac{1}{C_M} \left(\frac{\partial H}{\partial T} \right)_I dI \right] - 1 \right\} \quad (8.3)$$

where I and T are magnetization and final temperature and $I_s(T_i)$ and T_i are the initial magnetization and temperature. A sharp MCE maximum with a value of 60 K was observed at $T = 230 \text{ K}$ for $\Delta H = 350 \text{ kOe}$.

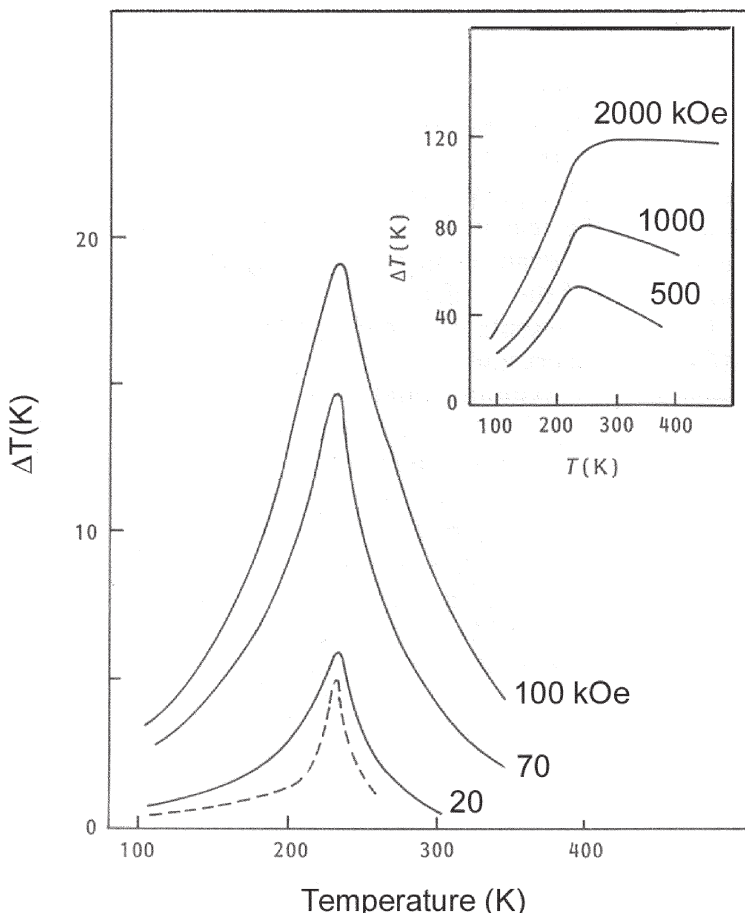


Figure 8.8. Temperature dependences of the MCE in Tb for different ΔH : —, calculations, - - -, experiment (Tishin 1990a). (Reprinted from Tishin 1990a, copyright 1990, with permission from Elsevier.)

The temperature dependences of the magnetic entropy change ΔS_M in Tb was evaluated from magnetization measurements by Dan'kov *et al* (1996) and on the basis of heat capacity and MCE data by Nikitin *et al* (1985a). In the latter case, the results of zero-field heat capacity measurements made by Jennings *et al* (1957) and equation (2.79) were used for the $\Delta S_M(T)$ calculation (the field dependence of the heat capacity was not taken into account). Later, ΔS_M for the heavy rare earths was calculated more exactly by Tishin (1994) (see figure 8.9), who took into account the field dependence of the heat capacity.

The heat capacity of Tb in the presence of a magnetic field was calculated by Nikitin *et al* (1985a) and Tishin (1988) on the basis of the

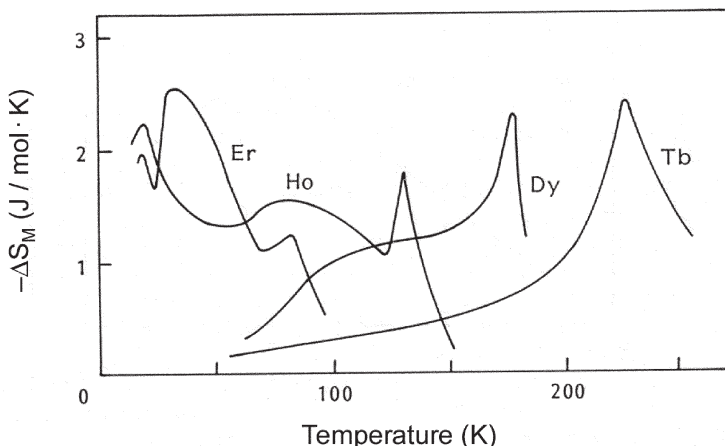


Figure 8.9. Temperature dependences of ΔS_M in Tb, Dy, Ho and Er induced by $\Delta H = 60.2$ kOe (Tishin 1994).

zero-field measurements of Jennings *et al* (1957) and MCE data with the help of equation (2.12). The results for $H = 60.2$ kOe are shown in the insert in figure 8.7.

Direct heat capacity measurements in the magnetic fields up to 75 kOe on the Tb single crystal were made by Chernishov *et al* (2002a). Figure 8.10 shows heat capacity temperature dependences of Tb single crystal in different magnetic fields applied along the crystallographic a-axis. In the magnetic

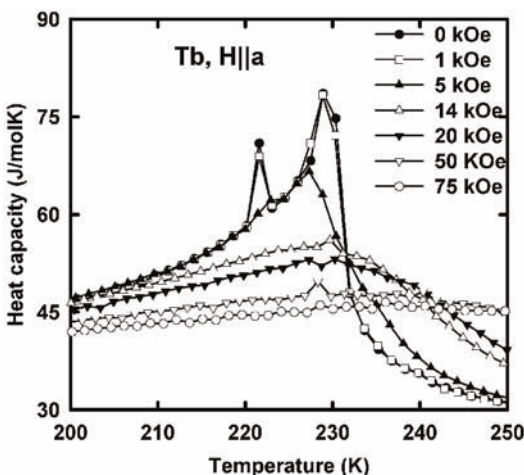


Figure 8.10. Temperature dependences of the heat capacity of Tb single crystal in different magnetic fields applied along the a-axis near the magnetic phase transitions (Chernyshov *et al* 2002a).

fields less than 5 kOe the curves display two maxima near T_N and T_C (the corresponding maxima on the zero-field curve were at 228.9 K and 221.6 K). With increasing magnetic field, the low-temperature maximum shifted to the higher-temperature region and the high-temperature maximum shifted to the low-temperature region as one could expect for T_C and T_N , respectively. For the fields higher than 5 kOe only one maximum was observed, which was suppressed in higher magnetic fields. From the heat capacity data the magnetic entropy change was determined—its temperature dependences for different ΔH are shown in figure 8.11(a). As one can see, in strong magnetic

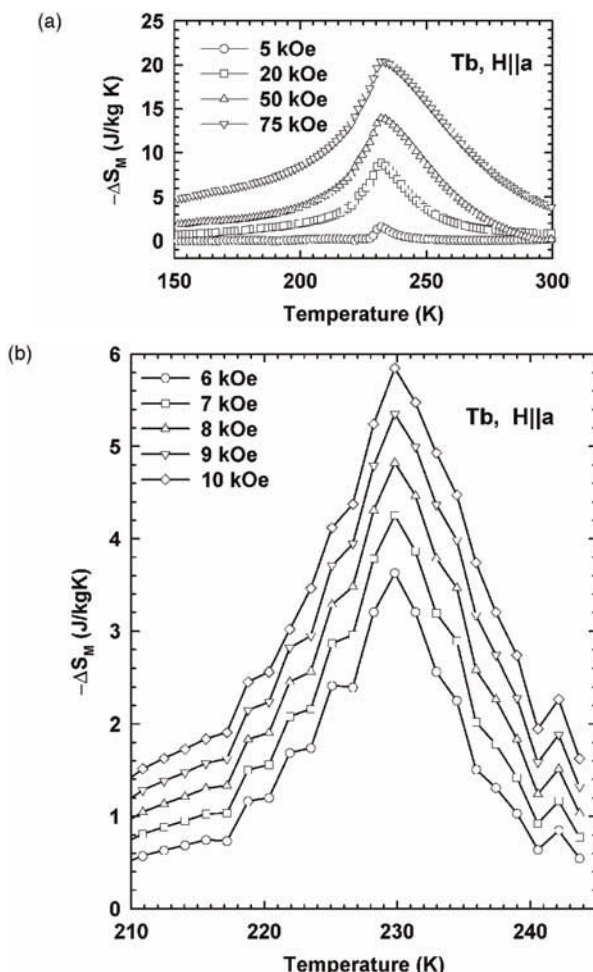


Figure 8.11. Temperature dependences of the magnetic entropy change in Tb single crystal (magnetic field was applied along the a-axis): (a) determined from heat capacity measurements; (b) determined from the magnetization data (Chernyshov *et al* 2002a).

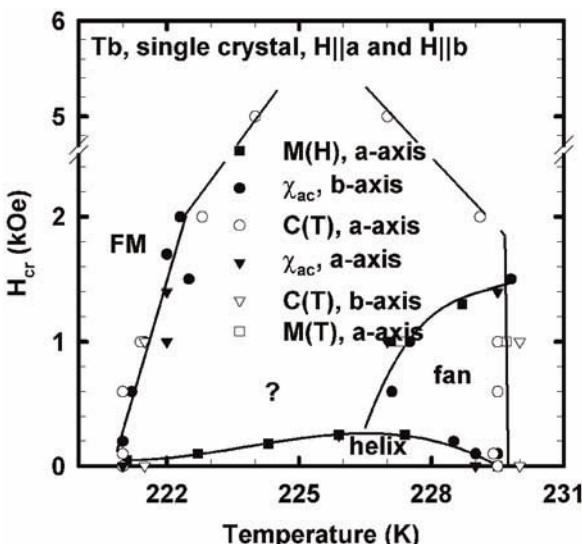


Figure 8.12. The magnetic phase diagram of the Tb single crystal constructed on the basis of magnetic and heat capacity measurements. The magnetic field was applied in the basal plane (Chernyshov *et al* 2002a).

fields only one maximum presents on $\Delta S_M(T)$ curves as in ferromagnets, because of complete suppression of the HAFM structure. Figure 8.11(b) shows $\Delta S_M(T)$ dependences for $\Delta H = 5-10$ kOe calculated from magnetization data. Chernyshov *et al* (2002a) singled out contributions in ΔS_M related to the paraprocess and HAFM–FM magnetic phase transition. According to the estimations made with the help of a magnetic phase diagram, magnetization data and the Clausius–Clapeyron equation (2.100), at 225 K the main contribution to ΔS_M for $\Delta H = 10$ kOe gives the paraprocess (~ -5 J/kg K) and the HAFM–FM transition (~ -0.5 J/kg K) only. Figure 8.12 represents the magnetic phase diagram of Tb single crystal obtained from magnetic and heat capacity measurements for a magnetic field applied in the basal plane. Besides FM, HAFM and paramagnetic phases the measurements allowed the fan magnetic phase and another distorted HAFM phase to be revealed—this latter structure should be close to the fan.

The thermal conductivity of Tb was studied by Powell and Jolliffe (1965), Aliev and Volkenshtein (1965a), Gallo (1965), Nellis and Legvold (1969) and Gschneidner (1993b). Temperature dependences of this quantity measured on Tb single crystal displayed essential anisotropy—the curve measured along the a-axis lay below the c-axis curve in the whole temperature range (Nellis and Legvold 1969). The thermal conductivity of Tb first decreased in the paramagnetic temperature range with decreasing temperature, displayed anomalies at magnetic phase transitions, and then

increased reaching maximum values at about 20 K (Nellis and Legvold 1969). With further cooling the thermal conductivity sharply decreased. In general features the temperature dependence of thermal conductivity in Tb was analogous to that observed in Gd (see figure 8.5). Numerical values of Tb thermal conductivity are presented in table A2.1 in appendix 2.

8.1.3 Dysprosium

The HAFM structure arises in Dy between $T_N \cong 180$ K and $T_C \cong 85$ K. Dy is characterized by much higher critical fields than Tb: the maximum H_{cr} value is about 11 kOe at $T_K = 165$ K (Bykhover *et al* 1990). At T_C the structural transition hexagonal–close-packed–orthorhombic structure occurs under magnetic transition from HAFM to FM phase (Darnell 1963).

Hudgins and Pavlovic (1965) performed detailed studies of the field and temperature dependences of the MCE in polycrystalline Dy in the fields up to 20 kOe and in the temperature interval from 77 to 320 K. The $\Delta T(H,T)$ curves were discussed in connection with the magnetic structure transformation. Later Tishin (1988) and Nikitin *et al* (1985a) studied the MCE in polycrystalline Dy in fields up to 60 kOe.

Investigations of the MCE by a direct method and magnetization of a Dy single crystal along the easy crystal a-axis were made by Nikitin *et al* (1979a) in magnetic fields up to 13 kOe. It was found that a field-induced HAFM–FM transition at H_{cr} causes a positive MCE ($\Delta T > 0$) within the temperature interval from 85 to 160 K. A change of sign of the MCE was found to take place at T_K , where H_{cr} had its maximum and $\partial H_{cr}/\partial T = 0$. According to the Clausius–Clapeyron equation (2.100) ΔS_M , and consequently ΔT , should be equal to zero at this temperature. It was concluded that T_K is a tricritical point in the magnetic phase diagram $H_{cr}(T)$ of Dy, where the first-order transition lines turn into a second-order transition line.

The MCE in Dy was also studied by a direct method by Benford (1979), Nikitin *et al* (1988a, 1991b) and Gschneidner and Pecharsky (2000b). Figure 8.13 shows temperature dependences of the MCE in a Dy single crystal measured with the field applied along the a- and b-axes (Tishin 1988; Nikitin *et al* 1991b). The MCE maximum observed for H applied along the a-axis at $T = 177.5$ K is associated with the HAFM–PM phase transition. The sharp increase of the MCE near $T \approx 90$ K corresponds to the FM–HAFM transition. For the temperature range above 90 K and below T_K (165 K) the MCE for $\Delta H = 10$ kOe is positive. Above T_K , in the region up to 178 K the MCE is negative. This behaviour can be understood on the basis of the Clausius–Clapeyron equation (2.100), equation (2.79) relating ΔT and ΔS_M and the magnetic H – T phase diagram of Dy (see, for example, figure 8.16). The magnetic field of 10 kOe is high enough to destroy the HAFM structure on the main part of the interval of its existence, and to cause the MCE corresponding to this process. Below T_K ,

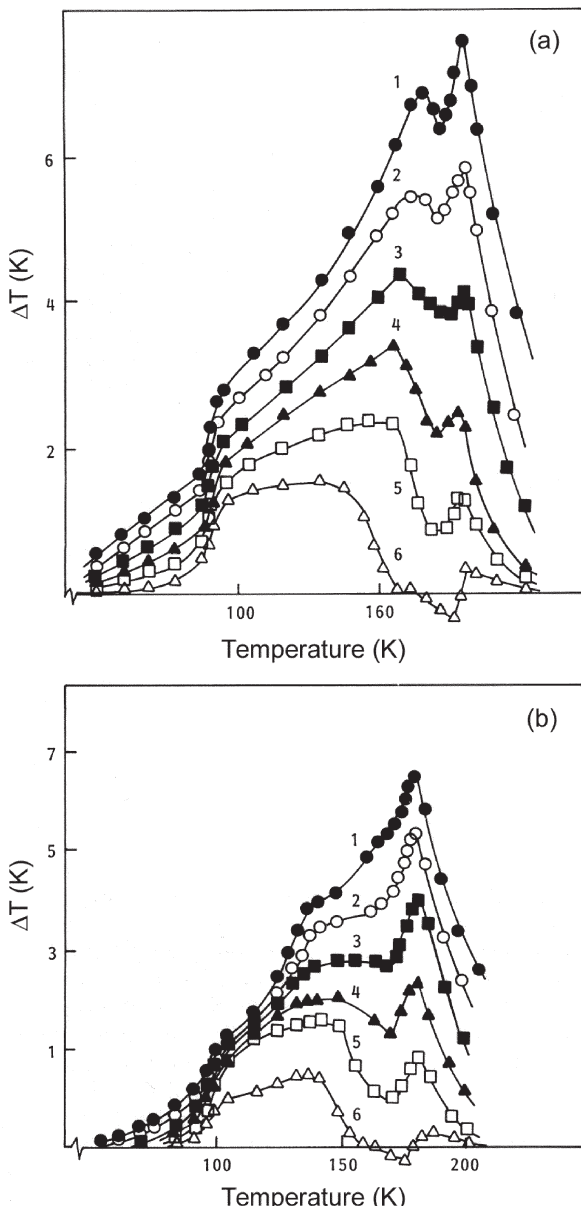


Figure 8.13. (a) Temperature dependences of ΔT in a Dy single crystal in a magnetic field applied along the a-axis: $\Delta H = (1) 60\text{ kOe}; (2) 50\text{ kOe}; (3) 40\text{ kOe}; (4) 30\text{ kOe}; (5) 20\text{ kOe}; (6) 10\text{ kOe}$. (b) Temperature dependences of ΔT in a Dy single crystal in a magnetic field applied along the b-axis: $\Delta H = (1) 60\text{ kOe}; (2) 50\text{ kOe}; (3) 40\text{ kOe}; (4) 30\text{ kOe}; (5) 20\text{ kOe}; (6) 10\text{ kOe}$ (Nikitin *et al* 1991b). (Reprinted from Nikitin *et al* 1991b, copyright 1991, with permission from Elsevier.)

$dH_{\text{cr}}/dT > 0$, which according to equation (2.100) corresponds to negative ΔS_M and positive ΔT . At $T = T_K$, dH_{cr}/dT is equal to zero and, consequently, ΔT should also be equal to zero, as observed in experiment. Above T_K , $dH_{\text{cr}}/dT < 0$ and ΔT should be negative. However, here the transition is of the second-order.

A substantial change of the $\Delta T(T)$ behaviour is observed when the field is increased. The broad plateaux in the temperature interval from 90 to 135 K and $H < 20$ kOe are due to the destruction of the HAFM structure by fields $H > H_{\text{cr}}$. In stronger fields the plateaux gradually disappear and an additional MCE maximum appears around 155–165 K, the temperature of the maximum position increasing as the field is increased. The minimum in high fields corresponds to the tricritical point $T_K = 165$ K. The general character of the MCE behaviour in fields applied along the b-axis is similar to that measured along the a-axis. The difference in MCE along a- and b-axes at low temperatures was explained by Nikitin *et al* (1991b) by a contribution from the change of magnetic basal-plane anisotropy energy. Gschneidner and Pecharsky (2000b) determined the MCE temperature dependences in polycrystalline ultra-pure Dy prepared by solid-state electrolysis on the basis of the heat capacity data. The peak value of the MCE near T_N for $\Delta H = 20$ kOe was ~ 2.1 K, which is two times higher than the value obtained by Nikitin *et al* (1991b) on single crystal Dy. The MCE peak value of 2.5 K for $\Delta H = 20$ kOe was obtained on polycrystalline Dy by Benford (1979) by a direct method.

Tishin (1998) and Nikitin *et al* (1991b) also measured the field dependence of the MCE in Dy for a magnetic field applied along the a-axis. The negative MCE field regions were observed in the temperature range corresponding to the existence of the HAFM structure above T_K —see figure 2.8. They are related to the antiferromagnetic-type paraprocess under transformation of HAFM structure by a magnetic field and were discussed in section 2.6. Below T_K there are jumps at the fields corresponding to H_{cr} , which are related to the destruction of the HAFM structure by the field-induced first-order metamagnetic transition.

Data on the magnetic entropy of Dy have been presented by Nikitin *et al* (1985a, 1991b,c), Nikitin and Tishin (1988), Foldeaki *et al* (1995) and Chenishov *et al* (2002b). Figure 8.9 shows the $\Delta S_M(T)$ curve for Dy for $\Delta H = 60.2$ kOe calculated on the basis of heat capacity and MCE data. The temperature dependence of the magnetic entropy $S_M(0, T)$ of a high-purity Dy single crystal was determined by Nikitin *et al* (1991c) on the basis of heat capacity measurements by integration of equation (2.12). The saturation high-temperature S_M value obtained in this way equals 23 J/mol K, which is in good agreement with the theoretical value from table 6.2. Foldeaki *et al* (1995) determined the temperature and field dependences of ΔS_M in polycrystalline Dy from the magnetization measurements. A positive magnetic entropy change was observed on the $\Delta S_M(H)$ curve at $T = 174$ K at low

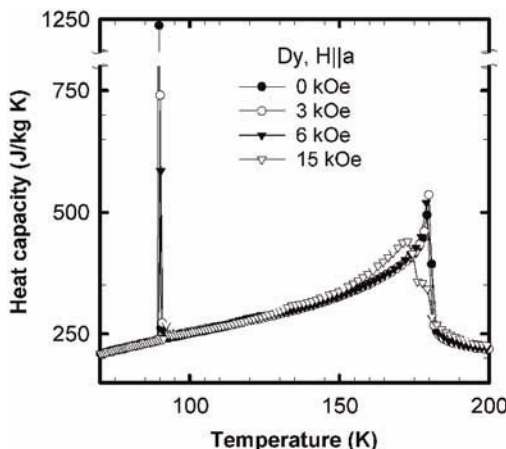


Figure 8.14. Temperature dependences of the heat capacity of Dy single crystal in various magnetic fields applied along the crystal a-axis (Chernyshov *et al* 2002b).

fields (below 1.5 kOe). The peak MCE and ΔS_M values obtained experimentally in Dy by various methods are presented in table 8.2.

The heat capacity of Dy was measured by Griffel *et al* (1956), Lounasmaa and Sundström (1966), Ramji Rao and Narayama Mytry (1978), Nikitin *et al* (1991c), Pecharsky *et al* (1996), Gschneidner *et al* (1997a) and Chernyshov *et al* (2002b). Maxima on the $C(T)$ curve were observed near T_N and T_C . It was shown that the value of the maximum near the HAFM–PM transition was in good agreement with that calculated with the help of MFA (Nikitin *et al* 1991c). Nikitin and Tishin (1987) using equation (2.155) and MCE data calculated the heat capacity of Dy in magnetic fields up to 60 kOe from the zero-field heat capacity measurements of Griffel *et al* (1956). In the field of 20 kOe, an additional maximum in the $C(T)$ curve appeared near 160 K, which was related by the authors to the occurrence of the fan structure. It disappeared in high magnetic field in accordance with the fan structure transformation into the ferromagnetic one.

Chernyshov *et al* (2002b,c) undertook investigations of magnetization, heat capacity, and magnetocaloric effect of high-purity Dy single crystal. Heat capacity temperature dependences measured in various magnetic fields applied along the crystal a-axis are shown in figure 8.14. The sharp maximum at 90 K corresponds to the first-order transition at T_C and the second anomaly at 180 K is due to the transition from paramagnetic to HAFM structure at T_N . The magnetic field caused a decrease of sharp peak amplitude and its disappearance in the field of 20 kOe. Chernyshov *et al* (2002b,c) determined the magnetic entropy change and MCE in Dy from the magnetization and heat capacity measurements and also measured the MCE directly in the fields up to 14 kOe. Figure 8.15 shows $\Delta T(H)$

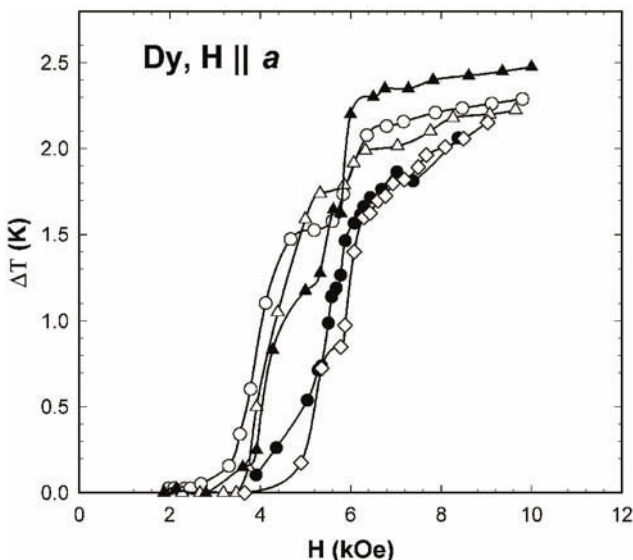


Figure 8.15. Magnetic field dependences of the MCE in Dy single crystal (magnetic field is applied along the a-axis) at different temperatures (Chernyshov *et al* 2002b).

dependences measured directly on a Dy single crystal for the field applied along the a-axis in the temperature range corresponding to the HAFM state above T_C . As one can see there are two jumps on the curves—one in low fields, corresponding to the destruction of the HAFM structure, and the other in higher fields. It was found that the low-field jump is characterized by temperature hysteresis displaying itself in the measurements made under heating and cooling, as should be expected for the first-order field-induced metamagnetic transition from HAFM to FM state. This hysteresis was not observed for the high-field jumps and the MCE was practically completely reversible in this field region, which allowed the authors to make a conclusion about the second-order nature of this transition. The high-field peculiarity was explained by an effect of commensurability between the magnetic helicoidal structure and crystal structure that takes place at 113.7 K, where the helicoid's turn angle is equal 30° (Wilkinson *et al* 1961, Greenough *et al* 1981). In order to describe the observed anomaly Chernyshov *et al* (2002b) used an expansion of the Landau–Ginsburg functional (Izyumov 1984) by the order parameters in the vicinity of the commensurability point. On the basis of this, the dependence of magnetization on magnetic field was determined and then by equation (2.16) the field dependence of the MCE near the commensurability point was determined. The results of calculations were in accordance with experiment, revealing anomalies related to commensurability.

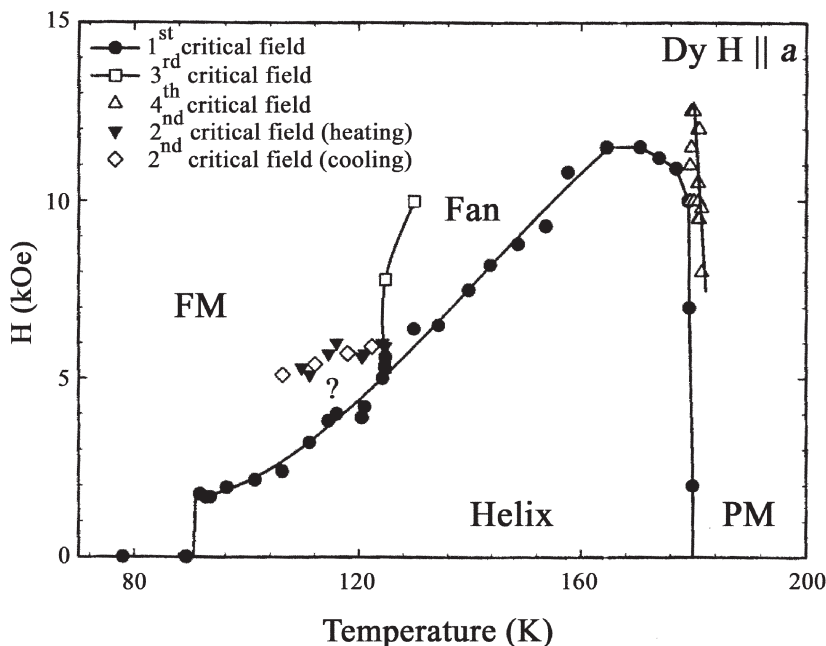


Figure 8.16. The magnetic phase diagram of high-purity Dy single crystal constructed from $\Delta T(H)$ curves measured directly for the field applied along the a-axis (Chernishov *et al* 2002c).

Figure 8.16 shows a magnetic phase $H-T$ diagram of the high-purity Dy single crystal constructed on the basis of $\Delta T(H)$ curves measured directly with the magnetic field applied along the a-axis. It is similar to the diagrams obtained previously (Wilkinson *et al* 1961, Nikitin *et al* 1979a) with respect to the major magnetic phases (PM, HAFM, FM and fan), but also have some additional features. One of them is a sharp increase of the HAFM–FM transition field (the first critical field corresponding to the low-field jump in figure 8.15) in the vicinity of the Curie temperature between 90 and 92 K. Chernishov *et al* (2002c) related it to the coexistence of HAFM and FM phases just above T_C . In the temperature region from 110 to 125 K in magnetic fields between 5 and 6 kOe there is an additional line associated with the second critical field (the high-field jump in figure 8.15) and explained by the authors by the commensurate effects. Another feature is the phase boundary line in the temperature interval from 179 to 182 K (the fourth critical field) corresponding to the anomalies in $\Delta T(H)$ curves found in this region. It was assumed that this is due to an intermediate ‘vortex’ state that according to the literature data may exist at these temperatures.

Magnetic entropy change temperature dependences determined for Dy single crystal for various ΔH by Chernyshov *et al* (2002b) for different

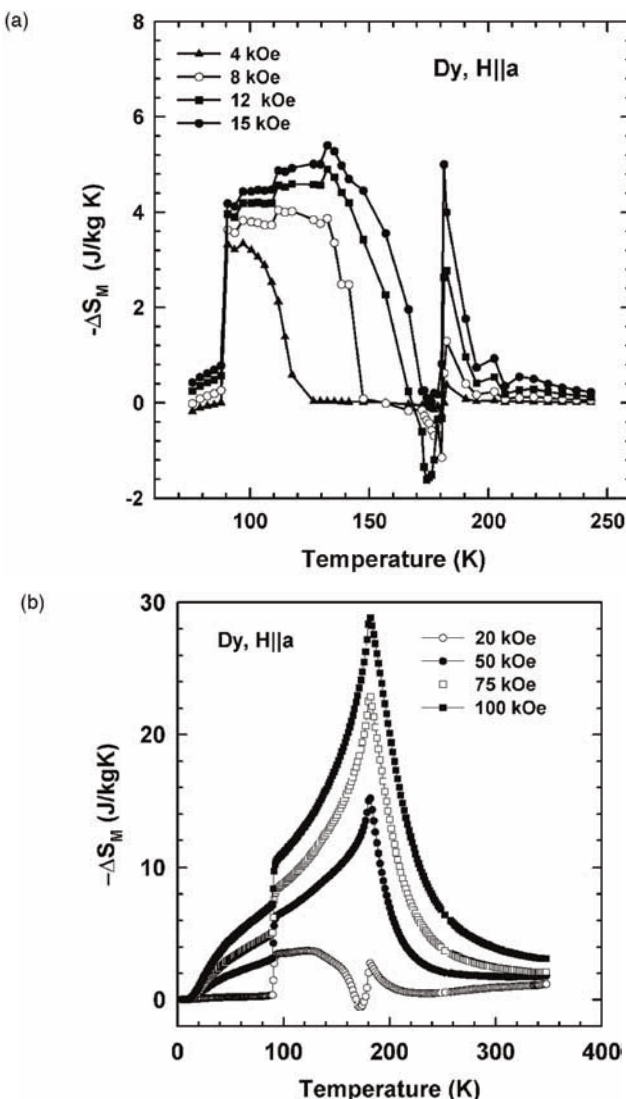


Figure 8.17. Temperature dependences of the magnetic entropy change in Dy single crystal (magnetic field is applied along the a-axis) for different ΔH : (a) up to 15 kOe (determined from magnetization); (b) in the range from 20 to 100 kOe (determined from heat capacity) (Chernyshov *et al* 2002b).

temperatures from magnetization and heat capacity data are shown in figure 8.17. In general features they are analogous to the $\Delta T(T)$ curves with the temperature regions of positive ΔS_M corresponding to the regions of negative ΔT (see figure 8.13). From the Clausius–Clapeyron equation (2.100),

on the basis of the magnetization data and constructed magnetic phase diagram, the authors estimated the magnetic entropy change related to the HAFM–FM magnetic phase transition at T_N as -3.6 J/kg K . Almost the same value (-3.4 J/kg K) had the lattice entropy change associated with the first-order structural phase transition and corresponding volume change, which was determined from the Clausius–Clapeyron equation in the form of equation (6.3). The value of the volume change ΔV in equation (6.3) was taken from the volume magnetostriction measurements and dT/dp was taken as the shift of T_C under pressure from the work of Nikitin *et al* (1991b). The obtained values are in quite good agreement with experimentally observed magnetic entropy change at T_C . The MCE temperature dependences determined from the heat capacity measurements were analogous to that measured by a direct method (figure 8.13), although the peak values near T_N in the former case were higher than obtained directly—see table 8.2.

In the paramagnetic region just above T_N , Chernyshov *et al* (2002b) observed significantly higher (about two times) values of the MCE in the investigated high-purity Dy single crystal than that reported previously (Nikitin *et al* 1979a). The difference disappeared in the high-temperature region. The observed effect was related by the authors to the existence of clusters with short-range AFM order in the paramagnetic region above T_N . The suppression of internal AFM structure of such clusters by a magnetic field should give negative MCE on the initial stage of the magnetization process due to the antiferromagnetic-type paraprocess, lowering the total MCE in the paramagnetic region. At higher temperatures the clusters will be destroyed and the effect will disappear. Higher MCE in the high-purity single crystal can be related to the existence of the clusters in a narrower temperature interval in this case.

Another interesting thermal effect was observed at the first-order transition at T_C in ultra-pure Dy obtained by a method of solid-state electrolysis (Pecharsky *et al* 1996, Gschneidner *et al* 1997a). This effect was superheating, i.e. cooling of the sample as a result of adding heat. It was revealed during the measurement of the heat capacity in the heat pulse calorimeter described in section 3.2.2.1. It was explained by the magnetic phase transformation causing by application of heat, at which the temperature of the material drops.

The thermal conductivity of Dy was investigated by Powell and Jolliffe (1965), Colvin and Arajs (1964), Gallo (1965), Boys and Legvold (1968) and Gschneidner (1993b). The values of thermal conductivity measured along the c-axis in Dy single crystal are higher than that measured along the a-axis in the paramagnetic range and the situation changes to the opposite in the magnetically ordered state (Boys and Legvold 1968). With cooling from the paramagnetic range the thermal conductivity first decreases and below T_N starts to increase, reaching maximum value at $\sim 25\text{ K}$. Further cooling causes rapid decrease of the thermal conductivity. At the temperatures of

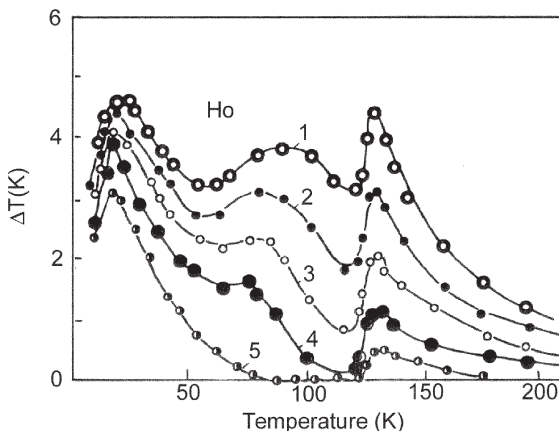


Figure 8.18. Temperature dependences of the MCE in polycrystalline Ho for various ΔH : (1) 60.2 kOe; (2) 50.2 kOe; (3) 40.3 kOe; (4) 30.1 kOe; (5) 20.1 kOe (Nikitin *et al* 1985a; Tishin 1988).

the magnetic phase transition (T_C and T_N) there are anomalies on the thermal conductivity. Colvin and Arajs (1964) measured temperature dependences of the thermal conductivity of Dy polycrystal in the temperature range from 5 to 305 K. Numerical values of Dy thermal conductivity are presented in table A2.1 in appendix 2.

8.1.4 Holmium

Direct measurements of the MCE in polycrystalline Ho were made by Nikitin *et al* (1985a)—see figure 8.18, where the MCE temperature dependences for various ΔH are shown. MCE maxima are observed at $T_C = 20$ K ($\Delta T = 4.6$ K for $\Delta H = 60.2$ kOe) and at $T_N = 132$ K ($\Delta T = 4.5$ K for $\Delta H = 60.2$ kOe). The MCE is large in the temperature interval from 20 to 132 K with $\Delta T = 3.2\text{--}4.6$ K for $\Delta H = 60.2$ kOe. Small MCE maxima are observed in the region of 70–90 K for $\Delta H = 30.1\text{--}60.2$ kOe. They are due to a complex temperature dependence of the critical field H_{cr} , which destroys the HAFM structure. Green *et al* (1988) found an MCE maximum in Ho near 136 K with a value of 6.1 K for $\Delta H = 70$ kOe.

Jayasuria *et al* (1985) and Lounasmaa and Sundström (1966) measured the heat capacity of Ho. Nikitin and Tishin (1987), on the basis of zero-field heat capacity of Jayasuria *et al* (1985) and measured MCE data, calculated $C(H, T)$ curves of Ho by equation (2.155)—see figure 8.19. For $H = 20$ kOe, which is higher than H_{cr} , a broad maximum appears in the $C(H, T)$ curve in the temperature range from 90 to 130 K. As the field is increased up to 60 kOe, this maximum disappears and only a plateau remains on the $C(H, T)$ curve. The authors related this maximum to the

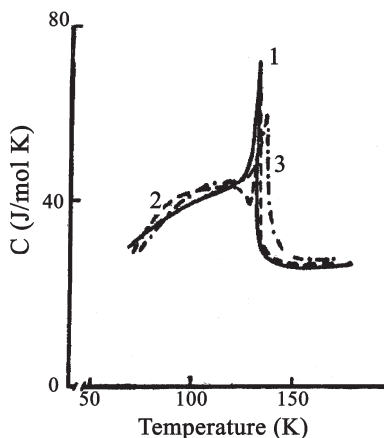


Figure 8.19. Temperature dependences of the heat capacity of Ho in various magnetic fields: $H = (1) 0$; (2) 20 kOe, (3) 60 kOe (Nikitin and Tishin 1987).

tricritical point on the magnetic phase diagram $H_{\text{cr}}(T)$. Figure 8.9 shows the $\Delta S_M(T)$ for Ho calculated by Tishin (1994) on the basis of the heat capacity and MCE data. It is seen that sharp ΔS_M maximum occurs near T_N .

The thermal conductivity of Ho was studied by Aliev and Volkenshtein (1965b), Powell and Jolliffe (1965), Nellis and Legvold (1969) and Gschneidner (1993b). The thermal conductivity of Ho single crystal measured along the c-axis is higher than that measured along the a-axis in the whole temperature range from 300 K to 5 K (Nellis and Legvold 1969). With temperature decreasing from the paramagnetic range the thermal conductivity decreases and then from ~ 110 K begins to rise, reaching a maximum value at about 50 K and decreasing with further cooling. The anomalies corresponding to the magnetic ordering temperatures were observed near the magnetic ordering temperatures on the thermal conductivity temperature dependences (Nellis and Legvold 1969). Numerical values of the Ho thermal conductivity are presented in table A2.1 in appendix 2.

8.1.5 Erbium

Nikitin *et al* (1985a) measured the MCE in polycrystalline Er by a direct method—see figure 8.20. The obtained $\Delta T(T)$ dependences revealed a maximum near the AFM-PM transition point T_N . For $\Delta H = 60.2$ kOe the maximum MCE value at T_N was 3.2 K. An extra maximum, which was attributed to the destruction of the AFM structure by a magnetic field, was observed at 35 K. The maximum value $\Delta T = 3.8$ K at this temperature exceeds that near T_N obtained for the same ΔH value. As well as Ho, Er shows a substantial MCE (about 3 K for $\Delta H = 60.2$ kOe) over a wide temperature interval from 30 to 85 K. Analogous $\Delta T(T)$ curves were

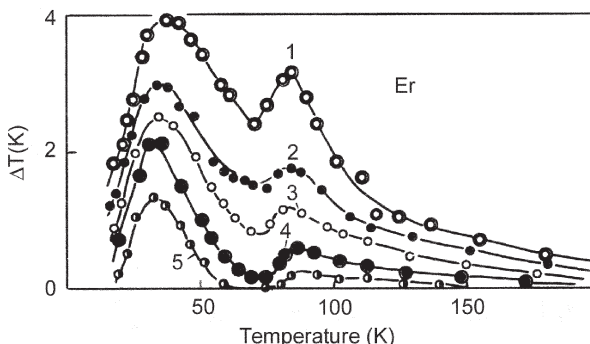


Figure 8.20. Temperature dependences of the MCE in polycrystalline Er for various ΔH : (1) 60.2 kOe; (2) 50.2 kOe; (3) 40.3 kOe; (4) 30.1 kOe; (5) 20.1 kOe (Nikitin *et al* 1985a; Tishin 1988).

obtained by Zimm *et al* (1988b) for polycrystalline Er. It was established that for $\Delta H = 75$ kOe the high-temperature (near T_N) and low-temperature MCE maxima become almost equal and amount to 4.7 K. Zimm *et al* (1988b) found that below 20 K a magnetization—demagnetization cycle causes sample heating. This was explained by a fairly large magnetic hysteresis observed in this temperature range.

The $\Delta S_M(T)$ curve of Er for $\Delta H = 60.2$ kOe is presented in figure 8.9. The ΔS_M maximum near T_N has a value of 1.2 J/mol K, while the low temperature maximum is much higher with $\Delta S_M = 2.5$ J/mol K.

The heat capacity of Er was studied by Skochdopole *et al* (1955), Dreyfus *et al* (1961), Krusius *et al* (1974), Hill *et al* (1984), Schmitzer *et al* (1987), Pecharsky *et al* (1993) and Gschneidner *et al* (1997a). The temperature dependence of the zero-field heat capacity of Er measured by Zimm *et al* (1988b) displayed a large step at 84 K corresponding to the AFM ordering along the c-axis. The sharp peak near 20 K was related to the first-order transition to a conical magnetic structure, and the broad shoulder from 30 to 80 K corresponded to the ordering in the basal plane. A magnetic field of 10 kOe wiped out the peak at 20 K but had only a small effect on the high-temperature anomaly.

The heat capacity of ultra-pure erbium prepared by solid state electrolysis measured by Gschneidner *et al* (1997a) is presented in figure 8.21. The observed anomalies are related to magnetic phase transformations: paramagnetism—c-axis modulated ferromagnetic spin structure at $T_N = 84$ K, the modulated structure—the cycloid at $T_{CY} = 52$ K and first-order transition from the cycloid to the conical phase at $T_C = 19$ K. The peculiarity near 25 K is related to the spin-slip transition between different commensurate AFM structures. The superheating (cooling under adding heat to the material) and supercooling (warming under removing heat from the material) effects were observed in ultra-pure Er by Gschneidner *et al* (1997a). Earlier superheating

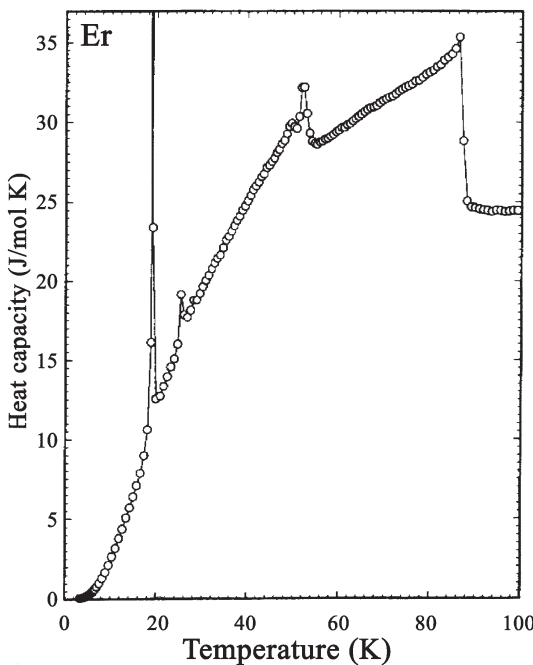


Figure 8.21. Temperature dependence of the zero-field heat capacity of ultra-pure polycrystalline Er (Gschneidner *et al* 1997a). (Copyright 1997 by the American Physical Society.)

was observed in ultra-pure Dy (Pecharsky *et al* 1996). A distinctive feature of the effects in Er was several successive temperature changes (four under heating and two under cooling) in comparison with only one temperature drop under superheating effect in Dy. The authors explained this behaviour by the passing of Er through several intermediate metastable magnetic states under the transition at T_C . These states arise due to the complex magnetic structure of Er. In ordinary (not ultra-pure) samples of Er and Dy the effects of supercooling and superheating were not observed. This was related by the authors to stresses introduced into a material by impurities and interaction with the magnetoelastic strain arising at the transition, which is one of its main driving forces. Such impurity stresses can slow down the magnetic phase transformation at the transition.

Zero field heat capacity of high-purity polycrystalline Er was thoroughly investigated by Pecharsky *et al* (1993) in the temperature interval 1.5–80 K. Besides the peaks at 19 K (conical phase transition) and 51.4 K (AFM ordering in the basal plane), additional anomalies at 25.1, 27.5, 42 and 48.9 K were revealed. The authors explained them by the spin-slip transitions between different commensurate AFM structures (Gibbs *et al* 1986, Bohr 1991).

The data about the thermal conductivity of Er are presented in the works of Aliev and Volkenshtein (1965b), Powell and Jolliffe (1965), Boys and Legvold (1968) and Gschneidner (1993b). According to the investigations of Boys and Legvold (1968) on Er single crystal, the thermal conductivity is higher along the c-axis than that along the b-axis in the paramagnetic region, and below ~ 70 K the c-axis values become smaller than the b-axis values. The thermal conductivity measured along the b-axis monotonically decreases with temperature decreasing from 300 K down to 5 K with small anomalies at the magnetic transition temperatures. Magnetic transitions have a more pronounced effect on the thermal conductivities measured along the b-axis, and also tend to decrease with cooling. However, at ~ 18 K in this case a thermal conductivity maximum of ~ 0.085 W/cm K is observed (Boys and Legvold 1968). Numerical values of the Er thermal conductivity are presented in table A2.1 in appendix 2.

8.1.6 Thulium

Figure 8.22 shows the temperature dependences of polycrystalline Tm measured directly by Nikitin *et al* (1985a). Near $T_N = 58$ K the MCE maximum with a value of 1.5 K for $\Delta H = 60.2$ kOe is observed. At lower

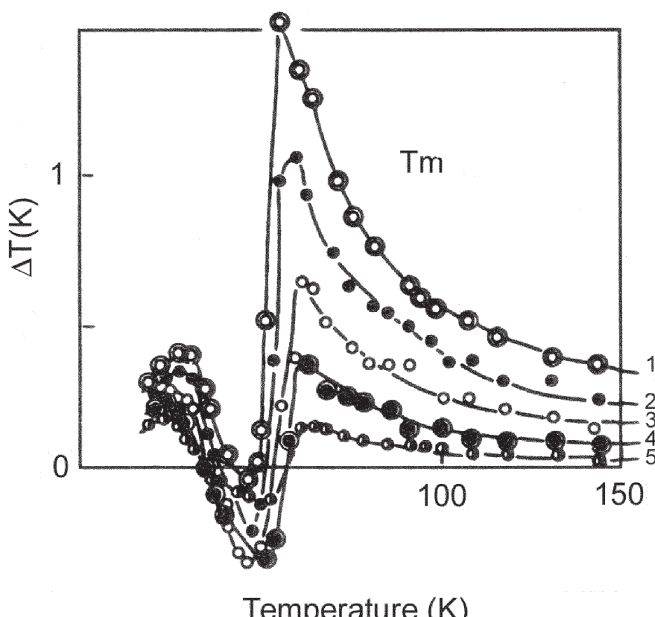


Figure 8.22. Temperature dependences of the MCE in polycrystalline Tm for various ΔH : (1) 60.2 kOe; (2) 50.2 kOe; (3) 40.3 kOe; (4) 30.1 kOe; (5) 20.1 kOe (Nikitin *et al* 1985a; Tishin 1988).

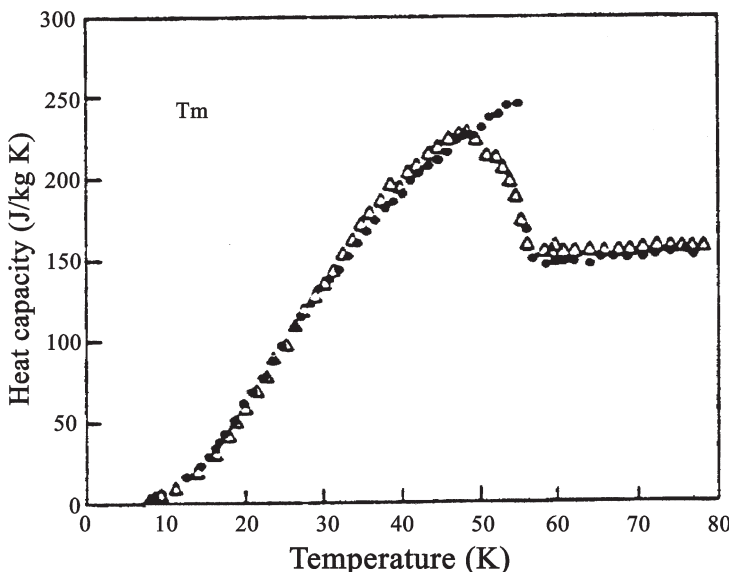


Figure 8.23. Temperature dependence of the heat capacity of polycrystalline thulium: zero field (●) and in a magnetic field of 30 kOe (△) (Zimm *et al* 1989). (Reprinted from Zimm *et al* 1989, copyright 1989, with permission from Elsevier.)

temperatures the MCE becomes negative, which may be due to the deformation of the AFM structure by the magnetic field and which is accompanied by a magnetic entropy increase. Analogous $\Delta T(T)$ curves were obtained by Zimm *et al* (1989), although the maximum ΔT values in corresponding magnetic fields were somewhat higher.

The temperature dependence of the zero-field heat capacity of Tm measured by Zimm *et al* (1989) showed a large step near T_N —see figure 8.23. Application of 30 kOe did not have any noticeable influence on the $C(T)$ curve except rounding of the step at T_N .

Thermal conductivity of Tm was reported in the works of Aliev and Volkenshtein (1965c), Edwards and Legvold (1968) and Gschneidner (1993b). The measurements made by Edwards and Legvold (1968) on Tm single crystal revealed essential anisotropy of the thermal conductivity in the paramagnetic region: at 300 K it was $\sim 0.24 \text{ W/cm K}$ for the c-axis direction and $\sim 0.14 \text{ W/cm K}$ for the b-axis direction. With cooling, the thermal conductivity of Tm decreased, reaching a minimum value of $\sim 0.09 \text{ W/cm K}$ near T_N for the measurements along the b-axis and $\sim 0.1 \text{ W/cm K}$ at $\sim 38 \text{ K}$ for the measurements along the c-axis, then increased displaying a maximum (0.25 W/cm K for the b-axis and ~ 0.21 for the c-axis) at $\sim 12 \text{ K}$ and decreased with further cooling (Edwards and Legvold 1968). The thermal conductivity values measured along the b-axis became higher than that measured along the c-axis below $\sim 40 \text{ K}$. Numerical

values of the Tm thermal conductivity are presented in table A2.1 in appendix 2.

8.1.7 Neodimium

Zimm *et al* (1990) measured directly the MCE in polycrystalline Nd in the temperature range from 5 to 35 K and in fields up to 70 kOe—figure 8.24. Two maxima were found on the temperature dependence of the MCE in Nd. The one near 20 K corresponds to magnetic ordering at the hexagonal sites, and the other, near 8 K, corresponds to ordering at the cubic sites. It should be noted that the latter maximum was much higher ($\Delta T \approx 2.5$ K at 10 K for $\Delta H = 70$ kOe) than the former ($\Delta T \approx 22$ K for $\Delta H = 70$ kOe). The authors related this difference to a large magnetocrystalline anisotropy because of which only the basal-plane component (the magnetic moments in the hexagonal sites order in the basal plane) of the external magnetic field in a crystallite can contribute to the magnetic ordering near T_N . The relatively weak MCE in Nd (as compared with the heavy RE metals) was explained by the anti-ferromagnetic structure and crystalline field effects. The latter factor reduces the maximum available magnetic entropy from $R \ln 10$ ($J = 9/2$) in the absence of crystal field splitting to the value of $R \ln 2$ ($J = 1/2$).

The heat capacity of Nd was investigated by Lounasmaa and Sundström (1967), Forgan *et al* (1979), Zimm *et al* (1990) and Pecharsky *et al* (1997a). Lounasmaa and Sundström (1967) found two maxima on the zero field $C(T)$ curve at about 8 K and 19 K corresponding to the magnetic phase transitions described above. Analogous results were obtained by Zimm *et al*

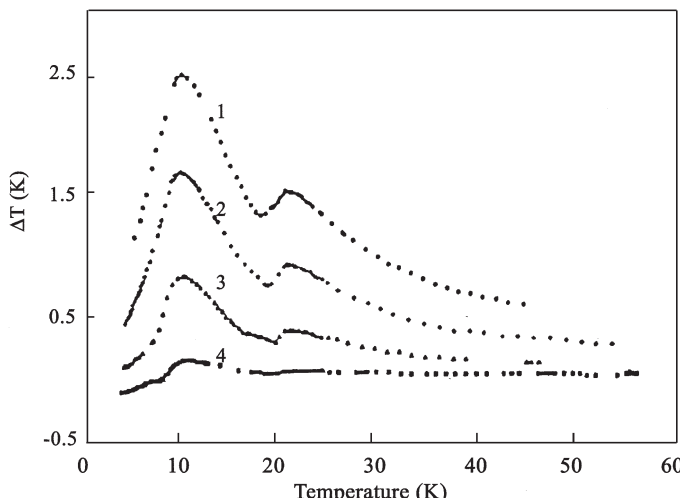


Figure 8.24. Temperature dependences of the MCE in polycrystalline Nd for different ΔH : (1) 70 kOe; (2) 50 kOe; (3) 30 kOe; (4) 10 kOe (Zimm *et al* 1990).

(1990). Forgan *et al* (1979) made heat capacity measurements on an electro-transport purified Nd sample, which revealed two sets of sharp peaks—two peaks at about 5 K (where there was only a shoulder on the $C(T)$ curves of Lounasmaa and Sundström (1967)) and three peaks in the temperature range from 7 K to 8 K. Essential volumetric heat capacity at low temperatures makes this material a possible candidate for application in passive magnetic regenerators in this temperature range—see section 11.1.

The room temperature value of thermal conductivity of polycrystalline Nd (0.165 W/cm K) is presented in the works of Powell and Jolliffe (1965) and Gschneidner (1993b).

8.1.8 Theoretically available MCE in heavy rare earth metals

Here the results of theoretical calculation of the MCE values in very high magnetic fields made by Tishin (1990a, 1998c) will be presented and discussed. Such a calculation is necessary for deeper understanding of the mechanisms of the magnetic ordering process in high magnetic fields and for identification of the ways of searching for materials with high magnetocaloric effects. Furthermore, modern experimental investigations in high magnetic fields up to 5 MOe and more are no longer something exotic. Since the MCE value in such fields can be extremely high, the possibility of its influence on the obtained experimental results needs to be accounted for.

Tishin (1990a, 1998c) made a computer simulation analysis of the MCE in rare earth metals and rare earth based materials based on the mean field approximation (MFA). The developed analysis was applied to calculate peak values of the MCE in rare earth metals (Tishin 1990a). The influence of such main thermodynamic parameters as magnetic field, temperature, magnetic ordering temperature and Debye temperature on the MCE in RE metals was investigated and the possible mechanisms of magnetic entropy change in the field region corresponding to the paraprocess were discussed. It was also shown that the Debye temperature has an essential influence on the MCE value in rare earth metals in a wide temperature range.

The calculations were made in the framework of approach described in section 2.4 (equations (2.58)–(2.63)) and section 3.2.2 with parameters of RE metals listed in table 8.3. The magnetic fields were assumed to significantly exceed the critical magnetic fields necessary to destroy the antiferromagnetic state in rare earth metals and, therefore, all calculations were performed for the magnetic phase transition from ferromagnetic to paramagnetic state.

The results of the numerical simulation should agree quite well with the experimental data for the heavy lanthanides only for large magnetic fields, i.e. for fields in which the contribution of the AFM–FM phase transition to the magnetic entropy is rather small. Consideration was made of the temperature interval from 10 K to 1000 K and in magnetic fields up to 40 MOe. The energy spectrum can become extremely distorted in such high

Table 8.3. Values of the maximum possible magnetic entropy change $-\Delta S_M^{\max}$, calculated values of the magnetic entropy change $-\Delta S_M^{\text{theor}}$ for $\Delta H = 6 \times 10^3$ and 10^4 kOe and maximum possible values of the magnetocaloric effect ΔT_{\max} , values of the H_{\max} , in which the MCE is different from ΔT_{\max} by at most 1% and the experimental maximum magnetic entropy change $-\Delta S_M^{\exp}$ near T_{ord} in heavy rare earth metals (Tishin 1990a).

Parameter	Rare earth metal						
	Gd	Tb	Dy	Ho	Er	Tm	
$-\Delta S_M^{\exp}$ (J/mol K)	17.3		21.3	23.1	23.6	23.1	21.3
$-\Delta S_M^{\exp}$ (J/mol K) ($\Delta H = 60$ kOe)	2.1		2.4	2.3	1.8	1.2	—
		($\Delta H = 70$ kOe)					
$-\Delta S_M^{\text{theor}}$ (J/mol K) ($\Delta H = 6 \times 10^3$ kOe)	15.8		19.4	21.4	22.3	22.6	21.0
$-\Delta S_M^{\text{theor}}$ (J/mol K) ($\Delta H = 10^4$ kOe)	16.8		20.6	22.5	23.1	22.7	21.0
ΔT_{\max} (K)	235		254	231	191	135	100
ΔH_{\max} ($\times 10^4$) kOe	2.2		2.8	2.6	2.4	1.6	1.0
T_{ord} (K)	293		230	178	135	85	60

magnetic fields. Therefore, this naturally may affect the real field dependence of the magnetic entropy, S_M , and ΔT . Phenomena like crossover are considered by the author to yield staircase-like $\Delta T(H)$ and $S_M(H)$ curves. But it was supposed that its contribution to the total value of the overall MCE and the entropy should be relatively small. The calculations reveal the fact that if the temperature is high (near 1000 K), the MCE and magnetic entropy continue to change even in the highest considered magnetic fields, while near the temperature of the phase transition to the paramagnetic state the value of the magnetic entropy saturates in a field of about 10 MOe. In high fields ($H > 10$ MOe), the magnetic entropy practically equals zero up to the point $T \approx T_C$, i.e. there is no magnetic contribution to the entropy. This result leads to the following conclusion: in fields higher than 1 MOe the magnetic moments of the rare earth ions must be nearly completely aligned in a wide range of temperatures up to the Curie temperature.

The calculations made by Tishin (1990a, 1998c) showed that the general behaviour of the MCE as a function of temperature is significantly transformed under the influence of a magnetic field. Anomalies in $\Delta T(T)$ curves are observed in magnetic fields up to 40 MOe, but the MCE continue to increase with temperature for $T > T_C$, when $H > 5$ MOe. This behaviour is characteristic for all investigated RE metals.

Figure 8.25 presents the temperature dependence of the maximum MCE for heavy lanthanides in the field of 6 MOe. Gadolinium has the minimum MCE at all considered temperatures. Tishin's (1998c) analysis led to the conclusion that at low temperatures the maximum MCE value (of heavy lanthanides) is determined by the Debye temperature, T_D (i.e. by the value

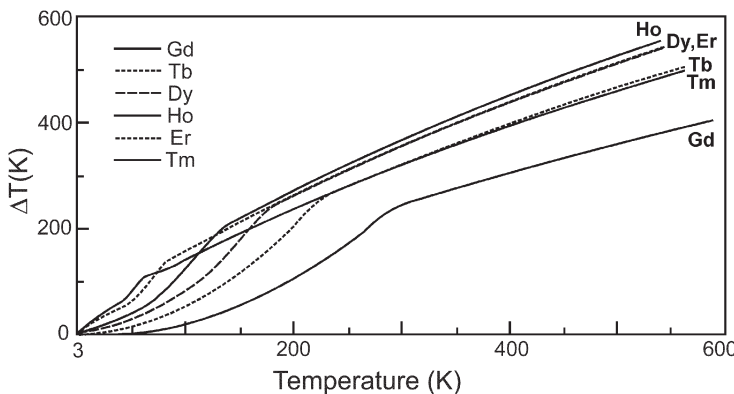


Figure 8.25. Calculated temperature dependences of the MCE in heavy rare earth metals Gd, Tb, Dy, Ho, Er and Tm induced by $\Delta H = 6$ MOe (Tishin 1990a). (Reprinted from Tishin 1990a, copyright 1990, with permission from Elsevier.)

of lattice heat capacity). When the temperature exceeds 230 K the maximum MCE in all REM follows the total angular moments, J , and/or the effective magnetic moment, μ_{eff} . The calculations show that Tb has the largest MCE in fields up to 2 MOe, while Er has the lowest. In higher fields Ho has the maximum value of MCE, and Gd the minimum. Furthermore, in high fields (although not in the saturation fields) the MCE is defined not only by the magnetic entropy, but also by a number of other parameters associated with the magnetic and crystal structures of the lanthanides.

Figure 8.26 shows field dependences of the magnetic entropy in the vicinity of the transition from ferromagnetic to paramagnetic state. As one

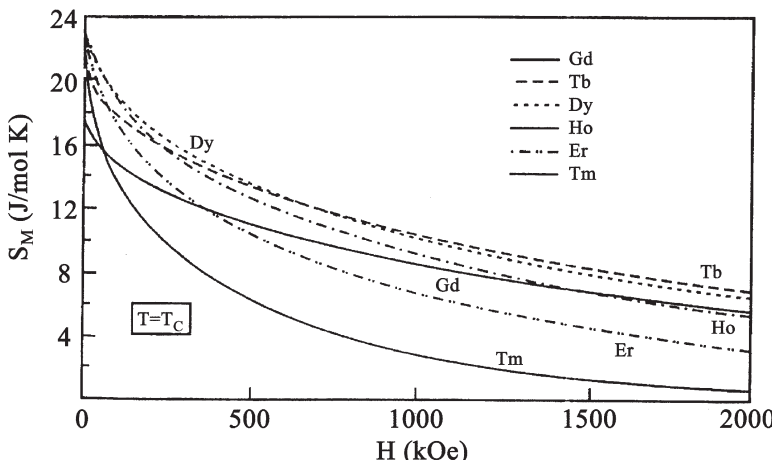


Figure 8.26. Calculated field dependences of the magnetic entropy near the transition from magnetically ordered to paramagnetic state in heavy rare earth metals (Tishin 1998c).

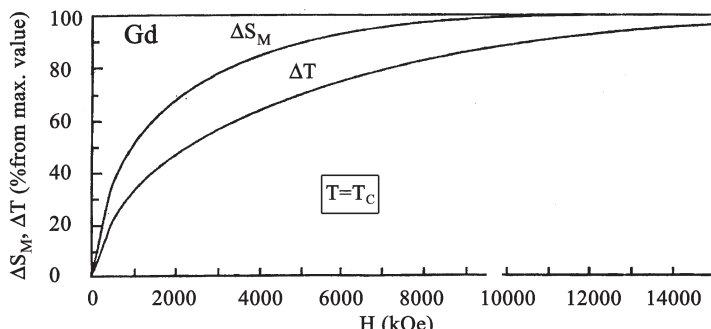


Figure 8.27. Calculated field dependences of the MCE and the magnetic entropy change in Gd at $T = T_C$ (Tishin 1998c).

can see, the curves can be arranged in order of increasing Curie temperatures of the RE metals, except Gd. The calculations also revealed that the MCE in RE metals continued to increase even when the entropy became almost equal to zero. Figure 8.27 presents the field dependence of the MCE and the magnetic entropy change (in percentage of the corresponding total value) at $T = T_C$ in gadolinium. It is seen that although $\Delta S_M = 0$ already at $H = 10$ MOe, the MCE continues to increase well above this field.

Calculations of the MCE value in the heavy RE metals as a function of the magnetic field at $T = T_{\text{ord}}$ (here $T_{\text{ord}} = T_C$ for Gd and T_N for the others RE metals), which are shown in figure 8.28, give satisfactory agreement with

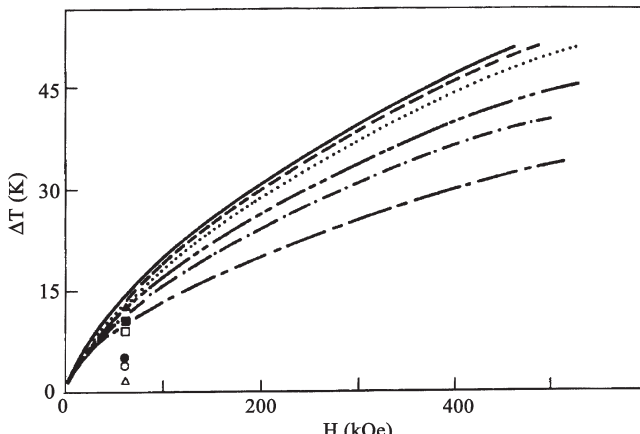


Figure 8.28. Calculated magnetic field dependences of the MCE in the heavy rare earth metals at T_{ord} : Tb (—); Dy (---); Gd (· · ·); Ho (- · -); Er (- - -); Tm (—). Experimental values for $\Delta H = 60$ kOe from the works of Brown (1976), Nikitin *et al* (1985a), Nikitin and Tishin (1988) and Tishin (1988) are given by symbols: Gd (▲), Tb (■), Dy (□), Ho (●), Er (○), Tm (△) (Tishin 1990a). (Reprinted from Tishin 1990a, copyright 1990, with permission from Elsevier.)

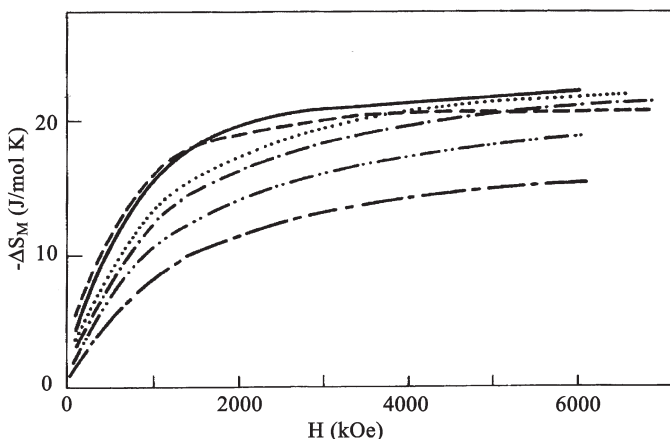


Figure 8.29. Calculated magnetic field dependences of the magnetic entropy change at T_{ord} for the heavy rare earth metals: Er (—), Ho (· · ·), Dy (- · -); Tm (— · —), Tb (— · — · —), Gd (— · — · — · —) (Tishin 1990a). (Reprinted from Tishin 1990a, copyright 1990, with permission from Elsevier.)

the experimental data for $\Delta H = 60$ kOe only for Gd, Tb and Dy (Tishin 1990a). This result is quite clear, since in Ho, Er and Tm the HAFM structure persists in much higher fields than in Tb and Dy. It follows from the experimental data that the behaviour of the $\Delta T(T)$ curves is strongly influenced by these structures in fields up to 60 kOe. One can suppose that in fields much higher than H_{cr} the MFA should describe the MCE quite well.

The results of MFA calculations of $\Delta S_M(T, H)$ in the heavy RE metals at $T = T_{\text{ord}}$ are shown in figure 8.29. One can see that a considerable rise in ΔS_M is observed only in fields below 2 MOe, whereas in fields of about 6 MOe the values of ΔS_M differ only slightly from their maximum values ΔS_M^{max} , which can be stated as maximum possible entropy S_M determined by equation (2.66) and listed in table 6.2. Table 8.3 presents ΔS_M^{max} , the values of ΔS_M calculated for $\Delta H = 6$ MOe and 10 MOe, and maximum experimental ΔS_M values for $\Delta H = 60$ kOe near T_{ord} (Brown 1976, Nikitin and Tishin 1988, Tishin 1988).

Table 8.3 also shows the maximum possible values of the magnetocaloric effect (ΔT_{max}) at $T = T_{\text{ord}}$, calculated by equation (2.79) on the basis of ΔS_M^{max} values and the calculated values of the fields $H_{\text{max}}(T_{\text{ord}})$, in which the MCE is different from ΔT_{max} by at most 1%. As one can see, an initial temperature rise of 100 K leads the MCE to increase by a factor 1.5–2. Such behaviour of ΔT_{max} corresponds to the functional dependence $\Delta T \approx T$, as follows from equation (2.79), since the factor $(\Delta S_M/C_{p,H})$ tends to a constant when H tends to infinity. The analysis made by Tishin (1990a) shows that the ΔT_{max} value in the series of heavy RE metals is directly proportional to the product $g_J T_{\text{ord}}$ —see figure 8.30.

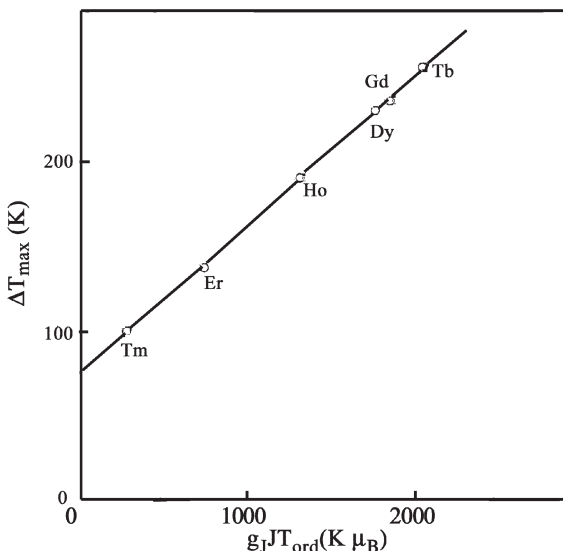


Figure 8.30. Dependence of maximum value of the magnetocaloric effect (ΔT_{\max}) in rare earth metals at $T = T_{\text{ord}}$ on the product $g_J J T_{\text{ord}}$ (Tishin 1990a). (Reprinted from Tishin 1990a, copyright 1990, with permission from Elsevier.)

From the classic point of view, the change of S_M value is usually related to the rotation of the magnetic moment vectors under the influence of the magnetic field (i.e. the S_M decreases with increasing magnetization in a magnetic material). It has been experimentally established that the value of ΔS_M measured in 60 kOe in rare earth metals and their alloys in the vicinity of their magnetic phase transition totals approximately from 8 to 10% of ΔS_M^{\max} (Tishin 1988). It should be noted that in rare earth intermetallic compounds the change of magnetic entropy can reach much higher values, close to about 90% of ΔS_M^{\max} for ΔH up to 100 kOe at low temperatures (Gschneidner *et al* 1996b). The magnetization of Gd at the Curie point practically does not change in 100 to 300 kOe (Ponamorev 1986). The MCE value measured in 100 kOe in Gd equals 19 K (Dan'kov *et al* 1998). But the calculations show that ΔT_{\max} in Gd is expected to be 234 K at $T = T_C$ (Tishin 1990a, 1998c). Thus, it appears that for most of the sample's temperature increase one should take into account a paraprocesses (occurring in the region where the sample already has single domain structure and the atomic magnetic moments are mostly aligned parallel to the field). According to Tishin (1998c), the magnetic entropy (and consequently the sample temperature) continues to change even in the region of the high field paraprocess, just because of the fact that the probability of atomic magnetic moment deflection from the field direction (due to the heat spin fluctuations) remains non-zero even in high magnetic fields. It is possible

that the values of ΔS_M , which have been observed in rare earth intermetallic compounds by Gschneidner *et al* (1994b), are large due to suppression of spin heat fluctuations in the low-temperature region in these compounds.

Besides MCE in the high-field region, Tishin (1998c) conducted numerical consideration of the influence of the Debye temperature on the MCE values. This question has not been sufficiently studied yet, either numerically or experimentally. To investigate the impact of the Debye temperature on the MCE one needs to take into account the effect of the temperature on the lattice entropy (it is worth noting that the concept of total entropy as a sum of different parts can be used without restrictions only for magnetic materials with localized magnetic moment, like RE elements). The entropy of a solid body is known to increase significantly when the Debye temperature decreases. For instance, it is easy to show that at 300 K a decrease of the Debye temperature from 184 K (Gd) to 50 K leads to a lattice entropy (S_l) increase of about 33 J/mol K (70%). When the Debye temperature increases from 184 K to 500 K this leads to an S_l change of only approximately 23 J/mol K (50%). The maximum possible magnetic entropy change ΔS_M^{\max} is determined by equation (2.66). So, on one hand the maximum MCE is limited by the total quantum number and the temperature of measurement. On the other hand, in general the MCE can vary due to the change of magnetic, lattice and electronic contributions to the heat capacity. The electronic part of the heat capacity gives a constant contribution to the heat capacity and does not change the MCE if $T = \text{const}$. The character of magnetic contributions to the heat capacity change (generally the magnetic contribution decreases in a magnetic field in ferromagnets) under exposure of a field is quite complicated and can be predicted only in general terms.

The influence of the Debye temperature value on the MCE was investigated for two rare earth metals, Gd ($T_{\text{ord}} = 293$ K) and Tm ($T_{\text{ord}} = 60$ K). The results are shown in figure 8.31. In Gd the change of T_D from 184 K (T_D value for Gd) to 20 K leads to the MCE decrease only by 0.07 K for $\Delta H = 20$ kOe, and T_D increase from 184 K up to 500 K causes the MCE increase by 0.45 K. So, in this case the Debye temperature change in wide range has only little impact on the MCE value. A contrary situation is observed in Tm. Here the T_D change from 190 K (T_D value for Tm) to 500 K increases the MCE peak value for $\Delta H = 100$ kOe from 6.4 K up to 12.6 K. In this case the change of T_D essentially changes the MCE.

However, the problem of which ways to change the Debye temperature in real magnetic materials still remains quite insufficiently investigated. From the qualitative point of view, the Debye temperature can be treated as the rigidity of the crystal lattice. The rigidity of a lattice can be changed in several ways. For instance, one may change the fabrication process by making it amorphous or by other processing means. The Debye temperature can also be significantly affected by addition of different elements to magnetic compounds. For example, additions of C, N or B are known to lead to a unit

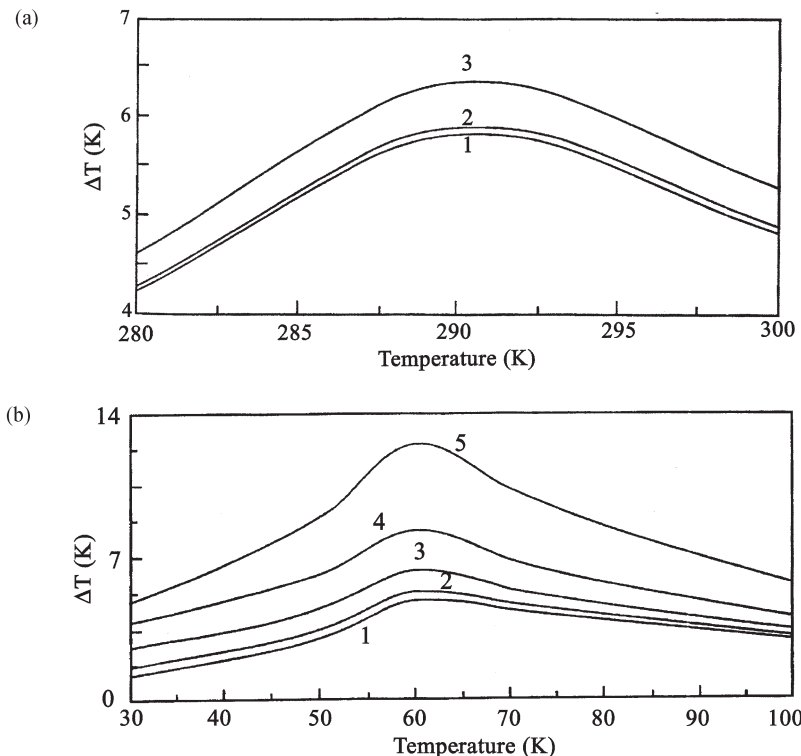


Figure 8.31. Calculated temperature dependences of the MCE (a) in Gd for $\Delta H = 20$ kOe and (b) in Tm for $\Delta H = 100$ kOe for different values of T_D : (a) (1) $T_D = 20$ K; (2) 184 K (Gd), (3) 500 K; (b) (1) $T_D = 20$ K, (2) 100 K, (3) 190 K (Tm), (4) 300 K, (5) 500 K. In calculations the following parameters were used: (a) for Gd $g_J = 2$, $J = 7/2$, $T_{\text{ord}} = 293$ K; (b) for Tm $g_J = 1.7$, $J = 6$, $T_{\text{ord}} = 60$ K (Tishin 1998c).

cell volume increase (swelling) of a magnetic material. However, this can also affect the MCE itself.

8.2 Rare earth alloys

8.2.1 Tb–Gd alloys

$\text{Tb}_x\text{Gd}_{1-x}$ alloys with $x < 0.94$ are strongly anisotropic easy-plane ferromagnets with a hard magnetization axis along the crystal c-axis (Nikitin *et al* 1980). These alloys display a spin-reorientation transition with the appearance of a magnetization component along the hard axis below some temperature. The MCE and magnetic entropy change in the alloys was investigated by Nikitin *et al* (1979b, 1980, 1981, 1988b), Gschneidner and

Pecharsky (2000b), Long *et al* (1994) and Xiyan *et al* (2001). Nikitin *et al* (1979b, 1980, 1981, 1988b) used a direct method of the MCE measured, Gschneidner and Pecharsky (2000b) determined it from heat capacity measurements and Long *et al* (1994) and Xiyan *et al* (2001) calculated $\Delta S_M(T)$ curves from magnetization.

The temperature dependences of the MCE measured in Tb_xGd_{1-x} alloys in fields applied in the basal plane (easy plane) have maxima near the Curie point (Nikitin *et al* 1981). An analogous picture was observed on polycrystalline Tb–Gd samples by Gschneidner and Pecharsky (2000b) and Long *et al* (1994). The measured MCE values are given in table 8.4.

The measurements along the hard c-axis revealed more complex MCE behaviour. The temperature dependence of the MCE in $Tb_{0.2}Gd_{0.8}$ alloy is shown in figure 8.32 (curves 1 and 2). A maximum of the positive MCE can be observed near $T_C = 282$ K, as in the case of H directed along the b-axis. However as the sample is cooled down, a sign change of the MCE takes place below T_C , where it becomes negative. The sign inversion temperature shifts towards lower temperatures in higher fields. Near T_C the MCE behaviour is correlated to the temperature dependences of the magnetization—see figure 8.32 and equation (2.16). For $H = 60$ kOe the specific magnetization $\sigma(T)$ curve (curve 3) has a form usually observed for ferromagnets and the MCE displays a maximum. For $H = 10$ kOe there is a maximum in the $\sigma(T)$ dependence. The maximum appears due to the ordering of the magnetic moments in the basal plane in fields, which are not high enough to orient them along the c-axis below T_C . The maximum in the $\Delta T(T)$ curve for $\Delta H = 10$ kOe is observed at the temperature where $\partial\sigma/\partial T$ is negative and its absolute value has a maximum (see curves 2 and 4 in figure 8.32). The negative MCE corresponds to positive $\partial\sigma/\partial T$.

Nikitin *et al* (1988b) considered the reasons for the appearance of a negative MCE in Tb–Gd alloys in the low-temperature range in fields applied along the hard axis. The total MCE was presented as consisting of three contributions:

$$\begin{aligned} \Delta T \approx -\frac{T}{C_{H,p}} & \left[\frac{\partial I_s}{\partial T} H \cos \Theta + \frac{\partial K_1}{\partial T} (\sin^2 \Theta - 1) + I_{RR} \left(\frac{\partial I_{Tb}}{\partial T} I_{Gd} + \frac{\partial I_{Gd}}{\partial T} I_{Tb} \right) \right. \\ & \times (\cos^2(\Theta_{Tb} - \Theta_{Gd}) - 1) \left. \right], \end{aligned} \quad (8.4)$$

where Θ is the angle between the total spontaneous magnetization vector \vec{I}_s and the c-axis, K_1 is the anisotropy constant, I_{RR} is the integral of the indirect exchange interaction between the Tb and Gd magnetic moments, I_{Tb} and I_{Gd} are the magnetizations of the Tb and Gd sublattices, respectively, and Θ_{Tb} and Θ_{Gd} are the angles between the sublattice magnetization vectors \vec{I}_{Tb} and \vec{I}_{Gd} and the c-axis. The first term, calculated by equation (2.16), is due to the variation of exchange interaction inside the Tb and Gd sublattices

Table 8.4. Magnetic ordering temperatures T_N or T_C , temperature of the maximum in the $\Delta T(T)$ curves (T_{\max}^T), temperature of the maximum in the $\Delta S_M(T)$ curves (T_{\max}^S) and maximum values of ΔS_M (at $T = T_{\max}^S$) and ΔT (at $T = T_{\max}^T$) induced by a magnetic field change ΔH and $\Delta T/\Delta H$ and $-\Delta S_M/\Delta H$ for heavy rare earth alloys. References are shown in brackets.

Element	T_C, T_N (K)	T_{\max}^T (K)	ΔT (K)	Peak MCE			ΔH (kOe)	$-\Delta S_M$ (J/kg K)	ΔH (kOe)	$-\Delta S_M/\Delta H \times 10^2$ (J/kg K kOe)
				ΔH (kOe)	$\Delta T/\Delta H \times 10^2$ (K/kOe)	T_{\max}^S (K)				
Gd _{0.3} Tb _{0.7}	253 [1]	252 [2]	9.1(b)[2]	60	15.2	—	—	—	—	—
Gd _{0.6} Tb _{0.4}	271 [1]	252 [1]	0.4(c)[1]	12	3.3	—	—	—	—	—
Gd _{0.8} Tb _{0.2}	282 [1]	270 [2]	8 (b)[2]	60	13.3	—	—	—	—	—
Gd _{0.74} Tb _{0.26}	280 [4]	281 [1]	2.2(b)[1]	8	27.5	—	—	—	—	—
Gd _{0.74} Tb _{0.26}	280 [4]	282 [2]	7.2(c)[2]	60	12	—	—	—	—	—
Gd _{0.74} Tb _{0.26}	280 [4]	282 [2]	0.9(c)[3]	9.1	9.9	—	—	—	—	—
Gd _{0.6} Tb _{0.4}	272 [5]	275 [4]	19 [4]	100	19	280 [4]	17.8 [4]	100	17.8	—
Gd _{0.8} Tb _{0.2}	284 [5]	—	5.6 [4]	20	28	275 [4]	6 [4]	20	30	—
Gd _{0.74} Tb _{0.26}	283 [17]	—	—	—	—	265 [5]	2.6 [5]	10	26	—
Gd _{0.75} Tb _{0.20} Nd _{0.05}	267 [17]	—	—	—	—	278 [5]	2.5 [5]	10	25	—
Gd _{0.25} Tb _{0.70} Nd _{0.05}	231 [17]	—	—	—	—	—	2.62 [17]	10	26.2	—
Gd _{0.25} Tb _{0.60} Nd _{0.15}	223 [17]	—	—	—	—	—	3.07 [17]	10	30.7	—
Gd _{0.2} Ho _{0.8}	160 [6]	160 [6]	7 [6]	60.2	11.6	—	—	—	—	—
Gd _{0.4} Ho _{0.6}	194 [6]	194 [6]	9 [6]	60.2	15	—	—	—	—	—
Gd _{0.6} Ho _{0.4}	230 [6]	230 [6]	9.5 [6]	60.2	15.8	—	—	—	—	—
Gd _{0.8} Ho _{0.2}	268 [6]	268 [6]	10 [6]	60.2	16.6	265 [7]	3.8 [7]	10	38	—
Gd _{0.2} Er _{0.8}	125 [6]	125 [6]	4 [6]	60.2	6.6	—	—	—	—	—
Gd _{0.4} Er _{0.6}	168 [6]	168 [6]	7 [6]	60.2	11.6	—	—	—	—	—
Gd _{0.6} Er _{0.4}	220 [6]	220 [6]	8 [6]	60.2	13.3	—	—	—	—	—
Gd _{0.69} Er _{0.31}	—	—	—	—	—	232 [8]	15.8 [8]	90	17.6	—
Gd _{0.84} Er _{0.16}	—	—	—	—	—	260 [7]	3.5 [7]	10	35	—

Gd _{0.9} Er _{0.1}	-	-	-	-	274 [8]	14 [8]	90	15.6	
Gd _{0.3} Dy _{0.7}	-	-	-	-	208 [9]	16 [9]	70	22.9	
Gd _{0.5} Dy _{0.49}	-	-	-	-	204 [9]	2.8 [9]	10	28	
Gd _{0.7} Dy _{0.3}	-	-	-	-	248 [9]	10.4 [9]	70	14.9	
Gd _{0.8} Dy _{0.2}	-	-	-	-	242 [9]	2 [9]	10	20	
Gd _{0.88} Dy _{0.12}	-	-	-	-	254 [10]	4.6 [10]	16	28.7	
Gd _{0.9} Dy _{0.1}	-	-	-	-	264 [10]	4.6 [10]	16	28.7	
Gd _{0.5} Dy _{0.5}	235 [11]	-	-	-	280 [9]	14 [9]	70	20	
Gd _{0.35} Dy _{0.35} Nd _{0.3}	165 [11]	-	-	-	280 [9]	3.6 [9]	10	36	
Tb _{0.1} Y _{0.9}	52 [10]	55 [12]	0.3([b] [12]	60	0.5	173 [12]	0.9([b] [12]	60	1.5
Tb _{0.63} Y _{0.37}	176 [10]	176 [12]	0.04([c] [12]	60	0.07				
Tb _{0.865} Y _{0.135}	205 [10]	205 [12]	5.6([b] [12]	60	9.3				
Dy _{0.7} Y _{0.3}	135 [13]	129 [13]	7([b] [12]	60	11.7				
Er _{0.8} La _{0.2}		45 [14]	3.7([la] [13]	60	6.2				
Tb _{0.25} Dy _{0.75}		45 [14]	5.4 [14]	70	7.7				
Tb _{0.5} Dy _{0.5}		44 [14]	0.8 [14]	10	8				
Tb _{0.75} Dy _{0.25}		194 [15]	0.7 [15]	13	5.4				
Er _{0.9} Pt _{0.1}		207 [15]	1.7 [15]	13	13.1				
Er _{0.8} Pt _{0.2}		218 [15]	2.1 [15]	13	16.2				
Er _{0.7} Pt _{0.25}		65.4 [16]	3.3 [16]	50	6.6				
Er _{0.8} Pt _{0.1}		49.2 [16]	50 [16]	4 [16]	50	8			
Er _{0.75} Pt _{0.25}		42.8 [16]	45 [16]	3.1 [16]	50	6.2			
Er _{0.7} Pt _{0.3}		38.7 [16]	40 [16]	2.9 [16]	50	5.8			

11. Nikitin *et al.* (1981); 2. Nikitin *et al.* (1988b); 3. Nikitin *et al.* (1980); 4. Gschneidner and Pecharsky (2000b); 5. Long *et al.* (1994); 6. Nikitin *et al.* (1985b); 7. Tishin (1990d); 8. Smaili and Chahine (1996); 9. Smaili and Chahine (1997); 10. Nikitin (1989); 11. Dai *et al.* (2000); 12. Nikitin and Tishin (1989); 13. Tishin (1988); 14. Zimm (1994); 15. Nikitin *et al.* (1989c); 16. Wu *et al.* (2002); 17. Xivan *et al.* (2001).

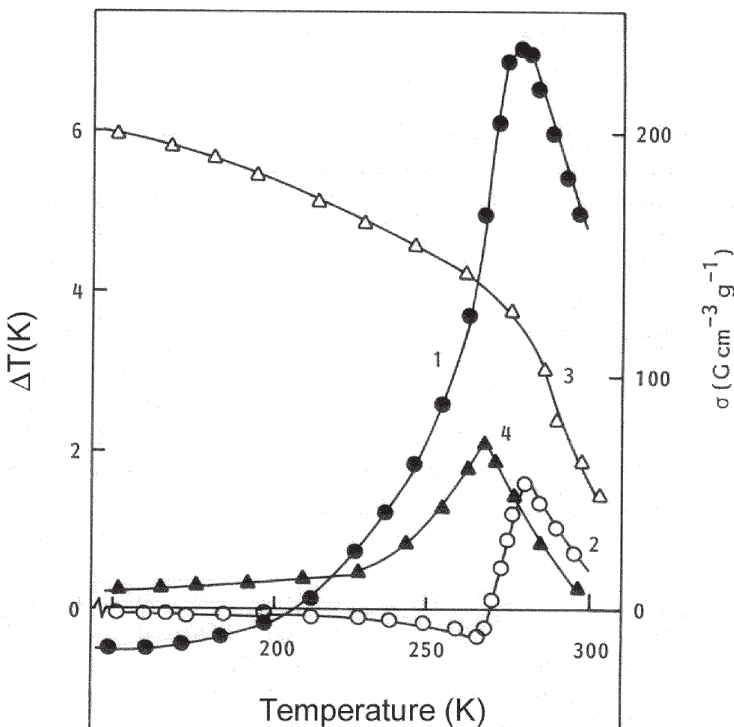


Figure 8.32. Temperature dependences of the MCE in $\text{Tb}_{0.2}\text{Gd}_{0.8}$ single crystal measured in the field applied along the crystal c-axis for $\Delta H = 60 \text{ kOe}$ (curve 1) and 10 kOe (curve 2). Curves 3 and 4 are the specific magnetization measured in the fields of 60 kOe and 10 kOe , respectively (Nikitin *et al* 1988b).

($H \cos \Theta$ is the projection of the field on the magnetization vector \vec{I}_s), i.e. the paraprocess. The second term in equation (8.4) is related to the rotation of \vec{I}_s from the basal plane to the c-axis against anisotropy forces. The last term describes the variation of the exchange interaction between Tb and Gd magnetic sublattices, which leads to a change of the angle between \vec{I}_{Tb} and \vec{I}_{Gd} and the formation of a noncollinear magnetic structure.

The calculations by equation (8.4) conducted for the $\text{Tb}_{0.2}\text{Gd}_{0.8}$ alloy on the basis of experimental data showed that for $\Delta H = 60 \text{ kOe}$ the anisotropy contribution to the MCE (the second term in equation (8.4)) is negative and its absolute value increases up to the temperature of the spin-reorientation transition near 223 K (where a magnetization component along the c-axis appears) and then remains constant (with a value of approximately -4 K). The contribution from the paraprocess is positive in all temperature ranges and has essential values near the Curie temperature. At $T = 223 \text{ K}$ it reaches a value of about 4.3 K . The last term in equation (8.4) is small and

negative below 223 K. The experimentally measured negative MCE below the temperature of the spin-reorientation transition 223 K for $\Delta H = 60$ kOe was in good accordance with the total MCE calculated as a sum of the three contributions considered (Nikitin *et al* 1988b).

Addition of Nd to $Tb_{26}Gd_{74}$ alloy decreased its Curie temperature and increased its magnetic entropy change (Xiyan *et al* 2001). The alloy $Gd_{0.25}Tb_{0.70}Nd_{0.05}$ ($T_C = 231$ K) revealed highest among other rare earth alloys absolute value of $\Delta S_M/\Delta H$ —see table 8.4. However, the $\Delta S_M(T)$ curve of this material is rather narrow—its full width at half maximum is about 5 K.

8.2.2 Gd–Dy, Gd–Ho and Gd–Er alloys

Magnetization studies of Fujii *et al* (1976) showed that in the Gd–Ho alloy system a PM–FM transition at the Curie temperature T_C takes place if the concentration of Gd exceeds 75 at%. If the Gd concentration is not higher than 75 wt% there are two magnetic phase transitions: PM–HAFM at T_N and HAFM–FM at T_C .

According to direct measurements made on polycrystalline Gd_xHo_{1-x} alloys by Nikitin *et al* (1985b) the magnetic structure changes are reflected on the $\Delta T(T)$ curves. In $Gd_{0.8}Ho_{0.2}$ a maximum in the $\Delta T(T)$ curve was found caused by the PM–FM transition. In the alloys with higher Ho concentrations, besides a high-temperature maximum related to the transition at T_N , the peculiarities due to the existence of HAFM were observed at lower temperatures. In $Gd_{0.2}Ho_{0.8}$ a broad MCE plateau occurs in the temperature interval from 40 to 140 K (for $\Delta H = 20$ kOe), which is associated to the HAFM–FM transition. For $\Delta H = 60$ kOe (this field is higher than the critical field of HAFM structure destruction) this plateau turned to a low-temperature shoulder on the maximum near T_N . On the alloys with $x = 0.4$ and 0.6 the bends associated with the HAFM structure transformation by magnetic field were observed in the low-temperature region. Tishin *et al* (1990d) determined $\Delta S_M(T)$ curves for the $Gd_{0.8}Ho_{0.2}$ alloy on the basis of magnetization measurements. The ΔS_M maximum was found near T_C for $\Delta H = 10$ kOe.

More complicated magnetic structures display Gd–Er alloys (Fujii *et al* 1976, Millhouse and Koehler 1970, Bozorth 1967). Below T_N , AFM structures arise if the Er concentration exceeds 30 at%, but they are not simple helicoidal: as in Er, spin oscillations along the crystal c-axis take place. The complex magnetic structures cause the appearance of maxima in the $\Delta T(T)$ curves at T_N and T_C , where a transition from AFM to a ferromagnetic spiral-type structure occurs (Nikitin *et al* 1985b). The latter maximum is observed in magnetic fields lower than the critical field. In the $Gd_{0.8}Er_{0.2}$ alloy there is one MCE maximum, which is due to the PM–FM transition, and for the others investigated alloys additional maxima at low

temperatures due to an AFM–ferromagnetic spiral transition exist. The magnetic entropy change temperature dependences were calculated from the magnetization data for $\text{Gd}_{0.84}\text{Er}_{0.16}$ alloy by Tishin (1990d) and for $\text{Gd}_{0.9}\text{Er}_{0.1}$ and $\text{Gd}_{0.69}\text{Er}_{0.31}$ alloys by Smaili and Chahine (1996) near the transition from paramagnetic to magnetically ordered state, where they revealed maxima. The peak MCE and ΔS_M values for Gd–Ho and Gd–Er alloys are presented in table 8.4.

Nikitin *et al* (1985b) noted that the value of MCE at the transition from paramagnetic to AFM structure T_N is proportional to T_N (see equation (2.16)), which in turn depends in rare earth metals and their alloys on the de Gennes factor as $T_N \approx G^{2/3}$ (here $G = (g_J - 1)^2 J(J + 1)$). This implies that $\Delta T(T_N)$ should be proportional to $G^{2/3}$. Such dependence was found in Gd–Ho and Gd–Er alloys.

The magnetic entropy change ΔS_M for Gd–Dy and $(\text{GdDy})_{1-x}\text{Nd}_x$ alloys was calculated by Burhanov *et al* (1991), Smaili and Chahine (1997) and Dai *et al* (2000) from the magnetization data. Maxima of ΔS_M were observed near the temperatures of transition from the paramagnetic to the magnetically ordered state. Burhanov *et al* (1991) revealed almost constant and close to Gd value of the peak ΔS_M in the $\text{Gd}_x\text{Dy}_{1-x}$ alloy system, although the Curie temperature decreased with increasing of Dy content. Dai *et al* (2000) investigated substitution of GdDy by the light rare earth metal Nd. The Curie temperature decreased with addition of Nd so as the peak magnetic entropy change value. The peak values of ΔS_M determined near T_C in the investigated alloys are presented in table 8.4.

8.2.3 Dy–Y, Tb–Y, Er–La and Er–Pr alloys

Child *et al* (1965) and Koehler *et al* (1963) established from neutron diffraction measurements that heavy rare earth metal–yttrium alloys order at T_N from a paramagnetic to an antiferromagnetic structure of the same type that exists in the corresponding pure RE metal. According to magnetization measurements the HAFM structure exists in $\text{Tb}_x\text{Y}_{1-x}$ alloys in the temperature range from liquid helium temperature up to T_N for $x = 0.1$ – 0.63 and for $x \geq 0.835$ the FM state arises at low temperatures below T_C ($T_C < T_N$) (Nikitin 1989). The easy and hard magnetization directions in $\text{Tb}_x\text{Y}_{1-x}$ alloys are crystal b- and c-axes, respectively.

Nikitin *et al* (1977a,b), Nikitin (1978), Nikitin and Andreenko (1981) and Nikitin and Tishin (1989) made direct MCE measurements in $\text{Tb}_x\text{Y}_{1-x}$ alloys in the magnetic fields up to 60 kOe. A tricritical point T_K was found on the magnetic phase diagram $H_{\text{cr}}(T)$ of the alloys in which FM, HAFM and PM phases arose under change of temperature. The $\Delta T(T)$ dependences of such alloys were analogous to those in dysprosium (see section 8.1.3). Below T_K the $\Delta T(H)$ curves displayed jumps at the critical values of the magnetic field H_{cr} . Nikitin (1989) considered the

contributions to the MCE arising at the field-induced HAFM–FM transition at $H = H_{\text{cr}}$ in $\text{Tb}_{0.865}\text{Y}_{0.135}$. The MCE at the transition was found from

$$\frac{C_{p,H}\Delta T(H_{\text{cr}})}{T} = S_{\text{HAFM}} - S_{\text{FM}} = \left(\frac{\partial G_{\text{FM}}}{\partial T} \right)_p - \left(\frac{\partial G_{\text{HAFM}}}{\partial T} \right)_p \quad (8.5)$$

where G_{FM} and G_{HAFM} are the Gibbs energy in the FM and HAFM states, respectively.

The Gibbs energy in the corresponding magnetic state was presented as

$$G = F_{\text{ex}} + E_{\text{me}} + E_A^{\text{b}} - HI \quad (8.6)$$

where F_{ex} is the free energy of the exchange interaction between the basal planes, E_{me} is the energy of the magnetoelastic interaction, E_A is the basal plane anisotropy energy, and I is the magnetization. From equations (8.5) and (8.6) it is possible to calculate the MCE due to the field-induced HAFM–FM transition at $H = H_{\text{cr}}$:

$$\Delta T(H_{\text{cr}}) \approx \frac{T}{C_{p,H}} \left(\frac{\partial \Delta F_{\text{ex}}}{\partial T} + \frac{\partial \Delta E_{\text{me}}}{\partial T} + \frac{\partial \Delta E_A^{\text{b}}}{\partial T} - H_{\text{cr}} \frac{\partial \Delta I}{\partial T} \right) \quad (8.7)$$

where Δ denotes the change of the corresponding parameter across the transition ($\Delta I = I_{\text{FM}} - I_{\text{HAFM}}$). The calculations conducted on the basis of experimental data on magnetostriction, anisotropy and magnetization showed that, for $T = 137$ and $K > T_C$ in $\text{Tb}_{0.835}\text{Y}_{0.135}$, the main contribution to $\Delta T(H_{\text{cr}})$ comes from interplane exchange and magnetoelastic energy changes. The last contribution is due to the giant magnetostriction arising at the field-induced HAFM–FM transition. As the temperature increases, the role of this contribution decreases and the negative exchange and positive Zeeman contributions become prevalent. Near the tricritical temperature $T_K = 190$ K these contributions compensate each other and $\Delta T(H_{\text{cr}}) = 0$. Experimental $\Delta T(H)$ dependences confirms the results of calculations: for temperatures below 190 K, ΔT is almost zero in the low-field region, then a positive jump occurs at $H = H_{\text{cr}}$ with subsequent ΔT increase due to the paraprocess, and at $T = 190$ K the jump disappears. For temperatures above 190 K, ΔT is negative in the low-field region where the antiferromagnetic-type paraprocess prevails. Similar $\Delta T(H)$ behaviour is observed in Dy, which has an analogous sequence of the magnetic phase transitions and magnetic phases (see figure 2.8).

Let us consider the role of various contributions in equation (8.7) on the value of the magnetocaloric effect arising at the field-induced first-order metamagnetic transition. According to experimental investigations in rare earth metals and their alloys, $\partial \Delta I / \partial T$ is usually negative, the magnetoelastic and magnetic and anisotropy terms are positive, and the exchange contribution term can be negative or positive (Nikitin 1989, Bykhover *et al* 1990, Tishin 1994). For materials with a magnetic phase H – T diagram with tricritical

point T_K (as in Dy and Tb) the sign of the exchange contribution (the first term in equation (8.7)) is positive for $T < T_K$ and negative for $T > T_K$. Another situation is realized for materials where the tricritical point is absent (as in some Tb–Y alloys)—the exchange contribution here is negative. So, as one can see from equation (8.7) the conditions to get large ΔT at the transition are large increasing with temperature of the exchange, magnetoelastic and anisotropic energies jumps and negative sign of $\partial\Delta I/\partial T$.

The temperature dependence of the MCE in $Tb_{0.1}Y_{0.9}$ alloy, which has only one HAFM phase below the ordering temperature T_N , was measured by Nikitin and Tishin (1989) and shows a maximum near T_N . Under further cooling the MCE became negative and monotonically increased in absolute value, remaining negative down to the lowest temperature investigated, 4.2 K. When the field was applied along the hard c-axis the positive MCE maximum near T_N became broader, and in the negative MCE temperature region a minimum at $T = 30$ K with $\Delta T = -0.17$ K at $\Delta H = 60$ kOe occurred. The observed form of the $\Delta T(T)$ curve measured along the c-axis was related to transformations of the alloy magnetic structure, which takes place not only in the case of magnetization along the easy b-axis, but also for magnetization along the hard c-axis. A ferromagnetic spiral seems to appear for the case that H is applied along the c-axis, in which the magnetization has a ferromagnetic component along the c-axis and its basal plane component remains helicoidal.

The temperature dependences of the MCE in $Tb_{0.63}Y_{0.37}$ alloy for H applied along the b-axis are shown in figure 8.33. For $H < 22$ kOe the MCE changes sign from positive to negative under cooling at low temperatures and displays a minimum with a value of -0.6 K at $T = 168$ K and $\Delta H = 15$ kOe. For magnetic field changes higher than 22 kOe, a negative MCE is not observed. This behaviour can be related by the complicated temperature dependence of the MCE contribution arising from the destruction of the HAFM structure (see the magnetic phase diagram $H_{cr}(T)$ in the inset in figure 8.33). Near T_N the MCE is mainly controlled by the para-process and has a rather sharp maximum. The authors explained the negative MCE in $Tb_{0.1}Y_{0.9}$ and $Tb_{0.63}Y_{0.37}$ alloys by the field-induced distortion of the HAFM structure, which reduces, on the first stage, the magnetic ordering and increases the magnetic entropy. The MCE maximum values near T_N in the Tb_xY_{1-x} alloy system are shown in table 8.4. The presented maximum ΔS_M value for $Tb_{0.63}Y_{0.37}$ was calculated by Nikitin and Tishin (1989) with the help of equation (2.79) on the basis of MCE and heat capacity data.

The field and temperature MCE dependences in $Dy_{0.7}Y_{0.3}$ single crystal were investigated by Tishin (1988) in the fields applied along the easy magnetization a-axis. The MCE measurements made by a direct method for $\Delta H = 20$ –50 kOe revealed two maxima: at $T = 7$ K and at the transition from paramagnetic to magnetically ordered state at $T_N = 135$ K, which were

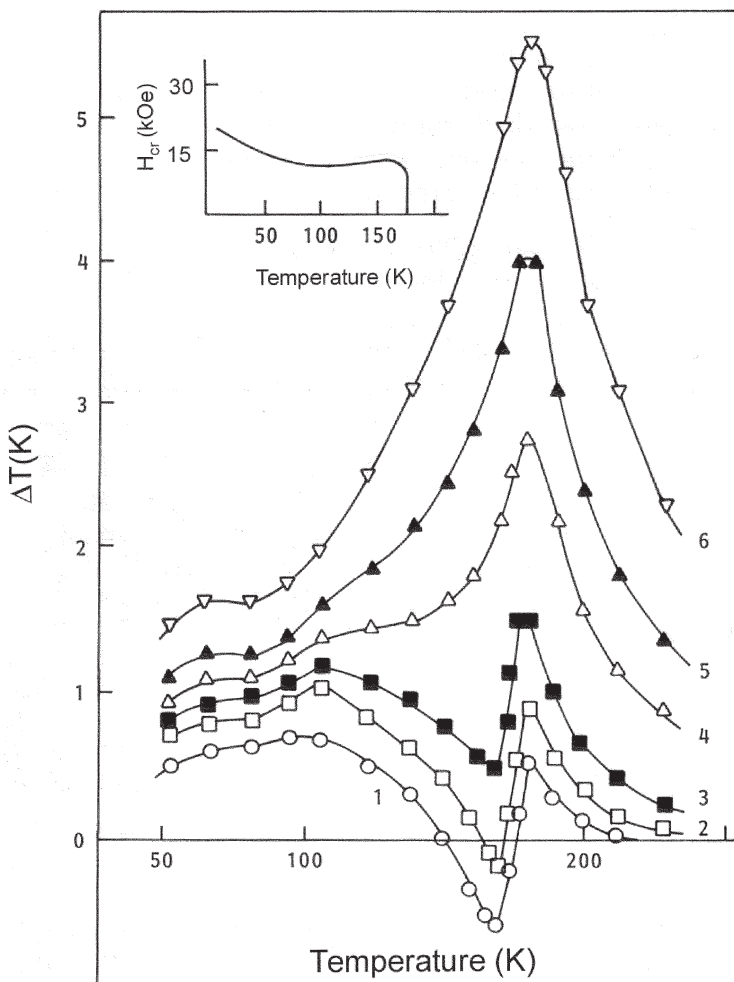


Figure 8.33. Temperature dependences of the MCE in $Tb_{0.63}Y_{0.37}$ alloy induced by a field applied along the crystal b-axis: $\Delta H = (1) 15\text{ kOe}; (2) 20\text{ kOe}; (3) 25\text{ kOe}; (4) 35\text{ kOe}; (5) 45\text{ kOe}; (6) 60\text{ kOe}$. The insert shows the magnetic phase diagram $H_{cr}(T)$ of the alloy (Nikitin and Tishin 1989).

explained by the complicated magnetic phase diagram $H_{cr}(T)$ of the alloy. For $\Delta H \leq 20\text{ kOe}$, the temperature dependence of the MCE displays one maximum near T_N . Negative MCE was observed in the temperature interval from 90 to 110 K for $\Delta H < 25\text{ kOe}$. By analogy with Dy, this was related to the formation of a fan structure under the effect of the magnetic field. The $\Delta T(H)$ curves are similar to those for Dy and provide evidence that the HAFM–FM transition is of first-order in the temperature interval from 4.2

to 110 K. In the region from 65 to 135 K this transition occurs via an intermediate fan structure. For temperatures from 65 K to 110 K the HAFM-fan transition is of first-order and above 110 K the transition is of second-order, where no jumps were observed in $\Delta T(H)$ dependences. At the tricritical point T_K , which is equal to 110 K, the MCE due to the destruction of the HAFM structure is equal to zero and because of this a minimum in the $\Delta T(T)$ curve near this temperature was observed.

Zimm (1994) measured the temperature dependences of the heat capacity and the MCE (by a direct method) of the polycrystalline $\text{Er}_{0.8}\text{La}_{0.2}$ alloy in the magnetic fields up to 70 kOe. Only one maximum and one anomaly, typical for ferromagnets, were observed in the $\Delta T(T)$ and $C(T)$ curves, respectively. Ferromagnetic ordering in $\text{Er}_{0.8}\text{La}_{0.2}$ was also established from magnetization measurements. The maximum ΔT value obtained in the $\text{Er}_{0.8}\text{La}_{0.2}$ alloy was somewhat larger than that in Er (see tables 8.4 and 8.2). The heat capacity data allowed calculation of the magnetic entropy value with the help of equation (6.1), which was found to be 111 J/kg K when the integration was made up to 100 K. The obtained value corresponds to $J = 7.8$, which is close to $J = 15/2$ for Er.

The heat capacity and MCE of $\text{Er}_{1-x}\text{Pr}_x$ alloys for x up to 0.5 were investigated by Gschneidner *et al* (2000d,e) and Wu *et al* (2002). Pure Er has four anomalies on the heat capacity on the temperature curve (see figure 8.21 and section 8.1.5)—near 84 K (T_N), near 52 K (T_{CY}), near 25 K (related to the commensurate AFM structure transformation) and 19 K (T_C). With addition of Pr to Er, T_N decreased and T_C increased with shifting of corresponding heat capacity anomalies. The peak at 25 K disappeared at $x = 0.05$ and the 52 K peak was rapidly lowered and also disappeared at $x \approx 0.07$. With further increase of x , the double peak structure on $C(T)$ merged into one peak for $x > 0.3$. The volumetric heat capacity temperature dependences for the $\text{Er}_{1-x}\text{Pr}_x$ system are shown in figure 8.34 for $x = 0, 0.1, 0.2, 0.25$ and 0.3 . Increasing the Pr concentration beyond $x = 0.3$ caused lowering of the heat capacity peak with its simultaneous shifting to the lower temperatures. On the basis of the heat capacity data Wu *et al* (2002) determined the MCE temperature dependences—see figure 8.35. As one can see there are anomalies on $\Delta T(T)$ curves corresponding to the temperatures of magnetic phase transitions. The high temperature anomaly in the investigated $\text{Er}_{1-x}\text{Pr}_x$ alloys is displayed as a peak and the low-temperature anomaly as a jump, which is characteristic for the first-order transitions.

8.2.4 Tb-Dy alloys

The MCE in the system of polycrystalline alloys $\text{Tb}_x\text{Dy}_{1-x}$ with $x = 0.25, 0.5$ and 0.75 was measured directly by Nikitin *et al* (1989c) in the fields up to 60 kOe. The $\Delta T(T)$ curves for $\Delta H = 13$ kOe (the maximum critical field H_{cr} for Dy is about 10 kOe (Nikitin *et al* 1991b)) in the alloys with

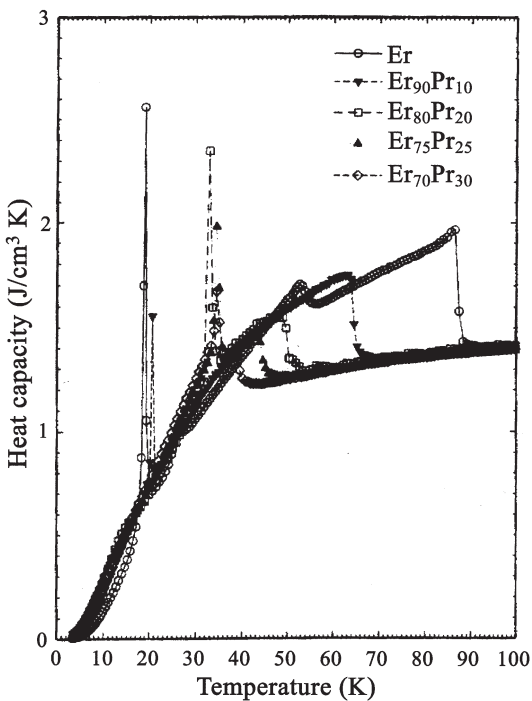


Figure 8.34. Temperature dependences of the zero-field volumetric heat capacity of Er and Er-Pr alloys (Wu *et al* 2002).

$x \leq 0.5$ have two maxima with a minimum between them corresponding to the tricritical temperature T_K , and resemble those for Gd-Ho alloys with high Ho content. For $\text{Tb}_{0.5}\text{Dy}_{0.5}$ alloy the value of the high temperature maximum at 207 K ($\Delta T = 1.7$ K), corresponding to the transition to the magnetically ordered state from a paramagnetic one, was higher than the low temperature maximum at 175 K ($\Delta T = 1.1$ K). For the alloy with $x = 0.25$ both maxima were of approximately the same height. The authors related the observed low and high temperature MCE maxima to the FM-HAFM and FM-PM transitions, respectively. It should be noted that the magnetization field and temperature dependences in $\text{Tb}_{0.5}\text{Dy}_{0.5}$ single crystal measured by Bykhover *et al* (1990) were typical for a material with HAFM structure. The MCE minimum due to the tricritical point was observed at $T = 190$ K for $\text{Tb}_{0.25}\text{Dy}_{0.75}$ and at $T = 200$ K for $\text{Tb}_{0.5}\text{Dy}_{0.5}$ for $\Delta H = 13$ kOe. A negative MCE appeared in $\text{Tb}_{0.25}\text{Dy}_{0.75}$ near 190 K and was related by the authors to the formation of a fan structure. For higher ΔH the low temperature MCE maximum disappeared.

So, as one can see from this chapter, the magnetocaloric properties of rare earth metals and their compounds have been investigated rather well.

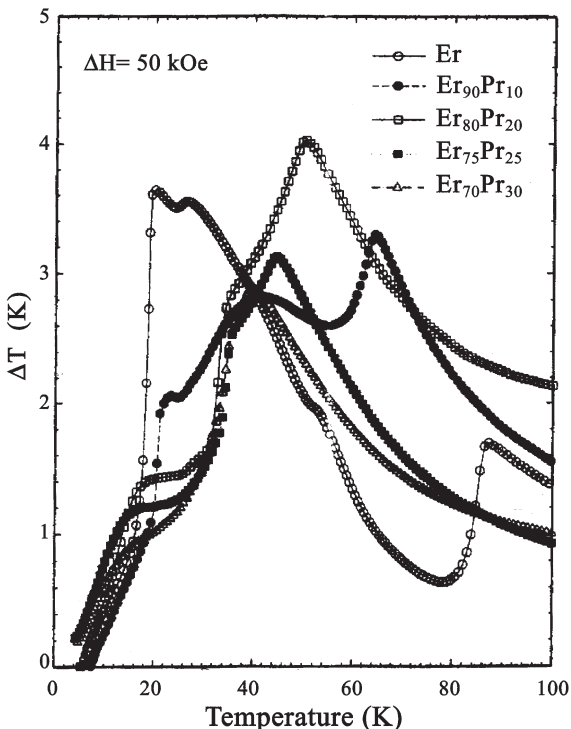


Figure 8.35. Temperature dependences of the MCE in Er and Er-Pr alloys induced by $\Delta H = 50$ kOe (Wu *et al* 2002).

The main amount of the obtained results concerns heavy rare earth metals and alloys. Among investigated heavy rare earth metals, Gd and Tb have the highest values of $\Delta T/\Delta H$ and $\Delta S_M/\Delta H$. Because Gd also has the Curie temperature of 294 K and wide $\Delta T(T)$ and $\Delta S_M(T)$ curves, it can be considered as the most promising material for magnetic refrigeration near room temperature. Gd- and Tb-based alloys have rather high magnetocaloric properties and their magnetic ordering temperature can be adjusted in a wide temperature range.

The rare earth metals and their alloys display various magnetic phases and phase transitions, displaying themselves in anomalies on magnetocaloric and magnetic entropy change temperature and field dependences. In the region of ferromagnetic phase existence the magnetocaloric effect in the rare earth metals and alloys is well described by the mean-field approximation. In Tb, Dy and the alloys based on these materials the first-order magnetic phase transition can be induced by temperature and the magnetic field changing. In Dy the first-order magnetic transition from HAFM to FM structure is accompanied by structural transition, as it takes place in

monoclinic $\text{Gd}_5(\text{Si}-\text{Ge})_4$ compounds at T_C , and by corresponding jumps on $\Delta T(T)$ and $\Delta S_M(T)$ curves, although they are not too high—about 1.6 K for $\Delta H = 10 \text{ kOe}$ and $\Delta S_M = -3.1 \text{ J/kg K}$ for $\Delta H = 20 \text{ kOe}$, respectively. The estimations made on the basis of the Clausius–Clapeyron equations showed that such ΔS_M can be explained by the lattice entropy change associated with first-order structural phase transition and corresponding volume change.

According to the thermodynamic consideration, the MCE at the field-induced first-order metamagnetic transition related to destruction of the HAFM structure can be presented as consisting of four contributions—the change of interplane exchange, magnetoelastic, anisotropy and magnetic energies under the transition. It should be noted that the changes themselves are not important, but their derivatives of temperature are. For the Tb–Y system it was shown that the main contributions for the MCE near T_N (HAFM–FM transition) come from the interplane exchange and magnetoelastic contributions arising because of the giant magnetostriction accompanying the transition. With increasing temperature, the role of the magnetoelastic contribution decreased. This result points to the important role of the magnetoelastic interactions in the formation of the MCE under the first-order field-induced metamagnetic transitions.

Chapter 9

Magnetocaloric effect in amorphous materials

In this chapter the magnetocaloric properties of amorphous materials are considered. The general feature of amorphous alloys is a broadness of magnetic transition from paramagnetic to magnetically ordered state, which is mostly related to fluctuation of the exchange interactions and crystalline electric field due to the structural disorder of these materials. The composition inhomogeneities and the possible presence of different crystalline phases can also contribute to this effect. The magnetic transition broadness leads to lower magnetic entropy change, magnetocaloric effect and heat capacity anomaly at the transition temperature because these values are directly proportional to the derivative of magnetization on temperature $\partial M/\partial T$ —see equations (2.9a), (2.16) and (2.161).

9.1 Amorphous alloys based on RE metals

The magnetization, heat capacity and magnetocaloric effect and magnetic entropy change on the basis of these data in amorphous $R_{0.7}M_{0.3-x}M'_x$ alloys (where $R = Gd, Dy, Er, Ho, Tb$; $M, M' = Ni, Fe, Co, Cu$) were studied by Liu *et al* (1996a,b) and Foldeaki *et al* (1997b, 1998b). The alloys were prepared by melt spinning in the form of thin ($30\text{--}40\ \mu\text{m}$) ribbons and their amorphism was confirmed by X-ray diffraction analysis.

Magnetic and Mössbauer measurements showed that below the Curie temperature the investigated alloys were ordered ferromagnetically for $R = Gd$ and displayed complex noncollinear magnetic structures for anisotropic R ions. The magnetic moment of the 3d ions was small or did not exist, so the magnetothermal properties were determined mainly by the R magnetic subsystem. The coercivity near the Curie temperature was negligible even in the alloys with anisotropic R ions, although magnetic saturation was not achieved in these alloys in high magnetic fields. The latter is related to the continuing transformation of the noncollinear magnetic structures

formed by highly anisotropic RE ions. The Curie temperatures of the alloys, obtained from magnetization measurements, are presented in table 9.1.

The zero-field heat capacity temperature dependences measured for the $\text{Gd}_{0.7}\text{Ni}_{0.3}$, $\text{Er}_{0.7}\text{Fe}_{0.3}$ and $\text{Gd}_{0.65}\text{Co}_{0.35}$ alloys revealed the absence of sharp discontinuity at T_C in these materials—no λ -type anomaly typical for ferromagnets was observed (Liu *et al* 1996a). Liu *et al* (1996a) modelled the heat capacity temperature dependence in amorphous materials on the basis of mean field approximation. It was supposed that an amorphous material could be presented as a number of clusters of atoms ordered ferromagnetically and having different magnetic ordering temperatures distributed around the Curie temperature of the material in accordance with Gaussian distribution. The consideration made for the $\text{Gd}_{0.7}\text{Ni}_{0.3}$ alloy showed that the sharp heat capacity anomaly at T_C obtained for zero magnetic ordering temperature standard deviation decreased and broadened with the deviation increasing. The anomaly completely disappeared for the deviation of 50 K (the Curie temperature in amorphous $\text{Gd}_{0.7}\text{Ni}_{0.3}$ alloy is 130 K). The heat capacity field dependence calculated for the deviation of 50 K for $\text{Gd}_{0.7}\text{Ni}_{0.3}$ alloy was in reasonably good agreement with experiment.

Figure 9.1 shows $\Delta S_M(T)$ and $\Delta T(T)$ curves for $\text{Gd}_{0.7}\text{Ni}_{0.3}$, $\text{Er}_{0.7}\text{Fe}_{0.3}$ and $\text{Gd}_{0.65}\text{Co}_{0.35}$ alloys determined from the heat capacity measurements. One can see that the curves have broad maxima near T_C typical for broad magnetic phase transitions in amorphous materials. For example, the full width of the $\Delta T(T)$ curve at half maximum for $\text{Gd}_{0.65}\text{Co}_{0.35}$ for $\Delta H = 80$ kOe is about 125 K. Further investigations of the magnetothermal properties of amorphous R-M alloys were made by Liu *et al* (1996b) and Foldeaki *et al* (1997b) on $\text{R}_{0.7}\text{Fe}_x\text{Ni}_{0.3-x}$ ($\text{R} = \text{Gd}, \text{Dy}$) and $\text{Gd}_{0.7}\text{Cu}_{0.3}$ melt-spun ribbons. It was found that the addition of Fe led to an increase of T_C from 130 to 300 K for $\text{Gd}_{0.7}\text{Fe}_x\text{Ni}_{0.3-x}$ alloys and from 35 to 110 K for $\text{Dy}_{0.7}\text{Fe}_x\text{Ni}_{0.3-x}$ alloys for x varied from 0 to 1. Gd-based alloys showed zero hysteresis in the whole temperature range, and in Dy-based alloys the coercive force decreased with increasing temperature and became zero near T_C . $\text{Dy}_{0.7}\text{Ni}_{0.3}$ alloy displayed the behaviour characteristic for spin glasses: under cooling in relatively low magnetic fields (up to 10 kOe) its magnetization increased near T_C , but then in the low-temperature range it decreased.

The magnetic entropy change temperature dependences in the amorphous alloys were determined by Liu *et al* (1996b) and Foldeaki *et al* (1997b) from the magnetization data. Broad maxima were observed in the $\Delta S_M(T)$ curves near T_C for both the Gd- and the Dy-based alloys, although for Gd the peak was sharper than for Dy-containing alloys. ΔS_M peak values for $\text{R}_{0.7}\text{Fe}_x\text{Ni}_{0.3-x}$ ($\text{R} = \text{Gd}, \text{Dy}; x = 0, 0.12$) and $\text{Gd}_{0.7}\text{Cu}_{0.3}$ alloys are presented in table 9.1. The substitution of Ni by Fe led to broadening of the ΔS_M maximum with a simultaneous reduction of its value in comparison with the initial alloy: 31% in $\text{Gd}_{0.7}\text{Fe}_{0.12}\text{Ni}_{0.18}$ and 12% for $\text{Dy}_{0.7}\text{Fe}_{0.12}\text{Ni}_{0.18}$.

Table 9.1. Magnetic ordering temperatures T_N or T_C , temperature of the maximum in the $\Delta T(T)$ curves (T_{\max}^T), temperature of the maximum in the $\Delta S_M(T)$ curves (T_{\max}^S) and maximum values of ΔS_M (at $T = T_{\max}^S$) and ΔT (at $T = T_{\max}^T$) induced by a magnetic field change ΔH and $\Delta T/\Delta H$ and $-\Delta S_M/\Delta H$ for amorphous alloys. References are shown in brackets.

Element	T_C (K)	T_{\max}^T (K)	Peak MCE			Peak – ΔS_M			
			ΔT (K)	ΔH (kOe)	$\Delta T/\Delta H \times 10^2$ (K/kOe)	T_{\max}^S (K)	$-\Delta S_M$ (J/kg K)	ΔH (kOe)	$-\Delta S_M/\Delta H \times 10^2$ (J/kg K kOe)
Gd _{0.7} Fe _{0.3}	297 [1]	—	—	—	—	287.5 [1]	1.5 [1]	10	15
Dy _{0.7} Fe _{0.3}	98.3 [1]	—	—	—	—	107.5 [1]	0.94 [1]	10	9.4
Er _{0.7} Fe _{0.3}	35 [2]	40 [2]	3.7 [2]	80	4.63	35 [2]	12.2 [2]	80	15.25
Gd _{0.7} Ni _{0.3}	129.6 [2]	35 [2]	2 [2]	40	5	35 [2]	6.7 [2]	40	16.75
Dy _{0.7} Ni _{0.3}	41 [1]	125 [2]	3.3 [2]	80	4.13	129.6 [1]	11.5 [1]	70	16.43
		125 [2]	1.8 [2]	40	4.5	129.6 [1]	2.45 [1]	10	24.5
		130 [3]	6 [3]	70	8.57	130 [3]	11 [3]	70	14.29
		35 [3]	3.5 [3]	70	5	48 [3]	10 [3]	70	15.29
Gd _{0.65} Co _{0.35}	180 [2]	210 [2]	2.8 [2]	80	3.5	45.5 [1]	10.7 [1]	70	15.5
		210 [2]	2.1 [2]	40	5.25	48 [3]	6.2 [3]	40	15.5
Gd _{0.7} Cu _{0.3}	154.1 [1]	—	—	—	—	200 [2]	3.6 [2]	80	4.5
Gd _{0.7} Fe _{0.12} Ni _{0.18}	189.4 [1]	—	—	—	—	200 [2]	2.6 [2]	40	6.5
Dy _{0.7} Fe _{0.12} Ni _{0.18}	63.2 [1]	—	—	—	—	144.4 [1]	8.19 [1]	70	11.7
NdFeAl	120 [4]	—	—	—	—	170 [1]	7.71 [1]	70	11
Fe _{0.9} Zr _{0.1}	237 [5]	—	—	—	—	70 [1]	9.48 [1]	70	13.54
		—	—	—	—	110 [4]	5.65 [4]	50	11.3
		—	—	—	—	2.98 [4]	20	14.9	75 ^f
		—	—	—	—	232 [5]	10.5 [*] [5]	14	71.4 ^f
		—	—	—	—	227 [5]	50 [*] [5]	70	—

Fe _{0.891} Ni _{0.009} Zr _{0.1}	255 [5]	—	—	—	—	247 [5]	11* [5]	14	78.6 [†]
Fe _{0.882} Ni _{0.018} Zr _{0.1}	275 [5]	—	—	—	—	263 [5]	11.5* [5]	14	82.1 [†]
Fe _{0.873} Ni _{0.027} Zr _{0.1}	288 [5]	—	—	—	—	272 [5]	12* [5]	14	85.7 [†]
Fe _{0.855} Al _{0.045} Zr _{0.1}	286 [5]	—	—	—	—	276 [5]	12.5* [5]	14	89.3 [†]
Fe _{0.855} Si _{0.045} Zr _{0.1}	303 [5]	—	—	—	—	292 [5]	12.5* [5]	14	89.3 [†]
Fe _{0.855} Gd _{0.045} Zr _{0.1}	315 [5]	—	—	—	—	300 [5]	12.5* [5]	14	89.3 [†]
Fe _{0.855} Ge _{0.045} Zr _{0.1}	310 [5]	—	—	—	—	298 [5]	12.5* [5]	14	89.3 [†]
Fe _{0.855} Sn _{0.045} Zr _{0.1}	315 [5]	—	—	—	—	307 [5]	12.5* [5]	14	89.3 [†]
Fe _{0.05} Co _{0.7} Si _{0.15} B _{0.1}	645 [6]	0.11 [6]	10	1.1	—	—	—	—	—
Pd ₄₀ Ni _{22.5} Fe _{17.5} P ₂₀	32 [7]	—	—	—	94 [7]	0.58 [7]	50	1.16	—

1. Foldeaki *et al.* (1997b); 2. Liu *et al.* (1996a); 3. Liu *et al.* (1996b); 4. Si *et al.* (1996); 5. Maeda *et al.* (2001a); 6. Belova and Stoliarov (1984); 7. Shen *et al.* (2002).

* In mJ/cm³K.

[†]In mJ/cm³KkOe.

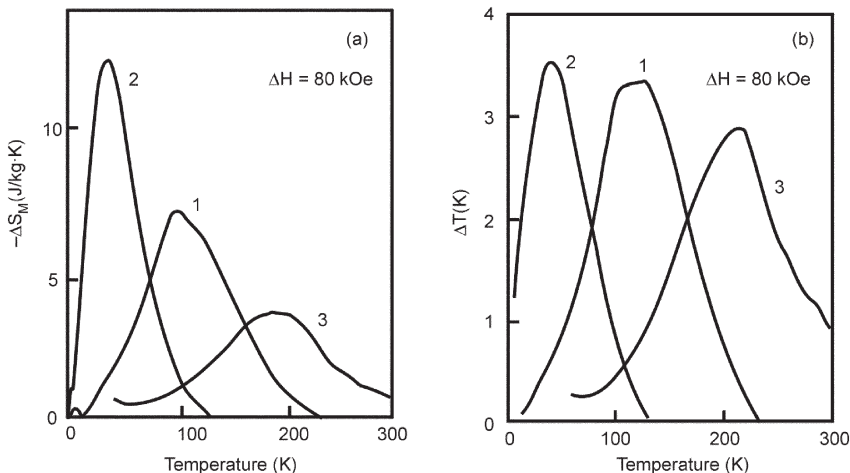


Figure 9.1. Temperature dependences of (a) the magnetic entropy change ΔS_M and (b) the MCE (b) induced by $\Delta H = 80$ kOe in (1) Gd_{0.7}Ni_{0.3}, (2) Er_{0.7}Fe_{0.3} and (3) Gd_{0.65}Co_{0.35} amorphous alloys (Liu *et al* 1996a).

for $\Delta H = 70$ kOe. In the Dy_{0.7}Ni_{0.3} alloy below 10 K, positive ΔS_M was induced by the application of a magnetic field, which can be related to the existence of a spin-glass-type state in this temperature interval. The ΔS_M peak broadening was explained by Liu *et al* (1996b) by the additional concentration fluctuations and further broadening of the exchange integral distribution arising from the substitution of Fe for part of Ni. Liu *et al* (1996b) estimated the MCE in Gd_{0.7}Ni_{0.3} alloy on the basis of the zero-field heat capacity and ΔS_M data calculated from magnetization. It was larger than that calculated by Liu *et al* (1996a) from the heat capacity measurements—see table 9.1.

Foldeaki *et al* (1998b) studied the influence of mechanical processing on the magnetocaloric properties of amorphous Gd_{0.7}Ni_{0.3} alloy. The heat capacity and magnetization of four samples were studied: as-cast ribbon fabricated by melt spinning, the powder obtained by grinding the ribbon, the amorphous powder mixed with silver powder, and the pellet cold-compressed from this mixture. The magnetic entropy change was determined from the heat capacity data. It was shown that mechanical treatment had an essential influence on the height and position of the peak on the $\Delta S_M(T)$ curve. The ribbon had the highest temperature of the peak position and highest peak ΔS_M . Grinding essentially (by a factor of 1.5) reduced ΔS_M and shifted the peak to the low-temperature region. For the ground powder the temperature of the peak was about 95 K (in the ribbon it was 130 K). Addition of silver restored the magnetic entropy change value almost to the initial value, although the transition temperature remained lower.

Pressing the silver and ground powder mixture into a pellet again reduced the ΔS_M peak value. The observed dependence of the magnetic entropy change on the mechanical treatment was related by the authors to the formation of Gd oxide and partial recrystallization during grinding. The authors concluded that the silver-bound pellet could not be considered as representative of the ribbon from which it was made in the investigations of the magnetocaloric properties.

The magnetic entropy change in amorphous melt-spun ribbon NdFeAl was calculated from magnetization by Si *et al* (2001a,b). This alloy displayed ferromagnetic properties with a Curie temperature of 120 K. The $-\Delta S_M$ maximum near T_C was rather sharp, with an absolute peak value of 5.65 J/kg K for $\Delta H = 70$ kOe. Although in the low-temperature region the alloy displayed hard magnetic properties near T_C , the coercive force was negligibly small. The amorphous sample was subjected to annealing well above crystallization temperature. The annealing caused the $-\Delta S_M$ maximum reduction by about 50% (Si *et al* 2001b).

Magnetic entropy change of the melt-spun Gd_xAg_{1-x} ($x = 0.5, 0.7, 0.75, 0.77, 0.8, 1$) alloy ribbons was calculated from magnetization by Fuerst *et al* (1994). It was established by x-ray diffraction and electron microscopy analysis that the alloys are the systems containing small crystalline particles in amorphous matrix. The Gd ribbon consisted of hexagonal Gd grains 500 nm in size. With the increasing Ag content, the amount of an amorphous Gd–Ag component increased. $Gd_{0.755}Ag_{0.255}$ ribbon contained Gd grains with a diameter of 10 nm embedded in an amorphous matrix with composition $Gd_{0.5}Ag_{0.5}$. This picture was preserved up to $x = 0.7$. In the $Gd_{0.5}Ag_{0.5}$ sample, crystalline GdAg grains (with a mean diameter of about 10 nm) but no gadolinium grains were found. The Gd ribbon displayed a $|\Delta S_M|$ maximum with a height of 2.5 J/kg K near 290 K for $\Delta H = 9$ kOe, which is lower than that of bulk Gd determined by the authors as 3 J/kg K. For the alloys with $0.7 \leq x \leq 0.8$ two broad maxima were observed on the $-\Delta S_M(T)$ curve, one near 280 K, and another in the temperature interval from 100 to 120 K. Their heights were 1.25, 0.75 and 0.1 J/kg K for the high-temperature maximum and 0.25, 0.6 and 0.9 J/kg K for the low-temperature maximum for $x = 0.8, 0.775, 0.7$ and $\Delta H = 9$ kOe, respectively. The authors related the high-temperature maximum to Gd grains, and the low-temperature one to the $Gd_{0.5}Ag_{0.5}$ amorphous matrix. The heights of maxima were changed in accordance with the change of the corresponding magnetic components (Gd and $Gd_{0.5}Ag_{0.5}$). At the same time their position on the temperature axis was almost constant. Analogous behaviour was observed in amorphous $Dy_{70}Zr_{30}$ and $Dy_{30}Zr_{70}$ ribbon alloys prepared by melt spinning (Giguere *et al* 1999a). These alloys were considered by the authors as consisting of randomly distributed magnetic clusters (Dy) in a nonmagnetic matrix (Zr). The alloys displayed one $-\Delta S_M$ maximum (ΔS_M was calculated from magnetization) near 120 K, the temperature of

clusters' magnetic moment freezing. For $Dy_{70}Zr_{30}$ the maximum height was about 11.5 J/kg K and for $Dy_{30}Zr_{70}$ about 4 J/kg K for $\Delta H = 70$ kOe. The peak $-\Delta S_M$ value decrease approximately corresponded to the decrease of Dy content.

The bulk amorphous alloy $Pd_{40}Ni_{22.5}Fe_{17.5}P_{20}$ is ordered ferromagnetically from the superparamagnetic state at about 32 K in zero-field and with further cooling turns to the spin-glass state at about 25 K (Shen *et al* 2002). However, the magnetic entropy change temperature dependences calculated from magnetization data revealed maxima at higher temperatures—at about 50 K for $\Delta H = 5$ kOe and 80 K for $\Delta H = 50$ kOe. In the spin-glass state the positive ΔS_M is observed for low fields. Magnetization measurements showed that in the spin-glass state the magnetization is directly proportional to the magnetic field and temperature. According to equation (2.70) this leads to the square-field dependence of ΔS_M , which was observed in amorphous alloy $Pd_{40}Ni_{22.5}Fe_{17.5}P_{20}$ experimentally (Shen *et al* 2002). It should be noted that such field dependence was observed also in the superparamagnetic region (see equation (2.81)).

The magnetic heat capacity and magnetization temperature dependences of Gd_xCo_{1-x} ($0.16 \leq x \leq 0.25$) amorphous alloys were studied theoretically by means of MFA by Aly (2001). These alloys are ferrimagnetic with compensation point for $x > 0.16$, and have high Curie temperatures (for $x = 0.16$ $T_C = 868$ K and for $x = 0.25$, $T_C = 740$ K). The calculated $C(T)$ dependences revealed λ -type anomaly near T_C . It was shown that the main contribution to the heat capacity comes from the Co sublattice.

9.2 Amorphous alloys based on transition metals

Magnetocaloric properties of the alloys of this type were studied by Maeda *et al* (1983) and Belova and Stoliarov (1984). Maeda *et al* (1983) studied the magnetic properties of amorphous $(Fe_{1-x}Ni_x)_{0.9}Zr_{0.1}$ ($x = 0, 0.01, 0.02, 0.03$) and $(Fe_{0.95}M_{0.05})_{0.9}Zr_{0.1}$ ($M = Al, Si, Ga, Ge, Sn$) alloys, prepared by melt-spinning and piston anvil-quenching techniques, in the magnetic fields up to 70 kOe. The $\Delta S_M(T)$ curves, obtained on the basis of these data, showed a behaviour usual for amorphous ferromagnets with a broad maximum near the Curie temperature T_C . The maximum ΔS_M values and T_C are presented in table 9.1. The values of T_C and ΔS_M increased with increasing x . Replacement of the M element in the $(Fe_{0.95}M_{0.05})Zr_{0.1}$ alloys had a small influence on the absolute peak ΔS_M value.

Belova and Stoliarov (1984) measured the MCE in a melt-spun ferromagnetic amorphous $Fe_{0.05}Co_{0.7}Si_{0.15}B_{0.10}$ ribbon by a direct method. In the $\Delta T(T)$ curve a maximum with a value of $\Delta T = 0.11$ K was observed near $T_C = 645$ K for $\Delta H = 10$ kOe. In the temperature range from 390 to 465 K an additional ΔT anomaly consisting of a maximum at about 410 K

and a minimum at about 440 K was found. It was related by the authors to the temperature dependence of the local magnetic anisotropy constant.

In conclusion, the investigated amorphous alloys revealed wide maxima on adiabatic temperature and magnetic entropy change temperature dependences near the transitions to a magnetically ordered state. This is related to the smeared character of the magnetic transitions in these materials due to structural and concentration heterogeneities close to the amorphous state. The spin-glass state in amorphous materials was characterized by positive ΔS_M , obviously because of the antiferromagnetic-type para-process. Although absolute peak magnetic entropy change values in the amorphous alloys are not small (maximum $-\Delta S_M/\Delta H$ value is about 16.75 J/kg K kOe for $\text{Er}_{0.7}\text{Fe}_{0.3}$ for $\Delta H = 40$ kOe), the MCE is rather small.

Chapter 10

Magnetocaloric effect in the systems with superparamagnetic properties

As shown in section 2.9, in the systems consisting of superparamagnetic particles, a value of the MCE should be higher than in regular paramagnets. Here we present the results of experimental investigations of the magnetocaloric properties of the superparamagnetic systems containing magnetic particles of nanometer sizes and molecular clusters.

10.1 Nanocomposite systems

One of the methods of obtaining superparamagnetic materials is rapid cooling of a corresponding melt, which is also used to produce amorphous materials. Shao *et al* (1996a,b) prepared nanocomposite ribbons of $\text{Gd}_{0.85}\text{Tb}_{0.15}$, $\text{Gd}_{0.85}\text{Y}_{0.15}$ and $\text{Gd}_{0.75}\text{Zr}_{0.25}$ alloys by a copper-sheathed rolling technique, which briefly consists of the following steps. The arc-melted and homogenized alloys were resolidified into amorphous particles about 20 nm in diameter by melt-spinning. These particles were then milled within a sealed agate bowl containing agate balls. By this method powder particles finer than mesh size 360 nm were obtained. As shown by X-ray analyses, the milling led to the formation of nanocrystallites of 10–20 nm size within the original amorphous particles, although part of them remained amorphous. The powder was then packed into an annealed copper tube, sealed at both ends and rolled into the copper-sheathed nanocomposite ribbon. The powder density in the ribbon was about 80% of that of the corresponding bulk alloy. On the samples prepared in this way the heat capacity, magnetic entropy change and magnetocaloric effect (directly) were measured.

Heat capacity measurements made on the ribbons in the temperature range from 280 to 310 K revealed its increase in all three samples with a maximum mean value of 57.9% for $\text{Gd}_{0.85}\text{Y}_{0.15}$. On the other hand, the Curie temperature in the ribbons was reduced. Shao *et al* (1996a) related these experimental results to the large amount of interface atoms arranged

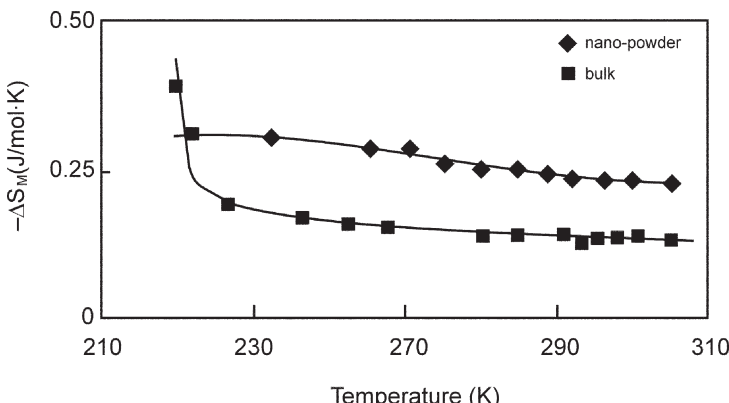


Figure 10.1. Temperature dependences of the magnetic entropy change induced by $\Delta H = 10$ kOe in $\text{Gd}_{0.85}\text{Y}_{0.15}$ alloy in bulk and nanosized states (Shao *et al* 1996a).

in disorder, which changed the interatomic distances and lowered the number of nearest neighbours.

Figure 10.1 shows temperature dependences of the magnetic entropy change of the nanopowder ribbon $\text{Gd}_{0.85}\text{Y}_{0.15}$ sample and bulk alloy with the same composition. The ribbon was considered to be in a superparamagnetic state (the Curie temperature of the bulk alloy is 240 K). As one can see, ΔS_M in the ribbon is higher than in bulk material in the temperature interval under consideration, which is typical for superparamagnets. The $\Delta T(T)$ curves of this alloy revealed analogous behaviour. At the same time no enhancement in the MCE was observed in the investigated nanopowder $\text{Gd}_{0.85}\text{Tb}_{0.15}$ and $\text{Gd}_{0.75}\text{Zn}_{0.25}$ ribbons in comparison with the corresponding bulk materials.

Much attention was paid by the investigators to the magnetocaloric properties of the nanocomposite compound $\text{Gd}_3\text{Ga}_{5-x}\text{Fe}_x\text{O}_{12}$ ($x < 2.5$), which is also known as gadolinium gallium iron garnet (GGIG) (McMichael *et al* 1993b, Shull *et al* 1993, Shull 1993a 1993b). Substitution of a few Fe atoms to gallium atoms in gadolinium gallium garnet (GGG) $\text{Gd}_3\text{Ga}_5\text{O}_{12}$ did not change its crystal structure. However, the magnetic properties of GGG were changed considerably (McMichael *et al* 1993a,b, Numazawa *et al* 1996). Pure GGG is a simple paramagnet in the temperature range above 0.8 K. Addition of Fe leads to superparamagnetic behaviour for $0 \leq x \leq 2.5$ and ferrimagnetic behaviour for $x \geq 2.5$. Shull *et al* (1993) supposed that the formation of magnetic nanosized clusters is due to the Gd–Gd interactions of the superexchange type via Fe atoms. Ferromagnetic resonance and Mössbauer spectroscopy data confirmed that GGIG contained magnetic nanosized clusters.

Figure 10.2 presents experimental temperature dependences of ΔS_M caused by the removal of 9 kOe determined from the magnetization data

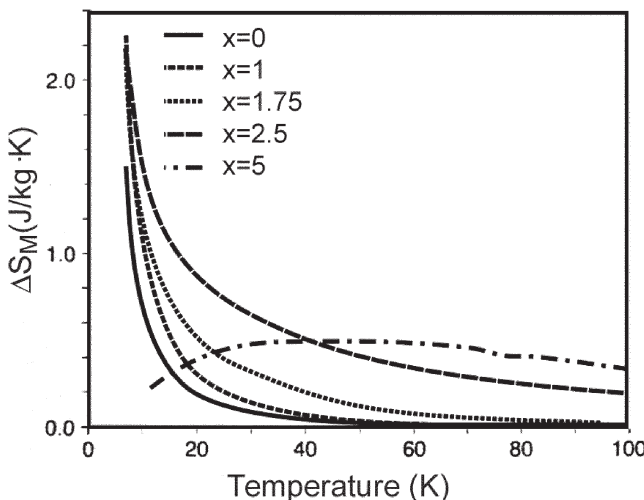


Figure 10.2. Temperature dependences of ΔS_M caused by removal of a magnetic field of 9 kOe in $Gd_3Ga_{5-x}Fe_xO_{12}$ ($0 \leq x \leq 5$) (McMichael *et al* 1993b).

for GGIG with $x = 0, 1, 1.75, 2.5, 5$. An obvious increase of ΔS_M in the high-temperature region can be seen with increasing of the iron content. This behaviour is in qualitative agreement with theoretical results calculated for different sizes of magnetic clusters (see figure 2.12) under the assumption that increasing of iron concentration causes increasing of the mean cluster size. Extrapolation shows that samples with smaller x have larger ΔS_M values below 6 K. Intersections of $\Delta S_M(T)$ curves for $x \neq 0$ with that of GGG occur at higher temperatures for higher x , which is also in accordance with theoretical predictions. Experimental results for $\Delta H = 50$ kOe showed that the addition of iron to GGG did not cause such strong magnetic entropy changes as for $\Delta H = 9$ kOe, but the enhancement was still significant for temperatures above 9 K. Shull *et al* (1993) also found out that in the sample with $x = 1.75$ no hysteresis losses were observed.

The enhancement of the magnetic entropy change in the superparamagnetic system consisting of iron oxide and iron nitride nanograins (with diameter of 10–35 nm) in a silver matrix was found by Yamamoto *et al* (2000a,b). The samples were prepared by the inert gas condensation technique, in which metallic iron and silver is coevaporated in an ultrahigh vacuum chamber filled with static helium gas. The oxide and nitride nanoparticles were formed by further heat treatment in an oxygen or NH_3 atmosphere. The content of iron in the samples was up to 40%. It was established that for the superparamagnetic iron oxide nanograin system (it was supposed that the oxide was ferrimagnetic γ - Fe_2O_3) the gain in ΔS_M in comparison with paramagnetic iron ammonium alum was about two orders of magnitude. A magnetic entropy change almost one order of magnitude larger than in the

iron oxide system was found in the superparamagnetic samples containing iron nitride (γ' -Fe₄N and ε -Fe₃N) nanograins. ΔS_M field and temperature dependence in the iron-oxide-containing material was satisfactorily described by a Langevin superparamagnetic model for high temperatures and low fields. For high fields and low temperatures the deviation from the Langevin behaviour was observed, which was related by the authors to the influence of exchange coupling between nanograins and magnetocrystalline anisotropy in the nanograins.

A number of studies are devoted to the investigation of the magnetocaloric properties of the systems of interacting superparamagnetic particles (which Mørup *et al* (1983) called superferromagnets). Pedersen *et al* (1997) studied a system consisting of particles of metastable iron–mercury alloy in a Hg matrix (Fe content was 0.5 wt%). From Mössbauer and magnetization measurements it was established that the particles magnetically interact with each other, which led to the establishing of a magnetically ordered state below about 100–150 K. ΔS_M temperature dependences were calculated from magnetization measurements. For $\Delta H = 10$ kOe the absolute value of ΔS_M was about 2.1×10^{-3} J/kg K and almost temperature independent in the temperature interval from 130 K to 200 K. For $\Delta H = 1$ kOe on the $-\Delta S_M(T)$ curve there was a broad maximum near 140 K with one order of magnitude lower height of 2.5×10^{-4} J/kg K. The estimations made by the authors showed that ΔS_M in the investigated system is much higher than in the case of an ordinary paramagnetic with the same Fe content: $-\Delta S_M = 1 \times 10^{-5}$ J/kg K for $\Delta H = 10$ kOe at 130 K. In the case of superparamagnetic material without interactions between particles the calculations gave $-\Delta S_M = 2.1 \times 10^{-5}$ J/kg K for at 130 K and 1.4×10^{-3} J/kg K at 200 K for $\Delta H = 10$ kOe. For $\Delta H = 1$ kOe, ΔS_M absolute values of the superparamagnet with noninteracting particles was about an order of magnitude lower than those experimentally obtained in the investigated Fe–Hg system.

McMichael *et al* (1993a,b) determined (from magnetization measurements) $\Delta S_M(T)$ curves for rapidly solidified Nd_{0.14}(Fe_{1-x}Al_x)_{0.8}B_{0.06} alloys ($x = 0, 0.1, 0.2$) for $\Delta H = 9$ kOe in the temperature range 290–500 K. X-ray analyses showed that the material, produced in the form of melt-spun ribbons, was structurally amorphous. The obtained $\Delta S_M(T)$ curves are shown in figure 10.3. As one can see, near the Curie temperatures (410, 405 and 360 K for $x = 0, 0.1, 0.2$, respectively, as determined from differential scanning calorimetry) there are broad peaks on the $\Delta S_M(T)$ curves. The obtained results were interpreted by the authors in the framework of mean field calculations made for superferromagnets—see figure 2.14 and related discussion in section 2.9. The experimental $\Delta S_M(T)$ curve for the alloy with $x = 0.2$ was shown to be in good agreement with that calculated for cluster magnetic moments of about $20 \mu_B$, which corresponds to about 10 atoms of Fe. The conclusion was made that the magnetic structure of the alloy can be regarded as consisting of regions with local concentration

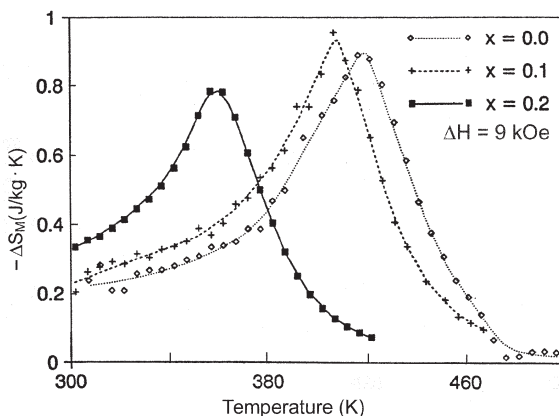


Figure 10.3. Temperature dependences of ΔS_M for $\Delta H = 9$ kOe in rapidly solidified $\text{Nd}_{0.14}(\text{Fe}_{1-x}\text{Al}_x)_{0.8}\text{B}_{0.06}$ alloys (McMichael *et al* 1993a). (Reprinted from McMichael *et al* 1993a, copyright 1993, with permission from Elsevier.)

fluctuations, rather than an assembly of distinct nanometre-sized magnetic particles dispersed in a nonmagnetic matrix. The magnetocaloric properties of the investigated alloys display the behaviour predicted for superferromagnet nanocomposites.

Cu-based water-quenched alloys $\text{Cu}_{0.783}\text{Ni}_{0.13}\text{Fe}_{0.087}$ and $\text{Cu}_{0.63}\text{Ni}_{0.22}\text{Fe}_{0.15}$ were investigated by Kokorin *et al* (1984). It was established that the alloys were inhomogeneous solid solutions consisting of a nonmagnetic matrix with low concentration of Fe and Ni, and ferromagnetic inclusions rich in Fe and Ni with mean dimension of 3–5 nm, randomly dispersed in the matrix. Subsequent annealing of the samples at 773–973 K led to an increase of the size of the inclusions. Also the number of inclusions and the concentration of Ni and Fe in the inclusions increased after annealing.

Magnetic susceptibility measurements made on $\text{Cu}_{0.783}\text{Ni}_{0.13}\text{Fe}_{0.087}$ alloy showed that at about 77 K for the as-quenched state and at about 300 K for the annealed state the alloy displayed a transition to a spin-glass-like state due to the interactions between the magnetic clusters (Kokorin and Perekos 1978). However, at this transition no MCE maximum was observed. The MCE maximum was found at higher temperatures corresponding to the superparamagnetic state of the alloy. It was attributed to the establishment of ferromagnetic order inside the inclusions according to the second term in equation (2.118). The maximum MCE value was $\Delta T \approx 10^{-2}$ K for $\Delta H = 15$ kOe at $T \approx 750$ K for the annealed alloy. The temperature of the ΔT maximum corresponds to the Curie temperature of the magnetic particles in the material, which equals 628 K for the as-quenched state and 740 K for the annealed state.

$\text{Cu}_{0.63}\text{Ni}_{0.22}\text{Fe}_{0.15}$ with higher magnetic component concentration was characterized by stronger interactions between the magnetic inclusions. It

displays superferromagnetic-type behaviour with ordering temperature T_1 (see equations (2.120) and (2.121)), which is close to the Curie temperature of the inclusions in the material. The MCE maximum of 0.015 K for $\Delta H = 15 \text{ kOe}$ was observed near 700 K where the magnetic susceptibility anomaly was also found (Kokorin *et al* 1984).

10.2 Molecular cluster systems

Examples of other systems displaying superparamagnetic properties are materials on the basis of molecular clusters. In the past two decades molecular chemistry has provided a diverse variety of magnetic clusters with nanometre range sizes and a high value of total spin ($S = 10\text{--}14$) and consequently the magnetic moment of the cluster. The molecular clusters are the objects with internal magnetic ordering, crystal structure and well-defined and uniform size and shape and in principle can be regarded as a single domain with nano-sized (few nm) magnetic particles. Their magnetic properties were studied and reviewed in a number of works—see Caneschi *et al* (1988, 1991), Sessoli *et al* (1993), Delfs *et al* (1993), Goldberg *et al* (1993), Abbati *et al* (1998), Blake *et al* (1994), Dobrovitski *et al* (1996), Dobrovitski and Zvezdin (1997), Zvezdin *et al* (1998) and Mukhin *et al* (1998).

There are many molecular clusters containing 3d transition metal atoms with a total ground state spin equal to 10 and higher. The total spin of the cluster is the result of internal magnetic ordering (usually antiferromagnetic in character with incomplete compensation) due to the superexchange interactions between 3d atoms via ligand ions. The total spin ground state 10 was established from magnetic measurements in the ‘ Fe_8 ’ cluster, whose formula is $[(\text{tacn})_6\text{Fe}_8\text{O}_2(\text{OH}_{12})]^{8+}$, where tacn is the organic ligand triazacyclononane (Wieghardt *et al* 1984, Delfs *et al* 1993). It arises from antiferromagnetic ordering of the eight iron spins ($S = 5/2$ each). Sangregorio *et al* (1997) obtained from a.c. susceptibility measurements the magnetic moment of Fe_8 cluster to be $20 \mu_B$. This is in agreement with $S = 10$ and $g = 2$, established earlier from electron paramagnetic resonance (EPR) measurements (Barra *et al* 1996).

Another example of a molecular cluster with the total spin $S = 10$ is dodecanuclear manganese cluster (‘ Mn_{12}ac ’) of formula $[\text{Mn}_{12}\text{O}_{12}(\text{CH}_3\text{COO})_{16}(\text{H}_2\text{O})_4]2\text{CH}_3\text{COOH}\cdot 4\text{H}_2\text{O}$, which is investigated the most completely (Caneschi *et al* 1991, Sessoli *et al* 1993, Lis 1980). The Mn_{12}ac cluster comprises four tetrahedrally coordinated Mn(IV) ions with $S = 3/2$ in the centre and eight Mn(III) ions with $S = 2$ in an external ring (Sessoli *et al* 1993). Mn(III) and Mn(IV) spins are coupled antiferromagnetically. The high spin ground state is combined with a strong easy axis anisotropy. Magnetic d.c. and a.c. susceptibility measurements revealed for Mn_{12}ac the behaviour characteristic for superparamagnets and confirmed

ground state with $S = 10$ and $g \approx 1.9$ (Caneschi *et al* 1991, Sessoli *et al* 1993). The magnetic moment of the cluster has essential temperature dependence reaching maximum value $\mu \approx 21 \mu_B$ in the temperature range of about 15–40 K and rapidly decreasing in the low-temperature region (Caneschi *et al* 1991, Sessoli *et al* 1993, Hennion *et al* 1997). The paramagnetic Curie temperature of $Mn_{12}ac$ was found to be very low, ~ 0.05 K (Novak *et al* 1995), suggesting negligible interactions between the clusters. The quantum tunnelling of magnetization exhibiting itself in the field hysteresis of pure molecular origin and steps in magnetization on the hysteresis loop was observed in $Mn_{12}ac$ below 3 K (Novak *et al* 1995, Hernandes *et al* 1997).

Molecular clusters comprising six manganese (Mn^{2+}) ions and six nitronyl–nitroxide radicals NITPh ($[Mn(hfac)_2NITPh]_6$, where hfac = hexafluoroacetylacetone) were synthesized and investigated by Caneschi *et al* (1988). From magnetization and EPR measurements it was established that their spin ground state is $S = 12$ with $g = 2$. It arises from antiferromagnetic coupling of Mn^{2+} ions ($S = 5/2$) and NITPh radicals ($S = 1/2$). The cluster magnetic moment changes with temperature, having a maximum value in the temperature range of about 10–50 K and decreasing with increasing temperature and below 10 K. The room-temperature magnetic moment is significantly higher than one can expect for uncorrelated Mn ions and radical spins.

In a hexanuclear Mn(III) cluster $NaMn_6$ ($[NaMn_6(OMe)_{12}(dbm)_6]^+$, dbm = dibenzoylmethane) the ground state with $S = 12$ and $g = 2$ is formed due to the ferromagnetic interactions between the Mn ions (Abbiati *et al* 1998). ‘ Mn_{10} ’ molecular clusters ($[Mn_{10}O_4(biphen)_4X_{12}]^{4-}$, $X = Cl^-$, Br^- , biphen = 2,2'-biphenoxide) were studied by Goldberg *et al* (1993 1995). Six Mn(II) and four Mn(III) ions in this mixed valence complex are ordered antiferromagnetically. The magnetic moment of the cluster at $T = 4.2$ K was $\sim 27.1 \mu_B$ for $X = Cl$ and $\sim 28.3 \mu_B$ for $X = Br$, which corresponds to $S = 14$ with $g = 2$ ground state. With temperature increasing the steady decrease of the magnetic moment is observed (for $\sim 20\%$ at 40 K as compared with 4.2 K) with no decrease in the low-temperature region (which is in contrast to the Mn_{12} cluster).

Theoretical calculations of the electronic structure of Mn_x ($x = 2–8$) and $(MnO)_x$ ($x \leq 9$) clusters were made by Pederson *et al* (1998) and Nayak and Jena (1998a,b). The equilibrium configurations and ground states of the clusters were established. It was found that $(MnO)_x$ clusters can have internal ferromagnetic ordering with total magnetic moments of $4–5 \mu_B$ per MnO unit. In particular, the $(MnO)_8$ cluster can have a ground state with the total moment of $40 \mu_B$. The ground states of Mn_4 , Mn_5 , Mn_6 , Mn_7 , and Mn_8 clusters are ferromagnetic with moments 20, 23, 26, 29 and $32 \mu_B$, respectively.

From the brief review presented here one can see that there are many nanosized magnetic molecules with high magnetic moments (much higher than have 4f transition metal atoms), which can exhibit superparamagnetic

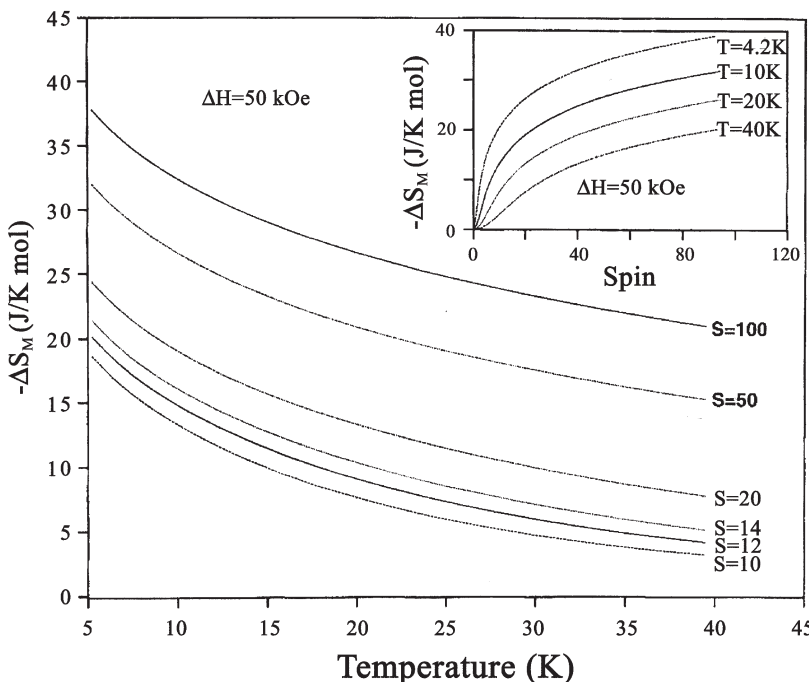


Figure 10.4. The calculated $\Delta S_M(T)$ curves for $\Delta H = 50\text{ kOe}$ for $S = 10, 12, 14, 20, 50$ and 100 . The insert shows $\Delta S_M(S)$ curves for $T = 4.2, 10, 20$ and 40 K (Spichkin *et al* 2001b).

properties. In the systems containing molecular clusters one can expect enhancement of the magnetocaloric properties, as it should be observed in superparamagnets.

Magnetocaloric properties of the superparamagnetic systems containing molecular clusters with high spins were considered in the work of Spichkin *et al* (2001b). The calculations of temperature, field and spin value dependences of the magnetic entropy change ΔS_M were made in the classical limit on the basis of equation (2.92) on the assumption that the cluster systems under investigation are superparamagnetic and isotropic in the whole temperature range. Figure 10.4 shows the temperature dependences of magnetic entropy change $\Delta S_M(T)$ caused by the magnetic field change $\Delta H = 50\text{ kOe}$ for $S = 10, 12, 14, 20, 50, 100$. The magnetic moment of the cluster was determined as $\mu = gS$ with $g = 2$. The insert in figure 10.4 shows ΔS_M on S dependences for $\Delta H = 50\text{ kOe}$ and $T = 4.2, 10, 20$ and 40 K . There is a considerable increase of ΔS_M with increase of S , which for $T = 4.2\text{ K}$ and $S = 100$ reaches the value of about 39 J/K mol . However the saturation on $\Delta S_M(S)$ dependences is not observed even for $T = 4.2\text{ K}$ and $S = 100$.

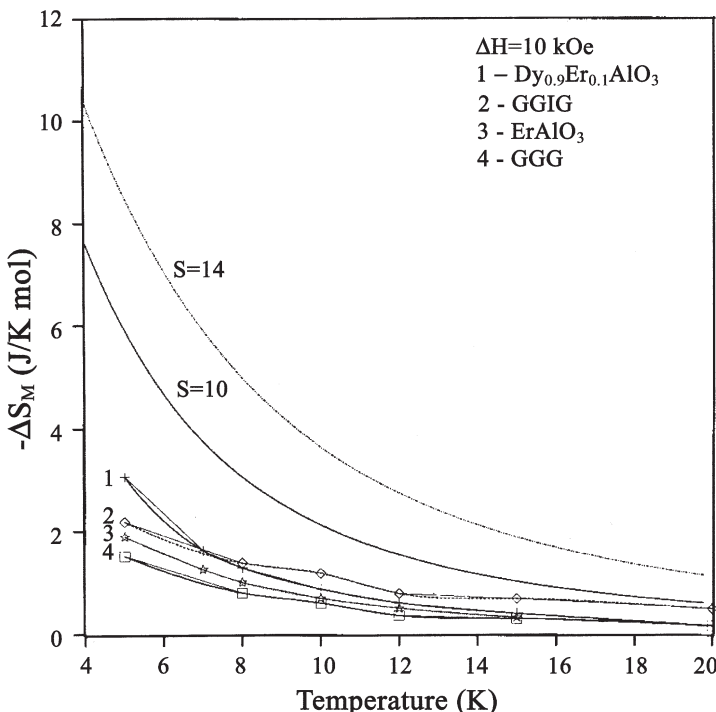


Figure 10.5. The calculated $\Delta S_M(T)$ curves for $\Delta H = 10 \text{ kOe}$ for the system consisting of molecular clusters with $S = 10$ and $\Delta S_M(T)$ dependences taken from literature for gadolinium gallium garnet (GGG) (Barclay and Steyert 1982a, Daudin *et al* 1982a, Shull *et al* 1993), gadolinium gallium iron garnet (GGIG) $\text{Gd}_3\text{Ga}_{3.25}\text{Fe}_{1.75}\text{O}_{12}$ (McMichael *et al* 1993b, Shull *et al* 1993), orthoaluminates ErAlO_3 (Kimura *et al* 1997a,b) and $\text{Dy}_{0.9}\text{Er}_{0.1}\text{AlO}_3$ (Tishin and Bozhkova 1997). The curve for ErAlO_3 was obtained by linear interpolation of data from (Kimura *et al* 1997a,b, Spichkin *et al* 2001b).

Figure 10.5 compares known $\Delta S_M(T)$ experimental data for gadolinium gallium garnet (GGG) (Barclay and Steyert 1982a, Daudin *et al* 1982a, Shull *et al* 1993), gadolinium gallium iron garnet (GGIG) $\text{Gd}_3\text{Ga}_{3.25}\text{Fe}_{1.75}\text{O}_{12}$ (McMichael *et al* 1993b, Shull *et al* 1993), erbium orthoaluminate ErAlO_3 (Kimura *et al* 1997a,b) and calculated data for $\text{Dy}_{0.9}\text{Er}_{0.1}\text{AlO}_3$ (Tishin and Bozhkova 1997) with $\Delta S_M(T)$ dependences calculated for $S = 10$ and 14 for $\Delta H = 10 \text{ kOe}$. As one can see, ΔS_M in $\text{J}/\text{mol K}$ units for the systems of superparamagnetic clusters exceeds that in known oxide compounds in the low-temperature region and is much higher in the liquid helium temperature range.

In real magnetic clusters there is some temperature dependence of its magnetic moment (Caneschi *et al* 1991, Sessoli *et al* 1993, Goldberg *et al* 1993, 1995, Hennion *et al* 1997). Figure 10.6 shows the $\Delta S_M(T)$ dependences

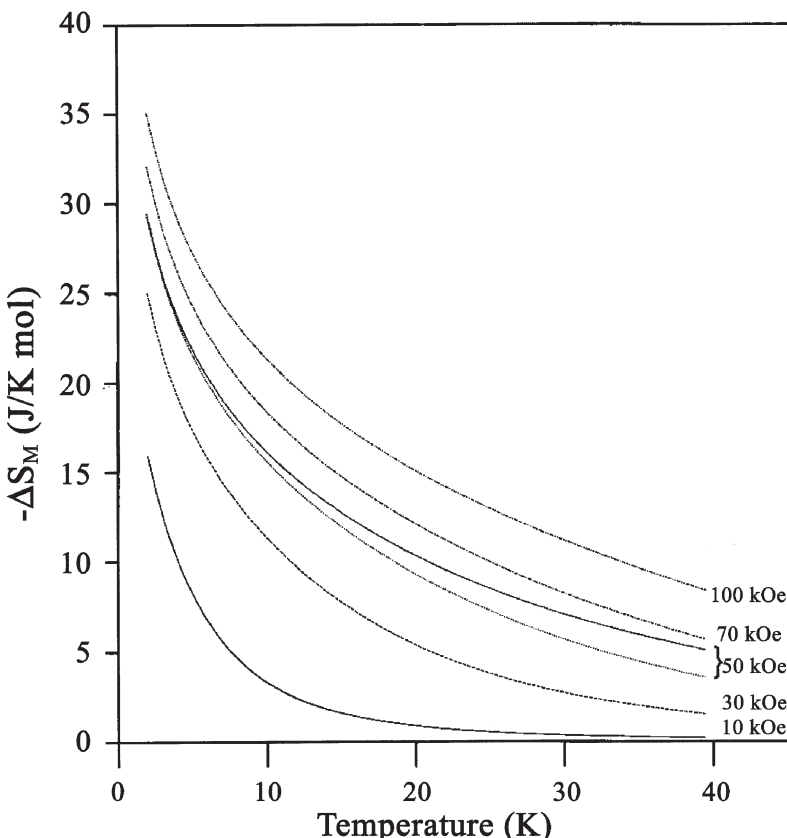


Figure 10.6. The calculated $\Delta S_M(T)$ curves for the Mn_{10} cluster with temperature dependent magnetic moment for $\Delta H = 10, 30, 50, 70$ and 100 kOe. For $\Delta H = 50$ kOe the result for the temperature independent magnetic moment of $28 \mu_B$ is also shown (—) (Spichkin *et al* 2001b).

calculated for the Mn_{10} cluster (maximum cluster magnetic moment is $28 \mu_B$ and $S = 14$) for $\Delta H = 10, 30, 50, 70$, and 100 kOe using experimental data on its $\mu(T)$ dependence (Hennion *et al* 1997, Novak *et al* 1995). For $\Delta H = 50$ kOe the curve calculated for constant cluster magnetic moment $\mu = 28 \mu_B$ is also shown (solid line). As one can see, the magnetic moment decrease does not have essential influence on the magnetocaloric properties of Mn_{10} . In the Mn_{12} cluster an essential decrease of μ is observed below ~ 15 K, which should cause a corresponding decrease of ΔS_M .

As shown by Zhang *et al* (2001b) the magnetic anisotropy has an essential effect on the cluster system magnetocaloric properties. The authors made investigations of Fe_8 molecular crystal and determined temperature dependences of ΔS_M in the fields up to 30 kOe. Since the crystal cell parameters

are rather large (the minimal value is 10.609 Å), the interaction between clusters in the crystals was recognized as negligible. However, the crystal had noticeable magnetic anisotropy, with an anisotropy field of about 50 kOe. Magnetization measurements showed that $M(H)$ curves of the crystal in the low-temperature region had the form typical for soft magnetic materials if the field was aligned along the easy magnetization axis, and were hard to saturate for the field directed along the hard axis. The obtained $\Delta S_M(T)$ curve measured along the easy axis revealed a maximum with a height of $\sim 5 \text{ J/kg K}$ at about 7.5 K for $\Delta H = 30 \text{ kOe}$. For the hard axis the maximum was much lower ($\sim 1.8 \text{ J/kg K}$) and positioned at about 10 K. Comparison of the obtained results with the theoretical $\Delta S_M(T)$ curve for an isotropic cluster system showed that ΔS_M of the latter is much higher in the temperature range below $\sim 7.5 \text{ K}$ and lower above this temperature. The observed effects were related by the authors to the influence of the anisotropy on the crystal magnetization temperature dependences. The anisotropy complicates population of low-spin states with increasing temperature, which provides more steady decreasing of magnetization in the same applied magnetic field in the case of an anisotropic system, also clearly observed in the experiment. The lowering of the magnetic entropy change in the anisotropic system in this case is explained by lower $\partial M / \partial T$ in the low-temperature range. It should be noted that experimental magnetization and ΔS_M temperature and field dependences in Fe_8 molecular crystal were fairly well explained in the frames of the statistical model, with the Hamiltonian taking into account anisotropy and Zeeman energies.

Torres *et al* (2000) carried out theoretical calculations and experimental measurements of magnetic entropy change in the systems containing Mn_{12} and Fe_8 molecular clusters with spin $S = 10$. The studied samples consisted of small crystallites with an average length of 10 µm (Mn_{12}) and 2 µm (Fe_8) embedded in an epoxy under the influence of the magnetic field of 50 kOe for 24 h. ZFC–FC magnetization measurements made in the field of 100 Oe revealed the blocking temperatures of 3 K for the Mn_{12} sample and 0.9 K for the Fe_8 sample. The blocking temperature corresponds to the transition under cooling from the superparamagnetic state to the blocking state, where the magnetic moments of the particles stabilize in a definite direction due to the impossibility of thermal agitation energy overcoming the potential barrier created by the magnetic anisotropy energy of the superparamagnetic particle. The experimental $-\Delta S_M(T)$ curve for the Mn_{12} for $\Delta H = 30 \text{ kOe}$ calculated from magnetization revealed a sharp maximum with a height of about 27 J/kg K near the blocking temperature of 3 K. With increasing temperature, ΔS_M rapidly decreased, reaching about 5 J/kg K at 4 K and remaining almost constant with further heating. Theoretical calculations of $\Delta S_M(T)$ curves were carried out from theoretically determined $M(T, H)$ dependences by equation (2.70). The total magnetic moment M was calculated as $M = M_+ - M_-$, where M_+ was the magnetic moment of the molecules

whose magnetic moments were directed along the positive easy axis in the presence of the magnetic field, and M_- was the magnetic moment of the molecules with the opposite moment orientation. M_+ and M_- were determined from the following differential equations:

$$\frac{dM_+}{dt} = -\Gamma_+ M_+ + \Gamma_- M_- \quad (10.1a)$$

$$\frac{dM_-}{dt} = -\Gamma_- M_- + \Gamma_+ M_+ \quad (10.1b)$$

where

$$\Gamma_\pm = v_\pm \exp\left(-\frac{U_\pm(H)}{k_B T}\right) \quad (10.1c)$$

is the rate of the transition between the two possible directions of the molecular magnetic moment, V is the volume of a molecular, and $U_\pm(H)$ is the magnetic anisotropy barrier height. In the expression for the magnetic anisotropy barrier the effect of quantum tunnelling of the magnetic moment across the barrier was taken into account. The variation of M in the magnetic field was calculated as

$$\frac{dM}{dH} = -\Gamma \frac{(M - M_{eq})}{r} \quad (10.2)$$

where $r = dH/dt$ is the sweeping rate of the applied magnetic field, $\Gamma = \Gamma_+ - \Gamma_-$, and M_{eq} is the equilibrium magnetic moment defined as

$$M_{eq}(H) = \frac{\Gamma_- - \Gamma_+}{\Gamma_- + \Gamma_+} M_s \quad (10.3)$$

where M_s is the saturation magnetic moment of the sample.

Fitting of the experimental $\Delta S_M(T)$ curve for Mn_{12} using the model described above gave good results for the field sweeping rate $r = 7 \times 10^{-3}$ Hz. Theoretical calculations showed that the value of the field sweeping rate had an essential influence on the form of $\Delta S_M(T)$ curves. With increasing r the position of the ΔS_M maximum shifted to the higher temperature range became wider and its height decreased: for Mn_{12} clusters the absolute value of ΔS_M maximum was reduced from 21 J/kg K for $r = 0.01$ Hz (the peak position ~ 3.7 K) down to 13 J/kg K for $r = 100$ Hz (the peak position ~ 7 K).

The heat capacity of Mn_{12} and Fe_8 clusters was studied by Novak *et al* (1995), Fominaya *et al* (1997 1999) and Gomes *et al* (2001). Gomes *et al* (2001) measured $C(T)$ dependences of Mn_{12} and Fe_8 below 3 K, where both cluster systems are in a blocked state. It was shown that the heat capacity could be regarded as consisting of four contributions: lattice contribution C_l , crystalline field contribution C_{cf} , hyperfine contribution C_{hf} and dipolar contribution C_{dip} . C_{hf} related to the nuclear magnetic

moment is negligible for Fe_8 and strong for Mn_{12} below 1 K due to the manganese nuclear moment of 5/2. C_{cf} is due to the crystal field effects and increases with increasing temperature, especially rapidly for Fe_8 . Dipolar contribution arises in a molecular cluster system because of essential dipole–dipole interaction between their high magnetic moments. For Fe_8 , experiment shows an essential decrease of the heat capacity below 1.3 K due to the establishing of the blocking state. However, non-negligible heat capacity was observed even in this state where thermally activated spin-reorientation is absent. This was explained by the authors by effects of quantum tunnelling of the cluster magnetic moments across the magnetic anisotropy energy barrier. An analogous picture was observed for the Mn_{12} cluster. In the low-temperature region below 0.5 K the heat capacity started again to increase, which was related to the role of the C_{hf} contribution.

The field dependence of the heat capacity of Mn_{12} single crystals at temperatures below 8.8 K was measured by Fominaya *et al* (1997, 1999). Above 3.5 K a pattern of peaks appeared at the magnetic fields of 4, 8 and 12 kOe. This was related by the authors to quantum tunnelling of the molecular spins through the magnetic anisotropy barrier due to crossing of spin-up and spin-down energetic levels of different magnetic quantum numbers under the effect of the magnetic field. The zero-field heat capacity of 20 µg Mn_{12} single crystal was found to monotonically increase from the value of $\sim 5 \times 10^{-8} \text{ J/K}$ at 3.2 K up to $\sim 3 \times 10^{-7} \text{ J/K}$ at 8.8 K. These results were in good agreement with those obtained by Novak *et al* (1995) on Mn_{12} powder. The Debye temperature of Mn_{12} was determined from the experimental data to be 41 K.

So, according to considerations presented in this chapter, the superparamagnetic systems display enhanced magnetocaloric properties in comparison with ordinary paramagnetic systems, which was predicted theoretically (see section 2.9). This effect is observed not only in the systems consisting of small magnetic particles, but also in magnetic molecular cluster systems. As shown in the work of Spichkin *et al* (2001b), the isotropic molecular cluster systems can have superior properties as the working bodies of magnetic cooling devices for the low-temperature range in comparison with systems traditionally used for these purposes, materials as garnets and ortho-aluminates. It should be noted that a patent for this application of the cluster materials has been taken out by Advanced Magnetic Technologies and Consulting Ltd. (Gubin *et al* 2001). However, the anisotropy effects in the molecular crystals can essentially affect their magnetocaloric properties.

Chapter 11

Application of the magnetocaloric effect and magnetic materials in refrigeration apparatuses

In this chapter we discuss the application of magnetic materials in refrigeration devices. The magnetic materials can be used in this field by two ways. As known, magnetic materials make additional contributions to the heat capacity related to the magnetic subsystem, which is especially large near the magnetic phase transition points. That is why the magnetic materials with the low ordering temperatures can provide high heat capacity in the low-temperature region where lattice and electronic heat capacities approach zero. This circumstance allows the use of such materials in passive magnetic regenerators—the devices serving to expand a conventional refrigerator temperature span. The described application of magnetic materials can be called ‘passive’ because here they only adsorb and desorb heat at different stages of the refrigerator cycle, do not produce heat themselves and operate without application of a magnetic field. In this way magnetic materials are used now in cryocoolers, essentially increasing their effectiveness. But more interesting and perspective application is related to the magnetocaloric effect inherent in magnetic materials. We mean the use of magnetic materials in magnetic refrigeration devices as working bodies, as a ‘heart’ of these devices. Such an application can be called ‘active’ (here a magnetic material produces heat under magnetization) and will be considered in detail in this chapter. It is worth noting, however, that in some cases both ‘passive’ and ‘active’ properties of a magnetic material are used simultaneously—for example, in so-called magnetically augmented regenerators, which are also discussed below.

11.1 Passive magnetic regenerators

A regenerator is a thermal device, which transfers heat between the parts of the regenerative thermodynamical refrigeration cycle of opposite directions

(from hot sink to cold load and from cold load to hot sink). When a high-temperature and high-pressured refrigerant gas (heat transfer fluid) passes through the regenerator it absorbs heat from the gas and when a low-temperature and low-pressured gas passes through the regenerator it returns heat to the gas. The regenerator serves to expand a refrigerator temperature span, since the temperature span produced by an adiabatic process itself is insufficient to achieve the desired temperature decrease, and to increase refrigerator efficiency. In regenerators working above 50 K (the upper stage of two-stage Gifford–McMahon cryocoolers) stainless steel or bronze are usually used. Lead is the conventional material for the lower-temperature regenerators.

In the temperature region below 15 K the heat capacity of conventional low-temperature stage regenerators in cryogenic refrigerators essentially decreases, since the lead volumetric heat capacity decreases and the regenerator efficiency is directly proportional to the heat capacity of the regenerator material. This happens because the lattice heat capacity of a solid is proportional to T^3 and the electronic heat capacity in metals is proportional to T (see section 2.11) and both these contributions approach zero in the low-temperature range. In cryocoolers utilizing helium gas this leads to a rapid decrease of refrigerator efficiency, because below 15 K the volumetric heat capacity (the heat capacity per unit volume) of compressed helium rapidly increases. A possible way to overcome this difficulty is to use in the regenerators the magnetic materials with low magnetic ordering temperatures instead of conventionally used lead. The maximum magnetic entropy change under transition from magnetically ordered to completely disordered (paramagnetic) state can be obtained from equation (2.66). According to equation (2.12) this entropy change should give additional magnetic contribution to the total heat capacity, which can play the main role in the low-temperature range where other contributions approach zero. The amount of this magnetic contribution near the magnetic transition temperature can be regarded roughly as directly proportional to the value determined by equation (2.66). Buschow *et al* (1975) suggested the rare earth compounds for use in low-temperature regenerators, based on the fact that in these materials the low magnetic ordering temperatures at which magnetic heat capacity peak occurs can be combined with high volumetric magnetic heat capacity in the phase transition temperature region. The latter is related to the oscillating nature of the exchange interaction in rare earth metals and their compounds, which does not necessarily require dilution of the magnetic ions (this reduces volumetric magnetic heat capacity) in order to achieve low ordering temperatures.

Hashimoto *et al* (1990) formulated the following requirements for magnetic materials with high magnetic heat capacity suitable for use in low-temperature magnetic regenerators: (1) the density of the magnetic ions in the material must be high; (2) the magnetic ions must have high

angular momentum quantum number; (3) the magnetic ordering temperature of the material must be low (in the range from 4 to 15 K) and be controllable. One more important parameter of the material for regenerators is its thermal conductivity. The material in regenerators is used in the form of particles, wires or plates. It is necessary to establish thermal equilibrium throughout the material during the cycle of the refrigerator. Otherwise only part of the material will participate in the heat exchange and the effectiveness of the regenerator will be reduced. The penetration depth of heat L_d in the material is determined as the length from the surface of the material to the place inside the material where the temperature reduces by e times from the temperature on the surface and can be described by the equation (Hashimoto *et al* 1990)

$$L_d = \left(\frac{k}{\pi\nu\rho C} \right)^{1/2} \quad (11.1)$$

where ν is the operation frequency of the regenerator (frequency of the alternating heat transfer fluid blow through the regenerator), k is thermal conductivity, ρ is the density and C is the volumetric heat capacity of the material. To achieve thermal equilibrium inside the magnetic material the dimension of the particles of magnetic material should be less than L_d . Thermal conductivity values of some metals, alloys, compounds and other materials are presented in table A2.1 in appendix 2.

11.1.1 Rare earth intermetallic compounds in passive regenerators

Bushow *et al* (1975) proposed a $Gd_xEr_{1-x}Rh$ system for use in low-temperature regenerators. The magnetic ordering temperatures in this system lie between $T_N = 3.2$ K for ErRh and $T_C = 24$ K for GdRh. The peak values of the heat capacity in ErRh and GdRh are on the level of about 0.9 J/K cm^3 , which is higher than the heat capacity of Pb.

Later RE–Ni and RE–Co intermetallic compounds were reported by Hashimoto and coworkers as suitable for application in the regenerators instead of Pb below 15 K (Yayama *et al* 1987, Sahashi *et al* 1990, Hashimoto *et al* 1990, 1992, Ke *et al* 1994, Long *et al* 1995c, Tsukagoshi *et al* 1996). Volumetric heat capacity temperature dependences of Er_3Ni , $ErNi$, $ErNi_2$, Er_3Co , $Er(Ni_{1-x}Co_x)_2$, $(Er-Yb)Ni$, $Er(Ni-Co)$, $Er_{1-x}Dy_xNi_2$ and $RNiGe$ ($R = Gd, Dy, Er$) compounds were investigated by Hashimoto and coworkers from the point of view of application in the regenerators. Figure 11.1 shows the heat capacity temperature dependences for some of the RE–Ni alloys (see also figure 6.12). As one can see the magnetic phase transition in the compounds provides volumetric heat capacity below 15 K much higher than that in Pb, although it is not higher than the volumetric heat capacity of compressed He (5 atm).

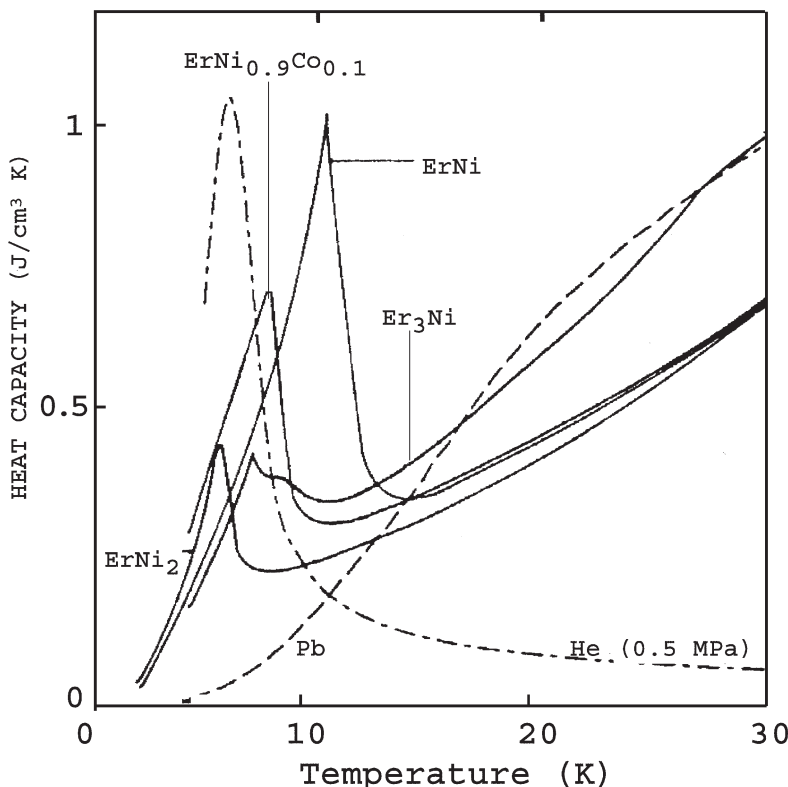


Figure 11.1. Temperature dependences of the volumetric heat capacity of Er_3Ni , ErNi , ErNi_2 and $\text{ErNi}_{0.9}\text{Co}_{0.1}$ compounds. For comparison the heat capacities of Pb and compressed He (5 atm) are also shown (Ke *et al* 1994).

According to estimations of McMahon and Gifford (1960), for effective work of the regenerator operating in a refrigerator using a gas as a heat transfer fluid, its material should have a volumetric heat capacity 3–5 times higher than that of the working gas. To verify effectiveness of the magnetic materials for use in the regenerators, Kuriyama *et al* (1990) partly replaced lead in the second (low-temperature) stage regenerator in a two-stage Gifford–McMahon (G-M) cryocooler by Er_3Ni . The regenerator contained of 141.2 g of Er_3Ni grains (0.1–0.3 mm in length) and 190.5 g of Pb spheres (0.2–0.3 mm in diameter). The second stage maximum expansion volume of the cryocooler was 25.4 cm³ and the first stage temperature maintained at 30–40 K. To compare the characteristics of the Er_3Ni -containing regenerator, the Pb regenerator filled with 383.2 g of Pb spheres with diameter of 0.2–0.3 mm was used. At the cryocooler reciprocating (rotational) speed (cryocooler motor cycle speed) of 18 rpm the minimal no-load temperature was 4.5 K for the Er_3Ni -containing regenerator and 6.28 K for the Pb

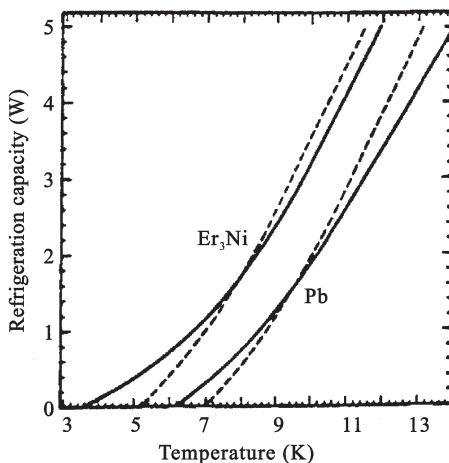


Figure 11.2. Dependence of the second stage refrigeration capacity of the Gifford–MacMahon cryocooler on the second stage temperature for Pb and Er₃Ni as materials in the second stage regenerators (—, reciprocating speed of the cryocooler 60 rpm; —, 24 rpm) (Hashimoto *et al* 1992, Kuriyama *et al* 1990).

regenerator. The optimized refrigeration capacity at reciprocating speed (which was 36 rpm) at 8 K was 1.2 W and 2.4 W for the Pb- and Er₃Ni-containing regenerators, respectively. Figure 11.2 shows the second stage refrigeration capacity of the G-M cryocooler as a function of the second stage temperature for regenerators containing Pb and Er₃Ni as a regenerator material. One can clearly see the advantage of the magnetic material, which can provide a lower second stage temperature and higher refrigeration capacity than Pb. Li *et al* (1990) measured, on the special test apparatus constructed for studying the thermal performance of cryogenic regenerators, the efficiency of the regenerators with Pb, Er₃Ni and Er_{0.5}Dy_{0.5}Ni₂ compounds in the temperature range from 4.2 to 35 K. It was shown that the efficiency of the magnetic materials is essentially higher than Pb below 15 K.

Er₃Ni has a broad heat capacity maximum near 7 K, which besides magnetic ordering process is related to the Schottky anomaly above the Néel temperature (see section 6.2). Above 15 K the volumetric heat capacity of Er₃Ni becomes comparable with that of Pb. These features make this material effective for application in low-temperature regenerators. It should be noted that Hershberg *et al* (1994) found an essential variability in the heat capacity data of Er₃Ni reported by various authors, in particular in the size of the heat capacity maximum. However, below 5 K the heat capacity of Er₃Ni rapidly decreases, which does not allow good refrigeration capacity to be obtained in a G-M cryocooler at liquid helium temperature using Er₃Ni in the second stage regenerator.

In the second stage regenerator in a G-M cryocooler the temperature of the hot end is usually about 30 K. At the same time the heat capacity peaks of the rare earth intermetallic magnetic materials with ordering temperatures below 15 K are rather narrow (about a few degrees at half maximum). Therefore it is impossible to cover the whole regenerator working temperature range from 30 K down to 4.2 K by one magnetic material. It was proposed to use a layered (hybrid) regenerator consisting of several layers of magnetic materials with magnetic ordering temperatures changing from high value (hot end of the regenerator) to low value (cold end of the regenerator) in accordance with temperature gradient in the regenerator (Hashimoto 1991, Hashimoto *et al* 1992).

Various layered regenerators were tried in the second stage of two-stage G-M cryocoolers. Ke *et al* (1994) used a hybrid second stage regenerator consisting of 240 g of Er_3Ni sphere particles with diameters from 0.2 to 0.5 mm (hot end) and of 250 g of $\text{ErNi}_{0.9}\text{Co}_{0.1}$ smashed particles with sizes from 0.2 to 0.5 mm (cold end). The regenerator was ~ 200 mm in length and 35 mm in diameter and was placed in the G-M cryocooler of RD210 type manufactured by Sumitomo Heavy Industries, Ltd. The minimal no-load temperature achieved was 2.7 K with no load put on the first expansion stage and cryocooler rotational speed of 48 rpm. The refrigeration capacity was almost the same for this hybrid regenerator and the regenerator completely consisting of Er_3Ni below 3.2 K, but at 4.2 K the refrigeration capacity was increased by 15.9% (0.95 W) in the hybrid regenerator. Employing the hybrid regenerator also allowed the refrigerator to be used with a first-stage load (0.4 W at 35 K), which was impossible with the Er_3Ni regenerator. Hashimoto *et al* (1994) and Kuriyama *et al* (1994) investigated characteristics of G-M cryocoolers with the hybrid second stage double-layer regenerators consisting of Er_3Co or Er_3Ni at the hot end plus $\text{Er}_{0.9}\text{Yb}_{0.1}\text{Ni}$ at the cold end (the ratio of the cold and hot magnetic components was 50:50). The maximum refrigeration capacity of 1.05 W at 4.2 K (the minimal no-load temperature was ~ 3.05 K) was achieved for the $\text{Er}_3\text{Co} + \text{Er}_{0.9}\text{Yb}_{0.1}\text{Ni}$ second stage regenerator with a hot end temperature of 30 K, a cryocooler reciprocating speed of 36 rpm, and the second stage maximum expansion volume of 25.7 cm^3 (Hashimoto *et al* 1994, Kuriyama *et al* 1994). The regenerator comprised 257 g of Er_3Co and 294 g of $\text{Er}_{0.9}\text{Yb}_{0.1}\text{Ni}$. For the regenerator with only Er_3Ni (542 g) the refrigeration capacity at the same conditions was 0.85 W and minimal no-load temperature was ~ 3.2 K. At the same time the regenerator consisting of 283 g Er_3Ni and 258 g $\text{Er}_{0.9}\text{Yb}_{0.1}\text{Ni}$ displayed a refrigeration power of 0.85 W at 4.2 K and minimal no-load temperature of ~ 3 K. Although the ratio of Er_3Co and $\text{Er}_{0.9}\text{Yb}_{0.1}\text{Ni}$ in the experimentally tested regenerator was 50:50, computer simulation showed that the optimum ratio providing maximum regenerator efficiency was about 60:40 and also confirmed more efficiency of the $\text{Er}_3\text{Co} + \text{Er}_{0.9}\text{Yb}_{0.1}\text{Ni}$ regenerator than the $\text{Er}_3\text{Ni} + \text{Er}_{0.9}\text{Yb}_{0.1}\text{Ni}$.

Takashi *et al* (1997) achieved a refrigeration capacity of 2.2 W at 4.2 K (the rotational speed was 42 rpm and the first stage temperature was 50 K with a heat load of 25 W) with the G-M cryocooler employing in the second stage the hybrid regenerator comprising Er_3Ni and $\text{ErNi}_{0.9}\text{Co}_{0.1}$. Such large refrigeration capacity was reached by increasing the second stage expansion volume up to 90.5 cm^3 and by application of mesh screens in the second stage regenerator. The regenerator (of inner diameter 55.1 mm) was divided by length into three equal parts by rectifiable meshes placed between felt mats. Two of the parts were filled with Er_3Ni and one (at the cold end) with $\text{ErNi}_{0.9}\text{Co}_{0.1}$. This was done to prevent flowing of helium gas to one side of the regenerator, which deteriorates the characteristics of the cryocooler, and in particular increases the minimal no-load temperature. Satoh *et al* (1996) used the hybrid regenerator composed of spherical particles of Pb (diameter 0.5–0.6 mm) at the hot end and $\text{ErNi}_{0.9}\text{Co}_{0.1}$ (diameter 0.2–0.3 mm) at the cold end with 500 g of each material. Besides using the hybrid regenerator, the intake/exhaust valve timing of the G-M cryocooler was also optimized in order to obtain maximum refrigeration capacity. The maximum refrigeration capacity of such a G-M cryocooler was 1.5 W at 4.2 K at the first stage temperature of 48.5 K (first stage heat load 40 W), a reciprocating speed of 60 rpm and a second stage maximum expansion volume of 37.7 cm^3 .

Triple-layer hybrid regenerators in the second stage of a two-stage G-M cryocooler were tested by Tsukagoshi *et al* (1996) and Hashimoto *et al* (1995). Tsukagoshi *et al* (1996) showed that a triple-layer regenerator composed of 25% $\text{Er}_{0.75}\text{Gd}_{0.25}\text{Ni}$ (hot end) + 25% Er_3Co (middle) + 50% $\text{Er}_{0.9}\text{Yb}_{0.1}\text{Ni}$ (cold end) provided superior cryocooler characteristics over a double-layer 50% $\text{Er}_{0.9}\text{Yb}_{0.1}\text{Ni}$ + 50% Er_3Co regenerator. For a rotational speed of 36 rpm and a second stage maximum expansion volume of $\sim 25.7\text{ cm}^3$, the refrigeration capacity of 1.05 W and 1.17 W was achieved at 4.2 K for the double-layer and triple-layer refrigerators, respectively. The double-layer regenerator comprised 283 g $\text{Er}_{0.9}\text{Yb}_{0.1}\text{Ni}$ and 275 g Er_3Co , and the triple-layer one 279 g $\text{Er}_{0.9}\text{Yb}_{0.1}\text{Ni}$, 138 g Er_3Co and 137 g $\text{Er}_{0.75}\text{Gd}_{0.25}\text{Ni}$. It should be noted that the heat capacity of $\text{Er}_{0.75}\text{Gd}_{0.25}\text{Ni}$ did not reveal maximum up to 30 K (maximum investigated temperature) but monotonically increased to about 0.85 J/K cm^3 at 30 K. In the work of Hashimoto *et al* (1995), a triple-layer regenerator consisting of 50% Er_3Co (hot end) + 30% $\text{Er}_{0.9}\text{Yb}_{0.1}\text{Ni}$ (middle) + 20% $\text{ErNi}_{0.8}\text{Co}_{0.2}$ (cold end) revealed somewhat better properties in comparison with the double-layer 50% $\text{Er}_{0.9}\text{Yb}_{0.1}\text{Ni}$ + 50% Er_3Co regenerator. The refrigeration capacity of the G-M cryocooler with the triple-layer regenerator was 1.11 W at 4.2 K (minimal no-load temperature 3.1 K) with the first stage temperature of 30 K and rotational speed of 36 rpm. At the same time, in the case of the single-layer regenerator with Er_3Ni the refrigeration capacity at 4.2 K was $\sim 0.6\text{ W}$ (minimal no-load temperature 3.2 K) at the same conditions.

Hashimoto *et al* (1995) did not give information about the weight of the magnetic materials in the regenerator and the second stage expansion volume.

Multi-layer regenerators including HoSb with a high volumetric heat capacity peak were studied by Nakane *et al* (1999). The heat capacity measurements of HoSb and DySb showed that these compounds have high and sharp heat capacity peaks with a height of 2.7 and 2 J/K cm³ at 5 and 9 K, respectively. According to Hashimoto *et al* (1998), in a multi-layered regenerator increasing the number of layers causes an increase in the volume of the partition between the layers, which reduces the regenerator effectiveness. Because of that the authors suggested using on the cold end a synthetic material in which two different materials are packed into one layer. This material was composed of HoSb and HoCu₂. Computer simulation of the regenerator effectiveness, which was estimated on the enthalpy basis (Seshake *et al* 1992), showed that the four-layer (Pb–Er₃Ni–HoCu₂–HoSb) and triple-layer (Pb–Er₃Ni–synthetic material (HoCu₂ + HoSb)) regenerator configurations have almost the same effectivenesses. In the experiments the particles of HoCu₂ had spherical form with diameters between 0.18 and 0.35 mm. HoSb particles were not spherical and were prepared from an arc-melted ingot, which was crushed and sifted through a sieve with a mesh having dimensions between 0.149 and 0.355 mm. Three triple-layer hybrid regenerators were tested: 58% Pb + 17% Er₃Ni + 25% HoCu₂, 58% Pb + 17% Er₃Ni + 25% HoSb and 58% Pb + 17% Er₃Ni + 25% synthetic material (13% (109.2 g) HoCu₂ + 12% (130 g) HoSb), where Pb was on the hot end. Pb and Er₃Ni were in the form of spherical particles with diameters from 0.2 to 0.3 mm and 0.18 to 0.35 mm, respectively. The materials were placed in the second stage of a G-M cryocooler. The temperature of the cold end of the first stage regenerator was fixed at 45 K (with 10 W of refrigeration capacity) and the reciprocating speed was 74 rpm. The cryocooler with the regenerator with HoCu₂ at the cold end demonstrated the highest cooling characteristics: its no-load minimal temperature was ~2.4 K and refrigeration capacity at 10 K was ~7.4 W. The no-load minimal temperature for regenerators with HoSb and the synthetic material was ~3 K and at 10 K they displayed 4 and 5 W of refrigeration capacity, respectively. All three refrigerator configurations studied had small differences in the refrigeration capacity on the second stage temperature behaviour below 6 K (at 6 K the refrigeration capacity was ~2.3 K), although this parameter was somewhat higher for the Pb–Er₃Ni–HoCu₂ configuration. However, the authors noted that because HoSb particles were not spherical, their packed volume decreased by 10% and this could decrease the refrigeration capacity achieved in the regenerators with this material.

Among other intermetallic compounds suitable for low-temperature regenerators RNiGe (R=Gd, Dy, Er), Er₆Ni₂Sn and Er₆Ni₂Pb, Er–Ag,

($\text{Pr}_{1-x}\text{Nd}_x\text{Ag}$, RGa_2 ($\text{R} = \text{Dy}, \text{Ho}$) and $\text{Dy}_{1-x}\text{Ho}_x\text{Ga}_2$ should be mentioned (Long *et al* 1995c, Gschneidner *et al* 1995, 1997b, Biwa *et al* 1996, Yagi *et al* 1997, 1998). Their heat capacity and magnetic properties were considered in chapter 6. The peak heat capacity values and temperatures corresponding to the peaks in the intermetallic compounds suitable for use in regenerators are summarized in table 11.1.

It should be noted that the intermetallic compounds have inherently poor mechanical properties—in particular, they are quite brittle. Because of this it is impossible to produce these materials in complex form, such as wires, sheets and so on. The best form in which intermetallic compounds can be used in the regenerators is small spherical particles. The dimensions of such particles are determined by requirements of thermal equilibrium inside the regenerator material during the refrigeration cycle, which is related to the thermal conductivity of the material—see equation (11.1). According to Hashimoto *et al* (1990) thermal conductivity of ErNi_2 , DyNi_2 and ErCo_2 is about $4 \times 10^{-3} \text{ W/cm K}$ at 4.2 K and about $4 \times 10^{-2} \text{ W/cm K}$ at 77 K ; the latter is an order of magnitude lower than thermal conductivity of Pb (note that with temperature decreasing, Pb thermal conductivity increases). Estimations of Hashimoto *et al* (1990) showed that the penetration depth of ErNi_2 at 4.2 K is $800 \mu\text{m}$ for typical operation frequency of 1 Hz . Lead is usually used in regenerators in the form of balls with diameters of $100\text{--}400 \mu\text{m}$. In accordance with the result of Hashimoto *et al* (1990), the same particle dimension is appropriate for rare earth intermetallic compounds. Such a range of the particle dimensions can give high packing density and uniformity of the regenerator material cross section in order to provide complete utilization of the regenerator volume and uniform heat transfer fluid pressure drop.

The simplest way to prepare such particles is to crush or grind the material and then to sieve it in order to obtain powder with the desired particle diameter. However, such material is highly susceptible to breakdown and fragmentation in use, with the formation of highly abrasive dust, which can quickly wear the seals and moving parts in the refrigerator, resulting in shortening its longevity. Besides, the dust can fill interstitial space between the particles and impede gas flow, increasing the pressure drop across the regenerator. The production process is characterized by low yield and the particles have irregular non-spherical shapes leading to low packing density, which causes a decrease of the regenerator efficiency and further destruction of the particles.

More suitable powders consisting of spherical intermetallic compound particles can be produced by gas or centrifugal atomization processes (Apri-gliano *et al* 1992, Hershberg *et al* 1994, Osborne *et al* 1994). However, the particles with diameters larger than $100 \mu\text{m}$ fabricated by gas atomization are characterized by prominent internal porosity and the essential fraction of the material is in the form of flakes or broken spheres, which reduces

Table 11.1. The values of magnetic phase transition temperatures (T_C , T_N , or other), peak values of the volumetric heat capacity C_{peak} and corresponding temperatures of the peak position T_{peak} . References are shown in brackets.

Compound	T_{pt} (K)	T_{peak} (K)	C_{peak} (J/K cm ³)
GdRh	24 [1]	20 [1]	0.93 [1]
Er ₃ Ni	5 [2]	7 [3]	0.35 [3]
		7.5 [4]	0.4 [4]
Nd ₃ Ni	–	6.5 [10]	0.64 [10]
ErNi ₂	6.2 [5]	6 [5]	0.35 [5]
Er _{0.8} Dy _{0.2} Ni ₂	–	9 [5]	0.43 [5]
Er _{0.4} Dy _{0.6} Ni ₂	–	14 [5]	0.62 [5]
DyNi ₂	20.55 [5]	21 [5]	0.82 [5]
HoNi ₂	–	12.5 [3]	0.7 [3]
Er _{0.5} Ho _{0.5} Ni ₂	–	9.5 [3]	0.54 [3]
ErNi	–	11 [3]	0.62 [3]
Er _{0.9} Yb _{0.1} Ni	–	9 [3]	0.82 [3]
ErNi _{0.9} Co _{0.1}	–	7 [6]	0.65 [6]
ErNi _{0.8} Co _{0.2}	–	6 [7]	0.75 [7]
Er ₃ Co	–	13 [7]	0.5 [7]
ErNiGe	3.3 [8]	3 [8]	0.52 [8]
Er ₆ Ni ₂ Sn	–	17.5 [9]	0.86 [9]
Er ₆ Ni ₂ Pb	–	17.5 [10]	0.8 [10]
HoSb	–	5 [11]	2.5 [11]
DySb	–	10 [11]	2.1 [11]
HoCu ₂	–	9 [11]	0.4 [11]
Er _{0.5} Ag _{0.5}	–	16 [12]	0.7 [12]
Er _{0.6} Ag _{0.4}	–	16 [12]	0.7 [12]
Er _{0.7} Ag _{0.3}	–	16 [12]	0.65 [12]
PrAg	–	10 [13]	1.08 [13]
Pr _{0.9} Nd _{0.1} Ag	–	11 [13]	1.2 [13]
Pr _{0.8} Nd _{0.2} Ag	–	10.5 [13]	1.05 [13]
Pr _{0.5} Nd _{0.5} Ag	–	12 [13]	1.3 [13]
Pr _{0.2} Nd _{0.8} Ag	–	17 [13]	0.9 [13]
NdAg	–	22 [13]	1.45 [13]
DyGa ₂	–	6.5 [14]	1.45 [14]
		9 [14]	1 [14]
HoGa ₂	–	7 [14]	0.6 [14]
		8.1 [14]	0.5 [14]
TbGa ₂	–	17.5 [14]	0.65 [14]
PrGa ₂	–	7.2 [14]	0.28 [14]
NdGa ₂	–	8 [14]	0.38 [14]
Dy _{0.5} Ho _{0.5} Ga ₂	–	10 [14]	0.35 [14]

1. Buschow *et al* (1975); 2. Buschow (1968); 3. Hashimoto *et al* (1992); 4. Pecharsky *et al* (1997a); 5. Hashimoto *et al* (1990); 6. Satoh *et al* (1996); 7. Hashimoto *et al* (1995); 8. Long *et al* (1995a); 9. Gschneidner *et al* (1997b); 10. Gschneidner *et al* (1995); 11. Nakane *et al* (1999); 12. Biwa *et al* (1996); 13. Yagi *et al* (1997); 14. Yagi *et al* (1998).

the yield of the final product. Er_3Ni powder was successfully produced by the centrifugal atomization process with a rotating quench bath (CA/RQB) (Osborne *et al* 1994, Hershberg *et al* 1994). In this process the molten alloy is poured on to a rapidly rotating refractory disk to produce spherical material droplets, which are then quenched in a concentric bath containing liquid quenchant rotating in the same direction as the disk but at a lower speed. The typical yield of Er_3Ni powder with particle dimensions between 150 and 355 μm in CA/RQB process was 30–40% (Osborne *et al* 1994). Scanning electron microscopy and cross-sectional optical micrographs showed that the obtained Er_3Ni particles were mostly spherical and essentially void free. It should be noted that the cost of fabrication of spherical intermetallic particles is high, which is mainly related to the expensive and sophisticated equipment required for the manufacturing process.

Pecharsky *et al* (1997a) tried to make amorphous Er_3Ni by rapid solidification with the help of the melt-spin method in order to improve its mechanical properties and possibly produce it in the form of sheets or ribbons. This attempt failed even at high cooling rates of about 10^6 K/s . Better results were achieved with alloys $\text{Er}_3(\text{Ni}_{0.98}\text{Ti}_{0.02})$ and $\text{Er}_3(\text{Ni}_{0.9}\text{Ti}_{0.1})$ which were made partly or probably completely amorphous and were quite flexible. However the heat capacity maximum at 7 K characteristic for Er_3Ni and observed in crystalline $\text{Er}_3(\text{Ni}_{0.98}\text{Ti}_{0.02})$ and $\text{Er}_3(\text{Ni}_{0.9}\text{Ti}_{0.1})$ disappeared in the amorphous state. At the same time the heat capacity of the amorphous alloys below 10 K was on the level of that in gas atomized commercial Nd.

The Cryofuel System Group from the University of Victoria (Canada) suggested the technology of fabrication of the monolithic regenerators comprising the particles of brittle intermetallic compounds obtained by crushing or grinding (Merida and Barclay 1998, Williamson 2001, Wysokinski *et al* 2002). The technology reduces the manufacturing cost of the regenerators and provides their structural integrity, eliminating the problems related to the abrasive dust described above. It consists of bonding the particles in a monolithic but porous regenerator bed with the help of a diluted epoxy mixture, which prevents the particles from moving during the cryocooler operation and excludes their fractioning. Because a small amount of epoxy is used, the particles are coated by thin epoxy layer of a sub-micron range (Wysokinski *et al* 2002), which does not deteriorate thermal exchange between the magnetic material of particles and the heat transfer gas. The conducted experiments confirmed that the characteristics of the G-M cryocoolers using monolithic regenerators did not degrade with time and the regenerators preserved their integrity. The experiments were made on the triple-layer regenerators consisting of Pb (spheres) + Er_3Ni (spheres) + $\text{ErNi}_{0.9}\text{Co}_{0.1}$ (grains). According to Merida and Barclay (1998), a G-M cryocooler with such a monolithic regenerator preserved its characteristics after 10 days of continuous operation, which corresponded

to $\sim 10^9$ cycles. Consider the results reported recently by Wysokinski *et al* 2002. The second stage regenerator in this work comprised 98.913 g of 0.3 mm in diameter Pb spheres, 183.689 g of 0.3 mm diameter Er₃Ni spheres and 58.946 g of ErNi_{0.9}Co_{0.1} grains with dimensions from 0.15 to 0.35 mm. The second stage expansion volume of the G-M cryocooler was 11.1 cm³, the regenerator volume was 56.1 cm³, its porosity was $\sim 36\%$ and the total surface area was 0.67 m². The total amount of epoxy used in the regenerator fabrication was ~ 0.85 g. It was diluted in acetone and poured through the regenerator, which was then blown off with nitrogen gas. The procedure was repeated 10 times and then the epoxy was cured. The experimental studies showed that using epoxy in the regenerator not only does not deteriorate the cryocooler characteristics, but also even improved some of them (the comparison was made with a conventional regenerator of the same composition), which was related to increasing the roughness of the epoxy-coated particles' surface and a corresponding increase of the heat transfer area. With the monolithic regenerator the minimal no-load second stage temperature of ~ 4.2 K was achieved at the rotational speed of ~ 90 rpm (the first stage no-load temperature was 34 K) with a standard commercial Leybold regenerator at the first stage. The observed higher gas flow pressure drop across the monolithic regenerator was explained by the reduction of the flow channel sizes due to the presence of epoxy coating.

11.1.2 Rare earth metals and their alloys in passive regenerators

Another material, which is used in low-temperature stage regenerators, is light rare earth metal neodymium. It has two magnetic phase transitions, at 7.8 and 19.2 K (Johansson *et al* 1970), with corresponding heat capacity maximums. The advantage of Nd is in its metallic nature with ductile mechanical properties inherent to the metallic state. This allows production of sound Nd spheres, wires, foils or even more complex articles in order to provide high efficiency heat exchange in the regenerators. Figure 11.3 shows the volumetric heat capacity temperature dependence of gas atomized commercial Nd (99% pure) measured by Pecharsky *et al* (1997a). As one can see Nd is superior to Pb below 15 K. Osborne *et al* (1994) prepared ellipsoidal Nd particles with average sizes between 180 and 355 μm by the centrifugal atomization process. The regenerator consisting of Nd perforated disks for use in a G-M refrigerator was fabricated by Chafe *et al* (1997). Such a construction should have a lower dead volume (a space in the regenerator occupied by the refrigerant gas) and pressure drop in comparison with regenerators filled with spheres of the working material. The disks were produced by means of the process analogous to that used to produce multi-filamentary superconducting wires. The holes in the disks had a mean equivalent diameter of 0.05 mm and occupied about 10% of the cross-sectional area. Each disk was 1 mm thick and weighed about 2.75 g. The test hybrid regenerator consisted

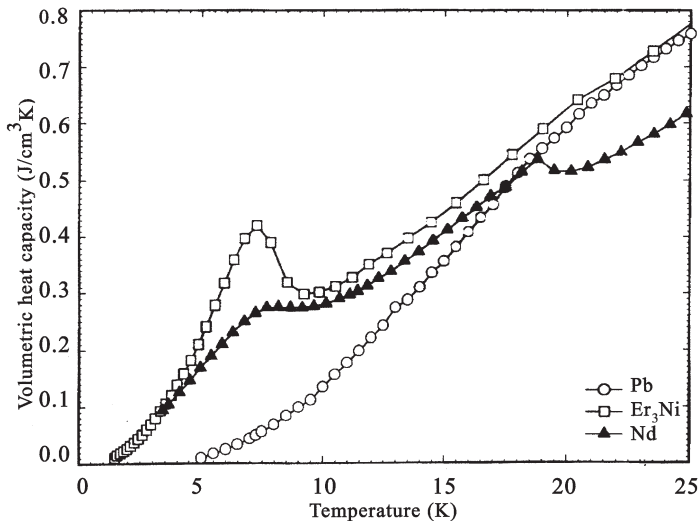


Figure 11.3. Temperature dependences of volumetric heat capacities of Nd, Er_3Ni and Pb in the low-temperature range (Pecharsky *et al* 1997a).

of a Pb spheres layer (occupying about 60% of the whole length of the regenerator, with a mass of 256 g) on the hot end and of 48 Nd disks set perpendicular to the gas flow on the cold end. The neighbouring disks were separated from each other by circular pieces of spun polyester cloth. A two-stage G-M refrigerator equipped with a second stage Nd regenerator as described showed 1 W of refrigeration capacity at 5.5 K and reached a minimal no-load operating temperature of about 4 K. These characteristics were somewhat worse than that using an all-Nd-sphere regenerator. The pressure drop was also higher than for the packed sphere regenerator. Later Chafe and Green (1998) proposed another construction of the Nd-based regenerator. The hybrid regenerator again consisted of Pb sphere and Nd parts. The Nd part was made up of a stack of sections of coiled Nd ribbons 0.32 cm wide. On the ribbon surface, small ridges providing spacing between ribbon sheets in the coiled sections were embossed during the preparation process. Two ribbons, one 0.025 cm thick with a 0.005 cm spacing ridge and another 0.018 cm thick with a 0.0025 cm spacing ridge, were prepared and used in the regenerator. Better results were achieved on the 0.025 cm ribbon. The regenerator with this ribbon had lower pressure drop in comparison with the all-sphere regenerator. It also provided higher cooling power (1 W at 4.75 K) and lower minimal no-load temperature (about 3 K) in a two-stage G-M refrigerator than the all-sphere regenerator.

Gschneidner *et al* (2000d,e), based on the results of the heat capacity measurements (see section 8.2.3), proposed to use $Er_{0.73}Pr_{0.27}$ and $Er_{0.5}Pr_{0.5}$

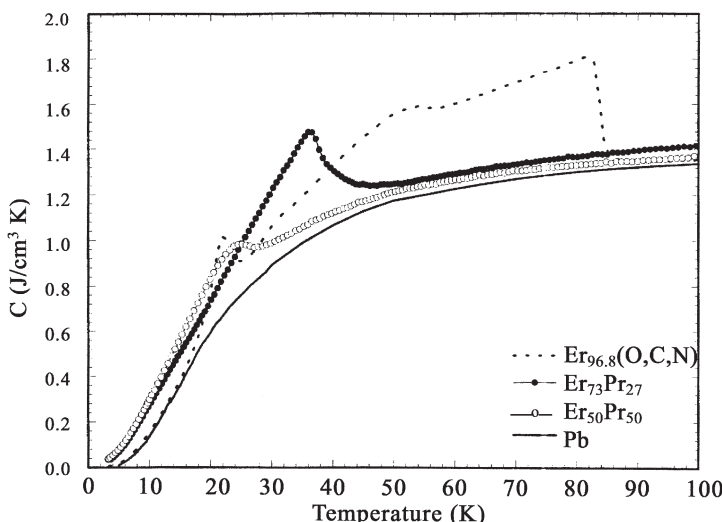


Figure 11.4. Temperature dependences of the volumetric heat capacities of $\text{Er}_{0.73}\text{Pr}_{0.27}$, $\text{Er}_{0.5}\text{Pr}_{0.5}$ and $\text{Er}_{0.968}\text{O}_{0.027}\text{N}_{0.003}\text{C}_{0.002}$ (Gschneidner *et al* 2000d).

alloys in the low-temperature regenerators working above 10 K. Figure 11.4 shows the volumetric heat capacity of these alloys along with that of lead. As one can see, below 40 K the heat capacity of the alloys is higher than that of lead. For the temperature range from 40 to 85 K, Gschneidner *et al* (2000d,e) suggested the interstitial alloy $\text{Er}_{0.968}\text{O}_{0.027}\text{N}_{0.003}\text{C}_{0.002}$, which is just Er purchased from a commercial vendor. The thermal conductivity of $\text{Er}_{0.968}\text{O}_{0.027}\text{N}_{0.003}\text{C}_{0.002}$ and Er–Pr alloys was determined to be an order of magnitude lower than that of Pb. The authors also pointed to good mechanical properties of the alloys, in particular their ductility and strength. This allows them to be used in various forms (wires, sheets, etc.) in regenerators. The other advantage is low oxidation capability of the alloys in comparison with light rare earths (such as Nd).

To produce fine rare earth metal powders, gas and centrifugal atomization processes are used (Osborne *et al* 1994, Hershberg *et al* 1994). The neodymium powder with particle sizes of 180–355 µm was produced by the centrifugal atomization process with a rotating quench bath (CA/RQB) by Osborne *et al* (1994). Some degradation of the initial material purity during the process was observed, which was reflected in changing the Nd heat capacity temperature dependence as compared with pure Nd. Miller *et al* (2000) prepared Gd, Er and $\text{Er}_{0.73}\text{Pr}_{0.27}$ powders using the plasma rotating electrode process (PREP). In this method a round bar of the necessary material rotates about its longitudinal axis and is melted by a plasma torch. The material is centrifugally ejected from the bar and solidified in the form of spherical particles. The heat capacity measured on the

produced $\text{Er}_{0.73}\text{Pr}_{0.27}$ powder with particle sizes of 100–250 μm was almost the same as on the initial material. This points to low contamination of the material during the process.

Wong and Seuntjens (1996) proposed a method of production of fine rare earth wires in order to fabricate wire cloth screens for utilization in the regenerators. In this method a rare earth metal or alloy ingot is put inside the copper jacket with an Nb barrier between the ingot and the jacket. This assembly is then extruded and the obtained extruded rod processed to final wire size by a standard wire drawing technology. Wires of Gd, Dy and $\text{Gd}_{0.6}\text{Dy}_{0.4}$ alloy with diameters of 254–817 μm were obtained.

11.2 Magnetic refrigeration

11.2.1 General consideration

In general, a magnetic refrigerator should include the following main parts: magnetic working body, magnetization system, hot and cold heat exchangers, and heat transfer fluid with a system providing its flow. The heat transfer fluid carries out coupling between the magnetic working material and heat exchangers and can be a gas or liquid depending on the working temperature range. The general operational principle of a refrigerator is as follows: the working material (refrigerant) absorbs heat at the low-temperature load (cold heat exchanger) and discharges heat at the high temperature sink (hot heat exchanger). As a result of cyclic repetition of this process the load is cooled. In magnetic refrigerators the working material is a magnetic material, which changes its temperature and entropy under the action of a magnetic field. For magnetic refrigeration a nonregenerative Carnot cycle and also magnetic type regenerative Brayton, Ericsson and AMR (active magnetic regenerator) cycles can be used (Barclay 1994).

Figure 11.5 illustrates the main thermodynamic cycles used for magnetic refrigeration. A Carnot cycle with a temperature span from T_{cold} to T_{hot} is shown in figure 11.5 by the rectangle ABCD in the total entropy–temperature (S – T) diagram. The heat Q_c , absorbed from the cooling load (at temperature T_{cold}) during one cycle of refrigeration, equals $T_{\text{cold}}\Delta S_M$, where $\Delta S_M = S_2 - S_1$. Increasing the temperature span beyond a certain optimal value leads to a significant loss of efficiency as point C in figure 11.5 tends to point G and the cycle becomes narrow. The temperature span of the Carnot cycle for a given T_{cold} and H is limited by the distance AG in figure 11.5 (i.e. by the MCE at $T = T_{\text{cold}}$ and the field change from 0 to H), when Q becomes zero. The lattice entropy of solids strongly increases above 20 K, which leads to a decrease of the Carnot cycle area (see rectangle abcd in figure 11.5). That is why applications of Carnot-type refrigerators are restricted to the temperature region below 20 K.

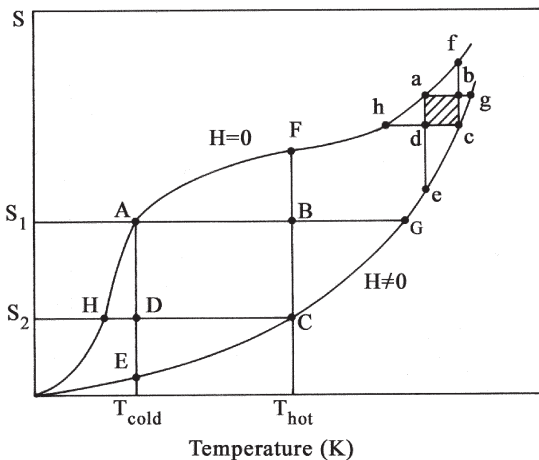


Figure 11.5. S - T diagram of thermodynamic cycles used for magnetic refrigeration. Two isofield $S(T)$ curves are shown: for $H = 0$ and $H \neq 0$ (Kuz'min and Tishin 1993a). (Reprinted from Kuz'min and Tishin 1993a, with permission from Elsevier.)

Magnetic refrigerators operating at higher temperatures have to employ other thermodynamic cycles, including processes at constant magnetic field. These cycles allow use of the area between the $S(T, H = 0)$ and $S(T, H \neq 0)$ curves in the S - T diagram more fully. The rectangles AFCE and AGCH present the Ericsson and Brayton cycles, respectively. The two cycles differ in the way the field change is accomplished—isothermally in the Ericsson cycle and adiabatically in the Brayton cycle. Realization of isofield processes in both of these cycles requires heat regeneration.

As noted in section 11.1, a regenerator is a thermal device serving to transfer heat between different parts of a regenerative thermodynamical refrigeration cycle, which allows the temperature span of the refrigeration device to increase. This is especially important in the case of magnetic refrigerators because the adiabatic temperature change (i.e. the magnetocaloric effect) in these devices is much less than in refrigerators utilizing gas as a refrigerant. Every magnetic refrigerator working on a regenerative cycle should include a regenerator in some form. Thermal energy in the magnetic regenerative cycles is absorbed by the regenerator during the high-field hot sink–cold load flow period (CE and GC lines in figure 11.5 for Ericsson and Brayton cycles, respectively) and returned to the heat transfer fluid during the low-field cold load–hot sink flow period (AF and HA lines in figure 11.5 for Ericsson and Brayton cycles, respectively). A magnetic regenerative refrigeration cycle can be presented as consisting of the following main parts: magnetization and heat transfer in the hot heat exchanger, regeneration with temperature dropping from T_{hot} to T_{cold} , demagnetization and heat transfer in the cold heat exchanger, regeneration with temperature increasing from T_{cold} to T_{hot} .

Let us introduce some concepts necessary for consideration of magnetic refrigeration cycles. According to the first law of thermodynamics, in the ideal refrigeration cycle the heat Q_h rejected at hot sink (at temperature T_{hot}) is related to heat Q_c absorbed from the cooling load (at temperature T_{cold}) and the work W_i consumed to accomplish this process as follows:

$$Q_c = Q_h - W_i. \quad (11.2)$$

Q_c , Q_h and the input work W_i are related to refrigeration capacity (cooling power) \dot{Q}_c , heat rejection at hot sink \dot{Q}_h and work rate in refrigerator \dot{W}_i as

$$\dot{Q}_c = Q_c \nu \quad (11.3a)$$

$$\dot{Q}_h = Q_h \nu \quad (11.3b)$$

$$\dot{W}_i = W_i \nu \quad (11.3c)$$

where ν is the operational frequency of the refrigerator.

For isothermal reversible heat transfer the corresponding entropy changes at hot (ΔS_h) and cold (ΔS_c) ends can be determined by the equations

$$\Delta S_h = \frac{Q_h}{T_{\text{hot}}} \quad (11.4a)$$

$$\Delta S_c = - \frac{Q_c}{T_{\text{cold}}}. \quad (11.4b)$$

The second law of thermodynamics requires that

$$\Delta S_h + \Delta S_c \geq 0 \quad (11.5)$$

from which one can obtain

$$W_i = Q_c \left(\frac{T_{\text{hot}}}{T_{\text{cold}}} - 1 \right). \quad (11.6)$$

The ratio refrigeration capacity (\dot{Q}_c)/power input (\dot{W}) (or heat lifted/work done) is called the coefficient of performance (COP) and in the case of an ideal cycle the COP is the Carnot value (see equation (11.6))

$$\text{COP}_{\text{Carnot}} = \frac{T_{\text{cold}}}{T_{\text{hot}} - T_{\text{cold}}}. \quad (11.7)$$

The efficiency η of a refrigerator is the ratio of its actual coefficient of performance to the Carnot coefficient of performance. It can also be determined as the ratio of Carnot (ideal) power input to actual input power required.

Magnetic regenerative refrigeration cycles were considered by Barclay (1991) and Cross *et al* (1987). Figure 11.6 illustrates the ideal magnetic Ericsson cycle, in which magnetic field is changed isothermally. The energy transfer to and from the magnetic material in low- and high-field stages of the cycle should be balanced in order to satisfy the law of energy conservation. This requirement implies the equality of areas $S_1ABS'_1$ and $S_2DCS'_2$,

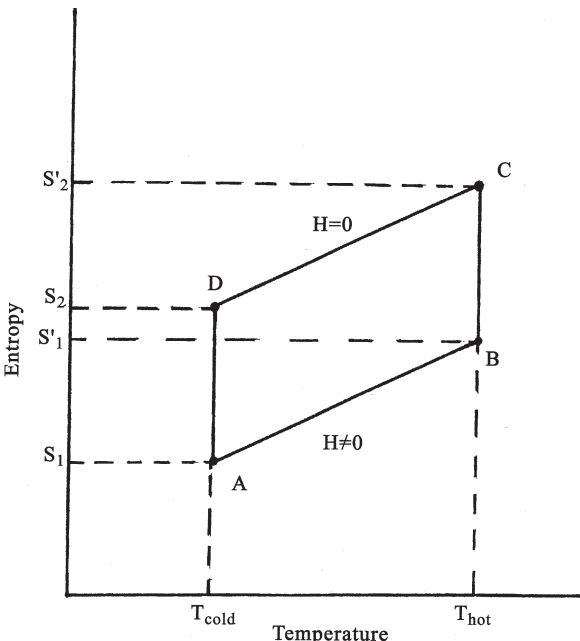


Figure 11.6. $S-T$ diagram of ideal magnetic Ericsson refrigeration cycle.

which are the heat Q_R absorbed and returned by the regenerator at the high- and low-field stages of the cycle, respectively. One more consequence follows from the conservation energy requirement: the entropy change (the distance between $S(T)$ curves for $H = 0$ and $H \neq 0$) in the cycle should be constant, i.e. $S_2 - S_1 = S'_2 - S'_1 = -\Delta S_M = \text{const.}$ and $S(T, H = 0)$ and $S(T, H \neq 0)$ are parallel. In this case the second law constraint (equation (11.5)) is fulfilled and the cycle is executed with maximum Carnot efficiency. Q_c and Q_h are determined by areas S_1ADS_2 and $S'_1BCS'_2$ areas in figure 11.6, respectively. The input work W_i is presented by the area ABCD. For an ideal Ericsson cycle the requirement $\Delta S_M = \text{const.}$ provides optimal performing conditions. In real magnetic materials ΔS_M has maximum value near the temperature of the magnetic phase transition (at which the material is used in magnetic refrigerators) and is decreased in the temperature region above and below the transition temperature. Cross *et al* (1987) regarded the influence of $\Delta S_M(T)$ dependence of such form on the effectiveness of the Ericsson magnetic cycle. It was shown that such a nonideal $\Delta S_M(T)$ curve would result in extra work required for cycle accomplishing and reduction of the refrigeration capacity (if $\Delta S_h = \Delta S_c$) in comparison with the ideal $\Delta S_M = \text{const.}$ case. It was also demonstrated that the Ericsson cycle is more effective with steeper $S(T)$ curves (with the condition of the same ΔS_M value), i.e. with lower heat capacity of the magnetic material. It

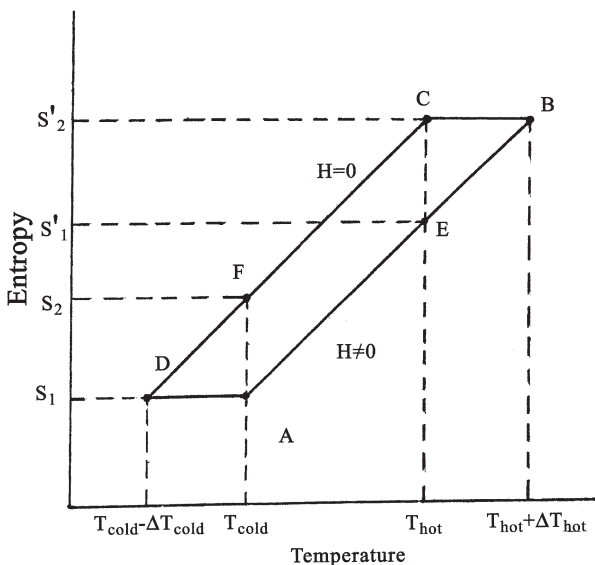


Figure 11.7. $S-T$ diagram of ideal magnetic Brayton refrigeration cycle.

should be noted that such material should also provide a higher magnetocaloric effect—see equation (2.16).

An ideal magnetic Brayton refrigeration cycle is shown in figure 11.7. In this cycle magnetization is accomplished adiabatically, in contrast to the Ericsson cycle. Consider the operation of the cycle starting from point C in figure 11.7, when the magnetic working material is at temperature T_{hot} . Adiabatic magnetization causes a rise in the temperature by the value of the magnetocaloric effect ΔT , so the temperature of the material becomes $T_{\text{hot}} + \Delta T$ (line C → B in figure 11.7). Then the magnetized material is set in thermal contact with the hot heat exchanger and is cooled back to the temperature T_{hot} (line B → E). Further cooling from T_{hot} down to T_{cold} is accomplished with the help of a regenerator (line E → A), which absorbs the heat Q_R determined by the area $S_1AES'_1$. After that the adiabatic demagnetization changes the magnetic material temperature from T_{cold} to $T_{\text{cold}} - \Delta T$ (line A → D) with subsequent warming back to T_{cold} (line D → F) as a result of interaction with the cold heat exchanger. Finally the regenerator returns to the magnetic material heat Q_R (line F → C and area $S_2FCS'_2$) and the cycle loop is closed in the point C. Q_c , Q_h and W_i in the Brayton cycle are represented by areas S_1DFS_2 , $S'_1EBS'_2$ and $ABCD$, respectively. If segments AE and CF are equal to zero, there is no regeneration ($Q_R = 0$) and we have a nonregenerative Brayton cycle. It should be noted that the Brayton cycle is characterized by less refrigeration capacity and larger heat rejection in comparison with the Ericsson cycle. Cross *et al* (1987) pointed out that the differences between real Ericsson and Brayton

cycles are small because of deviation from true isothermal and adiabatic magnetization in real processes. The response of these cycles to deviation of the working magnetic material $\Delta S_M(T)$ dependence from requirements for the ideal cycle ($\Delta S_M = \text{const.}$) is equivalent. The influence of the real $\Delta S_M(T)$ dependence on the parameters of the Ericsson and Brayton magnetic refrigeration cycles was also regarded by Dai (1992), Yan and Chen (1989), Chen and Yan (1991 1994). There is one more magnetic refrigeration cycle—the active magnetic regenerator (AMR) refrigeration cycle, which is based on the Brayton cycle. In the AMR cycle the magnetic material serves not only as a refrigerant but also as a regenerator. This cycle will be considered more thoroughly below.

In real magnetic regenerative refrigerators there are a number of irreversible processes occurring as a part of the refrigeration cycle, which produce additional entropy and reduces by this the effectiveness of the refrigerators. The effectiveness of the magnetic refrigerators was considered by Barclay (1984a,b 1991) Cross *et al* (1987) and Reid *et al* (1994). The rate of work in a real thermodynamic magnetic cycle can be presented as (Tolman and Fine 1948, Barclay 1984a,b, Barclay and Sarangi 1984)

$$\dot{W} = \dot{Q}_c \left(\frac{T_{\text{hot}}}{T_{\text{cold}}} - 1 \right) + \frac{\int_{T_{\text{cold}}}^{T_{\text{hot}}} \Delta \dot{S}_{\text{irr}} dT}{\int_{T_{\text{cold}}}^{T_{\text{hot}}} dT} \quad (11.8)$$

where

$$\Delta \dot{S}_{\text{irr}} = \Delta \dot{S}_{\text{ht}} + \Delta \dot{S}_{\text{vd}} + \Delta \dot{S}_{\text{ac}} \quad (11.9)$$

is the total entropy generation rate due to irreversible processes in the regenerator,

$$\Delta \dot{S}_{\text{vd}} = \frac{V_f \Delta P}{T_{\text{hot}}} \quad (11.10)$$

is the entropy generation rate due to viscous dissipation of the flow energy, ΔP is the pressure drop across the regenerator and V_f is the average volume flow rate,

$$\Delta \dot{S}_{\text{ac}} = \frac{kA}{L} \frac{(T_{\text{hot}} - T_{\text{cold}})^2}{T_{\text{hot}} T_{\text{cold}}} \quad (11.11)$$

is the entropy generation rate due to axial thermal conduction and gas dispersion along the regenerator, k is the effective thermal conductivity of the regenerator material, L is the regenerator length, A is the regenerator cross-sectional area,

$$\Delta \dot{S}_{\text{ht}} = \frac{\dot{Q}_R \Delta T_{\text{SF}}}{T^2} \quad (11.12)$$

is the entropy generation rate due to finite heat transfer between the heat transfer fluid and the magnetic material, \dot{Q}_R is the heat transfer rate in the regenerator, ΔT_{SF} is the mean temperature difference between the magnetic solid and the heat transfer fluid, which can be represented as

$$\Delta T_{SF} = \frac{T_{\text{hot}} - T_{\text{cold}}}{N_{\text{tu}} + 1}. \quad (11.13)$$

N_{tu} is the number of heat transfer units describing the regenerator and defined as

$$N_{\text{tu}} = \frac{kA_c}{\dot{m}C_f} \quad (11.14)$$

where A_c is the heat transfer area, $\dot{m}C_f$ is the thermal mass flow rate of the heat transfer fluid, and C_f is the fluid heat capacity. Among the above-mentioned contributions to $\Delta\dot{S}_{\text{irr}}$, the process due to the finite heat transfer in the regenerator is the main one. Another factor that can give essential contribution to the irreversibility in the regenerator is its finite thermal mass. As shown, the irreversibilities in the regenerator determine the general efficiency of the magnetic cooling device (Barclay 1984b, 1991). Indeed, as one can see from consideration of the S - T diagrams of the magnetic regenerative refrigeration cycles (figures 11.6 and 11.7), the heat transferred in the regenerator during the cycle, which is equal to $2Q_R$, is much higher than Q_c or Q_h . That is why even relatively small irreversibility in the regenerator can give a heat flow comparable with the cooling power \dot{Q}_c , resulting in very low effectiveness of the whole refrigerator.

Barclay (1984b) determined the efficiency of the magnetic refrigerator, suggesting that the irreversibilities in the regenerator related to the finite heat transfer and thermal mass are the main mechanisms reducing the efficiency of the refrigerator. Two temperature regions requiring regeneration were considered: from 20 to 150 K and from 150 to 300 K. It was assumed that in the first case the heat capacity of the regenerator material can be regarded as a constant and in the second case it is proportional to T . On the basis of equations (11.8), (11.9) and (11.12) the following expressions for the reverse efficiency were obtained (Barclay 1984a,b)

$$\frac{1}{\eta} = 1 + \frac{2(T_{\text{hot}} - T_{\text{cold}} - \Delta T_R)}{(N_{\text{tu}} + 1)(\Delta T_{\text{cold}} - \Delta T_R)} \quad (11.15)$$

for the temperature range from 150 to 300 K, and

$$\frac{1}{\eta} = 1 + \frac{2[T_{\text{hot}}^2 - T_{\text{cold}}^2 - \Delta T_R(T_{\text{hot}} - T_{\text{cold}})]}{(N_{\text{tu}} + 1)\{T_{\text{cold}}^2 - [T_{\text{cold}} - (\Delta T_{\text{cold}} - \Delta T_R)]\}} \quad (11.16)$$

for the temperature range from 20 to 150 K. In equations (11.15) and (11.16) ΔT_{cold} is the MCE at the cold end and ΔT_R is the thermal defect arising due to the finite thermal mass of the regenerator (for example, ΔT_R is the

difference between the real temperature reached in the high field regenerative part of the cycle cooling the magnetic material and T_{cold}). Estimations made on the basis of equations (11.15) and (11.16) for $N_{\text{tu}} = 200$, $\Delta T_R = 3 \text{ K}$ and $\Delta T_{\text{cold}} = 10 \text{ K}$ gave an efficiency of 52% in the temperature range from 20 to 150 K and 85% in the temperature range from 150 to 300 K. It should be noted that modern cryocoolers have efficiencies up to 50% (Walker and Bingham 1993).

Among other sources considered of irreversibility in the magnetic refrigerators' hot and cold heat exchangers with heat transfer were: pressure drop and longitudinal heat conduction; fluid pump inefficiency; the magnetization system and the process of magnetization; friction; seal leakage and various heat leaks (Barclay 1984b, 1991). The magnetization process can include irreversibilities due to the energy exchange between magnetic and crystal lattice subsystems of the magnetic material, losses for magnetic hysteresis and eddy currents induced in conductive magnetic materials by changing magnetic field, and parasitic heating in the magnet related to magnetic flux changes because of motion of the nonuniform magnetic material in the magnetic field. The lattice and magnetic subsystems in the magnetic material are strongly coupled with a spin-lattice relaxation time of the order of milliseconds for the rare earth based materials, which is much lower than periods of cycles used in magnetic refrigerators (0.1 Hz to several Hz) (Barclay 1991). A magnetic material is usually used in the refrigerators near Curie temperature, where the effects of magnetocrystalline anisotropy and magnetic hysteresis are small. The effects of eddy currents in the magnetic material and parasitic heating in the magnet can be minimized by careful design and use of a constant stream of the magnetic material in the magnet (wheel design of the refrigerator, which will be considered below). Magnetization/demagnetization of the magnetic material in magnetic refrigeration cycles is an analogue of compression/expansion in gas refrigeration cycles. It was shown by Barclay (1991) that these processes have approximately equal efficiency. Heat exchanging in hot and cold heat exchangers is much more efficient in the case of magnetic refrigerators because the rate of work produced by irreversible heat transfer is directly proportional to the temperature difference between the heat transfer fluid and the cooling bath at the start of heat exchange, i.e. adiabatic temperature change in compression or magnetization, which is much lower in the case of a magnetic material. Especially this concerns the hot heat exchanger. So, it was shown that all of the considered irreversibilities are essentially smaller than that related to the regeneration process and that the magnetic refrigerator is superior to or at least not worse than refrigerators with conventional gas cycles by these parameters. Besides, most of these irreversibilities can be eliminated by careful design.

According to considerations of Barclay (1984b 1991), the N_{tu} of the regenerator in magnetic refrigerators should be 10–20 times higher than in gas refrigerators. $N_{\text{tu}} = 500$ is required to provide an efficiency of 60% of

Carnot for the magnetic refrigerator operating in the temperature range between 20 and 300 K ($N_{tu} = 200$ gives $\eta = 38\%$ for this temperature range). $N_{tu} = 500$ is equivalent to the requirement of $25\,000\text{ m}^{-1}$ of specific area for the operational frequency of 0.5 Hz, which can be achieved for particles of $240\text{ }\mu\text{m}$ diameter in the regenerator (Barclay 1991). Decreasing the particle diameter increases the specific area, but also increases the pressure drop in the regenerator, to overcome which an additional fluid pump work is required.

Various possible designs of regenerators and their efficiencies were considered by Barclay and Sarangi (1984) on the basis of equations (11.8)–(11.14). The geometries of the regarded regenerators are presented in figure 11.8. They are: (a) tube channels in a solid block; (b) a stack of perforated plates arranged perpendicular to the heat transfer fluid direction; (c) a stack of solid plates arranged parallel to the heat transfer fluid direction; and (d) a packed bed of spherical particles (loose packed or sintered). The regenerators were characterized by the following geometrical parameters: L , overall length; a , height; b , width; t , plate thickness; s , plate spacing; and d , hole or particle diameter. The overall porosity (the total void fraction) was chosen to be 0.4 for all cases under consideration (this value is typical for a randomly packed bed of spherical particles). The following dimensional constraints were used under calculations: $0.01\text{ mm} \leq d \leq 1\text{ mm}$ for tube

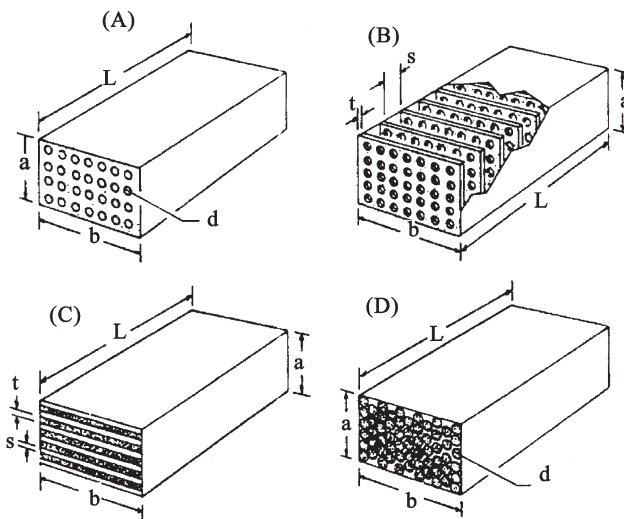


Figure 11.8. Possible geometries of regenerators, which can be used in magnetic refrigerators: (a) tube channels in a solid block; (b) a stack of perforated plates arranged perpendicular to the heat transfer fluid direction; (c) a stack of solid plates arranged parallel to the heat transfer fluid direction; (d) a packed bed of spherical particles (loose packed or sintered) (Barclay and Sarangi 1984).

channels in the solid block; $0.01 \text{ mm} \leq d \leq 1 \text{ mm}$, $0.01 \text{ mm} \leq t \leq 1 \text{ mm}$ and $0.2 \leq s/t \leq 0.6$ for the stack of perforated plates; $0.01 \text{ mm} \leq t \leq 1 \text{ mm}$ for the stack of solid plates; $0.01 \text{ mm} \leq d \leq 1 \text{ mm}$ for the packed bed of spherical particles; $0.3 \leq L/a \leq 30$ for all designs. The result of calculations for an operational frequency of 1 Hz showed that the highest efficiency of 0.936 ($t = 0.5 \text{ mm}$, $s/t = 0.2$, $L/a = 1.5$) had the perforated plate geometry. Almost the same efficiencies had the tube channels in a solid block ($\eta = 0.895$ for $d = 0.126 \text{ mm}$ and $L/a = 5.99$) and the stack of solid plates ($\eta = 0.902$ for $t = 0.126$ and $L/a = 5.99$) geometries. Packed beds were characterized by some smaller efficiency: $\eta = 0.823$ for $d = 0.316 \text{ mm}$ and $L/a = 3$ for loose packed particles and $\eta = 0.82$ for $d = 0.398 \text{ mm}$ and $L/a = 3.78$ for sintered particles. As one can see, the optimum aspect ratio of hole and particle diameters can be quite different. It was also established that lower operational frequencies led to higher efficiency, which can be related to increasing the effective amount of magnetic material.

11.2.2 Active magnetic regenerator refrigerators

In active magnetic regenerator (AMR) refrigerators magnetic material serves not only as a refrigerant providing temperature change as a result of adiabatic magnetization or demagnetization, but also as a regenerator for heat transfer fluid (van Geuns 1968, Steyert 1978a, Barclay and Steyert 1982b). One of the first constructions of magnetic refrigerator using AMR principle was suggested by van Geuns (1968). Figure 11.9(a) illustrates a schematic of an AMR refrigerator. A typical AMR refrigerator should include the following parts: a magnet, a regenerator bed with magnetic material, hot and cold heat exchangers, and a displacer or other device providing heat transfer fluid flow back and forth through the regenerator bed. An AMR cycle consists of two adiabatic steps (magnetization/demagnetization) and two isofield steps (corresponding to the heat transfer fluid flow through the regenerator). Consider the case when the heat capacity of the regenerator is infinite, so the heat capacity of the heat transfer fluid is much less than that of the regenerator, and that is why a temperature profile inside the regenerator in a steady regime does not change over the heat transfer fluid flow period. A simplified shape of the temperature profile inside the regenerator bed is shown in figure 11.9(b). At the first step of the cycle there is no fluid flow in the refrigerator, the displacer is in the right-most position (heat transfer fluid is in the cold head exchanger at the temperature T_{cold}) and the magnetic material is adiabatically magnetized, which causes a rise of its temperature on the value of the magnetocaloric effect (ΔT_{cold} at the cold end and ΔT_{hot} at the hot end). Then on the second step (warm blow step) the heat transfer fluid is forced by the displacer to pass through the regenerator from cold to hot heat exchanger at the constant magnetic field. This process corresponds to the upper line in figure 11.9(b). The fluid enters the regenerator at the temperature of T_{cold} and since the regenerator bed temperature rises

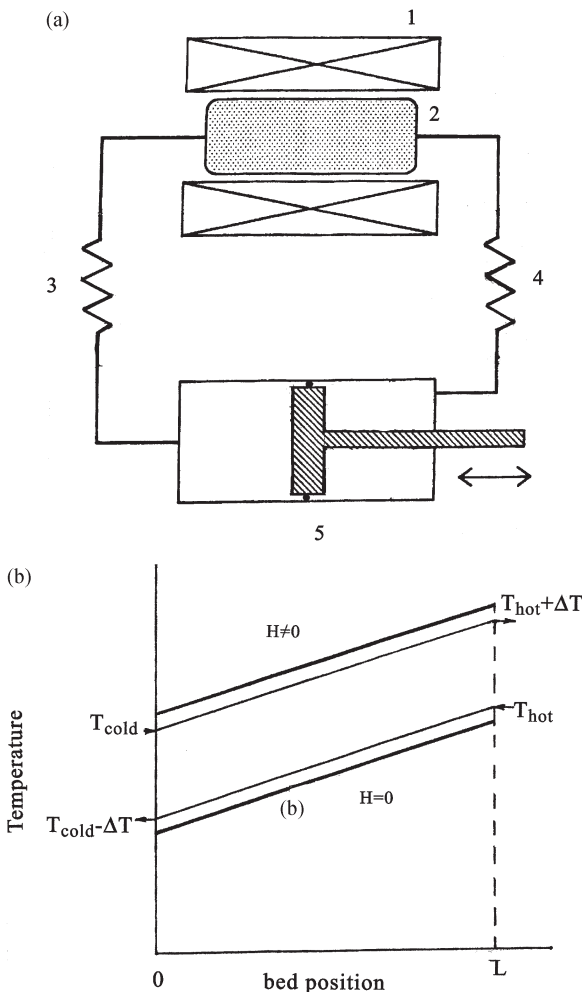


Figure 11.9. (a) Schematic drawing of AMR refrigerator: (1) magnet; (2) regenerator bed with magnetic material; (3) cold heat exchanger; (4) hot heat exchanger; (5) displacer. (b) Simplified temperature profiles inside the regenerator bed in AMRR: —, solid magnetic material, —, heat transfer fluid.

going from cold to hot end, the fluid temperature rises too, exiting the bed at the temperature $T_{hot} + \Delta T_{hot}$, higher than the temperature of the hot heat exchanger T_{hot} (it is assumed that there is an infinite heat transfer between the fluid and the solid magnetic material of the regenerator). Passing through the hot exchanger, the fluid temperature decreases to T_{hot} and the heat is rejected in the hot exchanger with a rate

$$\dot{Q}_h = \dot{m}_f C_f \Delta T_{hot} \quad (11.17)$$

where \dot{m}_f is the heat transfer fluid mass flow rate and C_f is the fluid heat capacity. On the third step the displacer is in the left-most position, the fluid flow is stopped and the regenerator bed is adiabatically demagnetized. Then on the final fourth step (cold blow step) the heat transfer fluid flow proceeds from the hot to the cold end—this process corresponds to the lower line in figure 11.9(b). The fluid enters the regenerator at the temperature T_{hot} , which is decreased at the regenerator exit down to the temperature of $T_{\text{cold}} - \Delta T_{\text{cold}}$, lower than T_{cold} , due to the heat exchange between the regenerator material and the fluid in the bed. Passing through the cold heat exchanger the fluid absorbs heat with the rate \dot{Q}_c , which determines the heat refrigeration capacity of the refrigerator

$$\dot{Q}_c = \dot{m}_f C_f \Delta T_{\text{cold}}. \quad (11.18)$$

Repetition of the cycle causes cooling at the cold end and warming at the hot end, because the heat is taken at the cold end and rejected at the hot one.

Cross *et al* (1987) and Reid *et al* (1994) considered an ideal AMR refrigeration cycle in which only reversible entropy flow from cold to hot end exists and there is no entropy production. This implies the condition of infinity of the thermal mass of the regenerator, an infinite heat transfer rate between the solid magnetic material and heat transfer fluid in the regenerator, and constancy of the fluid heat capacity over the refrigerator working temperature range. In this case one can write from equations (11.17) and (11.18) and from the requirement of conservation of the entropy flow following from the second law of thermodynamics

$$\frac{\dot{Q}_h}{\dot{Q}_c} = \frac{\dot{m}_f C_f \Delta T_{\text{hot}}}{\dot{m}_f C_f \Delta T_{\text{cold}}} = \frac{T_{\text{hot}} \Delta S}{T_{\text{cold}} \Delta S}. \quad (11.19)$$

Under the condition of the conservation of the fluid mass in the cycle it follows from equation (11.19) that, in an ideal AMR cycle with no entropy production, the following relation between the adiabatic temperature changes (MCE) ΔT_{cold} and ΔT_{hot} and absolute temperatures T_{cold} and T_{hot} at the cold and hot ends of the regenerator should be fulfilled

$$\frac{\Delta T_{\text{hot}}}{\Delta T_{\text{cold}}} = \frac{T_{\text{hot}}}{T_{\text{cold}}}. \quad (11.20)$$

Cross *et al* (1987) stated that the condition determined by equation (11.20) sets the optimum MCE on the temperature ($\Delta T(T)$) profile not only at the cold and hot ends of the regenerator but also inside the regenerator, because there is a constant entropy flux in the regenerator in the reversible case. It is clear from equation (11.20) that the optimum $\Delta T(T)$ profile is linear dependence of ΔT on T . According to Cross *et al* (1987) in the nonideal cycle the effect of the uniform generation of the entropy

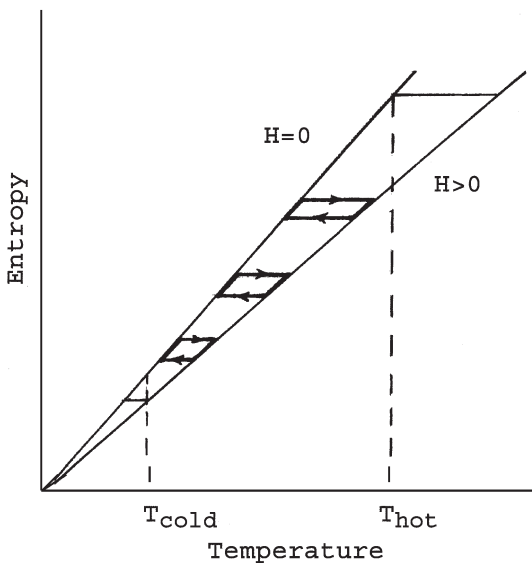


Figure 11.10. S - T diagram of the AMR refrigeration cycle.

throughout the regenerator can be taken into account by adding extra terms to ΔT_{cold}

$$\Delta T_{\text{cold}}(\text{nonideal}) = \Delta T_{\text{cold}} + \Delta T_{\text{SF}} + \Delta T_{\text{w}} \quad (11.21)$$

where ΔT_{SF} is the temperature difference between solid and fluid due to finite heat transfer and ΔT_{w} is the temperature change of the magnetic material related to its finite thermal mass. So the entropy production in the real nonideal AMR cycle should cause the change of ΔT on T dependence slope.

Cross *et al* (1987) showed, on the basis of equation (11.20), that ΔS_M in the AMR cycle should be directly proportional to T . So in the simple case of $S(T)$ dependences in the form of straight lines, the AMR cycle in S - T coordinates can have the shape shown by figure 11.10. According to Barclay (1991) and DeGregoria *et al* (1992) the elements of magnetic material in the AMR refrigerator working in the regime described above follow nonregenerative Brayton cycles, which are connected by the heat transfer fluid (see figure 11.10). The elements can also follow Carnot, Ericsson or some intermediate cycles if the work regime is changed—for example, if the magnetization/demagnetization stage is conducted under heat flow. Taussing *et al* (1986) assumed that the AMR cycle can be considered as consisting of a series of cascaded cycle refrigerators presented by the elements of the active magnetic regenerator. Such a scheme should provide constant entropy flow through the regenerator necessary for suggesting that equation (11.20) is valid inside

the regenerator. However, Hall *et al* (1996) later showed that such a cascaded approach is incorrect. Their arguments were as follows. Each solid element of the regenerator does not directly pump heat to the next-neighbour solid element, but all elements are accepting or rejecting heat to the heat transfer fluid at the same time and are coupled indirectly through the fluid. So the adjacent solid elements execute overlapping cycles, which is essentially different from the situation in the cascaded systems. Based on these point of view Hall *et al* (1996) also argued that the requirement of equation (11.20) should not be satisfied inside the regenerator, although it is still applicable at the boundaries of the regenerator. This implies that a linear $\Delta T(T)$ profile is not strictly required inside the regenerator bed for a reversible cycle, and furthermore there is no unique profile satisfying the zero entropy production criterion and there is an infinite number of such profiles. Based on the fact that the area inside thermodynamic cycle is equal to the work input in the cycle and is also proportional to the magnetocaloric effect, Hall *et al* (1996) gave another constraint on the $\Delta T(T)$ profile form in addition to the boundary conditions (11.20)

$$\dot{W}_i = \int f(\Delta T(T)) dT \quad (11.22)$$

where function $f(\Delta T(T))$ depends on the magnetic material properties and peculiarities of the heat transfer process between the magnetic material and the fluid.

Hall *et al* (1996) also considered the constraints imposed on the spatial distribution of the magnetocaloric effect ($\Delta T(r)$) inside the regenerator bed. It was shown that deviation of the $\Delta T(r)$ from the near-linear temperature profile in ordinary regenerators should be small because the magnetic work input weakly changes the energy of the system and is evenly distributed inside the regenerator. Entropy generation in the regenerator due to the finite heat transfer between the solid and the fluid was shown to be minimized if the exponent n in the general temperature profile $T(r) = ar^n$ (a is a constant) inside the regenerator is less than unity. Another constraint for the $\Delta T(r)$ profile was obtained from an analysis of relation between the input magnetic work and heat flow between the solid and the fluid in real regenerator and has the form

$$\frac{d\Delta T}{dT} > -1. \quad (11.23)$$

Equation (11.23) states that for the acceptable $\Delta T(r)$ dependence the MCE should not decrease by more than one degree per degree.

For modelling of the operation of AMR refrigerators with the packed regenerator bed the equations following from consideration of the energy conservation relations over the element of the regenerator assuming the absence of axial heat conduction are used (DeGregoria 1992, Matsumoto

and Hashimoto 1990)

$$L \frac{\partial T_f}{\partial t} = N_{tu}(T_b - T_f) \quad (11.24)$$

$$\frac{\partial T_b}{\partial t} = \frac{N_{tu}}{\Phi} (T_f - T_b) \quad (11.25)$$

where N_{tu} is the number of heat transfer units (see equation (11.14)), L is the regenerator bed length, T_b and T_f are the temperatures of the regenerator bed and the fluid, x and t are axial position and time, Φ is the heat capacity ratio of the fluid to bed

$$\Phi = \frac{m_b C_b(H, T)}{\dot{m}_f C_f \tau_f} \quad (11.26)$$

m_b is the bed mass, $C_b(H, T)$ is the bed heat capacity and τ_f is the time period of the fluid flow (blow period). As one can see this model is one-dimensional and allows temperature profiles to be obtained inside the regenerator along the axial direction. Equations (11.24) and (11.25) are solved numerically, in particular, by finite difference method. DeGregoria (1992) assumed the infinite regenerator bed mass, which allowed elimination of time dependence and essentially simplifies the calculations.

It should be noted that there are three possible AMR operating regimes, differing in the ratio of the thermal mass (product of mass on the heat capacity) values of the magnetic material and heat transfer fluid. Considered above was the case where the thermal mass of the regenerator magnetic material is higher than that of the fluid. It is realized, in particular, for the case of helium as a heat transfer fluid at relatively high temperatures (above 20 K). Another limiting case is when the thermal mass of the fluid is much higher than that of the regenerator. In this case the fluid serves as a regenerator for the magnetic material in the bed, and the AMR device becomes a magnetic refrigerator in which the magnetic material just executes a regenerative magnetic cycle (for example, Ericsson or Brayton cycles). Such a regime was used in the AMR refrigerator operating in the temperature range from 4.7 to 1.8 K with GGG as a working material and ^4He at 30 atm as a heat transfer fluid. The heat capacity of the liquid helium in this device is several times higher than that of the magnetic material. Numerical calculations showed that such a refrigerator should have a cooling power of 100 W with an efficiency of 40–50% of Carnot. In the intermediate region between these two limit cases, where thermal masses of the magnetic material and the fluid are comparable, and which can be realized for helium as a heat transfer fluid in the temperature region between 4 and 20 K, the analysis of AMR refrigerator work is the most complicated.

The practical designs of the AMR refrigerators can be divided into two groups. In the first group the heat transfer fluid flow is accomplished in a reciprocating manner with the help of the displacer, and in the second the

heat transfer fluid flow is realized in a steady regime by a pump. The reciprocating apparatus of the first type were considered and tested, for example, in the works of Zimm *et al* (1995 1996), Johnson and Zimm (1996), Kral and Zimm (1999), DeGregoria *et al* (1992) and Wang *et al* (1995).

Zimm *et al* (1995 1996) proposed an AMR refrigerator design in which two regenerator beds with magnetic materials were moved in a reciprocating manner in a superconducting magnet, provided magnetization/demagnetization of the magnetic material and the heat transfer fluid flow was produced by the displacer. The regenerator was designed to work between 10 and 3.5 K. The hot heat exchanger was cooled by a conventional G-M cryocooler operating at about 10 K. The overall design and schematic diagram of the AMR refrigerator are shown in figure 11.11. The magnetic field of 30 kOe was created by the Nb₃Sn superconducting solenoid conductively cooled by another G-M cryocooler to about 10 K. Two packed beds filled with ErNi (Curie temperature of about 10 K) particles were used as the active magnetic regenerators. The beds were made of G-10 glass–epoxy composite carrier and had a length of 8 cm and cross-section of 35 cm² with the porosity of the ErNi material being 0.4. The design of the bed assembly is shown in figure 11.12. Heat transfer fluid (helium gas in this case) is brought to the bed by two passages (inlet and outlet), one of which bypasses the other bed (see figure 11.12). This design made it possible to take the cold heat exchanger out of the magnetic field region. A room temperature drive reciprocated the bed assembly so that the beds were alternately placed inside the bore of the superconducting magnet. When one bed was inserted into the magnetic field the other bed was extracted from the field. Such a scheme allows one to cancel the magnetic forces, recover the magnetic work and reduce magnetic flux changes in the magnet, resulting in more efficient operation of the device. The necessary fluid flow was provided by a bellows displacer moving by a room temperature actuator. The helium gas pressure was chosen to be no more than 0.3 atm. At such pressure in the working temperature range, the heat capacity of the magnetic material was much higher than that of the heat transfer fluid. A bellows displacer forced helium gas to flow through the regenerator in forward and back directions. The working cycle in this device is analogous to that described above in connection with figure 11.9. The hot heat exchanger consisted of two parts connected by a thermal bus. The gas flow between the moving beds and stationary heat exchangers was provided with the help of flexible metal bellows. The whole system was surrounded by a thermal shield connected to the upper stage of the G-M cryocooler and placed in turn to a vacuum vessel. Modelling calculations predicted the device to have a cooling power of 1.6 W at 3.5 K for a helium flow of 1.3 g/sec and a helium pressure of 0.15 atm with a COP of about 30% of Carnot, and 3.2 W cooling power at 4.4 K with a COP of 52% of Carnot for a helium pressure of 0.3 atm (Zimm *et al* 1995). It was also shown that the cooling power should

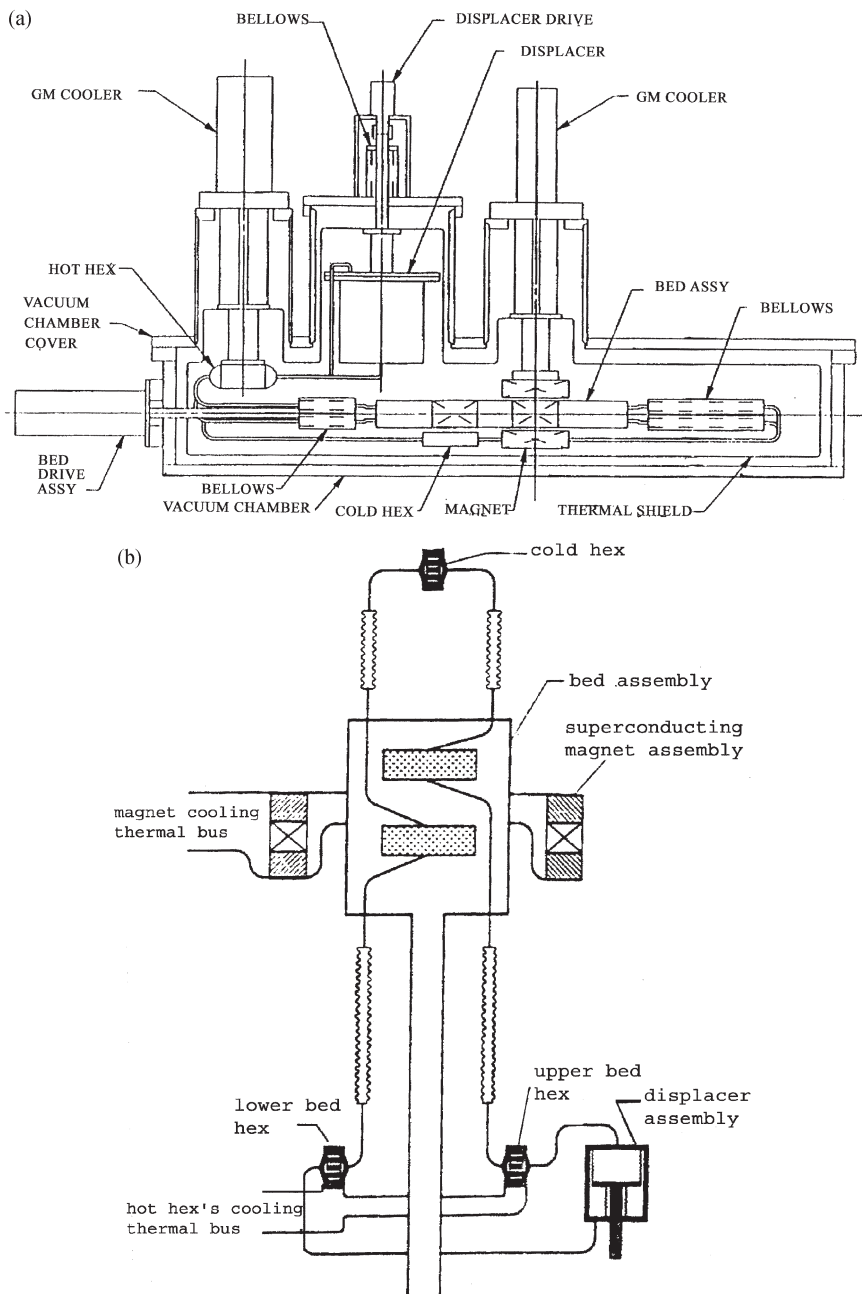


Figure 11.11. Reciprocating AMR refrigerator working between 3.5 and 10 K: (a) overall design; (b) schematic diagram explaining operational principle of the device (Kral and Zimm 1999, Zimm *et al* 1995).

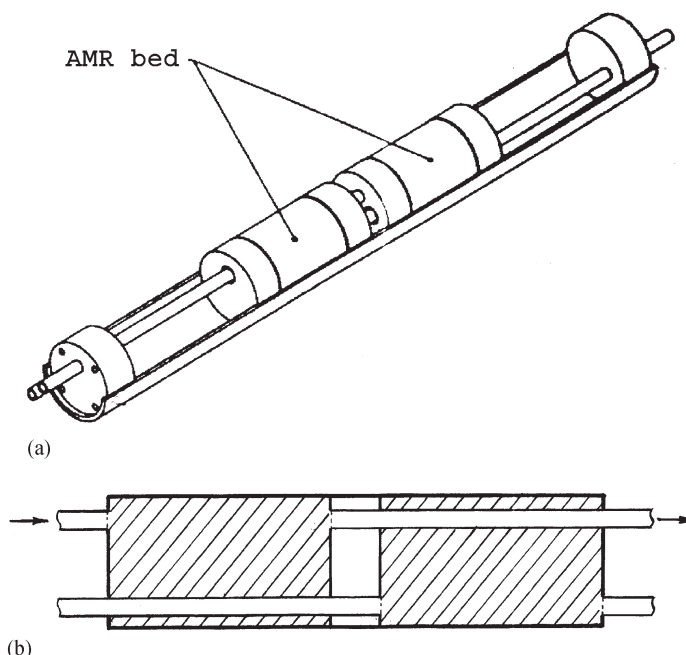


Figure 11.12. The regenerator bed assembly design for the AMR refrigerator operating between (a) 3.5 and 10 K and (b) its schematic diagram (a magnetic material is contained in the shaded region) (Zimm *et al* 1995, Johnson and Zimm 1996).

linearly depend on mass flow rate and should be relatively insensitive to the hot sink temperature. These predictions of the model were confirmed by experimental measurements on the refrigerator with this design made by Kral and Zimm (1999) for hot sink temperatures in the range of 9–13 K. The device was tested at different magnetic fields from 10 to 22.5 kOe, helium pressure of 0.5 atm and operating periods of 16 and 24 sec. The minimal no-load temperature of about 4.2 K was achieved for the magnetic field of 22.5 kOe and the cooling power in this case reached 1 W at about 6 K. An AMR refrigerator of the same design with a liquid nitrogen bath as the hot heat sink and helium as the heat transfer fluid was developed and tested by Zimm *et al* (1996). Here the magnetic field of 70 kOe was produced by an NbTi solenoid working at persistent mode and immersed into liquid helium in an annular dewar. 2 kg of 150 µm GdNi₂ particles (Curie temperature 75 K) in each of two regenerator beds was used as a refrigerant. According to Zimm *et al* (1996), in the no-load regime the temperature span from 82 K at the hot end down to 44 K in the cold heat exchanger was achieved. The cooling power of 2 W at 56 K and a maximum cooling power of 25 W at 76 K were obtained for a 81 K hot heat exchanger.

DeGregoria *et al* (1992), Zimm and DeGregoria (1993) and Wang *et al* (1995) used designs analogous to that described above, but a somewhat different design of the reciprocating AMR refrigerator, where two regenerator beds were fixed but the superconducting solenoid moved in order to alternately magnetize and demagnetize magnetic material in the beds. In the refrigerator of DeGregoria *et al* (1992), a magnetic field up to 70 kOe was created by NbTi superconducting solenoid. The regenerator bed had a length of about 9 cm with a cross section of 2.84 cm^2 and was filled with ground and sieved $\text{Er}_x\text{Gd}_{1-x}\text{Al}_2$ with particle sizes between 20 and 40 μm and porosity of 0.44. The period of the total refrigeration cycle was 10 s and a gas flow during testing was changed up to 0.59 g/s. For a magnetic field of 10 kOe, gas flow of 0.59 g/s and hot heat exchanger temperature of 19.25 K, a minimal no-load temperature of 9 K was achieved. GdNi_2 in the form of particles with dimensions between 10 μm and 20 μm was also employed in the refrigerator. In this case the operational period was 2.5 s and the hot heat capacity temperature was 77 K. The no-load temperature span for the magnetic field of 50 kOe was found to be 44 K (33 K was the cold heat exchanger temperature).

An example of the AMR refrigerator in which the heat transfer fluid flow is realized in steady manner is a rotary (wheel) AMR refrigerator (Steyert 1978a,b, Barclay 1991). It is schematically shown in figure 11.13. It consists of a rotating ring filled with porous magnetic regenerator material adapted for presumably radial heat transfer fluid flow with corresponding drive motor, a heat transfer fluid loop with hot and cold heat exchangers, a pump providing the fluid flow, and a magnet for magnetizing the part of the ring which is in the high-field region. Due to the ring rotation the magnetic material at the given element of the ring periodically magnetizes and demagnetizes adiabatically, which causes its heating and cooling due to the magnetocaloric effect. With the hot and cold head exchangers arrangement shown in figure 11.13 the inner part of the ring will be at the

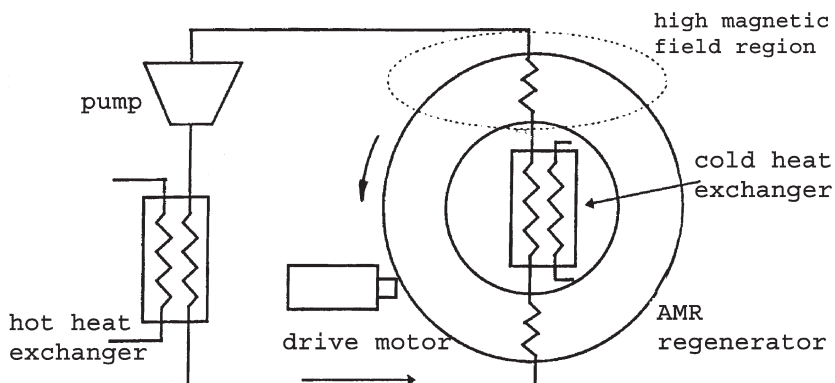


Figure 11.13. Schematic diagram of a rotary AMR refrigerator (Hall and Barclay 1998).

temperature T_{cold} and the outer part at the temperature T_{hot} , and the magnetic material serves not only as a refrigerant but also as a regenerator for the heat transfer fluid. So this apparatus works like AMR refrigerator in which the magnetic material segments in the ring execute the AMR refrigeration cycle, thus providing continuous refrigeration. The advantage of AMR refrigerators with steady unidirectional heat transfer fluid flow consists of the absence in this device of so-called dead volume inherent in the AMR refrigerators with reciprocating fluid flow. In the latter devices some amount of the heat transfer fluid is always in the connection lines between different parts of the refrigerator and never flows through the full loop, which reduces the efficiency of the refrigerator. It also should be noted that there is also steady magnetic material mass flow inside the magnet in the rotary AMR refrigerator. This solves problems related to changing of the magnetic field flux in the magnet if the magnetic material is periodically inserted and extracted from the magnet. The rotary AMR refrigerator is also characterized by low eddy current generation (Hall and Barclay 1998). The optimal operation of the rotary AMR refrigerators is determined by both magnetic material mass flow through the magnet and the heat transfer fluid flow through the magnetic regenerator (wheel) (Barclay 1991). The efficiency of the rotary AMR refrigerator was considered by Hall and Barclay (1998). It was shown that with the most optimistic assumptions about the refrigerator components performances an efficiency of 60% could be achieved for the temperature span from 100 to 300 K. A design for a rotary AMR air conditioner was proposed by Waynert *et al* (1994).

Another example of the AMR refrigerator with unidirectional heat transfer fluid flow is a reciprocating AMR refrigerator apparatus proposed by Lawton *et al* (1999). In this device two magnetic beds conduct reciprocating motion in a magnet as it takes place in the refrigerators of Zimm *et al* (1995, 1996) considered above. However, in contrast to the regarded designs, flow of the heat transfer fluid here is provided by a pump in one direction, which eliminates ineffectiveness related to dead volume. On the basis of the design proposed by Lawton *et al* (1999) a near-room temperature reciprocating AMR refrigerator was constructed and tested by Zimm *et al* (1998). The principle of its functioning is illustrated by figure 11.14. The beds are by turns moved in and out of the room-temperature bore of the superconducting NbTi solenoid immersed in liquid helium in a dewar and working in the persistent mode. Water was used as a heat transfer fluid. The working cycle of the device started with cooling of water by blowing it through the demagnetized bed located inside the magnetic area (this bed is in the bottom position in figure 11.14). Then the water was passed through the cold heat exchanger, picking up the thermal load from the cooling object. After this the water was blown through the magnetized bed located in the magnetic field area, where it absorbed the heat evolved in the magnetic material of the magnetized bed due to the MCE. Next the water passed

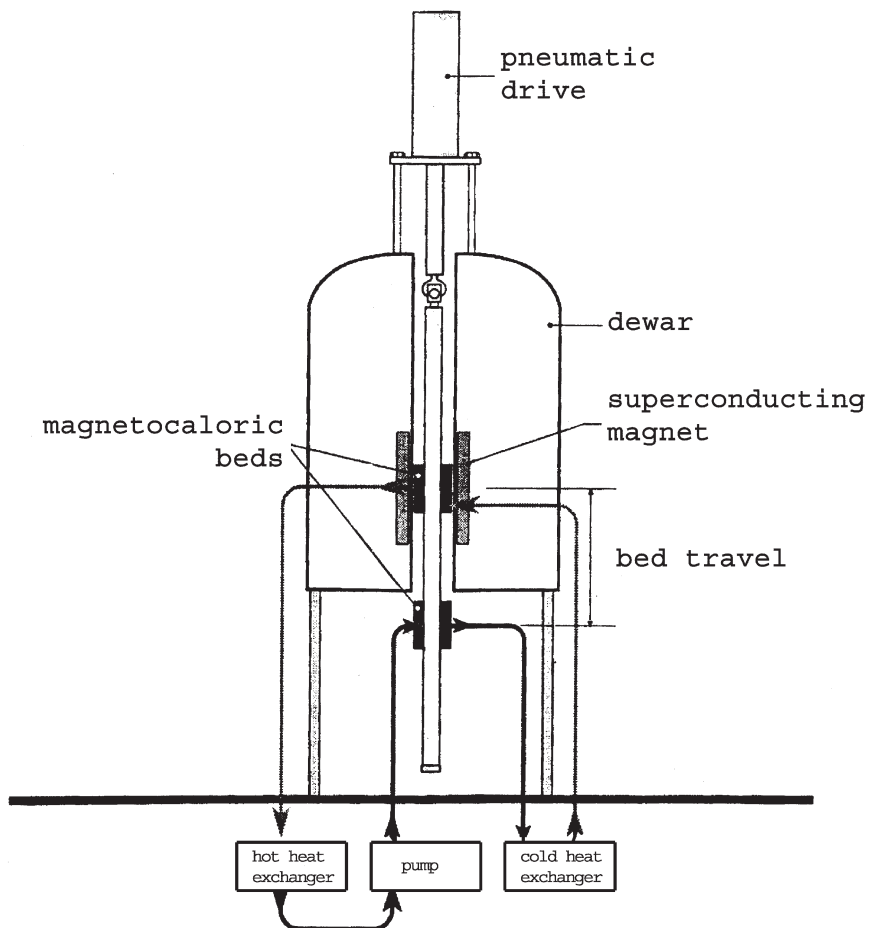


Figure 11.14. Design of the near-room-temperature reciprocating AMR refrigerator (Zimm *et al* 1998, Gschneidner *et al* 2001).

through the hot heat exchanger, giving up the heat absorbed from the magnetized bed. The cycle was finished by removing the magnetized bed from the magnet and replacing it by the demagnetized one. During the movement of the beds the water flow was stopped. Then the upper bed was set in the position out of the solenoid and above it, the heat flow circuit from the pump to the cold heat exchanger (in figure 11.14 it is connected to the lower bed) was switched to the upper bed by a switching valve of special design, and the cycle was repeated with the same heat transfer fluid flow direction in the refrigerator (although in the regenerator beds the flow direction was reversed). The superconducting solenoid produced a field up to 50 kOe. Each regenerative bed was composed of 1.5 kg of Gd

spheres with diameter between 150 and 300 µm made by the plasma-rotating electrode process. The device operated with a total cycle time of 6 s (0.17 Hz) and a fluid flow rate time of 2 s in one direction. The process of the bed insertion into the magnet took 1 s and the maximum net magnetic force was about 2500 N.

The heat capacity of water used as a heat transfer fluid and trapped in the regenerator beds (porosity of 0.36) was close to the gadolinium heat capacity, which implied that the device operated in the regime intermediate between limit cases, when the heat transfer fluid serves as a regenerator and when the magnetic material serves as a regenerator. However, it was experimentally shown that the flow rate up to 3 l/min did not essentially change the temperature profile inside the regenerator. Essential changes of the temperature profile during the water blow period corresponding to the intermediate regime were observed for a flow rate of 6 l/min. The observed decrease of the cooling power of the device in the high flow rate range, which led to the appearance of a maximum on cooling power on flow rate dependence, was explained by this effect. For a magnetic field of 50 kOe, such a maximum corresponded to a flow rate of about 4.5 l/min.

The cooling power of 600 W was reached by the near-room temperature reciprocating AMR refrigerator for a temperature span of 10 K, a magnetic field of 50 kOe and a flow rate of 5 l/min. The efficiency of the device was less than 50% of Carnot. The cooling power and efficiency decreased with temperature span increasing, which was related by the authors to gadolinium magnetocaloric properties. When the seal friction in the elastomer seals around the magnetocaloric beds was subtracted, the maximum efficiency was 60% of Carnot. The maximum achieved temperature span was 38 K with a cooling power of 120 W. For a magnetic field of 15 kOe (this value can be produced by a NdFeB permanent magnet), a flow rate of 4 l/min, and a cooling power of 180 W, an efficiency of 20% was obtained for the temperature span of 16 K (Gschneidner *et al* 1999).

An important part of a magnetic refrigerator is a magnetic system for magnetization/demagnetization of the refrigerant. At present, superconducting magnets cooling with liquid helium are used in magnetic refrigerators. It is unacceptable for such applications as domestic refrigerators, automotive conditioners, etc. and inconvenient for other applications. Using permanent magnets can solve this problem. However, it is difficult to achieve a magnetic field higher than 15 kOe even with the magnetic material having the highest values of maximum energy production at present, NdFeB. This reduces the value of the magnetocaloric effect which can be achieved in the refrigeration device and its cooling power and efficiency. Lee and Jiles (2000) proposed new permanent magnet design. The design was based on a hollow cylindrical permanent magnet array consisting of permanent magnet segments in which magnetization vectors were arranged according to the rotation theorem of Halbach (1980). It was shown that in order to increase magnetic field

inside the magnet gap the following modifications of the basic design should be made: the cylindrical form of the magnet cross section should be changed to an ellipsoidal one (the maximum magnetic flux density should occur at an ellipticity of 2), magnetic flux concentrators should be included in the array close to the magnet air gap (FeVCo was proposed for that) and the magnet should be surrounded by a soft iron magnetic shell to provide a flux return path. According to calculations, such a design can provide a magnetic field of about 30 kOe in $23.5 \text{ mm}^2 \times 15.2 \text{ mm}$ pole gap for NdFeB with 12 kOe remanence.

11.2.3 Magnetically augmented regenerators in gas refrigerators

As shown in section 11.1, using magnetic materials with high magnetic heat capacity in the low-temperature region in passive regenerators of gas cryocoolers allows one to essentially increase performances of such devices. Jeong and Smith (1994) proposed to magnetize and demagnetize the magnetic material in the regenerator in coordination with different stages of the gas cycle in order to match heat capacities of the regenerator material and heat transfer fluid (helium gas). Magnetic material in this case ideally does not change its temperature during the cycle, magnetic work is not done, and the only result of using such a scheme is the enhancement of the regeneration within a conventional gas cycle. It was shown that such a design, called a magnetically augmented regenerator and proposed to be applied in G-M cryocoolers, can increase their efficiency. The modelling was made for gadolinium gallium garnet as a low-temperature stage regenerator material. Later Smith and Nellis (1995) suggested using magnetic material in the gas cycle not only for regeneration of a gas but also as a refrigerant, so that there are two working substances in such devices—gas and the magnetic material. Such devices were regarded by Smith and Nellis (1995), Nellis and Smith (1996) and Yayama *et al* (2000). Consider the principle of operation of G-M cryocooler with a magnetically augmented regenerator following Yayama *et al* (2000). The schematic diagram of the device is shown in figure 11.15. It comprises a compressor, two valves V_1 and V_2 , a regenerator with magnetic material, a magnet and a displacer (piston). A and B here denote high-pressure and low-pressure spaces, respectively. At the first stage a piston is at the bottom and high-pressure helium gas (heat transfer fluid) is introduced into the space A and the regenerator through the open valve V_1 . Then the magnetic material in the regenerator is demagnetized adiabatically so that its temperature decreases. At the third stage the helium gas is forced out of space A to space B through the regenerator by the piston (it is now in the top position), which causes helium gas cooling due to heat exchange between the regenerator and the gas. The process is performed under isobaric conditions with open valve V_1 . After that the valve V_1 is closed and the valve V_2 is opened, reducing the pressure in the space B and causing expansion of the

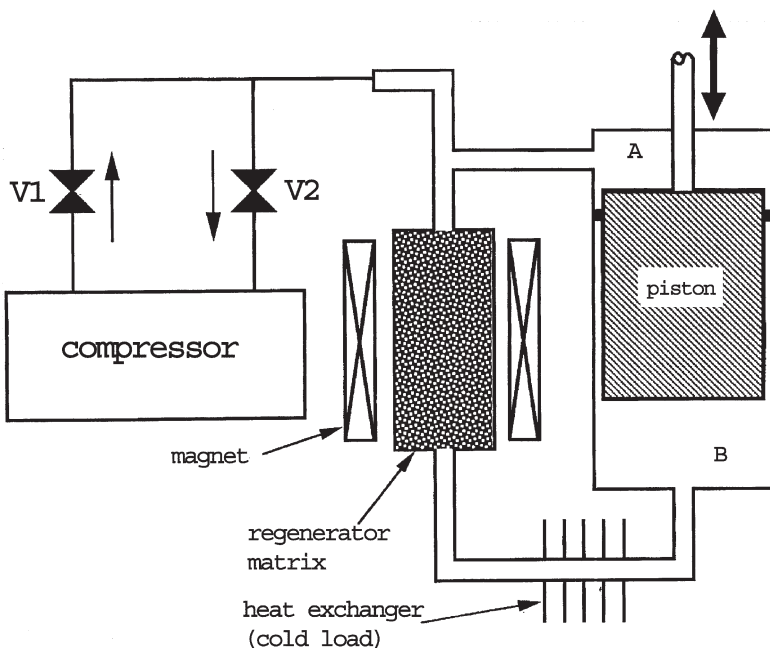


Figure 11.15. Schematic diagram of the G-M cryocooler with magnetically augmented regenerator (Yayama *et al* 2000).

helium gas, and removing heat from the cold load at the cold heat exchanger. At the fifth stage the magnetic material in the regenerator is adiabatically magnetized with its temperature increasing. At the final stage the displacer is moved back to the bottom and the helium gas is moved from space B to space A through the heat exchanger and hot regenerator. By this process the heat taken from the heat exchanger and the magnetic regenerator is transferred by the helium gas to the hot sink. So, one can see that in this cycle the magnetic material in the regenerator is used simultaneously as a regenerator for heat transfer fluid in the gas refrigeration process and as a refrigerant in the magnetic refrigeration process. It should be noted that in real G-M cryocoolers the displacer and regenerator are incorporated in one unit.

The device operation modelling made by Yayama *et al* (2000) for a regenerator of 2.8 cm diameter and 8.5 cm length filled with spherical ErNi particles with a diameter of 250 µm, high pressure of 20 atm and low pressure of 8 atm, helium flow rate 2 g/s and temperature span of the device between 4 and 30 K. The maximum cooling power of the device was determined to be 0.36 W at 4 K for a magnetic field of 50 kOe. For magnetic fields below 5 kOe, a cooling capacity of 0.31 W was obtained for the optimum magnetic field change between 2.2 and 4.2 kOe. Calculations of Nellis and Smith (1996) showed that a cooling capacity of 1.4 W at 4.2 K

can be achieved in the device using gadolinium gallium garnet as a magnetic material and operating with a hot sink at 12 K, low and high pressures of 3 and 6 atm, an operational frequency of 83 mHz and a magnetic field change between 10 and 40 kOe.

11.2.4 Hybrid magnetic working bodies

To provide effective operation of the magnetic refrigerator the magnetic material used as a working body in regenerative cycles should satisfy special requirements superimposed on $\Delta S_M(T)$ and $\Delta T(T)$ dependences in a wide temperature range. In the case of the Ericsson and Brayton cycles it is the requirement about constancy of the magnetic entropy change ($\Delta S_M(T) = \text{const.}$) between T_{cold} and T_{hot} , and in the case of an AMR cycle they are conditions (11.20), (11.22) and (11.23). At the same time $\Delta S_M(T)$ and $\Delta T(T)$ dependences of magnetic materials are characterized by peaks near magnetic phase transition temperatures and rapid decrease of ΔS_M and ΔT values when moving away from these temperatures. It is very difficult to fabricate the single phase material with necessary $\Delta S_M(T)$ and $\Delta T(T)$ dependences. As was shown by Reid *et al* (1994), mixing of the particles of different magnetic materials may cause an essential entropy generation in such a composite working body during the refrigeration cycle. It is related to the difference between the temperatures of the adjacent particles of the different materials, since they exhibited different magnetic entropy change and magnetocaloric effect in a given magnetic field. Hashimoto *et al* (1987) suggested using complex (hybrid) magnetic material comprising layers of different magnetic materials in necessary proportion and arranged in necessary order determined by their magnetic ordering temperatures. The hybrid material consisting of layers of $\text{ErAl}_{2.15}$, $\text{HoAl}_{2.15}$ and $(\text{Ho}_{0.5}\text{Dy}_{0.5})\text{Al}_{2.15}$ (their Curie temperatures lie in the interval from 10 to 50 K) in a molar ratio of 0.312:0.198:0.490 was prepared in order to obtain constant ΔS_M in the temperature range from 10 to 50 K. Experimental measurements confirmed almost constant ΔS_M behaviour in the required temperature range. Tishin (1990d-f) and Burkhanov *et al* (1991) for the first time considered complex magnetic bodies on the basis of rare earth alloys Gd-Tb, Gd-Dy and Tb-Dy in order to obtain maximum refrigerant capacity—this question will be considered later, in section 11.3.

The problem of determination of the required prorate of the different magnetic materials in the hybrid material was considered by Dai (1992) and Smaïli and Chahine (1996 1997 1998). Dai (1992), based on the requirement of minimal heat release on the regenerative parts of the Ericsson cycle (this automatically implies $\Delta S_M = \text{const.}$ in the temperature interval of the cycle), considered the case of the magnetic working body consisting of Gd and Tb and suitable for the temperature interval from 240 to 300 K.

For $\Delta H = 20$ and 80 kOe the materials with $0.726:274$ and $0.740:0.260$ of Gd:Tb were found to be optimal for Ericsson cycle.

Smaïli and Chahine (1996, 1997) regarded the hybrid magnetic material for an Ericsson cycle consisting of layers of n magnetic materials in the $y_1:y_2:\dots:y_n$ proportions with different magnetic transition temperatures $T_0^1, T_0^2, \dots, T_0^n$ appropriately arranged in the required temperature range from T_{cold} to T_{hot} . The magnetic entropy change of the material was presented as

$$\Delta S_M = \sum_{j=1}^n y_j \Delta S_{Mj} \quad (11.27)$$

where ΔS_{Mj} is the magnetic entropy change of the j th material. The requirement $\Delta S_M = \text{const.}$ can be in this case written as

$$\sum_{j=1}^n y_i [\Delta S_{Mj}(T_0^{i+1}) - \Delta S_{Mj}(T_0^i)] = 0. \quad (11.28)$$

By combination of equation (11.28) with the condition $\sum_{j=1}^n y_i = 1$, the following equations set was obtained:

$$\begin{bmatrix} \alpha_{11} & \alpha_{12} & \cdots & \alpha_{1n} \\ \alpha_{21} & \alpha_{22} & \cdots & \alpha_{2n} \\ \cdots & \cdots & \alpha_{ij} & \cdots \\ \alpha_{n1} & \cdots & \alpha_{nn-1} & \alpha_{nn} \end{bmatrix} \begin{bmatrix} y_1 \\ y_2 \\ \vdots \\ y_n \end{bmatrix} = \begin{bmatrix} 0 \\ 0 \\ \vdots \\ 1 \end{bmatrix} \quad (11.29)$$

where α_{ij} are determined in this case as

$$\alpha_{ij} = \begin{cases} \Delta S_{Mj}(T_0^{i+1}) - \Delta S_{Mj}(T_0^i) & \text{if } i \leq n-1, \\ 1 & \text{if } i = n. \end{cases} \quad (11.30)$$

The numerical solution of equation set (11.29) gives optimum values of y_i . By this method, a two-layered hybrid magnetic working body comprising Gd_{0.9}Er_{0.1} and Gd_{0.69}Er_{0.31} alloys for the temperature range from 225 to 280 K and magnetic working bodies consisting of up to five layers of Gd_{1-x}Dy_x alloys ($x = 0, 0.12, 0.28, 0.49, 0.70$) for the temperature range from 200 to 300 K were optimized. Experimental data for ΔS_M for (Gd_{0.9}Er_{0.1})_{0.56}(Gd_{0.69}Er_{0.31})_{0.44} material confirmed the results of calculations— ΔS_M was constant in the required temperature range.

This method was also applied by Smaïli and Chahine (1998) for optimization of the composition of the magnetic working body for an AMR refrigerator. In this case instead of constraint $\Delta S_M = \text{const.}$ suitable for the an Ericsson magnetic cycle, the following equation reflecting adiabatic magnetization operational conditions in the AMR cycle was used:

$$S(H = 0, T) = S(H \neq 0, T + \Delta T) \quad (11.31)$$

where S is the total entropy. Correspondingly S should be used in equation (11.27) instead of ΔS_M and equations (11.30) become

$$\begin{aligned}\alpha_{ij} = & S_j(H, T_0^{i+1} + \Delta T(T_0^{i+1})) - S_j(H, T_0^i + \Delta T(T_0^i)) \\ & - S_j(0, T_0^{i+1}) + S_j(0, T_0^i).\end{aligned}\quad (11.32)$$

Using the method described, Smaïli and Chahine (1998) optimized the hybrid magnetic working material consisting of Gd–Dy alloys to the desired $\Delta T(T)$ profile. This allowed them to calculate the parameters of an AMR refrigerator with different $\Delta T(T)$ profiles inside the regenerator. The desired profiles were described by a function

$$f(T) = k_T T_{\text{hot}} \left(\frac{T}{T_{\text{hot}}} \right)^\zeta \quad (11.33)$$

where k_T is a constant and ζ is an exponent ($\zeta \geq 0$). The constant k_T was determined by iteration procedure on the basis of given ζ , properties of the magnetic material and equations (11.27), (11.29) and (11.32). The profiles with ζ from 0 to 3 were used in the calculations. It was shown that there is no unique $\Delta T(T)$ profile for a reversible AMR cycle. Any monotone increasing profile was recognized to be suitable, but the profiles with $1 \leq \zeta \leq 2$ provided the maximum values of cooling power and COP.

11.2.5 Magnetic refrigerators working on the Ericsson cycle

One example of such a device is a magnetic refrigerator working near room temperature proposed by Brown (1976). Its schematic drawing and operational principle are shown in figure 11.16. The regenerator consists of a vertical column with fluid (0.4 dm^3 , 80% water and 20% alcohol), so that the fluid serves in this case as a regenerator for the magnetic material (refrigerant). The magnetic working material immersed in the regenerator consists of 1 mol of 1 mm thick Gd plates, separated by screen wire to allow the regeneration fluid to pass through in the vertical direction. The working material is held stationary in a water-cooled electromagnet while the tube containing the fluid oscillates up and down. The cold end hot heat exchangers are on the bottom and on the top of the column (they are denoted as load and cooling loop, respectively, in figure 11.16).

The first stage (figure 11.16(a)) is isothermal magnetization, with the working material in the upper position in the magnetic field of the electromagnet. During this stage the magnetic material rejects heat by the hot heat exchanger. Then, at a constant field of 70 kOe, the magnetic material is moved downwards (figure 11.16(b)). The field is then switched off and the magnetic material absorbs heat from the load at the temperature of the cold end of the device due to the magnetocaloric effect (Fig 11.16(c)). At the last stage the working material passes back through the regenerator

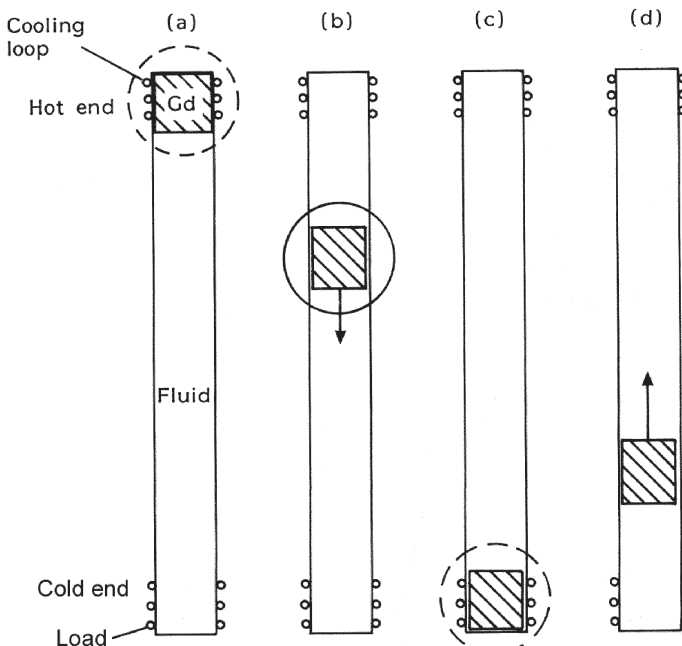


Figure 11.16. Magnetic regenerator proposed by Brown (1976). A solid circle indicates that the magnetic field is switched on, and a broken circle that the field is switched off (Brown 1976).

column (figure 11.16(d)). Then the cycle is repeated. If initially the regenerator fluid was at room temperature, after about 50 cycles the temperature at the top reached $+46^{\circ}\text{C}$ and the temperature at the bottom reached -1°C . The temperature gradient in this device is maintained in the regenerator column. In spite of the essential temperature span, the device was characterized by low cooling power. The main shortcoming of the device was the destruction of the temperature gradient in the regenerator under movement of the magnetic material through the column.

Matsumoto *et al* (1988) proposed an Ericsson magnetic refrigerator working in the temperature range from 20 to 77 K with lead as a regenerator. The magnetization/demagnetization in the device was performed by charging and discharging of the superconducting magnet, creating the field of 50 kOe. The operational principle of the device shown in figure 11.17 is analogous to that considered above to the refrigerator of Brown (1976) except that here the magnetic material (refrigerant) is fixed and the regenerator is moved (its moving stroke was 40 cm) up and down with respect to the magnetic material during the cycle. Helium gas was used as a heat transfer fluid to maintain the temperature of the hot end of the device. Figure 11.18 shows the overall design of the refrigerator without the driving motor. Two pieces of sintered

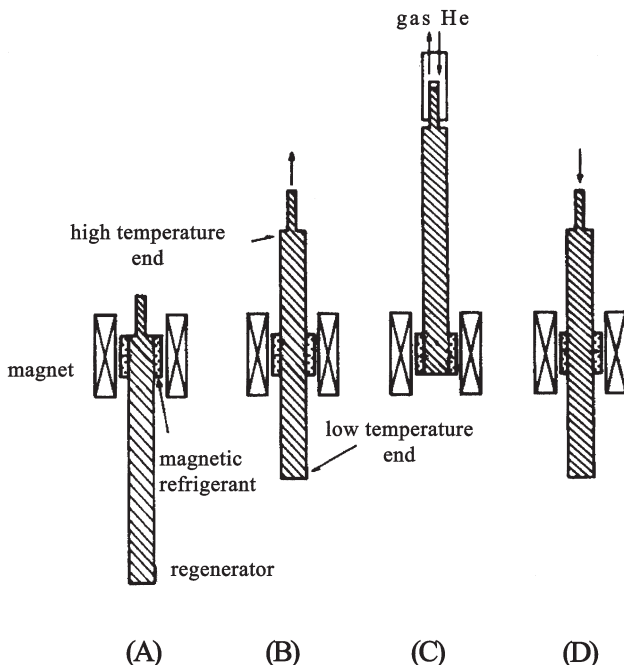


Figure 11.17. Operational principle of the Ericsson magnetic refrigerator with lead regenerator: (A) magnetization, (B) isofield cooling, (C) demagnetization, (D) isofield heating (Matsumoto *et al* 1988).

$\text{DyAl}_{2.2}$ with dimensions of $20 \times 80 \times 7$ mm were used as a magnetic working body. The regenerator consisted of hard lead (an alloy of lead and antimony) and had a volume of 377 cm^3 and a length of 49 cm. The heat transfer surfaces of the magnetic material and the regenerator were machined in order to provide better heat exchange. The magnetic material was pressed to the regenerator by a spring. The total cycle consists of 65 s for both isofield heating and cooling, 90 s for heat absorption, 80 s for heat rejection, and 45 s for magnet charge and discharge. The regenerator of the device with an initial temperature of 51 K after 11 cycles had a temperature of 58.7 K at the hot end and 50.3 K at the cold end.

11.2.6 Magnetic refrigerators working on the Carnot cycle

Below 15–20 K the nonregenerative Carnot cycle can be effective for use in magnetic refrigerators. This cycle is represented by rectangle ABCD in the $S-T$ diagram in figure 11.5. It consists of two adiabatic processes (magnetization and demagnetization) and two isothermal processes (magnetization and demagnetization). In the ideal Carnot cycle the heat Q_c absorbed from the cooling load (at temperature T_{cold}) and the heat Q_h rejected at the hot

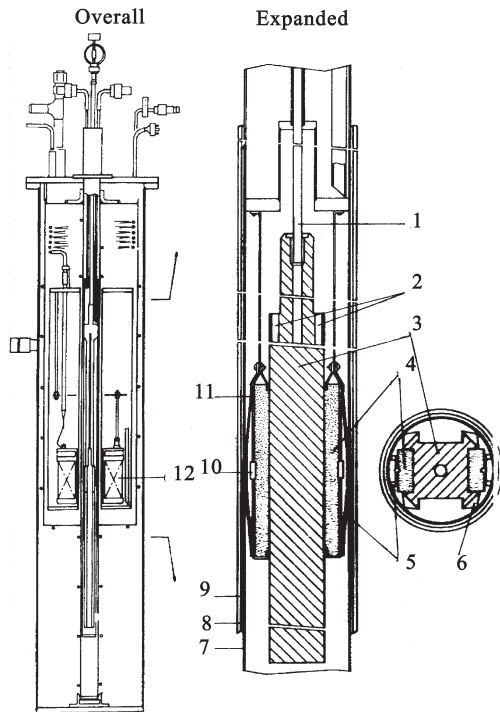


Figure 11.18. Overall design of the Ericsson magnetic refrigerator with lead regenerator: (1) driving rod; (2) hot heat exchanger; (3) regenerator; (4) magnetic working body; (5) holder spring; (6) regenerator guide; (7) can; (8) vacuum; (9) 77 K shield; (10) resistor thermometer; (11) magnetic material holder; (12) magnet (Matsumoto *et al* 1988).

sink (at temperature T_{hot}) can be represented as $T_{\text{cold}}\Delta S_M$ and $T_{\text{hot}}\Delta S_M$, respectively, where $\Delta S_M = S_2 - S_1$.

A Carnot-type refrigeration device was proposed in the work of Daunt and Heer (1949) and can be represented in general by the schematic diagram shown in figure 11.19. It comprises a magnetic working body (working material), two thermal switches and a magnet. The cycle starts at the point B in figure 11.5, where the working material is in contact with the heat reservoir, and the upper thermal switch is closed and the lower one is open. During isothermal magnetization (line BC in figure 11.5) the temperature of the working material is higher than the temperature of the heat reservoir T_{hot} and the heat Q_h is released to the reservoir. At the next step—adiabatic demagnetization—the magnetic field is partially removed with both upper and lower heat switches open. As a result of this process (line CD in figure 11.5) the temperature of the working material decreases. In the subsequent isothermal demagnetization (line DA in figure 11.5) the magnetic field is reduced to zero, and the lower heat switch is closed and the upper switch

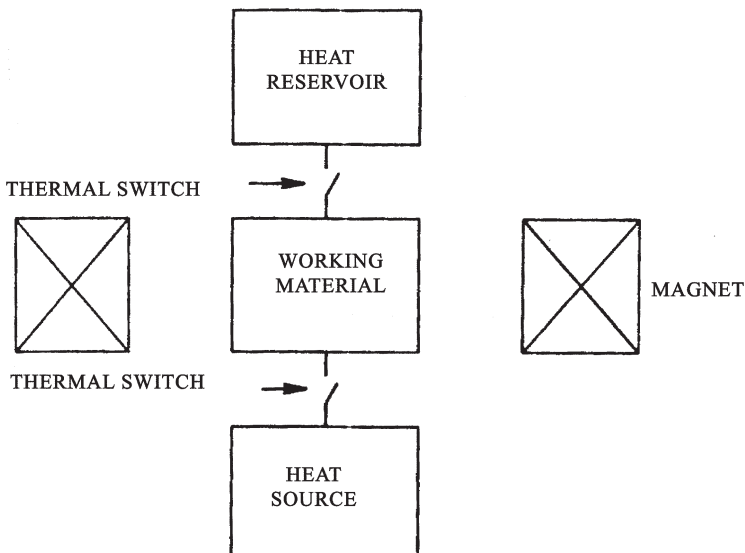


Figure 11.19. Schematic diagram of magnetic Carnot-type refrigerator (Daunt and Heer 1949, Steyert 1978a).

is open. In this process the temperature of the working material is lower than the heat source temperature and the heat Q_c is absorbed from the heat source. The cycle is completed by adiabatic magnetization (line AB in figure 11.5) with both heat switches open, leading to the working material heating back to the initial point A.

Carnot-type magnetic refrigerators can be divided into two main groups—with moving and with stationary magnetic working material. In the former case the magnetic material magnetizes and demagnetizes by insertion and removal from a magnet, and in the latter case these processes are conducted by switching a magnet on and off or by moving it with respect to the material.

A reciprocating magnetic refrigerator with moving magnetic material was proposed in the works of Delpuech *et al* (1981) and Beranger *et al* (1982). A schematic drawing of the apparatus is shown in figure 11.20. For operation it is immersed in a liquid helium bath, which serves as the hot reservoir. The heat source is a bath of superfluid HeII. It can be cooled with the help of an auxiliary refrigerator. The superconducting magnet (9) creates the field of 50 kOe. Correcting superconducting magnet (11) was used to obtain the necessary magnetic field profile. Under operation two identical magnetic working elements (10) are moved periodically up and down with the help of a bar (8). In the position shown in figure 11.20 the upper magnetic element is magnetized in the magnet in thermal contact with the liquid helium bath at 4.2 K. Then it is moved down and demagnetized in the middle He II bath (heat

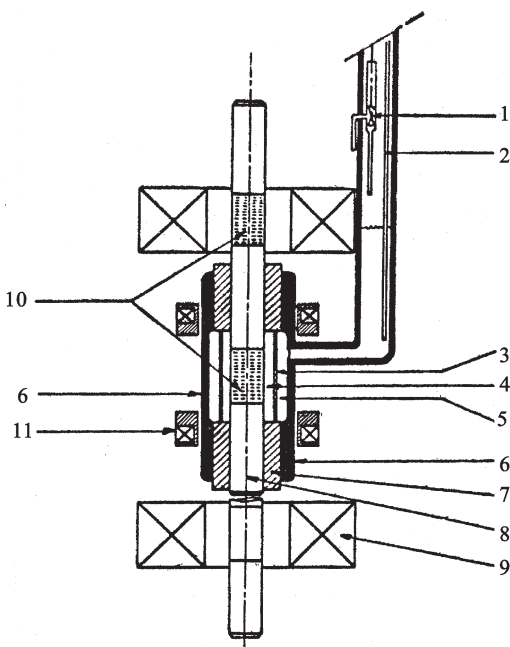


Figure 11.20. Schematic drawing of the reciprocating double action magnetic refrigerator: (1) expansion valve; (2) level gauge; (3) copper wall; (4) He II bath; (5) refrigerator bath (saturated He II); (6) insulator; (7) bearing; (8) magnetic bar; (9) superconducting magnet (Delpuech *et al* 1981). (Reprinted from Delpuech *et al* 1981, copyright 1981, with permission from Elsevier.)

source). Simultaneously the lower magnetic element is magnetized in the second superconducting magnet. Guide bearings (7) together with an isolator (6) isolate the middle bath from the 4.2 K liquid helium bath. The copper wall (3) provides thermal contact of the middle bath with the auxiliary refrigerator bath (5). In the reciprocating moving process described, the magnetic working elements are alternately put in contact with a 4.2 K heat reservoir and the low-temperature heat source. The authors used HoPO_4 , $\text{Gd}_2(\text{SO}_4)_3$ and gadolinium gallium garnet (GGG) as working bodies (Delpuech *et al* 1981, Beranger *et al* 1982). For HoPO_4 the temperature limit of 1.98 K was achieved and the useful cooling power at 2.1 K was 0.12 W for an operational frequency of 0.3 Hz. With $\text{Gd}_2(\text{SO}_4)_3$ as the working body the minimal temperature was 1.67 K with 0.36 W useful cooling power at 2.1 K. The apparatus with two GGG single crystals 2 cm long and 2.4 cm in diameter gave a minimal temperature of 1.38 K (operational frequency of 0.8 Hz), a useful cooling power of 1.2 W at 1.8 K (0.95 Hz) and an efficiency of 45%.

A rotary Carnot-type magnetic refrigerator configuration was proposed by Hakuraku and Ogata (1986a). In their construction 12 GGG elements

with dimensions $1.2 \times 1.4 \times 7.5$ cm were arranged around a rotor outer circumference. The ceramic rotor with 10 cm diameter and 10 cm length was surrounded by a housing (thermal insulator) made of glass ceramics. The housing had windows open in order to provide thermal contact with liquid 4.2 K helium and the low-temperature cooling chamber. The housing–rotor unit was surrounded by a superconducting magnet and the whole construction was embedded in liquid helium at 4.2 K. The rotor was rotated by a room-temperature driving motor. Under rotation the GGG elements were magnetized and demagnetized, executing a Carnot refrigeration cycle. Such a device showed 1.79 W useful cooling power at 1.8 K with an efficiency of 34% at a rotational speed of 24 rpm and a magnetic field of 30 kOe. Steyert (1978b) considered wheel construction of a Carnot-type refrigerator analogous to that regarded in section 11.2.2. The Carnot magnetic refrigeration cycle in this case was provided by appropriate configuration of the magnetic field. A possible construction of a Carnot-type magnetic refrigerator working below 20 K on a rotating principle and utilizing the strong anisotropy of a DyAlO_3 single crystal was proposed by Kuz'min and Tishin (1991)—see figure 11.21. DyAlO_3 has $\mu_{\text{eff}} = 6.88 \mu_B$ along the [010] direction (b-axis) and $\mu_{\text{eff}} = 0.8 \mu_B$ along the [001] direction (c-axis) (Kolmakova *et al* 1990). The working material, having the shape of a cylinder cut along the [100] direction (a-axis), rotates from the b-axis to the c-axis. The rotation of the single crystal with a volume of 10 cm^3 requires about 75 J. The rotation causes magnetization/demagnetization and, consequently, cooling/heating due to the MCE necessary for executing the magnetic refrigeration cycle. The device allows use of a superconducting solenoid operating in a persistent mode for producing the field. The advantages of this design are its simplicity and the possibility of miniaturization.

Another group of magnetic Carnot-type refrigerators is the devices with stationary magnetic working body and switching magnetic field. The first device of this type was proposed by Daunt and Heer (1949) and realized in the works of Heer *et al* (1953, 1954). These apparatuses were the first

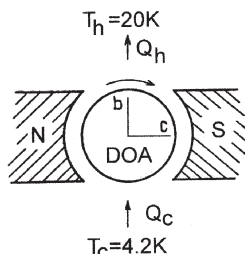


Figure 11.21. Construction of a magnetic refrigerator using DyAlO_3 as a working body. The axis of rotation is parallel to the crystal a-axis (Kuz'min and Tishin 1991).

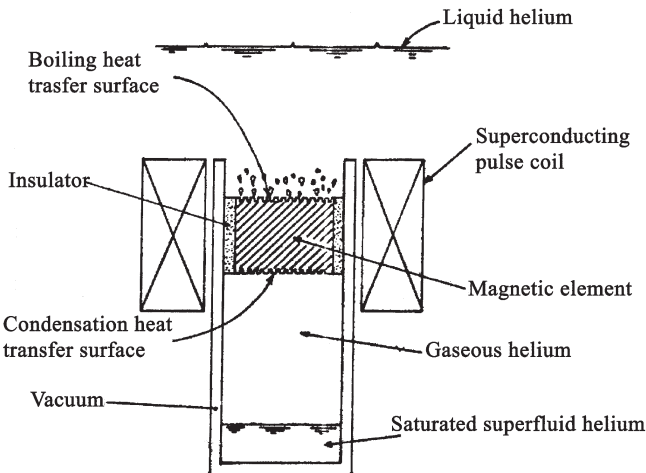


Figure 11.22. Schematic drawing of Carnot-type magnetic refrigerator with stationary magnetic working body and thermal siphon-type heat switches (Hakuraku and Ogata 1985).

models of magnetic refrigerators. Their design and characteristics were considered in section 2.13. The key elements in the Carnot-type refrigerators with stationary magnetic working body are the heat switches. In the refrigerators of Heer *et al* (1953, 1954), superconducting heat switches were used. Magnetic refrigerators with thermal siphon-type heat switches were proposed by Nakagome *et al* (1984), Numazawa *et al* (1984), and Hakuraku and Ogata (1985, 1986b). Figure 11.22 illustrates a possible design of a magnetic refrigerator with such heat switches. The operational principle of the heat switches is based on the differences in heat transfer rates in different heat transfer modes: condensation, boiling, convection and conduction. The heat exchange with hot heat reservoir (liquid helium) and cold heat source is conducted in the refrigerator through separate surfaces of the magnetic working material. The upper surface of the magnetic material is exposed to liquid helium and the lower surface to the gaseous helium. The side surface of the material is thermally insulated. When the magnetic material is heated in a magnetization process to a temperature higher than liquid helium temperature, heat is transferred from the material to the liquid by boiling and to the gas by conduction. However, the boiling heat transfer rate is about two orders of magnitude higher than the conductive one. So it can be considered that the upper heat switch is closed and the lower heat switch is open. When the magnetic material is cooled during demagnetization below the saturated temperature of the gas, condensation happens on the lower surface of the magnetic material. Heat is transferred in this case from the magnetic material to the gas through condensation heat transfer and to the liquid helium by conduction. Because the condensation heat transfer rate is

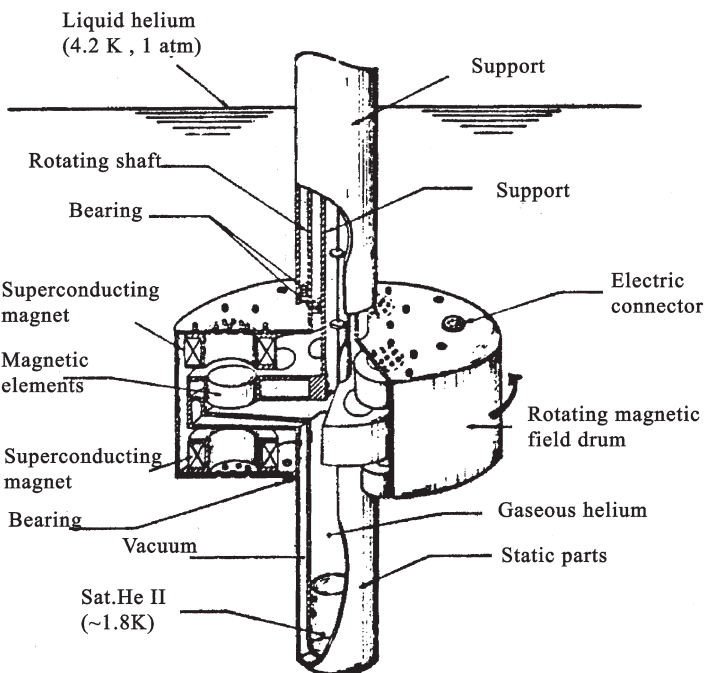


Figure 11.23. Schematic drawing of Carnot-type rotating magnetic refrigerator (Hakuraku and Ogata 1986b). (Reprinted from Hakuraku and Ogata 1986b, copyright 1986, with permission from Elsevier.)

about 20 times higher than the conductive heat transfer rate, the situation implies a closed low temperature heat switch and an open high temperature switch. The magnetization and demagnetization in the device shown in figure 11.22 are accomplished by switching on and off the superconducting magnet. An experimental device with construction based on the schematic drawing in figure 11.22, working in the temperature interval 1.8–4.2 K with GGG as a working body, a magnetic field of 30 kOe and an operational frequency 0.3 Hz, showed useful cooling power of 0.6 W at 1.8 K (Hakuraku and Ogata 1985). Another method of the magnetic field changing was proposed by Hakuraku and Ogata (1986c) in the construction shown in figure 11.23. Here eight GGG cylinders, 5 cm in diameter and 1.6 cm long, are placed around the static disc at equal intervals. As in the device in figure 11.22 the upper surface of the cylinders serves for heat transfer to the hot reservoir and the lower surface serves as a lower temperature heat transfer surface. The heat switches in this device work as described above. Three pairs of superconducting Helmholtz coils working in the persistent mode are placed around the GGG cylinders on the rotating drum. Under rotation of the drum the magnetic field applied to the magnetic working elements varies

and the elements are alternately magnetized and demagnetized. The heat switches in this device work automatically as described above and the magnetic material executes the Carnot cycle. For a magnetic field of 29.4 kOe and an operational frequency of 0.2 Hz, the minimum temperature of 1.9 K and the useful cooling power of 1.5 W at 2.1 K were achieved in the device.

Heat switches of another design were proposed by Kashani *et al* (1995, 1996) for the Carnot-type magnetic refrigerator working in the temperature interval from about 2 to 10 K with GGG as a magnetic working body. The heat switches in this case are two matching surfaces separated by a narrow gap. When the gap is filled with helium the switch is on and when the gap is empty the switch is off. Helium is delivered to and extracted from the switch with the help of an activated carbon pump. Its operational principle is based on the capability of carbon to absorb helium under cooling and to desorb it under heating. In order to provide sufficient thermal conductivity in the low-temperature heat switch, liquid superfluid helium was used, and in the high-temperature heat switch, gaseous helium was used. The refrigeration device operating by the principle described in the temperature interval from 9.6 to 1.8 K provided 30 mW of cooling for 150 s with an efficiency of 25% for a magnetic field of 65 kOe (Kashani *et al* 1996).

Bézaguet *et al* (1994) proposed a magnetic refrigerator with a static 10.1 kg single crystal GGG working body operating a quasi-Carnot cycle between 1.8 and 4.5 K. The working body was magnetized and demagnetized by a pulsed-field 35 kOe superconducting magnet. Thermal switching to the hot reservoir and heat source were provided by flushing of the working body by liquid helium from 4.5 and 1.8 K liquid helium baths. During adiabatic magnetization/demagnetization the magnetic material was thermally isolated with the help of mechanically actuated valves. According to estimations the device can provide cooling power of about 25 W.

The construction of the Carnot-type magnetic refrigerator working at 20 K with a mechanical upper heat switch was proposed by Ohira *et al* (1997). A cylindrical shaped GGG single crystal of 4 cm diameter and 10 cm height was used as a working body and a Gifford–McMahon refrigerator was used as a hot reservoir. The heat switch was made of high thermal conductivity copper and placed near the upper surface of the magnetic working material. At isothermal magnetization, the heat switch mechanically contacts the magnetic material, making thermal connection between the material and the hot reservoir. Such a refrigerator gave a cooling power of 0.21 W at 20 K with a cycle frequency of 0.002 Hz and magnetic field of 80 kOe. Mechanical thermal switches were also considered by Seyfert (1990). One of them was a mechanical shutter covering the upper (warm) surface of the magnetic working material and thermally isolating it from the hot reservoir. Another was a sliding bar alternately connecting the magnetic working material with the hot reservoir or cold heat source at the relevant parts of the Carnot cycle.

11.3 Working materials for magnetic refrigerators

For magnetic refrigerators working with a Carnot cycle below 20 K, oxides with low magnetic ordering temperatures such as $R_3Ga_5O_{12}$ and $RAIO_3$ were proposed (Barclay and Steyert 1982a, Hashimoto 1986, Kuz'min and Tishin 1991, 1993b). Barclay and Steyert (1982a) showed that among various gadolinium oxide compounds the gadolinium gallium garnet is the most suitable one as a working material for magnetic refrigerators in the temperature range between 2 and 20 K. As was discussed in section 5.1.2, Kimura *et al* (1988) obtained $\Delta T(T)$ curves for dysprosium gallium garnet $Dy_3Ga_5O_{12}$ (DGG)—see figure 5.9. Although this compound is antiferromagnet with a Néel temperature of 0.373 K, maxima on $\Delta T(T)$ curves were observed at higher temperatures—for $\Delta H = 50$ kOe at about 14 K. $\Delta T/\Delta H$ values in this compound were rather high—about 0.24 K/kOe for $\Delta H = 50$ kOe.

Kuz'min and Tishin (1991, 1993b) and Kimura *et al* (1995) have devoted their investigations to rare earth orthoaluminates with perovskite structure. From the MFA calculations made by Kuz'min and Tishin (1991) it was shown that $DyAlO_3$ and $GdAlO_3$ are the most advantageous compounds among the orthoaluminates. The results of calculations are illustrated by figure 11.24, where the dependence of the field change on the temperature of a hot sink T_{hot} in the Carnot cycle (the temperature of the cold load T_{cold} was supposed to be 4.2 K) for $DyAlO_3$ and $GdAlO_3$ are presented. The borderline between the region where $DyAlO_3$ is more effective than $GdAlO_3$ and vice versa is almost exactly a straight line. As one can see, $DyAlO_3$ is more efficient in weak and moderate fields, while $GdAlO_3$ is better within the strong-field region. Magnetization measurements of

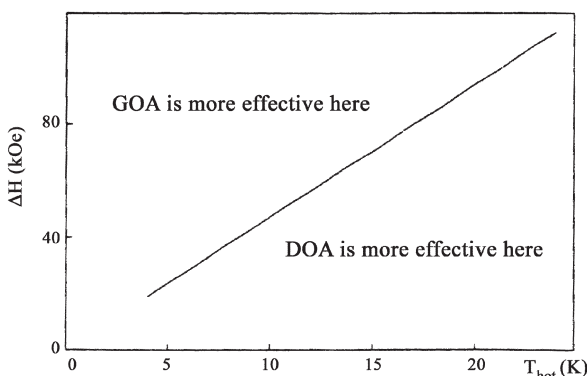


Figure 11.24. The dependence of the field change on the temperature of a hot sink T_{hot} in the Carnot cycle (the temperature of the cold load T_{cold} is supposed to be 4.2 K) for $DyAlO_3$ and $GdAlO_3$ (Kuz'min and Tishin 1991).

Kimura *et al* (1995) showed that ErAlO₃ single crystal was a promising material for temperatures below 20 K. According to theoretical calculations made by Tishin and Bozkova (1997) some success can also be expected from the Dy_xEr_{1-x}AlO₃ orthoaluminates.

Daudin *et al* (1982a) suggested a solid solution between DyVO₄ and Gd₃Ga₅O₁₂ as a working material for use in an Ericsson cycle in the low-temperature range. Tomokiyo *et al* (1985) proposed Dy₃Ga₅O₁₂ to be used in an Ericsson cycle below 20 K.

Brown (1976) suggested using gadolinium as a working material in a magnetic refrigerator working near room temperature (see section 11.2.5). Later gadolinium was usually used in experimental magnetic refrigerators working near room temperature because of its high magnetocaloric properties (ΔT and ΔS_M), its metallic nature making it easily machinable. The possibility of using rare earth metals and some of their alloys as working bodies in magnetic refrigerators was investigated in the works of Tishin (1990a,d-f), Burkhanov *et al* (1991), Nikitin and Tishin (1988).

A magnetic material suitable for application for the purposes of magnetic refrigeration first of all should have high ΔT and ΔS_M values in available magnetic fields. One should remember that $\Delta T(H)$ and $\Delta S_M(H)$ dependences usually have nonlinear character and the MCE growth in high fields is lower than in low fields (see, for example, figure 8.3). So increasing of the magnetic field strength cannot give a proportional increasing of the MCE. The form of $\Delta T(T)$ and $\Delta S_M(T)$ curves also can have essential meaning. For application in Ericsson and Brayton magnetic refrigeration cycles, a magnetic working material should have a magnetic entropy change ΔS_M constant in the cycle temperature span. In most cases it is better for the material to have wide $\Delta T(T)$ and $\Delta S_M(T)$ dependences. Wood and Potter (1985) proposed a quantitative criterion of efficiency of the working material called maximum refrigerant capacity $(\Delta S_M \Delta T_{cyc})_{max}$, where $\Delta T_{cyc} = T_{hot} - T_{cold}$ is the operating temperature range of a cycle. The higher the $(\Delta S_M \Delta T_{cyc})_{max}$ value, the more effective the material is for the given ΔH . This value also determines T_{hot} and T_{cold} for which the material can be most effective. $(\Delta S_M \Delta T_{cyc})_{max}$ corresponds to a cycle area in the $S-T$ plane (i.e. to the net work in the cycle) that is maximized for a given material. ΔS_M is supposed to be constant over the cycle. However, in real cycles this condition is usually violated due to various irreversible processes. According to Wood and Potter (1985), the value of the refrigerant capacity that might be realized in a real cycle in magnetic refrigerators is about half of the computed maximum refrigerant capacity value defined above. To optimize refrigerator performance and cost by choosing the proper magnetic field value it is more convenient to use the specific maximum refrigerant capacity $(\Delta S_M \Delta T_{cyc})_{max}/H$ corresponding to a field change from 0 to H .

According to the temperature dependence of ΔS_M (see figure 8.8) the heavy rare earth metals are efficient within certain narrow temperature intervals. Tishin (1990e,f) determined the refrigerant capacities of the rare

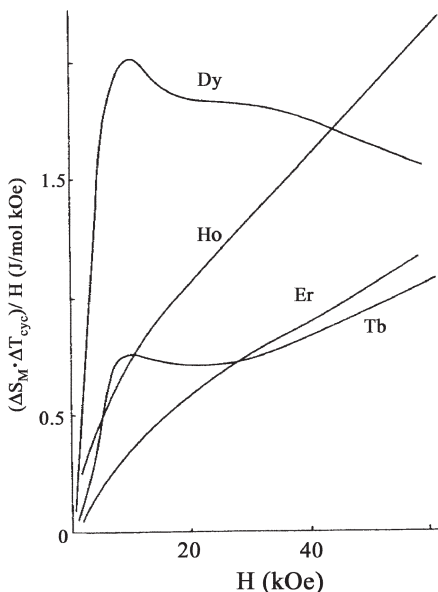


Figure 11.25. Magnetic field dependence of the specific refrigerant capacity in Dy, Ho, Er and Tb (Tishin 1990f).

earth metals in the temperature interval from 20 to 300 K for $H = 60$ kOe. It was established that Ho is the most suitable for cycles from 20 to 135 K, where its maximum refrigerant capacity reaches 129 J/mol (or 6.88 J/cm³). Er is good enough for the range from 20 to 85 K with $(\Delta S_M \Delta T_{cyc})_{\max} = 72$ J/mol (or 3.9 J/cm³). For Dy the maximum refrigerant capacity is 82.4 J/mol (or 4.35 J/cm³) in the temperature interval from 100 to 190 K. Gd had $(\Delta S_M \Delta T_{cyc})_{\max} = 51.8$ J/mol (or 2.59 J/cm³) for temperatures from 185 to 300 K. Tishin (1990f) also considered dependences of $(\Delta S_M \Delta T_{cyc})_{\max}/H$ on H for Tb, Er, Ho and Dy—see figure 11.25. It was shown that Dy is the most promising material among them for $H < 45$ kOe—its $(\Delta S_M \Delta T_{cyc})_{\max}/H$ reached a maximum value of about 2 J/mol kOe for $H \approx 11$ kOe. The specific refrigerant capacity of Ho increased with field almost linearly, exceeding the value of Dy for $H > 45$ kOe. A comparison of the refrigerant capacity of AFM rare earth metals and alloys with the results of Wood and Potter (1985) made by Tishin (1990e,f) showed that the materials where AFM structure was destroyed by a relatively small magnetic field were often more advantageous as magnetic working bodies for refrigerators than ferromagnets.

The refrigerant capacity of Gd–Tb, Gd–Dy, Gd–Er and Gd–Ho alloys with high Gd concentration was investigated in the works of Tishin (1990a,d–f) and Nikitin and Tishin (1988). Figure 11.26 shows calculated field dependences of the specific maximum refrigerant capacity for Gd–Tb

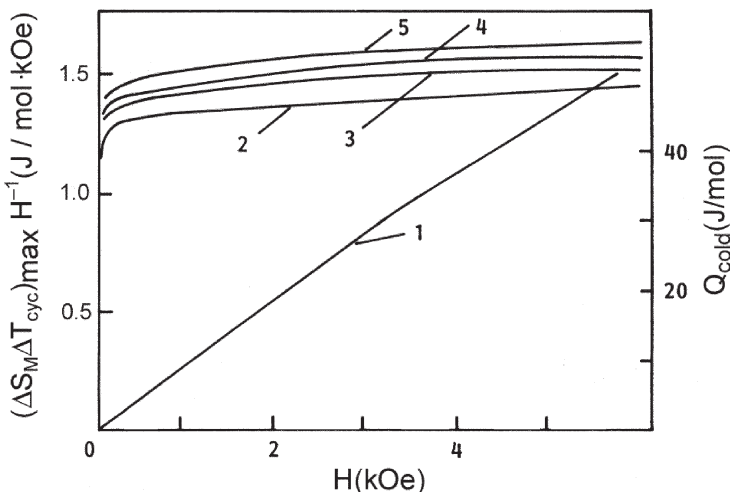


Figure 11.26. Magnetic field dependences of the specific maximum refrigerant capacity $(\Delta S_M \Delta T_{cyc})_{max}/H$ for Tb_xGd_{1-x} alloys: (2) $x = 0$; (3) 0.1; (4) 0.2; (5) 0.3. Curve (1) represents heat transferred by Gd from load per cycle of refrigeration (Tishin 1990a). (Reprinted from Tishin 1990a, copyright 1990, with permission from Elsevier.)

alloys (Tishin 1990a). $\Delta S_M(T)$ curves for these alloys were determined with the help of MFA (Gd-Tb alloys with Gd content higher than 6 at% are ordered ferromagnetically). As can be seen, with increasing Tb content, the specific maximum refrigerant capacity increases with the field. For $H \leq 10$ kOe a sharp increase in the refrigerant capacity is observed. Analysis of the data led to the conclusions that Gd-Tb alloys are more effective as magnetic refrigerants near room temperature than pure Gd, and that Gd and its alloys with Tb have high specific refrigerant capacity over a wide range of fields from 10 to 60 kOe, which enables relatively weak fields to be used in magnetic refrigerators with these working bodies.

Figure 11.27 shows the maximum refrigerant capacity of Gd-Tb, Gd-Dy, Gd-Er and Gd-Ho alloys for $H = 60$ kOe as a function of Gd content. These binary alloys with high Gd content have Curie temperatures close to room temperature. Their $\Delta S_M(T)$ curves were measured and calculated on the basis of MFA. As one can see from figure 11.27, Gd-Dy alloys have the maximum refrigerant capacity in the room-temperature region—79.2/mol for the temperature interval from 110 to 300 K (Nikitin and Tishin 1988). At the same time in the low-temperature region Gd-Ho alloys have high refrigerant capacity values. For $T_{hot} = 300$ K, $T_{cold} = 20$ K and $H = 60$ kOe a maximum refrigeration capacity of 60.5 J/mol is shown by Gd_{0.8}Ho_{0.2} alloy. According to the obtained data this alloy can be recommended for use as a working material for a magnetic refrigerator operating from 20 K to room temperature.

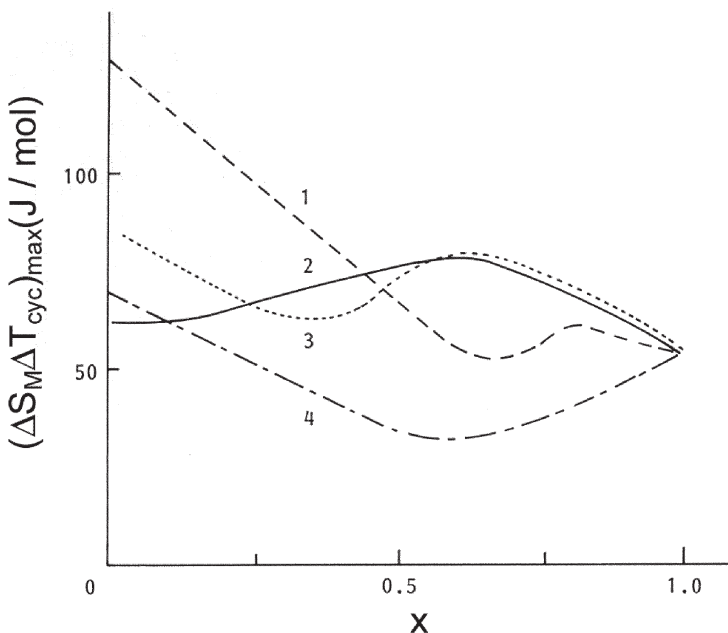


Figure 11.27. Dependence of maximum refrigerant capacity on Gd content ($H = 60$ kOe) for: (1) $\text{Gd}_x\text{Ho}_{1-x}$; (2) $\text{Gd}_x\text{Tb}_{1-x}$; (3) $\text{Gd}_x\text{Dy}_{1-x}$ and (4) $\text{Gd}_x\text{Er}_{1-x}$ alloys (Nikitin and Tishin 1988).

Tishin (1990d–f) and Burkhanov *et al* (1991) also considered complex magnetic working bodies on the basis of rare earth metals and their alloys. It was shown that for a complex working material made of $\text{Gd}_{0.9}\text{Tb}_{0.1}$ and $\text{Gd}_{0.4}\text{Tb}_{0.6}$ in the ratio of 0.78:0.22 the value $\Delta S_M = 0.3$ J/mol K for $\Delta H = 10$ kOe can be achieved in the temperature interval from 255 to 295 K. Burkhanov *et al* (1991) studied Gd–Dy alloys experimentally and found that a complex working body consisting of 59% Gd and 41% $\text{Gd}_{0.9}\text{Dy}_{0.1}$ is a promising refrigerant for the room-temperature region. This material has the effective Curie temperature below room temperature and $\Delta S_M = 0.8$ J/mol K at 10 °C for $\Delta H = 16$ kOe. Ternary working bodies consisting of Gd–Tb and Tb–Dy alloys and rare earth metals Ho and Dy for the temperature interval from 20 to 300 K were considered by Tishin (1990e,f). It was shown that the best result can be achieved with Ho, $\text{Tb}_{0.5}\text{Dy}_{0.5}$ and $\text{Gd}_{0.6}\text{Tb}_{0.4}$, each of them working in the intervals 20–135, 135–215 and 215–300 K, respectively. For this working body $(\Delta S_M \Delta T_{cyc})_{\max} = 269$ J/mol for $\Delta H = 60$ kOe.

Gschneidner and Pecharsky (2000a, 2001) suggested a new parameter for characterization of magnetocaloric properties and determination of suitability of magnetic material for working bodies in magnetic refrigerators, which takes into account not only the value of magnetocaloric effect (ΔT and ΔS_M) but also the width of $\Delta T(T)$ and $\Delta S_M(T)$ curves. The parameter

was called the relative cooling power (RCP) and was determined as a product of ΔT or ΔS_M peak value and the full width at half maximum (δT_{FWHM}) of the $\Delta T(T)$ or $\Delta S_M(T)$ curves. So the relative cooling power (RCP) based on the magnetic entropy change has the form

$$RCP(S) = -\Delta S_M(\max) \times \delta T_{FWHM} \quad (11.34)$$

and the RCP based on the adiabatic temperature change has the form

$$RCP(T) = \Delta T(\max) \times \delta T_{FWHM}. \quad (11.35)$$

According to Gschneidner and Pecharsky (2000a) $RCP(S)$ gives a value close to $4/3$ times the refrigerant capacity discussed above in the same temperature range. Parameter $RCP(T)$ has no physical meaning (its dimension is K^2). RCP allows easy comparison of different magnetic materials from the point of view of application for magnetic refrigeration—larger RCP points to better magnetocaloric material. Because RCP increases with magnetic field change ΔH increasing, it is convenient to use normalized RCP— $RCP(S)/\Delta H$ and $RCP(T)/\Delta H$. In some cases RCP can give a more correct result than the refrigerant capacity. For example, if the $\Delta S_M(T)$ curve has very gently sloping shoulders then it is impossible to calculate the refrigerant capacity, which is just the maximal square under the $\Delta S_M(T)$ curve, because this parameter is just increasing with increasing temperature interval and does not reveal a maximum.

Gschneidner and Pecharsky (2000a, 2001) considered the available experimental results on MCE by means of RCP. It was shown that among rare earth metals Gd has the best RCP values: its $RCP(S)$ lies between ~ 2 and $\sim 14 J/cm^3$ and the $RCP(T)$ lies between ~ 240 and $\sim 2000 K^2$ for ΔH of 20 to 100 kOe ($RCP(S)/\Delta H = 111 mJ/cm^3 kOe$ and $RCP(T)/\Delta H = 16.12 K^2/kOe$ for $\Delta H = 60$ kOe). Tb and Dy are also characterized by essential RCP values ($RCP(T)$ for Tb is ~ 620 K^2 and for Dy is ~ 820 K^2 for $\Delta H = 70$ kOe), which make them suitable for using in the temperature ranges 210–250 K and 160–200 K, respectively (Gschneidner and Pecharsky 2001). For $Gd_{1-x}Dy_x$ alloys, the $RCP(S)$ for $\Delta H = 70$ kOe was determined to be ~ 11 , 8, 11 and $8 J/cm^3$ for $x = 0.12$, 0.28, 0.49 and 0.7, respectively ($RCP(S)/\Delta H = 157 mJ/cm^3 kOe$ for $x = 0.12$).

High RCP was also found by Gschneidner and Pecharsky (2000a, 2001) in $GdNiIn$, $GdZn$, Fe–Rh, RAI_2 and RCO_2 compounds, $(Gd_{1-x}Er_x)NiAl$ phases, lanthanum–manganese perovskites and gadolinium silicides (system Gd_5Si_4 – Gd_5Ge_4). $GdNiIn$ with $T_C = 94$ K has $RCP(S)/\Delta H = 118 mJ/cm^3 kOe$ ($\Delta H = 90$ kOe) and $RCP(T)/\Delta H = 7.14 K^2/kOe$. $GdZn$ with higher Curie temperature ($T_C = 270$ K) has $RCP(S)/\Delta H = 112 mJ/cm^3 kOe$ ($\Delta H = 100$ kOe) and $RCP(T)/\Delta H = 11.13 K^2/kOe$ ($\Delta H = 100$ kOe). Alloys Fe–Rh with first-order magnetic transition somewhat above room temperature revealed high magnetocaloric properties but they strongly depended on heat treatment, and the magnetic behaviour of these alloys was irreversible. For

quenched $\text{Fe}_{0.49}\text{Rh}_{0.51}$ $\text{RCP}(T)/\Delta H = -4.62 \text{ K}^2/\text{kOe}$ and for annealed $\text{Fe}_{0.49}\text{Rh}_{0.51}$ this value is $-1.95 \text{ K}^2/\text{kOe}$ ($\Delta H = 19.5 \text{ kOe}$). Annaorazov *et al* (1992) determined the specific refrigerant capacity of $\text{Fe}_{0.49}\text{Rh}_{0.51}$. Rather high values were obtained: for $\Delta H = 19.5 \text{ kOe}$ ($\Delta S_M \Delta T_{\text{cyc}}/H = 6.41 \text{ J/kg kOe} = 44.49 \text{ mJ/cm}^3 \text{ kOe}$ for the annealed sample in the temperature range from 309 to 347.7 K and 13.52 J/kg kOe ($93.83 \text{ mJ/cm}^3 \text{ kOe}$) for the quenched sample in the temperature range 295 to 312.2 K.

In the RAI_2 system the highest RCP was found in HoAl_2 ($\text{RCP}(S)/\Delta H = 101 \text{ mJ/cm}^3 \text{ kOe}$ for $\Delta H = 40 \text{ kOe}$) and $(\text{Dy}_{0.4}\text{Er}_{0.6})\text{Al}_2$ ($\text{RCP}(S)/\Delta H = 107 \text{ mJ/cm}^3 \text{ kOe}$ for $\Delta H = 50 \text{ kOe}$ and $\text{RCP}(T)/\Delta H = 6.88 \text{ K}^2/\text{kOe}$ for $\Delta H = 100 \text{ kOe}$). In GdAl_2 with $T_C = 167 \text{ K}$, RCP was lower: $\text{RCP}(S)/\Delta H = 89.5 \text{ mJ/cm}^3 \text{ kOe}$ and $\text{RCP}(T)/\Delta H = 6.84 \text{ K}^2/\text{kOe}$ for $\Delta H = 50 \text{ kOe}$. For RCO_2 ($\text{R} = \text{Er}, \text{Ho}, \text{Dy}$) compounds with first-order transition to magnetically ordered state the highest $\text{RCP}(S)/\Delta H = 83.1 \text{ mJ/cm}^3 \text{ kOe}$ ($\Delta H = 70 \text{ kOe}$) was observed in HoCo_2 ($T_C = 82 \text{ K}$) and the highest $\text{RCP}(T)/\Delta H = 2.11 \text{ K}^2/\text{kOe}$ ($\Delta H = 70 \text{ kOe}$) for ErCo_2 ($T_C = 35 \text{ K}$). The alloys $(\text{Gd}_{1-x}\text{Er}_x)\text{NiAl}$ have multiple magnetic phase transitions. This provides almost flat $\Delta S_M(T)$ behaviour in a wide temperature range (see figure 6.16). The highest RCP in this row of materials exhibits $(\text{Gd}_{0.54}\text{Er}_{0.46})\text{NiAl}$ (the upper magnetic ordering temperature 37 K, $\text{RCP}(S)/\Delta H = 93.7 \text{ mJ/cm}^3 \text{ kOe}$ and $\text{RCP}(T)/\Delta H = 4.98 \text{ K}^2/\text{kOe}$) and $(\text{Gd}_{0.4}\text{Er}_{0.6})\text{NiAl}$ (the upper magnetic ordering temperature 32 K, $\text{RCP}(T)/\Delta H = 9.29 \text{ K}^2/\text{kOe}$ and $\text{RCP}(S)/\Delta H = 85.5 \text{ mJ/cm}^3 \text{ kOe}$). High RCP values were also found in manganites. For example, normalized $\text{RCP}(S)$ is $57.9 \text{ mJ/cm}^3 \text{ kOe}$ for $\text{La}_{0.925}\text{Na}_{0.075}\text{MnO}_3$ ($\Delta H = 10 \text{ kOe}$, $T_C = 193 \text{ K}$) and $28.3 \text{ mJ/cm}^3 \text{ kOe}$ for $\text{La}_{0.8}\text{Ca}_{0.2}\text{MnO}_3$ ($\Delta H = 15 \text{ kOe}$, $T_C = 230 \text{ K}$). The latter compound is characterized by the highest $|\Delta S_M|/\Delta H$ value among the manganites (in J/kg K kOe , see table 5.2). Using various dopants it is possible to change magnetic ordering temperatures of the manganites in a wide range. $\text{Gd}_5(\text{Si}_x\text{Ge}_{1-x})_4$ compounds display high magnetocaloric properties in the whole concentration region. In high temperature orthorhombic region ($0.5 < x \leq 1$) Gd_5Si_4 has $\text{RCP}(S)/\Delta H = 88.8 \text{ mJ/cm}^3 \text{ kOe}$ and $\text{RCP}(T)/\Delta H = 10.92 \text{ K}^2/\text{kOe}$ ($\Delta H = 50 \text{ kOe}$, $T_C = 336 \text{ K}$) and $\text{Gd}_5\text{Si}_{2.06}\text{Ge}_{1.94}$ has $\text{RCP}(S)/\Delta H = 95.9 \text{ mJ/cm}^3 \text{ kOe}$ and $\text{RCP}(T)/\Delta H = 9.6 \text{ K}^2/\text{kOe}$ ($\Delta H = 50 \text{ kOe}$, $T_C = 306 \text{ K}$). In monoclinic concentration region ($0.24 \leq x \leq 0.5$) the highest RCP values were found in $\text{Gd}_5\text{Si}_{1.5}\text{Ge}_{2.5}$ ($T_C = 217 \text{ K}$): $\text{RCP}(S)/\Delta H = 103 \text{ mJ/cm}^3 \text{ kOe}$ and $\text{RCP}(T)/\Delta H = 9.9 \text{ K}^2/\text{kOe}$ ($\Delta H = 50 \text{ kOe}$). High RCP values also have $\text{Gd}_5\text{Si}_2\text{Ge}_2$ compound because of its Curie temperature suitable for use in the room-temperature region. In the low-temperature orthorhombic phase the maximum RCP was observed in $\text{Gd}_5\text{Si}_{0.33}\text{Ge}_{3.67}$ with $T_C = 68 \text{ K}$ $\text{RCP}(S)/\Delta H = 120.5 \text{ mJ/cm}^3 \text{ kOe}$ for $\Delta H = 50 \text{ kOe}$. The magnetocaloric parameters of the regarded metals, alloys and compounds allowing conclusions to be made about their applicability for magnetic refrigeration are summarized in table 11.2.

Table 11.2. Parameters of the materials with high magnetocaloric properties: a temperature of magnetic phase transition T_{pt} or maximum T_{max} in $\Delta S_M(T)$ or $\Delta T(T)$ curves, specific maximum refrigerant capacity ($(\Delta S_M \Delta T_{\text{cyc}})_{\text{max}}/H$), maximal $\Delta S_M/\Delta H$ and $\Delta T/\Delta H$ values, specific relative cooling power based on the magnetic entropy change ($\text{RCP}(S)/\Delta H$) and on the adiabatic temperature change ($\text{RCP}(T)/\Delta H$), and effective MCE value ΔT_{eff} . For $\text{Dy}_3\text{Ga}_5\text{O}_{12}$ the value of $\Delta S_M/\Delta H$ at the temperature of 1.2 K corresponding to the maximum on $\Delta T(T)$ curve is presented. References are shown in brackets.

Material	T_{pt} or T_{max} (K)	H (J/mol kOe) (mJ/cm ³ kOe)	$\frac{(\Delta S_M \Delta T_{\text{cyc}})_{\text{max}}}{H}$	$\frac{\Delta S_M}{\Delta H}$	$\frac{\text{RCP}(S)}{\Delta H}$ (J/mol kOe) (mJ/cm ³ kOe)	$\frac{\Delta T}{\Delta H}$ (K/kOe)	$\frac{\Delta T_{\text{eff}}}{\Delta H}$ $\times 10^4$ (kOe ⁻¹)	$\frac{\text{RCP}(T)}{\Delta H}$ (K ² /kOe)	$\frac{\Delta H}{\Delta H}$ (kOe)
			$(\Delta S_M \Delta T_{\text{cyc}})_{\text{max}}$	ΔS_M	ΔT	ΔT_{eff}	ΔH	ΔH	ΔH
$\text{Dy}_3\text{Ga}_5\text{O}_{12}$	14 [1] 12 [1] 294 [2]	— — 0.86 [3] (43.2) [3]	— 270 (1.54) [4]	— (111) [4] —	— 0.207 [4] —	0.24 [1] 0.3 [1] —	1.71 250 7	3.36 3.75 16.12 [4]	50 30 60
Gd	— — —	— — —	— — —	— — —	0.29 [2] — —	— — —	— — —	— — —	60 60 20
Tb	231 [4]	1.1 [3] (56.9) [3]	— — (2.72) [4]	— — (62.4) [4]	— — 0.149 [4] 0.25 [6]	— — — —	— — — —	— — — —	12 12 60 60
Dy	180 [8]	1.6 [3] (84.1) [3]	— —	— —	— — 0.143 [6]	— — —	— — —	— — —	75 75 20
GdNiIn	93.5 [11]	—	— (1.39) [4] 51.92 [11]	— — —	— — —	— — —	— — —	— — —	70 70 90

GdZn	270 [12]	-	(0.86) [4]	(112) [4]	0.106 [4]	3.93	11.13 [4]	100
			24.76 [12]	-	-	-	-	100
			37.85 [12]	-	0.15 [12]	5.56	-	20
			(-11.48) [14]	(-212.46)	-0.662 [14]	-21.15	-6.62	19.5
			-183.72 [14]	-3.4	-	-	-	19.5
			(-25.06) [14]	(-175.1)	-0.708 [14]	-22.62	-4.04	6.5
			-401 [14]	-6.4	-	-	-	6.5
			(0.85) [4]	(89.5) [4]	0.076 [4]	4.55	6.84 [4]	50
GdAl ₂	167 [4]	-	32.11 [15]	(101) [4]	0.105 [15]	6.29	-	50
			44.4 [15]	-	0.15 [4]	50	-	40
			(3.9) [4]	-	-	-	-	80
			-	112.3 [16]	-	-	-	50
			140.3 [16]	-	0.23 [16]	76.67	-	20
			(2.56) [4]	(107) [4]	-	-	-	50
			97.8 [17]	-	-	-	-	50
			-	0.125 [4]	39.56	6.88 [4]	100	
			(4.5) [4]	(77) [4]	0.169 [4]	48.29	2.11 [4]	70
			118 [19]	-	-	-	-	70
			(3.2) [4]	(83.1) [4]	-	-	-	70
			88.8 [19]	-	-	-	-	70
			-	0.085 [4]	10.37	1.44 [4]	60	
			(2.04) [4]	(93.7) [4]	-	-	-	50
			63.9 [17]	-	-	-	-	50
			-	0.089 [4]	24.05	4.98 [4]	100	
			(1.9) [4]	(85.5) [4]	-	-	-	100
			72.2 [17]	0.202 [4]	63.13	9.29 [4]	50	
			(0.827) [10]	(57.9) [10]	-	-	-	10
			30.2 [20]	-	-	-	-	10

Table 11.2. Continued.

Material	T_{pt} or T_{max} (K)	$\frac{(\Delta S_M \Delta T_{\text{cyc}})_{\text{max}}}{H}$	$-\frac{\Delta S_M}{\Delta H}$	$-\frac{\text{RCP}(S)}{\Delta H}$	$\frac{\Delta T}{\Delta H}$	$\frac{\Delta T_{\text{eff}}}{\times 10^4}$	$\frac{\text{RCP}(T)}{\Delta H}$
		(J/mol kOe) (mJ/cm ³ kOe)	(mJ/mol K kOe) (mJ/cm ³ K kOe)	(J/mol kOe) (mJ/cm ³ kOe)	(K/kOe)	(kOe ⁻¹)	(K ² /kOe)
La _{0.8} Ca _{0.2} MnO ₃	230 [21]	—	(2.18) [10]	(28.3) [10]	—	—	—
Gd ₅ Si ₁₄	336 [4]	—	81.3 [21] (1.23) [4]	(88.8) [4]	0.176 [4]	0.0524	10.92 [4]
Gd ₅ Si _{2.06} Ge _{1.94}	306 [4]	—	161.8 [22] (1.41) [4]	—	—	—	50
Gd ₅ Si ₂ Ge ₂	276 [4]	—	187.2 [22] (2.8) [4]	(95.9) [4] (67.2) [4]	0.16 [4] 0.3 [4]	5.23 10.87	9.6 [4] 6.3 [4]
Gd ₅ Si _{1.5} Ge _{2.5}	217 [4]	—	365.4 [23] 691.4 [23]	—	—	—	50
Gd ₅ Si _{0.33} Ge _{3.67}	68 [10]	—	(4.46) [4] (5.74) [4]	(103) [4] (121) [4]	0.31 [4] 0.224 [4]	14.29 17.5	9.9 [4] 4.04 [4]
Gd ₇ Pd ₃	323 [25]	—	913.3 [24] (1.13) [25]	(30)	—	—	50
MnFeP _{0.65} As _{0.35}	212 [26]	—	181.8 [25] 103.7 [26]	—	5.26	—	50
MnFeP _{0.5} As _{0.5}	287 [26]	—	(4.5) [26] 65.5 [26]	(63.4) 1.842	—	—	50
MnFeP _{0.35} As _{0.65}	332 [26]	—	(2.7) [26] 51.1 [26]	(76.7) 1.35	—	—	50
MnAs	318 [27]	—	(2.1) [26] 83.1 [28]	(54.4) 1.44	—	—	50

MnAs _{0.7} Si _{0.3}	220 [29]	—	77.7 [29] (3.6) [29]	1.15 (53.3)	—	—	—	—	50
Ni _{0.526} Mn _{0.231} Ga _{0.243}	297 [30]	—	94.3 [30] (2.9) [30]	0.141 (4.4)	—	—	—	—	50
Ni _{0.501} Mn _{0.207} Ga _{0.296}	219 [31]	—	—222.5 [31] (−6.1) [31]	−0.359 (−9.1)	—	—	—	—	50
LaFe _{1.4} Si _{1.6}	208 [32]	—	318.4 [32] (2.82)	7.9 (70)	—	—	—	—	50
LaFe _{11.7} Si _{1.3}	188 [33]	—	586.7 [32] (5.19)	7.1 (62.9)	—	—	—	—	20
LaFe _{11.57} Si _{1.43} H _{1.3}	291 [34]	—	480.8 [33] (4.22)	10.63 (93.2)	—	—	—	—	20
			1036.1 [33] (9.1)	10.67 (93.6)	—	—	—	—	20
			—	—	0.286 [33] 0.345 [34]	15.2 11.86	1.46 —	14 —	20
			992.5 [34] (8.72)	—	—	—	—	—	20

1. Kimura *et al.* (1988); 2. Dan'kov *et al.* (1998); 3. Tishin (1990f); 4. Gschneidner and Pecharsky (2001); 5. Dankov *et al.* (1992); 6. Tishin (1988); 7. Chernyshov *et al.* (2002a); 8. Bykhov *et al.* (1990); 9. Nikitin *et al.* (1991b); 10. Gschneidner and Pecharsky (2000a); 11. Canepa *et al.* (1999); 12. Pecharsky and Gschneidner (1999b); 13. Nikitin *et al.* (1990); 14. Annaorazov *et al.* (1992); 15. Dankov *et al.* (2000); 16. Ilyin *et al.* (2001); 17. Korte *et al.* (1998a); 18. Tishin *et al.* (2002); 19. Foldeaki *et al.* (1998a); 20. Zhong *et al.* (1998a); 21. Guo *et al.* (1997a); 22. Gschneidner *et al.* (1999); 23. Pecharsky and Gschneidner (1997); 24. Pecharsky and Gschneidner (1998); 25. Canepa *et al.* (2002); 26. Tegus *et al.* (2002); 27. Hashimoto *et al.* (2002b); 28. Wada and Tanabe (2001); 29. Wada *et al.* (2002); 30. Hu *et al.* (2001c); 31. Hu *et al.* (2001b); 32. Hu *et al.* (2001d); 33. Hu *et al.* (2002a); 34. Fujieda *et al.* (2002).

Among compounds with high magnetocaloric properties investigated recently Gd_7Pd_3 , $\text{MnFeP}_{1-x}\text{As}_x$, $\text{MnAs}_{1-x}\text{Sb}_x$, Ni_2MnGa and $\text{La}(\text{M}_{1-x}\text{M}'_x)_{13}$ ($\text{M} = \text{Fe}, \text{Ni}; \text{M}' = \text{Si}, \text{Al}$) compounds should be mentioned. Gd_7Pd_3 has high Curie temperature (323 K) and relatively high magnetic entropy change, although its adiabatic temperature change is not too large—see table 11.2. Tegus *et al* (2002b) determined the refrigerant capacity of $\text{MnFeP}_{1-x}\text{As}_x$ ($x = 0.25\text{--}0.65$) for the temperature span from $T_C - 25\text{ K}$ to $T_C + 25\text{ K}$. The maximum value of the specific refrigerant capacity of 1.92 J/mol kOe (for $\Delta H = 50\text{ kOe}$) was found in $\text{MnFeP}_{0.65}\text{As}_{0.35}$. The specific magnetic entropy change in this system is also high—in $\text{MnFeP}_{0.65}\text{As}_{0.35}$ this parameter is $103.7\text{ mJ/mol K kOe}$. In accordance with magnetic measurements, another promising system is $\text{MnAs}_{1-x}\text{Sb}_x$. MnAs displays the best magnetocaloric properties in this system, but the others compounds also have high magnetocaloric properties up to $x = 0.3$. Non-stoichiometric Heusler alloys $\text{Ni}_{0.515}\text{Mn}_{0.227}\text{Ga}_{0.258}$, $\text{Ni}_{0.501}\text{Mn}_{0.207}\text{Ga}_{0.296}$, $\text{Ni}_{0.526}\text{Mn}_{0.231}\text{Ga}_{0.243}$ and $\text{Ni}_{0.53}\text{Mn}_{0.22}\text{Ga}_{0.25}$ reveal essential specific magnetic entropy change values near the first-order structural transition from the high-temperature austenite to the low-temperature martensite phase. Especially high magnetic entropy change is observed in low magnetic fields. However, the peak on the $\Delta S_M(T)$ curve in these compounds is narrow (full width at half maximum about 1.5 K), which leads to low RCP values. Among $\text{La}(\text{M}_{1-x}\text{M}'_x)_{13}$ ($\text{M} = \text{Fe}, \text{Ni}; \text{M}' = \text{Si}, \text{Al}$) compounds $\text{LaFe}_{13-x}\text{Si}_x$ with low Si content ($x \leq 1.6$), which display first-order magnetic phase transition at T_C , show the highest magnetocaloric properties. The specific magnetic entropy change in these compounds is large in low magnetic fields and rapidly decreases with the field increasing. However, specific RCP(S) remains high because of increasing of δT_{FWHM} of the maximum on the $\Delta S_M(T)$ curve with the magnetic field increasing—see data for $\text{LaFe}_{11.7}\text{Si}_{1.3}$ in table 11.2. $\Delta T/\Delta H$ in $\text{LaFe}_{11.7}\text{Si}_{1.3}$ is also high—direct measurement in the field of 14 kOe gave the value of 0.286 K/kOe , which is on the level of that observed in the $\text{Gd}_5(\text{Si}-\text{Ge})_5$ system. However, the peak on $\Delta T(T)$ curve in $\text{LaFe}_{11.7}\text{Si}_{1.3}$ is narrow ($\delta T_{\text{FWHM}} \approx 5\text{ K}$ for $\Delta H = 14\text{ kOe}$). Because of that, the specific RCP(T) is not high—about $1.46\text{ K}^2/\text{kOe}$.

Pecharsky and Gschneidner (2001b) showed that in deciding which magnetic material is more suitable for application in magnetic refrigerators from the point of view of their magnetic entropy change, it is necessary to use the values of ΔS_M calculated per unit of volume. That is because high magnetic field can be created by permanent magnets (and other magnets too) in rather small volume, and the higher the volumetric magnetic entropy change the more effective is the material for magnetic cooling under the same conditions. Because of that, the values in the table 11.2 characterizing magnetic entropy change are given also per cm^3 . As one can see, the highest $\Delta S_M/\Delta H$, RCP(S) and $\Delta T/\Delta H$ are observed in $\text{Fe}_{0.49}\text{Rh}_{0.51}$.

alloy, which, however, displays essential magnetic irreversibility and is expensive. The nonstoichiometric Heusler alloys, $\text{LaFe}_{13-x}\text{Si}_x$ compounds with low Si content ($x \leq 1.6$) and monoclinic $\text{Gd}_5(\text{Si}-\text{Ge})_4$ compounds also have high $\Delta S_M/\Delta H$ values. The $\text{LaFe}_{13-x}\text{Si}_x$ and $\text{Gd}_5(\text{Si}-\text{Ge})_4$ compounds are characterized by large specific RCP(S). The $\text{Gd}_5(\text{Si}-\text{Ge})_4$ compounds also have essential RCP(T), which cannot be said about $\text{LaFe}_{13-x}\text{Si}_x$ compounds where the peak on $\Delta T(T)$ is rather narrow. Gadolinium has the highest specific RCP(T) value ($16.12 \text{ K}^2/\text{kOe}$), which together with large specific RCP(S) ($111 \text{ mJ/cm}^3 \text{ kOe}$), Curie temperature and metallic properties makes it one of the most suitable materials for using in magnetic refrigerators working in the room-temperature range.

As follows from equation (2.16), the value of the magnetocaloric effect ΔT is directly proportional to temperature. In order to obtain a parameter capable of characterizing the magnetocaloric effect irrespective of initial temperature, Tishin *et al* (2002) proposed an effective MCE value ΔT_{eff}

$$\Delta T_{\text{eff}} = \frac{\Delta T}{T\Delta H} \quad (11.36)$$

which is also shown in table 11.2. According to equation (2.79) this parameter should be high for materials with high $\Delta S_M/\Delta H C_H$ values. The latter can occur not only in the case of large $\Delta S_M/\Delta H$ but also when C_H is small. Such a situation can be realized in the low-temperature region, where electronic and lattice contribution to the heat capacities approaches zero for materials with low magnetic heat capacity (or if it is suppressed by a magnetic field). As one can see, the highest ΔT_{eff} value among the materials presented in table 11.2 is observed in $\text{Dy}_3\text{Ga}_5\text{O}_{12}$, which should be recognized as one of the best known of today's materials by this parameter. The next are HoAl_2 ($7.77 \times 10^{-3} \text{ kOe}^{-1}$) and $(\text{Gd}_{0.4}\text{Er}_{0.6})\text{NiAl}$ ($6.31 \times 10^{-3} \text{ kOe}^{-1}$). For other materials presented in table 11.2, ΔT_{eff} is less than $5 \times 10^{-3} \text{ kOe}^{-1}$. High ΔT_{eff} in $\text{Dy}_3\text{Ga}_5\text{O}_{12}$ can be related to large $\Delta S_M/\Delta H$ values ($-\Delta S_M/\Delta H \approx 0.27 \text{ J/mol K kOe}$ for $\Delta H = 30 \text{ kOe}$ at 12 K) and low heat capacity near the temperature where ΔT maximum occurs. Magnetization measurements showed that this compound is an anti-ferromagnet with T_N of 2.54 K (Landau *et al* 1971, Li *et al* 1986). However, Tomokiyo *et al* (1985), from the heat capacity measurements, and later Kimura *et al* (1988) from direct measurements, found a maximum on $\Delta T(T)$ curves at higher temperatures—for $\Delta H = 50 \text{ kOe}$ at about 14 K (see figure 5.9). No maximum was observed on $\Delta S_M(T)$ curves of $\text{Dy}_3\text{Ga}_5\text{O}_{12}$ —the magnetic entropy change absolute value monotonically increased with temperature decreasing down to 4.2 K (see figure 5.8). According to the measurements made by Tomokiyo *et al* (1985) the zero-field heat capacity of $\text{Dy}_3\text{Ga}_5\text{O}_{12}$ revealed a sharp maximum at T_N , a minimum at about 4 K and then a broad Schottky-type maximum at about 15 K . In magnetic fields higher than 30 kOe the heat capacity monotonically

increased up to 20 K. The lattice heat capacity contribution in this region was low and the main heat capacity comes from the magnetic subsystem. For $\Delta H = 30$ kOe the MCE maximum is observed at about 12 K. The heat capacity at this temperature and magnetic field is about 17 J/mol K (in comparison: the heat capacity of Gd near T_C , where ΔT maximum is observed, is about 40 J/mol K in the field of 50 kOe) and ΔS_M is about 8 J/mol K. It follows from equation (2.79) that the peak ΔT value should be ~ 5.7 K, which is close to that observed experimentally (~ 9 K). So, the parameter ΔT_{eff} allows us to determine a material where $\Delta S_M/\Delta H$ is high and heat capacity is low, which is very desirable for magnetic refrigerant materials and, in such a way, should be as high as possible for the materials most suitable for magnetic refrigeration.

Tishin *et al* (2002) made an analysis of the dependence of the MCE properties on the shift of temperature of the magnetic phase transition ($\Delta T_{\text{pt}}/\Delta H$) in a row of magnetic materials with high MCE including Gd and materials with first-order magnetic phase transitions. It was established that the dependence of normalized RCP(S) on $\Delta T_{\text{pt}}/\Delta H$ was linear—see figure 11.28. The obtained regularity shows that the materials with high $\Delta T_{\text{pt}}/\Delta H$ should have large RCP. This criterion can be used for easy searching of the magnetocaloric materials appropriate for using in effective magnetic refrigerators—it is only necessary to measure the shift of magnetic phase transition temperature in the magnetic field. This conclusion was also obtained on the basis of consideration of the magnetocaloric effect influence on the magnetic state of a magnetic material made in section 2.7. It was pointed out that advanced magnetic materials capable of making a new step in solving the problem of construction of commercially available magnetic refrigerators should have values of the magnetic ordering shift of 0.8–1 K/kOe or higher in the magnetic fields of 30–50 kOe (Tishin *et al* 2002).

It is necessary to note that for application of a material in magnetic refrigerators not only the magnetocaloric parameters discussed above are important. The cost of initial materials and fabrication of the final working body, thermoconductivity, long-term stability, toxicity, mechanical durability and some other factors also have to be taken into account. For example, despite Fe–Rh alloys having the highest known value of the MCE near room temperature and in the range of fields up to 20 kOe among magnetocaloric materials, these alloys cannot be widely used in magnetic refrigerators because of high cost of Rh and should be considered only as a solid physical demonstration of the capabilities of magnetic refrigeration materials and a guiding line in development of new magnetic refrigerants.

In this chapter we have considered the application of magnetic materials in refrigerators and cryocoolers. The passive regenerators of the cryocoolers are the devices where the materials with high magnetic heat capacity and low magnetic ordering temperatures are used. Numerous experimental investigations made in this field allowed determination of the materials most suitable

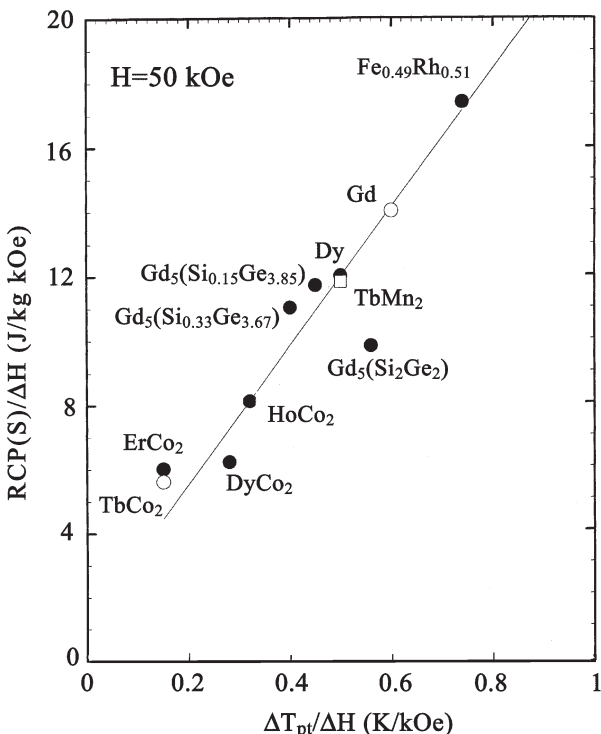


Figure 11.28. The dependence of the normalized relative cooling power on the shift of the magnetic transition temperature in a magnetic field of 50 kOe (in the case of $Fe_{0.49}Rh_{0.51}$ the data for $H = 20$ kOe were used) (Tishin *et al* 2002).

for this purpose. Among them such typical representatives as intermetallic compounds Er_3Ni , $ErNi_2$, $ErNi_{0.9}Co_{0.1}$, rare earth metal Nd, interstitial alloy based on Er and Er–Pr alloys should be mentioned. It was also shown that the hybrid regenerators consisting of layers of the magnetic materials could be effective. Various forms of magnetic materials such as wires, perforated plates, foils and spherical particles were tried in the regenerators. Spherical particles have essential advantages in comparison with others and is the only possible form in the case of intermetallic compounds because of their mechanical properties. It was shown that passive magnetic regenerators considerably increase the effectiveness of the conventional gas cycle cryocoolers, such as the Gifford–McMahon cryocooler.

We also considered magnetic thermodynamic refrigeration cycles, such as Carnot, and regenerator Bryton, Ericsson and active magnetic regenerator (AMR) cycles, and operational principles of magnetic refrigerators. The devices working on the Carnot cycle are effective in the low-temperature range (below 20 K), where regeneration is not needed. For higher

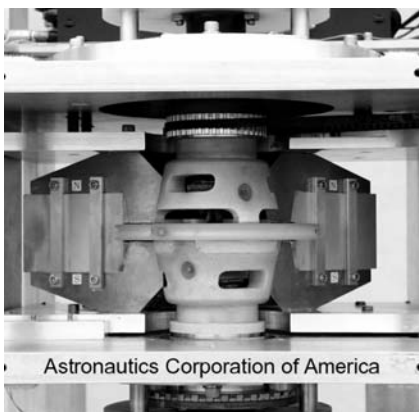


Figure 11.29. A magnetic refrigerator using a permanent magnet working in the room-temperature range, designed by Astronautics Corporation of America using magnetocaloric material characterized by Ames Laboratory (by the courtesy of Astronautics Corporation of America (USA)).

temperatures the regenerator cycles are suitable. Theoretical estimations showed that the critical part in the magnetic regenerator cooling devices is a regenerator, which determines the effectiveness of the whole device. From this point of view the best design is active magnetic regenerator refrigerator (AMRR) where the magnetic working body can also fulfil the functions of a regenerator. Two main designs of AMRR were proposed: reciprocating and wheel-type. The latter design has considerable advantages. In May 2002 Astronautics Corporation of America together with Ames Laboratory presented a magnetic refrigerator working in the room-temperature range. It is composed of a wheel that turns through the field of a permanent magnet—this part of the device is shown in figure 11.29. The wheel is packed with spherical particles of gadolinium that act as the refrigerant in the AMR cycle. The heat transfer is via water that is pumped through the wheel and heat exchangers. This and other achievements made in the field of magnetic refrigeration design shows that a magnetic refrigerator is not only a theoretical construction but already has been realized in practice. The potential advantages of magnetic refrigerators discussed in this chapter can make them competitive with traditional refrigerators working on gas-vapour cycles.

The question about an effective working body is one of the key questions in the development of magnetic refrigerators along with their optimal design. At present there is a considerable amount of magnetic materials displaying high magnetocaloric properties in a wide temperature range. Rare earth metals have an advantage related to their metallic nature: they are easily machinable. Rare earth metal gadolinium is characterized by one of the best magnetocaloric parameter sets and is often used in experimental

magnetic refrigerators working near room temperature. The $\text{Gd}_5(\text{Si}-\text{Ge})_4$ and $\text{La}(\text{Fe}-\text{Si})_{13}$ systems should be regarded as the most promising of those. The compounds belonging to these systems display high magnetic entropy and adiabatic temperature change and their magnetic ordering temperatures can be tuned in a wide range. At the same time, such intermetallic compounds with first-order transition as $\text{Fe}-\text{Rh}$, MnAs and $\text{MnFe}(\text{As}-\text{P})$ can be considered as a beautiful fundamental demonstration of future prospects of increasing MCE and magnetic entropy change values. However, it should be noted that searching and development of new effective magnetocaloric materials, as before, remains an actual and important task.

Chapter 12

Conclusion

In this book we have considered an interesting phenomenon, which has important fundamental and practical applications—the magnetocaloric effect (MCE), displaying itself in changing magnetic entropy and temperature of a magnetic material under application of a magnetic field. We have discussed theoretical approaches to the MCE, methods of its investigation, currently available experimental results on magnetocaloric phenomena in a numerous number of materials, and the application of magnetic materials in conventional and magnetic refrigeration devices.

A general thermodynamic approach, Landau theory of second-order phase transitions and mean field approximation (MFA) are usually used for description of the MCE. These models allowed us to establish a set of important regularities and to fulfil calculations of the MCE in various magnetic materials, which were later confirmed by experimental measurements. In particular, positive magnetic entropy change under application of the magnetic field observed in some magnetic materials with antiferromagnetic, ferromagnetic or more complex noncollinear magnetic structures (in simple collinear spin structures such as ferromagnets it is always negative) can be explained using MFA by the disordering action of the magnetic field on these spin structures (antiferromagnetic-type paraprocess). Recently the authors of this book, by means of the thermodynamic approach, considered the contributions to the magnetic entropy change arising under magnetization and established the condition necessary to achieve the highest MCE (this question is discussed in section 2.4). Thermodynamic consideration of the magnetocaloric effect at the first- and second-order magnetic transitions were made in the works of Tishin (1998a) and Tishin *et al* (1999a, 2002) and Pecharsky *et al* (2001). It was shown that the value of the magnetic transition temperature shift under the action of the magnetic field can be regarded as the upper limit of the specific MCE value per ΔH ($\Delta T/\Delta H$) (Tishin 1998a, Tishin *et al* 2002). This gives a new criterion for searching materials with high MCE properties—they should have essential magnetic transition temperature shift in the magnetic field. It should be noted that this indication can be easily established

experimentally. In the recent works of von Ranke *et al* (1998a,b 2000a, 2001a) the MCE in intermetallic compounds RAI_2 , RNi_2 (R =rare earth element) and PrNi_5 was determined with the help of quantum-mechanical calculations taking into account crystal field effects.

Experimental methods of the MCE determination can be divided into direct and indirect. The former are based on the direct measurement of adiabatic temperature change in a magnetic material induced by applying (or removing) a magnetic field. In the latter methods the magnetic entropy and adiabatic temperature changes can be calculated indirectly, in particular, from the heat capacity or magnetization temperature and field dependences. The reliability of determination of the MCE properties on the basis of the heat capacity measurements was determined in a number of works (for example, by Dan'kov *et al* 1988). The magnetic entropy change can be calculated from the magnetization data on the basis of Maxwell equation (2.9a). As argued by Gschneidner *et al* (2000c), this method should give correct results even near the first-order transitions. However, in some cases, the results of direct and indirect measurements can have certain difference and this problem needs further detailed consideration.

Today there is a considerable amount of experimental investigation of the MCE in various magnetic materials with different types of magnetic ordering and magnetic phase transitions, the main part being undertaken in order to find a material with high magnetocaloric properties suitable for application in magnetic refrigerators. However, the MCE is also a sensitive tool allowing study of magnetic phase transformations occurring under the action of temperature and magnetic field and determination of magnetic interactions in the material under investigation. For these purposes the MCE was successfully used for rare earth metals and their alloys, where the MCE anomalies were found at the Curie, Néel, tricritical points and field-induced metamagnetic transitions. Chernishov *et al* (2002a–c) using MCE and heat capacity measurements found new peculiarities in the magnetic phase diagrams of Tb and Dy. In high purity Dy essential (up to two times) increasing of the MCE (in comparison with previously reported results) in the paramagnetic region near the Néel temperature related to the existence of clusters with short-range antiferromagnetic order was suggested (Chernishov *et al* 2002c). A set of fine peculiarities in the magnetic behaviour of rare earth garnets was revealed by the MCE (see section 5.1.1). Interactions between various magnetic sublattices in the garnets were also determined from the MCE measurements.

From the practical point of view the magnetocaloric materials should have large adiabatic temperature and magnetic entropy changes (ΔS_M and ΔT). As shown by Pecharsky and Gschneidner (2001b), these two parameters do not have direct relationship: if a material has a large heat capacity this leads in accordance with equation (2.79) to a reduced MCE even for high magnetic entropy change. Such a situation is observed, for example, in doped

perovskite-type manganese oxides considered in section 5.2.3. Among the materials with high magnetocaloric properties one should first of all mention $\text{Fe}_{0.49}\text{Rh}_{0.51}$ alloy, which in its quenched state reveals the highest values of the MCE among the magnetic materials investigated to date (Annaorazov *et al* 1992). However, this alloy cannot be used in practice because of its essential magnetic irreversibility and high cost. It (its magnetocaloric characteristics) can only serve as some kind of reference point in the development of new perspective magnetocaloric materials. Other materials with high magnetocaloric properties, which makes them in principle suitable for use in magnetic refrigerators, are heavy rare earth metals and some of their alloys, intermetallic compounds RCO_2 , RAI_2 , $\text{La}(\text{Fe}-\text{Si})_{13}$, $\text{Gd}_5(\text{Si}-\text{Ge})_4$ system, MnAs and $\text{MnFeP}_{1-x}\text{As}_x$ system. Among them $\text{La}(\text{Fe}-\text{Si})_{13}$ and $\text{Gd}_5(\text{Si}-\text{Ge})_4$ systems should be marked out. $\text{La}(\text{Fe}-\text{Si})_{13}$ alloys with low Si content and first-order magnetic transition at T_C have high $\Delta S_M/\Delta H$, $\Delta T/\Delta H$ and relative cooling power (RCP) values. Recently it was shown that by introduction of hydrogen the Curie temperature of the alloys can be increased up to room temperature values with preservation of their high magnetocaloric characteristics (the alloy $\text{LaFe}_{11.57}\text{Si}_{1.43}\text{H}_{1.3}$ —see table 11.2) (Fujieda *et al* 2002). The $\text{Gd}_5(\text{Si}-\text{Ge})_4$ system is also characterized by considerable values of magnetocaloric parameters $\Delta S_M/\Delta H$, $\Delta T/\Delta H$ and RCP in a wide temperature range. The magnetic ordering temperatures in this system can be tuned from liquid nitrogen up to room temperatures. This system and its magnetocaloric properties are thoroughly studied in the works of Gschneidner and Pecharsky and the technology of preparation of these compounds is rather well developed. It should be noted that high MCE is observed in the materials with first-order temperature or field-induced magnetic phase transition, where magnetization is changed sharply, which leads to essential ΔS_M values. If such materials have not large heat capacity, ΔT values are also high. Frequently the first-order magnetic phase transition is accompanied by essential magnetovolume effects (magnetostriiction, thermal expansion, etc.), or even by crystal structure change, as takes place, for example, in MnAs , $\text{Gd}_5(\text{Si}-\text{Ge})_4$ and Dy . The magnetovolume effects in such materials give essential contribution to the magnetic entropy change. However the character of magnetoelastic, magnetic anisotropy and exchange energy change influence on the MCE value under the first-order transitions is not investigated in detail and requires further studies.

Besides high magnetocaloric properties, the materials suitable for use in magnetic refrigerators should also have low toxicity, sufficient thermoconductivity, long term stability and mechanical durability, and low cost. The price of materials consists not only of the cost of initial materials but also of the preparation process cost. This determines the importance of development of effective and cheap technological processes of material preparation. Some elements apparently can never be used in the magnetocaloric materials suitable

for wide practical applications because of their high price. Among them are ruthenium, palladium, osmium, iridium, platinum, silver, gold and rhodium (which forms half of the $\text{Fe}_{0.49}\text{Rh}_{0.51}$ alloy mentioned above). Such elements as beryllium, cadmium, mercury, tellurium, lead and arsenic are toxic and their presence may complicate the practical use of materials based on them. On the basis of the analysis of the magnetocaloric materials existing at present, it is natural to expect that Fe or Co will be widely used in future in the alloys and compounds with high magnetocaloric properties suitable for practical applications.

Development of effective design is very important in the creation of magnetic refrigeration devices along with the question of magnetic working bodies. It was shown that below 20 K the Carnot magnetic refrigeration cycle is effective and for higher temperatures regenerator cycles should be used. Among the latter the most suitable is an active magnetic regenerator (AMR) refrigeration cycle. In May 2002 Astronautics Corporation of America together with Ames Laboratory presented the wheel-type magnetic refrigerator working in the room-temperature range on the AMR cycle. The magnetic refrigeration devices have a set of advantages in comparison with conventional gas-vapour cycle refrigerators, among which are high efficiency and reliability, energy and cost-saving potential. Room-temperature magnetic refrigerators are also environmentally friendly, because they do not use toxic and volatile liquid refrigerants with negative influence on the Earth's atmosphere. Recent achievements in this field give hope that the magnetic refrigeration technology will find practical application in industry and life. For example, in spite of the high price of the first magnetic refrigerator prototype working near room temperature, it can be used in such applications as extraction of water from air in a desert by a condensation method (Pecharsky 2002). Solar-generated electricity can be used in this case as a power source for the refrigerator.

In conclusion, we should say that in this book we tried to give, as far as possible, a comprehensive and clear presentation of the MCE problem, which is rapidly developing at the present time. We hope that our book will help investigators and engineers working in the field of MCE and its practical applications.

Appendix 1

Units used in the book

In this appendix we will consider units used in our book and conversion relations between them. More detailed information about this question can be found in the following references: Smith (1970), Vigoureux (1971), Brown (1984), Jiles (1998).

The International System of Units (SI) is based on seven base units: metre (length), kilogram (mass), second (time), ampere (electric current), kelvin (thermodynamic temperature), mole (amount of substance), and candela (luminous intensity). Other SI units, including units for magnetism, are derived units and can be expressed in terms of base units using mathematical operations of multiplication and division.

In scientific literature, Gaussian and CGS (centimetre-gram-second) unit systems are often used. The CGS system has three base units: centimetre (length), gram (mass), and second (time). However new definitions are needed in this case for units of electricity and magnetism. It is necessary, in particular, to introduce a unit of electric charge, which can be done in two ways—on the basis of Coulomb's law describing the force of interaction between two static electric charges, or with the help of the law of force between currents (moving charges) flowing in parallel wires. In the first case we deal with the electrostatic unit (e.s.u.) subsystem, and in the second with the electromagnetic unit (e.m.u.) subsystem. In the e.m.u. system the unit of charge is called abcoulomb and in the e.s.u. system it is called statcoulomb, and they are related as abcoulomb/statcoulomb = c , where c is the speed of light in free space (see table A1.3). An analogous relation is valid for current units in e.m.u. and e.s.u. systems—abampere and statampere, respectively. In the Gaussian system for charge, current, electric field intensity and other primarily electric quantities, the e.s.u. subsystem is used; and for magnetic field, magnetic induction, magnetization, magnetic moment and other primarily magnetic quantities, the e.m.u. subsystem is used. The relations between magnetic induction \vec{B} , magnetic field (magnetic field strength) \vec{H} , magnetization \vec{M} and magnetic polarization (intensity of magnetization) \vec{J} and magnetic susceptibility χ in isotropic medium, together with relations for magnetic moment \vec{m} , energy of magnetic

Table A1.1. Relations between various magnetic values in Gaussian and SI systems.

Quantity	Gaussian	SI (Sommerfeld)	SI (Kennelly)
Magnetic induction (B)	$\vec{B} = \vec{H} + 4\pi\vec{M}$	$\vec{B} = \mu_0(\vec{H} + \vec{M})$	$\vec{B} = \mu_0\vec{H} + \vec{J}$
Magnetization (M)	$\vec{M} = \chi\vec{H}$	$\vec{M} = \chi_S\vec{H}$	$\vec{M} = \vec{J}/\mu_0$
Magnetic polarization (J)	$\vec{J} = \vec{M}$	$\vec{J} = \mu_0\vec{M}$	$\vec{J} = \chi_K\vec{H}$
Torque on the moment ($\vec{\tau}$)	$\vec{\tau} = \vec{m} \times \vec{H}$	$\vec{\tau} = \vec{m} \times \vec{B}$	$\vec{\tau} = \vec{m} \times \vec{H}$
Energy of the moment (E)	$E = -\vec{m} \cdot \vec{H}$	$E = -\vec{m} \cdot \vec{B}$	$E = -\vec{m} \cdot \vec{H}$

moment (in free space) E and torque on the moment (in free space) $\vec{\tau}$ in the Gaussian system, are presented in table A1.1. Magnetization M and magnetic polarization J , which are the magnetic moment of a unit volume, are identical in the Gaussian system. As one can see from table A1.1, in free space in the Gaussian system $\vec{B} = \vec{H}$.

In the SI system in the relations between B , H , M and J the quantity μ_0 appears, which is called the permeability of free space and is defined as

$$\mu_0 = 4\pi \times 10^{-7} H/m \quad (\text{N/A}^2 \text{ or Wb/Am}). \quad (\text{A1.1})$$

It is related to permittivity of free space ϵ_0 as

$$\mu_0\epsilon_0 = c^{-2} \quad (\text{A1.2})$$

where c is the speed of light in free space. In contrast to the Gaussian system, in the SI system $\vec{B} = \mu_0\vec{H}$ even in free space—see table A1.1. Using the SI system the relationship between B , H , M and J can be presented in two ways according to the Sommerfeld and Kennelly conventions. These two treatments differ in definition of the magnetic moment of a current loop. In the Sommerfeld convention the moment is defined as a production of the current on the loop square and in the Kennelly convention this quantity is additionally multiplied by μ_0 . Accordingly, there are different formulae for the energy of the magnetic moment and torque on the moment in the magnetic field in free space (see table A1.1). Magnetic moment per unit volume has various names in Sommerfeld and Kennelly conventions (magnetization and magnetic polarization, respectively) and is measured in different units—see table A1.2. According to Jiles (1998), the Sommerfeld convention was accepted for magnetism measurements by the International Union for Pure and Applied Physics (IUPAP) and was adopted by the magnetism community. Magnetic volume susceptibilities χ_S and χ_K are also measured in different units in Sommerfeld and Kennelly conventions. Table A1.2 presents base, some derived and magnetic and electric units in Gaussian and SI systems and corresponding conversion factors. Some physical constants, which are useful in thermal and magnetic investigations, are shown in table A1.3.

Table A1.2. Magnetic and electric units in Gaussian and SI systems and corresponding conversion factors.

Quantity	SI	Gaussian	Conversion factor
Length	metre (m)	centimetre (cm)	$1\text{ m} = 10^2 \text{ cm}$
Mass	kilogram (kg)	gram (g)	$1\text{ kg} = 10^3 \text{ g}$
Time	second (s)	second (s)	$1\text{ s} = 1\text{ s}$
Electric current	ampere (A)	esu	$1\text{ A} = 0.1c \text{ esu}$
Thermodynamic temperature	kelvin (K)	—	—
Amount of substance	mole (mol)	—	—
Density, mass density	kg/m^3	g/cm^3	$1\text{ kg/m}^3 = 10^{-3} \text{ g/cm}^3$
Force	newton (N) = m kg s^2	dyne (dyn) = cm g s^2	$1\text{ N} = 10^5 \text{ dyn}$
Pressure, stress	pascal (Pa) = N/m^2	dyn/cm^2	$1\text{ Pa} = 10 \text{ dyn/cm}^2$
Energy, work, quantity of heat	joule (J) = Nm	erg (erg) = dyn cm	$1\text{ J} = 10^7 \text{ erg}$
Power	watt (W) = J/s	erg/s	$1\text{ W} = 10^7 \text{ erg/s}$
Moment of force	N m	dyn cm	$1\text{ N m} = 10^7 \text{ dyne cm}$
Heat flux density	W/m^2	—	—
Specific heat capacity, specific entropy	J/(kg K)	—	—
Molar heat capacity, molar entropy	J/(mol K)	—	—
Thermal conductivity	W/(m K)	—	—
Molar heat capacity, molar entropy	J/(mol K)	coulomb (C) = As	$1\text{ C} = 0.1c \text{ esu}$
Electric charge, quantity of electricity	volt (V) = W/A	esu	$1\text{ V} = 10^8 c^{-1} \text{ esu}$
Electric potential difference, electromotive force	V/m	esu/cm	$1\text{ V/m} = 10^6 c^{-1} \text{ esu/cm}$
Electric field strength	farad (F) = C/V	cm	$1\text{ F} = 10^{-9} c^2 \text{ cm}$
Capacitance	ohm (Ω)	s/cm	$1\text{ } \Omega = 10^9 c^{-2} \text{ s/cm}$
Electric resistance	henry (H) = Wb/A	s^2/cm	$1\text{ H} = 10^9 c^{-2} \text{ s}^2/\text{cm}$
Inductance	weber (Wb) = Vs	maxwell (Mx) = G cm^2	$1\text{ Wb} = 10^8 \text{ Mx}$
Magnetic flux	tesla (T) = Wb/m^2	gauss (G)	$1\text{ T} = 10^4 \text{ G}$
Magnetic field (magnetic field strength)	A/m	oersted (Oe)	$1\text{ A/m} = 4\pi \times 10^{-3} \text{ Oe}$

Magnetization (volume magnetization)	A/m	emu/cm^3	$1 \text{ A/m} = 10^{-3} \text{ emu}/\text{cm}^3$
Magnetic polarization (intensity of magnetization)	$\text{T} = \text{Wb}/\text{m}^2$	G	$1 \text{ T} = 10^4 / 4\pi \text{ emu}/\text{cm}^3$
	A m^2 (Sommerfeld)	$\text{emu} = \text{G cm}^3 = \text{erg}/\text{G}$	$1 \text{ A m}^2 = 10^3 \text{ emu}$
Magnetic moment	Wb m (Kennelly)		$1 \text{ Wb m} = 10^3 \text{ emu}$
	$(\text{A m}^2)/\text{kg}$	emu/g	$1 (\text{A m}^2)/\text{kg} = 1 \text{ emu/g}$
Mass magnetization (magnetic moment per unit mass)	dimensionless	dimensionless	$1(\text{SI}) = 1/4\pi \text{ (Gaussian)}$
Volume magnetic susceptibility ($\chi = M/H$)			

esu and emu denote corresponding units in e.s.u. and e.m.u. subsystems; c is the speed of light in free space (29979245800 cm/s).

Table A1.3. Some physical constants.

Quantity	SI	Gaussian
Speed of light in free space (c)	299792458 m/s	29979245800cm/s
Planck constant ($\hbar = h/2\pi$)	$1.05457266(63) \times 10^{-34} \text{ Js}$	$1.05457266(63) \times 10^{-27} \text{ ergs}$
Avogadro's number (N_A)	$6.0221367(36) \times 10^{23} \text{ mol}^{-1}$	—
Atomic mass constant, m (C^{12})/12 (m_u)	$1.6605402(10) \times 10^{-27} \text{ kg}$	$1.6605402(10) \times 10^{-24} \text{ g}$
Molar gas constant (R)	$8.314510(70) \text{ J/(mol K)}$	$8.314510(70) \times 10^7 \text{ erg/(mol K)}$
Boltzmann constant (k_B)	$1.380658(12) \times 10^{-23} \text{ J/K}$	$1.380658(12) \times 10^{-16} \text{ erg/K}$
Elementary charge (e)	$1.60217733(49) \times 10^{-19} \text{ C}$	$4.8032068(14) \times 10^{-10} \text{ esu}$
Bohr magneton (μ_B)	$9.2740154(31) \times 10^{-24} \text{ J/T}$	$9.2740154(31) \times 10^{-21} \text{ erg/G}$
Bohr radius (a_0)	$0.529177249(24) \times 10^{-10} \text{ m}$	$0.529177249(24) \times 10^{-8} \text{ cm}$
Permeability of vacuum (μ_0)	$4\pi 10^{-7} \text{ H/m (N/A}^2)$	—
Permittivity of vacuum (ϵ_0)	$1/\mu_0 c^2 = 8.854187817 \times 10^{-12} \text{ F/m}$	—

Let us now consider the units which are used in this book for the specific heat capacity and magnetic entropy change. In the literature concerning magnetocaloric effect the following units can be found: J/kg K, J/cm³ K, J/mol K, J/g-at K and J/mol(atoms)K. J/kg K and J/mol K are the units of specific heat capacity and entropy and molar heat capacity and entropy, respectively, in the SI system. They are related between themselves and with J/cm³ K as follows:

$$1 \text{ J/mol K} = (10^3/M_m) \text{ J/kg K} \quad (\text{A1.3})$$

$$1 \text{ J/cm}^3 \text{ K} = (10^3/\rho) \text{ J/kg K} \quad (\text{A1.4})$$

where ρ is the density (g/cm³) and M_m is the molar mass, which can be calculated for the matter with, for example, the molecular formula $A_xB_yC_z$ as

$$M_m = xA_A + yA_B + zA_C \quad (\text{A1.5})$$

where A_A , A_B and A_C are atomic weights of the corresponding atoms. As follows from equations (A1.3) and (A1.4)

$$1 \text{ J/mol K} = (\rho/M_m) \text{ J/cm}^3 \text{ K} \quad (\text{A1.6})$$

The unit J/g-at K is related to J/mol K as

$$1 \text{ J/g-at K} = n_a \text{ J/mol K}. \quad (\text{A1.7})$$

where n_a is a total number of atoms in the molecule. If a molecule contains only one atom, as in pure metals Fe, Co, Gd, etc., then $1 \text{ J/g-at K} = 1 \text{ J/mol K}$. The units J/g-at K and J/mol(atoms) K are equal. The unit 1 mJ used in some tables in this book is equal to 10^{-3} J. Sometimes one more unit called ‘calorie’ is used in the literature as a measure of heat. According to NIST Special Publication 330 (2001) several calories are in use: a calorie labelled ‘at 15 °C’ ($1 \text{ cal}_{15} = 4.1855 \text{ J}$); a calorie labelled ‘IT’ (International table) ($1 \text{ cal}_{\text{IT}} = 4.1868 \text{ J}$); and a calorie labelled ‘thermochemical’ ($1 \text{ cal}_{\text{th}} = 4.184 \text{ J}$).

Appendix 2

Magnetic, thermal and physical properties of some metals, alloys, compounds and other materials

Table A2.1 presents magnetic, thermal and physical properties of some metals, alloys, compounds and other materials. The data about magnetic parameters of rare earth metals, their alloys and compounds with rare earth elements can also be found in the books and reviews of Taylor and Darby (1972), Wallace (1973), Buschow (1977), Kirchmayer and Poldy (1978), Pfranger *et al* (1982), Kirchmayer and Poldy (1982) and Gschneidner (1993b).

Table A2.1. Curie temperature T_C , Néel temperature T_N , saturation magnetization I_s , saturation magnetic moment per atom μ_0 at 0 K, effective magnetic moment μ_{eff} per magnetic atom, Debye temperature T_D , density ρ , heat capacity C (heat capacity at T_C means peak value of the heat capacity near T_C) in zero magnetic field and thermal conductivity λ for some metals, alloys, compounds and other materials. References are shown in brackets.

Substance	T_C (K)	T_N (K)	I_s (emu/g)	μ_0 (μ_B)	μ_{eff} (μ_B)	T_D (K)	ρ (g/cm^3)	C ($\text{J}/\text{kg}\cdot\text{K}$) ($\text{J}/\text{mol}\cdot\text{K}$)	λ ($\text{J}/\text{cm}\cdot\text{K}$)
Fe	1043 [1]	—	217.75 (293 K) [1] 221.89 (0 K) [1]	2.218 [1]	—	470 [64]	7.874 [1]	~77 (T_C) [2] ~76 (T_C) [4] ~44 (923 K) [4] 25 (295 K) [3]	0.72 (373 K) [3] 0.8 (293 K) [3] 0.98 (173 K) [3] 1.32 (103 K) [3]
Co	1394 [1]	—	169 (293 K) [1] 170 (0 K) [1]	1.714 [1]	—	445 [64]	8.78 [1]	—	—
Ni	636 [1]	—	54.39 (288 K) [1] 57.5 (0 K) [1]	0.604 [1]	—	450 [64]	8.90 [1]	~31.8 (T_C) [70] ~39.5 (T_C) [4] ~33.8 (573 K) [4] 26.1 (293 K) [3]	0.83 (373 K) [3] 0.91 (293 K) [3] 1.14 (173 K) [3] 1.56 (103 K) [3]
Al	—	—	—	—	—	428 [64]	2.707 [3]	24.4 (293 K) [3] 2.37 (293 K) [3] 2.42 (173 K) [3] 3.02 (103 K) [3]	2.4 (373 K) [3] 2.37 (293 K) [3] 2.42 (173 K) [3]

Table A2.1. Continued.

Substance	T_C (K)	T_N (K)	I_s (emu/g)	μ_0 (μ_B)	μ_{eff} (μ_B)	T_D (K)	ρ (g/cm ³)	C (J/kg·K)	λ (J/cm·K)
Cu	—	—	—	—	—	343 [64]	8.954 [3]	24.4 (293 K) [3]	3.91 (373 K) [3] 3.98 (293 K) [3]
								4.2 (173 K) [3]	
								4.83 (103 K) [3]	
								~5 (80 K) [65]	
								~50 (18 K) [65]	
								~11 (3.5 K) [65]	
Ag	—	—	—	—	—	225 [64]	10.524 [3]	25.5 (293 K) [3]	4.22 (373 K) [3] 4.27 (293 K) [3]
								4.31 (173 K) [3]	
								4.49 (103 K) [3]	
								~10.5 (20 K) [25]	
								~2.5 (3 K) [25]	
Pb	—	—	—	—	—	105 [64]	11.373 [3]	0 (~5 K) [6] 2.6 (10 K) [6] 13.9 (25 K) [6] 26.9 (293 K) [3]	0.34 (373 K) [3] 0.35 (293 K) [3] 0.37 (173 K) [3] 0.4 (103 K) [3]
								~0.45 (50 K) [5]	
								~5 (6 K) [5]	
Gd	293.4 [7]	—	—	7.98 [7]	7.63 [7]	169 [7]	7.8 [7]	37.1 (298 K) [7] ~30 (350 K) [8] ~60 (T_C) [8] ~4 (20 K) [8]	0.105 (298 K) [7] 0.091 (291 K) [9] ~0.11 (310 K ^c) [10] ~0.106 (310 K ^a) [10]

Tb	219.5 [7]	230.0 [7]	-	9.34 [7]	9.77 [7]	169.6 [7]	8.23 (hep) [7]	28.9 (298 K) [7]	0.111 (298 K) [7]
						8.219	~79.5 (T_N) [11]	0.103 (291 K) [9]	
						(ortho) [7]	~48 (200 K) [11]	~0.16 (300 K ^c) [10]	
								~0.095 (300 K ^a) [10]	
								~0.175 (100 K ^c) [10]	
								~0.124 (100 K ^a) [10]	
								~0.294 (~20 K ^c) [10]	
								~0.2 (~20 K ^a) [10]	
Dy	89 [7]	179 [7]	-	10.33 [7]	10.83 [7]	192 [7]	8.551 [7]	27.7 (298 K) [7]	0.107 (298 K) [7]
							~81.3 (T_N) [12]	~0.19 (300 K) [13]	
							~40.6 (100 K) [12]	0.104 (291 K) [9]	
							~203 (T_C) [12]	~0.117 (300 K ^c) [14]	
							~32.5 (70 K) [12]	~0.102 (300 K ^a) [14]	
								~0.95 (100 K ^c) [14]	
								~0.102 (100 K ^a) [14]	
								~0.133 (~25 K ^c) [14]	
								~0.165 (~25 K ^a) [14]	
Ho	20 [7]	132 [7]	-	10.34 [7]	11.2 [7]	175 [7]	8.795 [7]	27.2 (298 K) [7]	0.162 (298 K) [7]
							~26 (150 K) [15]	0.106 (291 K) [9]	
							~69 (T_N) [15]	~0.22 (300 K ^c) [10]	
							~39 (100 K) [15]	~0.14 (300 K ^a) [10]	
								~0.16 (100 K ^c) [10]	
								~0.128 (100 K ^a) [10]	
								~0.184 (~50 K ^c) [10]	
								~0.152 (~50 K ^a) [10]	

Table A2.1. Continued.

Substance	T_C (K)	T_N (K)	I_s (emu/g)	μ_0 (μ_B)	μ_{eff} (μ_B)	T_D (K)	ρ (g/cm ³)	C (J/kg·K) (J/mol·K)	λ (J/cm·K)
Er	20 [7]	85 [7]	—	9.1 [7]	9.9 [7]	177 [7]	9.066 [7]	28.1 (298 K) [7] ~24.5 (100 K) [16] ~35.5 (T_N) [16] ~2.5 (10 K) [16]	0.145 (298 K) [7] 0.138 (291 K) [9] ~0.185 (300 K ^c) [14]
Tm	32 [7]	58 [7]	—	7.14 [7]	7.61 [7]	179 [7]	9.321 [7]	27 (298 K) [7] ~27 (70 K) [17] ~42.2 (T_N) [17] ~10 (20 K) [17]	0.169 (298 K) [7] ~0.24 (300 K ^c) [18] ~0.14 (300 K ^a) [18] ~0.203 (100 K ^c) [18] ~0.115 (100 K ^a) [18] ~0.21 (~12 K ^c) [18] ~0.25 (~12 K ^a) [18]
Nd	—	19.9 (hex. sites); 7.5 (cub. sites) [7]	—	2.2 [7]	3.45 [7]	163 [7]	7.008 [7]	27.4 (298 K) [7] ~12.8 (25 K) [19] ~3.5 (5 K) [19]	0.165 (298 K) [7] 0.165 (291 K) [9]
Yb	—	—	—	—	—	109 [7]	6.903 [7]	26.7 (298 K) [7]	0.385 (298 K) [7]
Lu	—	—	—	—	—	183.2 [7]	9.841 [7]	26.8 (298 K) [7]	0.164 (298 K) [7]
								~0.23 (300 K ^c) [14] ~0.14 (300 K ^a) [14] ~0.28 (100 K ^c) [14] ~0.16 (100 K ^a) [14]	

MnAs	312 [20]	—	3.4 [20]	4.95 [20]	—	6.18 [71]	—	~55 (450 K) [21] ~580 (T_c) [21] ~55 (200 K) [21]
Gd ₃ Ga ₅ O ₁₂	—	—	—	—	4.58 [22]	—	7.09 ^c	376.34 (300 K) [23] ~0.6 (70 K, sc ^b) [24] ~5 (20 K, sc ^a) [25]
Dy ₃ Ga ₅ O ₁₂	—	0.373 [26]	—	—	4.15 ([111]) [27]	—	7.32 ^c	157.52 (100 K) [23] ~1.2 (3 K, sc ^a) [25] 0.92 (10 K) [23] ~0.5 (30 K) [25] 9.71 (2 K) [23]
Dy ₃ Al ₅ O ₁₂	—	2.54 [30]	—	—	5.25 ([111]) [22]	—	—	~11 (12 K) [28] ~0.18 (10 K) [29] ~0.8 (2 K) [26] ~0.3 (4.5 K) [29] ~25 (T_N) [26] ~0.07 (2 K) [29] ~0.7 (0.1 K) [26]
LaAlO ₃	—	—	—	—	—	—	748 [73]	~1.2 (4 K) [35] ~0.6 (20 K) [31] ~44.1 (T_N) [35] ~1.5 (11 K) [31] ~1.7 (1.5 K) [35]
DyAlO ₃	—	3.52 [32]	—	—	6.88 (b-axis) [22]	—	7.701 ^c	105.8 (298 K) [73] 0.136 (300 K) [73] ([110]) 0.44 (77 K) [73]
ErAlO ₃	—	0.6 [33]	—	—	4.35 (c-axis) [34]	—	7.953 ^c	~1.5 (20 K) [31] ~4 (11 K) [31] ~1.3 (4.2 K) [31] (c-axis)
								~8 (25 K) [31] ~12 (18 K) [31] ~2.5 (4.2 K) [31] (c-axis)

Table A2.1. Continued.

Substance	T_C (K)	T_N (K)	I_s (emu/g)	μ_0 (μ_B)	μ_{eff} (μ_B)	T_D (K)	ρ (g/cm^3)	C ($J/\text{kg}\cdot\text{K}$) ($\text{J}/\text{mol}\cdot\text{K}$)	λ ($\text{J}/\text{cm}\cdot\text{K}$)
LaMnO ₃	—	136 [36]	—	—	—	—	—	~120 (350 K) [36] ~92 (200 K) [36] ~82 (T_N) [36] ~18 (50 K) [36]	~0.01 (300 K) [37] (~0.0085) (100 K) [37] (~0.005) (20 K) [37]
La _{0.7} Ca _{0.3} MnO ₃	255 [37]	—	—	—	—	—	—	~0.012 (300 K) [37] ~0.026 (100 K) [37]	~0.035 (30 K) [37]
La _{0.67} Ca _{0.33} MnO ₃	263 [38]	—	—	—	—	—	—	~120 (300 K) [38] ~190 (T_C) [38] ~45 (100 K) [38] ~14 (50 K) [38]	— ~0.9 (5 K) [40]
GdVO ₄	—	2.5 [39]	—	—	7.9 (a-axis) 7.0 (c-axis) [40]	5.47 ^c	—	~10 (15 K) [40]	~0.9 (5 K) [40]
DyVO ₄	—	3 [40]	—	—	8.6 (a-axis) 7.0 (c-axis) [40]	5.72 ^c	—	~0.4 (28 K) [40] ~0.15 (5 K) [40]	—
CeAl ₂	—	3.8 [66]	—	—	—	4.933 ^c	—	~0.12 (295 K) [43] ~0.01 (10 K) [43]	—
PrAl ₂	33 [41]	—	—	—	—	5.009 ^c	—	~0.17 (295 K) [43] ~0.08 (100 K) [43] ~0.12 (14 K) [43]	—

NdAl ₂	65 [41]	–	2.5 [41]	3.1 [41]	–	5.143 ^c	–	~0.17 (295 K) [43]
–	–	–	–	–	–	~0.09 (100 K) [43]	~0.09 (100 K) [43]	~0.09 (100 K) [43]
SmAl ₂	123 [41]	–	–	–	–	~0.15 (295 K) [43]	~0.15 (295 K) [43]	~0.11 (22 K) [43]
GdAl ₂	170 [41]	–	7.0 [41]	7.92 [41]	–	5.693 ^c	~0.095 (295 K) [43]	~0.014 (10 K) [43]
–	167 [42]	–	–	–	–	~74 (350 K) [69]	~0.022 (10 K) [43]	~0.022 (10 K) [43]
TbAl ₂	114 [41]	–	–	8.1 [41]	9.82 [41]	–	~5 (25 K) [69]	~0.02 (10 K) [43]
DyAl ₂	58 [41]	–	–	9.1 [41]	9.7 [41]	–	~0.15 (295 K) [43]	~0.03 (10 K) [43]
–	63.9 [67]	–	–	–	10.65 [67]	–	~0.16 (295 K) [41]	~0.03 (10 K) [43]
HoAl ₂	27 [41]	–	–	7.86 [41]	10.8 [68]	–	~3 (10 K) [67]	~0.03 (10 K) [67]
–	–	–	–	–	–	6.097 ^c	~15 (35 K) [68]	~0.18 (295 K) [43]
–	–	–	–	–	–	6.209 ^c	~26 (T _C) [68]	~0.02 (10 K) [43]
ErAl ₂	14.5 [41]	–	–	7.6 [41]	9.87 [41]	–	~9 (10 K) [68]	~0.19 (295 K) [43]
–	13.6 [42]	–	–	–	–	~35 (80 K) [67]	~0.15 (170 K) [43]	~0.02 (10 K) [43]
–	–	–	–	–	–	~7 (20 K) [67]	~0.02 (10 K) [43]	~0.3 (170 K) [44]
TmAl ₂	–	–	–	–	–	6.312 ^c	–	~0.07 (12 K) [44]
PrAl ₂	–	14 [46]	–	–	–	7.928 ^c	–	~0.22 (295 K) [43]
–	–	–	–	–	–	~23.5 (25 K) [45]	~0.01 (10 K) [43]	~0.06 (17 K) [45]
–	–	–	–	3.44 [41]	–	~9.4 (12.5 K) [45]	~31.4 (10 K) [45]	~0.012 (3.5 K) [45]
–	–	–	–	–	–	~3.1 (5 K) [45]	~3.1 (5 K) [45]	~3.1 (5 K) [45]

Table A2.1. Continued.

Substance	T_C (K)	T_N (K)	I_s (emu/g)	μ_0 (μ_B)	μ_{eff} (μ_B)	T_D (K)	ρ (g/cm^3)	C ($J/\text{kg}\cdot\text{K}$) ($\text{J}/\text{mol}\cdot\text{K}$)	λ ($\text{J}/\text{cm}\cdot\text{K}$)
NdAg	—	22 [41]	—	—	3.64 [41]	—	8.158 ^c	~21.6 (25 K) [45] ~46.4 (T_N) [45] ~6.2 (10 K) [45]	~0.1 (15 K) [45] ~0.04 (4 K) [45]
ErAg	—	21 [41]	—	—	9.22 [41]	—	10.083 ^c	~9 (25 K) [47] ~10 (16 K) [47] ~1 (5 K) [47]	~0.075 (11 K) [45] ~0.03 (2 K) [45]
DyGa ₂	—	11 [48]	—	—	~9.1 [74]	—	8.076 ^c	~7.5 (20 K) [49] ~37.4 (9 K) [49] ~54.2 (6.5 K) [49]	~0.011 (20 K) [49] ~0.004 (5 K) [49]
Er ₃ Ni	—	7.7 [50]	—	7.1 [50]	9.85 [50]	—	9.29 ^c	~0.8 ^d (25 K) [51] ~0.3 ^d (10 K) [51] ~0.43 ^d (T_N) [51] ~0.25 ^d (5 K) [51]	~0.02 (50 K) [52] ~0.003 (5 K) [52]
ErNi	12 [50]	—	—	8.1 [50]	9.8 [50]	—	9.632 ^c	~16.4 (30 K) [53] ~7 (15 K) [52] ~14.1 (T_C) [53] ~4.7 (5 K) [53]	~0.07 (50 K) [52] ~0.03 (7 K) [52]
ErNi ₂	6 [42]	—	—	6.9 [50]	9.55 [50]	—	10.446 ^c	~58 (250 K) [54] ~55 (100 K) [54] ~8.3 (20 K) [54] ~1.4 (T_C) [54]	~0.05 (50 K) [52] ~0.003 (3 K) [52]

DyNi ₂	20 [42]	—	—	8.8 [50]	10.5 [50]	—	—	10.15 ^c	—	~19 (35 K) [55]	~0.05 (50 K) [52]
—	—	—	—	—	—	—	—	—	~12 (25 K) [55]	~0.015 (6 K) [52]	
—	—	—	—	—	—	—	—	—	~25 (T_C) [55]	—	
—	—	—	—	—	—	—	—	—	~7 (10 K) [55]	—	
ErCo ₂	35 [56]	—	—	7 ^b [57]	9.84 [56]	207 [72]	10.388 ^c	—	~55 (60 K) [56]	~0.03 (50 K) [52]	
—	—	—	—	—	—	—	—	—	~1427 (T_C) [56]	~0.06 (3.5 K) [52]	
Gd ₃ Si ₄	345.7 [58]	—	—	7.52 [58]	7.85 [58]	213.7 [59]	6.97 ^c [58]	—	~27.5 (30 K) [56]	—	
—	—	—	—	—	—	—	—	—	~386.4 (T_C) [59]	—	
—	—	—	—	—	—	—	—	—	~242.6 (200 K) [59]	—	
—	—	—	—	—	—	—	—	—	~175.2 (100 K) [59]	—	
Gd ₃ Ge ₄	—	15 [60]	—	—	2.02 [60]	8.1 [60]	—	8.04 ^c	—	—	—
Gd ₃ Si ₂ Ge ₂	276 [61]	—	—	125 (272.8 K, 55 kOe) [62]	7.36 [75]	—	—	7.52 ^c	—	~243 (350 K) [62]	—
—	—	—	—	—	—	—	—	—	~828 (T_C) [62]	—	
Tb ₅ Si ₄	225.1 [63]	—	—	—	—	10.27 [63]	—	7.206 ^c	—	~198 (100 K) [62]	—
—	—	—	—	—	—	—	—	—	~90 (50 K) [62]	—	
—	—	—	—	—	—	—	—	—	~252 (300 K) [63]	—	
Tb ₅ Si ₂ Ge ₂	100.1 [63]	—	—	—	8.92 [76]	10.21 [63]	—	7.773 ^c	—	~414 (T_C) [63]	—
—	—	—	—	—	—	—	—	—	~207 (100 K) [63]	—	
—	—	—	—	—	—	—	—	—	~117 (50 K) [63]	—	
—	—	—	—	—	—	—	—	—	~252 (300 K) [63]	—	
—	—	—	—	—	—	—	—	—	~550 (T_C) [63]	—	
—	—	—	—	—	—	—	—	—	~126 (50 K) [63]	—	

Table A2.1. Continued.

Substance	T_C (K)	T_N (K)	I_s (emu/g)	μ_0 (μ_B)	μ_{eff} (μ_B)	T_D (K)	ρ (g/cm^3)	C ($\text{J}/\text{kg}\cdot\text{K}$) ($\text{J}/\text{mol}\cdot\text{K}$)	λ ($\text{J}/\text{cm}\cdot\text{K}$)
Brass (30% Zn)	—	—	—	—	—	—	8.522 [3]	(385) (295 K) [3]	0.73 (103 K) 0.89 (173 K) 1.09 (293 K)
Bronze (25% Sn)	—	—	—	—	—	—	8.666 [3]	(343) (295 K) [3]	1.33 (373 K) [3] 0.26 (293 K) [3]
Stainless steel	—	—	—	—	—	—	8 [3]	(460) (295 K) [3]	0.12 (173 K) [3] 0.135 (293 K) [3] 0.005 (10 K) [47]
AISI 316	—	—	—	—	—	—	—	—	—
SUS304	—	—	—	—	—	—	—	—	—
Al_2O_3 (poly crystalline)	—	—	—	—	—	—	3.9 [3]	(725) (273 K) [3] 73.9 (273 K) [3] (940) (400 K) [3] 95.8 (400 K) [3]	0.4 (273 K) [3] 0.26 (400 K) [3]
Al_2O_3 (single crystal (sapphire))	—	—	—	—	—	—	3.98 [3]	(725) (273 K) [3] (940) (400 K) [3]	0.52 (273 K) [3] 0.32 (400 K) [3]
Cardboard	—	—	—	—	—	—	0.79 [3]	—	$1.4 \cdot 10^{-3}$ (273 293 K) [3]
Glass wool	—	—	—	—	—	—	0.064-0.16 [3]	—	$4 \cdot 10^{-4}$ (293 K) [3]
Acrylic (Plexiglas)	—	—	—	—	—	—	1.18 [3]	—	$1.4 \cdot 10^{-3}$ (318 K) [3]

Epoxy (bisphenol A (EP), east)	-	-	-	1.2 [3]	-	$\sim 2.2 \cdot 10^{-3}$ (297-
Polyamide (nylon 6,6)	-	-	-	1.12 [3]	(1470) (273-322 K) [3]	$2.5 \cdot 10^{-3}$ (273-
Polyethylene (HDPE)	-	-	-	0.96 [3]	(2260) [3]	$3.3 \cdot 10^{-3}$ [3]
Polyimide	-	-	-	1.43 [3]	(1130) [3]	$3.5 \cdot 10^{-3}$ [3]
Polystyrene (expanded)	-	-	-	0.013-0.03 [3]	-	$3.5 \cdot 10^{-4}$ (277-
Polytetrafluoro-ethylene (Teflon)	-	-	-	2.2 [3]	(1050) (293 K) [3]	$2.5 \cdot 10^{-3}$ (293 K) [3]
Rubber (hard)	-	-	-	-	1.2 [3]	$2.5 \cdot 10^{-3}$ (100 K) [52]
Oak	-	-	-	-	0.6 [3]	$6 \cdot 10^{-4}$ (5 K) [52]
Wool (sheep)	-	-	-	-	-	$5 \cdot 10^{-4}$ (293 K) [3]

^a sc = single crystal. ^b Per formula unit. ^c Density, determined from crystallographic data; calculated or taken from JCPDS (Joint Committee Powder Diffraction Standard) PDF-2 data base.

1. Bozorth (1978); 2. Kohlhaas *et al.* (1966); 3. Lienhard and Lienhard (2002); 4. Hirschler and Rocker (1966); 5. Hashimoto *et al.* (1990); 6. Pecharsky *et al.* (1997a); 7. Gschneidner (1993b); 8. Dan'kov *et al.* (1998); 9. Powell and Jolliffe (1965); 10. Nellis and Legvold (1969); 11. Chernishov *et al.* (2002a); 12. Chernishov *et al.* (2002b); 13. Colvin and Arajs (1964); 14. Boys and Legvold (1968); 15. Jayasuria *et al.* (1997a); 16. Gschneidner *et al.* (1997a); 17. Zinn *et al.* (1989); 18. Edwards and Legvold (1968); 19. Pecharsky *et al.* (1997a); 20. Adachi (1961); 21. Krokozinski *et al.* (1982); 22. Kuz'min and Tishin (1991); 23. Dai *et al.* (1988); 24. Slack and Oliver (1971); 25. Numazawa *et al.* (1983); 26. Filippi *et al.* (1977); 27. Kimura *et al.* (1988); 28. Tomokyo *et al.* (1985); 29. Numazawa *et al.* (1990); 30. Landau *et al.* (1971); 31. Kimura *et al.* (1997b); 32. Schuchert *et al.* (1969); 33. Sivadierre and Quezel-Ambrunaz (1971); 34. Bonville *et al.* (1980); 35. Ball *et al.* (1963); 36. Hlopkin *et al.* (2000); 37. Cohn *et al.* (1997); 38. Chivelder *et al.* (1998); 39. Fischer *et al.* (1991); 40. Kimura *et al.* (1998); 41. Taylor and Darby (1972); 42. Gschneidner *et al.* (1996a); 43. Bauer *et al.* (1980); 44. Zinn *et al.* (1988a); 45. Yagi *et al.* (1997); 46. Brun *et al.* (1974); 47. Biwa *et al.* (1996); 48. Gignoux *et al.* (1998); 50. Buschow (1977); 51. Gschneidner *et al.* (1995); 52. Ogawa *et al.* (1991); 53. Hashimoto *et al.* (1992); 54. Melero *et al.* (1995); 55. Tomokyo *et al.* (1986); 56. Tishin *et al.* (2002); 57. Chikazumi (1964); 58. Spichkin *et al.* (2001a); 59. Serdyuk *et al.* (1985); 60. Holzberg *et al.* (1967); 61. Gschneidner and Pecharsky (2000a); 62. Pecharsky and Gschneidner (1997e); 63. Huang *et al.* (2002); 64. Kittel (1986); 65. Berman and MacDonald (1952); 66. Barbara *et al.* (1996b); 68. Hashimoto *et al.* (1986); 69. Dan'kov *et al.* (2000); 70. Gopal (1966); 71. Babichev (1991); 72. Giguere *et al.* (1999a); 73. Schnelle *et al.* (2001); 74. Baranov *et al.* (1988); 75. Pecharsky and Gschneidner (1998); 76. Thuy *et al.* (2002).

References

- Abatti G L, Corina A, Fabretti A C, Caneschi A and Gattechi D 1998 *Inorg. Chem.* **37** 1430
- Abramovich A I, Michurin A V, Gorbenko O Yu and Kaul A R 2001 *Phys. Solid State* **43** 715
- Adachi K 1961 *J. Phys. Soc. Japan.* **16** 2187
- Ahiezer A I and Pomeranchuk I Y 1944 *J. Eksp. Teor. Fiz.* **14** 342
- Ahiezer A I, Bariahtar V G and Peletinskii S V 1967 *Spin waves* (Moscow: Nauka) p 368
- Akulov N S and Kirensky L W 1940 *J. Phys.* **3** 31
- Aliev N G and N V Volkenshtein 1965a *J. Eksp. Theor. Phys.* **49** 24
- Aliev N G and N V Volkenshtein 1965b *Fiz. Tverd. Tela* **7** 2560
- Aliev N G and N V Volkenshtein 1965c *J. Eksp. Theor. Phys.* **49** 1450
- Alkhafaji M T and Ali N 1997 *J. Alloys and Comp.* **250** 659
- Aly S H 2001 *J. Magn. Magn. Mater.* **232** 168
- Amaitsu A, Moritomo Y, Tomioka Y, Arima T and Tokura Y 1995 *Nature* **373** 407
- Ambler E and R P Hudson 1955 *Rep. Progr. Phys.* **18** 255
- Anderson E E 1964 *Proc. Int. Conf. Magn.* (Nottingham 1964) p 660
- Andreenko A S, Nikitin S A, Spichkin Y I and Tishin A M 1991 *Fiz. Tverd. Tela* **33** 2463
- Annaorazov M P, Asatryan K A, Nikitin S A, Tishin A M and Tyurin A L 1991 *Pisma Zh. Tekh. Phys.* **12** 38
- Annaorazov M P, Asatryan K A, Myalikgulyev G, Nikitin S A, Tishin A M and Tyurin A L 1992 *Cryogenics* **32** 867
- Annaorazov M P, Nikitin S A, Tyurin A L, Asatryan K A and Dovletova A Kh 1996 *J. Appl. Phys.* **79** 1689
- Antyukhov A M, Antonov A V, Ivanov I A and Volchenkova M I 1984 *Sov. Phys.–Solid State* **26** 325
- Aoki Y, Urakawa J, Sugawara H, Sato H, Markin P E, Bostrem I S and Baranov N V 2000 *Phys. Rev. B* **62** 8935
- Aprigliano L F, Green G, Chafe J, O'Connor L, Biancanello F and Ridder S 1992 *Adv. Cryog. Eng.* **37B** 1003
- Arajs S and R V Colvin 1964 *J. Appl. Phys.* **35** 1053
- Argyriou D N, Mitchell J F, Potter C D, Hinks D G, Jorgensen J D and Bader S D 1996 *Phys. Rev. Lett.* **76** 3826
- Asamitsu A, Moritomo Y, Tomioka Y, Amira T and Tokura Y 1995 *Nature* **373** 407
- Atoji M 1974 *Solid State Comm.* **14** 1074
- Azhar A A, Mitescu C D, Johanson W R, Zimm C B and Barclay J A 1985 *J. Appl. Phys.* **57** 3235

- Baazov N G and Manjavidze A G 1983 *Investigation of Rare Earth Magnets by Neutron Methods* (Metsnireba, Tbilisi)
- Babichev A P 1991 The Density of Compounds in *Physical Values. The Handbook*. eds I S Grigoriev and E Z Meilikhov (Moscow: Energoatomizdat)
- Babkin E V and Urinov H O 1987 *Sov. Phys.–Solid State* **29** 133
- Babkin E V and Urinov H O 1989 *Sov. Phys. J.* **32** 899
- Bagguley D M S. and Howe F A 1986 *J. Magn. Magn. Mater.* **58** 191
- Ball M, Leask M J M, Wolf W P and Wyatt A F G 1963 *J. Appl. Phys.* **34** 1104
- Banerjee S K 1964 *Phys. Lett.* **12** 16
- Baranov N V, Markin P E and Sinicin E V 1988 *Fiz. Met. Metalloved.* **65** 538
- Baranov N V, Markin P E and Hrudev Yu A 1992 *Pisma J. Techn. Phys.* **18** 20
- Barbara B, Baruchel J X, Buevoz J L, Rossignol H F and Schweizer J 1977 *Solid State Commun.* **24** 481
- Barclay J A and Steyert W A 1982a *Cryogenics* **22** 73
- Barclay J A and Steyert W A 1982b USA patent 4,332,135
- Barclay J A 1984a *Proc. 21st Space Congress* (Cocoa Beach, FL)
- Barclay J A 1984b *Proc. 22nd Nat'l Heat Transf. Conf.* (Niagara Falls, N.Y., August 1984)
- Barclay J A and Sarangi S 1984 *Cryog. Proc. Equip.* 51
- Barclay J A 1991 *Workshop on Magnetic Refrigeration and Conventional Refrigeration Techniques, 18th International Conference on Refrigeration* (Montreal, 15 August 1991)
- Barclay J A 1994 *J. Alloys. Comp.* 207/208 355
- Barra A L, Debrunner P, Gatteschi D, Schulz C E and Sessoli R 1996 *Europhys. Lett.* **35** 133
- Barratt J, Lees M R and Mck Paul D 1996 *Appl. Phys. Lett.* **68** 424
- Bartolomé F, Kuz'min M D, Merino R I, and Bartolomé J 1994 *IEEE Trans. Magn.* **30** 960
- Bauer E, Gratz E and Adam G 1986 *J. Phys.* **16** 493
- Bazarov I P 1964 *Thermodynamics* (Oxford, New York: Pergamon Press)
- Bean C P and Rodbell D S 1962 *Phys. Rev.* **126** 104
- Beaudry B J and Gschneidner K A Jr 1978 in *Handbook on the Physics and Chemistry of Rare Earth* ed by K A Gschneidner Jr and L Eyring (Amsterdam: Elsevier) **1** 173
- Belov K P 1961a *Magnetic Transformations* (New York: Consultants Bureau)
- Belov K P 1961b *J. Eksp. Teor. Phys.* **41** 692
- Belov K P and Nikitin S A 1965 *Phys. Stat. Sol.* **12** 453
- Belov K P 1968 *Helv. Phys. Acta* **41** 679
- Belov K P, Talalaeva E V, Chernikova L A and Ivanovskii V I 1968 *JETP Lett.* **7** 331
- Belov K P, Talalaeva E V, Chernikova L A and Ivanovskii V I 1969 *Pisma JETP* **9** 671
- Belov K P and Nikitin S A 1970a *Izv. AN SSSR Ser. Fiz.* **34** 957
- Belov K P and Nikitin S A 1970b *J. Eksp. Teor. Phys.* **58** 937
- Belov K P, Chernikova L A, Talalaeva E V, Levitin R Z, Kudriavceva T V, Amadesi S and Ivanovskii V I 1970 *J. Eksp. Teor. Phys.* **58** 1923
- Belov K P, Nikitin S A, Talalaeva E V, Chernikova L A, Kudriavceva T V, Tihonov V V and Ivanovskii V I 1971 *J. Exp. Theor. Phys.* **61** 1101
- Belov K P, Talalaeva E V, Chernikova L A, Kudriavceva T V and Ivanovskii V I 1972 *J. Eksp. Teor. Phys.* **62** 2183
- Belov K P, Talalaeva E V, Chernikova L A, Kudriavceva T V, Ivanovskii V I, Yahro G A and Amadezi S 1973 *Vest. Mosk. Univ. Ser. Fizika, Astronomia.* **N1** 113
- Belov K P, Talalaeva E V, Chernikova L A, Andreenko A S and Ivanovskii V I 1974 *Sov. Phys. JETP* **39** 316

- Belov K P, Talalaeva E V, Chernikova L A, Ivanova T I, Ivanovskii V I and Kozakov G V 1977 *Sov. Phys. JETP* **45** 307
- Belova B M and Stoliarov V L 1984 *Fiz. Tverd. Tela* **26** 851
- Benford S M 1979 *J. Appl. Phys.* **50** 1868
- Benford S M and Brown G V 1981 *J. Appl. Phys.* **52** 2110
- Bennett L H, McMichael R D, Swartzendruber L J, Shull R D and Watson R E 1992 *J. Magn. Magn. Mater.* **104-107** 1094
- Bennett L H, McMichael R D, Shull R D and Swartzendruber L J 1993 *J. Appl. Phys.* **73** 6507
- Beranger R, Bon Mardion G, Claudet G, Delpuech C, Lacaze A F and Lacaze A A 1982 *Adv. Cryog. Eng.* **27** 703
- Berman R and MacDonald D K C 1952 *Proc. Roy. Soc. (London)* **A211** 122
- Bertran E, Foriat V, Herpin A and Meriel P 1956 *C.R. Acad. Sci., Paris* **243** 898
- Bézaguet A, Casas-Cubillos J, Lebrun Ph, Losserand-Madoux R, Marquet M, Schmidt-Ricker M and Seyfert P 1994 *Cryogenics* **34** 227
- Biwa T, Yagi W and Mizutani U 1996 *Jpn. J. Appl. Phys.* **35** 2244
- Blake A J, Grant C M, Parsons S, Rawson J M and Winpenny R E P 1994 *J. Chem. Soc. Chem. Comm.* **20** 2363
- Blazey K W, Rohrer H and Webster R 1971 *Phys. Rev. B* **4** 2287
- Bloch D and Lemaire R 1970 *Phys. Rev. B* **2** 2648
- Bloch D, Chaisse F, Givord F and Voiron J 1971 *J. de Phys.* **32** 659
- Bloch D, Edwards D M, Shimizu M and Voiron J 1975 *J. Phys. F: Met. Phys.* **5** 1217
- Bloembergen N 1949 *Physica* **15** 588
- Blois de R W and Rodbell D S 1963 *J. Appl. Phys.* **34** 1101
- Bohigas X, Tejada J, del Barco E, Zhang X X and Sales M 1998 *Appl. Phys. Lett.* **73** 390
- Bohigas X, del Barco E, Sales M and Tejada J 1999 *J. Magn. Magn. Mater.* **196-197** 455
- Bohigas X, Tejada J, Marínez-Sarrión M L, Tripp S and Black R 2000 *J. Magn. Magn. Mater.* **208** 85
- Bohr J 1991 *Surface Structures, Magnetic Structures and Small Inclusions, as Studied by X-ray Diffraction* (Riso-R-585) p 69
- Bonville P, Hodges J A and Imbert P 1980 *J. Physique* **41** 1213
- Borovikov V S, Kaner N E, Litvinenko Yu I, Fishman A M and Shapiro V V 1981 *J. Eksp. Teor. Phys.* **53** 816
- Bose T K, Chahine R, Gopal B R, Foldeaki M, Barman A, Gosh M., De S K and Chatterjee S 1998 *Cryogenics* **38** 849
- Bouchaud J P, Fruchart R, Pauthenet R, Guillot M, Bartholin H and Chaisse F 1966 *J. Appl. Phys.* **37** 971
- Boys D W and S Legvold 1968 *Phys. Rev.* **174** 377
- Bozorth R M 1967 *J. Appl. Phys.* **38** 1366
- Bozorth R M 1978 *Ferromagnetism* (New York: IEEE Press) p 968
- Bredy P and Seyfert P 1988 *Cryogenics* **28** 605
- Brown G V 1976 *J. Appl. Phys.* **47** 3673
- Brown W F 1984 *IEEE Trans. Magn.* **20** 112
- Brun T, Sinha S, Wakabayashi N, Lander G, Edwards L and Spedding F 1970 *Phys. Rev. B* **1** 1251
- Brun T O, Lander G H, Price D L, Felcher G P and Reddy J F 1974 *Phys. Rev. B* **9** 248
- Burkhanov G S, Dan'kov S Yu, Nikitin S A, Tishin A M and Chistiakov O D 1991 *Sov. Tech. Phys. Lett.* **17** 353

- Buschow K H J 1968 *J. Less-Common Metals* **16** 45
Buschow K H J, Olijhoek J F and Miedema A R 1975 *Cryogenics* **15** 261
Buschow K H J 1977 *Rep. Progr. Phys.* **40** 1179
Busey R H and Giauque W F 1952 *J. Amer. Chem. Soc.* **74** 3157
Bykhover S E, Nikitin S A, Spichkin Yu I, Tishin A M and Umhaeva Z S 1990 *Sov. Phys. JETP* **70** 1114
Cable J W, Wollan E O, Koehler W C and Wilkinson M K 1965 *Phys. Rev.* **140** 1896
Cable J W and Wollan E O 1968 *Phys. Rev.* **165** 733
Canepa F, Napoletano M, Palenzona A, Merlo F and Cirafici S 1999 *J. Phys. D: Appl. Phys.* **32** 2721
Canepa F, Manfrinetti P, Palenzona A, Cirafici S, Merlo F and Cimberle M R 2000 *Intermetallics* **8** 267
Canepa F, Napoletano M and Cirafici S 2002 *Intermetallics* **10** 731
Caneschi A, Gatteschi D, Laugier J, Rey P, Sessoli R and Zanchini C 1988 *J. Am. Chem. Soc.* **110** 2795
Caneschi A, Gatteschi D and Sessoli R 1991 *J. Am. Chem. Soc.* **113** 5873
Chafe J N, Green G F and Hendricks J B 1997 *Cryocoolers* **9** 653
Chafe J N and Green G 1998 *Adv. Cryog. Eng.* **43** 1589
Chaudhary S, Sunul Kumar V, Roy S B, Chaddah P, Krishnakumar S R, Sathe V G, Kumar A and Sarma D D 1999 *J. Magn. Magn. Mater.* **202** 47
Chen J and Yan Z 1991 *J. Appl. Phys.* **69** 6245
Chen J and Yan Z 1994 *J. Appl. Phys.* **75** 1249
Chen D Y, Patel S and Shaw D T 1994 *J. Magn. Magn. Mater.* **134** 75
Chen D Y, Patel S and Shaw D T 1995 *J. Magn. Magn. Mater.* **146** 175
Chen P, Du Y W and Ni G 2000 *Europhys. Lett.* **52** 589
Chen P and Du Y W 2001 *J. Phys. D: Appl. Phys.* **34** 1868
Chernishov A S, Ilyn M I, Tishin A M, Gorbenko O Yu, Amelichev V A, Mudretsova S N, Mairova A F and Gütler B 2001 unpublished results
Chernishov A S, Tishin A M, Gschneidner K A Jr, Pecharsky V K and Pecharsky A O 2002a to be published
Chernishov A S, Tishin A M, Gschneidner K A Jr, Pecharsky V K and Pecharsky A O 2002b to be published
Chernishov A S, Tishin A M, Gschneidner K A Jr, Pecharsky A O, Pecharsky V K and Lograsso T A 2002c *Proc. Int. Cryogen. Mater. Conf. (ICMC)* (American Institute of Physics) **48** 19
Chikazumi S 1964 *Physics of Magnetism* (New York: Wiley)
Child H, Koehler W, Wollan E and Cable I 1965 *Phys. Rev. A* **138** 1655
Chivelder L, Abrego Castillo I, McN Alford N, Tomka G J, Riedi P C, MacManus-Driscoll J, Akther Hossain A K M and Cohen L F 1998 *J. Magn. Magn. Mater.* **189** 274
Choe W, Pecharsky V K, Pecharsky A O, Gschneidner K A Jr, Young V G and Miller G J 2000 *Phys. Rev. Lett.* **84** 4617
Clark A E and Callen E 1968 *J. Appl. Phys.* **39** 5972
Clark A E and Callen E 1969 *Phys. Rev. Lett.* **23** 307
Clark A E and Alben R S 1970 *J. Appl. Phys.* **41** 1195
Clement J R and E H Quinell 1952 *Phys. Rev.* **85** 502
Coey J M D, Viret M, Ranno L and Ounadjela K 1995 *Phys. Rev. Lett.* **75** 3910
Coey J M D, Viret M and von Molnar S 1999 *Adv. Phys.* **48** 167
Coey J M D 2001 *J. All. Comp.* **326** 2

- Cohn J L, Neumeier J J, Popoviciu C P, McClellan K J and Leventouri Th 1997 *Phys. Rev. B* **56** R8495
- Collins S C and J Zimmerman 1953 *Phys. Rev.* **90** 991
- Colvin R V and S Arajs 1964 *Phys. Rev.* **133** A1076
- Corak W S, Garfunkel M P, Satterthwaite C B and Wexler A 1955 *Phys. Rev.* **98** 1699
- Cross C R, Barclay J A, DeGregoria A J, Jaeger S R and Johnson J W 1987 *Cryogenic Eng. Conf.* (June 1987)
- Dai W, Gmelin E and Kremer R 1988 *J. Phys. D: Appl. Phys.* **21** 628
- Dai W 1992 *J. Appl. Phys.* **71** 5272
- Dai P, Zhang J, Mook H A, Liou S H, Dowben P A and Plummer E W 1996 *Phys. Rev. B* **54** 3694
- Dai W, Shen B G, Li D X and Gao Z X 2000 *J. All. Comp.* **311** 22
- Dan'kov S Yu, Ivanova T I and Tishin A M 1992 *Pisma JTP* **18** 35
- Dan'kov S Yu, Spichkin Yu I and Tishin A M 1996 *J. Magn. Magn. Mater.* **152** 208
- Dan'kov S Yu, Tishin A M, Pecharsky V K and Gschneidner K A Jr. 1997 *Rev. Sci. Instrum.* **68** 2432
- Dan'kov S Yu, Tishin A M, Pecharsky V K and Gschneidner K A Jr. 1998 *Phys. Rev. B* **57** 3478
- Dan'kov S Yu, Ivchenko V V, Tishin A M, Gschneidner K A Jr. and Pecharsky V K 2000 *Adv. Cryog. Eng.* **46** 397
- Darby J, Hatton J, Rollin B V, Seymour E F W and Silsbee H B 1951 *Proc. Phys. Soc.* **64** 861
- Darnell F J 1963 *Phys. Rev.* **130** 1825
- Das I and Rawat R 2000 *Solid State Commun.* **115** 207
- Daudin B, Lacaze A A and Salce B 1982a *Cryogenics* **22** 439
- Daudin B, Lagnier R and Salce B 1982b *J. Magn. Magn. Mater.* **27** 315
- Daunt J G and Heer C V 1949 *Phys. Rev.* **76** 985
- Debye P 1926 *Ann. Physik* **81** 1154
- DeGregoria A J 1992 *Adv. Cryog. Eng.* **37B** 867
- DeGregoria A J, Feuling L J, Laatsch J F, Rowe J R, Trueblood J R and Wang A A 1992 *Adv. Cryog. Eng.* **37B** 875
- Delfs C, Gatteschi D, Pardi L, Sessoli R, Wieghardt K and Hanke D 1993 *Inorg. Chem.* **32** 3099
- Delpuech C, Beranger R, Bon Mardion G, Claudet G and Lacaze A A 1981 *Cryogenics* **21** 579
- Deportes J, Givord D and Ziebeck K R A 1981 *J. Appl. Phys.* **52** 2074
- Dobrovitski V V, Zvezdin A K and Popkov A F 1996 *Adv. Phys. (Uspehi Fiz. Nauk, Moscow)* **166** 439
- Dobrovitski V V and Zvezdin A K 1997 *Europhys. Lett.* **38** 377
- Dörr M, Loenhaupt M, Hahn W, Brück E, Hagmusa I H, Klaase J C P and Rotter M 1999 *Physica B* **262** 340
- Dreyfus B, Goodman B B, Lacaze A and Trolliet G 1961 *C.R. Acad. Sci.* **253** 1764
- Drillat A, Baruchel J, Bates S and Palmer S B 1984 *J. Magn. Magn. Mater.* **44** 232
- Druzhinin V V, Zapasski S P and Povishev V M 1975 *Fiz. Tverd. Tela* **17** 23
- Druzhinin V V, Ponomarev B K and Zapasski S P 1977 *Sov. Phys.-Solid State* **19** 25
- Druzhinin V V, Melnikov V M and Shkarubski VV 1979 *Sov. Phys.-Solid State* **21** 1002
- Duc N H, Hien T D, Brommer P E and Franse J J M 1992a *J. Magn. Magn. Mater.* **104-107** 1252

- Duc N H, Hien T D, Levitin R Z, Markosyan A S, Brommer P E and Franse J J M 1992b *Physica B* **167** 232
- Duc N H and Goto T 1999 Itinerant electron metamagnetism of Co sublattice in the lanthanide–cobalt intermetallics *Handbook of the Physics and Chemistry of Rare Earth* ed. K A Gschneidner Jr and L Eyring (Amsterdam: Elsevier) **26** p 177
- Duc N H and Kim Anh D T 2002 *J. Magn. Magn. Mater.* **242–245** 873
- Duc N H, Kim Anh D T and Brommer P E 2002 *Physica B* **319** 1
- Duong N P, Klaasse J C P, Brück E, Hagmusa I H, de Boer F R and Buschow K H J 2000 *J. All. Comp.* **309** L10
- Duyckaerts G 1939a *Physica* **6** 401
- Duyckaerts G 1939b *Physica* **6** 817
- Edwards D M, Green A C M and Kubo K 1999 *J. Phys.: Condens. Mat.* **11** 2791
- Edwards L R and S Legvold 1968 *Phys. Rev.* **176** 753
- Engelhardt J, Asen-Palmer M, Kleeberg Ch, Annaorazov M, Kattwinkel A, Barner K and Gmelin E 1999 *Phys. Stat. Sol. (b)* **211** 789
- Eriksson O, Nordström L, Brooks M S S and Johansson B 1988 *Phys. Rev. Lett.* **60** 2523
- Estermann I, Friedberg S A and Goldman J E 1952 *Phys. Rev.* **87** 582
- Filippi J, Lašjaunias J C, Ravex A, Tcheou F and Rossat-Mignod J 1977 *Solid St. Commun.* **23** 613
- Finkel A V, Vorobev V V and Palatnik M I 1971 *Phys. Stat. Sol. (b)* **47** 53K
- Finkel A V 1978 *Structure of Rare Earth Metals* (Moscow: Metallurgiay)
- Fisher R A, Brodale G E, Homung E W and Gianque W F 1973 *J. Chem. Phys.* **59** 4652
- Fischer B, Hoffmann J, Kahle H G and Paul W 1991 *J. Magn. Magn. Mater.* **94** 79
- Flippen R B and Darnell F J 1963 *J. Appl. Phys.* **34** 1094
- Foldeaki M, Chahine R and Bose T K 1995 *J. Appl. Phys.* **77** 3528
- Foldeaki M, Schnelle W, Gmelin E, Benard P, Koszegi B, Giguere A, Chahine R and Bose T K 1997a *J. Appl. Phys.* **82** 309
- Foldeaki M, Giguère A., Gopal B R, Chahine R, Bose T K, Liu X Y and Barclay J A 1997b *J. Magn. Magn. Mater.* **174** 295
- Foldeaki M, Giguere A, Chahine R and Bose T K 1998a *Adv. Cryog. Eng.* **43** 1533
- Foldeaki M, Chahine R, Gopal B R, Bose T K, Liu X Y and Barclay J A 1998b *J. Appl. Phys.* **83** 2727
- Fominaya F, Villain J, Gandit P, Chaussy J and Caneschi A 1997 *Phys. Rev. B* **79** 1126
- Fominaya F, Villain J, Fournier T, Gandit P, Chaussy J and Caneschi A 1999 *Phys. Rev. B* **59** 519
- Forgan E M, Muirhead C M, Jones D W and Gschneidner K A Jr 1979 *J. Phys. F* **9** 651
- Fuerst C D, Herbst J F, Mishra R K and McMichael R D 1994 *J. Appl. Phys.* **76** 6301
- Fujieda S, Fujita A and Fukamichi K 2002 *Appl. Phys. Lett.* **81** 1276
- Fujii H, Hashimoto Y and Meshima A 1976 *J. Phys. Soc. Japan* **41** 1176
- Fujita A and Fukamichi K 1999 *IEEE Trans. Magn.* **35** 3796
- Fujita A, Akamatsu Y and Fukamichi K 1999 *J. Appl. Phys.* **85** 4756
- Gallo C F 1965 *J. Appl. Phys.* **36** 3410
- Gamari-Seale H, Anagnostopoulos T and Yakinthos J K 1979 *J. Appl. Phys.* **50** 434
- Garrett C G B 1954 *Magnetic Cooling* (Harvard, University Press)
- Geller S and Bala B 1956 *Acta Cryst.* **9** 1019
- Gennes de P G 1960 *Phys. Rev.* **118** 141
- Geuns van J R 1968 US Patent 3,413,814
- Giauque W F 1927 *J. Amer. Chem. Soc.* **49** 1864

- Giauque W F and MacDougall D P 1933 *Phys. Rev.* **43** 768
- Gibbs D, Bohr J, Axe J D, Moncton D E and D'Amico K L 1986 *Phys. Rev. B* **34** 8182
- Gignoux D, Givord D, Givord F and Lemaire R 1979 *J. Magn. Magn. Mater.* **10** 288
- Gignoux D, Gomez-Sal J C and Paccard D 1984 *Solid State Commun.* **49** 75
- Gignoux D, Schmitt D, Takeuchi A and Zhang F Y 1991 *J. Magn. Magn. Mater.* **97** 15
- Giguere A, Foldeaki M, Schnelle W and Gmelin E 1999a *J. Phys. Condens. Matter* **11** 6969
- Giguere A, Foldeaki M, Dunlap R A and Chahine R 1999b *Phys. Rev. B* **59** 431
- Giguere A, Foldeaki M, Gopal B R, Chahine R, Bose T K, Frydman A and Barclay J A 1999c *Phys. Rev. Lett.* **83** 2262
- Givord D and Lemaire R 1974 *IEEE Trans. Magn.* **10** 109
- Glorieux G, Thoen J, Bednarz G, White M A and Geldart D J W 1995 *Phys. Rev. B* **52** 12770
- Goldberg D P, Caneschi A and Lippard S J 1993 *J. Am. Chem. Soc.* **115** 9299
- Goldberg D P, Caneschi A, Delfs C D, Sessoli R J and Lippard S J 1995 *Am. Phys. Soc.* **117** 5789
- Gomes A M, Novak M A, Nunes W C and Rapp R E 2001 *J. Magn. Magn. Mater.* **226–230** 2015
- Gomes A M, Reis M S, Oliveira I S, Guimarães A P and Takeuchi A Y 2002 *J. Magn. Magn. Mater.* **242–245** 870
- Goodenough J 1955 *Phys. Rev.* **100** 564
- Gopal B R, Chahine R, Foldeaki M and Bose T K 1995 *Rev. Sci. Instrum.* **66** 232
- Gopal B R, Chahine R and Bose T K 1997 *Rev. Sci. Instrum.* **68** 1818
- Gopal E S R 1966 *Specific Heats at Low Temperatures* (New York: Plenum Press)
- Gorkov L P and Sokol A V 1987 *Pisma JETP* **46** 333
- Gorkov L P 1998 *Uspehi Fiz. Nauk* **168** 665
- Gorter C J 1934 *Phys. Zeit.* **35** 923
- Gratz E 1983 *Solid State Commun.* **48** 825
- Gratz E, Bauer E, Hausen R, Maikis M, Haen P and Markosyan A S 1993 *Int. J. Mod. Phys. B* **7** 366
- Green G, Patton W and Stevens J 1988 *Adv. Cryog. Eng.* **33** 777
- Greenough R D, Blackie G N and Palmer S B 1981 *J. Phys. C* **14** 9
- Greenough R D and Hettiarachchi N F 1983 *J. Magn. Magn. Mater.* **31–34** 178
- Grewen N and Steglich F 1991 in *Handbook on the Physics and Chemistry of Rare Earth* ed K A Gschneidner Jr and L Eyring (Amsterdam: Elsevier) **14** 343
- Griffel M, Skochdopole R E and Spedding F H 1954 *Phys. Rev.* **93** 657
- Griffel M, Skochdopole R E and Spedding F H 1956 *J. Chem. Phys.* **25** 75
- Gschneidner K A Jr. 1993a *J. Alloys Comp.* **193** 1
- Gschneidner K A Jr 1993b in *Handbook on the Physics and Chemistry of Rare Earth* ed K A Gschneidner Jr and L Eyring (Amsterdam: Elsevier) **Cumulative Index 1–15** 509
- Gschneidner K A Jr, Takeya H, Moorman J O and Pecharsky V K 1994a *Appl. Phys. Lett.* **64** 253
- Gschneidner K A Jr, Takeya H, Moorman J O, Pecharsky V K, Malik S K and Zimm C B 1994b *Adv. Cryog. Eng.* **39** 1457
- Gschneidner K A Jr, Pecharsky V K and Gailloux M J 1995 *Cryocoolers* **8** 685
- Gschneidner K A Jr, Pecharsky V K, Gailloux M J and Takeya H 1996a *Adv. Cryog. Eng.* **42** 465
- Gschneidner K A Jr, Pecharsky V K and Malik S K 1996b *Adv. Cryog. Eng.* **42** 475

- Gschneidner K A Jr. and Pecharsky V K 1997 Magnetic refrigeration in *Rare Earths: Science, Technology and Applications III* ed R G Bautista, C O Bounds, T W Ellis and B T Kilbourn (The Minerals, Metals and Material Society) p 209
- Gschneidner K A Jr, Pecharsky V K and Fort D 1997a *Phys. Rev. Lett.* **78** 4281
- Gschneidner K A Jr, Pecharsky V K, Osborne M S, Moorman J O, Anderson I E, Pasker D and Eastwood M L 1997b *Cryocoolers* **9** 669
- Gschneidner K A Jr and Pecharsky V K 1999 *J. Appl. Phys.* **85** 5365
- Gschneidner K A Jr, Pecharsky V K, Pecharsky A O and Zimm C B 1999 *Mater. Sci. Forum* **315–317** 69
- Gschneidner K A Jr and Pecharsky V K 2000a *Annu. Rev. Mater. Sci.* **30** 387
- Gschneidner K A Jr and Pecharsky V K 2000b *Mater. Sci. Eng. A* **287** 301
- Gschneidner K A Jr, Pecharsky V K, Pecharsky A O, Ivchenko V V and Levin E M 2000a *J. All. Comp.* **303–304** 214
- Gschneidner K A Jr, Pecharsky A O, Pecharsky V K, Lograsso T A and Schlagel D L 2000b *Rare Earth and Actinides: Science, Technology and Applications* **IV** 63
- Gschneidner K A Jr, Pecharsky V K, Brück E, Duijn H G M and Levin E M 2000c *Phys. Rev. Lett.* **85** 4190
- Gschneidner K A Jr, Pecharsky A O and Pecharsky V K 2000d *Proc. 11th International Cryocooler Conference* (Keystone, Colorado, 20–22 June 2000) Paper N 35
- Gschneidner K A Jr, Pecharsky V K and Pecharsky A O 2000e *The Science of Alloys for the 21st Century: A Hume-Rothery Celebration* (ed E A Turchi, R D Shull and A Gonis) 201
- Gschneidner K A Jr, Pecharsky V K, Zimm C B and Sternberg A 2001 *Proc. Domotecnica Appliance Eng. Conf.* (7–9 March 2001) 170
- Gschneidner K A Jr and Pecharsky V K 2002 Intermetallic compounds for magnetic refrigeration in *Intermetallic Compounds—Principles and Practice* ed J H Westbrook and R L Fleischer (New York: Wiley) vol 3
- Gu G, Cai J, Yang W and Du Y 1998 *J. Appl. Phys.* **84** 3798
- Gubin S P, Zvezdin A K, Mishenko A S, Spichkin Y I and Tishin A M 2001 *Russian Patent 2177124*
- Guo Z B, Du Y W, Zhu J S, Huang H, Ding W P and Feng D 1997a *Phys. Rev. Lett.* **78** 1142
- Guo Z B, Zhang J R, Huang H, Ding W P and Du Y W 1997b *Appl. Phys. Lett.* **70** 904
- Guo Z B, Yang W, Shen Y T and Du Y W 1998 *Solid State Commun.* **105** 89
- Guthrie G, Friedberg S A and Goldman J E 1955 *Phys. Rev.* **98** 1181
- Haas de W J, Wiersma E C and Kramers H A 1933a *Nature* **131** 719
- Haas de W J, Wiersma E C and Kramers H A 1933b *C.R. Acad. Sci. (Paris)* **196** 1975
- Haas de W J, Wiersma E C and Kramers H A 1933c *Physica* **1** 1
- Habenschuss M C, Stassis C, Sinha S K, Deckman H W and Spedding F H 1974 *Phys. Rev. B* **10** 1020
- Hagmusa I H, Brück E, de Boer F R and Buschow K H J 1999 *J. Magn. Magn. Mater.* **196–197** 625
- Hagmusa I H, Klaasse J C P, Brück E, de Boer F R and Buschow K H J 2000 *J. All. Comp.* **297** 21
- Hakuraku Y and Ogata H 1985 *Jap. J. Appl. Phys.* **24** 1538
- Hakuraku Y and Ogata H 1986a *J. Appl. Phys.* **60** 3266
- Hakuraku Y and Ogata H 1986b *Cryogenics* **26** 171
- Hakuraku Y and Ogata H 1986c *Jap. J. Appl. Phys.* **25** 140

- Halbach K 1980 *Nucl. Instrum. Meth.* **169** 1
- Hall J L, Reid C E, Spearing I G and Barclay J A 1996 *Adv. Cryog. Eng.* **41** 1653
- Hall J L and Barclay J A 1998 *Adv. Cryog. Eng.* **43**
- Hashimoto T, Numusawa T, Shino M and Okada T 1981 *Cryogenics* **21** 647
- Hashimoto T, Namasawa T, Watanabe Y, Sato A, Nakagome H, Horigami O, Takayama S and Watanabe M 1982 *Proc. ICEC 9* (Guildford, UK: Butterworths) 26
- Hashimoto T 1986 *Adv. Cryog. Eng. Mater.* **32** 261
- Hashimoto T, Matsumoto K, Kurihara T, Numazawa T, Tomokiyo A, Yayama H, Goto T, Todo S and Sahashi M 1986 *Adv. Cryog. Eng.* **32** 279
- Hashimoto T, Kuzuhara T, Sahashi M, Inomata K, Tomokiyo A and Yayama H 1987 *J. Appl. Phys.* **62** 3873
- Hashimoto T, Ogawa M and Li R 1990 *Cryogenics* **30** 192
- Hashimoto T 1991 *Workshop Magn. Refr. Convekt. Refrig. Techniques, 18th International Congress of Refrigeration* (Montreal, August 15).
- Hashimoto T, Ogawa M, Hayashi A, Makino M, Li R and Aoki K 1992 *Adv. Cryog. Eng.* **37B** 859
- Hashimoto T, Yabuki M, Eda T, Kuriyama T and Nakagome H 1994 *Adv. Cryog. Eng.* **40** 655
- Hashimoto T, Tsukagoshi T, Nitta H, Yabuki M, Kuriyama T and Nakagome H 1995 *Cryocoolers* **8** 677
- Hashimoto T, Nakane H, Tsukagoshi T and Nakagome H 1998 *Adv. Cryog. Eng.* **43** 1541
- Hatton J and Rolling B V 1949 *Proc. Roy. Soc. A* **199** 222
- Heer C V and Daunt J G 1949 *Phys. Rev.* **76** 854
- Heer C V, Barnes C B and Daunt J G 1953 *Phys. Rev.* **91** 412
- Heer C V, Barnes C B and Daunt J G 1954 *Rev. Sci. Instrum.* **25** 1088
- Helmholdt R B, Palstra T T M, Nieuwenhuys G J, Mydosh J A, van der Kraan A M and Buschow K H J 1986 *Phys. Rev. B* **34** 169
- Hennion M, Pardi L, Mirebeau I, Suard E, Sessoli R and Caneschi A 1997 *Phys. Rev. B* **56** 8819
- Hennion M, Moussa F, Biotteau G, Rodriguez-Carvajal J, Pinsard L and Revcolevschi A. 1998 *Phys. Rev. Lett.* **81** 1957
- Hernandes J M, Zhang X X, Luis F, Tejada J, Friedman J R, Sarachik M P and Ziolo R 1997 *Phys. Rev. B* **55** 5858
- Herpin A and Meriel P 1957 *J. Phys. et Rad.* **24S** 2033
- Hershberg E L, Anderson I E, Osborne M G, Hundley M F and Smith J L 1994 *Adv. Cryog. Eng.* **40** 617
- Herz R and Kronmüller H 1978 *Phys. Stat. Sol. (a)* **47** 451
- Hill R W, Cosier J and Hukin D A 1984 *J. Phys. F* **14** 1267
- Hilscher G, Pillmayr N, Schmitzer C and Gratz E 1988 *Phys. Rev. B* **37** 3480
- Himcinschi C, Burzo E and Deville J P 2001 *Mater. Sci. Forum* **373-376** 521
- Hirschler W and Rocker W 1966 *Z. angew Phys.* **21** 368
- Hlopkin M N, Panova G H, Shikov A A, Siniavskii V F and Shuliatiev D A 2000 *Fiz. Tverd. Tela* **42** 111
- Hobden M V and N Kurti 1959 *Phil. Mag.* **4** 1092
- Holtzberg F, Gambino R J and McGuire T R 1967 *J. Phys. Chem. Solids* **28** 2283
- Horowitz M, Silvidi A A, Malakker S F and Daunt J G 1952 *Phys. Rev.* **88** 1182
- Hu F, Shen B and Sun J 2000a *Appl. Phys. Lett.* **76** 3460
- Hu F X, Shen B G, Sun J R, Cheng Z H and Zhang X X 2000b *J. Phys.: Condens. Matter.* **12** L691

- Hu F X, Shen B G, Sun J R and Cheng Z H 2001a *Phys. Rev. B* **64** 012409
Hu F X, Shen B G, Sun J R and Cheng Z H 2001b *Appl. Phys. Lett.* **78** 3675
Hu F X, Shen B G, Sun J R and Wu G H 2001c *Phys. Rev. B* **64** 132412–1
Hu F X, Sun J R, Wu G H and Shen B G 2001d *J. Appl. Phys.* **90** 5216
Hu F X, Shen B G, Sun J R, Pakhomov A B, Wong C Y, Zhang X X, Zhang S Y, Wang C J and Cheng Z H 2001e *IEEE Trans. Magn.* **37** 2328
Hu F X, Shen B G, Sun J R, Wang G J and Cheng Z H 2002a *Appl. Phys. Lett.* **80** 826
Hu F X, Wang G J, Wang J, Sun Z G, Dong C, Chen H, Zhang X X, Sun J R, Cheng Z H and Shen B G 2002b *J. Appl. Phys.* **91** 7836
Hu F X, Ilyn M, Tishin A M, Sun J R, Wang G J, Chen Y F, Wang F, Cheng Z H and Shen B G 2003 *J. Appl. Phys.* **93** 5503
Huang H, Pecharsky A O, Pecharsky V K and Gschneidner K A Jr 2002 *Adv. Cryog. Eng.* **48** 11
Hudgins A C and Pavlovic A S 1965 *J. Appl. Phys.* **36** 3628
Hueso L E, Sande P, Miguéns D R, Rivas J, Rivadulla F and López-Quintela M A 2002 *J. Appl. Phys.* **91** 9943
Hume-Rothery W 1961 *Elements of Structural Metallurgy* (London: Institute of Metals)
Ibarra M R and Algarabel P A 1994 *Phys. Rev. B* **50** 4196
Ibarra M R, Algarabel P A, Marquina C, Blasco J and García J 1995 *Phys. Rev. Lett.* **75** 3541
Ibarra M R, De Teresa J M, Algarabel P A, Marquina C, Garcia-Landa B, Morellon L, Ritter C, Mahendiran R and Del Moral A 2000 *Magnetostriction in Mixed Valant Magnetic Oxides, Modern Trends in Magnetostriction Study and Application* ed M R J Gibbs (Dordrecht: Kluwer) p 171
Iglesias J E and Steinfink H 1972 *J. Less-Common. Metals* **26** 45
Ikeda K, Gschneidner K A Jr, Tsang T W E and Schmidt F A 1982 *Solid State Commun.* **41** 889
Ilyn M I, Tishin A M, Gschneidner K A Jr, Pecharsky V K and Pecharsky A O 2000 *Proc. 11th Int. Cryocooler Conf.* (June 2000, Colorado, USA)
Ilyn M I, Tishin A M, Pecharsky V K, Pecharsky A O and Gschneidner K A Jr 2001 *CEC/ICMC* (Madison, WI, 16–20 July 2001)
Imai H, Wada H and Shiga M 1995 *J. Magn. Magn. Mater.* **140–144** 835
Inoue T, Sankar S G, Craig R S, Wallace W E and Gschneidner K A Jr 1977 in *Crystal Field Effects in Metals and Alloys* ed A Furrer (Plenum: New York) 143
Inoue J and Shimizu M 1982 *J. Phys. F* **12** 1811
Itoh M, Natori I, Kubota S and Motoya K 1994 *J. Phys. Soc. Japan* **63** 1486
Ivanovskii V I 1959 *Fiz. Met. Metalloved.* **7** 29
Ivanovskii V I 1960 *Izv. Visch. Uchebn. Zaved. Fizika* **N 5** 108
Ivanovskii V I and Denisov P P 1966a *Izv. Visch. Uchebn. Zaved. Fizika* **N 3** 135
Ivanovskii V I and Denisov P P 1966b *Izv. Visch. Uchebn. Zaved. Fizika* **N 6** 147
Ivtchenko V V 1998 MS thesis (M.V. Lomonosov Moscow State University, Physics Faculty)
Ivtchenko V V, Pecharsky V K and Gschneidner K A Jr 2000 *Adv. Cryog. Eng.* **46** 405
Izyumov Y A 1984 *Usp. Fiz. Nauk* **144** 493
Jayaraman A 1991 *High Pressure Studies: Metals, Alloys and Compounds; Handbook on the Physics and Chemistry of Rare Earths* ed K A Gschneidner Jr and L Eyring (Amsterdam: Elsevier) **1** Ch 9
Jayasuriya K D, Campbell S Y and Stewart W A 1985 *J. Phys. F* **15** 225

- Jee C S, Lin C L, Mihalisin T and Wang X Q 1996 *J. Appl. Phys.* **79** 5403
 Jennings L, Stanton R and Spedding F 1957 *J. Chem. Phys.* **27** 909
 Jeong S and Smith J L Jr 1994 *Adv. Cryog. Eng.* **39** 1399
 Jiles D 1998 *Introduction to Magnetism and Magnetic Materials* (London, New York: Chapman and Hall)
 Jin S G, Liu L M, Wang Y L and Chen B X 1991 *J. Appl. Phys.* **70** 6275
 Jin S, Tiefel T H, McCormack M, Fastnacht R A, Fastnacht R A, Ramesh R and Chen L H 1994 *Science* **264** 413
 Johansson J, Lebech B, Nielsen N, Bjerum-Moller H and Mackintosh A 1970 *Phys. Rev. Lett.* **25** 254
 Johanson W R, Pierce G, Zimm C B and Barclay J A 1988 *J. Appl. Phys.* **64** 5892
 Johnson J W and Zimm J A 1996 *J. Appl. Phys.* **79** 2171
 Ju H L, Know C, Li Q, Greene R L and Venkatesan T 1994 *Appl. Phys. Lett.* **65** 2108
 Ju H L and Sohn H 1997 *J. Magn. Magn. Mater.* **167** 200
 Ju H L, Nam Y S, Lee J E and Shin H S 2000 *J. Magn. Magn. Mater.* **219** 1
 Kamarad J, Arnold Z and Ibarra M R 1995 *J. Magn. Magn. Mater.* **140–144 Pt 2** 837
 Kamilov I K, Musaev G M, Magomedov M M, Aliev H K and Shahshaev G M 1975 *Fiz. Tverd. Tela* **17** 543
 Kappel G, Fisher G and Jaegle A 1976 *Phys. Stat. Sol. (a)* **34** 691
 Kashani A, Helvenstein B P M, McCormack F J, Spivak A L and Kittel P 1995 *Cryo-coolers* **8** 637
 Kashani A, Helvenstein B P M, McCormack F J and Spivak A L 1996 *Adv. Cryog. Eng.* **41** 1313
 Kazei Z A, Kolmakova N P, Levitin R Z, Platonov V V, Sidorenko A A and Tatsenko O M 1998 *Physica B* **246** 483
 Kazei Z A, Kolmakova N P, Platonov V V, Sidorenko A A and Tatsenko O M 2000 *J. Eksp. Theor. Phys.* **91** 524
 Kazei Z A, Kriste A, Kolmakova N P, von Ortenberg M, Platonov V V, Puhlmann N, Sidorenko A A, Stolpe I and Tatsenko OM 2001 *J. Magn. Magn. Mater.* **224** 76
 Ke G, Makuchi H and Hashimoto T 1994 *Adv. Cryog. Eng.* **40** 639
 Kimura H, Maeda H and Sato M 1988 *J. Mater. Sci.* **23** 809
 Kimura H, Numazawa T, Sato M, Ikeya T and Fukuda T 1995 *J. Appl. Phys.* **77** 432
 Kimura H, Numazawa T, Sato M, Ikeya T, Fukuda T and Fujioka K 1997a *Proc. 16th Int. Cryogenic Engineering Conf./Int. Cryogenic Materials Conf.* (Oxford: Elsevier) 2069
 Kimura H, Numazawa V, Sato M, Ikeya T, Fukuda T and Fujioka K 1997b *J. Mater. Sci.* **32** 5743
 Kimura H, Sato M, Terada Y, Shimamura K, Fukuda T and Miyashita S 1998 *J. Mater. Sci.* **33** 2379
 Kirchmayer H R and Poldy C A 1978 *J. Magn. Magn. Mater.* **8** 1
 Kirchmayer H R and C A Poldy 1982 Magnetic properties of intermetallic compounds of rare earth metals in *Handbook of the Physics and Chemistry of Rare Earths* ed K A Gschneidner Jr and L Eyring (Amsterdam: Elsevier) **2** 55
 Kittel C 1958 *Elementary Statistical Physics* (New York: Wiley)
 Kittel C 1960 *Phys. Rev.* **120** 335
 Kittel C 1969 *Thermal Physics* (New York: Wiley)
 Kittel C 1986 *Introduction to Solid State Physics* (New York: Wiley)
 Klerk de D 1956 in *Encyclopedia of Physics. Low Temperature Physics* ed S Flugge (Berlin, Gottingen, Heidelberg: Springer) **15** 38

- Knizek K 1992 *J. Solid State Chem.* **100** 292
- Kobayashi H, Onodera H, Yamaguchi Y and Yamamoto H 1991 *Phys. Rev. B* **43** 728
- Koehler W, Child H, Wollan E and Cable J 1963 *J. Appl. Phys.* **34** 1335
- Kohlhaas R 1967 in *Magnetismus: Structur und Eigenschaften Magnetisher Festkorper* VEB Deutscher Verlag fur Grundstoffindustrie (Leipzig) 134
- Kohlhaas R, Rocker W and Hirschler W 1966 *Z. Naturforsch* **21** 183
- Kok J A and Keesom W H 1937 *Physica* **4** 835
- Kokorin V V and Perekos A E 1978 *Pisma JETP* **27** 500
- Kokorin V V, Minkov A V and Osipenko I A 1984 *Fiz. Met. Metalloved.* **57(1)** 197
- Kolmakova N P, Krynetskii I B, Lukina M M and Mukhin A A 1990 *Phys. Stat. Sol. (b)* **159** 845
- Korn J and Kohlhaas R 1969 *Z. angew. Phys.* **26** 119
- Korte B J, Pecharsky V K and Gschneidner K A Jr 1998a *Adv. Cryog. Eng.* **43** 1737
- Korte B J, Pecharsky V K and Gschneidner K A Jr 1998b *J. Appl. Phys.* **84** 5677
- Kokorin V V, Minkov A V and Osipenko I A 1984 *Fiz. Met. Metalloved.* **57(1)** 197
- Kouvel J S and Hartelius C C 1962 *J. Appl. Phys.* **33** Suppl. 1343
- Kral S F and Zimm C B 1999 *CEC'99*
- Kripyakevich P I, Zarechnyuk O S, Gladyshevsky E I and Bodak O I 1968 *Z. Anorg. Chem.* **358** 90
- Krokoszinski H J, Santandrea C, Gmelin E and Barner K 1982 *Phys. Stat. Sol. (b)* **113** 185
- Krusius M, Pickett G R and Veuro M C 1974 *Solid State Commun.* **14** 191
- Kuhrt C, Schittny T and Barner K 1985 *Phys. Stat. Sol. (a)* **91** 105
- Kuriyama T, Hakamada R, Nakagome H, Tokai Y, Sahashi M, Li R, Yoshida O, Matsumoto K and Hashimoto T 1990 *Adv. Cryog. Eng.* **35B** 1261
- Kuriyama T, Takahashi M, Nakagome H, Hashimoto T, Nitta H and Yabuki M 1994 *Adv. Cryog. Eng.* **39** 1335
- Kurti N and Simon F 1934 *Nature* **133** 907
- Kurti N 1960 *Cryogenics* **1** 2
- Kurti N and Simon F E 1934 *Nature* **133** 907
- Kurti N and Simon F E 1935 *Proc. Roy. Soc. A* **149** 152
- Kurti N, Rolling B V and Simon F E 1936 *Physica* **3** 266
- Kurti N, Robinson F N B, Simon F and Spohr D A 1956 *Nature* **178** 450
- Kushino A, Aoki Y, Yamasaki N Y, Namiki T, Ishisaki Y, Matsuda T D, Ohashi T, Mitsuda K and Yazawa T 2001 *J. Appl. Phys.* **90** 5812
- Kushino A, Aoki Y, Yamasaki N Y, Ishisaki Y, Ohashi T and Mitsuda K 2002 *Low Temperature Detectors* **605** 383
- Kuwahara H, Tomioka Y, Asamitsu A and Tokura Y 1995 *Science* **270** 961
- Kuwahara H, Tomioka Y, Moritomo Y, Asamitsu A, Kasai M, Kumai R and Tokura Y 1996 *Science* **272** 80
- Kuz'min M D and Tishin A M 1991 *J. Phys. D: Appl. Phys.* **24** 2039
- Kuz'min M D and Tishin A M 1992 *Cryogenics* **32** 545
- Kuz'min M D and Tishin A M 1993a *Cryogenics* **33** 868
- Kuz'min M D and Tishin A M 1993b *J. Appl. Phys.* **73** 4083
- Labroo S, Ali N and Robinson P 1990 *J. Appl. Phys.* **67** 5292
- Lanchester P C, Robinson K, Baker D P, Williams I S, Street R and Gopal E S R 1980 *J. Magn. Magn. Mater.* **15–18** 461
- Landau L D and Lifshitz E M 1958 *Statistical Physics* (New York: Pergamon)
- Landau D P, Keen B E, Schneider B and Wolf W P 1971 *Phys. Rev. B* **3** 2310

- Langevin P 1905 *Ann. Chem. Phys.* **5** 70
- Lawton L M Jr, Zimm C B and Jastrab A G 1999 US patent 5,934,078
- Lee E W and Pourarian F 1976 *Phys. Stat. Sol. (a)* **33** 483
- Lee S J and Jiles D C 2000 *IEEE Trans. Magn.* **36** 3105
- Leontiev P I 1988 Ph.D. thesis (Moscow State University, Moscow)
- Levitin R Z, Snegirev V V, Kopylov A V, Lagutin A S and Gerber A 1997 *J. Magn. Magn. Mater.* **170** 223
- Li R, Numazawa T, Hashimoto T, Tomokiyo A, Goto T and Todo S 1986 *Adv. Cryog. Eng.* **32** 287
- Lienhard J H IV and Lienhard J H V 2002 *A Heat Transfer Texbook* (Cambridge, MA: Phlogiston Press) 749
- Lima A L, Oliveira I S, Gomes A M and von Ranke P J 2002 *Phys. Rev. B* **65** 172411
- Lindley E J, Rainford B D and McK Paul D 1988 *J. Phys. (Paris)* **49** C8
- Lis T 1980 *Acta Crystallogr. B* **36** 2042
- Litvinenko Y G, Eremenko V V and Myatlik V I 1973 *Sov. Phys.—Solid State* **15** 871
- Liu X Y, Barclay J A, Gopal R B, Foldeaki M, Chahine R, Bose T K, Schuler P J and LaCombe J L 1996a *J. Appl. Phys.* **79** 1630
- Liu X Y, Barclay J A, Foldeaki M, Gopal R B, Chahine R and Bose T K 1996b *Adv. Cryog. Eng.* **42** 431
- Long Y, Zhou S Z and Zhao J 1994 *Chinese Sci. Bull.* **39** 367
- Long Y, Fu H, Hashimoto T, Matsumoto K, Onishi A and Satoh T 1995a *J. Appl. Phys.* **78** 7410
- Long Y, Hashiguchi T, Hashimoto T, Okamura M and Sori N 1995b *J. Appl. Phys.* **77** 2214
- Long Y, Fu H, Hashimoto T, Matsumoto K, Onishi A and Satoh T 1995c *J. Appl. Phys.* **78** 7410
- Lounasmaa O V 1962 *Phys. Rev.* **128** 1136
- Lounasmaa O V and Sundström L J 1966 *Phys. Rev.* **150** 399
- Luis F, Kuz'min M D, Bartolomé F, Orera V M and Bartolomé J. 1998 *Phys. Rev. B* **58** 798
- Luong N H, Chau N, Huong P M, Minh D L, Chau N N, Cong B T and Kurisu M 2002 *J. Magn. Magn. Mater.* **242–245** 760
- Maeda H, Sato M and Uehara M 1983 *J. Japan Inst. Metals* **47** 688
- Majumdar S, Sampathkumaran E V, Paulose P L, Bitterlich H, Löser W and Behr G 2000 *Phys. Rev. B* **62** 14207
- Marquina C, Ibarra M R, de la Fuente C and del Moral A 1995 *J. Magn. Magn. Mater.* **140–144** 809
- Matsumoto G 1970 *J. Phys. Soc. Japan* **29** 615
- Matsumoto K, Ito T and Hashimoto T 1988 *Adv. Cryog. Eng.* **33** 743
- Matsumoto K and Hashimoto T 1990 *Cryogenics* **30** 840
- McAlister S P 1984 *J. Phys. F* **14** 2167
- McEwen K A 1991 Magnetic and transport properties of the rare earths in *Handbook on the Physics and Chemistry of Rare Earths* ed K A Gschneidner Jr and L Eyring (Amsterdam: Elsevier) 1 p 411
- McMahon H O and Gifford W E 1960 *Adv. Cryog. Eng.* **5** 354
- McMichael R D, Shull R D, Swartzendruber L J and Bennett L H 1992 *J. Magn. Magn. Mater.* **111** 29
- McMichael R D, Shull R D, Bennett L H, Fuerst C D and Herbst J F 1993a *Nanostruct. Mater.* **2** 277

- McMichael R D, Ritter J J and Shull R D 1993b *J. Appl. Phys.* **73** 6946
Melero J J, Burriel R and Ibarra M R 1995 *J. Magn. Magn. Mater.* **140–144** 841
Mendelssohn K and H M Rosenberg 1961 in *Solid State Physics* ed F Seitz and T Turnbull (New York: Academic) **12** 223
Merida W R and J A Barclay 1998 *Adv. Cryog. Eng.* **43B** 1597
Milton J E and Scott T A 1967 *Phys. Rev.* **160** 387
Miller S A, Nicholson J D, Gschneidner K A Jr, Pecharsky A O and Pecharsky V K 2000 *11th Int. Cryocooler Conf.* (Keystone, Colorado, 20 June 2000) Paper N 33
Millhouse A and Koehler W 1970 *Colloq. Int. CNRS* **102/2** 213
Millis A J, Littlewood P B and Shraiman B I 1995 *Phys. Rev. Lett.* **74** 5144
Minakata R, Shiga M and Nakamura Y 1976 *J. Phys. Soc. Japan* **41** 1435
Mira J, Rivas J, Rivadulla F, Vázquez-Vázquez C and López-Quintela M A 1999 *Phys. Rev. B* **60** 2998
Mira J, Rivas J, Hueso L E, Rivadulla F, López-Quintela M A, Senaris-Rodrígues M A and Ramos C 2001 *Phys. Rev. B* **65** 024418
Mira J, Rivas J, Hueso L E, Rivadulla F and López-Quintela M A 2002 *J. Appl. Phys.* **91** 8903
Mizokawa T and Fujimori A 1997 *Phys. Rev. B* **56** R493
Moldover M R, Sjolander G and Weyhmann W 1971 *Phys. Rev. Lett.* **26** 1257
Morelli D T, Mance A M, Mantese J V and Micheli A L 1996 *J. Appl. Phys.* **79** 373
Morellon L, Algarabel P A, Ibarra M R, Blasco J, García-Lannda B, Arnold Z and Albertini F 1998 *Phys. Rev. B* **58** R14721
Morellon L, Magen C, Algarabel P A, Ibarra M R and Ritter C 2001 *J. Appl. Phys.* **79** 1318
Moreo A, Yunoki S and Dagotto E 1999 *Science* **283** 2034
Mørup M, Madsen M B, Franck J, Villadsen J and Koch C J W 1983 *J. Magn. Magn. Mater.* **40** 163
Mørup S and Christiansen G 1993 *J. Appl. Phys.* **73** 6955
Mukhin A A, Travkin V D, Zvezdin A K, Lebedev S P, Caneshi A and Gatteschi D 1998 *Europhys. Lett.* **44** 778
Müller K A, Fauth F, Fischer S, Koch M, Furrer A and Lacorre P 1998 *Appl. Phys. Lett.* **73** 1056
Nagaev E L 1996 *Uspehi Fiz. Nauk* **166** 833
Naiden E P and Zhilyakov S M 1997 *Phys. Solid State* **39** 967
Nakagome H, Tanji N, Horigami O, Numazawa T, Watanabe Y and Hashimoto T 1984 *Adv. Cryog. Eng.* **29** 581
Nakane H, Hashimoto T, Numazawa T, Okamura M, Kuriyama T and Ohtani Y 1999 *CEC-ICMC* (Montreal, Canada)
Napoletano M, Canepa F, Manfrinetti P and Merlo F 2000 *J. Mater Chem.* **10** 1663
Narasimhan K S V, Rao V U S, Bergner R L and Wallace W E 1975 *J. Appl. Phys.* **46** 4957
Nayak S K and Jena P 1998a *Chem. Phys. Lett.* **289** 473
Nayak S K and Jena P 1998b *Phys. Rev. Lett.* **81** 2970
Néel L 1954 *Compt. Rend.* **239** 8
Nellis W J and Legvold S 1969 *Phys. Rev.* **180** 581
Nellis G F and Smith J L Jr 1996 *Adv. Cryog. Eng.* **41** 1665
Nikitin S A, Talalaeva E V, Chernikova L A and Andreenko A S 1973 *J. Eksp. Teor. Phys.* **65** 2058
Nikitin S A and Bisliev A M 1974 *Fiz. Met. Metalloved.* **37** 81

- Nikitin S A, Talalaeva E V, Chernikova L A and Andreenko A S 1975 *Fiz. Met. Metalloved.* **40** 96
- Nikitin S A, Andreenko A S, Chuprikov G E and Posyado V P 1977a *Sov. Phys. JETP* **46** 118
- Nikitin S A, Andreenko A S, Chuprikov G E and Posyado V P 1977b *J. Eksp. Teor. Phys.* **73** 228
- Nikitin S A 1978 *Izv. Acad. Nauk SSSR, Ser. Fiz.* **42** 1707
- Nikitin S A, Talalaeva E V, Chernikova L A, Chuprikov G E, Ivanova T I, Kazakov G V and Yarkho G A 1978 *Sov. Phys. JETP* **47** 105
- Nikitin S A, Andreenko A S and Pronin V A 1979a *Sov. Phys.—Solid State* **21** 1616
- Nikitin S A, Andreenko A S, Zvezdin A K and Popkov A F 1979b *Sov. Phys. JETP* **49** 1090
- Nikitin S A, Andreenko A S, Zvezdin A K and Popkov A F 1980 *Bull. Acad. Sci. USSR, Phys. Ser.* **44(7)** 14
- Nikitin S A and Andreenko A S 1981 *Phys. Met. Metallogr.* **52(1)** 55
- Nikitin S A, Andreenko A S and Chuprikov G E 1981 *Vestn. Mosk. Univ. Ser. 3* **22** 64
- Nikitin S A, Andreenko A S, Tishin A M, Arkharov A M and Zherdev A A 1985a *Phys. Met. Metallogr.* **60** 56
- Nikitin S A, Andreenko A S, Tishin A M, Arkharov A M and Zherdev A A 1985b *Phys. Met. Metallogr.* **59(2)** 104
- Nikitin S A and Tishin A M 1987 *Sov. Phys. Solid. State* **29** 1615
- Nikitin S A, Popov Y F, Torchinova R S, Tishin A M and Arkharov I A 1987 *Solid State Phys.* **29** 572
- Nikitin S A and Tishin A M 1988 *Sov. Tech. Phys. Lett.* **14** 327
- Nikitin S A, Tishin A M, Bykhover S E and Redko S V 1988a *Moscow Univ. Phys. Bull.* **43** 96
- Nikitin S A, Tishin A M and Redko S V 1988b *Phys. Met. Metallogr.* **66** 77
- Nikitin S A 1989 *Magnetocaloric Properties of Rare Earth Metals and their Alloys* (Moscow, MGU) p 248
- Nikitin S A and Tishin A M 1989 *Phys. Met. Metallogr.* **67(2)** 59
- Nikitin S A, Spichkin Yu I and Tishin A M 1989a *Fiz. Tverd. Tela* 31 250
- Nikitin S A, Tishin A M and Bykhover S E 1989b *Phys. Stat. Sol. (a)* **114** K99
- Nikitin S A, Tishin A M and Leontev P I 1989c *Phys. Stat. Sol. (a)* **113** K117
- Nikitin S A, Myalikguliev G, Tishin A M, Annorazov M P, Astaryan K A and Tyurin A L 1990 *Phys. Lett. A* **148** 363
- Nikitin S A and Tishin A M 1991 *Cryogenics* **31** 166
- Nikitin S A, Tishin A M, Kuz'min M D and Spichkin Yu I 1991a *Phys. Lett. A* **153** 155
- Nikitin S A, Tishin A M and Leontev P I 1991b *J. Magn. Magn. Mater.* **92** 405
- Nikitin S A, Tishin A M, Savchenkova S F, Spichkin Yu I, Chistykov O D, Redko S V and Nesterov Yu A 1991c *J. Magn. Magn. Mater.* **96** 26
- Nikitin S A, Spichkin Yu I, Tishin A M and Chistiakov O D 1991d *Vestn. Mosk. Univ. Ser. 3* **32** 90
- Nikolaev V I, Dubovcev I A, Ugodnikov G G and Yakimov S S 1966 *Izv. AN SSSR Ser. Fiz.* **30** 949
- NIST Special Publication 330* 2001 *The International System of Units* ed B N Taylor
- Niu X J, Gschneidner K A Jr, Pecharsky A O and Pecharsky V K 2001 *J. Magn. Magn. Mater.* **234** 193
- Noakes J E and Arrott A S 1973 *Proc. 18th Ann. Conf. Magn. Magn. Mater.* **2** 899

- Nojiri N, Shimamoto Y, Miura N, Hase M, Uchinokura K, Kojima H, Tanaka I and Shibuya Y 1995 *Phys. Rev. B* **52** 12749
- Novak M A, Sessoli R, Caneschi A and Gatteschi D 1995 *J. Magn. Magn. Mater.* **146** 211
- Numazawa T, Watanabe Y, Hashimoto T, Sato A, Nakagome H, Horigami O, Takayama S and Watanabe M 1983 *Proc. ICEC* **9** 30
- Numazawa T, Hashimoto T, Nakagome H, Tanji N and Horigami O 1984 *Adv. Cryog. Eng.* **29** 589
- Numazawa T, Kimura H, Sato A, Maeda H, Shimamura K and Fukuda T 1996 *Adv. Cryog. Eng.* **42** 459
- Oesterreicher H and Parker F T 1984 *J. Appl. Phys.* **55** 4334
- Ogawa M, Li R and Hashimoto T 1991 *Cryogenics* **31** 405
- Ohira K, Matsuo S and Furumoto H 1997 *Proc. 16th Int. Cryogenic Engineering Conf./Int. Cryogenic Materials Conf.* p 403
- Okamoto T, Nagata H, Fujii H and Makihara Y 1987 *J. Magn. Magn. Mater.* **70** 139
- Okazaki T, Miyasawa R and Takami S 1993 *Materials Transactions JIM* **34** 1
- Oliveira de N A, von Ranke P J and Tovar Costa M V 2002 *J. Appl. Phys.* **91** 8879
- Onn D G, Meyer H and Remeika J P 1967 *Phys. Rev.* **156** 663
- Osborne M G, Anderson I E, Gschneidner K A Jr, Gaoilloux M J and Ellis T W 1994 *Adv. Cryog. Eng.* **40** 631
- Pakhomov A S 1962 *Vestnik Mosk. Univers. Ser. Fizika*. **N 1** 3
- Pakhomov A S and Gusev A A 1964 *Fiz. Met. Metalloved.* **18** 156
- Palstra T T M, Mydosh J A, Nieuwenhuys G J, van der Kraan A M and Buschow K H J 1983 *J. Magn. Magn. Mater.* **36** 290
- Palstra T T M, Mydosh J A, Nieuwenhuys G J and Buschow K H J 1985 *Phys. Rev. B* **31** 4622
- Parkinson D H, Simon F E and Spedding F H 1951 *Proc. Roy. Soc.* **207A** 137
- Pecharsky V K, Gschneidner K A Jr and Fort D 1993 *Phys. Rev. B* **47** 5063
- Pecharsky V K and Gschneidner K A Jr 1996 *Adv. Cryog. Eng.* **42** 423
- Pecharsky V K, Gschneidner K A Jr and Fort D 1996 *Scr. Mater.* **35** 843
- Pecharsky V K and Gschneidner K A Jr 1997a *Appl. Phys. Lett.* **70** 3299
- Pecharsky V K and Gschneidner K A Jr 1997b *J. Magn. Magn. Mater.* **167** L179
- Pecharsky V K and Gschneidner K A Jr 1997c *Phys. Rev. Lett.* **78** 4494
- Pecharsky V K and Gschneidner K A Jr. 1997d *J. All. Comp.* **260** 98
- Pecharsky V K, Gschneidner K A Jr, McCallum R W and Dennis K W 1997a *Cryocoolers* **9** 663
- Pecharsky V K, Moorman J O and Gschneidner K A Jr 1997b *Rev. Sci. Instrum.* **68** 4196
- Pecharsky V K and Gschneidner K A Jr 1998 *Adv. Cryog. Eng.* **43** 1729
- Pecharsky V K and Gschneidner K A Jr 1999a *J. Appl. Phys.* **86** 565
- Pecharsky V K and Gschneidner K A Jr 1999b *Cryocoolers* **10** 629
- Pecharsky V K, Gschneidner K A Jr, Dan'kov S Yu and Tishin A M 1999 *Cryocoolers* **10** 639
- Pecharsky V K and Gschneidner K A Jr 2001a *Adv. Mater.* **13** 683
- Pecharsky V K and Gschneidner K A Jr 2001b *J. Appl. Phys.* **90** 4614
- Pecharsky V K, Gschneidner K A Jr, Pecharsky A O and Tishin A M 2001 *Phys. Rev. B* **64** 144406
- Pecharsky V K 2002 Private communication.
- Pedersen M S, Mørup S, Linderoth S, Johansson C and Hanson M 1997 *J. Phys.: Condens. Matter.* **9** 7173

- Pederson M R, Reuse F and Khanna S N 1998 *Phys. Rev. B* **58** 5632
- Pérez F, Werner T, Wosnitza J, Löhneysen H and Tanaka H 1998 *Phys. Rev. B* **58** 9316
- Peshkov V P 1964 *Sov. Phys. JETP* **19** 1023
- Peshkov V P 1965 *Zh. Eksp. Theor. Fiz.* **48** 997
- Petric G 1969 *Z. Phys.* **221** 431
- Pfranger R, Plusa D, Szymura S and B Wyslocki 1982 *Postepy Fizyki* **33** 111
- Pillmayer N, Schmitzer C, Gratz E, Hilscher G and Sechovsky V 1987 *J. Magn. Magn. Mater.* **70** 162
- Ponomarev B K 1972 *J. Eksp. Teor. Phys.* **63** 199
- Ponomarev B K 1983 *Instr. Exp. Tech.* **26** 659
- Ponomarev B K 1986 *J. Magn. Magn. Mater.* **61** 129
- Potter H H 1934 *Proc. Roy. Soc. A* **146** 362
- Powell R W and Jolliffe B W 1965 *Phys. Lett.* **14** 171
- Prince E 1957 *Acta Cryst.* **10** 787
- Pszczola J and Krop K 1986 *J. Magn. Magn. Mater.* **59** 95
- Radaelli P G, Cox D E, Marezio M, Cheong S W, Schiffer P E and Ramirez A P 1995 *Phys. Rev. Lett.* **75** 4488
- Ramirez A P, Schiffer P, Cheong S W, Chen C H, Bao W, Palstra T T M, Gammel P L, Bishop D J and Zegarski B 1996 *Phys. Rev. Lett.* **76** 3188
- Ramji Rao R and Narayama Mytry J V S S 1978 *J. Low Temp. Phys.* **33** 413
- Ranke, von P J, Pecharsky V K and Gschneidner K A Jr 1998a *Phys. Rev. B* **58** 12110
- Ranke, von P J, Pecharsky V K, Gschneidner K A Jr and Korte B J 1998b *Phys. Rev. B* **58** 14436
- Ranke, von P J, de Oliveira I G, Guimarães A P and de Silva X A 2000a *Phys. Rev. B* **61** 447
- Ranke, von P J, Lima A L, Nobrega E P, da Silva X A, Guimarães A P and Oliveira I S 2000b *Phys. Rev. B* **63** 02442
- Ranke, von P J, Nóbrega E P, de Oliveira I G, Gomes A and Sarthour R S 2001a *Phys. Rev. B* **63** 184406
- Ranke, von P J, de Oliveira N A, Tovar Costa M V, Nobrega E P, Caldas A and de Oliveira I G 2001b *J. Magn. Magn. Mater.* **226–230** 970
- Rawat R and Das I 2001a *J. Phys.: Condens. Matter* **13** L379
- Rawat R and Das I 2001b *J. Phys.: Condens. Matter* **13** L57
- Rawat R and Das I 2001c *Phys. Rev. B* **64** 052407
- Raychaudhuri A K, Guha A, Das I, Rawat R and Rao C N R 2001 *Phys. Rev. B* **64** 165111
- Rayne J 1954 *Phys. Rev.* **95** 1428
- Reid C E, Barclay J A, Hall J L and Sarangi S 1994 *J. All. Comp.* **207–208** 366
- Rocker W and Kohlhaas R 1967 *Z. angew Phys.* **23** 146
- Romanov A Y and Sulin V P 1997 *Phys. Met. Metallogr.* **83** 111
- Sahashi M, Niu H, Tokai Y, Inomata K, Hashimoto T, Kuzuhara T, Tomokiyo A and Yayama H 1987 *IEEE Trans. Magn.* **MAG-23** 2853
- Sahashi M, Tokai Y, Kuriyama T, Nakagome H, Li R, Ogawa M and Hashimoto T 1990 *Adv. Cryog. Eng.* **35** 1175
- Sampathkumaran E V, Das I, Rawat R and Majumdar S 2000 *Appl. Phys. Lett.* **77** 418
- Sande P, Hueso L E, Miguens D R, Rivas J, Rivadulla F and López-Quintela M A 2001 *Appl. Phys. Lett.* **79** 2040
- Sangregorio C, Ohm T, Paulsen C, Sessoli R and Gatteschi D 1997 *Phys. Rev. Lett.* **78** 4645
- Saito A T, Tutai A, Sahashi M and Hashimoto T 1995 *Jpn. J. Appl. Phys.* **34** L171

- Saito K, Yamamura Y, Mayer J, Kobayashi H, Miyazaki Y, Ensling J, Gütlich P, Leniewska B and Sorai M 2001 *J. Magn. Magn. Mater.* **225** 381
- Sato K, Isikawa Y and Mori K 1982 *J. Appl. Phys.* **53** 8222
- Sato K, Isikawa Y, Mori K and Miyazaki T 1990 *J. Appl. Phys.* **67** 5300
- Satoh T, Onishi A, Li R, Asami H and Kanazawa Y 1996 *Adv. Cryog. Eng.* **41** 1631
- Schiffer P, Ramirez A P, Huse D A and Valentino A J 1994 *Phys. Rev. Lett.* **73** 2500
- Schiffer P, Ramirez A P, Bao W and Cheng S W 1995 *Phys Rev. Lett.* **75** 3336
- Schmitzer C, Hilscher G, Vajda P and Daou J N 1987 *J. Phys. F* **17** 865
- Schnelle W, Fischer R and Gmelin E 2001 *J. Phys. D: Appl. Phys.* **34** 846
- Schobinger-Papamantellos P and Niggli A 1981 *J. Phys. Chem. Solids* **42** 583
- Schuchert H, Hufner S and Faulhaber R 1969 *Z. Phys.* **222** 105
- Schünemann J W, Lange A, Govor G A, Bärner K and Gmelin E 1992 *J. All. Comp.* **178** 237
- Selte K, Kjekshus A, Andersen A F and Zieba A 1977 *J. Phys. Chem. Solids* **38** 719
- Serdyuk U V, Krentsis R P and Geld P V 1985 *J. Less-Common Metals* **111** 347
- Seshake H, Eda T, Matsumoto K and Hashimoto T 1992 *Adv. Cryog. Eng.* **37B** 995
- Sessoli R, Tsai H L, Schake A R, Wang S, Vincent J B, Folting K, Gatteschi D, Christou G and Hendrickson D N 1993 *J. Am. Chem. Soc.* **115** 1804
- Seyfert P 1990 *Adv. Cryog. Eng.* **35** 1087
- Shao Y, Zhang J, Lai J K L and Shek C H 1996a *J. Appl. Phys.* **80** 76
- Shao Y Z, Lai J K L and Shek C H 1996b *J. Magn. Magn. Mater.* **163** 103
- Shen T D, Schwarz R B, Coulter J A and Thompson J D 2002 *J. Appl. Phys.* **91** 5240
- Shepard M, Henning P F, Cao G and Crow J E 1998 *J. Appl. Phys.* **83** 6989
- Shull R D 1993a *AIP Conf. Proc.* **273** 628
- Shull R D 1993b *IEEE Trans. Magn.* **29** 2614
- Shull R D, McMichael R D and Ritter J J 1993 *Nanostructured Mater.* **2** 205
- Si L, Ding J, Wang L, Li Y, Tan H and Yao B 2001a *J. All. Comp.* **316** 260
- Si L, Ding J, Li Y and Wang X Z 2001b *Mater. Sci. Forum* **360–362** 553
- Siek S, Szytula A and Leciejewicz J 1981 *Solid State Comm.* **39** 863
- Silin V P, Wagner D and Zverev V M 1995 *Phys. Lett. A* **199** 395
- Sill R L and Esau E D 1984 *J. Appl. Phys.* **55** 1844
- Simon F E 1939 *C.R. Congr. sur le Magnetisme* (Strasbourg) 3 1
- Sivardiére J and Quezel-Ambrunaz S 1971 *Compt. Rend. B* **273** 619
- Skochdopole R E, Griffel M and Spedding F H 1955 *J. Chem. Phys.* **23** 2258
- Slack G A and D W Oliver 1971 *Phys. Rev. B* **4** 592
- Smaili A and Chahine R 1996 *Adv. Cryog. Eng.* **42** 445
- Smaili A and Chahine R 1997 *J. Appl. Phys.* **81** 824
- Smaili A and Chahine R 1998 *Cryogenics* **38** 247
- Smart J S 1966 *Effective Field Theories of Magnetism* (Philadelphia, London: W B Saunders)
- Smith G S, Tharp A G and Johnson Q 1967 *Acta Cryst.* **22** 940
- Smith D H 1970 *Contemp. Phys.* **11** 287
- Smith J L Jr and Nellis G F 1995 *Cryocoolers* **8** 647
- Smolyaninova V N, Biswas A, Zhang X, Kim X H, Kim Bog-Gi, Cheong S W and Greene R L 2000 *Phys. Rev. B* **62** R6093
- Songlin, Dagula, Tegus O, Brück E, de Boer F R and Buschow K H J 2002a *J. All. Comp.* **337** 269
- Songlin, Dagula, Tegus O, Brück E, de Boer F R and Buschow K H J 2002b *J. All. Comp.* **334** 249

- Spichkin Y I, Pecharsky V K and Gschneidner K A Jr 2001a *J. Appl. Phys.* **89** 1738
 Spichkin Y I, Zvezdin A K, Gubin S P, Mishenko A S and Tishin A M 2001b *J. Phys. D: Appl. Phys.* **34** 1162
- Steinitz M O, Kahrizi M, Tindall D A, Astrom H U and Benediktsson G 1987 *Phys. Rev. B* **35** 8747
- Stewart G R 1984 *Rev. Mod. Phys.* **56** 755
- Stewart A M and Collocott S J 1989 *J. Phys.: Condens. Matter* **1** 677
- Steyert W A 1978a *J. Appl. Phys.* **49** 1216
- Steyert W A 1978b *J. Appl. Phys.* **49** 1227
- Stout J W and Hadley W B 1964 *J. Chem. Phys.* **40** 55
- Strässle Th, Furrer A and Miller K A 2000a *Physica B* **276–278** 944
- Strässle Th, Furrer A, Lacorre P and Müller K A 2000b *J. All. Comp* **303–304** 228
- Srnat K, Hoffer G and Ray A E 1966 *IEEE Trans. Magn.* **2** 489
- Sucksmith W, Clark C A, Oliver D J and Thompson J E 1953 *Rev. Mod. Phys.* **25** 34
- Sun J R, Hu F X and Shen B G 2000a *Phys. Rev. Lett.* **85** 4191
- Sun Y, Xu X and Zhang Y 2000b *J. Magn. Magn. Mater.* **219** 183
- Sun Y, Tong W and Zhang Y 2001 *J. Magn. Magn. Mater.* **232** 205
- Sun Y, Tong W, Liu N and Zhang Y 2002a *J. Magn. Magn. Mater.* **238** 25
- Sun Y, Salamon M B and Chun S H 2002b *J. Appl. Phys.* **92** 3235
- Swalin R A 1962 *Thermodynamics of Solids* (New York: Wiley)
- Sychev V V 1986 *Complex Thermodynamic Systems* (Moscow: Energoatomizdat)
- Szewczyk A, Szymczak H, Wiśniewski A, Piotrowski K, Kartaszyński R, Dabrowski B,
 Kolesník S and Bukowski Z 2000 *Appl. Phys. Lett.* **77** 1026
- Szytula A 1992 *J. All. Comp.* **178** 1
- Takashi I, Masashi N, Kouki N and Hideto Y 1997 *Cryocoolers* **9** 617
- Tanaka J and Mitsuhashi T 1984 *J. Phys. Soc. Japan* **53** 24
- Tang W H, Liang J K, Rao G H and Yan X 1994 *Phys. Stat. Sol.* **141** 217
- Tang T, Gu K M, Cao Q Q, Wang D H, Zhang S Y and Du Y W 2000 *J. Magn. Magn. Mater.* **222** 110
- Tanoue S, Gschneidner K A Jr and McCallum R W 1992 *J. Magn. Magn. Mater.* **103** 129
- Taussig C P, Gallaher G R, Smith J L Jr and Iwasa Y 1986 *4th Int. Cyocooler Conf.*
 (Easton, Maryland, September 1986)
- Taylor K N R and Darby M I 1972 *Physics of Rare Earth Solids* (London: Chapman and Hall)
- Tegus O, Brück E, Klaasse J C P, Buschow K H J and Boer F R 2001 *IEEE Trans. Magn.* **37** 2169
- Tegus O, Brück E, Buschow K H J and de Boer F R 2002a *Nature* **415** 150
- Tegus O, Brück E, Zhang L, Dagula, Buschow K H J and de Boer F R 2002b *Physica B* **319** 174
- Tegus O, Duong N P, Dagula W, Zhang L, Brück E, Buschow K H J and de Boer F R
 2002c *J. Appl. Phys.* **91** 8528
- Tegus O, Dagula O, Brück E, Zhang L, de Boer F R and Buschow K H J 2002d *J. Appl. Phys.* **91** 8534
- Thuy N P, Tai L T, Hien N T, Nong N V, Vihn T Q, Thang P D, Nguyen T P and Molinié
 P 2000a *Proc. Asia Pacific Phys. Conf.* 8 (Taiwan, 6–10 August 2000)
- Thuy N P, Nong N V, Tai L T, Vihn T Q, Kim Anh D T, Quang P H, Thang P D and Long
 N T 2000b *Proc. Vietnam Germany Phys. and Tech. Seminar* (Hochimin City, 3–8
 April 2000)

- Thuy N P, Nong N V, Hien N T, Tai L T, Vinh T Q, Thang P D and Brück E 2002 *J. Magn. Magn. Mater.* **242–245** 841
- Tiablikov S V 1956 *Fiz. Met. Metalloved.* **2** 193
- Tishin A M 1988 *Magnetocaloric Effect in Heavy Rare Earth Metals and their Alloys* (PhD thesis, Moscow State University)
- Tishin A M 1990a *Cryogenics* **30** 127
- Tishin A M 1990b *Sov. Tech. Phys. Lett.* **16** 47
- Tishin A M 1990c *J. Techn. Phys.* **60** 205
- Tishin A M 1990d *Cryogenics* **30** 720
- Tishin A M 1990e *Moscow Univ. Phys. Bull.* **45(2)** 98
- Tishin A M 1990f *J. Appl. Phys.* **68** 6480
- Tishin A M 1990g *Proc. Int. Cryocool. Conf.* (Plymouth, MA, 25–26 October) p 247
- Tishin A M and Kuz'min M D 1991 unpublished results
- Tishin A M 1994 *Magnetic, Magnetothermal and Magnetoelastic Properties of Heavy Rare Earth Metals and their Alloys in the Region of Magnetic Phase Transitions* DSc thesis, Moscow State University
- Tishin A M and Martynenko O P 1995 *Physics of Rare Earth Metals in the Vicinity of Magnetic Phase Transitions* (Moscow: Nauka)
- Tishin A M 1997 *J. Alloys Comp.* **250** 635
- Tishin A M and Bozkova L P 1997 *J. Appl. Phys.* **81** 1000
- Tishin A M 1998a *J. Magn. Magn. Mater.* **184** 62
- Tishin A M 1998b *unpublished results*
- Tishin A M 1998c *Adv. Cryog. Eng.* **43** 1549
- Tishin A M, Gschneidner K A Jr and Pecharsky V K 1999a *Phys. Rev. B* **59** 503
- Tishin A M, Spichkin Yu I and Bohr J 1999b in *Static and Dynamic Stresses Handbook of the Physics and Chemistry of Rare Earth* ed by K A Gschneidner Jr and L Eyring (Amsterdam: Elsevier) **26** p 87
- Tishin A M, Pecharsky V K, Pecharsky A O and Gschneidner K A Jr 2002 unpublished results
- Tokai Y, Takahashi A, Sahashi M and Hashimoto T 1992 *Proc. 7th Int. Conf.* (Santa Fe, NM, 17–19 November) p 484
- Tokura Y, Tomioka Y, Kuwahara H and Kasai M 1996 *Physica C* **263** 544
- Tokura Y and Tomioka Y 1999 *J. Magn. Magn. Mater.* **200** 1
- Tolman R C and Fine P C 1948 *Rev. Mod. Phys.* **20** 51
- Tomokiyo A, Yayama H, Hashimoto T, Aomine T, Nishida M and Sakaguchi S 1985 *Cryogenics* **25** 271
- Tomokiyo A, Yayama H, Wakabayashi H, Kuzuhara T, Hashimoto T, Sahashi M and Inomata K 1986 *Adv. Cryog. Eng.* **32** 295
- Tomioka Y, Asamitu A and Tokura Y 1995 *Phys. Rev. Lett.* **74** 5108
- Torres F, Hernández J M, Bohigas X and Tejada J 2000 *Appl. Phys. Lett.* **77** 3248
- Troyanchuk I O, Trukhanov S V, Khalyavin D D and Szymczak H 2000 *J. Magn. Magn. Mater.* **208** 217
- Tsukagoshi T, Nitta H, Yoshida A, Matsumoto K, Hashimoto T, Kuriyama T, Takahashi M, Ohtani Y and Nakagome H 1996 *Adv. Cryog. Eng.* **41** 1623
- Venturini G, Malaman B, Tomala K and Szytula A 1992 *Phys. Rev. B* **46** 207
- Vigoureux P *Units and Standards of Electromagnetism* (London: Wykeham)
- Vinh T Q, Hein N T, Nong N V, Long N T, Tai L T, Thuy N P, Thang P D, Brück E and Duijn H G M 1999 *Proc. 3rd Int. Workshop on Materials Science* (Hanoi, 2–4 November 1999) 258

- Visser D W, Ramirez A P and Subramanian M A 1997 *Phys. Rev. Lett.* **78** 3947
- Voiron J and Bloch B 1971 *J. Phys. France* **32** 949
- Voiron J, Breton A and Chaussy J 1974 *Phys. Lett. A* **50** 17
- Vonsovskii S V 1974 *Magnetism* (Jerusalem: Israel Program Sci. Translations)
- Wada H, Nishigori M and Shiga M 1993 *J. Phys. Soc. Japan* **62** 1337
- Wada H, Yamaguchi H and Shiga M 1996 *J. Magn. Magn. Mater.* **152** 165
- Wada H, Tomekawa S and Shiga M 1999 *Cryogenics* **39** 915
- Wada H, Tanabe Y, Hagiwara K and Shiga M 2000 *J. Magn. Magn. Mater.* **218** 203
- Wada H and Tanabe Y 2001 *Appl. Phys. Lett.* **79** 3302
- Wada H, Tanabe Y, Shiga M, Sugawara H and Sato H 2001 *J. All. Comp.* **316** 245
- Wada H, Taniguchi K and Tanabe Y 2002 *Mater. Transact.* **43** 73
- Wagner D, Romanov A Y and Silin V P 1996 *J. Eksp. Teor. Phys.* **106** 1753
- Walker G and Bingham E R 1993 *Low Capacity Cryogenic Refrigeration* (The University of Calgary, Alberta, Canada: Department of Mechanical Engineering)
- Wallace W E 1973 *Rare Earth Intermetallics* (New York: Academic)
- Wang A A, Johnson J W, Niemi R W, Sternberg A A and Zimm C B 1995 *Cryocoolers* **8** 665
- Wang F W, Zhang X X and Hu F X 2000 *Appl. Phys. Lett.* **77** 1360
- Wang Z M, Ni G, Xu Q Y, Sang H and Du Y W 2001a *J. Appl. Phys.* **90** 5689
- Wang Z M, Ni G, Xu Q Y, Sang H and Du Y W 2001b *J. Magn. Magn. Mater.* **234** 371
- Wang D, Tang S, Liu H, Li S, Zhang J and Du Y 2001c *Jpn. J. Appl. Phys.* **40** 6815
- Wang Z M, Tang T, Wang Y P, Zhang S Y and Du Y W 2002a *J. Magn. Magn. Mater.* **246** 254
- Wang D H, Liu H D, Tang S L, Tang T, Wen J F and Du Y W 2002b *Solid State Commun.* **121** 199
- Wang D H, Liu H D, Tang S L, Yang S, Huang S and Du Y 2002c *Phys. Lett. A* **297** 247
- Warburg E 1881 *Ann. Phys.* **13** 141
- Waynert J A, Nilles M J, Campbell H G and Zimm C B 1994 *Int. CFC and Halon Alternatives Conference* (Washington, DC, 24–27 October 1994)
- Weiss P and Piccard A 1918 *Compt. Rend.* **166** 352
- Weiss P and Forrer R 1924 *Compt. Rend.* **178** 1347
- Weiss P and Forrer R 1926 *Ann. Phys.* **5** 153
- Wen G H, Zheng R K, Zhang X X, Wang W H, Chen J L and Wu G H 2002 *J. Appl. Phys.* **91** 8537
- White G K 1989 *J. Phys.: Condens. Matter* **1** 6987
- Wieghardt K, Phol K, Jibril I and Huttner G 1984 *Angew. Chem.* **23** 77
- Wilkinson M K, Koehler W C, Wollan E O and Cable J W 1961 *J. Appl. Phys.* **32** 48
- Williamson R 2001 Individual Project Report, CFS, University of Victoria
- Wong T and Seuntjens J M 1996 *Adv. Cryog. Eng.* **42** 439
- Wood M E and Potter W H 1985 *Cryogenics* **25** 667
- Woodfield B F, Wilson M L and Byers J M 1997 *Phys. Rev. Lett.* **78** 3201
- Wu Y L, Pecharsky A O, Pecharsky V K and Gschneidner K A Jr 2002 *Adv. Cryog. Eng.* **48** 3
- Wysokinski T W, Xu Xiangdong and Barclay J A 2002 *Cryogenics* **42** 691
- Xiyan Z, Ling Y, Shijie Z, Linlin Q and Zhinong L 2001 *Mater. Trans.* **42** 2622
- Xu Q Y, Gu K M, Liang X L, Ni G, Wang Z M, Sang H and Du Y W 2001 *J. Appl. Phys.* **90** 524
- Xu Y, Memmert U and Hartmann U 2002 *J. Magn. Magn. Mater.* **242–245** 698

- Yagi W, Iwata H and Mizutani U 1997 *Jpn. J. Appl. Phys.* **36** 5638
Yagi W, Iwata H and Mizutani U 1998 *Jpn. J. Appl. Phys.* **37** 4787
Yamamoto T A, Tanaka M, Nakayama T, Nishimaki K, Nakagawa T, Katsura M and Niihara K 2000a *Jpn. J. Appl. Phys.* **39** 4761
Yamamoto T A, Tanaka M, Shiomi K, Nakayama T, Nishimaki K, Nakagawa T, Numazawa T, Katsura M and Niihara K 2000b *Mat. Res. Soc. Symp. Proc.* **581** 297
Yan Z and Chen J 1989 *J. Appl. Phys.* **66** 2228
Yayama H, Tomokiyo A, Hashimoto T, Kuzuhara T, Li R, Sahashi M and Inomata K 1987 *IEEE Trans. Magn.* **MAG-23** 2850
Yayama H, Hatta Y, Makimoto Y and Tomokiyo A 2000 *Jpn. J. Appl. Phys.* **39** 4220
Yunoki S, Hu J, Malvezzi A L, Moreo A, Furukawa N and Dagotto E 1998 *Phys. Rev. Lett.* **80** 845
Zach R, Guillot M and Fruchart R 1990 *J. Magn. Magn. Mater.* **89** 221
Zaharov A I, Kadomceva A M, Levitin R Z and Poniatovski E G 1964 *J. Eksp. Teor. Phys.* **46** 2003.
Zener C 1951 *Phys. Rev.* **82** 403
Zhang X X, Tejada J, Xin Y, Sun G F, Wong K W and Bohigas X 1996 *Appl. Phys. Lett.* **69** 3596
Zhang Y X, Liu Z G, Zhang H H and Xu X N 2000a *Mater. Letters* **45** 91
Zhang X X, Wen G H, Wang F W, Wang W H, Yu C H and Wu G H 2000b *Appl. Phys. Lett.* **77** 3072
Zhang X X, Wang F W and Wen G H 2001a *J. Phys.: Condens. Matter* **13** L747
Zhang X X, Wei H L, Zhang Z Q and Zhang L 2001b *Phys. Rev. Lett.* **87** 157203-1
Zhong W, Chen W, Ding W, Zhang N, Du Y and Yan Q 1998a *Solid State Commun.* **106** 55
Zhong W, Chen W, Ding W P, Zhang N, Du Y W and Yan Q J 1998b *Eur. Phys. J. B* **3** 169
Zhong W, Chen W, Ding W P, Zhang N, Hu A, Du Y W and Yan Q J 1999 *J. Magn. Magn. Mater.* **195** 112
Zhou T J, Yu Z, Zhong W, Xu X N, Zhang H H and Du Y W 1999 *J. Appl. Phys.* **85** 7975
Zhilyakov S M, Naiden E P and Riabtsev G I 1993 *Izv. VUZov Fizika* **10** 63
Zhilyakov S M, Riabtsev G I and Naiden E P 1994 *Fiz. Tverd. Tela* **36** 2402
Zieba A, Shapira Y and Foner S 1982 *Phys. Lett. A* **82** 243
Zimm C B, Campenni C K and Barclay J A 1988a *J. Appl. Phys.* **63** 4294
Zimm C B, Karl P L, Barclay J A, Green G F and Patton W G 1988b *Proc. 5th Int. Cryocooler Conf.* (Monterey, CA, USA) p 49
Zimm C B, Barclay J A, Harkness H H, Green G F and Patton W G 1989 *Cryogenics* **29** 937
Zimm C B, Ratzmann P M, Barclay J A, Green G F and Chafe J N 1990 *Adv. Cryog. Eng.* **36** 763
Zimm C B, Ludeman E M, Severson M C and Herring T A 1992 *Adv. Cryog. Eng.* **37B** 883
Zimm C B and DeGregoria A J 1993 *AIP Conf. Proc.* p 471
Zimm C B 1994 *Adv. Cryog. Eng.* **40** 647
Zimm C B, Jastrub A G and Johnson J W 1995 *Cryocoolers* **8** 657
Zimm C B, Johnson J W and Murphy R W 1996 *Adv. Cryog. Eng.* **41** 1675
Zimm C B, Jastrub A, Sternberg A, Pecharsky V, Gschneidner K A Jr, Osborne M and Anderson I 1998 *Adv. Cryog. Eng.* **43** 1759
Znamenskii B V and Fakidov I G 1962 *Phys. Met. Metalloved.* **N 2** 312
Zvezdin A K, Dobrovitski V V, Harmon B N and Katsnelson M I 1998 *Phys. Rev. B* **58** R14733

Index

- adiabatic conditions, 1, 41
adiabatic demagnetization, 62
 nuclear, 67
adiabatic heat-pulse calorimeter, 87, 90
adiabatic-isobaric process, 7, 17, 19
adiabatic-isochoric process, 7, 61
adiabatic magnetization, 7, 8
adiabatic shield, 90, 93
alloy
 Dy-Y, 322, 324
 Er-La, 322, 326
 Er-Pr, 322, 326, 327, 328, 363–365, 414
 Fe-Rh, 105, 109–112, 406, 407, 412,
 414, 417, 420, 421
 Fe-Si, 104, 122
 Gd-Dy, 79, 321, 322, 389, 390,
 403–406
 Gd-Dy-Nd, 322
 Gd-Er, 79, 321, 322, 390, 403–405
 Gd-Ho, 321, 322, 327, 403–405
 Gd-Lu, 276
 Gd-Tb, 389, 403–405
 Gd-Tb-Nd, 321
 Heusler, 120, 125, 412, 413
metastable Fe-Hg, 341
Mn-Cu, 119
Ni-Mn, 199
Ni-Cu, 119
Tb-Dy, 326, 327, 389
Tb-Gd, 316, 317, 320
Tb-Y, 284, 322–325, 329
 water-quenched, 342
amplitude modulated spin structure, 255
amorphous, 209
 Er_3Ni , 361, 362
 $\text{Er}_3(\text{Ni}_{0.98}\text{Ti}_{0.02})$, 361
 $\text{Er}_3(\text{Ni}_{0.9}\text{Ti}_{0.1})$, 361
Fe-M-Zr ($M = \text{Al, Ga, Ge, Sn}$), 336
 $(\text{Fe-Ni})_{0.9}\text{Zr}_{0.1}$, 336
 (Gd-Co) , 336
material, 330
melt-spun ribbon, 335, 336, 341, 342
Pd-Ni-Fe-P, 336
 $\text{R}_{0.7}\text{Mn}_{0.3-x}\text{M}'_x$ ($\text{R} = \text{Gd, Dy, Er, Ho, Tb}$; $\text{M}' = \text{Ni, Fe, Co, Cu}$), 330,
 331, 334, 337
anisotropy
 constant, 99, 103, 123, 170–172, 279,
 317
form, 124
in-plane, 25
magnetocrystalline, 8, 25, 121, 139,
 171, 195, 227, 251, 270, 287, 308,
 341, 347, 348
single-ion, 25
uniaxial, 25, 174, 197
antiferromagnet, 19, 22, 32, 56
 helicoidal (HAFM), 35, 39, 61, 217,
 276, 284, 287, 293, 294, 296–299,
 302, 313, 321, 323, 324, 326–329
itinerant, 244
spiral structure, 60
surface, 124
two-dimensional, 56
antiferromagnetic canting state, 164
antiferromagnetic layered spin structure,
 256
anvil-quenching technique, 336
Arrott plot, 155, 191, 204, 229, 230
atomic volume, 60

- Avogadro's number, 16
 austenitic phase, 120, 121, 412
 band structure, 54
 barocaloric effect, 62
 blocking state of superparamagnet, 154, 348–350
 blocking temperature, 348
 blow period, 379
 Born–von Karman model, 54
 Brillouin function, 11, 34
 cadmium, 65
 calcium fluoride, 67
 canted spin structure, 245, 273
 caret-type maximum
 on heat capacity temperature dependence, 188, 194, 205
 on $\Delta S_M(T)$ dependence, 268
 centrifugal atomization process, 359, 361, 362, 364
 cerium ethylsulfate
 ($\text{Ce}(\text{C}_2\text{H}_5\text{SO}_4)_3 \cdot 9\text{H}_2\text{O}$), 64
 cerium fluoride (CeF_3), 64
 cerium manganese nitride, 66
 charge ordering, 143, 145, 159, 162–164, 167
 chrome alum, 65
 chrome potassium alum, 68
 Clausius–Clapeyron equation, 31, 36, 81, 112, 113, 238, 293, 294, 300, 301, 329
 cluster glass, 164
 coefficient
 of performance (COP), 367, 380, 391
 of thermal expansion, 6, 52, 59–61, 94, 95
 Steven's, 244
 thermodynamic, 9
 coercive force, 162, 221, 222, 244, 269, 270, 273, 330, 331, 335
 commensurability effect (point), 298, 299
 commensurate spin structure (phase), 195, 304, 305, 326
 compensation temperature (point), 33, 128, 129, 142, 168, 169, 211, 214, 336
 compounds
 $\text{CrS}_{1.17}$, 109, 112
 CrTe , 105
 Cr_3Te_4 , 105
 DySb , 358
 (Er-Dy)Sb, 250
 Fe_5Si_3 , 122
 $\text{Gd}_4(\text{Bi-Sb})_3$, 247
 $\text{Gd}_2(\text{SO}_4)_3$, 396
 HoSb , 358
 HoPO_4 , 396
 LaFeSi , 110
 $\text{Li}_{0.1}\text{Mn}_{0.9}\text{Se}$, 109, 112
 mixed-valence, 144
 MnAs , 105, 112–117, 412, 417, 420, 421
 $\text{MnAs}_{1-x}\text{P}_x$, 115, 116
 $\text{MnAs}_{1-x}\text{P}_x$, 117
 $\text{MnAs}_{1-x}\text{Sb}_x$, 412
 $\text{Mn}_{2-x}\text{Cr}_x\text{Sb}$, 109, 112, 122
 $\text{Mn}_{1.9}\text{Cr}_{0.1}\text{Sb}$, 112
 $\text{Mn}_{1.95}\text{Cr}_{0.05}\text{Sb}$, 109
 $\text{Mn}_{3-y-z}\text{Cr}_y\text{AlC}_{1+z}$, 123
 $\text{Mn}_{1-x}\text{Fe}_x\text{As}$, 116
 $\text{Mn}_{5-x}\text{Fe}_x\text{Si}_3$, 122
 $\text{MnFeP}_{1-x}\text{As}_x$, 117–119, 412, 417, 420, 421
 Mn_3GaC , 112
 Mn_5Ge_3 , 109
 Mn_3Ge_2 , 109, 112
 $\text{Mn}_5\text{Ge}_{3-x}\text{Sb}_x$ –122
 MnP , 105, 112, 113, 115
 Mn_5Si_3 , 109, 122, 123
 $\text{Mn}_{1-x}\text{V}_x\text{As}$, 116
 $\text{Mn}_{0.95}\text{V}_{0.05}\text{As}$, 109
 NiAs , 113, 116, 117
 $\text{Ni}_2(\text{Mn}_{1-x}\text{M}_x)\text{Sn}$ ($\text{M} = \text{V}, \text{Nb}$), 123
 Ni_2MnGa , 412
 RbMnBr_3 , 123
 YbAs , 250
 compressibility (isothermal), 53
 constant
 anisotropy, 49
 Boltzmann, 11
 gas, 15, 53
 Planck's, 54
 conductivity
 axial, 370, 372, 378
 electrical, 105

- thermal, 104, 105, 136, 139, 143, 167, 177, 190, 195, 210, 244, 281, 284, 287, 293, 294, 301–303, 306, 307, 309, 353, 359, 364, 370, 429
- conical spin structure, 277, 304, 305
- cooling power, 367, 371, 380, 382, 386, 388, 391, 397, 399
- normalized relative (RCP), 406
- relative (RCP), 406, 412–415, 420
- useful, 397, 399
- covalent-like bonds, 259, 261
- Coulomb's law, 422
- critical field, 223, 276, 294, 299, 302, 309, 321, 322, 326
- crystal field splitting, 133
- crystal structure
- anti-Th₃P₄-type, 247
 - antiperovskite-type, 193
 - bcc, 60
 - CeCu₂-type, 193
 - CeNiSi₂-type, 253
 - CsCl-type, 194, 195
 - Cu₃Au-type, 187
 - Cu₂Mg-type, 179
 - Cu₂Sb-type, 254
 - cubic, 50, 51, 164
 - cubic NaZn₁₃-type, 220, 221
 - double hcp (dhcp), 60, 277
 - fcc, 60, 119
 - hexagonal, 50, 113
 - hexagonal AlB₂-type, 196, 257, 258
 - hexagonal close-packed (hcp), 276, 294
 - hexagonal MgZn₂-type, 243
 - hexagonal Ni₂In-type, 200
 - hexagonal Th₂Ni₁₇-type, 215
 - Laves phase, 179, 201, 225
 - layered, 247, 254
 - MgCu₂-type, 231
 - monoclinic, 259, 261, 266, 268, 269, 271, 273, 275
 - monoclinic Gd₅Si₄-type, 261
 - monoclinic Gd₅Si₂Ge₂-type, 261, 268, 270, 271
 - orthorhombic, 113, 146, 156, 162, 194, 255, 258, 268, 269, 271, 273, 275, 294
 - orthorhombic Gd₅Ge₄-type, 261
 - orthorhombic Gd₅Si₄-type, 261, 270, 271, 273
 - orthorhombic Sm₅Ge₄-type, 261, 268, 271, 273
 - orthorhombic TiNiSi-type, 209
 - perovskite-type, 112, 137
 - rhombohedral, 146, 156, 164, 193
 - rhombohedral Th₂Zn₁₇-type, 215
 - Sr₃T₂O₇-type, 158
 - tetragonal, 256
 - tetragonal CeFeSi-type, 254
 - tetragonal Pr₇Co₆Al₇-type, 244
 - tetragonal ThMn₁₂-type, 225, 245
 - tetragonal ThCr₂Si₂-type, 251
 - tetragonal zircon-type, 175, 176
 - tetragonal Zr₅Si₄, 271
 - Th₇Fe₃-type, 194
 - transition 9, 115, 116, 118, 175, 226, 294
 - ZrNiAl-type, 209
- crystal structure change, 113, 115
- crystallite, 44
- crystallization temperature, 335
- Curie:
- constant, 12, 14, 16
 - law, 12
 - local temperature, 43
 - point (temperature), 9, 13, 14
- cluster, 347, 348
- with short-range magnetic order, 301
- clustered system, 46
- convention:
- Kennelly, 423
 - Sommerfeld, 423
- corundum, 174
- crossover, 177, 207, 309
- cryostat, 76, 90–92
- cryocooler, 352
- Gifford–McMahon, 352, 354–358, 361, 380, 387, 388, 400, 414
 - magnetic, 62
- crystalline electric field, 57, 58, 61, 64, 179, 144, 210, 184–186, 188, 189, 193, 198, 204, 205, 207, 227, 244–246, 250, 250, 252, 254, 308, 330, 419
- coefficient, 27
- Curie–Weiss law, 13, 139, 176

- Co, 96–104
 Cu, 104, 105, 136
 cycloid (spin structure), 277, 304
 dead volume, 362
 in AMR refrigerator, 384
 Debye
 interpolation formula, 15
 temperature, 15, 23, 31, 53, 59, 97, 309,
 310, 315, 350, 429
 Debye's model, 53, 54
 de Gennes factor, 270, 273, 322
 degeneracy, 57
 differential thermal analysis, 170, 341
 dislocations, 136
 displacer, 374–376, 380, 387, 388
 domain wall, 8
 Dulong–Petit limit, 23, 53, 98,
 dysprosium ethylsulfate
 (Dy(C₂H₅SO₄)₃·9H₂O), 64
 Dy, 39, 41, 42, 61, 284, 291, 295, 294,
 296–302, 310–313, 322–325, 326,
 403–406, 419
 high-purity, 297, 299, 301
 ultra-pure, 296, 297, 301, 305
 eddy (Foucault) currents, 9, 71, 76, 77,
 372, 384
 effective exchange field, 12
 eigenvalues, 11
 elastic modulus, 7
 elastocaloric effect, 58–61
 electrical resistivity, 156, 219, 255,
 256
 electron density of states, 54, 205,
 207
 electronic microscopy, 335
 electronic paramagnetic resonance
 (EPR), 343, 344
 electrons
 itinerant, 144, 179, 220, 226, 243, 245,
 245
 3d, 242
 5d, 226
 4f, 226, 243
 energy
 anisotropy, 287, 296, 323, 324, 329,
 348, 349, 420
 exchange interaction, 284, 323, 324,
 329, 420
 free, 4
 Gibbs free, 4, 323
 internal, 4, 56
 magnetic free, 11, 123, 132
 magnetoelastic, 9, 284, 323, 324, 329,
 420
 single-ion crystalline field, 250
 thermal agitation, 1, 67, 133
 Zeeman, 287, 323, 348
 enthalpy, 28, 29, 358
 entropy, 1, 4, 14
 electronic, 14, 15, 63, 111, 219, 220,
 243, 315
 magnetic, 1, 14, 16, 34, 35, 63, 156,
 180, 181, 227, 243, 246, 250, 296,
 307, 315
 lattice, 14, 15, 63, 111, 132, 134, 219,
 329, 365
 total, 14
 volumetric magnetic, 412
 exchange:
 antiferromagnetic interactions, 33
 double interactions, 144, 145, 158, 161
 field, 33
 indirect interactions, 317
 integral, 12, 34, 56
 integral distribution, 334
 interactions, 12, 35, 47, 57, 63, 113,
 113, 130, 144, 169, 185, 205, 227,
 247, 281, 352
 oscillating indirect, 276
 parameter, 113
 RKKI-type interactions, 197, 270
 expansion volume
 maximum, 356, 357
 eutectic composition, 194
 Er, 277, 284, 291, 303, 304, 305, 306,
 310–313, 326, 328, 364, 403
 high-purity, 305
 ultra-pure, 304
 Eu, 60
 EuS, 26, 94
 fan magnetic (spin) structure, 35, 217,
 276, 284, 287, 293, 297, 299, 326,
 327

- FC (field cooled) magnetization measurement, 147, 204, 348
- Fermi–Dirac statistics, 54
- Fermi level, 54
- Fermi surface, 111
- ferrimagnet, 32
- ferromagnet, 9
- inhomogeneous, 42, 43
 - easy-plane, 316
- ferromagnetic resonance, 339
- ferromagnetic spiral-type (spin structure), 321, 322, 324
- ferrites, 126
- field-induced
- ferromagnet, 39
- metamagnetic transition, 114, 117, 118, 163, 175, 179, 192, 200, 219, 220, 222, 223, 226, 252, 254–256, 271, 296, 298, 419
- film
- Ni, 124
 - $\gamma\text{-Fe}_2\text{O}_3$, 124
- Foucault (eddy) currents, 9, 71, 76, 77, 372, 384
- free electron model, 54
- gas, 55
- Fe, 96–101, 103
- gadolinium sulfate ($\text{Gd}_2(\text{SO}_4)_2 \cdot 8\text{H}_2\text{O}$), 64
- garnets 32, 126, 419
- aluminium rare earth ($\text{R}_3\text{Al}_5\text{O}_{12}$), 126, 131, 401
 - $\text{Dy}_3\text{Al}_5\text{O}_{12}$, 133, 177
 - ($\text{Dy-Gd})_3\text{Ga}_5\text{O}_{12}$, 137
 - dysprosium aluminium (DAG, $\text{Dy}_3\text{Al}_5\text{O}_{12}$), 133, 134, 136, 139, 140, 401
 - dysprosium gallium (DGG, $\text{Dy}_3\text{Ga}_5\text{O}_{12}$), 131, 133–137, 177, 402, 413
 - ($\text{Er-Y})_3\text{Al}_5\text{O}_{12}$, 131, 136
- gadolinium gallium (GGG, $\text{Gd}_3\text{Ga}_5\text{O}_{12}$), 46, 85, 86, 131–134, 136, 137, 211, 346, 387, 389, 396, 397, 399–402
- gadolinium gallium iron (GGIG, $\text{Gd}_3\text{Ga}_x\text{Fe}_{5-x}\text{O}_{12}$), 127, 128, 346
- gadolinium iron ($\text{Gd}_3\text{Fe}_5\text{O}_{12}$), 32, 34, 35, 127, 128, 169, 211
- gallium rare earth ($\text{R}_3\text{Ga}_5\text{O}_{12}$), 126, 131
- rare earth iron ($\text{R}_2\text{Fe}_5\text{O}_{12}$, $\text{R} = \text{Gd}, \text{Tb}, \text{Dy}, \text{Ho}, \text{Er}, \text{Tm}, \text{Yb}, \text{Y}$), 33, 126–128, 130, 214
- $\text{Lu}_3\text{Al}_5\text{O}_{12}$, 133
 - $\text{Yb}_3\text{Fe}_5\text{O}_{12}$, 130, 131
 - ($\text{Yb-Y})_3\text{Fe}_5\text{O}_{12}$, 130, 131)
 - $\text{Y}_3\text{Al}_5\text{O}_{12}$, 133
 - $\text{Y}_3\text{Fe}_5\text{O}_{12}$, 127, 130
- gas atomization process, 359, 364
- Gaussian distribution, 331
- generalized coordinates, 28
- thermodynamic quantities, 5
- germanides, 247, 250
- $\text{CeCu}_{0.86}\text{Ge}_2$, 253
 - Gd_5Ge_4 , 258, 259
 - GdRu_2Ge_2 , 253
 - HoTiGe , 254
 - LaFe_2Ge_2 , 251
 - $\text{PrCu}_{0.76}\text{Ge}_2$, 253, 254
 - RMn_2Ge_2 ($\text{R} = \text{La}, \text{Y}, \text{Gd}, \text{Tb}, \text{Dy}$), 247, 251, 256
 - RNiGe ($\text{R} = \text{Gd}, \text{Dy}, \text{Er}$), 358
 - Tb_5Ge_4 , 271
- g*-factor, 11, 132
- Gifford–McMahon cryocooler, 352, 354–358, 361, 380, 387, 388, 400, 414
- Gd, 41, 42, 56, 60, 61, 72, 77, 79, 80, 83–85, 87–89, 97, 110, 123, 117, 119, 121, 158, 162, 194, 206, 214, 221, 222, 224, 238, 250, 251, 261, 269, 275, 277–281, 283, 287, 294, 310–316, 328, 364, 385, 386, 389–391, 402–404, 406, 413, 414, 416
- Gd_2O_3 , 281, 335
- Hamiltonian, 11, 12, 25, 205, 207, 250, 348
- Heisenberg, 57
- Ising, 57

- heat capacity, 6, 52, 86, 103
 crystalline field (contribution), 349,
 350
 dipolar (contribution), 349, 350
 electronic, 14, 15, 53, 54, 166, 219, 227,
 245, 251, 351, 352, 413
 hyperfine (contribution), 349, 350
 lattice, 15, 53, 166, 198, 209, 219, 227,
 245, 251, 311, 349, 351, 352, 413
 magnetic, 15, 53, 56, 352
 molar, 53
 spin wave, 55, 56
 Schottky nuclear (contribution), 198
 volumetric, 194, 195, 197, 208, 309,
 326, 352–355, 358, 362–364
 λ -type anomaly, 137, 143, 188, 191,
 193–195, 201, 205, 208, 210, 217,
 231, 244, 245, 247, 254, 256, 277,
 281, 336
 heat exchanger, 365, 369
 heat transfer fluid, 352, 359, 365
 Heusler alloy, 120, 125, 412, 413
 hexagonal axis, 101
 hexagonal ferrites, 170, 171
 $\text{BaFe}_{12-x}\text{Co}_x\text{Ti}_x\text{O}_{19}$, 170
 $\text{BaCa}_{2-x}\text{Zn}_x\text{Fe}_{16}\text{O}_{27}$, 170
 $\text{BaCo}_{1.65}\text{Fe}_{0.35}^{2+}\text{Fe}_{16}^{3+}\text{O}_{27}$, 172
 CoZn-W , 171
 Co_xW , 172
 Ho, 58, 60, 61, 77, 284, 291, 301, 302,
 310–313, 403, 405
 Hund rule, 144
 hybridization, 144, 219, 226
 hydrogen, 225
 hydrogenated, 225
 hyperfine splitting, 64
 hysteresis, 9
 loop, 223
 loss, 340
 magnetic field, 121, 175, 219, 221–223,
 244, 261, 276, 344, 372
 temperature, 19, 113, 117, 165,
 221–223, 298
 ZFC-FC temperature, 154
 interactions
 antiferromagnetic exchange, 33
 dipole, 47, 57, 63, 66, 350
 double exchange, 144, 145, 158, 161
 exchange, 12, 35, 47, 57, 63, 113, 113,
 130, 144, 169, 185, 205, 227, 247,
 281, 352
 indirect exchange, 317
 magnetoelastic, 10, 125, 156
 oscillating indirect exchange, 276
 quadrupolar, 195, 250
 RKKI-type exchange, 197, 270
 superexchange, 144, 145, 158, 339,
 343
 intermetallic compounds, 37, 179, 314,
 315, 353
 $\text{Ce}_2\text{Fe}_{17}$, 214
 $\text{Ce}(\text{Fe-Co})_2$, 217, 219
 DyCu_2 , 195
 $\text{Dy}(\text{Co-Si})_2$, 242
 $(\text{Dy-Gd})\text{Co}_2$, 243
 $(\text{Dy-Er})\text{Al}_2$, 180, 186, 188, 189, 209,
 407
 $(\text{Dy-Ho})\text{Ga}_2$, 196, 197, 359
 ErAg , 195, 246, 358
 Er_2Al , 193
 ErAl_2 , 83–85, 87–89
 Er_3AlC_x , 193
 ErAgGa , 193
 Er_3Co , 244, 353, 356, 357
 $\text{Er}(\text{Co-Ni})_2$, 240–242, 353
 $\text{Er}(\text{Ni-Co})$, 353, 354, 356, 357, 361,
 362, 414
 ErNi , 353, 354, 380, 388
 $(\text{Er-Gd})\text{Ni}$, 357
 $(\text{Er-Y})\text{Ni}$, 201
 $(\text{Er-Yb})\text{Ni}$, 353, 356, 357
 ErNi_2 , 353, 354, 359
 $(\text{Er-Dy})\text{Ni}_2$, 205, 353, 355
 Er_3Ni , 195, 244, 353–356, 358
 $\text{Er}_3(\text{Ni-Ti})$, 208
 $\text{Er}_6\text{Ni}_2\text{Sn}$, 208, 358
 $\text{Er}_6\text{Ni}_2\text{Pb}$, 208, 358
 Gd_3Al_2 , 191, 192
 $(\text{Gd-Er})\text{Al}_2$, 189, 209, 383
 $(\text{Gd-Er})\text{NiAl}$, 209, 210, 244, 246, 406,
 407, 413
 $(\text{Gd-Dy})\text{Al}_2$, 180
 $(\text{Gd-Dy-Er})\text{CoAl}$, 244
 $(\text{Gd-R})\text{Co}_2$ ($\text{R} = \text{Tb}, \text{Lu}, \text{Y}$), 243
 Gd_2In , 199, 200

- GdNiGa, 209
 GdNiIn, 209, 406
 Gd_3Pd_4 , 193, 194
 GdPd, 194
 Gd_7Pd_3 , 194, 412
 GdRh, 194, 195, 246
 (Gd-Er)Rh, 353
 GdZn, 194, 406
 HoCu₂, 359
 HoNi₂, 189
 $\text{Ho}_{0.5}\text{Dy}_{0.5}\text{Al}_{2.25}$, 187
 LaCo₂, 220
 LaCo₁₃, 220
 LaFe₁₃, 220
 La(Fe-Co)_{11.83}Al_{1.17}, 221
 La(Fe_{0.98}Co_{0.02})_{11.7}Al_{1.3}, 221
 LaFe_{11.44}Si_{1.56}H_{1.0}, 225
 LaFe_{11.57}Si_{1.43}H_{1.3}, 225
 LaFe_{11.2}Co_{0.7}Si_{1.1}, 225
 La(M_{1-x}M'_x)₁₃ (M = Fe, Ni; M' = Si, Al), 220–225, 246, 275, 412, 413, 417, 420
 LuCo₂, 226, 227, 241
 Lu₂Fe₁₇, 214, 217, 218
 Nd₇Co₆Al₇, 244
 Nd₂Fe₁₇, 217
 (Pr-Nd)Ag, 195, 359
 Pr₂Fe₁₇, 214
 PrNi₅, 205, 207, 419
 RAg (R = Pr, Nd, Er), 195
 RAI₂ (R = Y, Ce, Pr, Nd, Sm, Gd, Tb, Ho, Er, Dy, Tm, La, Lu), 179, 180, 184, 185, 187, 188, 190, 246, 406, 407, 413, 419, 420
 RAI_{2.2} (R = Er, Ho, Dy), 187, 393
 RAI_{2.15} (R = Er, Ho, Ho-Dy), 389
 RAI₃, 187
 RCo₂ (R = Gd, Tb, Dy, Ho, Er), 225–232, 242–244, 246, 359, 406, 407, 420
 (R-Y)Co₂ (R = Er, Ho, Dy), 243
 RCoAl (R = Gd, Tb, Dy, Ho), 243, 344
 RGa₂ (R = Pr, Nd, Gd, Tb, Dy, Ho, Er), 196, 197, 198, 246, 359
 RFe₂ (R = Tb, Er, Y), 211, 214
 RFe₃ (R = Ho, Y), 211, 214
 RFe₄Al₈ (R = Y, Er), 225
 (R-Ce)₂Fe₁₇ (R = Y, Pr), 214
 RMn₂ (R = Y, Gd, Tb, Er), 244, 245
 RMn₄Al₈ (R = Y, Nd, Gd, Dy, Er), 245, 246
 RNi (R = Gd, Ho, Er), 200, 201, 205, 210, 211, 244, 246, 353, 354
 RNi₂ (R = Pr, Gd, Tb, Dy, Ho, Er, Lu, La), 189, 201, 204–207, 210, 211, 244, 246, 353, 354, 359, 382, 383, 414, 419
 RNi₅, 200, 205
 R₃Ni (R = Pr, Nd, Er), 200, 207, 208, 210, 211, 246, 361, 362, 414
 RNiGe (R = Gd, Dy, Er), 209, 210, 353
 Tb_{0.8}Er_{0.2}Co₂, 243
 (Tb-Gd)Al₂, 190
 (Tb-Y)Fe₂, 211, 214
 TmAg, 194, 195
 TmCu, 194–196
 YCo₂, 220, 226
 Y₂Fe₁₇, 214–218
 Invar compounds, 220
 ionic radius, 156
 iron, 96–101, 103
 α-Fe, 221, 222
 iron ammonium alum, 66, 340
 irreversible process (in a refrigeration cycle), 370
 irreversibility (in a regenerator), 371
 Ising
 model, 143
 lattice, 57
 isobaric conditions, 7, 8
 isothermal process, 393, 394
 itinerant electrons, 144, 179, 220, 226, 243, 243, 245
 itinerant magnetism, 217
 interstitial impurities, 281
 Jahn-Teller effect, 143, 156, 175–177
 Kramer doublets, 132, 133
 Landau theory of second order phase transitions, 9, 27, 42, 56, 97, 230, 418
 Landau–Ginsburg functional, 298
 Langevin function, 13

- lanthanum cobaltate ($\text{La}_{1-x}\text{Sr}_x\text{CoO}_3$), 164
latent heat, 28
Laves phase, 179, 201, 217, 220, 225, 244
lead (Pd), 65, 201, 208, 246, 352, 353–355, 357, 358, 359, 361, 362–364
localized magnetism, 217, 226
lock-in amplifier, 76–79
longitudinal spin wave (structure), 277
Lorentz number, 105
La, 60
Lu, 284
- magnetic
clusters, 44, 48
commensurate phases, 195
cryocooler, 62
effective field, 64
field strength, 422
critical field, 35, 120, 122
incommensurate phases, 195
induction, 422
moment, 4, 11, 13, 45, 276, 311, 422, 42 phase diagram ($H-T$), 41, 112, 123, 276, 287, 294, 299, 301, 303, 322–324
polarization, 422, 423
refrigerators, 14, 62, 65, 139, 365, 366
spin fluctuations, 184
susceptibility, 422, 423
working body, 65, 365, 389, 390, 391, 405
- magnetic entropy change, 16, 17–20, 49, 81
magnetic moment, 4, 11
atomic, 11
effective, 13, 311, 429
localized, 276
nuclear, 349
saturation magnetic, 45
spontaneous, 13
magnetic phase separation, 126
magnetic working body, 65, 365
hybrid (complex) 389, 390, 391, 405
magnetism
itinerant, 217
localized, 217, 226
- magnetization 9, 422, 423
axis, 139, (176, 348 (easy)), (172, 348 (hard))
mean, 43
remanent, 261
saturation, 9, 222, 429
specific, 112, 261
spontaneous, 10, 12, 49, 56, 101
cycle, 9
magnetization axis, 139
easy, 176, 348
hard, 172, 348
- magnetocaloric effect (MCE), 1
anisotropic (contribution), 49, 50, 172, 279, 320
effective, 413
giant, 273
of paraprocess, 8, 172, 279
specific, 42, 126
- magnetoelastic
coupling, 156
effect, 156
strain, 305
- magneton
Bohr, 67
nuclear, 67
- magnetoresistance effect 155, 254, 256
colossal, 126, 143, 145, 154, 159
magnetostructural transition, 275
magnetostriction, 7, 62, 94, 95, 240
constants, 51, 103
forced volume, 262
giant, 323, 329
spontaneous, 27, 226
spontaneous volume, 238, 301
volume, 301
- magnetovolume effect, 9, 246, 420
nonreversible, 9
- magnons, 55
magnon mechanism of thermal conductivity, 105, 284
- manganese ammonium sulfate
 $(\text{MnSO}_4(\text{NH}_4)_2\text{SO}_4)$, 64, 65
- manganese spinel ferrites chromites
 $(\text{MnFe}_{2-x}\text{Cr}_x\text{O}_4)$, 168, 169
- manganites, 126, 143
 LaMnO_3 , 144, 146, 166

- La_{0.67}A_{0.33}MnO₃** (A = Ca, Ba, Sr), 143, 146
(La-Ag)MnO₃, 161, 162
(La-Ca)Mn₂O₇, 158, 159
(La-Ca)MnO₃, 147, 154–159, 162, 166, 167, 407
La_{0.75}Ca_{0.25}MnO₃, 146
La_{2/3}Ca_{1/3}MnO₃, 146, 156, 159
(La-Ca-Pd)MnO₃, 157
(La-Ca-Ti)MnO₃, 157
La_{2/3}(Ca_{1-x}Sr_x)_{1/3}MnO₃, 146, 156
(La-Er-Ca)MnO₃, 156
(La-Gd-Sr)MnO₃, 159
(La-K)MnO₃, 161
(La-Na)MnO₃, 161, 407
(La-Nd-Ca)MnO₃, 156, 158
(La-Nd-Ca)(Mn-Cr)O₃, 157, 158
(La-Nd-Pb)MnO₃, 167, 168
(La-Pb)MnO₃, 167, 168
(La-Sr)MnO₃, 146, 147, 159, 166
(La-Sr)(Mn-Cr)O₃, 160, 168
(La-Y-Ca)MnO₃, 159
(La-Y-Sr)MnO₃, 159, 160
(La-Yb-Ca)Mn₂O₇, 159
La_{0.875}Sr_{0.125}MnO₃, 143
La_{2/3}Sr_{1/3}MnO₃, 146, 156, 159
La_{0.06}Y_{0.07}Ca_{0.33}MnO₃, 146
Nd_{0.7}Ba_{0.3}MnO₃, 166
Nd_{0.5}Sr_{0.5}MnO₃, 146
(NdSm)_{1/2}Sr_{1/2}MnO₃, 146
Pr_{0.63}Ca_{0.37}MnO₃, 146, 164
Pr_{0.5}Sr_{0.5}MnO₃, 146, 162, 164, 168
(Pr-Nd)_{0.5}Sr_{0.5}MnO₃, 162
(R-Sr)MnO₃ (R = Nd, Pr), 154
(Sm-Sr)MnO₃, 95, 165
Sm_{0.6}Sr_{0.4}MnO₃, 95
martensite phase, 120, 121, 412
martensitic–austenitic transition, 121, 125
Maxwell equations, 5, 17
mean field, 45
mean field approximation (MFA), 10, 12, 25, 33, 44, 48, 49, 56, 57, 79, 85, 97, 98, 105, 125, 133, 134, 139, 159, 185, 186, 205, 214, 221, 246, 252, 280, 281, 287, 289, 297, 309, 313, 328, 331, 336, 401, 404, 418
three-dimensional, 186, 205
- mechanical strain, 103
melt spinning, 334, 336, 338, 361
mesh screen, 357
metals
 3d transition, 14, 96–98, 123, 125
 heavy rare earth, 33, 60, 81, 97, 98
 lanthanide, 60
metamagnetic transition, 114, 117, 118, 163, 175, 179, 192, 200, 219, 220, 222, 223, 226, 252, 254–256, 271, 296, 298, 419
metamagnetism, 242
metastable process, 9
methods (of magnetic susceptibility measurement)
 force-balance, 64
 inductance, 64, 66
methods (of MCE measurement)
 adiabatic magnetization, 85
direct, 69
heat capacity measurements, 86
indirect, 69, 77, 81
magneto-optical, 70
magnetization and thermal expansion measurement, 94
non-contact, 77
pulsed magnetic field, 69, 70–73, 89
ramped magnetic field, 69
switch-on technique, 69, 89
thermoacoustic, 77, 78
mictomagnetic ordering, 220
minimal no-load temperature, 356–358, 362, 363, 382, 383
mixed magnesium-zinc ferrite
 MgOZnO·2Fe₂O₃, 170
modulated spin structure, 256, 304
molar
 mass, 427
 ratio, 389
 volume, 54
mole, 16
molecular field, 12, 34, 56, 226
molecular cluster, 338, 343, 345
 Fe₈, 343, 347–350
 Mn_x (x = 2–8), 344
 Mn₁₀, 344, 347
 Mn₁₂, 343, 347–350
 MnO_x (x ≤ 9), 344

- molecular cluster (*continued*)
 NaMn₆, 344
 system, 350
- Monte-Carlo method, 25, 47, 48, 49, 145
- Mössbauer spectroscopy, 330, 339, 341
- nanocomposite, 44
 compound, 339, 340
 Dy-Zr, 230
 ribbons, 338, 339
 system, 47, 338, 340
- nanocrystallite, 338
- nanograins, 340, 341
- nanopowder ribbon, 339
- nanosize
 crystal structure, 230
 particles, 44
- Neél
 model, 33
 temperature, 41
- neodymium gallate (NdGaO₃), 142
- Neumann and Kopp law, 53
- neutron scattering (diffraction), 33, 145, 185, 197, 207, 217, 251, 256, 273, 277, 322
- nickel-chromite (NiFeCrO₄), 169
- no-load regime (of refrigerator), 382
- no-load temperature, minimal, 356–358
- noncollinear spin structure, 269
- nuclear resonance, 67
- nuclear magnetic moment, 349
- number of heat transfer units, 371–373, 379
- Nd, 277, 308, 309, 361, 362, 364, 414
- Ni, 96–104
- operational frequency (of refrigerator), 353, 359, 367, 389, 396
- orbital ordering, 126, 143
- orthoaluminates (REOA, RAlO₃, R = rare earth), 126, 137, 139, 401, 402
 GdAlO₃, 139, 401
 DyAlO₃, 139, 141, 142, 177, 397, 401
 (Dy-Er)AlO₃, 139, 142, 346, 401
 ErAlO₃, 139, 141, 142, 346, 401
 HoAlO₃, 139, 141, 142
 LaAlO₃, 142
- orthoferrites (RFeO₃, R = Yb, Er, Tm), 142
 ErFeO₃, 142
 TmFeO₃, 142
- oscillating spin structure, 321
- oxide compounds, 126
- packing density (of regenerator), 359
- paramagnet
 nuclear, 67
 electronic, 67
- paramagnetic salt, 62, 64, 65
- paramagnetic state, 12
- paramagnetism, exchange-enhanced Pauli, 226
- paraprocess, 8, 33, 96, 103, 238, 240, 293, 309, 314, 320, 323, 324
- antiferromagnetic-type, 34, 122, 127–130, 169, 195, 200, 214, 231, 252, 253, 258, 287, 296, 301, 323, 418
- ferromagnetic-type, 34, 35, 127–130, 168, 169
- high-field, 314
- partition function, 10, 11, 53, 57
- penetration depth, 353, 359
- permanent magnet, 109
- permeability of free space, 423
- permittivity of free space, 423
- perovskites, 137
- perovskites RMeO₃, 142
 CaRuO₃, 143
 rare earth orthoferrites (RFeO₃, R = Yb, Er, Tm), 142
 neodymium gallate (NdGaO₃), 142
 (Sr-Ca)RuO₃, 143
 SrRuO₃, 143
- phase separation, 143, 145, 154
- phonons, 105, 284
- plasma-rotating electrode process, 386
- Plexiglas, 70, 75
- point charge model, 201, 244
- porosity, 362, 380
 internal, 359
 overall, 373
- potassium chrome alum, 66
- pressure drop (in a regenerator), 370, 372

- Pb (lead), 65, 201, 208, 246, 352, 353–355, 357, 358, 359, 361, 362–364
- quantum tunnelling (of magnetization), 344, 349, 315
- quasi-adiabatic, 41
- refrigerator
- AMR, 374, 375, 377, 379–384, 390, 391, 416
 - efficiency, 352, 367, 370–374, 384, 386, 396, 397
 - magnetic, 14, 62, 65, 139, 365, 366
 - no-load regime, 382
 - operation frequency, 353
 - reciprocating AMR, 380, 381, 383–385
 - rotary (wheel) AMR, 383, 384, 421
 - rotary Carnot, 396, 399
- refrigerant capacity, 14, 357, 367, 406
- maximum, 402, 404
 - specific, 412
 - specific maximum, 402–404
- refrigeration:
- capacity, 355–357, 363
 - power, 356
- regenerator, 208, 351, 352
- dead volume, 384
 - double-layer, 356
 - efficiency, 356
 - four-layer, 358
 - Gifford–McMahon (G-M), 362, 363
 - irreversibility, 371
 - Laybold, 362
 - layered (hybrid), 356, 357, 414
 - magnetically augmented, 351, 387, 388
 - material $\text{Er}_{0.968}\text{O}_{0.027}\text{N}_{0.003}\text{C}_{0.002}$, 364
 - monolithic, 361
 - multi-layer, 358
 - packing density, 359
 - passive magnetic, 309, 351
 - pressure drop, 370, 372
 - second-stage, 355, 356
 - temperature span, 351, 352, 366, 382, 386, 388, 392
 - thermal mass, 376, 377
 - triple-layer hybrid, 357, 358
- refrigeration thermodynamical cycle
- active magnetic regenerator (AMR), 365, 370, 376, 377, 391, 415
 - gas, 372
 - irreversible, 370, 371
 - magnetic-type regenerative Brayton, 365, 366, 369, 370, 377, 379, 389, 402, 415
 - magnetic-type regenerative Ericsson, 365–370, 377, 379, 389–392, 415
 - nonregenerative Carnot, 365, 377, 393, 397, 400, 401, 415, 421
 - regenerative, 351
- rotational speed, 356
- scanning electron microscopy, 156, 361
- Schottky
- anomaly, 58, 132, 166, 188, 193, 195, 205, 208, 210, 244, 245, 355, 413
 - effect, 57, 58
 - heat capacity contribution, 198
- s-d model, 226, 243
- second law of thermodynamics, 6
- semiadiabatic conditions, 91, 92
- short-range order, 31
- siderite (FeCO_3), 70, 174
- silicides, 247, 250
- Dy_5Si_4 , 268
 - $\text{Dy}_5\text{Si}_3\text{Ge}_1$, 269
 - GdFeSi , 254, 259, 275
 - Gd_2PdSi_3 , 258
 - GdPd , 255
 - $\text{Gd}_2\text{Pd}_2\text{Si}_3$, 275
 - $\text{Gd}_5\text{Si}_{0.33}\text{Ge}_{3.67}$, 269
 - $\text{Gd}_5\text{Si}_1\text{Ge}_3$, 261, 275
 - $\text{Gd}_5\text{Si}_{1.8}\text{Ge}_{2.2}$, 222, 266
 - $\text{Gd}_5\text{Si}_{1.72}\text{Ge}_{2.28}$, 275
 - $\text{Gd}_5\text{Si}_2\text{Ge}_2$, 238, 240, 261, 266, 271, 274, 275, 407
 - $\text{Gd}_5\text{Si}_{1.985}\text{Ge}_{1.985}\text{Ni}_{0.03}$, 274
 - $\text{Gd}_5\text{Si}_{1.985}\text{Ge}_{1.985}\text{Ga}_{0.03}$, 274
 - Gd_5Si_4 , 258, 407
 - $(\text{Gd-Pr})_5\text{Si}_4$, 273
 - $(\text{Gd-Tb})_5\text{Si}_4$, 270
 - NdMn_2Si_2 , 256, 257, 275
 - PrCo_2Si_2 , 255, 256
 - $\text{Pr}_{0.8}\text{La}_{0.2}\text{Co}_2\text{Si}_2$, 255, 256
 - $(\text{RR}')_5(\text{Si-Ge})_4$, 247, 275

- silicides (*continued*)
R₅(Si-Ge)₄ (R = Nd, Pr, Gd, Tb, Dy), 110, 114, 119, 121, 135, 231, 247, 258–261, 268, 269, 271, 273–275, 329, 407, 412, 413, 417, 420
Tb₂PdSi₃, 257
Tb₅Si₄, 270, 271
Tb₅(Si-Ge)₄, 270–272
(b Tb-Gd)₅(Si-Ge)₄, 269, 270
skyscraper shape of $\Delta S_M(T)$, $\Delta T(T)$
 curves, 231
sol-gel method, 156
solid state reaction, 156
specific MCE, 42, 126
spinel Li₂Fe₅Cr₅O₁₆, 169, 170, 214
spin angular momentum, 25
spin fluctuations, 184
spin glass, 154, 164, 193, 331, 334, 336, 337, 342
spin-lattice relaxation time, 18, 372
spin reorientation transition, 142,
 170–172, 188, 194, 200, 226, 231,
 243, 269, 277, 278, 316, 320, 321
spin-slip transition, 304, 305
spin structure
 amplitude modulated, 255
 antiferromagnetic helicoidal (HAFM),
 35, 39, 61, 217, 276, 284, 287, 293,
 294, 296–299, 302, 313, 321, 323,
 324, 326–329
 antiferromagnetic layered, 256
 canting, 164
 commensurate, 195, 304, 305, 326
 conical, 277, 304, 305, 60
 cycloid, 277, 304
 fan, 35, 217, 276, 284, 287, 293, 297,
 299, 326, 327
 ferromagnetic spiral-type, 321, 322,
 324
 incommensurate, 195
 longitudinal spin wave, 277
 modulated, 256, 304
 noncollinear, 269
 oscillating, 321
 spiral, 200
 vortex, 299
spin waves, 55, 166, 198
- staircase-like MCE and ΔS_M
 temperature dependences, 310
statistical sum, 10
stoichiometry violation, 217
structural
 disorder, 330
 heterogeneities, 337
 transition, 31, 60–62, 146, 222, 247,
 261, 266, 275, 301, 328, 329
sum rule, 45, 46, 48
supercooling, 304, 305
superexchange (interactions), 144, 145,
 158, 339, 343
superferromagnet, 48, 154
superheating, 301, 304, 305
superparamagnetic
 behaviour, 339
 Langevin model, 341
 particle, 338, 348
 state, 336, 348
 system, 44, 338, 340, 345, 346, 350
superparamagnet, 45, 339, 341–345
Si, 104
Sm, 60
SmCo₅, 75, 76
- table-like $\Delta S_M(T)$ dependence
 behaviour, 209, 221, 244, 246
- Teflon, 74, 75, 78
- thermal conductivity, 104, 105, 136, 139,
 143, 167, 177, 190, 195, 210, 244,
 281, 284, 287, 293, 294, 301–303,
 306, 307, 309, 353, 359, 364, 370, 429
- thermal expansion, 146, 156, 220, 245
- thermal mass, 371, 379
- thermal mass flow rate, 371, 376
- thermal (heat) switch
 gas, 65, 90, 91
 superconducting, 65, 66, 398
 thermal siphon-type, 398
- thermal shield, 68
- thermocouple 69–72
 differential, 70, 71, 72
- thermodynamic potential, 28
- total angular momentum operator, 12
- total surface area, 362
- transitions
 charge-ordering, 162–164, 167

- crystal structure 9, 115, 116, 118, 175, 226, 294
- magnetic first order, 9, 28, 81, 109, 111–113, 115–122, 125, 126, 146, 155, 156, 165, 179, 187, 195, 198, 219–223, 225–228, 231, 232, 238, 241–243, 245–247, 251, 252, 256, 261, 266, 269, 271, 274–276, 284, 294, 298, 304, 323, 325, 326, 328, 406, 407, 412, 414, 418, 420
- magnetic order–order, 31, 56
- magnetic second order, 9, 81, 117, 146, 155, 159, 166, 195, 200, 221, 226, 231, 238, 241–243, 246, 261, 266, 269, 271, 273, 276, 277, 294, 296, 298, 326, 418
- magnetostructural, 275
- martensitic–austenitic, 121, 125
- metamagnetic field-induced, 114, 117, 118, 163, 175, 179, 192, 200, 219, 220, 222, 223, 226, 252, 254–256, 271, 296, 298, 419
- orthorhombic–rhombohedral crystal phase, 159
- reversible structure, 120
- spin reorientation, 142, 170–172, 188, 194, 200, 226, 231, 243, 269, 277, 278, 316, 320, 321
- spin–slip, 304, 305
- structural, 31, 60–62, 146, 222, 247, 261, 266, 275, 301, 328, 329
- tricritical point, 294, 296, 303, 322, 323, 326, 327, 419
- Tb, 97, 252, 269, 284, 287–294, 310–313, 328, 403, 404, 406, 419
- Tm, 277, 284, 306–308, 310–316
- units, 422
- unit system
- CGS, 422
 - e.m.u. (subsystem), 422
 - e.s.u. (subsystem), 422
 - Gaussian, 422, 423
 - SI, 422, 413
- vanadites (RVO_4), 126, 177
- DyVO_4 , 175–177, 402
 - (Dy-Gd) VO_4 , 175, 177
 - GdVO_4 , 177
 - PrVO_4 , 177, 178
- vortex (spin structure), 299
- wire
- Gd, 365
 - $\text{Gd}_{0.6}\text{Dy}_{0.4}$, 365
 - Dy, 365
- x-ray, 176, 187, 193, 208, 220, 222, 229, 268, 269, 270, 271, 273, 330, 335, 341
- yttrium (Y), 226
- yttrium iron garnet, 69
- $\text{Y}_2\text{Fe}_5\text{O}_{12}$, 32
 - Yb, 60, 159, 276
 - YbPO_4 , 177
- Zeeman effect, 177
- ZFC (zero field cooled) magnetization measurement, 147, 204, 348

